Laboratory and Field Asphalt Fatigue Performance

Matching Theory with Practice

F. P. Pramesti

Laboratory and Field
Asphalt Fatigue Performance
Matching Theory with Practice

Laboratory and Field
Asphalt Fatigue Performance
Matching Theory with Practice

Proefschrift

ter verkrijging van de graad van doctor
aan de Technische Universiteit Delft,
op gezag van de Rector Magnificus prof. ir. K.C.A.M. Luyben,
voorzitter van het College voor Promoties,
in het openbaar te verdedigen op
woensdag 17 juni 2015 om 10:00 uur

door

Florentina Pungky Pramesti

Magister Teknik in Civil Engineering,
Institut Teknologi Bandung, Indonesië
geboren te Madiun, Indonesië

Dit proefschrift is goedgekeurd door de promotor:
Prof. dr. ir. A. A. A. Molenaar

Toegevoegd promotor
ir. M. F. C. van de Ven

Samenstelling promotiecommissie:

Rector Magnificus,	Technische Universiteit Delft, voorzitter
Prof. dr. ir. A. A. A. Molenaar,	Technische Universiteit Delft, promotor
ir. M. F. C. van de Ven,	Technische Universiteit Delft, copromotor

Onafhankelijke leden:

Prof. dr. ir. S. M. J. G. Erkens,	Technische Universiteit Delft
Prof. K. van Breugel,	Technische Universiteit Delft
Dr. ir. J. Groenendijk,	KOAC-NPC, the Netherlands
Dr. Ing. S. Portas,	Università degli Studi di Cagliari, Italy
Prof. Dr. M. O. Hamzah,	University Sains Malaysia, Malaysia

I dedicate this dissertation to my beloved mother, TH. Sri Soemarmi,
my husband, Senot Sangadji
and my son, Quanta A. Sangadji.

Acknowledgements

The only name that appears on the cover of this thesis is my name. However in producing this book, many great people have generously contributed their ideas, thoughts, energy, and talents. I owe my gratitude to them without whom this thesis would never be possible. They also made my doctoral study an unforgettable experience.

> *Teachers, colleagues and friends, from whom I have learnt essential skills of critical thinking.....*

My deepest gratitude is to my Promotor, Professor Molenaar. He is the one who introduced me to the field of pavement fatigue, a highly complex phenomenon but at the same time very attractive to study. He shared with me his knowledge. I am deeply grateful to him for the long discussions that helped me to sort out the technical details of my work. His patience and support has helped me overcome many crises. I am also thankful to him for encouraging the use of correct grammar in my writings and for carefully reading and commenting on countless revisions of this manuscript.

My co-promotor, Associate Professor Martin van de Ven, has always been there to give advice and, for sure, to listen. His insightful comments and constructive criticisms at different stages of my research have helped me sharpening my ideas.

I would like to acknowledge the Directorate General of Higher Education, Ministry of National Education, the Government of Republic of Indonesia for providing the doctoral scholarship which make this PhD research possible. I thank also my colleagues at the Jurusan Teknik Sipil, Universitas Sebelas Maret, Solo, Indonesia for their supports. I acknowledge PT Olah Bumi Mandiri for providing the Retona, a natural bitumen discussed in part of this research.

I am also indebted to the technicians who helped and supported me in all different stages of the experiments. Marco Poot has been very instrumental in performing many tests and realizing the BOEF test setup design as well as in acquiring many good quality data. Jan Willem has helped me preparing the specimens with his skilful hands. Dirk helped in solving many problems. Jacqueline made the complicated administration easy. I thank them as well as Jan Moraal and Michele for many good coffee times together.

Truly, the members of the Road and Railway Engineering group have contributed in so many ways, either in some of works carried out in this thesis or making my experience in the lab one of the most exciting moments in my life. Finite element modelling would be confusing without Milliyon. Jian has helped to understand self-healing asphalt. Staring at the PC monitor would be boring without Maider and Sadegh also Mingliang, Guillermo and Chen, my officemates. Making Asphalt Concrete slabs would not be so enjoyable without Ning and Jingang, also Ruben, Mandela, Salil and Ilnaz. Dr. Lambert Houben, thank you for supporting me with all the books, papers and reports. Dr. Virginie Wiktor and Frits Stas, thank you for the discussions. Also I thank the support of Alem, Oscar, Mo, Gang, Dongxing, Yue,

Diederik, Mohamad, Yuan, Pengpeng, Mauricio, Dongya, Chang, Maria, Nico. If your name is not mentioned, it is only because of the limitation of my memory but not your existence. Thank you very much.

> *Friends, from whom I have learnt not to forget that*
> *life is always beautiful.....*

Many friends have helped, influenced and shaped me to be a better person. To my close friends Niken, Dewi, Ida, I am glad that we share the wondrous zest of life, the bad and the good. Yuli, Julian, Andre, Thomas, Caesar, Awi, Sayuta, Sisca, Stevie, Tya, Sandra, Julius, Alma, Dwi, Xander, Piet, Enny, Juanfran, Karina, Ronald, you have made my days in Delft hard to forget. My friends; bang Junaedi, Fossy, Erizaldy, Dieky, Yazdi, Budi, Adhi, Isnaeni, Ajeng, Lasmini, Orchidea, Agung, Meinar and their family, Fiona, Yudha, Nugroho, Mutia, July, Sandy and many of the PPI-Delft members; thank you for sharing your great friendship.

To ISC choir members, thanks for the great times we sing together and for letting me raise my hand and 'stop' the song, otherwise you'll sing 'forever'. Fr. Avin and Rev. Waltraut thank you for believing me and giving me the chance to lead the flock. To Ruben and Oom Henk, thanks for showing the meaning of loyalty. The ISC community, you are all awesome!

> *...My parents and family for everything. You made me*
> *into who I am.*

Theresia Sri Sumarmi, my mom, often impressed her students, including me, with her stories about many great places in the world when she taught in junior high school back then in my hometown, Caruban. I regret that I could not bring her to visit these places due to her frail condition. Mom, throughout my life, you have showed me that your selfless act of nurturing and giving are a completed circle when goodness is returned. During the writing of this dissertation, however, you are gradually losing your memory. I do hope only beautiful memories linger in your mind and you always know that I love you to the fullest. I dedicate this dissertation to you.

Raised by a single mom have strengthen the relationship between me and my siblings. Mas Pram, mbak Yanti, mas Lupi, mbak Thithing, Puguh and Dian, have shared many good times and lessons with me. Their prayers and supports are always my strength. My in-laws, both from the Prayogo's and the Pierngadi's, my nieces and nephews, always cheer up my life. For this I thank them.

> *...and for my precious; Senot and Quanta Sangadji,*

Senot Sangadji, your patience, endless support and love, always encourage and strengthen me throughout difficult times. Quanta, each time you moved to new places, courageously you said: 'that's fine, Mom. I can handle it'. To me that is inspiring. And often you pose many tough questions and critics which push me to think harder and do better. Thanks, dear! Both of you make this challenging journey of being a wife, a mother and a PhD student colourful and fun.

Summary

This thesis investigates the relationship between predicted and observed fatigue life of asphalt. This study also investigates the positive effects of modifying bitumen with Retona, a bitumen modifier produced in Indonesia from natural asphalt rock sources, on pavement performance in terms of increased resistance to fatigue and permanent deformation.

Classical pavement fatigue analysis assumes cracking to initiate from the bottom of the pavement and propagates to the top. However, when relating 'predicted' pavement fatigue life to 'observed' fatigue life, one immediately encounters a 'conflict' with theory because in practice cracks are also initiated at the pavement surface. This thesis also attempts to explain the phenomenon of surface or top-down cracking.

In the past, many studies were made to validate design procedures by matching predicted performance with field performance. However, this project, only takes into account the studies that were carried out in the Netherlands and by Dutch researchers elsewhere. Test results performed in the 1990's on three pavement sections on the accelerated pavement testing facility Lintrack, then owned by the Section of Road and Railway Engineering, Department of Civil Engineering Delft University of Technology, have therefore been used in this study. The Lintrack research provided a large amount of valuable data with respect to pavement performance and was therefore perfectly suited for a study to match theory with practice.

To achieve these goals, several steps were taken. Firstly, the data obtained from observations made on the Lintrack accelerated pavement test sections (built in 1990) were studied. The sections were simple two-layered pavement systems consisting of a gravel asphalt concrete (GAC) layer overlying a sand subgrade. The data consisted of information on the geometry and material characteristics of the test pavements, loading and environmental conditions, deflection test results and visual condition data in terms of cracking and permanent deformation.

Secondly, a fatigue cracking prediction model was developed based on laboratory data obtained from four point bending (4PB) tests on the same material type. To more accurately simulate the fatigue behaviour of a real pavement in the laboratory, a new test setup termed as the "beam on elastic foundation" (BOEF) test was developed. Since the GAC pavement sections built in 1990 had been removed, the GAC (GAC 1990) material was not available anymore. Therefore, a new GAC (GAC 2010) mixture needed to be produced and considerable efforts were made to produce the GAC 2010 mixture such that it truly replicated the GAC 1990 mixture. Material characterization tests performed to understand better the GAC 2010 mixture included, in addition to the two mentioned fatigue tests; monotonic uniaxial

tension and compression tests, indirect tension tests, mastic healing tests and tests on the recovered bitumen such as penetration and Dynamic Shear Rheometer tests.

The analysis of the Lintrack APT sections was carried out by determining; (1) the pavement life based on the back calculated modulus of the asphalt layer for different probability of survival levels, and (2) the magnitude of damage that was initiated at the bottom of the asphalt layer expressed by means of Miner's damage ratio.

The cumulative damage ratio, $\Sigma ni/Nfi$ (Miner's ratio), was calculated based on the tensile strain at the bottom of the asphalt layer at different temperatures that occurred during the Lintrack tests and the fatigue relationships that were obtained from 4PB and BOEF fatigue laboratory tests.

It is shown that the observed pavement life based on the back-calculated asphalt modulus from deflection measurements is longer than the pavement life calculated on the basis of damage initiation at the bottom of the asphalt layer. The results showed that for all three Lintrack sections, the BOEF based predictions exhibited a better agreement as evidenced from the smaller shift factor between "field stiffness reduction" lifetime and the lifetime based on "fatigue" predictions. Therefore, BOEF test based fatigue models are highly recommended to be used for predicting pavement life in practice.

This study has shown that it is very difficult to relate cracking visible at the surface of the pavement to the initiation of fatigue damage at the bottom of the asphalt layer.

Finite element simulations using detailed tyre–pavement contact pressure modelling have been carried out. The results showed that significant tensile strains had developed at the pavement surface. The magnitude of these tensile strains was such that they can be held responsible for the development of surface cracking. It should be noted however that surface cracking cannot be explained using a stress based analysis.

This study clearly showed that permanent deformation (in this study this was permanent deformation of the subgrade) exhibits significant effects on the formation of longitudinal cracks at the edges of the wheel paths.

The study on modifying GAC with Retona showed that the GAC+Retona mixture exhibits better mechanical properties compared to the reference GAC mixture. The Retona modified mixture showed a higher fatigue life and higher resistance to permanent deformation compared to the reference GAC mixture.

Samenvatting

Dit proefschrift onderzoekt het verband tussen de vermoeiingslevensduur van asfalt zoals die voorspeld wordt en zoals die waargenomen wordt. Daarnaast wordt onderzocht wat de positieve effecten zijn van modificatie van bitumen met Retona - een product dat in Indonesië geproduceerd wordt uit bitumen houdende rots - op het gedrag van wegverhardingen met betrekking tot verbeterde vermoeiingsweerstand en verbeterde weerstand tegen blijvende vervorming.

Als men de voorspelde vermoeiingslevensduur wil relateren aan de waargenomen vermoeiingslevensduur loopt men direct tegen het probleem aan dat de theorie in veel gevallen niet voorspelt wat er in werkelijkheid gebeurt. In de klassieke vermoeiingstheorie wordt er vanuit gegaan dat scheurvorming onderin de asfaltlaag geïnitieerd wordt, terwijl in werkelijkheid veel scheurvorming aan het wegoppervlak ontstaat. Dit proefschrift probeert ook dit fenomeen te verklaren.

In het verleden zijn wereldwijd veel studies verricht om ontwerpmethoden te valideren door voorspeld gedrag te relateren aan het in werkelijkheid waargenomen gedrag. Voor deze studie is echter alleen gebruik gemaakt van resultaten van onderzoek zoals die in Nederland aan dit onderwerp zijn verkregen en van onderzoeksresultaten die door Nederlandse onderzoekers elders zijn verkregen. Het onderzoek dat in de negentiger jaren op drie wegsecties is uitgevoerd met de Lintrack, een apparaat waarmee verhardingen versneld op ware grootte kunnen worden beproefd en dat in die tijd eigendom was van de Weg- en Spoorwegbouwkunde sectie van de afdeling Civiele Techniek der TU Delft, vormt het hart van het onderzoek. Het Lintrack onderzoek heeft namelijk een schat aan informatie opgeleverd over het gedrag van wegverhardingen en was daarom bij uitstek geschikt om voor dit onderzoek te worden gebruikt.

Verschillende stappen moesten worden gezet om de gestelde doelen van dit onderzoek te kunnen bereiken. Allereerst was het nodig om de gegevens verkregen op de Lintracksecties (die gebouwd zijn in 1990) te bestuderen. Deze secties waren eenvoudige tweelagensystemen bestaande uit een laag grindasfaltbeton op een ondergrond van zand. De beschikbare data betroffen geometrie en materiaalkarakteristieken, belasting- en klimaatgegevens, resultaten van deflectiemetingen en visuele inspectiegegevens van de secties met betrekking tot scheurvorming en blijvende vervorming.

Daarnaast is een model ontwikkeld om de vermoeiingsscheurvorming te kunnen voorspellen. Dit model is gebaseerd op vierpuntsbuig vermoeiingsproeven uitgevoerd op hetzelfde materiaal. Daarnaast is een nieuwe proef ontwikkeld waarbij een balk rustend op een elastische fundering wordt beproefd. Dit is de zogenaamde BOEF-test. Deze proef is ontwikkeld

omdat het een betere simulatie van de werkelijkheid is dan de vierpuntsbuigproef.

Omdat de Lintracksecties uit 1990 waren gesloopt was het grindasfaltbeton mengsel uit 1990 (GAC 1990) niet meer beschikbaar en daarom is een zo goed mogelijke kopie van dat mengsel gemaakt (GAC 2010). Ter karakterisering van dit mengsel zijn, naast de hierboven genoemde vermoeiingsproeven, monotone uniaxiale druk- en trekproeven uitgevoerd alsmede indirecte trekproeven en proeven ter bepaling van het zelfherstellend vermogen van de mastiek. Op het teruggewonnen bitumen zijn penetratieproeven en proeven met de "dynamic shear rheometer" uitgevoerd.

De analyse van de Lintracksecties is op twee manieren uitgevoerd. (1) Allereerst is de levensduur voor verschillende overlevingskansen berekend op basis van de teruggerekende modulus van de asfaltlaag. (2) Daarnaast is de levensduur voor verschillende overlevingskansen berekend op basis van de hoeveelheid schade, uitgedrukt in Miner's schadegetal, die onderin de asfaltlaag initieerde.

Miner's cumulatieve schadegetal, $\Sigma n_i/N_{fi}$ (Miner's ratio), is berekend uitgaande van de rek die onderin de asfaltlaag van de Lintracksecties bij verschillende temperatuurniveau's was gemeten en de vermoeiingsrelaties zoals die met de vierpuntsbuigproef en de BOEF-test waren bepaald.

Aangetoond is dat de levensduur berekend op basis van de afname van de asfaltstijfheid, berekend uit deflectiemetingen, langer is dan de levensduur die berekend werd op basis van Miner's cumulatieve schadegetal. Voor alle drie secties bleek dat het verschil tussen beide levensduren het kleinste was indien Miner's schadegetal werd berekend op basis van de BOEF vermoeiingsresultaten. Daarom wordt het gebruik van vermoeiingsresultaten, bepaald met de BOEF-test, sterk aanbevolen voor het dikteontwerp.

Deze studie heeft aangetoond dat het heel lastig is om aan het wegoppervlak zichtbare scheurvorming te relateren aan vermoeiingsschade die initieert aan de onderkant van de asfaltlaag.

Eindige elementenanalyses die uitgevoerd zijn met een nauwkeurige modellering van de contactspanningen in het band-wegdek-contactvlak hebben aangetoond dat aan het wegoppervlak grote rekken optreden die aanleiding kunnen geven tot vermoeiingsscheurvorming aan het wegoppervlak. Opgemerkt dient te worden dat een analyse op basis van de optredende spanningen niet tot zo'n conclusie leidt.

De studie heeft verder duidelijk aangetoond dat de, aan de randen van het wielspoor in de Lintrackvakken, opgetreden scheurvorming sterk gerelateerd

is aan de opgetreden spoorvorming. In de Lintrackvakken was deze spoorvorming het gevolg van blijvende vervorming van de ondergrond.

De studie naar het effect van het modificeren van grindasfaltbeton met Retona heeft aangetoond dat het gemodificeerde mengsel in vergelijking met het niet gemodificeerde referentiemengsel betere mechanische eigenschappen heeft, zoals een langere vermoeiingslevensduur en een betere weerstand tegen permanente deformatie.

Table of contents

This page is intentionally left blank

Chapter 1
Introduction and scope of the study

1.1.   Introduction

As a consequence of dynamic repeated loading during its service life, an asphalt pavement fails due to material fatigue marked by cracking or other damage. This indicates that the pavement needs to be maintained to provide a constant level of service as required by the user. To bridge these two sides of 'demand versus supply', good planning of maintenance, repair, and rehabilitation must be applied. The ability to predict when maintenance has to be executed is the prerequisite to extent the service life of asphalt pavements and to save money as well as resources. Therefore, an accurate prediction of the pavement life is needed.

In order to be able to make accurate performance predictions, the fatigue behaviour and characteristic of the applied asphalt mixtures should be known but Edwards [1] already ascertained that it is also necessary to employ a cumulative damage rule in cases when the loadings are variable in nature and time.

Accumulated fatigue damage is commonly calculated using Miner's law and the damage calculated by means of that law is usually defined as the ratio of applied number of load repetitions, n, over the allowable number of load repetitions, N.

Fatigue characteristics of asphalt mixtures are usually determined in the laboratory using specific tests; the European Standard specifies several methods. One of them is the bending beam test where a constant sinusoidal loading is applied on an asphalt concrete beam until the number of load repetitions to failure is obtained [2]. In the Netherlands the Four Point Bending Test (4PB test) has been selected for this purpose. In this case, fatigue life is defined as the number of constant strain applications until the specimen stiffness reaches half of its initial value.

It is a well-known fact, however, that the results of this test cannot be used directly for pavement life predictions. The reason is that the stress and strain conditions which are imposed to the beam specimen in either a load or displacement controlled 4PB test are quite different from those occurring in practice. Because of this, calibration of the laboratory determined fatigue relations to match the fatigue behaviour observed in the field is required.

Pavement fatigue failure is observed visually the field in the form of surface cracking. It is hard, however, to determine where these cracks initiated; is one dealing with a top-down or bottom-up process? Traffic induced fatigue cracking is assumed to be bottom up cracking, as in theory the largest tensile stress and strain occur at the bottom of the pavement layer.

As Sun et al [3] described, one of the meaningful interpretations of fatigue damage in practice is by relating damage in terms of the number of load repetitions obtained from the predictive models to the percentage fatigue cracking visible at the pavement surface. There is, however, enough information provided by others (e.g. Groenendijk [4]) that such an approach, relating the calculated cumulative damage ratio n/N to the visible amount of cracking, is not as straightforward as it may seem.

In 1990 the Road and Railroad Research Laboratory (RRRL) of the Delft University of Technology (DUT) built an accelerated pavement testing system (APT) called Lintrack which allows large number of realistic wheel loads to be applied in a limited period of time. Four pavement sections consisting of a gravel asphalt concrete (GAC) top layer on a sand subgrade were tested by means of the Lintrack. During these tests, several parameters were measured such as strain at the bottom of the asphalt layer, temperature, and surface cracking. This information provides a great opportunity to relate the n/N ratio to the cracking visible at the pavement surface or, in other words, to calibrate the fatigue life which is determined in the laboratory to real life fatigue performance.

Bridging this gap between theoretical predictions and practical observations was defined as the main objective of the research described in this thesis. A second objective was inspired by the fact that pavements in Indonesia are prone to permanent deformation due to high temperatures and fatigue damage caused by repetitive heavy traffic loads. It is obvious that modification of asphalt mixtures could be an option to cope with these harsh conditions. Modifying the asphalt mixtures by means of polymers is an effective but costly option. Another possibility is to use RETONA which is a material produced from abundantly available natural asphalt rock resources on Buton island (Indonesia). The second objective of this research was, therefore, to investigate the potential benefits of modifying bitumen by means of RETONA in increasing the resistance to fatigue and permanent deformation.

1.2. Thesis goals

The disparity between fatigue life predictions and observations is large. Therefore, fatigue life predictions based on a models obtained from laboratory tests need to be in better agreement with the results from observations.

As can be seen in Figure 1.1., the goal of this thesis is to investigate the relationship between fatigue life predictions and observations. To achieve this goal, several steps must be attained. Firstly the data obtained from observations made on the Lintrack accelerated pavement test sections need to be studied. These data consist of information on the geometry and material characteristics of the test pavements, loading and environment conditions, deflection test results and data on the visual condition of the test sections in terms of cracking and permanent deformation. It is recalled that these sections were simple two layer pavement systems consisting of a gravel asphalt concrete layer on top of a sand subgrade. These sections were constructed in 1990.

Secondly, a predictive model is built on laboratory data obtained on the same type of material (called GAC 2010), collected by means of four point bending tests. In order to simulate more accurately the fatigue behaviour of a real pavement in the laboratory, a new test setup was designed. In this new test the same beam as used in the four points bending test is placed on top of an elastic support. This new test is called the "beam on elastic foundation" (BOEF) test.
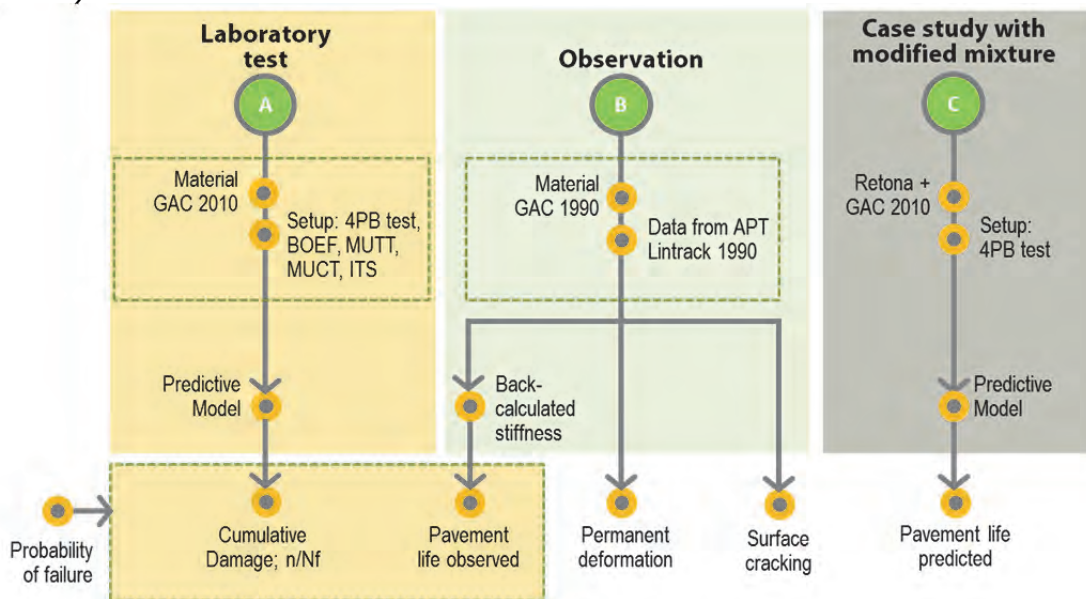
Figure 1.1. Approach to relate fatigue life predictions based on laboratory tests to field observations

In summary, this work aims to compare fatigue life predicted using GAC 2010 fatigue data with the fatigue life that was observed on accelerated pavement test sections (GAC 1990).

When relating 'predicted' pavement fatigue life with 'observed' fatigue life, one will immediately encounter a 'conflict' with theory because in practice cracks are also initiated at the pavement surface and not only at the bottom of the pavement where "classic" pavement fatigue analyses assume cracking

to start. This thesis is, therefore, also an attempt to explain the surface – top down – cracking process.

Retona is a bitumen modifier which is produced in Indonesia from natural asphalt rock sources. As the author is coming from Indonesia it was also decided to investigate in this research the benefits that could be obtained in terms of increased fatigue and permanent deformation resistance by modifying bitumen with Retona.

1.3. Scope of the Study

In the past, a large number of studies have tried to match predicted performance with field performance to validate design procedures. The amount of work done in this specific field is so extensive that it is simply impossible to cover it all. For this particular project it has been, therefore, decided to only take into account the studies that were done in the Netherlands or by Dutch researchers.

In achieving the purpose of the study of matching predictions with observations, pavement fatigue behavior as observed on the pavement sections tested by means of the Lintrack accelerated pavement testing machine were taken as the reference. Since the Lintrack 1990 sections are removed, the GAC 1990 material was not available anymore. Therefore, a new mixture called GAC 2010 which was similar to GAC 1990 needed to be produced. Major efforts needed to be made to produce the GAC 2010 mixture such that it was an as good as possible copy of the GAC 1990 mixture.

1.4. Outline of the Dissertation

This thesis is divided into 8 chapters. Introduction into the problem and goal and scope of the thesis are elaborated in Chapter 1. Chapter 2 provides the results of a literature survey on the fatigue behavior and performance of asphalt pavements. Laboratory fatigue tests and field fatigue performance of pavement are discussed. The role of accelerated pavement testing in predicting the fatigue performance of asphalt pavements is also elaborated. The study regarding the relationship between laboratory fatigue testing and field performance is carried out in order to describe the main issues and missing links in matching the theory of pavement fatigue behavior with practice. This will lead into Chapter 3 in which a detailed research plan is discussed.

Chapter 4 focuses specifically on the characterization of the gravel asphalt concrete base course mixture as used in this research. Characterization of the mixture components as well as mechanical properties of Gravel Asphalt concrete are highlighted. The chapter also describes the two fatigue test used

in this research namely the four point bending (4PB) test and the beam on elastic foundation (BOEF) test. The chapter concludes with a comparison between the two test main features, the results and the limitations.

Chapter 5 describes the characterization of a gravel asphalt concrete base course mixture in which Retona is used as a modifier. The Retona material properties and its function in the mixture are elaborated. The same test procedures used for the GAC in chapter 4 were used for this type of mixture. The potentials benefits as well as the limitations of the Retona modification are highlighted.

A detailed discussion of the comparison of the lifetime predictions based on 4PB & BOEF tests with the cracking performance observed in Lintrack test sections is then presented in Chapter 6.

Attempts to elucidate the surface cracking phenomena in relation with permanent deformation have been done by performing finite element simulations which are discussed in chapter 7.

Finally, some general conclusions and an outlook towards future research in this area are presented in chapter 8.

1.5.   References

[1]   P. R. Edwards, *Cumulative Damage in Fatigue with Particular Reference to the Effects of Residual Stresses*. London, UK: Her Majesty's Stationery Office, 1971.
[2]   NEN-EN-12697, "Bituminous Mixtures-Test methods for hot mix asphalt," in *Part 24; Resistance to fatigue*, ed: Comite Europeen de Normalisation, 2007.
[3]   L. Sun, R. P. E. Hudson, and Z. Zhang, "Empirical-Mechanistic Method Based Stochastic Modeling of Fatigue Damage to Predict Flexible Pavement Cracking for Transportation Infrastructure Management," *Journal Of Transportation Engineering © ASCE,* pp. 109-117, March/April 2003.
[4]   J. Groenendijk, "Accelerated Testing and surface cracking of asphaltic concrete pavements," PhD, Delft University of Technology, Delft The Netherlands, 1998.

This page is intentionally left blank

Chapter 2
Literature review on fatigue of asphalt pavements observed in the field and predicted by means of design tools

2.1. Introduction; overview of matching theory and practice

Although advanced modelling is available nowadays, many countries still use so called empirical methods such as the AASHTO design method [1]. Many other countries are using catalogue based methods which are developed by combining performance observations with, to a more or lesser extent, calculations on stresses and strains as well as results of material tests. Other countries use so called mechanistic-empirical design procedures which are based on the application of multi-layer linear elastic models, or simple finite element methods, characterization of the stiffness as well as the fatigue resistance and resistance to permanent deformation of the pavement materials by means of testing or by estimating these material characteristics by means of charts, nomographs *et cetera*. The lifetime predictions made by means of these methods are then multiplied with "calibration factors", which in fact take into account all the "unknown" factors, to match theory with practice. Such calibration factors are determined by comparing the predicted performance with the performance which is observed on specific test sections. These test sections can either be real pavements subjected to real traffic or specially constructed test pavements subjected to accelerated testing by means of so called Accelerated Pavement Testing (APT) devices. Using the later implies that the test is carried out under well controlled conditions which makes the analyses less complicated.

The expectation is that in the years to come not much will change with respect to the use of advanced design systems. This is simply because advanced models require advanced material tests which cannot be done at most of the road material testing laboratories. Of course this situation differs from country to country. In France and the Netherlands for example, fatigue testing, triaxial testing, etc. have become common practice but in many other countries, and especially in developing countries, laboratories that can do such tests are still a rarity and it is not likely that this situation will change significantly in the coming years.

Although linear elastic multi-layer theory combined with appropriate material characterization is used for many years in making pavement designs and

performance predictions, the question is whether such an approach is really able to predict pavement performance with a high degree of accuracy. It will be clear that it will never be possible to fully simulate the *nonlinear* behavior of unbound aggregates by means of *linear* elasticity. Nevertheless, sub-layering of granular base and sub-base courses in such a way that a single base or sub-base layer is divided into a number of sub-layers to which a modulus is assigned which is reflecting the stress conditions in those layers, has shown to be a reasonable way to overcome the non-linearity problem. Another problem is how to apply laboratory fatigue tests on asphalt mixtures for pavement life predictions. The conditions in the field differ considerably from the lab conditions and it is a well-known fact that calibration factors of a significant magnitude are needed to "match" predictions with observations.

2.2. Fatigue cracking of asphalt pavements; why it is important to study

This research will be limited to fatigue cracking of asphalt pavements. One of the reasons for doing so is that the asphalt layer forms a significant part of the pavement structure's costs so it is important to get the required thickness right. Furthermore, cracking of the asphalt layer (even when it is thin) will reduce its bending stiffness and the consequence of that is that all layers below the asphalt layer will be subjected to higher stresses and might suffer from early damage. Also cracks in the pavement will allow moisture to enter the structure which in turn will result in loss of stiffness and bearing capacity of the layers below, especially if these layers are unbound layers. A combination of cracks and moisture will eventually result in potholes which have a severe effect on the riding quality of the pavement.

The effect of cracks on other pavement performance indicators is perhaps best illustrated by the models for rutting and potholing as incorporated in the Highway Design Model III [2]. These models are given below.

The models for rutting are given in Equation 2.1 and 2.3:

$$RDM = AGER^{0.166} \, SNC^{-0.502} \, COMP^{-2.3} \, NE_4^{ERM} \qquad (2.1)$$

$$ERM = 0.092 + 0.0384 \, DEF - 0.009 \, RH + 0.00158 \, MMP \, . \, CRX \qquad (2.2)$$

$$RDS = 2.063 \, RDM^{0.532} \, SNC^{-0.442} \, COMP^{-.1664} \, NE_4^{ERS} \qquad (2.3)$$

$$ERS = -0.009 \, RH + 0.00116 \, MMP \, . \, CRX \qquad (2.4)$$

Where:
RDM = mean rut depth (mm);
AGER = age of pavement (years);
SNC = modified structural number;

COMP = compaction index of the pavement relative to a standard;
NE_4 = number of 80 kN equivalent single axles (damage power 4) (ESA);
DEF = mean Benkelman beam peak deflection under an 80 kN axle load (mm);
RH = rehabilitation state. 0 for new pavements; 1 for overlaid pavements;
MMP = mean monthly precipitation (m/month);
CRX = cracked area (%);
RDS = standard deviation of the rut depth (mm);

These equations show that the amount of cracking has a significant effect on permanent deformation especially in conditions where the monthly precipitation is high.

The initiation of potholes is, according to HDM III, not related to the amount of cracking but the growth of the area showing potholes is, as is shown in Equation 2.5:

$$\Delta APOT = \min (\Delta APOT_{CR} + \Delta APOT_{RV} + \Delta APOT_{PE}; 10) \qquad (2.5)$$

$$\Delta APOT_{CR} = \min (2 * CRW * U; 6) \qquad (2.6)$$

$$U = ((1 + CQ) * (YAX / SNC)) / 2.7 HS \qquad (2.7)$$

Where:
$\Delta APOT$ = change in total pothole area per year (%);
$\Delta APOT_{CR}$ = change in pothole area due to cracking;
$\Delta APOT_{RV}$ = change in pothole area due to raveling;
$\Delta APOT_{PE}$ = change in pothole area due to enlarging of existing potholes;
CRW = percentage of area showing wide cracking (%);
CQ = construction quality factor; 0 is no fault; 1 when pavement is faulty, such as early stripping;
YAX = annual flow of all vehicles (millions/lane/year);
HS = total thickness of bituminous surfacing (mm);

When the extension of the pothole area equations are examined in more detail then one will notice that changes in the cracked area have approximately a two times bigger effect than the changes in the raveled area.

These relationships, which were all based on statistical analyses of actual pavement performance data, clearly show the effect cracking has on the development of damage types like rutting and pothole formation. Since these damage types (especially potholing) strongly affect driving speed, driving comfort, safety and vehicle operating costs, cracking indirectly influences the functional performance of pavements. All in all it means that analyzing and predicting the cracking performance of pavements is important.

Cracking can be initiated because of a large number of reasons. It has been decided to limit this thesis to fatigue cracking due to repeated wheel loads. Fatigue cracking due to repeated temperature cycles is not considered because they are not relevant for the country where the author of this thesis is coming from and also not for the Netherlands where the winters are too mild to cause a significant amount of this type of cracking to develop. Also reflective cracking initiated in cemented base courses will not be considered because the origin of these cracks is not in the asphalt layer itself.

2.3.   Scope of the literature review

In the past a large number of studies were done to validate design procedures by trying to match predicted performance with field performance. The amount of work done in this specific field is so extensive that it is simply impossible to cover it all in a literature survey. Therefore, for this particular project it has been decided to only take into account the studies that were done in the Netherlands or by Dutch researchers. This implies that this literature survey is limited to the following work:
-   investigations done as part of the SHRP-NL project [3, 4];
-   work done by researchers of the Roads and Railways Research Laboratory (RRRL) of the Delft University of Technology (DUT) related to the test sections built as part of the OECD FORCE project [5, 6];
-   work done by researchers of RRRL as part of the investigations done by means of the DUT's accelerated pavement testing (APT) facility LINTRACK [7-9]
-   work done by MSc student Visser of DUT on sections tested in Texas with the APT device available in Texas [10];
-   work done by the Dutch CROW committee B12 on the prediction of surface cracking in pavements [11, 12];
-   work done by PhD student Groenendijk of DUT and PhD student Myers of the University of Florida on surface cracking [7, 13];
-   work done by researchers of the structural mechanics group of the Civil Engineering Faculty of the Delft University of Technology [14].
-   work done by researchers of the Royal Shell laboratories in Amsterdam in matching beam fatigue with field fatigue [15].

Major issues that will be discussed in the literature review are among other:
-   How large were the calibration factors that were needed to match theory with practice?
-   What were the factors that complicated matching theory with practice?
-   Were there any unknowns in the analysis for which (major) assumptions needed to be made and what was the magnitude/effect of these assumptions?
-   Is the cracking observed at the surface of pavements, bottom-up or top down cracking or both?
-   Irrespective which type of cracking it is, were the researchers able to predict these different types of cracking?

2.4. Fatigue

In order to be able to predict fatigue cracking of asphalt pavements, understanding the basic concept of fatigue is the starting point.

Fatigue, which is often described as the development of cracks due to repeated loading, is difficult to predict but the prediction of fatigue properties and the determination of fatigue resistance is important in order to be able to estimate the structural behavior of the road during its service life. It is difficult to obtain the right input parameters for fatigue life predictions, but maybe it is even more difficult to understand how cracks develop and propagate.

Determination of fatigue properties in the laboratory is not enough to predict field performance, because some aspects like lateral traffic wander, geometry differences between the lab specimen and the real pavement, and healing are not taken into account. Therefore, shift factors of significant magnitude need to be applied on fatigue relationships derived from laboratory fatigue tests in order to make them applicable for field predictions.

Furthermore, many of the pavement design procedures, for example the RHED (Road and Hydraulic Engineering Division of the Dutch Ministry of Transport, Public Works and Water Management) method or the SPDM (The Shell Pavement Design Manual, 1978, 1985), do not consider visible cracking at the pavement surface as a design criterion but are using Miner's ratio, being the ratio of applied number of load repetitions to the allowable number, as an indication of damage. The relation between this ratio and the amount of visible cracking is not clear.

The design methods are aiming to prevent the development of fatigue cracking at the bottom of the pavement layer. But many pavements also show a large amount of top down cracking and although this damage type is the reason for a significant amount of maintenance it is remarkable to note that this type of cracking is not taken into account in any of the design systems. It will be obvious that top down cracking has nothing to do with the tensile strain at the bottom of the asphalt layer [16]. This implies that it is difficult to relate visible cracking to Miner's ratio which is calculated using the tensile strain at the bottom of the asphalt layer as input.

All in all it is clear that prediction of visible fatigue cracking is not an easy task to do and this thesis is devoted to get a better understanding of the relationship between visible fatigue crack patterns and stresses and strains that are calculated at various locations in the asphalt pavement. In order to be able to correlate stresses and strains to cracking, damage functions or fatigue relationships need to be known. One aspect that complicates the prediction of visible cracking is the fact that the result of fatigue testing as performed in the lab is not directly applicable for practical purposes.

Accelerated pavement tests (APT) allow visible damage to be related to predicted damage in a much better way than real life pavement sections do.

This is simply because of the fact that the conditions in AP tests are much better known and contolled. Therefore, results obtained from accelerated pavement testing (APT) and the analysis thereof should be discussed in this literature survey. APT is considered to be an important step between theory and practice. If it is not possible to predict what happens in APT then it will be almost impossible to predict what happens in real pavements.

In this literature review attention will be paid to the prediction of the fatigue resistance of asphalt mixtures using laboratory tests and correlations that were made between beam fatigue tests and fatigue tests on fully supported beams and slabs. Furthermore, results of fatigue cracking analyses done on real pavements will be discussed and finally, attention will be paid to results of accelerated pavement tests that were done for fatigue modelling purposes. A limited overview will be given of what other researchers did and after that an overview will be given of those aspects which still need to be investigated.

2.5.   Fatigue life prediction using laboratory tests

Fatigue properties are derived through testing in the laboratory. In the European Standard bituminous mixtures are ranked on the basis of their resistance to fatigue. Furthermore, these tests provide input data for predicting pavement performance. Fatigue testing is also used to determine whether mixtures as designed and laid comply to the specifications set for them [17] and to determine whether mixture modifications by means of for example polymers and other products result in the desired improvement of the fatigue resistance of these modified mixtures.

The principle of a laboratory fatigue test is applying a repeated loading to the specimen until failure. Trapezoidal, prismatic or cylindrical shaped asphalt mixture specimens can be used depending on the type of test. The test can be carried out in either stress controlled or strain controlled mode. The principles of these two loading modes are described in Figure 2.1. In the 'stress controlled mode' (also called 'load controlled mode') a sinusoidal force with constant amplitude is applied to the specimens. At a given moment the amplitude of the sinusoidal displacement will start to increase until failure/fracture occurs. In a 'strain controlled test' (also called 'displacement controlled' test) the force is changing to keep the displacement at a constant level. It is common practice to declare the specimen as 'failed' when the amplitude of the applied load has reduced to 50% of its initial value [3]. Based on the test results, relationships between the applied strain level and the number of load repetitions to failure are derived. These types of tests have been done for many decades and Figure 2.2 is an example of stress and strain controlled fatigue test results obtained by Epps and Monismith as early as 1972 [18].
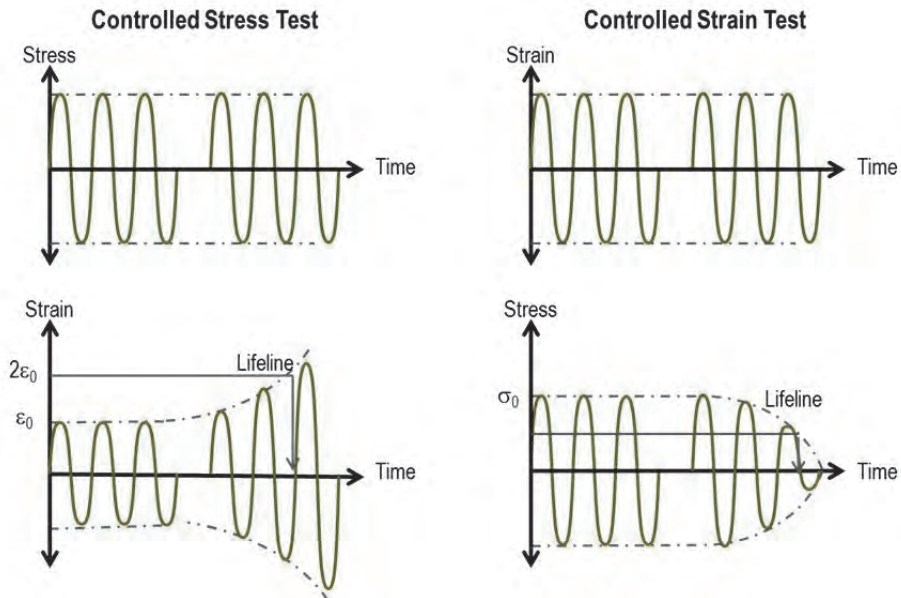
Figure 2.1. Stress controlled and strain controlled loading scheme [19]
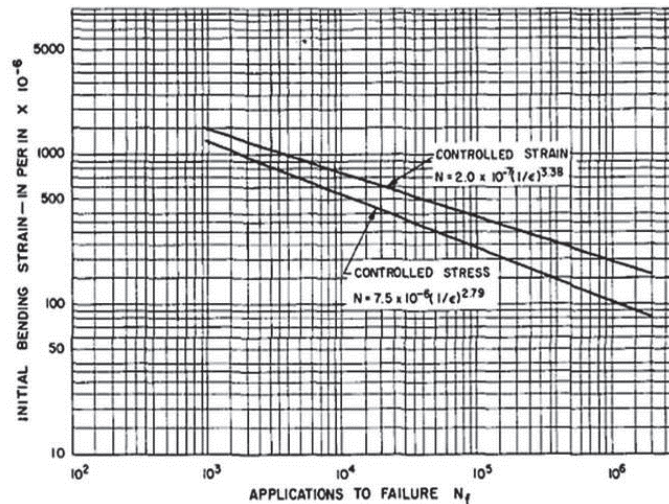
Figure 2.2. Fatigue lines resulting from stress and strain controlled tests
(Epps and Monismith, [18])

It appears that the number of load repetitions to failure in a constant displacement (strain) type of test is about 4 times the number of load repetitions in a constant load (stress) fatigue tests.

Fatigue damage in a viscoelastic material is quite often explained by the energy dissipated during the fatigue test. The principle of energy dissipation is shown in Figure 2.3.c. [20]. Figure 2.3 shows a comparison between a linear elastic material and a visco-elastic material. Energy dissipation does not occur in linear elastic materials. When unloading a linear elastic material, all the energy stored in the sample during loading is completely recovered.

A visco-elastic material shows a different pattern when it is unloaded. In this case not all the energy that is stored in the material will be recovered. Some of it is "used" for heating up the material and some of it might be used to

damage the material. This energy loss is called dissipated energy and is equal to the area within the load vs deflection loop
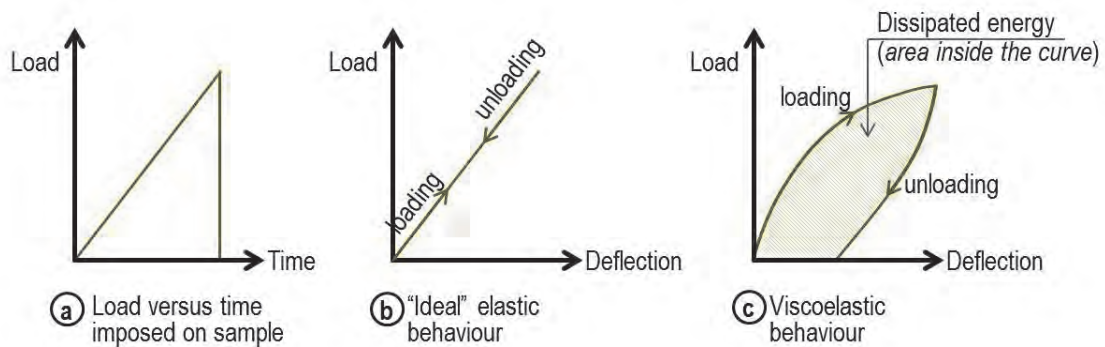
Figure 2.3. The dissipated energy approach on visco-elastic mixture [20]

When a sinusoidal loading is applied to a visco-elastic material, a phase lag is observed between the load and measured deflection [21]. As a result of this, a 'hysteresis' loop will be obtained as depicted in Figure 2.4.

Figure 2.4 shows how the dissipated energy per cycle is changing in a load (stress) and displacement (strain) controlled test. In a load controlled test the dissipated energy per cycle increases with increasing number of load repetitions while it is decreasing in a displacement controlled fatigue test. The figure also shows how the dissipated energy is accumulating during both tests.

When a sinusoidal load signal is used, the amount of energy which is dissipated per load cycle can be calculated using Equation 2.8.

$$W_i = \pi \sigma_i \varepsilon_i \sin \phi_i \tag{2.8}$$

Where
W_i = dissipated energy at cycle i
σ_i = stress amplitude at cycle i
ε_i = strain amplitude at cycle i
ϕ_i = phase lag at cycle i

Van Dijk [15] postulated that there is no difference in the results of load and displacement controlled fatigue tests when the number of load repetitions to failure is related to the cumulative amount of dissipated energy. In both tests the specimens will fail after the same number of load repetitions when the same amount of energy is dissipated. Van Dijk presented a relationship in terms of "cumulative dissipated energy" versus number of loading cycles, as follows:

$$W = \pi \sum_{i=0}^{i=N} \sigma_i \varepsilon_i \sin \phi_i = AN^Z \tag{2.9}$$

Where W is cumulative dissipated energy to failure, N is number of load repetition and A and z are experimentally determined coefficients. For different types of mixtures this relationship is shown in Figure 2.5.
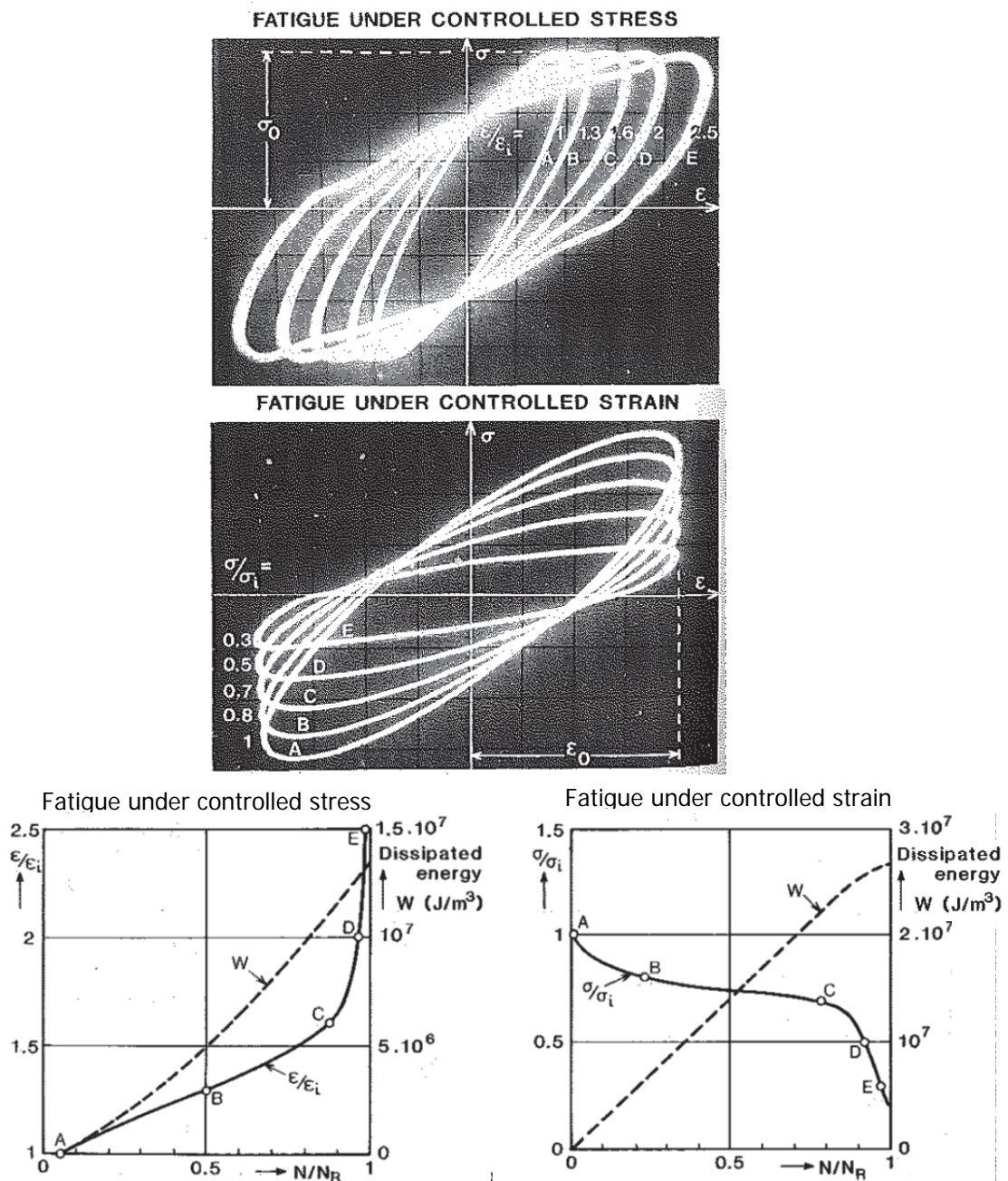
Figure 2.4. Hysteresis loop obtained from plotting load versus deflection and variation of dissipated energy per load cycle during controlled stress and strain fatigue tests. [20]
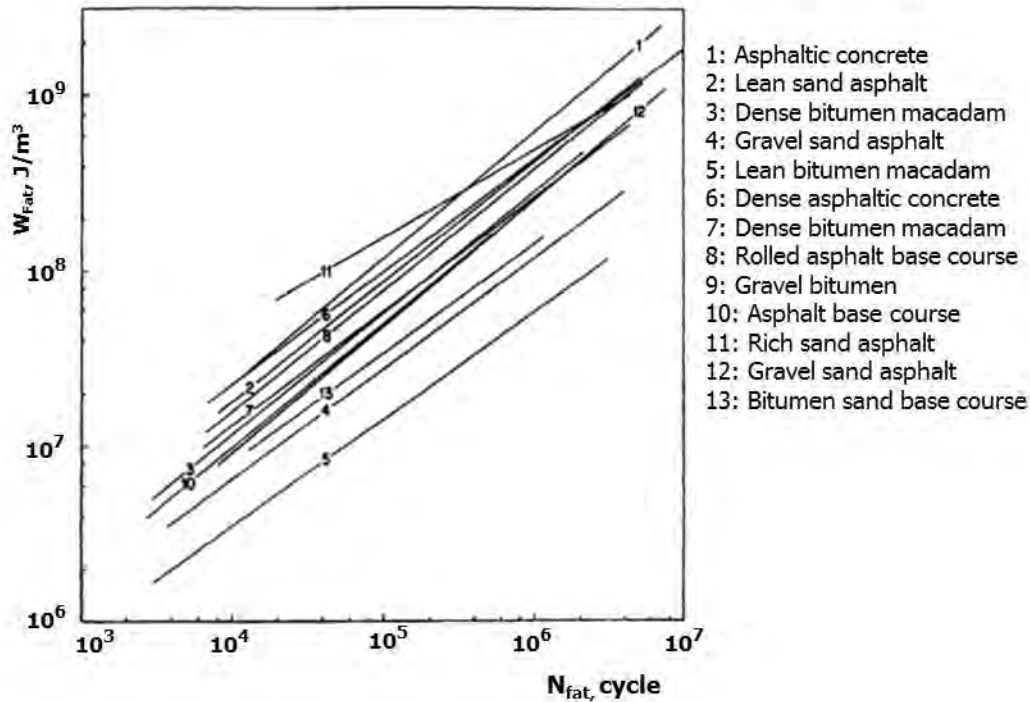
Figure 2.5 Cumulative amount of dissipated energy versus fatigue life for a series of mixtures [22]

.

Pronk [23] stated that instead of the total amount of dissipated energy, the change in dissipated energy per period (cycle) is the most relevant parameter. This is because energy is also dissipated because of generation of heat and the change in energy dissipation is due to damage development. Pronk also underlined that a fatigue life prediction based on dissipated energy is more appropriate than the prediction based on the tensile strain criterion. This indicates that a flexible pavement design system incorporating visco-elastic material behavior seems to be more appropriate than a system based on linear elastic theory. Programs like VEROAD [24], KENLAYER[25] and ViscoRoute[26] are good examples of such a design system but for some reason such more advanced systems never got widely used.

2.6. Factors influencing laboratory fatigue results

Researchers developed several laboratory test methods to predict the fatigue life of an asphalt mixture. Each method however, has a different working procedure and produces a different result. In this part of the chapter results obtained on beam type specimens tested in 4PB and in direct tension will be discussed. Furthermore, work that is done to determine the effect of a beam being fully supported during the fatigue test will be reported.

2.6.1. Beam fatigue tests

In the European Standard [17], bending tests and direct and indirect tensile tests methods are described for characterizing the fatigue of bituminous mixtures. Li [20] did extensive research on three types of fatigue tests being the uniaxial tension-compression test (UTC), four point bending (4PB) test and indirect tension test (ITT). These tests are shown in Figure 2.6. Li showed that not only the type of loading has a big influence on the results of fatigue tests but also that the result is strongly dependent on the type of tests and, in case of bending tests such as the 4PB test, on the specimen geometry as well [20]. The UTC and ITT appeared not to be affected by the specimen size.
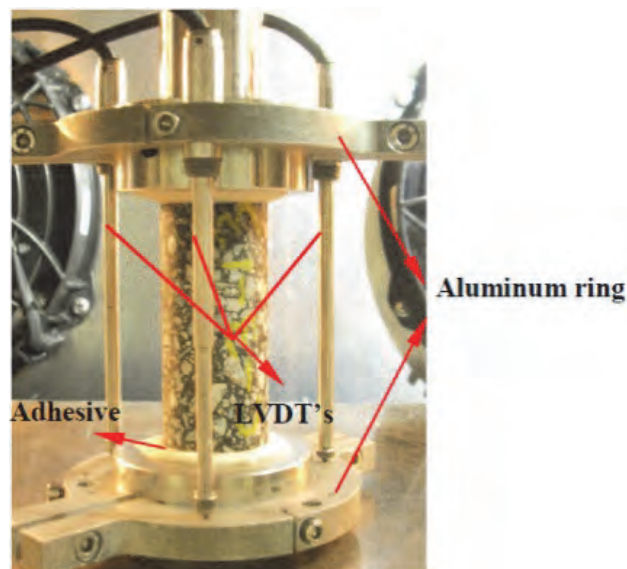
(a)
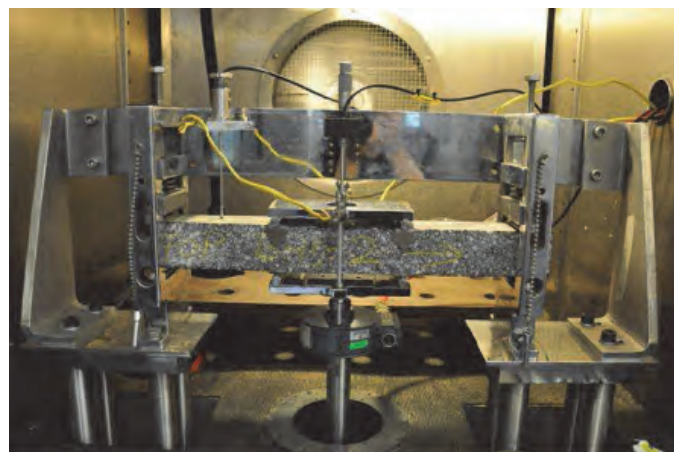
(b)

Figure 2.6. Typical fatigue test setup (a) close up of the uniaxial tension and compression test (b) 4 point bending test, after Li [20]

(c)
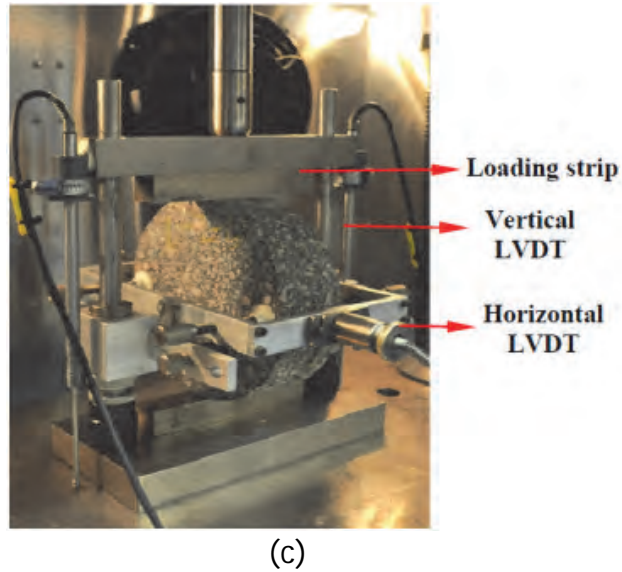
Figure 2.6. Typical fatigue test setup (c) indirect tension test, after Li [20]

Using the 4PB Test, Li [20] investigated the effect of specimen size on the fatigue life of a typical Dense Asphalt Concrete 0/8 mixture (DAC 0/8). In order to limit the effect of inhomogeneity Li used a relatively fine grained mixture which is shown in Table 2.1. Table 2.2 shows the different specimen sizes which were cut from blocks prepared using a shear press box compactor [27]. This machine produced compacted blocks with dimensions of 450x150x150. The average air void of the specimens was 3.5%.

Table 2.1. DAC 0/8 mixture composition [20]

Sieve (mm)	Scottish crushed granite		Norwegian Bestone	Crushed sand	Wigras 40K	Binder
	8-5.6	5.6-4	6-2	2-0.063	0.18-0.063	
Wt. %	11.2	19.6	21.5	33.2	7.9	6.5

Table 2.2. 4PB fatigue test program and the specimen's dimension [20]

Loading mode	Specimen size	Dimension of the beam [mm]	Test condition
strain-controlled	size 0.5	$l \times w \times h = 400 \times 50 \times 25$	• Temp.: 20 °C • Freq.: 10 Hz • Waveform: sinusoidal
	size 1.0	$l \times w \times h = 400 \times 50 \times 50$	
	size 1.5	$l \times w \times h = 400 \times 50 \times 75$	
Stress and strain-controlled	size 1.0	$l \times w \times h = 400 \times 50 \times 50$	• Temp.: 5 °C • Freq.: 10 Hz • Waveform: sinusoidal

Figure 2.7 shows the different 4PB test fatigue lines as obtained by Li. The figure shows that the 4PB fatigue results are significantly influenced by the specimen size. At the same strain level the higher height/length ratio results

in a shorter fatigue life. The stress controlled tests were only performed on one size and at one temperature. The reason behind this was that Li only wanted to show the difference between strain controlled and stress controlled loading modes. Therefore, Li decided it was not necessary to test all three specimen sizes and that doing tests at only one temperature was sufficient for this purpose. The temperature of 5°C was chosen because at such a low temperature, the influence of the permanent deformation on the stress controlled fatigue test results is low [20].
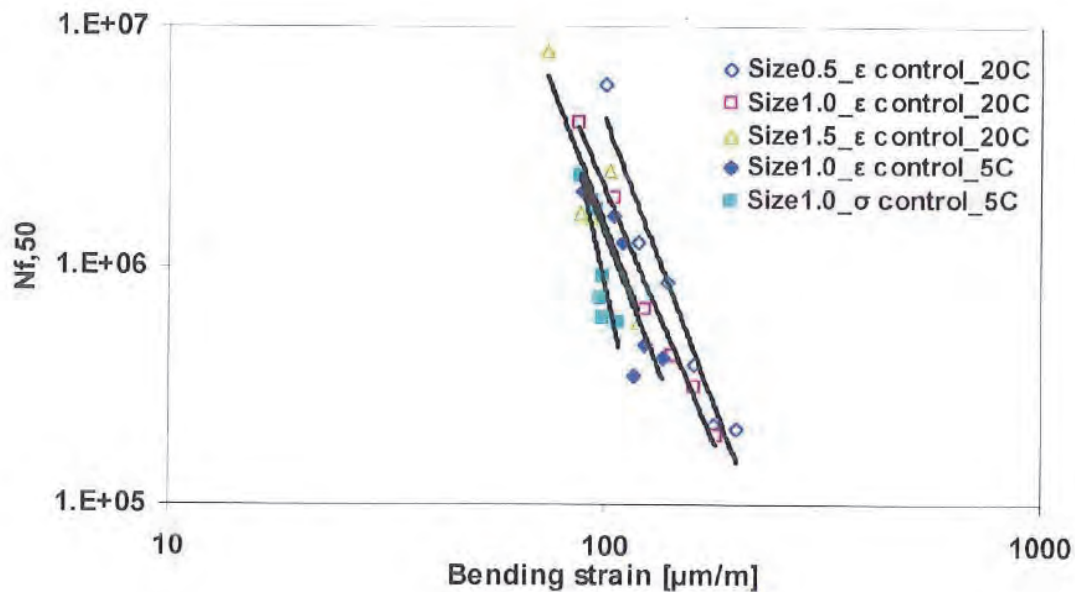
Figure 2.7 Strain based fatigue life relationships determined by means of the 4PB test, after Li [20]

Before Li came to his conclusion, Molenaar [16], Tseng and Lytton [28] and Groenendijk [7] already hypothesized and showed that laboratory fatigue tests are providing only specimen properties rather than mixture properties. The only *material property* that can be obtained from laboratory fatigue testing is the slope of the fatigue line. Molenaar also indicated that the value of this parameter can be obtained in a much more practical way by means of resilient modulus testing. The intercept value is dependent on the geometry of the specimen.

Pronk [23] and Varaus et al [29] compared the 2PB test and 4PB test. By employing Weibull's theory, Pronk showed that the lifetime obtained by means of a four point bending test is 2.8 times longer than the one from a two point bending test. The prediction appeared to be in good agreement with real test results. Pronk discussed the difference between the fatigue life resulting from 2PB and 4PB test, while Varaus et al focused on the difference in the stiffness moduli resulting from these two test methods. Varaus claims that at 15°C the stiffness moduli in the 4PB test are higher than the stiffness moduli in the 2PB test. When comparing the 4PB with the UTC and ITT; Li, however, concluded that the stiffness moduli obtained with the 4PB and UTC

test at 20°C are close to each other but are higher than the stiffness moduli obtained with the ITS.

2.6.2. Effect of support conditions

A laboratory fatigue test which is believed to be a closer representation of what is happening in the road is the Beam on Elastic Foundation (BOEF) test. A considerable amount of literature has been published on the BOEF test [30-35].

The set up basically consists of an asphalt mixture beam placed on top of a rubber slab which is functioning as a supporting foundation. During the test the horizontal tensile strain at the bottom of the beam can be measured with strain gauges or can be determined by means of measuring the horizontal displacement between two points at the bottom part of the beam using a linear variable differential transformer (LVDT). A typical test configuration is shown in Figure 2.8.

Majidzadeh [35] mentioned that for a beam on an elastic foundation or an asphalt slab placed on an elastic layer the effect of creep is probably negligible. In this way these tests could simulate fatigue in a way which is closer to field conditions.
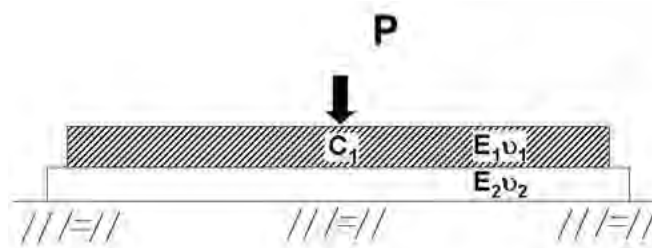
Figure 2.8. Typical test set-up of a BOEF test according to Majidzadeh [35]

In part of Molenaar's PhD research [36], uniaxial tension fatigue tests were performed, allowing creep to occur. Next to that, Molenaar also performed BOEF tests which were only briefly described in [30]. The results of these BOEF tests are, however, reported in detail by Thewessen e.a. [37]. In these tests beams with dimensions of length x width x height of 900 x 50 x 60 mm were glued on a rubber subgrade to ensure full friction (adhesion) between beam and subgrade. In these BOEF tests, the crack did not fully propagate through the beam because the crack tip was entering the compressive zone. This complicated significantly the development of relationships between the stress intensity factor K at the tip of the crack and the crack speed dc/dN to such an extent that no meaningful relations could be developed. Part of the problem was also caused by the fact that the crack length was difficult to measure given the technique used and because sometimes a significant different crack length was observed on either side of the beam. Therefore, they rejected this test as being suitable for crack growth investigations.

Choi [33] investigated the effect of a moving wheel load on top of a beam on an elastic foundation (see Figure 2.9.a). The wheel had a solid rubber tyre; its width was just less than 50 mm.

Instead of gluing the beam on the rubber foundation Choi overcame the slip problem by placing restraints around the beam also at each end of the top surface [33]. In this paper Choi does not describe these restraints in detail but it is explained that the restraints added negligible stresses but ensured that the beam remained centrally placed within the mould directly under the path of the wheel load. However, since the interface between the specimen and the rubber remains free, neither full friction nor full slip between the beam and the rubber foundation was achieved. This could have influenced the test result. The strain under the beam was measured by means of pairs of strain gauges glued centrally to the underside of each beam.

Choi compared the fatigue life of a particular dense asphalt mixture tested in the BOEF set-up at 10°C, 20°C and 30°C with the fatigue life of the same mixture determined with the two point trapezoidal test and the uniaxial fatigue test. The two point trapezoidal test and the uniaxial fatigue test were performed at a frequency of 10 Hz. The BOEF tests were performed at the rate of testing of 40 passes to the minute, which is giving a pulse duration at the bottom of the beam of 'a little under a second'. The paper stated that loading frequency of the three types of tests are in agreement. Choi concluded that at 20°C and 30°C the BOEF test gives a higher fatigue life than the trapezoidal and uniaxial test while at 10°C the three different tests give approximately the same result. Choi reported that the difference between the fatigue life of the trapezoidal test and the fatigue life of the beam on elastic foundation is a factor of about 2 at 20°C and of about 2.8 at 30°C.

(a)   (b)
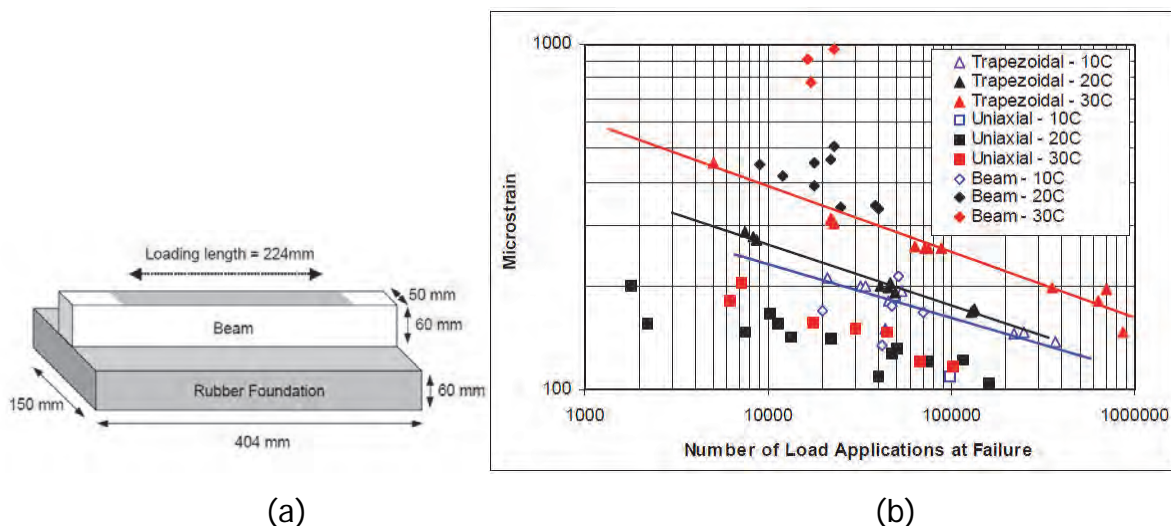
Figure 2.9. BOEF experiment as performed by Choi et al and results obtained [27]

Several points may be drawn from the paper. Magnitudes and direction (push-pull mode) of the loading for both two point trapezoidal test and the uniaxial fatigue test were not mentioned. Moreover the loading frequency of

the three tests are questionable whether they were in agreement or not. When discussing the result, it is not clear how Choi reached to this conclusion because Figure 2.9.b shows that at 20°C the shift factor is 20 while at 30°C it is 170! The 2P bending (trapezoidal) fatigue test was a load controlled test with a full sine loading. At 20°C the difference between the uniaxial and trapezoidal test seems to be a factor of around 20. Such a difference, however, seems to be unrealistically high.

Important work on relating beam fatigue to fatigue of fully supported asphalt slabs has been done by Shell [15]. Van Dijk compared the fatigue life of a typical asphalt mixture obtained in a 3PB fatigue test set up with the fatigue life of the same mixture tested in a laboratory wheel tracking machine. The beam specimens, with dimensions of 230x30x20 mm, were tested with a 3PB fatigue test set up in the constant stress, constant strain and constant dissipated energy mode.

Slabs with dimensions of 950 x 440 x 40 mm (length x width x height) of the same asphalt mixture were also tested in a wheel tracking test (WTT). A wheel with a rubber tire was used to load the slabs with a speed of approximately 7 km/h and a maximum load of 1500N. The size of the contact area was dependent on the wheel load and varied between 1500 – 3000 mm^2. During the tests the strains developing at the bottom of the slabs were measured using strain gauges.

During testing, the measured strains developed like shown in Figure 2.10. It is interesting to note that a good correlation was obtained between the change in strain and the visible damage.

The relations between the 3PB and the WTT tests are shown in Figure 2.11. From this graph it was concluded that the difference between N1 and N2 stages is related fairly well to the difference between the fatigue result measured in the 3PB constant stress and 3PB constant strain tests. The N1 stage was indicating the initiation of hairline cracks while the N2 stage indicated the formation of real cracks. The results also revealed that the initiation of the hairline cracks in the WTT could be predicted from the 3PB fatigue test results in the constant stress loading mode. Furthermore, Van Dijk concluded that the number of load repetitions to failure in the slab could best be predicted using the 3PB strain controlled fatigue test. However, close observation of Figure 2.11 learns that the number of load repetitions to failure might better be predicted using constant dissipated energy based fatigue lines.
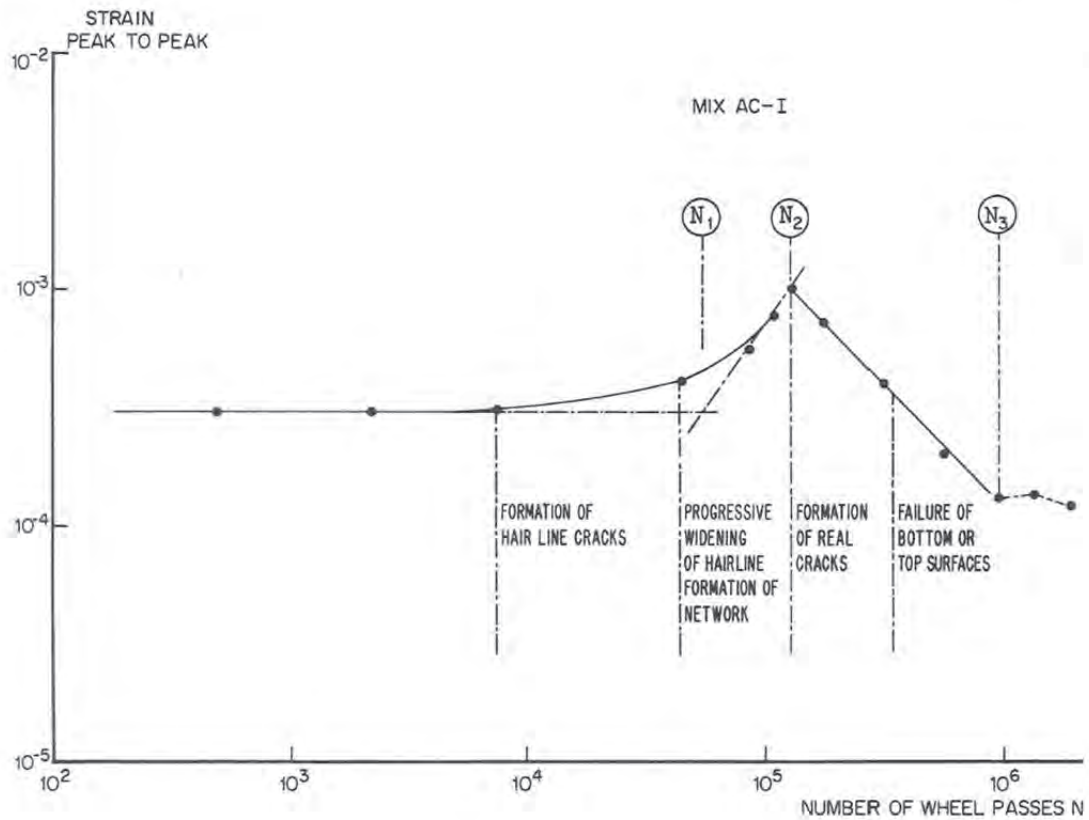
Figure 2.10. Crack development in relation to tensile strain and number of wheel passes [15]

The 3 point beam bending fatigue test as used by Shell in the 1970's is no longer used. It is replaced by the 4 point beam bending tests and tension/compression uni-axial tests. In both tests, the specimen size is significantly larger than those used by Shell. Furthermore, asphalt pavements in many parts of the world are thicker than the 40 mm used in Shell's WTT. All this implies that the basis for using constant displacement 4 point bending results for design purposes is rather weak.
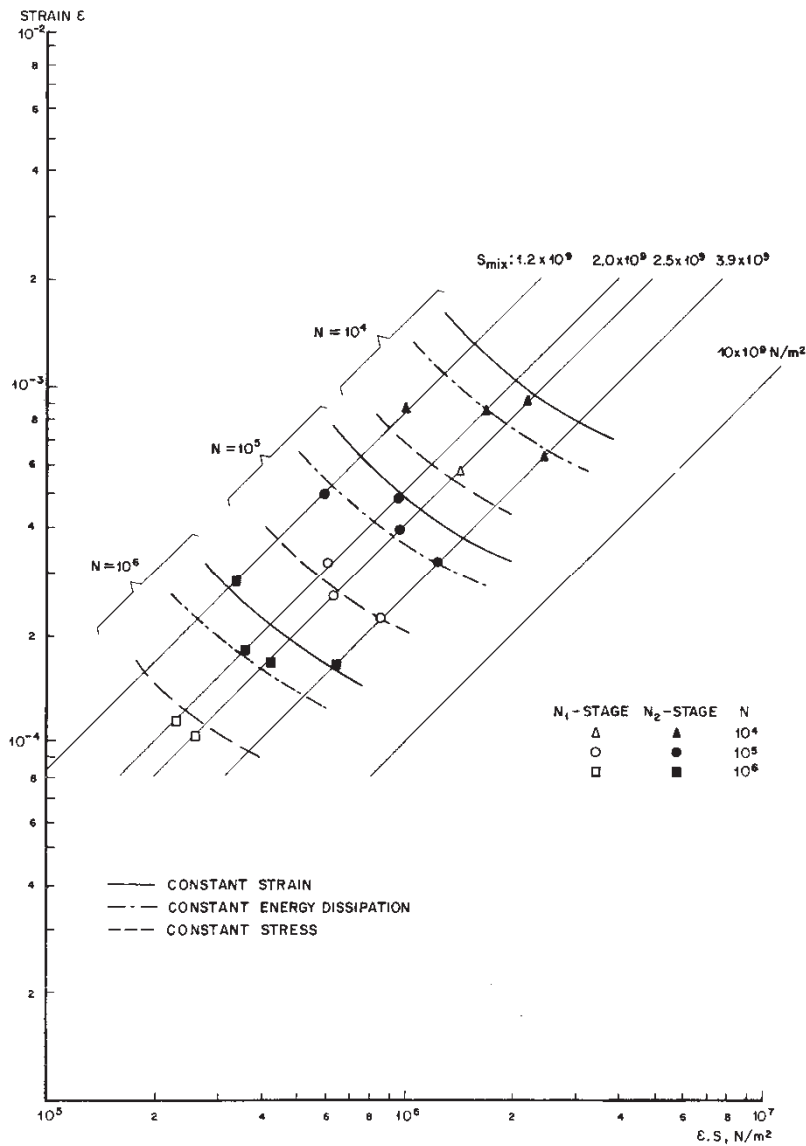
Figure 2.11. The relation between WTT and 3PB fatigue test [15]

2.7. Field fatigue observations

In the SHRP-NL Technical Report 1995 published by CROW diagrams are presented that show the relation between Miner's ratio and the percentage of cracked area as observed on a number of test pavements [3, 4]. Miner's ratio is the cumulative amount of damage which is calculated using Equation 2.10.

$$\text{Miner's ratio} = \frac{n}{N} \tag{2.10}$$

In the equation "n" is the number of applied load repetitions and "N" is the predicted number of those load repetitions until failure. In the SHRP-NL analyses "N" is determined by calculating the tensile strain at the bottom of

the asphalt layer due to a standard axle load using a multilayer linear elastic program and fatigue relations that were determined by means of 4PB fatigue tests. Shift factors were used to account for lateral wander and healing.

The investigation was carried out on 190 test sections. The data collected consisted of visual condition data; traffic data; falling weight deflectometer data and data from drilled cores [3]. The latter two data sets were used to back calculate the stiffness of the different pavement layers which were then used as input in the multilayer analyses.

The main results of the investigation are shown in Figure 2.12 where the x and y ordinate of the graph represent Miner's ratio and the percentage of cracking in the wheel track respectively. The graphs show the amount of surface cracking (shown as triangle point▲) and cracking through the entire asphalt layer (shown as square point■). The lines in the graphs show the 85%, 50% and 15% reliability curves.

Figure 2.12.(a) shows that in almost all cases Miner's ratio is lower than 1. Nevertheless, many of the pavement sections show cracking. This is also the case when only the amount of cracking that developed through the entire layer is considered (see Figure 2.12.(b)). This could imply that the observed cracking is not the bottom up fatigue cracking which is predicted by means of the theoretical analyses and/or the used fatigue relation and/or the used correction factors are not correct.

Schmorak [3] showed in the 190 test sections investigation that all cracking observed on roads with an asphalt concrete thickness of more than ±0.16 m was surface cracking only. Cracking over the full thickness of the pavement (often combined with surface cracking) was only observed on thinner road sections (see Table 2.3). It was then concluded that in the thick pavements all cracks had originated at the surface while in the thinner pavements the cracks have propagated over the full depth of the asphalt layer.

Table 2.3. Nature of cracking in relation to the asphalt concrete thickness [3]

Asphalt thickness > (m)	Test sections with full crack propagation (%)
0.04	26.9
0.08	25.5
0.12	20.0
0.16	3.2
0.20	4.2
0.24	0.0
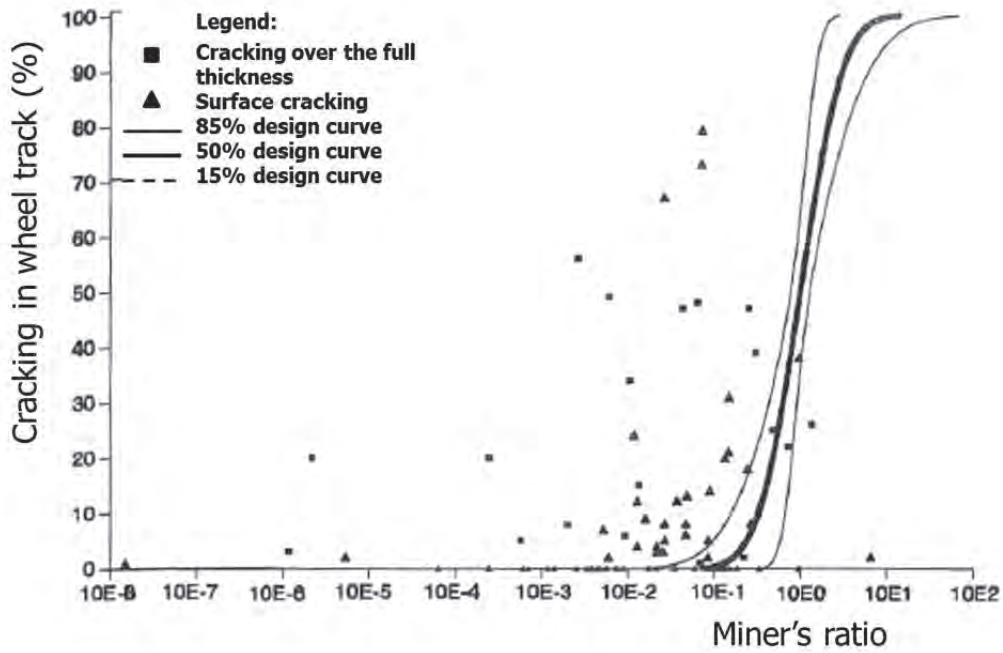
(a)
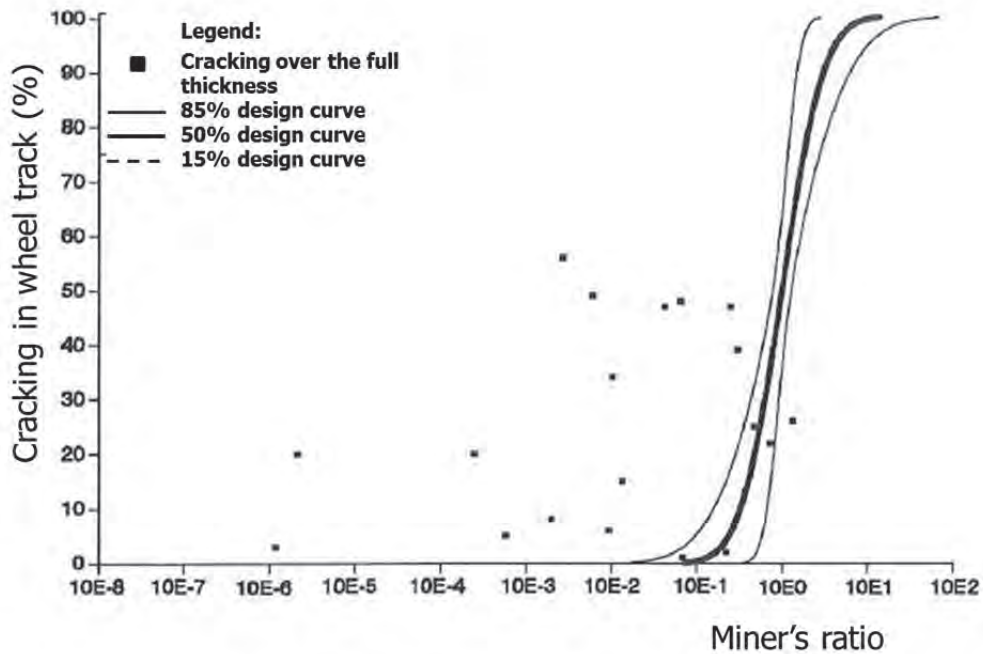
(b)

Figure 2.12. (a) Calculated Miner's ratio's versus quantity of all cracks in wheel tracks (all test sections) (b) calculated Miner's ratio's versus quantity of cracking in the wheel tracks that propagated through the entire layer [4]

Figure 2.13 is the same as Figure 2.12 but now the data points are marked according to the thickness of the asphalt layer. The figure does not show a clear relation between Miner's damage ratio and the amount of visible cracking even not for the thinner pavement sections.
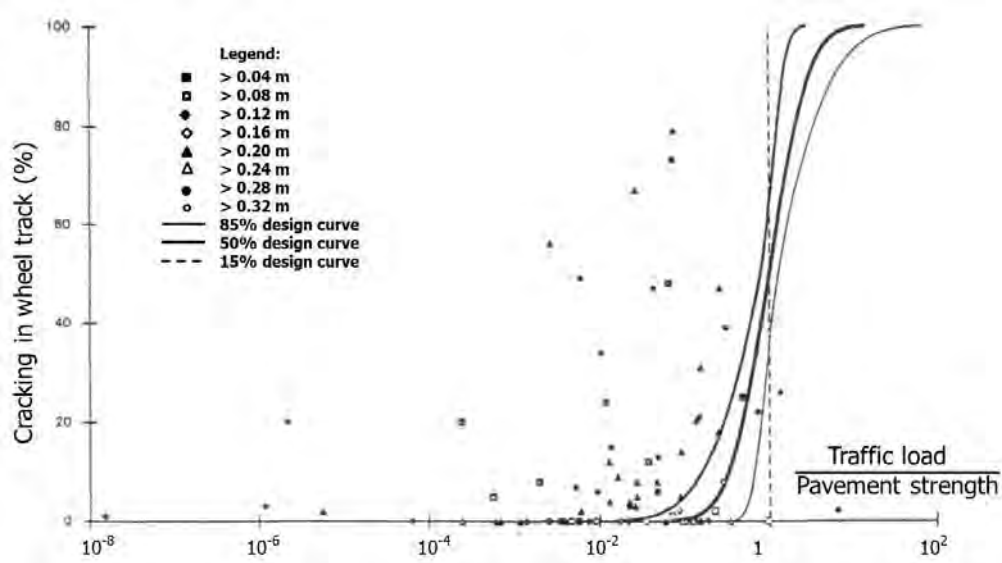
Figure 2.13. Calculated Miner-value versus quantity of cracks in wheel tracks observed on sections with different thickness [3]

Schmorak concluded that the total sample of test sections used in this project contained few or no sections where the structural fatigue life did reach a significant value. However, many of the test sections did show a significant amount of cracking and, therefore, it was concluded that most of the observed cracking should be surface cracking. This surface cracking usually stays confined in the top layer in case of thick pavements but will develop rapidly through the entire asphalt concrete thickness in thinner pavements.

Furthermore, the SHRP-NL results indicate that Miner's ratio, defined as the ratio between number of applied load repetitions (n) and the fatigue life of the asphalt concrete at the bottom of the pavement (N), does not tell anything about the presence of surface cracking.

Finally, it can be concluded that establishing shift factors between laboratory and field fatigue is a very difficult undertaking when it has to be based on analyses of field data. It seems that such shift factors only can be determined when field tests are done under very well controlled conditions such as occur in accelerated pavement tests.

The same SHRP-NL data base was used by Miradi [38] who developed models to predict the amount of cracking in dense asphalt concrete wearing courses 11 years after construction. Using various AI (artificial intelligence) techniques she came up with a ranking of the most important explaining variables. The result is shown in Table 2.4. From Table 2.4 it becomes evident that the number of "cold days" and "traffic" are the two most important parameters.

Table 2.4. The five most important input variables for predicting Meq (cracking) 11 years after construction

Method	Setting	Variable 1	Variable 2	Variable 3	Variable 4	Variable 5
Regression trees	Leave-one-out cross validation	Cold days	Traffic	Voids content	Bitumen content	
Genetic polynomial	Polynomial degree = 3	Cold days	Traffic	Bitumen content	Voids content	Rain
Artificial neural network (WWF)	Leave-one-out cross validation	Traffic	Cold days	Voids content	Bitumen content	Rain
Rough sets	2-class output	Voids content	Bitumen content	Traffic		
Correlation-based subset selection (bidirectional search)	Greedy stepwise search Leave-one-out cross validation	Cold days	Voids content	Bitumen content		
Correlation-based subset selection (genetic search)	Genetic Search Leave-one-out cross validation	Cold days	Bitumen content	Voids content		
Wrappers of ANN (genetic search)	Genetic Search Leave-one-out cross validation	Voids content				
Relief ranking filter	K=20 Nearest neighbor (equal influence) Leave-one-out cross validation	Cold days	Traffic	Bitumen content	Voids content	

Note: Meq = 0.25 * amount [% surface area] of light cracking + amount of moderate + 5 * amount of severe cracking

Miradi then used the Artificial Neural Network (ANN) techniques to develop a model to predict the amount of equivalent moderate cracking damage (Meq) using these two parameters as well as the bitumen and void content as explaining variables. After that a sensitivity study was made to determine the relative importance of each parameter. It was shown that if the bitumen content increases the amount of cracking 11 years after construction decreases. Furthermore, it was shown that if 'Traffic' or 'Cold days' increased, the amount of cracking increased as well. From the pavement engineering point of view, these results are all in agreement with practice.

Although "Traffic" showed to have a large influence on the cracking development, also climate (expressed in number of cold days) had a significant influence and should, therefore, be taken into account in cracking analyses. The idea behind the influence of the number of cold days is that the asphalt mixture ages during the hot summer days and becomes brittle as a result of that. Brittle mixtures, because of having lost their relaxation

capacity, will by definition show more cracking when exposed to low temperatures for a longer period of time.

2.8. Top down and bottom up cracking

Before discussing accelerated pavement testing, attention will be paid to the issue of top down vs bottom up cracking. As discussed in the previous section, the SHRP-NL technical report 1995 [4] stresses the importance of making a distinction between bottom up and top down cracking. There was a clear difference between the crack formation that was predicted by means of bottom up fatigue analyses and the amount of cracking visible at the pavement surface. The extent and severity of cracks visible on pavement surfaces were recorded via visual inspections, but from these inspections no distinction could be made between top down and bottom up cracks which were assumed to be those cracks which had grown through the entire layer. The presence of the latter type of cracking had to be proven by means of cores taken on places with cracks.

Although most of the surface cracks detected on the SHRP-NL test sections appeared to be in the wheel paths, one still could hypothesize that these surface cracks (top down cracking) are related to excessive hardening of the surface layer because of ageing due to the ambient effects such as: temperature, sunshine. However, these surface cracks were also reported by Groenendijk who carried out research with the Lintrack APT device. In spite of the fact that this device was operating in a hall and the test pavements, therefore, were protected from rain and solar radiation, Groenendijk concluded, by means of coring, that the majority of the cracks visible on section I, having a thickness of 150 mm, after 2.5 Million cycles had originated at the pavement surface [7]. One important remark should, however, be made here; the crack patterns observed by Groenendijk were like the ones shown in Figure 2.14. The surface cracks observed were almost exclusively transverse cracks (see Figure 2.15)
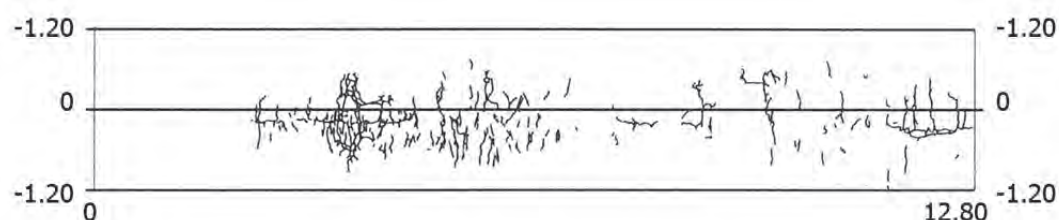
Figure 2.14. Total crack pattern Lintrack lane I after 4×10^6 load repetitions
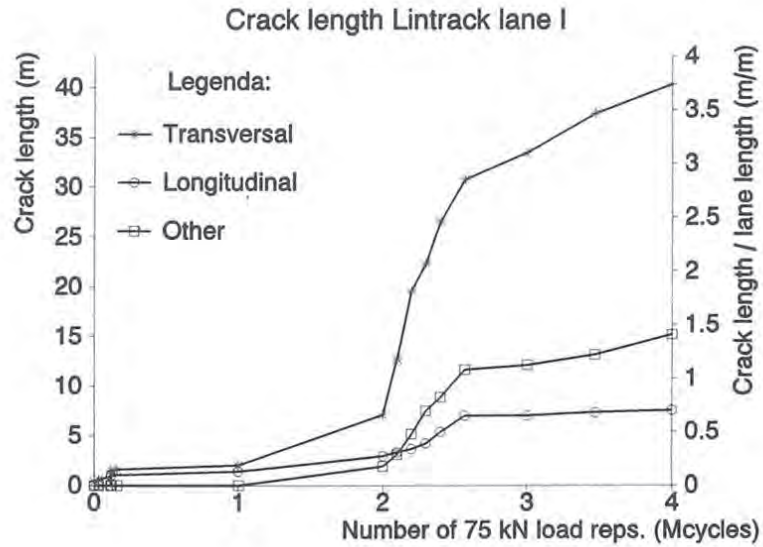
Figure 2.15. Crack length development Lintrack section I

These surface cracks are of a different nature than those observed in practice. In practice, wheel load associated surface cracks show up as longitudinal cracks at the edges of the wheel paths. Therefore, It might be hypothesized that the surface cracks monitored by Groenendijk were mainly compaction cracks (Groenendijk reported that there were many small compaction cracks after construction) which had grown as a result of the wheel load.

This transversal cracking was also observed on the thinner section VB. However, on the other thinner section VA most of the observed cracks were longitudinal cracks although there was also a significant amount of transversal cracks (see Figure 2.16).
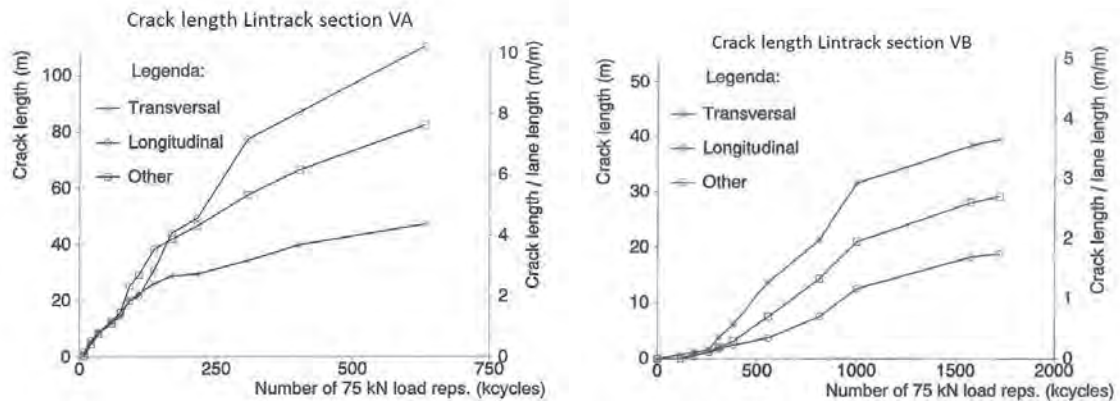
(a)   (b)

Figure 2.16. Crack length development at Lintrack section VA and section VB

Based on Groenendijk's data obtained on the thinner Lintrack sections VA and VB (both had a thickness of 80 mm), Molenaar [39] concluded that at the moment when 20% of the wheel track area of these sections was cracked,

the average asphalt stiffness of these sections was reduced to approximately 50% of its initial value (based on deflection measurements). It is recalled that in a 4PB fatigue test, the number of load repetitions to a stiffness reduction of 50% is usually taken as the fatigue point. On the thinner sections, however, it was difficult to decide whether the cracking started top down or bottom up, because most of the cores taken on a crack showed that the crack had developed through the entire asphalt layer. It was assumed that most of this "through and through" cracking was due to bottom up cracking but no proof could be found that this was really the case.

2.8.1. Early work in trying to explain surface/top down cracking

It is interesting to note that as early as 1967 Verstraeten [40], already pointed to the importance of horizontal shear stresses acting on the pavement surface in the tire contact area and their effect on the occurrence of tensile stresses and strains at the pavement surface. It should be mentioned that Verstraeten did not only consider shear stresses due to braking but also shear stresses that occur under free rolling and driven wheels. Later on Gerrard and Wardle [41] made the occurrence of tensile strains at the pavement surface due to shear forces in the contact area very explicit in the design manual they had developed. Inspired by their work, Molenaar [36] made extensive analyses on stresses and strains at the surface of pavements in the vicinity of the tire and showed that cracks visible at the pavement surface of pavement structures, having a so-called surface curvature index of less than 100 μm, are most probably top down cracks. The surface curvature index (SCI) was defined as the difference between the maximum deflection and the deflection measured at a distance of 500 mm from the load centre. In this analyses a 50 kN load was applied on a 300 mm diameter loading area (falling weight deflectometer configuration). Molenaar arrived to this conclusion after making extensive calculations using the CIRCLY computer program [42, 43] which allows to take into account horizontal shear force distributions that are acting in the tire-pavement contact area. Based on the load configuration used and the assumed shear stress distribution (see Figure 2.17) Molenaar related the tensile strain occurring at the pavement surface at the tire edge to the stiffness of the surface layer following:

$$\text{Log } \varepsilon_{te} = 4.822 - 1.049 \text{ Log } E_1 \qquad (2.11)$$

Where:

ε_{te} = tensile strain at the tire edge
E_1 = stiffness of the top layer [MPa]
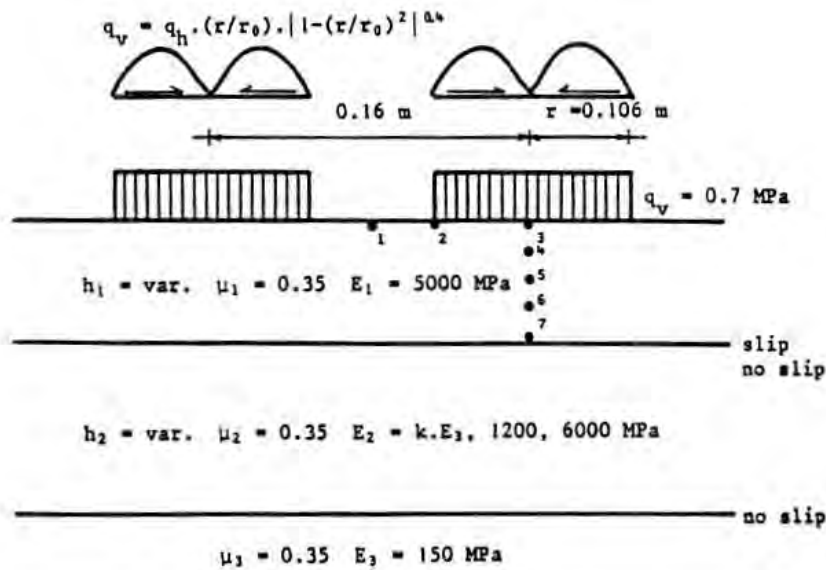
Figure 2.17. Load configuration and shear stress distribution as used by Molenaar [36]

This finding reported by Molenaar [36], is supported by work of van Gurp and Wennink [44]. Van Gurp and Wennink developed relationships between the SCI_{300} (defined as the maximum deflection minus the deflection measured at a distance of 300 mm from the center of a 50 kN FWD load, in μm) and the tensile strain at several locations in the pavement including tensile strains at the surface next to the tire edge. In their analyses they used the BISAR computer program and modelled the tire contact pressures as shown in Figure 2.18. Their predictions show that especially for pavements with a fairly high bending stiffness, surface fatigue cracking becomes dominant over fatigue cracking that is initiated at the bottom of the asphalt layer.

At the time Molenaar was doing his analyses, the Dutch Study Center for Road Construction SCW, later called CROW, had also started research into the reasons behind the occurrence of surface cracking. For this reason, the SCW B12 study committee did extensive analyses on a number of pavements involving falling weight deflectometer measurements, coring, mixture composition tests, analyses on the recovered binders, fatigue tests as well as tests on the buildup and relaxation of temperature stresses. Next to that extensive multilayer analyses were carried out. The results of this extensive research program are reported in [12, 45]. The wearing courses of the test sections in their study, all showed a significant amount of longitudinal surface cracking which was overwhelmingly concentrated in the wheel track area. Only very limited transverse cracking was observed (see Table 2.5). Falling weight deflectometer measurements were taken in and between the wheel paths. These results showed that at 66% of all measurement locations the deflections in the wheel paths were higher than between the wheel paths indicating that structural deterioration had taken place. Although this was the case, only surface cracking was observed on all sections. The penetration of the binders recovered from the wearing courses was ranging from 21 to 36 indicating that significant hardening had occurred since the penetration of the

virgin binder was 80/100 in all cases. All wearing courses had a void content of 5.1% or less except for one section where it was 7.2%; this was the section showing the highest amount of cracking.
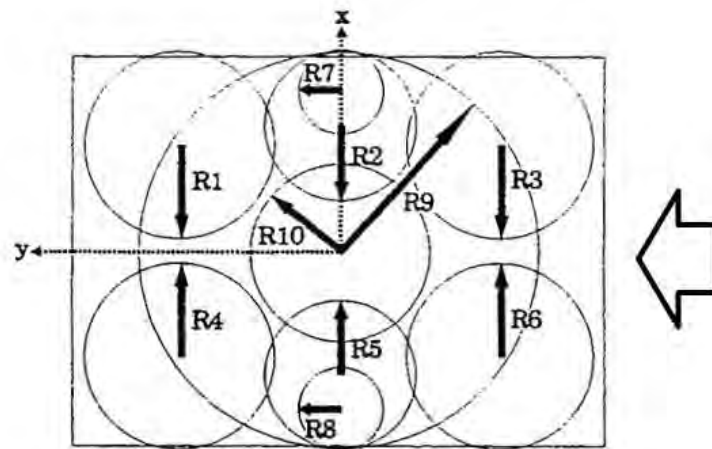
	Position [mm]		Radius	Stress [kPa]		
Load	X	Y	[mm]	X	Y	Z
1	60	90	52.6	-200	0	400
2	70	0	42.6	-200	0	0
3	60	-90	52.6	-200	0	400
4	-60	90	52.6	-200	0	400
5	-70	0	42.6	-200	0	0
6	-60	-90	52.57	-200	0	400
7	90	0	22.6	-180	0	0
8	-90	0	22.6	-180	0	0
9	0	0	112.6	0	150	750
10	0	0	50	0	-60	750

Figure 2.18. Schematisation of the contact stresses under a tyre as used by van Gurp and Wennink.

The following relation was found:

$$\varepsilon_{r1,t} = 194.895 - 20.7769 \ Log \ SCI_{300} \tag{2.12}$$

Where:

$\varepsilon_{r1,t}$ = tensile strain at pavement surface [μm/m]

Table 2.5. Visual condition survey conducted by SCW-Study committee B12 after Gerritsen [45].

Section		Cracking*					
		1984			1986		
		T	L	A	T	L	A
		(m)	(m)	(m)	(m)	(m)	(m)
IA	in**	1	130	0	0	17	-
	out**	1	4	0	0	6	-
IB	in	1	96	8	0	3	-
	out	1	5	3	0	49	-
IC	in	2	82	1	1	41	-
	out	1	9	0	0	32	-
ID	in	6	53	9	2	15	-
	out	5	11	1	3	29	-
IE	in	0	43	0	0	10	-
	out	0	4	0	0	7	-
IF	in	0	58	0	0	1	-
	out	1	43	0	0	13	-
3B	in	0	12	0	3	8	0
	out	0	4	0	1	3	0
3C	in	2	21	1	8	45	4
	out	2	5	0	2	8	0
4	in	11	34	21	26	58	53
	out	7	10	6	43	19	9

```
*    T    = transverse cracking
     L    = longitudinal cracking
     A    = alligator cracking
**   in   = inside the wheelpaths
     out  = outside the wheelpaths
```

Although the researchers assumed a certain horizontal inward shear distribution under the tire at the pavement surface, the tensile strain at the pavement surface as a result of this could not completely explain the occurrence of surface cracks. However, when the work strain was used in the fatigue relation, it was possible to explain surface cracking. Workstrain ε_w was defined as follows:

$$\varepsilon_w = \sqrt{\frac{2\Delta W_b}{S_{mix}}} \tag{2.13}$$

Where:

ε_w	= workstrain
ΔW_b	= energy of distortion which can be calculated with any linear elastic multilayer program
S_{mix}	= stiffness of the wearing course

The fatigue life was calculated using

$$N = \left\{ \frac{\left(3S_{mix}\pi \sin\varphi\right)}{\left(2\left(1+\nu\right)A\psi\right)} \right\}^{1/(z-1)} \varepsilon_w^{2/(z-1)}$$ (2.14)

Where:

N	=	number of load repetitions to failure
φ	=	phase angle between stress and strain as determined by means of stiffness tests
ν	=	Poisson's ratio
A, z	=	material parameters coming from the relation $W_f = A\,N^z$
W_f	=	total amount of dissipated energy in a fatigue test till failure
Ψ	=	$W_f/(N \cdot W_1)$; Ψ depends on whether the fatigue test is load or displacement controlled
W_1	=	amount of energy dissipated in the first cycle of a fatigue test

The authors concluded among other:
- Although the bitumen in the test sections had hardened to a substantial degree, most cracking surveyed had to be attributed to wheel-load induced factors. Nevertheless, thermal stresses seemed to have an effect as well.
- Cracking seemed to be initiated by traffic loads while propagation was probably due to temperature variations.
- Early ageing of the bitumen of the surface course should be prevented implying that attention should be paid to sufficiently thick bitumen films implying a sufficiently high bitumen content and a shift to coarser aggregate compositions. Furthermore, attention needs to be paid to the void content and degree of compaction.
- The work strain parameter seems to be a powerful parameter since it allows damage cq fatigue to be predicted at locations where this would not be possible using the classical approach.
- Failure criteria based on, for example, the Mohr-Coulomb model should be developed.

2.8.2. Finite element modelling, work done by Groenendijk, Delft University of Technology

Based on the findings reported above, it became clear that the actual contact pressure distribution could play a big role in the development of longitudinal top down cracking in the wheel paths which is so often observed. At the time the research mentioned in the previous section was done, such information was not available. It only became available when the South Africans had developed their VRSPTA [46, 47].
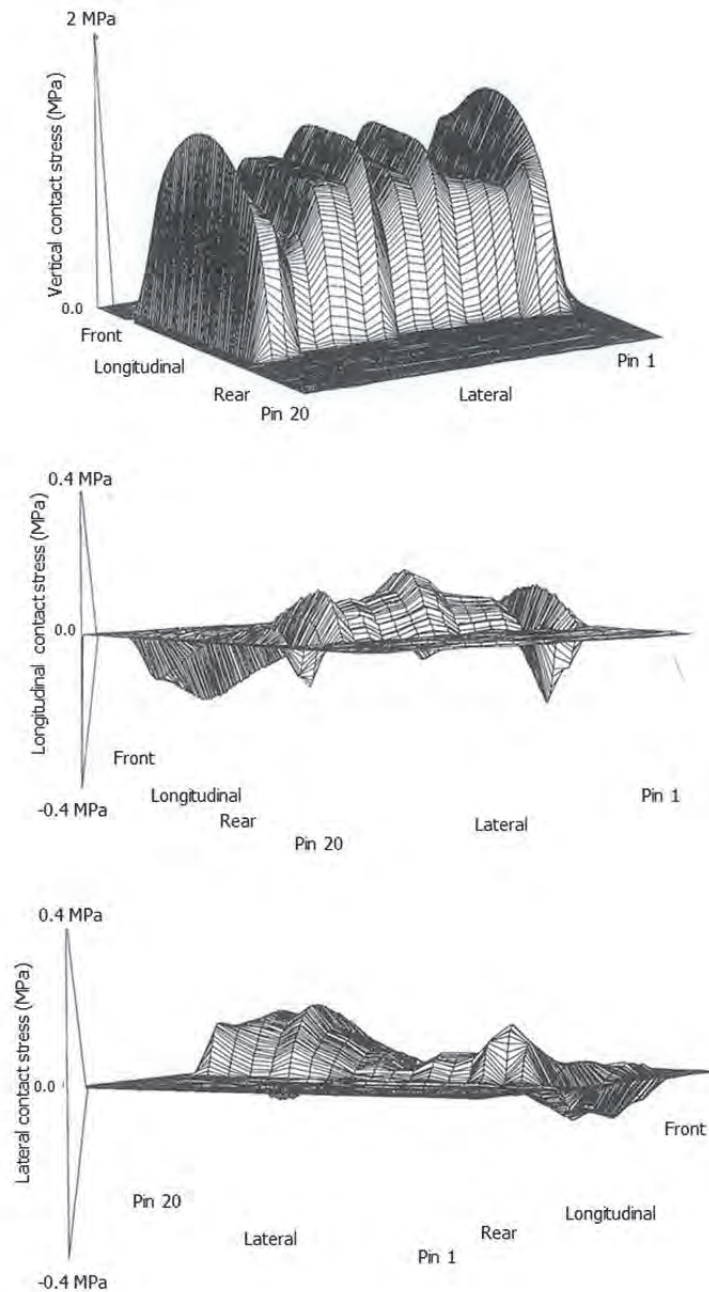
Figure 2.19. Example of contact pressure distributions as measured by Groenendijk [6] on a smooth tyre R160AZ, 75 kN, 950 kPa, 0.3 m/s

This device has been used by Groenendijk to determine the contact stress distribution under the tire that was used in the Lintrack experiments [7]. Examples of the distributions measured are shown in Figure 2.19. It was showed that especially the vertical stress distribution is very much dependent on the combination of wheel load and tire pressure.

Groenendijk used the CAPA finite element program [48] in analyzing the effect of contact pressure distributions, ageing of the top layer, and the presence of transversal compaction cracks on the development of surface cracking. Figure 2.20 shows the contact pressure distribution used in most of this analyses and Figure 2.21 shows the finite element mesh used.
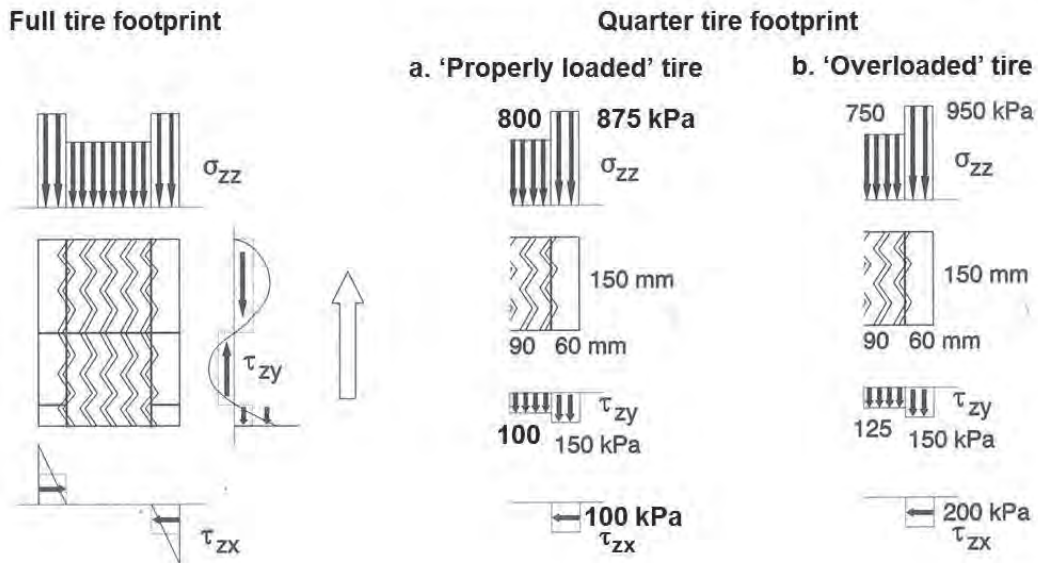
Figure 2.20. 3D wheel schematization for CAPA input
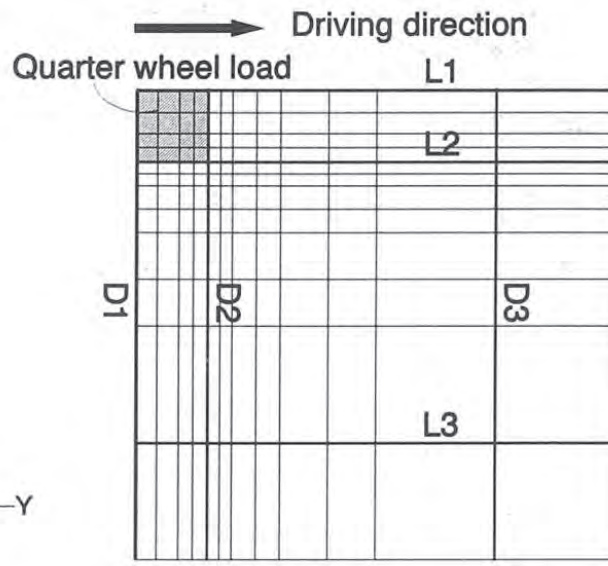
Figure 2.21. Finite element mesh used, after Groenendijk [7]

After an extensive analyses, Groenendijk concluded that given the rather low inward shear stresses as well as the rather uniform vertical stress distribution under the tire as used in his analyses, top down cracking could not well be explained. However, surface cracking will be triggered when tires are under-inflated with respect to the wheel load such that very high peak stresses occur at the tire edge. He, furthermore, showed that ageing of the top layer will increase the possibility of surface cracks. He stated that the effect of ageing on the occurrence of surface cracks is larger than the effect of the contact stress distribution. He also concluded that surface cracks which are already there because of shrinkage and, more importantly, those as a result of compaction, will certainly propagate because of the contact stresses. In the situation where the crack tip was at the wheel load edge, both the longitudinal and transversal crack will propagate faster horizontally than

vertically. Horizontal cracks, however, would not propagate beyond the wheel path.

Finally, he concluded "*that it is unlikely that contact stress distributions alone should be held responsible for the surface cracking often found in pavements, but they undoubtedly play an important role together with climatic influences like bitumen ageing and low-temperature cracking. Therefore, it is recommended that close approximations of the actual contact stress distributions should be taken into account in pavement design and analysis*"

2.8.3. Finite element modelling, work done by Myers, University of Florida

Using finite element modelling, Myers [13] tried to identify the mechanisms causing the development and propagation of longitudinal wheel path cracks at the surface of an asphalt pavement. To study the crack propagation 2D and 3D simulations were carried out with the commercial finite element software ABAQUS. In the model, Myers applied pre-cracking in the top of the asphalt layers with a variation of the crack position transversally under the wheel. Table 2.6 shows the structural parameters considered for the pavement structures investigated. A radial tire as shown in Figure 2.22 was used. This figure also shows the 2D finite element representation of the tire.

Table 2.6. Pavement structures used for FEM analysis, after Myers [13]

Parameters	Variation
Surface Layer Thickness, h_1, (in)	4; 8
Base Layer Thickness, h_2, (in)	12
Subgrade Thickness, h_3, (in)	90
Crack Length, a, (in)	0.25; 0.5; 0.75; 1.0; 1.5
Surface Layer Modulus, E_1, (ksi)	800; 1200
Base Layer Modulus , E_2, (ksi)	20.3; 44.5
Subgrade Modulus, E_3, (ksi)	14.5

Her findings show that the primary cause of the initiation of longitudinal wheel path surface cracks appears to be the generation of high tensile stresses underneath the treads of radial and wide-base (super single) radial truck tires.

It was found that the tire structure had a significant influence on contact stress distributions especially the lateral contact stresses rather than the vertical stresses. According to Myers it is, therefore, crucial to measure tire-pavement interface stresses, including lateral stresses, in the evaluation of pavement cracking performance.
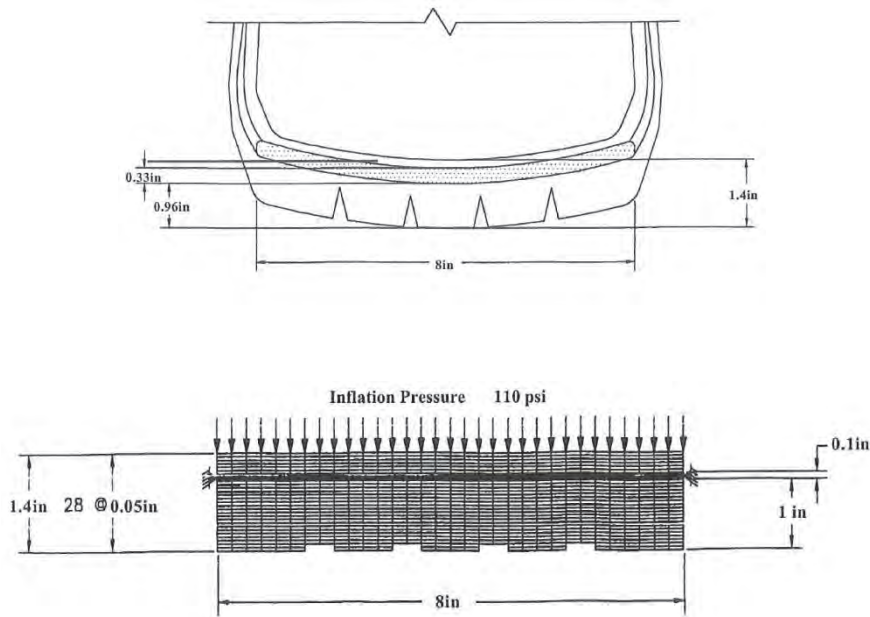
Figure 2.22. The cross section and the finite element representation of the typical radial tire, after Myers [13]

2.9. Accelerated pavement testing

According to NCHRP Synthesis 235 full scale accelerated pavement testing (APT) is defined as the controlled application of a prototype wheel loading, at or above the appropriate legal load limit to a prototype or actual, layered, structural pavement system to determine pavement response and performance under a controlled, accelerated, accumulation of damage in a compressed time period [49].

APT offers controlled conditions which allow performance tests to be conducted that can validate performance prediction models in a more reliable way. Although APT conditions are not 100% the same as real life conditions because of differences in terms of accelerated application of traffic loads (rest periods), ageing of materials, etc. APT allows the wheel loading to be applied, strains to be measured as well as other performance tests to be done under more or less controlled conditions. Especially, when placed in a shelter also the environmental conditions can be controlled. Anyway, the better controlled the conditions are, the better one should be able to predict the observed performance. As a golden rule one could state: "if we cannot predict what happens in APT then we will never be successful in predicting real life pavement performance" [39].

In 2004 there were 35 APT facilities around the world, but only 18 of them were actively operated [50]. Some of these APT facilities are operating in Europe, for example: Lintrack (the Netherlands); Manège de Fatigue of LCPC in Nantes (France); the mobile Heavy Vehicle Simulator (HVS)-Nordic

Countries (Sweden and Finland), Mobile Load Simulator (MLS) at EMPA (Switzerland) and BASt Mobile Linear Test Track (Germany). The question, however, is whether all these devices are equally suited to study pavement fatigue.

This issue was treated in a paper by Molenaar [39] which discussed extensively the requirements that should be set to Accelerated Pavement Testing facilities in order to be able to successfully use their results for modeling and predicting field pavement performance. In other words: are all APT devices for instance, equally suited to simulate pavement fatigue as a result of fast moving heavy traffic? APT programs performed by means of LINTRACK were used as case studies to support his findings which are given here-after.

- Testing asphalt pavements at low speeds and elevated temperatures will mostly reveal information about the resistance to permanent deformation behavior of the pavement and the materials used, unless the pavement materials used are stiff (concrete and asphalt with a high stiffness). Testing at low speeds and elevated temperatures is not suitable to obtain information about the fatigue resistance of pavements and the materials used in it.
- Doing tests at elevated temperatures and low speeds on asphalt pavements mostly implies that the permanent deformation which is observed is mostly caused by plastic flow of the skeleton and not really by viscous deformation of the bituminous mortar.
- When the pavement materials are stiff and elastic, fatigue studies can be done with APT's at low speed.

Molenaar, therefore, concluded that devices such as Lintrack, the South African HVS, and the Australian ALF are not very well suited for asphalt pavement fatigue studies while the French Manège de Fatigue is. Nevertheless, devices operating at low speed are extensively used for fatigue studies.

Dutch researchers have worked with devices operating at high speed (Manège de Fatigue and TxMLS) as well as with devices operating at a low speed (Lintrack). Results of their work when using these devices will be reported here.

2.9.1. Force Project

In 1988 a project called FORCE (First OECD Road Common Experiment) was conducted by the Road Transport Research programme of the Organization for Economic Co-operation and Development (OECD). The aim of the project was to develop a relation/connection between theory and laboratory testing on the one hand and field performance on the other, and to understand better the effect of traffic on road pavement behaviour.

(a)
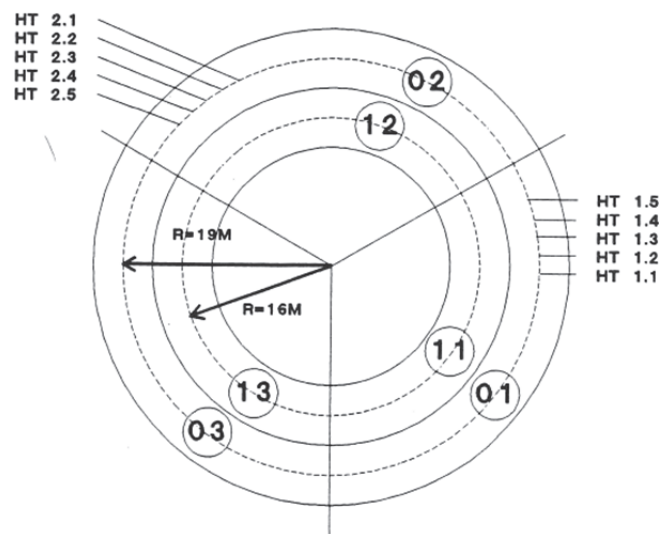
(b)

Figure 2.23. (a). LCPC's "Manège de Fatigue" (b). Section 01 and 02 and the location of the strain gauges of the FORCE project for the Dutch research team [5, 6].

The project was carried out in Nantes, France, in an accelerated pavement testing facility called "Manège de Fatigue". In this circular facility wheel loads can be simulated as high as 150 kN at speeds between 0 and 100 km/h. Figure 2.23 shows the circular fatigue test track of LCPC For the FORCE project pavement sections consisting of two asphalt layers laid on top of a granular base were built and tested.

Stas [5] did research on sections 01 and 11 (see Figure 2.23.b). The main objective was to determine a cracking performance model. The asphalt thickness of section 01 and 11 was 60 mm. Section 01 and 11 were trafficked by a 115 kN and 100 kN axle load respectively. Stas reports two models that describe the development of the amount of cracking as a function of the applied number of load repetitions. These models are the so called P_v and S_v model; they are shown in Equations 2.15 and 2.16.

$$P_V = 1 - \left(\frac{n}{N}\right)^b \qquad (2.15)$$

Where

P_v = the visual condition index defined as number ranging from 1 (no distress) to 0 (terminal level of acceptability)

n = number of wheel load repetitions

N = Pavement life, number of wheel load repetitions until Pv = 0

b = curve fit parameter that defines the degree of curvature of the performance curve,

$$S_V = (S_f - S_0)e^{-\left(\frac{\rho}{n}\right)^\beta} \qquad (2.16)$$

Where

S_v = condition at a specific value of applied wheel load repetitions, expressed as percentage cracked area

S_f = asymptotic value of final distress

S_0 = initial condition

ρ = curve fit parameter that denotes the expected number of wheel load repetitions to a S-value of (1-1/e) x 100%

β = curve fit parameter that defines the degree of curvature of the performance curve

n = number of wheel load repetitions

A comparison of both models to the observed data for section 01 is shown in Figure 2.24. It is clear that the simple Pv model can only be used to predict limited amounts of damage, it does not describe the "full" cracking development.
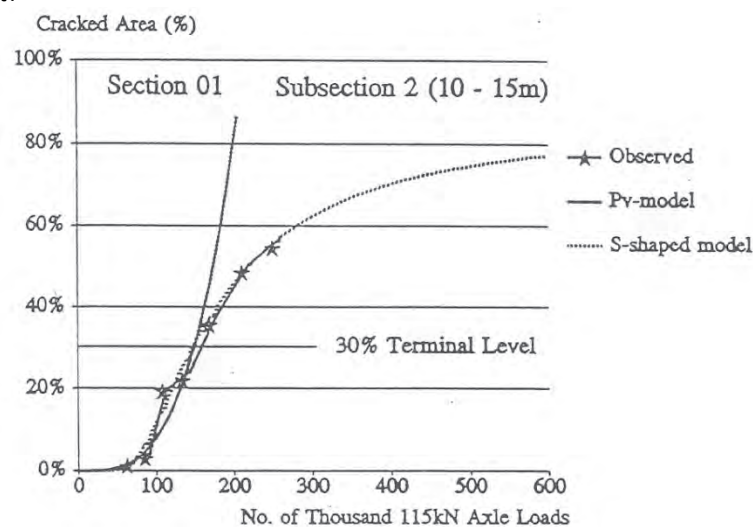
Figure 2.24. Pv and Sv model compared with the observed data

It is important to mention that a 73 mm thick overlay was placed on section 01 after 25900 wheel load repetitions because the 60 mm asphalt layer showed extensive cracking after that number of load repetitions.

Holster [6] analysed sections 01 and 02 (see Figure 2.23.b) of the FORCE project. As mentioned previously, the asphalt thickness of section 01 was 60 mm while for section 02 it was 120 mm. These sections were trafficked by a 115 kN axle load at speeds varying between 72 and 86 km/h. In his report Holster compared the observed pavement response in terms of measured strains and visual distress with the response predicted using the results of laboratory experiments, layer moduli back-calculated from deflection measurements and linear elastic multilayer analyses.

He examined the strain measurements results and compared the strains measured due to a falling weight load to those which were calculated with Bisar. From Figure 2.25.a. it can be seen that for section 01 all the measurements below 500μm/m show an acceptable agreement between predicted and measured pavement response. But above that value the predictions are always lower than the measurement values. For section 02 (Figure 2.25.b.), the strain values calculated using BISAR are in all cases higher than the strain measured at the bottom. Holster concluded that for section 2 the difference between predicted and measured pavement response is about 20% (around 25 μm/m). When all the data are put in one figure and a regression analysis is made, as is shown in Figure 2.26, one may notice that the difference between measured and predicted becomes pronounced at strain levels higher than 400 μm/m.
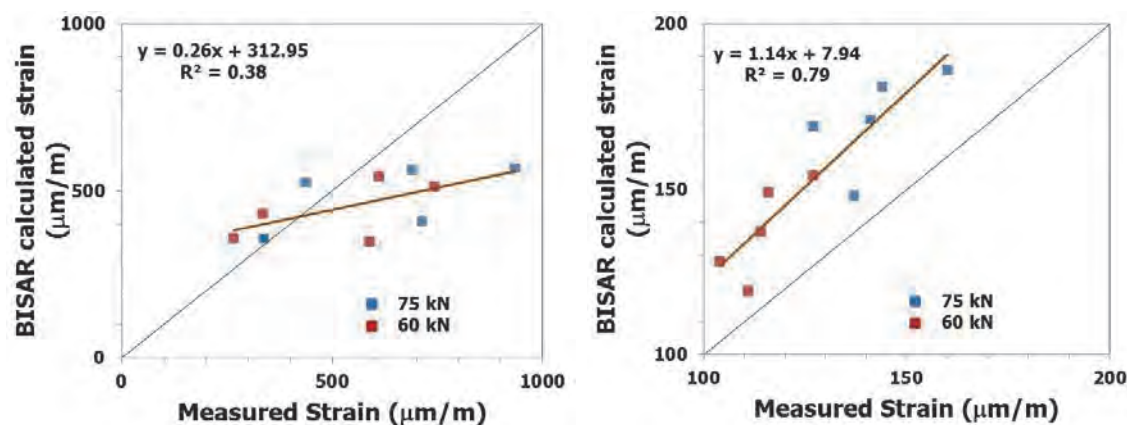
a. Section 01 (60 mm asphalt layer)   b. Section 02 (120 mm asphalt layer)

Figure 2.25. Comparison of calculated and measured asphalt strain due to FWD loading [6]
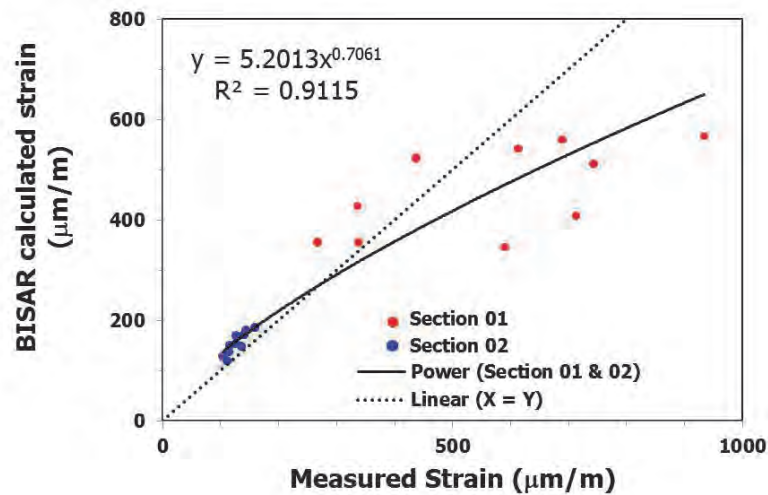
Figure 2.26. Calculated and measured asphalt strain for section 01 and section 02

Holster also calculated the fatigue life of section 01 using the tensile strains measured at the bottom of the asphalt layer at five locations and compared it with the fatigue characteristics of the asphalt mixture as determined by means of 4PB fatigue tests. The tests were carried out at the RRR Laboratory of the DUT [51]. This comparison is shown in Figure 2.27. It should be noted that the fatigue relations shown in Figure 2.27 are already corrected for influences like lateral wander (correction factor = 2.5) and healing (correction factor = 4). It appears from this figure that the fatigue life should have been between 2×10^4 and 2×10^6 load repetitions. When healing is not taken into account, which is a reasonable assumption since the back calculated asphalt layer stiffness was very high > 10,000 MPa, these numbers are 2.5×10^3 and 0.5×10^6. According to the cracking patterns that were determined after certain numbers of load repetitions (see Figure 2.28), the pavement started to crack at location 4 after 72,600 repetitions, at location 5 after 95,000, at location 3 after 113,000, at location 2 after 177,000 repetitions. Crack initiation at location 1 is difficult to determine because it looks like cracks started to develop there as a result of crack propagation from the neighbouring area rather than because of initiation at location 1. Except for location 1, the order of calculated number of load repetitions to failure as derived from Figure 2.27 (4-5-3-2) is approximately the same as the order of the number of load repetitions at which cracking appeared as shown in Figure 2.28 (5-3/4-2).

Therefore, It can be concluded that for this pavement there is a reasonable agreement between the calculated pavement life based on the tensile strain measured at the bottom of the asphalt layer and the appearance of cracking at the pavement surface.
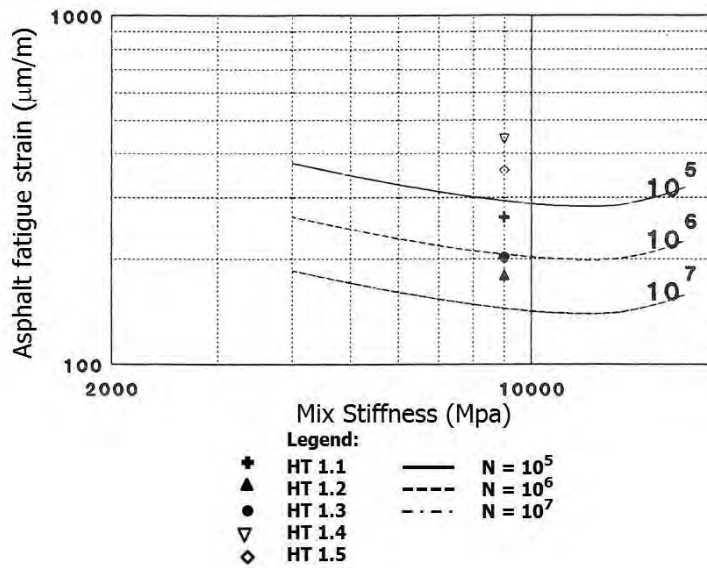
Figure 2.27. Fatigue relation based on Four Point Bending Test
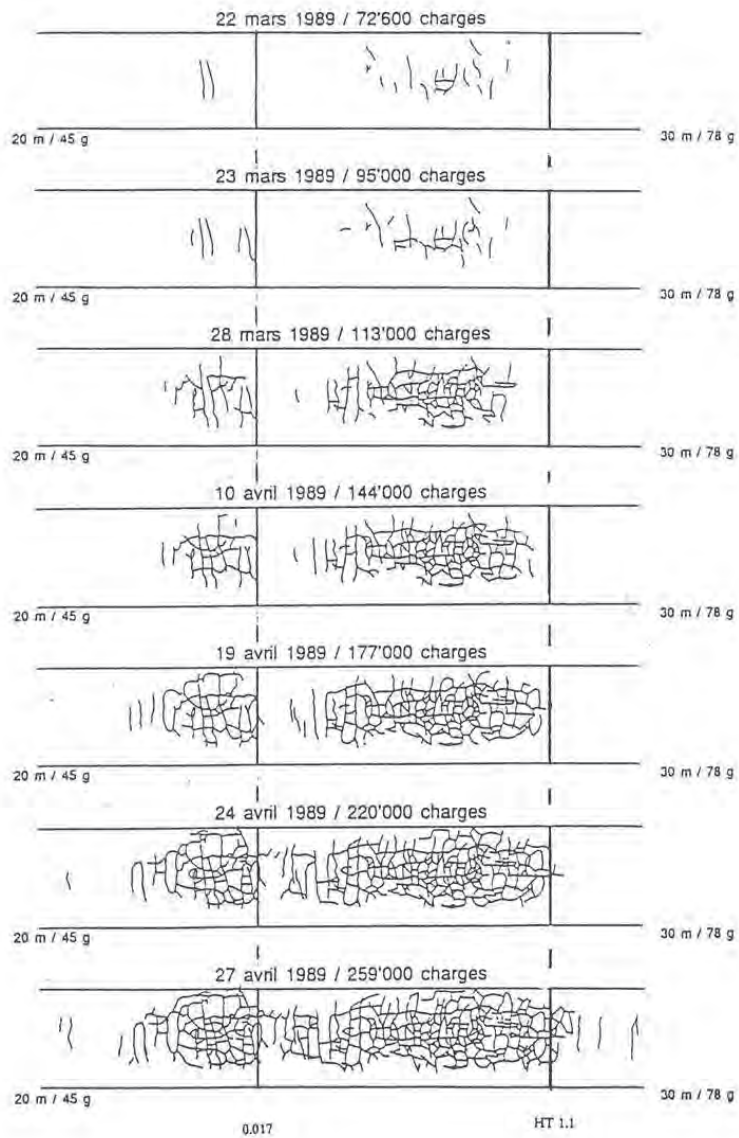
Figure 2.28. (a) Cracking pattern of section 01 from 20 to 30m
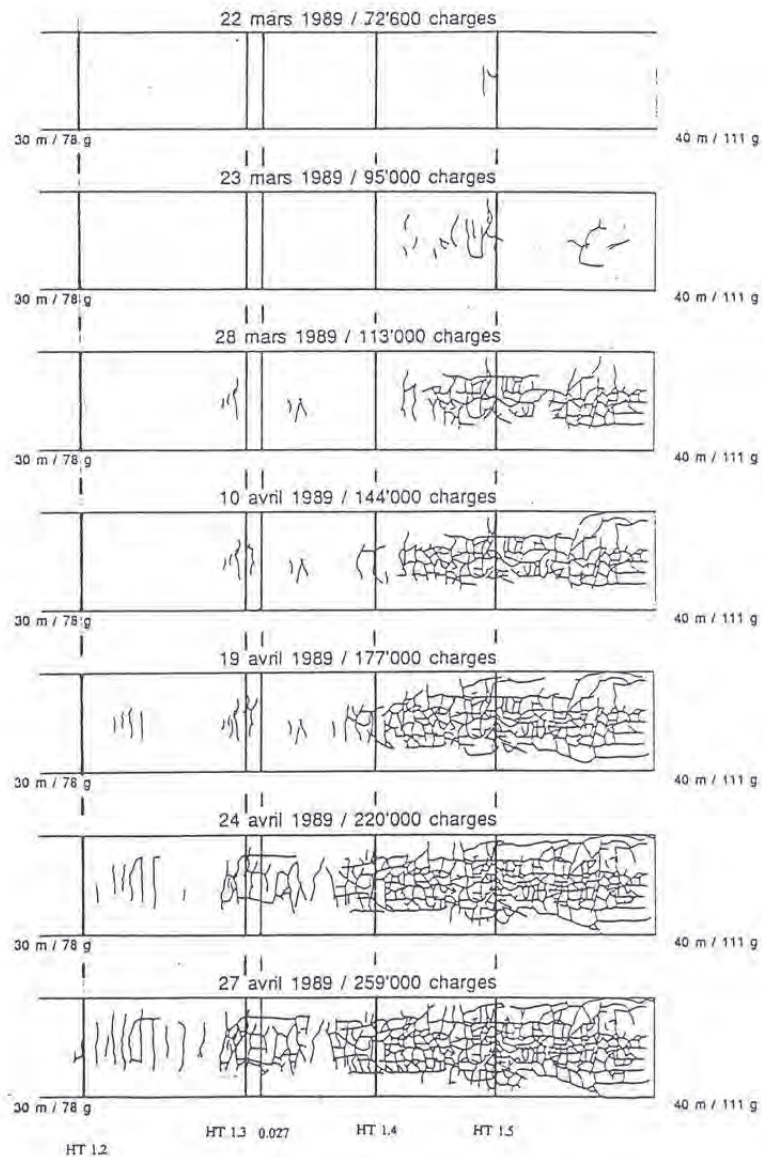
Figure 2.28. (b) Cracking pattern of section 01 from 30 to 40m

2.9.2. Texas Mobile Load Simulator

In 1994 Visser [10] analysed results that were obtained using the TxMLS (The Texas Mobile Load Simulator). The TxMLS is an APT device that consists of wheels which are attached to an oval bogies rail (Figure 2.29). The load is delivered via the weight of the structure against the bogie and can be changed. The carrousel contained 6 bogies of which 2 were driven. The advantage of this APT device is the large number of load repetitions that can be applied in a short time at a reasonable speed. With its twelve circulating axles, traffic loads can be applied at a rate of more than 10.000 equivalent real axle loads per hour [52]. Due to the closed loop this mobile equipment can be transported to track/test sites to simulate the effect of future traffic loads to the pavement under investigation. Because of the high operating and maintenance costs the device has been taken out of service.

The track tested during Visser's research was a four layer system consisting of a 50 mm thick asphalt surface layer; a 300 mm thick flexible base (granular base); 150 mm lime treated subgrade and a subgrade of sand with some clay layers deeper in the subgrade. The top layer was a so-called "type D" hot-mix asphalt layer according to the Texan specifications. The average air void of specimens after loading with the MLS was 10.4% while the voids content of specimens taken from areas that were not subjected to the TxMLS loading was 13.5%. The bitumen content was estimated to be 9% by volume. For this particular research the applied axle load during testing was pre-set at 75.6 kN and the average speed was 19.2 km/h.
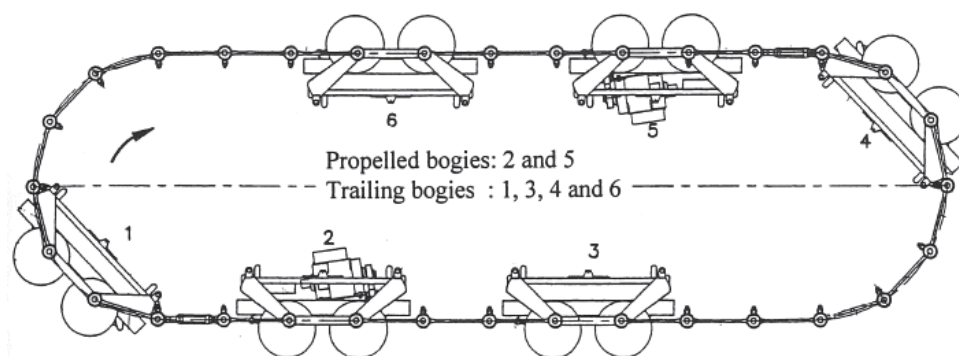
Figure 2.29. The closed loop bogie of the TxMLS [10]

Visser collected a huge amount of data from the tested pavements including falling weight deflectometer test data and data obtained from laboratory tests on the pavement materials. However, one basic piece of information was missing being fatigue test data. Therefore, he had to make major assumptions on the fatigue characteristics of the asphalt mixture used in the test sections. He decided to estimate the fatigue characteristics using the Shell equations (Shell) [53] and the Asphalt Institute (MS-1) [54] method. The most important differences between the fatigue lines estimated by means of these methods are:
  - The slope of the fatigue line has a fixed value of -5 in the Shell equation, and -3.29 in the MS-1 method
  - Shell developed the equations using displacement controlled tests while the MS-1 fatigue characteristics are based on force controlled tests.

A comparison between the Shell and MS-1 fatigue lines for Vb=9% (binder volume); Va=13.5% (voids content) and a mix stiffness of 3000 MPa (the Vb, Va and Smix values were average values for the asphalt mixture as laid) is shown in Figure 2.30.
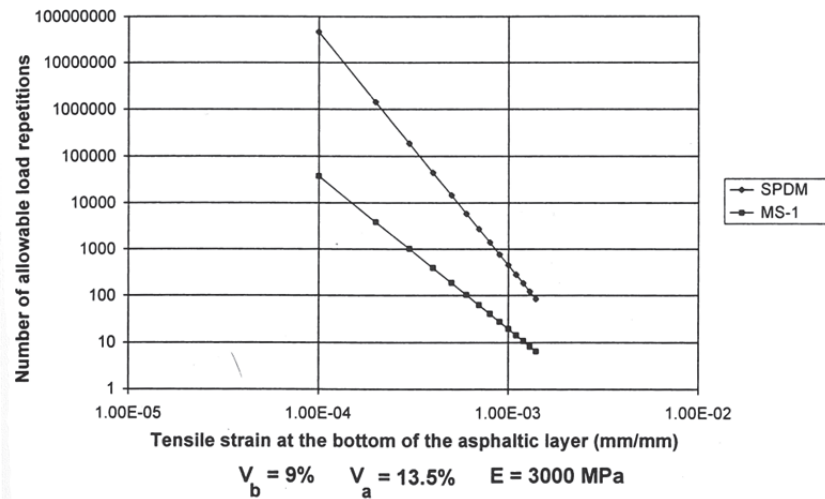
Figure 2.30. The comparison of the fatigue lines of the SPDM and MS-1 method for E=3000 MPa based on assumptions made by Visser [10].

Based on the calculated tensile strain at the bottom of the asphalt layer and using the fatigue characteristics mentioned above, Visser calculated the pavement life and compared the predicted number of axle loads with the number of axle loads that were needed till 45% of the trafficked lane was cracked. The next step was to calculate a shift factor to match the predicted number with the observed number of axle loads (See Equation 2.17).

$$SF = \frac{N_a}{N_p} \qquad (2.17)$$

Where:
N_a = actual number of load repetitions to 45% cracking,
N_p = predicted number of load repetitions

The shift factors (SF) as calculated for a number of locations are shown in Table 2.7. It should be noted that N_p is calculated using the average values for layer thicknesses, layer moduli, etc.

As can be seen from Table 2.7, the SF based on the Shell fatigue line is fairly close to 1. Secondly one will note that the discrepancy between the SF of Shell and SF of MS-1 is quite high. The main reasons are that the Shell relation is based on constant displacement fatigue tests while the MS-1 relation is based on constant force fatigue tests. Furthermore, the MS-1 relation is predicting 10% cracked area while the shift factor is based on comparing the number of load repetitions to 45% cracking.

One of the things Visser's work is clearly pointing at is that knowing the material characteristics (for example fatigue characteristics) as function of the actual loading conditions is vital in order to be able to compare predicted with observed fatigue performance.

Table 2.7. Shift factor based on Shell and MS-1 fatigue relationships

Position	Shift factor Shell fatigue line	Shift factor MS-1 fatigue line	Position	Shift factor Shell fatigue line	Shift factor MS-1 fatigue line
A1	1.21	320	C1	1.70	367
A2	57.9	3812	C2	4.70	704
A3	4.96	788	C3	4.24	836
A4	9.95	863	C4	2.48	465

In his report Visser made some comments with respect to the type of information that was missing. These comments are listed below since they are considered to be very important showing that doing APT research is much more than just operating the APT device.

Visser concluded that: *"Of the pavement structure parameters, the layer thickness and number of layers were known. However, the difference in thickness of the asphaltic layers was only encountered after testing. If a construction log-book had existed and some rod and level measurements after the construction of each layer were executed, this information would have been available. Another possibility would have been to execute drillings outside the tested area, to obtain further information.*

The material information had seven main problems:
- *tests on the asphaltic materials were executed using different types of tests in a very limited temperature and frequency domain;*
- *tests were only executed on cores drilled after loading the pavement;*
- *no performance related tests were executed;*
- *the executed tests didn't relate to a specific design method, which makes validation of an empirical-mechanistic design method an impossible task;*
- *hardly anything was known about the variation of the material characteristics over the pavement area, partly because it was unknown from which area the cores resulted, partly because no other types of measurements were executed to obtain for instance information about the density of the material.*
- *hardly any information was available about the mix-composition;*
- *no information was available about the change of the material parameters over time.*

For further tests it is advisable to take into account the above mentioned comments.

Of the environmentally important parameters only average air-temperatures were available for the total duration of the test. The author believes that the breakdown of the weather station should have given the same type of alert as the breakdown of the APT-device. Other environmentally important

parameters, which could have been monitored if the weather station wouldn't have broken down, are:

- *moisture in the structure;*
- *pavement temperature;*
- *humidity;*
- *solar radiation;*
- *water tables;*
- *subgrade.*

It is advisable to measure these items in future tests.

No documented information about the construction was available. For future test-site this information should be tried to retrieve."

2.9.3. Lintrack

Lintrack (Linear TRACKing device) is an accelerated pavement testing facility jointly owned by the Road and Railroad Research Laboratory (RRRL) of the Delft University of Technology (DUT) and the Road and Hydraulic Engineering Division (RHED) of the Dutch Ministry of Transport, Public Works and Water Management. The loading system of LINTRACK can be equipped with a dual or a single wheel, the latter can be equipped with a super single tire, and loads between 15 and 100 kN can be applied. Figure 2.31 shows the Lintrack facility. The total running length of the wheel is 12 m but due to the acceleration and deceleration in the beginning and the end, the maximum constant speed of 20 km/h is reached in the central 4 meter of the section. Lintrack can simulate both one and bi-direction traffic. The Lintrack device is protected from climatic influences -such as rain and sunshine- by means of a mobile hall. The entire equipment and the mobile hall are mounted on rails across the length of the test area, so they can be moved sideways easily to access other test sections [7].

Many tests have been done by means of Lintrack. For this thesis the test program to validate the RHED pavement design method is of importance and these results are extensively used in this research.

The aim of the RHED pavement design manual (RHED 1994) was to design a flexible pavement in such a way that fatigue cracking at the bottom of the asphalt concrete only occurs after the design number of load repetitions. Because of the fact that most of the Dutch highways at that time showed a very limited amount of bottom up cracking, the Ministry of Transportation was wondering whether the manual was resulting in overdesigned pavements [39].

Figure 2.31. APT facility Lintrack

For this purpose, four identical lanes (section I to IV) were built by a contractor in 1990 on the test field of the RRRL. These pavements consisted of 150 mm Gravel Asphalt Concrete (GAC) structures laid on top of a compacted sand subgrade. Each section was 16 m long and 4 m wide. After testing of lane I, it was decided to perform another test with the same loading condition but on a thinner construction. Therefore, the asphalt thickness of the second test lane (II) was reduced by milling it in May 1995 from 150 to 80 mm and the same was done for the third lane (III) in June 1996. These milled off sections with a thickness of 80 mm asphalt were called 'VA' and 'VB' respectively. Table 2.8. provides the details of the thickness and the loading conditions of the three sections [7].

Table 2.8. Details of the three Lintrack sections used in this thesis

Section's name		Asphalt thickness [mm]		Asphalt mixture	Load characteristic
I		150 (80+70)		GAC	super single F = 75 kN, p = 950 kPa
II	**V$_A$**	150	80	GAC	super single F = 75 kN, p = 950 kPa
III	**V$_B$**	150	80	GAC	super single F = 50 kN, p = 700 kPa

GAC : gravel asphalt concrete; F = wheel load, p = tire pressure

A gravel asphalt concrete mixture was used since at that time it was commonly used as a base course mixture for all flexible pavements in the Netherlands. The air voids of the compacted GAC was approximately 4.5% and the 40/60 pen bitumen content was approximately 4% by total mass of aggregates.

During the Lintrack tests the following measurements were made:
- horizontal strain measurements at the bottom of the asphalt layer, both in the transversal (DT) and longitudinal (DL) direction;
- vertical stress in the subgrade, 0.15 m below the asphalt;
- pavement and surrounding temperature;

- transverse profile measurements to determine the amount of permanent deformation;
- surface deflection measurements using a falling weight deflectometer;
- visual condition surveys;
- photographic registration of the pavement surface;
- collection of climatic data.

Moreover, the asphalt concrete was extensively tested in order to determine its stiffness modulus as function of temperature and load frequency and its fatigue resistance.

In his research on these Lintrack sections Groenendijk [7], Groenendijk and Vogelzang [9] and Bhairo [55] focused on two aspects being:
   a. correlation of the observed performance with predicted performance
   b. modelling of the surface cracking phenomenon.

For the last objective, extensive studies on tyre–pavement contact stress distributions were done and the results of this work have been discussed in the previous section.

The fact that combining different types of measurements and matching theory with practice is not an easy task is extensively discussed by Groenendijk and is illustrated by means of some examples here-after. Figure 2.32 for example shows the amount of cracking observed at section I after 2.5 million load repetitions while Figures 2.33 and 2.34 show how the peak strains changed with increasing number of load repetitions.
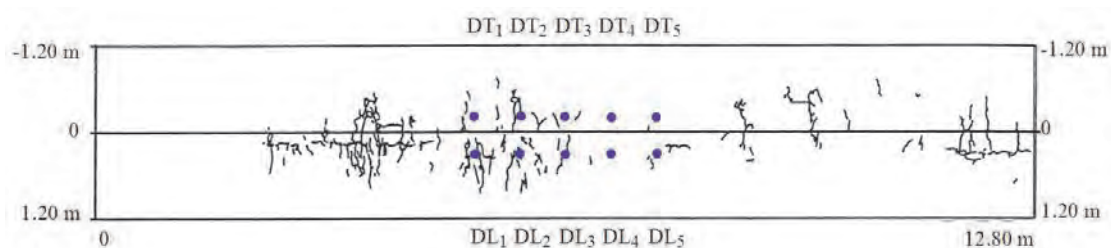
Figure 2.32. Overview of cracks observed on Lintrack section I after 2.5 M cycles (adapted from Groenendijk [7])
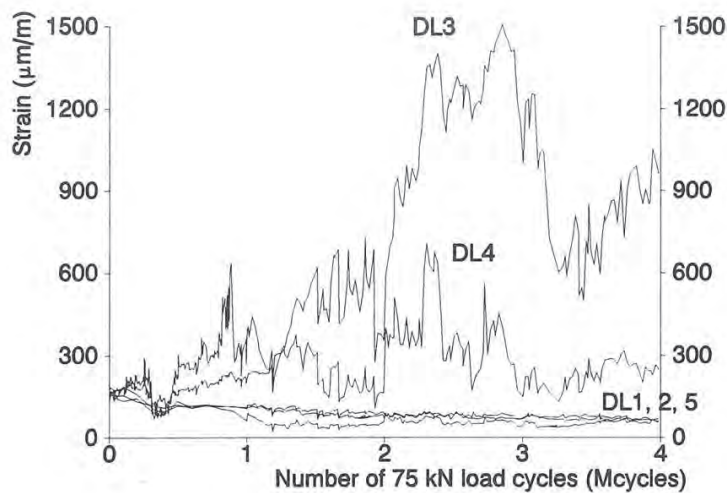
Figure 2.33. Strain peak development on longitudinal direction (Lintrack section I, corrected to 15°C)
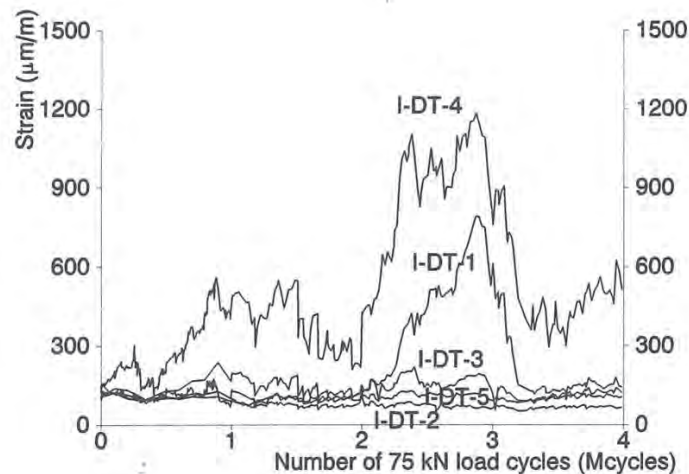
Figure 2.34. Strain peak development on transversal direction (Lintrack section I, corrected to 15°C)

The figures show that the large increase in tensile strain that has been observed in locations DL3 and DL4 (locations of longitudinal strain gauges) and at the I-DT-1 and I-DT-4 locations (locations of transversal strain gauges) is not or hardly reflected in the crack pattern visible at the top of the pavement. Only 4 out of the 10 strain gauges (DL3, DL4, I-DT-4, I-DT-1) are giving such high strains values that one can consider the pavement to be 'fatigued' at those locations. At location 4 both strain gauges indicate 'fatigue' while no damage at the pavement surface was visible. Coring at location 3 later on showed that a hairline crack was crossing the DL3 gauge perpendicular but this crack did not propagate through the entire thickness. The observations made above imply that 'measuring damage' is something else than 'seeing damage'. This certainly complicates attempts in matching observed with predicted damage.

Another problem which complicated significantly the analyses made by Groenendijk was the fact that especially during testing of section I long rest periods (some were as long as a few months) occurred because the Lintrack device was out of order because of maintenance. It was very difficult to estimate the effects of these prolonged rest periods, during which the pavement had time to recover, on its performance.

A very important question when analyzing pavement performance is how 'end of pavement life' is defined. From a road user point of view end of pavement life is defined as the moment where traffic safety, because of a poor pavement condition, becomes an issue, or when the vehicle operating costs start to increase sharply and travel speed significantly decreases. When pavement design systems like the SPDM are used, traffic safety etc. are not the design parameters; the thickness design of the pavement is controlled by fatigue of the asphalt layer. The question then really is 'what is end of pavement life'?

Groenendijk in his work answered this question by putting in one chart the cracking behaviour, rut depth development, and back calculated asphalt modulus as function of the number of load repetitions. Examples of these charts are given in Figures 2.35 and 2.36.
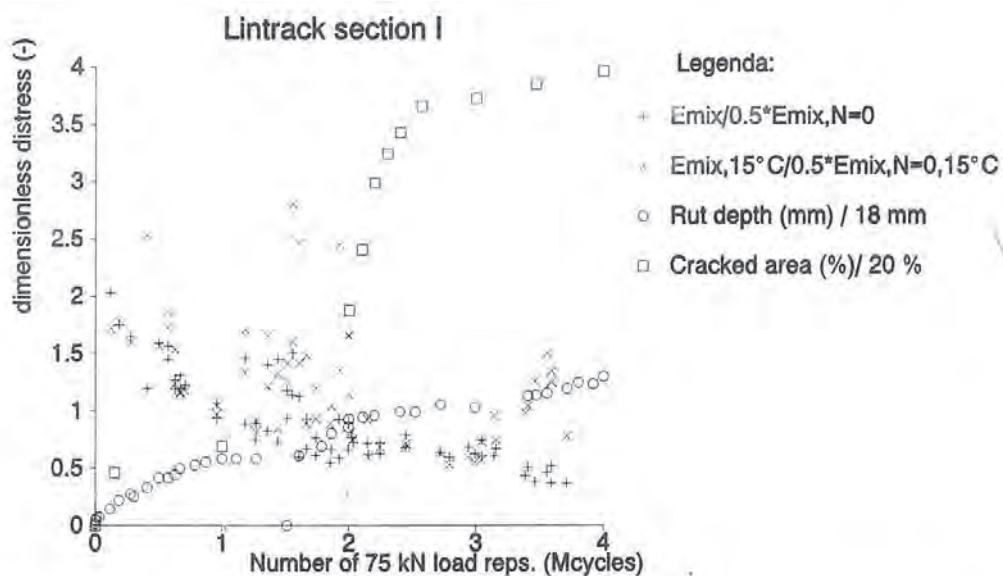
Figure 2.35. Development of condition parameters versus loading cycles of Lintrack Section I
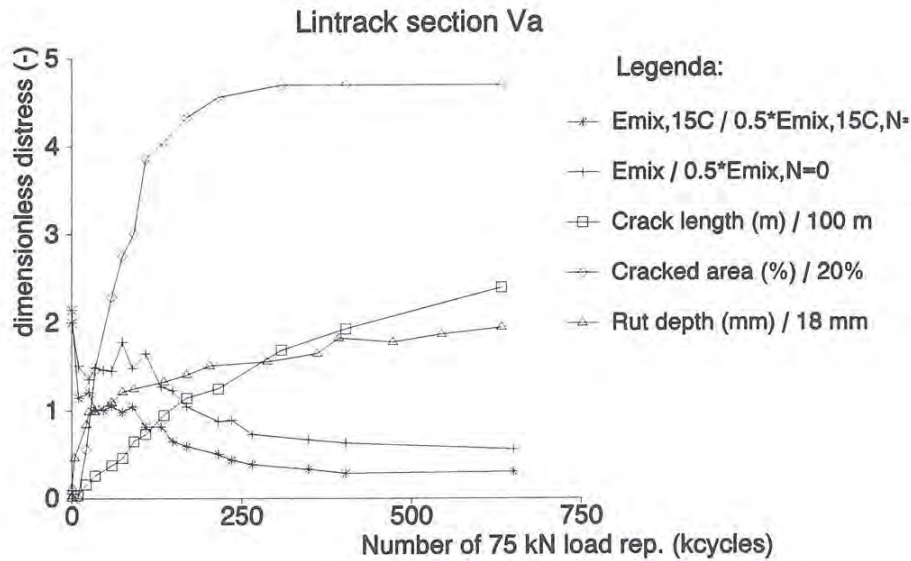
Figure 2.36. Development of condition parameters versus loading cycles of Lintrack Section VA

The number of load repetitions at which the asphalt modulus had decreased to 50 % of its initial value was proposed as 'end of pavement life' because a similar definition is used in laboratory fatigue tests. From the figures one can derive that this moment coincided with the number of load repetitions at which the size of the cracked area amounted approximately 20%. It is interesting to note that in section I cracking increased rapidly after this amount had been reached.

Using this definition Groenendijk concluded that for all sections, the observed fatigue life was longer than the fatigue life that was predicted using multi-layer linear elastic theory and fatigue relations. For section 1 a shift factor around 5 to 15 was needed to match the predicted fatigue life with the observed fatigue life. The shift factor was 1 to 10 for section VA and 2 to 25 for section VB. The magnitude of the shift factor depended on how certain influence factors like healing were taken into account and on the fatigue relation used. One of the problems was that fatigue data were only determined at a loading frequency of 30 Hz and temperatures of 0°C and 20°C, while during the Lintrack tests the loading frequency was between 3 and 8 Hz and temperatures during testing varied between -6°C and 26°C. Using results from tension tests and by applying fracture mechanics principles, Groenendijk estimated fatigue relationships applicable for the Lintrack loading and temperature conditions but in doing so some major assumptions had to be made.

Groenendijk, furthermore, showed that the subgrade strain criterion to be used for the sand subgrade (which was typical for sand subgrade in the Netherlands) was between the 50% and 85% confidence level subgrade strain criteria as mentioned in the Shell Pavement Design Manual (see Figure 2.37).

N 10^8

$\epsilon_3 = 2.8 \times 10^{-2} \times N^{-0.25}$

50% Confidence level

95% Confidence level

Section I

Section Vb

Section Va

10^7

10^6

10^5

10^4

10^{-4} 10^{-3} 10^{-2}
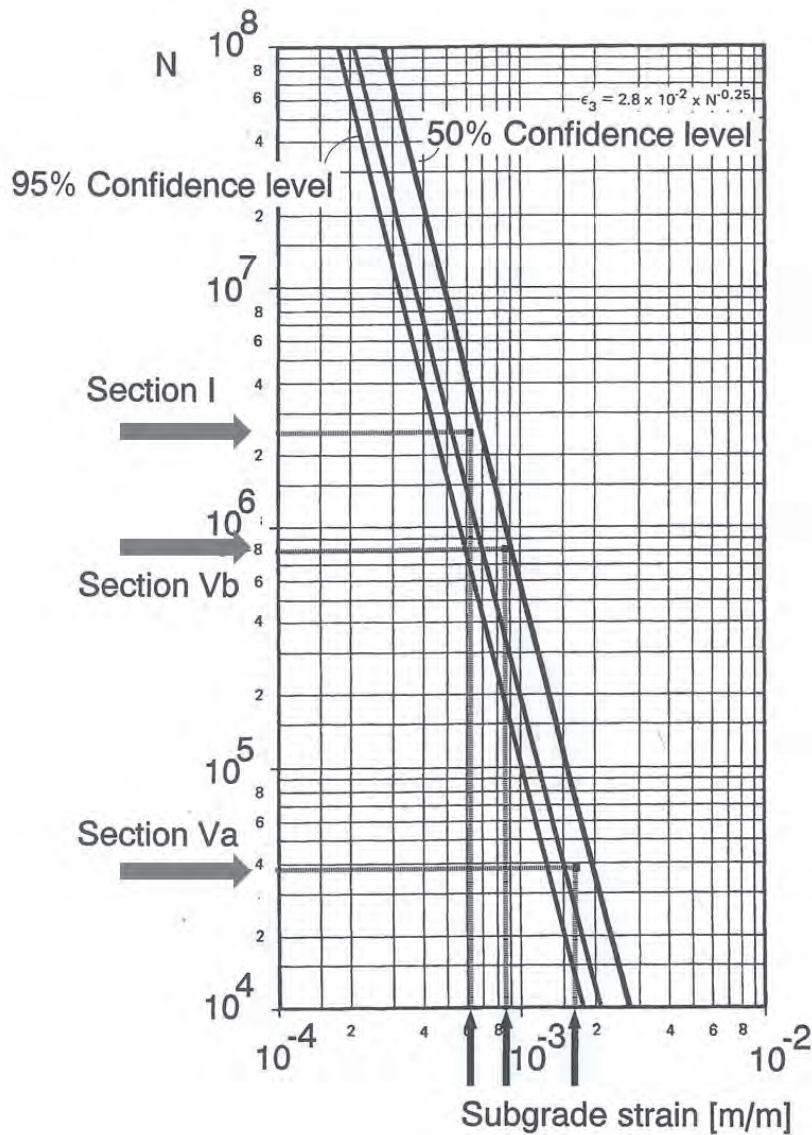
Subgrade strain [m/m]

Figure 2.37. Lintrack result on the Chart RS Shell subgrade strain criterion with 85% and 95% confidence limit

2.9.4. Conclusions on APT

Based on the work done in the FORCE project and by Visser and Groenendijk one can conclude that matching theory to practice, even in controlled APT conditions, is not an easy task. As mentioned before APT research should be supported with extensive and appropriate laboratory research. Furthermore, the effects of changing environmental conditions (temperature and moisture) should either be excluded by doing the experiments in environmentally controlled conditions or by carefully monitoring the changes in environmental conditions during the tests.

2.10. Advanced modelling to match theory with practice

In 1997 the Road and Railway Engineering Group and the Structural Mechanics Group of the Civil Engineering Faculty of the Delft University of Technology started the Asphalt Concrete response (ACRe) project. One of the primary goals of this project was to developed material models which have the capability to describe the nonlinear response of asphalt mixtures as well as damage initiation and propagation [14, 56, 57]. The ACRe model was developed based on the hierarchical single surface (HISS) criterion proposed by Desai [1986]. By implementing it into a 3D FEM (CAPA), which enables to simulate the non-linear dynamic response of the pavement, it is believed that the model has the ability to explain the damage development of asphalt mixes in pavement layers [37]. The model has been used successfully to model for example the semi-circular bending (SCB) test, the indirect tension test (ITT) [14] and was also very successfully used to model the behaviour of asphalt surfacing on orthotropic steel bridge decks [58].

The background of this modelling work will not be presented here. The interested reader is referred to the available literature [14, 58-61]. Here only the work that was done for Kraton B.V. in evaluating the benefits that could be achieved by using their polymer modifications will be summarized. This work has been reported in among other [62].

In an extensive laboratory testing program, the failure envelopes of different polymer modified mixtures as well as other mixtures were determined by means of uni-axial tension and uni-axial compression tests. Examples of such envelopes are shown in Figure 2.38.
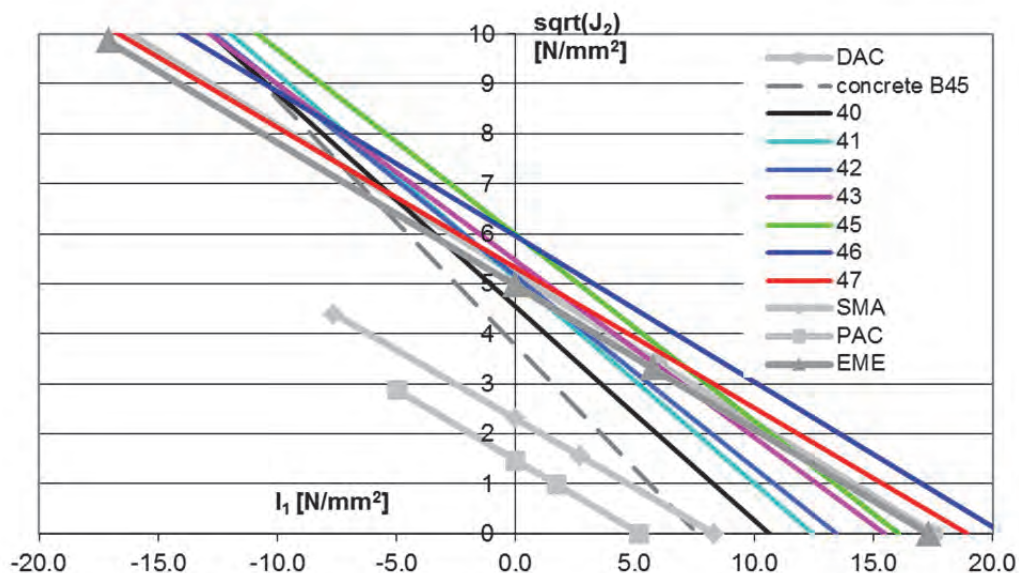
Figure 2.38. Ultimate slopes of the tested mixtures at T = 5°C and strain rate = 0.1 %/s together with concrete (Concrete B45), Dense Asphalt Concrete (DAC), Stone Mastic Asphalt (SMA), Porous Asphalt Concrete (PAC) and base course mix Enrobé à Module Elevé (EME) [62]

The material model, which was used to describe the response of the asphalt mixtures is based on the flow surface proposed originally by Desai [60, 63] and further developed by Scarpas [61, 64] (1997), Erkens [14], Liu [59] and Medani [58] resulting in the Asphalt Concrete Response (ACRe) material model.

The ACRe model is relatively simple in terms of number of material parameters and every parameter has a clear physical meaning. The surface is continuous and hence avoids discontinuity problems of multi-surface models.

In the stress invariant space, the chosen form of the model yield function F is given by:

$$F = \frac{J_2}{p_a^2} - \left[-\alpha \left(\frac{I_1 - R}{p_a} \right)^n + \gamma \left(\frac{I_1 - R}{p_a} \right)^2 \right] = 0 \qquad (2.18)$$

where I_1 and J_2 are the first and second stress invariants, p_a is the atmospheric pressure, α, β, γ, n and R are the model parameters depending on the material characteristics.

In 3D space, Equation 2.18 represents a closed surface, as shown in Figure 2.39. The value of the yield function F determines the response of the material to a state of stress. For F<0, the state of stress is within the yield surface and the response of the material is elastic. For F=0, the state of stress is on the yield surface and the response of the material is inelastic. States of stress outside the yield surface cannot exist.
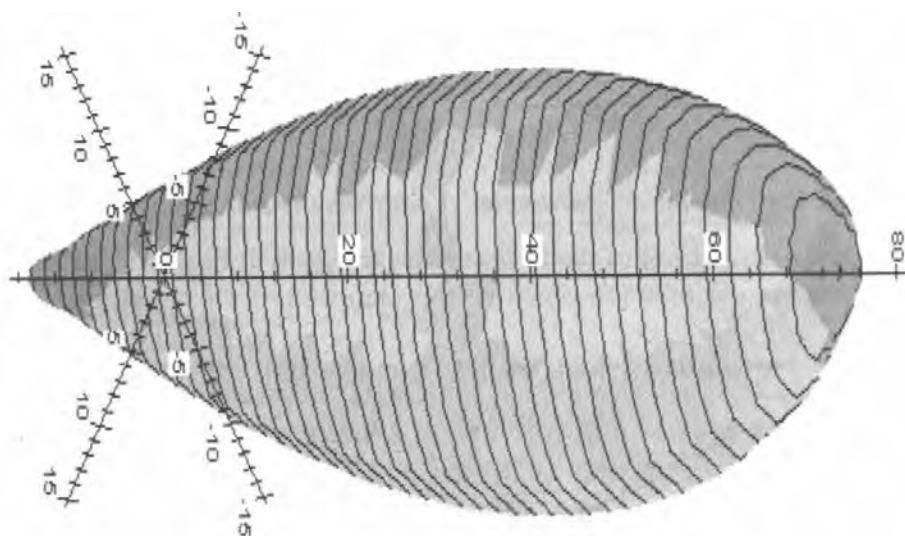
Figure 2.39. Schematic representation of Desai response surface

The constitutive framework of the material model is based on the theory of rate dependent consistent plasticity as proposed by Scarpas and Blaauwendraad (1998) [64] and Liu (2003) [59].

The parameters of the material model were determined using the results of uni-axial monotonic compression and tension tests, and the dependency of the material properties on strain rate and temperature was taken into account. This allowed defining a flow surface at any given combination of strain rate and temperature.

In order to interpret the FEM simulation results, it was necessary to introduce a definition of damage. Damage was defined as the cumulative amount of plastic strain (ε^p) in the material. In mathematical terms, damage denoted as ξ can be defined as:

$$\xi = \sqrt{d\varepsilon_{ij}^p : d\varepsilon_{ij}^p} = \sqrt{d\varepsilon_{xx}^p \cdot d\varepsilon_{xx}^p + d\varepsilon_{yy}^p \cdot d\varepsilon_{yy}^p + d\varepsilon_{zz}^p \cdot d\varepsilon_{zz}^p + d\varepsilon_{xy}^p \cdot d\varepsilon_{xy}^p + d\varepsilon_{yz}^p \cdot d\varepsilon_{yz}^p + d\varepsilon_{xz}^p \cdot d\varepsilon_{xz}^p} \qquad (2.19)$$

The total damage can be divided into volumetric and deviatoric (shear) components. The volumetric damage can further be subdivided into compressive volumetric deformation and tensile volumetric deformation.

This helps in understanding what kind of damage is developed. Compressive volumetric damage is associated with permanent deformation of the material (rutting). Tensile volumetric damage is associated with cracking. Deviatoric damage is the result of tensile-compressive states of stress and can lead to Mode II (the sliding or shearing mode) associated cracking.

The ultimate goal of this investigation was to acquire insight into the mechanical performance of polymer modified asphalt mixtures in actual pavement structures. The behaviour of the pavement structure was simulated by means of the finite element system CAPA-3D. The finite element mesh, Figure 2.40, consisted of 20-noded brick elements for the simulation of the different layers in the pavement. Because of symmetry, only a quarter of the pavement was modelled. The pavement profile was assumed to consist of three material layers. The bottom layer represented a layer of soil with a thickness of 15 m. The middle layer represented a base material with a thickness of 0.3 m. Both the subgrade and the base layer were assumed to behave linear elastically. The top-layer represented the asphalt layer. The temperature of the asphalt mixture was assumed to be 20°C. The modulus of the asphalt layer depended on the strain rate and was determined in an iterative way. The reference mixture (mixture nr 40) had been compared with a polymer modified mixture (mix 45) (Figure 2.38 gives the yield surfaces of mixtures 40 and 45). In the finite element analyses, two different top layer thicknesses, 0.15 m and 0.25 m, were investigated. The thicker (0.25 m) non-modified asphalt pavement was compared to the thinner (0.15 m) modified pavement.
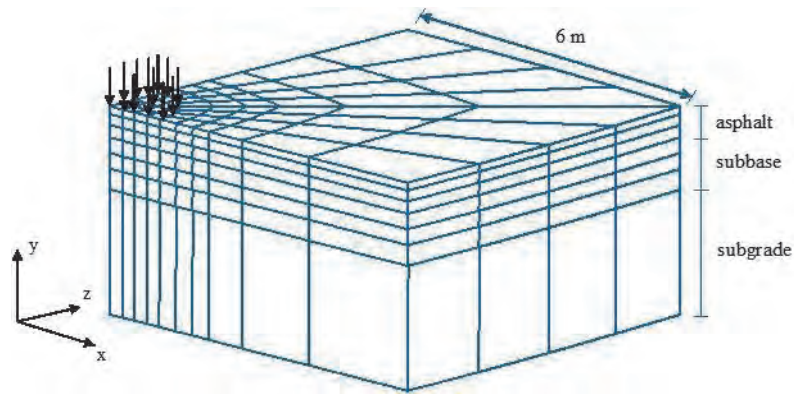
Figure 2.40. Finite element mesh for stationary load analyses [62]

The dynamic analysis option of CAPA-3D was utilized to subject the model to a series of successive half-sinusoidal pulses each of 25 ms duration and 0.8 MPa stress amplitude. Figure 2.41 shows the development and propagation of the total damage in the asphalt layer as the number of load cycles increased.

At the top of the asphalt layer of the non-modified pavement, a damage concentration can be identified in the vicinity of the wheel. Although the volumetric and deviatoric damage are not shown separately projected, the results clearly showed that this damage concentration is of volumetric nature, which indicates the gradual development of permanent deformation.

In the non-modified pavement intense tensile damage can be observed developing at the bottom of the layer directly under the wheel, see Figure 2.41. This indicates the tendency of initiation and gradual development of tensile cracking at the bottom of the layer.

Both figures show the development and propagation of damage in the asphalt layer as the number of load cycles increased. A notable difference between the two structures is that in the thick non-modified structure damage starts directly under the wheel and propagates rather quickly into the body of the pavement. After 9000 load cycles another area of severe damage occurs at the bottom of the pavement. In the modified thinner structure the maximum damage is about 4 times smaller than in the non-modified structure. The damage occurs mainly in the area under the wheel. Lower in the structure there is hardly any effect from the load.
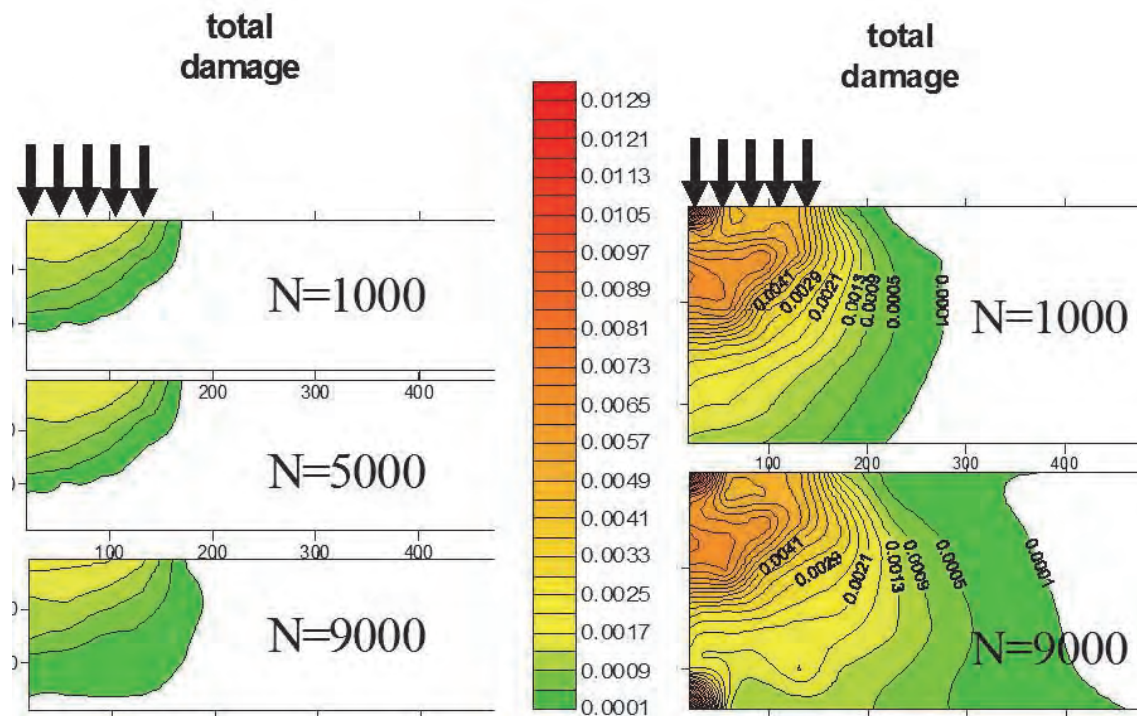
Figure 2.41. Development of damage in pavement structure. Left: polymer modified asphalt mixture, 150 mm asphalt pavement. Right: reference, non-modified asphalt mixture, 250 mm asphalt pavement [62]

It was concluded that, for a given mixture, depending on the thickness of the asphalt layer, different damage patterns and mechanisms develop under the load within the body of the pavement. By comparing the magnitude of damage, it was concluded that the pavement with the polymer modified mix demonstrates less damage accumulation than the pavement with the non-modified mixture, even with a 40% thickness reduction. In the case of the modified mixture, there is less damage development and propagation and the damage concentrates mostly in the vicinity of the wheel. The highest damage levels always occur inside the body of the pavement with the non-modified mix 40.

The beauty of this type of analysis is that it allows a detailed analysis to be made of damage initiation and propagation including the effects of stress redistribution due to local damage development.

In spite of its beauty, the disadvantage of such an approach is still the large amount of computation time that was needed to only make a limited analysis up to 9000 load repetitions. The fact that temperature conditions were quite variable during the Lintrack tests will further complicate the use of this approach in analyzing the performance of the Lintrack sections.

2.11. Findings and conclusions

In this sections findings and conclusions are reported which are related to the 'major issues' which were defined in the beginning of section 2.3. For sake of completeness these 'major issues' are given below.

- How large were the calibration factors that were needed to match theory with practice?
- What were the factors that complicated matching theory with practice?
- Were there any unknowns in the analysis for which (major) assumptions were needed and what was the magnitude/effect of these assumptions?
- Is the cracking observed at the surface of pavements bottom-up or top down cracking or both?
- Irrespective which type of cracking it is, were the researchers able to predict these different types of cracking?

Fatigue of real pavements is a complex phenomenon which is influenced by a large number of variables. Field observations reported by committee B-12 from CROW and by SHRP-NL 95 (Schmorak) show that many cracks originate at the surface and that bottom up fatigue cracking, which is the decisive parameter in currently used pavement thickness design systems, only seems to occur in pavements with a thin AC thickness. This immediately implies that many of the calibration factors developed to match fatigue cracking visible at the pavement surface to tensile strains occurring at the bottom of the asphalt layer should be treated with caution.

Furthermore, the calibration factors as reported in this literature survey are of significant magnitude implying a significant mismatch between theory and practice. This indicates that one is still dealing with a large number of unknowns on which assumptions have to be made. The question is whether the large mismatch is caused by using a wrong theory to calculate stresses and strains (for example elastic vs visco-elastic) or by using inaccurate transfer functions for damage predictions based on the calculated stresses and strains or because of other reasons.

Different laboratory fatigue tests result in different fatigue models. These results are influenced by specimen size, temperature, loading mode and type, and test setup for example 4PB test, 3PB test, or uniaxial tension/compression test. The widely used fatigue model in the Netherlands is based on data resulted from 4PB tests.

None of these tests, do take into account the fact that in reality an asphalt slab is supported by a base course and a subgrade. The use of supporting foundation under a beam specimen is believed to be a closer simulation of what is happening in the road, and the effect of the continuous support of a beam when subjected to fatigue has clearly been indicated. Thus, the question remains whether the current standard laboratory fatigue tests are useful for producing fatigue relations which can be used in pavement design.

From the literature survey it also became clear that establishing shift factors based on laboratory tests and design calculations on the one hand and analyses of field data on the other, is a very difficult undertaking. It seems that reliable shift factors only can only be determined when field tests are done under very well controlled conditions such as occur in accelerated pavement tests.

APT's offer more realistic 'pavement conditions' than the laboratory test do and will, to some extent, provide more reliable and well controlled 'field data' than field observations made on in service roads. However, quite some variation was observed on APT test sections as shown by Groenendijk, Stas, Holster and Visser. These variations are variations in layer thickness and material characteristics as well as variations in the number of load repetitions resulting in visible damage. This further complicates matching theory with APT observations. These variations, however, do indicate that probabilistic concepts, taking into account these variations, should be applied in pavement design. Unfortunately this is seldom done and if it is done it is mostly done in a simplistic way.

Things are further complicated by the fact that Lintrack observations showed that excessively high strain values measured at the bottom of the asphalt layer do not necessarily imply that cracking is visible at the pavement surface.

Advanced modelling, e.g. such as done for the Kraton mixtures by using CAPA, seems to offer possibilities to match theory with practice. These computer simulations have the capability to analyse in detail the damage initiation and propagation including the effects of stress redistribution due to local damage development. Furthermore, these advanced models open up possibilities to link 'simple' tests like a monotonic indirect tension test to pavement performance predictions. Such a link would bring theory much closer to practice because 'simple' tests can be performed in any road material testing laboratory while advanced testing like e.g. fatigue testing cannot. Some complications remain however, such as the large variability of field and accelerated pavement test sections in terms of layer thickness and material characteristics. Moreover, the long computation times required make these approaches less suitable for practical use.

Surface cracking is a major defect that seems to appear before cracks initiated at the bottom layer of the asphalt appear at the surface. Although in some researches cracking through the entire asphalt layer was detected, it is difficult to determine whether this cracking, was top down or bottom up. Field and APT observations lead to the conclusion that especially for thick asphalt layers, surface cracking develops before the bottom up cracking. Several studies were performed in attempt to understand the crack propagation mechanism; however, no comprehensive model has yet been successful in explaining the mechanism.

All this research shows that top down cracking is an important issue implying that it should be taken into account in design systems.

All in all it can be concluded that the findings of this literature study indicate that none of the 'major issues' is actually solved and that still much work needs to be done to relate predictions to field performance without the need of using shift or calibration factors of significant magnitude and not clearly defined origin.

2.12. References

[1]   AASHTO, "AASHTO Guide for Design of Pavement Structures 1993," ed. Washington D.C., 1993.

[2]   W.D.O. Paterson, *Road Deterioration and Maintenance Effects*. Baltimore, U.S.A.: John Hopkins University Press, 1987.

[3]   Nora Schmorak and Arthur van Dommelen, "Analysis of The Structural BEhaviour of Asphalt Concrete Pavements in SHRP-NL Test Sections," in *Road Safety in Europe and STrategic Highway Research Program (SHRP)*, Prague, Czech Republic, , 1995.

[4]   C.R.O.W., "Term Views on pavements. Technical Report SHRP-NL period 1990-1995 (in Dutch)," ed. Dutch centre for research & Contract standardization in Civil & Traffic Engineering, 1996.

[5]   W.F. Stas, A.A.A. Molenaar, and C.A.P.M. van Gurp, "Evaluation of the Structural Condition of Test Pavements F.O.R.C.E. Project," Delft University of Technology, Delft The Netherlands, June 1991.

[6]   A. M. Holster, A.A.A. Molenaar, H.G. van den Bosch, and C. A. P. M. v. Gurp, "Comparison between Observed and Predicted Pavement Response, Part I: Measuring Report," Delft University of Technology, Delft The Netherlands, January 1991.

[7]   J. Groenendijk, "Accelerated Testing and surface cracking of asphaltic concrete pavements," PhD, Delft University of Technology, Delft The Netherlands, 1998.

[8]   J. Groenendijk, C. H. Vogelzang, A. Miradi, A. A. A. Molenaar, and L. J. M. Dohmen, "Linear tracking performance tests on full-depth asphalt pavement," in *Pavement Research Issues*, ed. Washington, 1997, pp. 39-47.

[9]   J. Groenendijk and C.H. Vogelzang, "Pavement Performance Under LINTRACK Accelerated Loading, Extending measurement report and interpretation report section Vb," Delft University of Technology, Delft, The Netherlands, 1998.

[10]   A. F. H. M. Visser, "Evaluation of Pavement Performance Under TxMLS loading," Delft University of Technology, Delft The Netherlands, February 1998.

[11]   A.H. Gerritsen, C.A.P.M. van Gurp, J.P.J. M. van der Heide, A.A.A. Molenaar, and A.C. Pronk, "Prediction and Prevention of Surface Cracking in Asphaltic Pavement," in *International Conference on the*

Structural Design of Asphalt Pavement, Ann Arbor, MI, USA, 1988, pp. 378-391.

[12] P.A.J.C. Kunst, J.P.J. van der Heide, C.A.P.M. van Gurp, F. van Gorkum, P.C. Hopman, A.A.A. Molenaar*, et al.*, "Surface Cracking in Asphalt Layers," C.R.O.W. , Ede The Netherlands, March 1990.

[13] L. A. Myers, "Development and Propagation of Surface-Initiated Longitudinal Wheel Path Cracks in Flexible Highway Pavements," PhD, University of Florida, Florida, USA, 2000.

[14] S. M. J. G. Erkens, "Asphalt Concrete Response - Determination, Modeling and Prediction," PhD, Delft University of Technology, Delft The Netherlands, 2002.

[15] W. v. Dijk, "Practical Fatigue Characterization of Bituminous Mixes," in *Association of Asphalt Paving Technologists, Technical Sessions*, Phoenix, Arizona, 1975, pp. 38-74.

[16] A. A. A. Molenaar, "Prediction of Fatigue Cracking in Asphalt Pavements, Do We Follow the Right Approach?," in *2007 Annual Meeting of Transportation Research Board*, 2007.

[17] NEN-EN-12697, "Bituminous Mixtures-Test methods for hot mix asphalt," in *Part 24; Resistance to fatigue*, ed: Comite Europeen de Normalisation, 2007.

[18] J. A. Epps and C. L. Monismith, "Fatigue of Asphalt Concrete Mixture - Summary of Existing Information," in *Fatigue of Compacted Bituminous Aggregate Mixture*, *1972*, pp. 19-45.

[19] F. Bonnaure, A. Gravois, and J. Udron, "A new method for predicting the fatigue life of bituminous mixes," in *Association of Asphalt Paving Technologists Proceedings*, 1980.

[20] N. Li, "Asphalt Mixture Fatigue Testing; Influence of Test Type and Specimen Size," PhD, Delft University of Technology, Delft The Netherlands, 2013.

[21] L. Francken and C. Clauwaert, "Characterization and structural assessment of bound materials for flexible road structures," in *Proceedings 6th International Conference on the Structural Design of Asphalt Pavements, Ann Arbor*, 1987, pp. 130-144.

[22] W. Van Dijk and W. Visser, "Energy Approach to Fatigue for Pavement Design," in *Association of Asphalt Paving Technologists Proc*, 1977.

[23] A. C. Pronk, "Comparison of 2 and 4 point fatigue Tests and Healing in a 4 Point Dynamic Bending test based on the Dissipated Energy Concept," in *The 8th International Conference on Asphalt Pavement* Seattle, Washington, 1997, pp. 987-994.

[24] P. Hopman, "VEROAD: A viscoelastic multilayer computer program," *Transportation Research Record: Journal of the Transportation Research Board,* vol. 1539, pp. 72-80, 1996.

[25] Y. H. Huang, *Pavement analysis and design*. Upper Saddle River, NJ: Pearson Education, 2012.

[26] A. Chabot, O. Chupin, L. Deloffre, and D. Duhamel, "ViscoRoute 2.0 A," *Road Materials and Pavement Design,* vol. 11, pp. 227-250, 2010.

[27] J. Qiu, N. Li, F. P. Pramesti, A.A.A. Molenaar, and M.F.C. van de Ven, "Evaluating Laboratory Compaction of Asphalt Mixtures using the Shear Box Compactor," *Journal of Testing and Evaluation,* vol. 40, p. 9, 2012.

[28] K.-H. Tseng and R. L. Lytton, "Fatigue Damage Properties of Asphaltic Concrete Pavements," *Transportation Research Record,* 1990.

[29] M. Varaus, P. Hyzl, V. Soucek, and O. Vacin, "Comparison of stiffness moduli using 2-point and 4-point bending tests," in *The 2nd Workshop on Four Point Bending,* , University of Minho, Guimaraes, Portugal, 2009.

[30] A.A.A. Molenaar, J.C.P. Heerkens, and J.H.M.Verhoeven, "Effects of Stress Adsorbing Membrane Interlayers," in *Proceeding of AAPT*, 1986, pp. 206-219.

[31] Q. Liu, "Induction Healing of Porous Asphalt Concrete," PhD, Delft University of Technology, Delft The Netherlands, 2012.

[32] S. Vismara, A.A.A. Molenaar, M. Crispino, and M.R. Poot, "Towards a Better Understanding of the Benefits of Geosynthetics Embedded in Asphalt Pavements," in *2012 Annual Meeting of Transportation Research Board*, Washington 2012.

[33] Y.K. Choi, N.H. Thom, and A. C. Collop, "Fatigue Damage Accumulation measured using Different Laboratory Techniques," in *4th International Symposium Maintenance And Rehabilitation Of Pavemetns And Technological Control*, Belfast, 2005.

[34] J. Qiu, A.A.A. Molenaar, M.F.C. Van De Ven, and S. Wu, "Development of An autonomous Setup for Evaluating Self HEaling capability of Asphalt Mixtures," in *2012 Annual Meeting of Transportation Research Board*, 2012.

[35] K. Majidzadeh, E. M. Kauffmann, and D. V. Ramsamooj, "Application of Fracture Mechanics in the Analysis of Pavement Fatigue," *Journal of Association of Asphalt Paving Technologist,* vol. Vol. 40, pp. Page 227-246, 1971.

[36] A.A.A. Molenaar, "Structural Performance and Design of Flexible Road Construction and Asphalt Concrete Overlays," PhD, Delft University of Technology, Delft The Netherlands, 1983.

[37] H.P.M. Thewessen and A. A. A. Molenaar, "Investigation into the crack growth behavior of some Dutch asphalt concrete mixtures (in Dutch)," Road and Railway Research Laboratory; Delft University of Technology; Delft, Delft, The Netherlands, 1981.

[38] M. Miradi, "Knowledge Discovery and Pavement Performance: Intelligent Data Mining," PhD, Delft University of Technology, Delft The Netherlands, 2009.

[39] A. A. A. Molenaar, "What Do We Learn from Accelerated Pavement Testing," presented at the International Advanced Technologies in Asphalt Pavements (ATAP) 2010 Symposium, Korea, 2010.

[40] J. Verstraeten, "Stresses and Displacements in Elastic Layered Systems," in *2nd International Conference on the Structural Design Asphalt Pavements*, Ann Arbor, 1967, pp. 283-290.

[41] C.M. Gerrard and L.J. Wardle, "Stresses, Strains and Displacements in Three-Layer Systems Undervarious Traffic Loads," Australian Road Research Board, Vermont, 1976.

[42] L. J. Wardle, *Program CIRCLY : a computer program for the analysis of multiple complex circular loads on layered anisotropic media : user's manual / by L. J. Wardle.*: Mount Waverley, Vic. : Division of Applied Geomechanics, Commonwealth Scientific and Industrial Research Organization., 1977.

[43] L. Wardle. (9 May 2014). *CIRCLY and Mechanistic Pavement Design: The Past, Present and Towards the Future*.

[44] C.A.P.M. Van Gurp and P.M. Wennink, "Design, Structural Evaluation and Overlay Design of Rural Roads (in Dutch)," KOAC-WMD Consultants, Apeldoorn, The Netherlands, 1997.

[45] A.H. Gerritsen, C.A.P.M. Van Gurp, J.P.J. Van der Heide, A.A.A. Molenaar, and A.C. Pronk, "Prediction and Prevention of Surface Cracking in Asphaltic Pavements. , ," in *6th Int. Conf. Structural Design of Asphalt Pavements*, Ann Arbor, Michigan, July 13-17, 1987,.

[46] M. De Beer, C. Fisher, and F. J. Jooste, "Determination of Pneumatic Tyre/Pavement Interface Contact Stresses Under Moving Loads and Some Effects on Pavements with Thin Asphalt Surfacing Layers," in *Proceedings of the 8th International Conference on Asphalt Pavements*, 1997, pp. 10-14.

[47] M. De Beer, "Tyre/Pavement Interface Stresses measured with the Vehicle-Road Surface Pressure Transducer Array (VRSPTA) System (i.e. "3-D Loadcell"); Part I: The VRSPTA System: Some Technical Detail. Unpublished Confidential Technical Note I/PA/11/95," Pavement Engineering Technology, Transportek, CSIR, June 1995.

[48] A. Scarpas, "CAPA-3D Finite Elements System User's Manual, Parts I, II and III, ," Department of Structural Mechanics, Faculty of Civil Engineering, Delft University of Technology, Delft, The Netherlands, 1992.

[49] J. B. Metcalf, "NCHRP Synthesis of Highway Practice 235: Application of Full-Scale Accelerated Pavement Testing.," in *Transportation Research Board, National Research Council, Washington, D.C.,* , 1996, p. 110 p.

[50] K. G. Sharp, "Full Scale Accelerated Pavement Testing: a Southern Hemisphere and Asian Perspective," in *2nd International Conference on Accelerated Pavement Testing*, Minnesota USA, 2004.

[51] C.A.P.M. van Gurp and J. Elzenaar, "Interim Report: Fatigue Test on Asphalt Mix, Project FORCE Road and Railroad Research Laboratory," Faculty of Civil Engineering, Delft University of Technology, August 1989.

[52] F. Hugo, "Some factors affecting the design and use of the Texas Mobile Load Simulator," *ASTM Special Technical Publication,* vol. 1225, pp. 67-67, 1994.

[53] Shell_1978, "Shell Pavement Design Manual, Asphalt Pavement and Overlays for Road Traffic," ed. Shell International Petroleum Company, 1978.

[54] Asphalt_Institute_1982, "Research and Development of the Asphalt Institute Thickness Design Manual (MS-1)," ed. The Asphalt Institute, August 1982.

[55] P. D. Bhairo, "Comparison of the predicted and Observed Pavement Life of LINTRACK Test Lane Va," Delft University of Technology, Delft, The Netherlands, 1997.

[56] S.M.J.G. Erkens and M.R. Poot, "Additional Compression Test on ACRe," TU Delft, The Netherlands, March 2000.

[57] X. Liu, T.O. Medani, W. Sutjiadi, and A. Scarpas, "FEM Simulation of the Response of Polymer Modified Asphalt Mixtures," TU Delft, The Netherlands, September 2007.

[58] T. O. Medani, "Design Principles of Surfacings on Orthotropic Steel Bridge Decks," PhD, Delft University of Technology, Delft The Netherlands, 2006.

[59] X. Liu, "Numerical modelling of porous media response under static and dynamic load conditions," PhD, Delft University of Technology, Delft The Netherlands, 2003.

[60] C. S. Desai, S. Somasundaram, and G. Frantziskonis, "A hierarchical approach for constitutive modelling of geologic materials," *International Journal for Numerical and Analytical Methods in Geomechanics,* vol. 10, pp. 225-257, 1986.

[61] A. Scarpas, R. Al-Khoury, C. Van Gurp, and S. Erkens, "Finite element simulation of damage development in asphalt concrete pavements," in *Eighth International Conference on Asphalt Pavements*, Washington, 1997.

[62] E.J. Scholten, A.A.A. Molenaar, M.F.C. Van de Ven, M.R. Poot, X. Liu, and A. Scarpas, "Advanced Testing of SBS Modified Asphalt Base Courses," in *2nd European Airport Pavement Workshop - CROW*, 2009, pp. 1-11.

[63] C. S. Desai, "A general basis for yield, failure and potential functions in plasticity," *International Journal for Numerical and Analytical Methods in Geomechanics,* vol. 4, pp. 361-375, 1980.

[64] A. Scarpas and J. Blaauwendraad, "Experimental calibration of a constitutive model for asphaltic concrete," in *Proc. of the Euro-C Conference on the Computational Modelling of Concrete Structures* Badgastein, Austria 1998, pp. 193-202.

Chapter 3
Experimental program

3.1.   What we learned from previous research

In Chapter 2 it was shown that it is difficult to get a good match between the fatigue life observed in the field and the predicted fatigue life. Major influence factors are unknown traffic conditions, variability in layer thicknesses and material characteristics, environmental factors that cannot be controlled, etc. Also in case of APT sections there is a clear difference between the observed fatigue life and the fatigue life prediction based on using a multilayer pavement model and laboratory fatigue tests. This disparity has been attributed to different factors such as differences in geometry and support conditions between specimens tested in the laboratory and asphalt layers in a pavement. Furthermore, differences in the loading conditions, rest periods in between load pulses, healing and lateral wander, contribute to this disparity.

Top down versus bottom up cracking is also an important point. All pavement design systems such as RHED and SPDM only consider the initiation of cracks at the bottom of the asphalt layer (typically in base layers), while in reality surface cracking (typically starting in the wearing course) is a major defect that mostly even appears before crack initiation at the bottom.

All these issues also complicate the evaluation of the effect of modified binders to the fatigue life. Such effects can be studied to some extent by means of laboratory tests, i.e. fatigue tests. However, as was shown in chapter 2, evaluation of the effects of bitumen modifications in real life situations is still a big step. A decision on whether modifications are beneficial cannot only be based on laboratory testing but should include a complete and correct design analysis.

In this research the effect of a bitumen modifier on the crack and fatigue resistance of the GAC (Gravel Asphalt Concrete) was investigated as well. For this purpose, sets of 4PB test fatigue-stiffness tests, Monotonic Uniaxial Compression tests (MUCT), Monotonic Uniaxial Tension tests (MUTT), and healing tests were also performed on the gravel asphalt concrete mixture modified with Retona, a natural rock asphalt found in Buton Island, Indonesia.

3.2. Research methodology

In attempting to reconcile pavement fatigue life predictions to in-service fatigue life observations, a framework as depicted in Figure 3.1 was proposed. The workflow comprises of two blocks:
[a] analysis of the observed crack damage and fatigue behavior of the Lintrack APT sections (green color).
[b] prediction of this behavior using laboratory tests supported by stress strain analyses.

Point A in Figure 3.1 represents the work that was done on the Lintrack sections I, VA and VB, starting in 1990. The sections were simple two layer structures consisting of an asphalt layer (GAC) on a sand subgrade. The dimensions of the pavement structures (thickness * length * width) were 150 x 16,000 x 4,000 mm for section I and 80 x 16,000 x 4,000 mm for section VA and VB.

A free rolling super single tire was applied to the sections at a speed of 20 km/h. This speed results in a loading frequency of approximately 3 Hz and 8 Hz in the transversal and longitudinal directions respectively [1]. The daily temperature according to the nearest weather station varied between -6°C and 26°C. The strain at the bottom of the pavement was measured using embedded strain gauges both in transversal and longitudinal directions. Also falling weight deflectometer measurements were performed at the strain gauge positions.

The behavior of the Lintrack sections is extensively explained by Groenendijk [2, 3]. This was explained to some extent in chapter 2 of this thesis. Some important details of Groenendijk's work will be discussed further in chapter 6. In this research the development of surface cracking, permanent deformation and back-calculated stiffness as reported by Groenendijk, will be used (point 1, 2, and 3, Figure 3.1). Furthermore, pavement life analyses will be made leading to 'observed fatigue life' indicators.

Point B in Figure 3.1 shows the prediction aspect of this study. In order to develop a model which can predict the fatigue life, a set of laboratory tests and multi-layer analyses will be performed. The laboratory tests will consist of fatigue tests on beam specimens (point 5) and mechanical tests (point 4) to characterize the GAC. Two different bending test setups, namely the Four Point Bending test (4PB) and the Beam on Elastic Foundation (BOEF) test, will be used to obtain a comprehensive view of the fatigue behavior of the GAC mixture. These results with the support of the stress-strain analysis will be used to predict the fatigue life of the GAC.

In point C the fatigue life prediction and observation will be compared. This will lead to a development of a shift factor, bridging the observation (practice) and the prediction (theory).
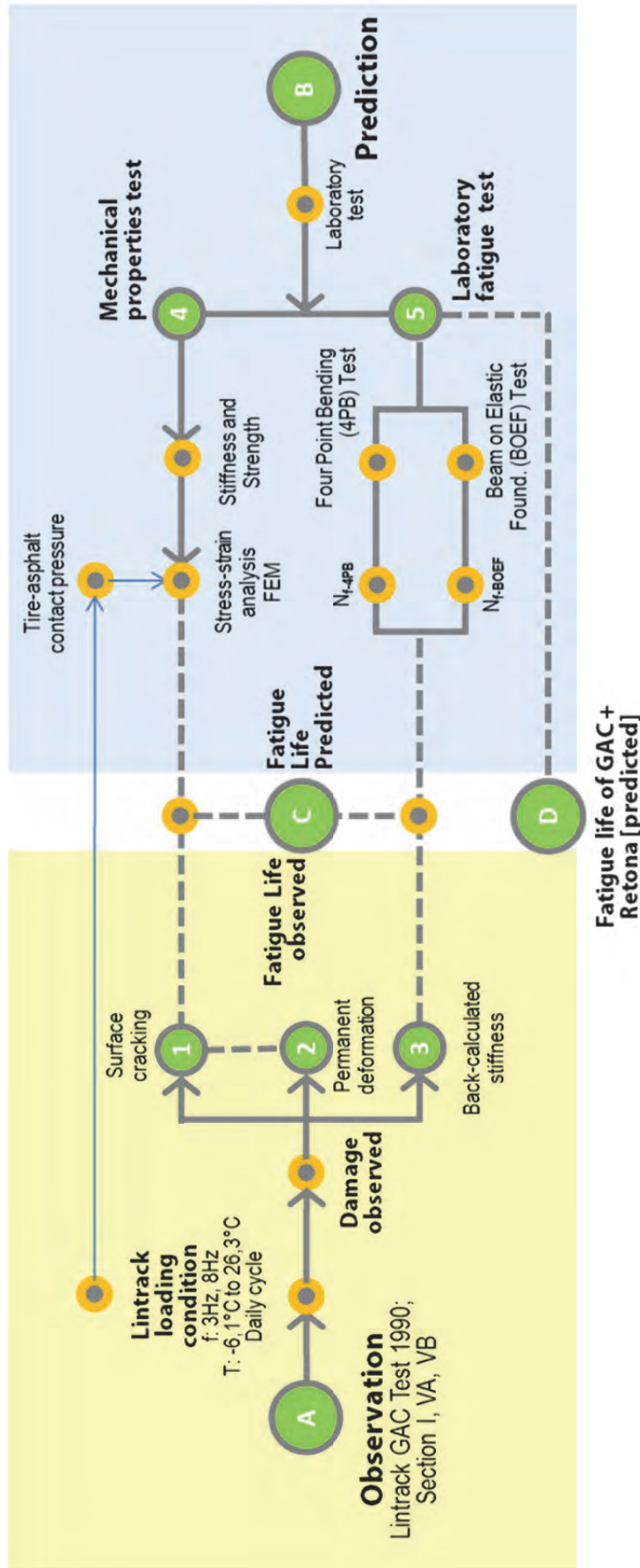
Figure 3.1. Research workflow to match the prediction with the observation

3.3.   Material, mixture design and experimental program

3.3.1. Material and specimen production

The asphalt mixture tested in this research was a base course mixture that was used in the Lintrack sections. It was a GAC (gravel asphalt concrete) 57 type 0/32 for traffic class IV (class IV indicates the mixture is used on heavily trafficked highways). The maximum aggregate grain size in the mixture was 32 mm, the bitumen content was 3.85% by mass (8.9 % by volume) and the design void content was 4.5%. For the mixture, a Q8 bitumen 40/60 was used with a penetration of 42 (0.1 mm) and a softening point of 50 (°C). The mix composition of the GAC is shown in Table 3.1.

Table 3.1. The composition of the gravel asphalt concrete mixture.

Sieve size	% Weight (with Bitumen)					Cumulative
(mm)	Gravel	River sand	'plaatzand'	Filler	Bitumen	
31.5 mm						
22.4 mm	5.22					5.22
16 mm	13.62					18.85
11.1 mm	12.44					31.28
8 mm	8.67					39.95
5.6 mm	8.56					48.52
4 mm	4.36					52.88
2 mm	0.75	1.01	0.15			54.79
500 μm		4.14	2.58			61.51
180 μm		4.82	16.57			82.89
90 μm				0.60		83.49
63 μm	0.16	0.31	6.44	0.23		90.63
passing 63 μm	0.05	0.02	0.03	5.43		96.15
bitumen 40/60					3.85	100.00
Total	100					

The process to produce the GAC blocks is shown in Figure 3.2. Table 3.2 shows how the specimens are cut and drilled from the blocks. The gravel asphalt material consists of river gravel aggregate, fore-shore sand ('plaatzand'), river sand, Wigro filler and bitumen 40/60 [4]. It was mixed at the target temperature of $180 \pm 5 °C$. The mixture was then carefully fed into the shear box compactor. A vertical stress of 0.75 MPa and a shear angle of 4 degrees were used to compact the mixture [5]. This resulted in a block with certain dimensions.

Beam and cylindrical specimens were cut from each block. The measured air voids varied from 3.3 to 6.67%. The distribution of the air voids of all specimens is shown in Figure 3.3. Only specimens with an air voids between 3.75% to 5.25% were used as test specimens.
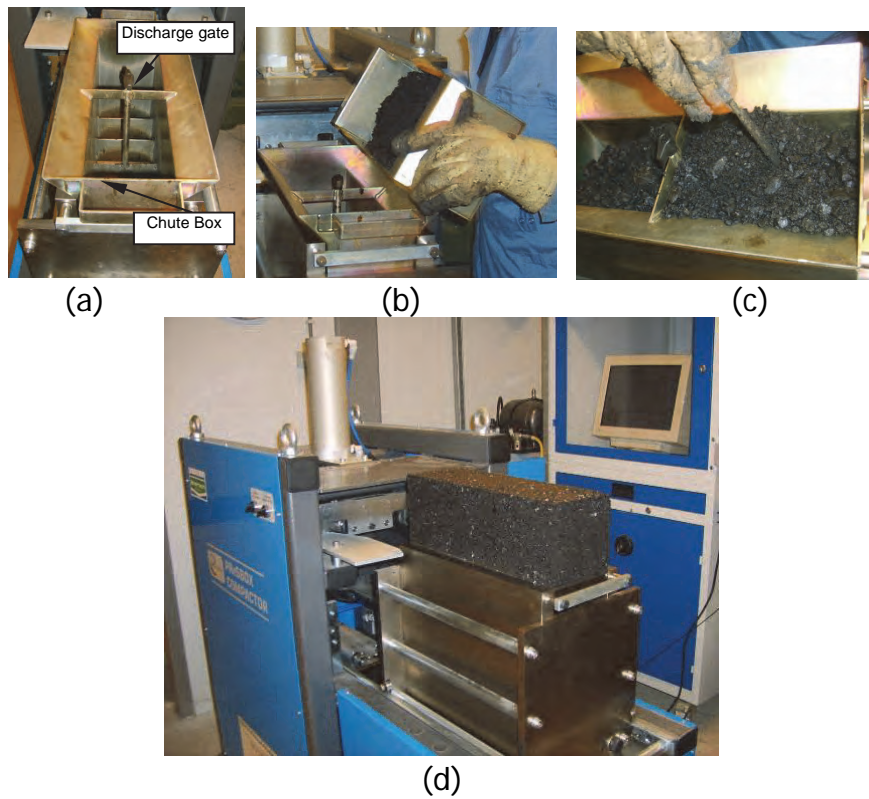
Figure 3.2. Illustration of the shear box compactor and the compaction process: (a). the chute box and the discharge gate; (b). feeding; (c). laying; (d). the ejected block from the shear box compactor. [6]

Table 3.2. Overview of specimen's geometry
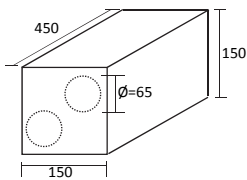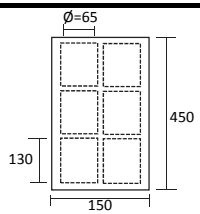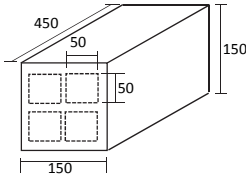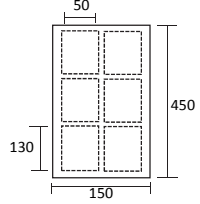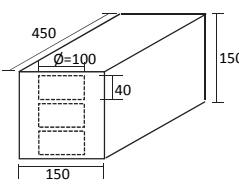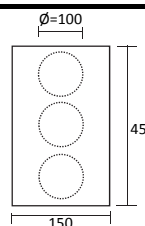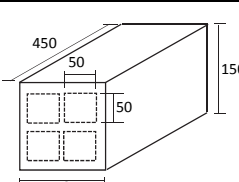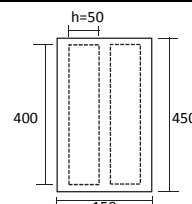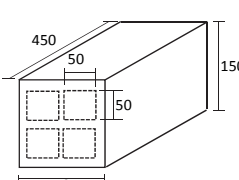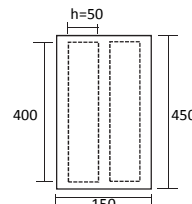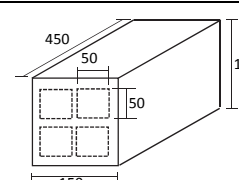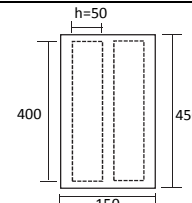
Test	Dimension (mm) n	Coring/sawing (all in mm)	Top view (all in mm)
Monotonic Uniaxial Compression test (MUCT)	$\varnothing 65*130$ (Cylinder) 18		
Monotonic Uniaxial Tension test (MUTT)	$50*50*130$ (beam) 18		

Table 3.2. Overview of specimen's geometry (continued)

Test	Dimension (mm) n	Coring/sawing (all in mm)	Top view (all in mm)
Indirect Tension Test (Monotonic) (ITT)	∅100*40 (Cylinder) 12		
Four Point Bending test for Stiffness (FPBT)	50*50*400 (Beam) 4		
Four Point Bending test for Fatigue (FPBT)	50*50*400 (Beam) 45		
Beam on Elastic foundation for fatigue (BOEF)	50*50*400 (Beam) 5		
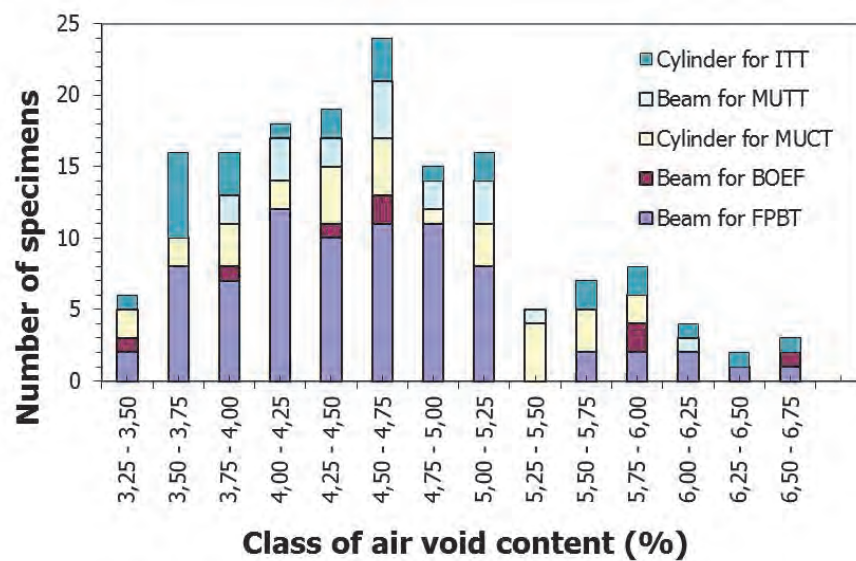
Figure 3.3. The distribution of the air voids of all GAC specimens

3.3.2. Four Point Bending Test

The specimens used for the 4PB (and BOEF) test were, as shown in Table 3.2, 400 mm long, 50 mm wide and 50 mm high. These sizes are always used in the Netherlands and the test frames are developed for those sizes. In order to comply with the European norms, the big aggregate size used in the mixture would require larger specimens. However, it is also mentioned in the European norm that the beam should have a certain slenderness in which the effective length between the outer clamps L should be at least six times the maximum value of the width and/or the height [7]. Using the standard test frames with a length of 3 x 118.5 mm, it is hard to achieve this slenderness requirement if 3 x D aggregate size is chosen to drive the dimension of the beam. Therefore, it was decided to use the sizes as mentioned above [5].

The 4PB tests were carried out for two purposes; firstly, to determine the flexural stiffness and to develop a master curve for the mixture stiffness. Secondly, to develop a fatigue relationship for the GAC mixture. The stiffness tests were performed in the constant displacement mode using a sinusoidal strain signal with an amplitude of 50μm (100 μm peak to peak) whereas the stiffness was determined after 100 cycles. The experimental program is shown in Table 3.3.

The fatigue tests were performed at frequencies of 3 and 8 Hz (see Table 3.4). The reason to choose these frequencies was that they were similar to the loading frequencies occurring in the Lintrack test sections. Bhairo [1] reported that when back calculating the measured transverse and longitudinal strain, the loading frequency had to be estimated to obtain the proper mixture stiffness. Bhairo estimated equivalent loading frequencies of 3 Hz and 8 Hz respectively for the transverse and longitudinal direction. Such values were also reported by Groenendijk [8] and Bouman [9] for section I. For the thinner sections VA and VB, with a thickness of 80 mm the equivalent frequency differed only 1 Hz from the ones determined for section I. Since this difference is insignificant, it can be neglected and, therefore, frequencies of 3 Hz and 8 Hz were used in the fatigue tests [1].

Since the 4PB test is extensively used in this research, more details about this test is given in the paragraph below and further in chapter 4. The principle of the 4PB test is explained in Figure 3.4.a. A displacement controlled or load controlled sinusoidal signal (see Figure 3.4.a.) is applied via the inner clamps at the middle of the beam. The movement of the clamps are controlled by an actuator as shown in Figure 3.4.b. This test can be used to determine the fatigue life of materials under bending forces and can be performed at different loading frequencies and temperatures [10]. Since the load and displacement are continuously measured during the test, parameters such as flexural stiffness, tensile stress, tensile strain, phase angle, and dissipated energy can be determined. Fatigue relationships are usually described in the form of equation (3.1).

$$N_f = a\, \varepsilon^n$$

$$\mathrm{Log}N_f = \mathrm{Log}\,a + n\,\mathrm{Log}\,\varepsilon \qquad\qquad (3.1)$$

Where Nf is the number of displacement controlled load repetitions until the specimen fails. The failure/fatigue life is usually defined as the number of cycles at which the stiffness is half of its initial value. ε is the applied strain (μm/m) and 'a' and 'n' are regression constants [10].

Table 3.3 The test program of Four Point Bending test (Stiffness)

T(°C)	f (Hz)	Nr of
Temp	frequency	specimen
5	0.5; 1; 2; 4; 8	4
10	0.5; 1; 2; 4; 8	
15	0.5; 1; 2; 4; 8	
20	0.5; 1; 2; 4; 8	
25	0.5; 1; 2; 4; 8	
30	0.5; 1; 2; 4; 8	

Table 3.4 The test program of Four Point Bending test (Fatigue)

T(°C)	f (Hz)	nr of spec
Temp	frequency	
5°	3	9
	8	9
20°	3	7
	8	7
30°	8	7
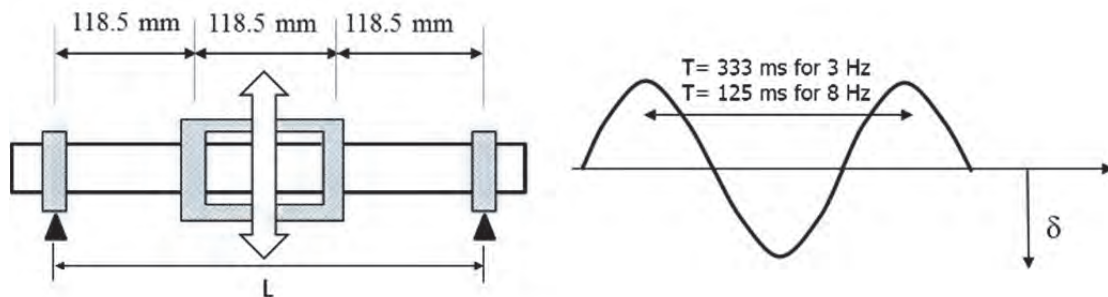
(a)
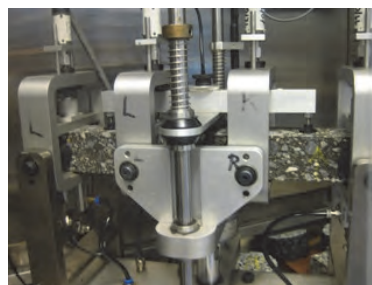
(b)

Figure 3.4. (a) the principle of the 4PB test [10],
(b) 4PB test set-up used at RRRL-DUT

3.3.3. Beam on Elastic Foundation

A laboratory set up called beam on elastic foundation (BOEF) was also used to simulate more appropriately the fatigue behavior of a real pavement in the laboratory.

The setup of the BOEF test and the applied loading are shown in Figure 3.5. In this test a beam is placed on top of an elastic (rubber) foundation. The specimen dimensions and volumetric characteristics are the same as for the 4PB test. The objective of this test is to simulate the fatigue behavior of asphalt mixtures in a more realistic way since in this case the beam is fully supported which is also the case for an asphalt layer in a pavement.

(a)

(b)
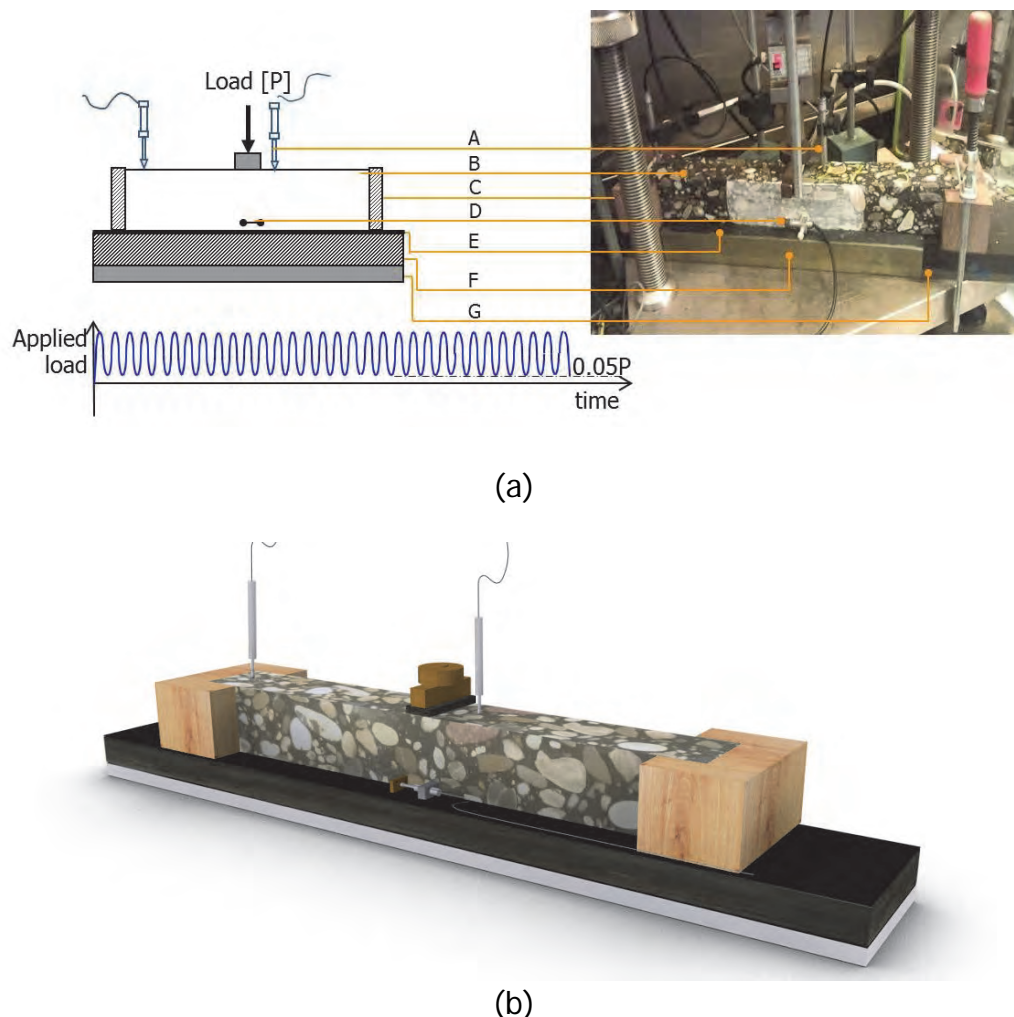
Figure 3.5. (a) The setup of the BOEF test and the haversine loading applied to the beam, where 0.05P is the preload. Where A: LVDT for vertical displacement; B: Beam 50 x 50 x 400 mm; C: Wooden C-Shape Support; D: LVDT for horizontal displacement; E: Latex sheet; F: Rubber foundation; G: Steel plate. (b) Artist impression of BOEF test setup.

A steel plate (600 x 100 x 11 mm) which is stiff enough to hold the applied load was placed under the rubber subgrade. Based on Qiu's [11] work a soft rubber (600 x 100 x 24 mm) with a Young's modulus of 6.5 MPa was selected to act as elastic foundation. The use of such a low Young's modulus elastic foundation is necessary in order to accelerate fatigue development and crack propagation; no notch to initiate cracking was applied on the beam. In order to reduce the friction between foundation and beam, a latex sheet was placed on top of the rubber. Then the GAC beam was placed on top of the sheet. Two 50 mm high C shaped pieces of wood were put at the two ends of the beam, loosely enough to keep the beam in position during the cyclic loading application (Due to the very low friction, the beam might slide away; this was overcome by means of these two C shaped wooden blocks).

The load level used in the BOEF test was chosen such that fatigue occurred within a reasonable period of time. Vismara [12] suggested to use load levels between 30 to 60% of the indirect tensile strength (at 5°C). However, when a tensile stress of 60% of the GAC's indirect tensile strength was applied, which corresponds to 3kN, the beam did break within 5 minutes and the vertical and horizontal displacement showed a lot of scatter. Therefore, it was decided to limit the maximum load level to 2.5kN. Finally, five load levels were selected being: 2.5; 2.25; 2.0; 1.75; and 1.5 kN. The test was carried out at 5°C and with a frequency of 8 Hz (see Table 3.5). The vertical displacement was measured using two LVDT's, one at a distance of 35 mm from the center of the load and one at 10 mm from the edge of the beam. This was done to measure the curvature of the beam during the test since this is an indicator of the maximum tensile strain under the center of the load. The tensile strain at the bottom of the beam under the load center was calculated from the horizontal displacement that was measured over a distance of 25.4 mm (1 inch) by means of an LVDT. This device was placed at the location where the crack was assumed to initiate (this assumption proved to be correct). This LVDT was attached 8 mm above the bottom of the beam to prevent it from touching the rubber foundation.

Table 3.5 The test program of the Beam on Elastic Foundation

Temp	frequency	P	nr of spec
(°C)	(Hz)	(kN)	
5	8	2.5	1
		2.25	1
		2	1
		1.75	1
		1.5	1

The reasons to do the BOEF tests at 5°C were twofold. Firstly, the test conditions should be such that the results would not be influenced by any permanent deformation that might occur under the loading strip. That was why tests at 20°C and 30°C were not done. Secondly, time limitations did not allow doing the tests at other temperatures. In conclusion: the BOEF tests

were performed in a stress controlled mode at 5°C and a frequency of 8Hz [5].

3.3.4. Monotonic Uniaxial Compression Test (MUCT)

The compression test set-up consists of a MTS 150 KN hydraulic actuator mounted in the 3D space frame. The force that is applied with this actuator is measured with a 200 kN load cell. An insulated temperature controlled cabinet maintains the temperature in a range of 0°C to 40°C.
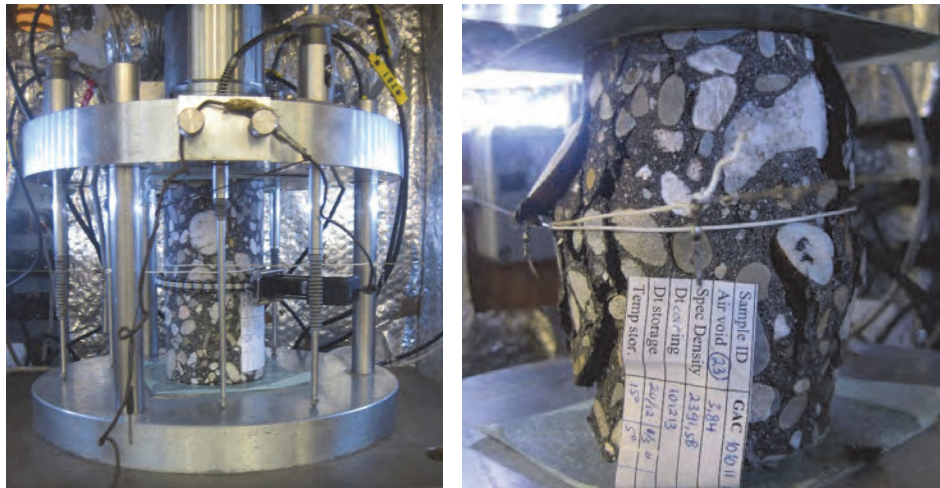
Figure 3.6. Set-up of the uniaxial compression test (left) and a specimen after testing (right)

Three LVDTs with a range of ±10 mm were placed between two loading plates to measure and control the deformation of the specimen in the axial direction. Three other LVDTs with a range of ±1 mm were also placed between the plates in order to be able to obtain more accurate displacement measurements in the beginning of the test. The 10 mm LVDTs have the ability to measure 20 mm axial deformation in total, while the 1 mm LVDTs can measure 2 mm in total.

The total radial deformation of the specimen was measured with two devices being an extensometer and a kevlar string. As Figure 3.6 shows, the extensometer has a roller chain and is wrapped around the center of the specimen. Also the string was wrapped around the middle of the specimen and was connected to two potentiometers. The extensometer provides accurate information about the magnitude of the radial displacement in the beginning of the test when the displacement is very small, while the string provides good quality information about the larger displacements which occur at a later stage of the test. A friction reduction system, consisting of a thin steel plate and a thin layer of a biological plastic foil covered at both sides with a thin layer of grease, was placed on top and bottom between the specimen and the plate.

Similar to the other tests, only specimens with an air voids between 4 and 5% are used. The specimen dimensions and the way they were drilled from the GAC block were described in Table 3.2. In a compression test it is essential to keep the top and bottom side of the specimen smooth and parallel. This condition was achieved by polishing the specimens.

Several BISAR calculations were made to determine the strain rate at the bottom of GAC layer in the Lintrack sections that occurred during a wheel passage. The simulation results and the determination of the strain rates are described in Appendix 3A. The relationship between the strain rate and the modulus of elasticity for section I & VA is shown in Figure 3.7.

The monthly average air temperature from Rotterdam weather station (www.knmi.nl) [13] during the Lintrack performance test varied from -6 °C to 26°C. While according to Groenendijk [2], the pavement temperature ranged from 0°C to 30°C. Based on these ranges it was decided to do the test at three temperatures being 5°C, 20°C and 30°C. Since the stiffness of the mixture at certain temperatures and loading frequencies are known, the strain rates can be determined and they are depicted in Table 3.6. The testing program is shown in Table 3.7.
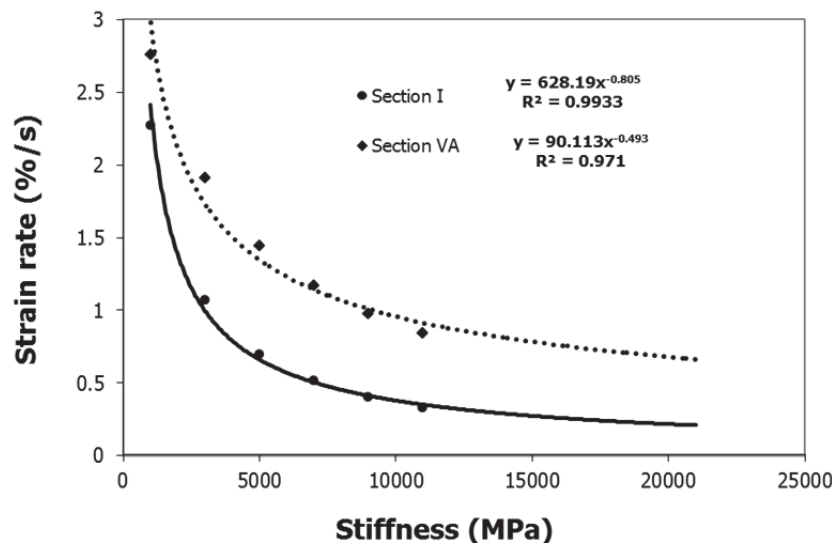
Figure 3.7. Stiffness versus strain rate of GAC Lintrack section I and VA (from BISAR calculation)

Table 3.6. Combination of the strain rate for each temperature

Temp [°C]	Stiffness [MPa]	Transversal & longitudinal direction	
		$\dot{\varepsilon}$	Strain rate chosen
30	2000-3000	2.76 – 0.15	3 ; 2 ; 1 ; 0.1
20	5000-7000	1.44 – 0.06	2 ; 1; 0,1 ; 0.05
5	20000-21000	0.349 – 0.019	1 ; 0,5 ; 0,1 ; 0.01

Table 3.7 The test program of MUCT and MUTT

Monotonic Uniaxial Compression Test			Monotonic Uniaxial Tension Test		
Temp	Strain rate	nr of spec	Temp	Strain rate	nr of spec
(°C)	$\dot{\varepsilon}$ (%/s)	n	(°C)	$\dot{\varepsilon}$ (%/s)	n
5	0.01	1	5	0.01	1
	0.1	1		0.1	1
	0.5	1		0.5	1
	1	1		1	1
20	0.05	1	20	0.05	1
	0.1	1		0.1	1
	1	1		1	1
	2	1		2	1
30	0.1	1	30	0.1	1
	1	1		1	1
	2	1		2	1
	3	1		3	1

3.3.5. Monotonic Uniaxial Tension Test (MUTT)

In order to attain comparable results the MUTT testing program was kept the same with the MUCT testing program. The air voids of the specimens was between 4% and 5%. How the specimens were cut from the blocks is shown in Table 3.2.

The reason of using rectangular specimens instead of cylinders was because several blocks had already been sawn into beams with an air voids in the range of 4% to 5%.
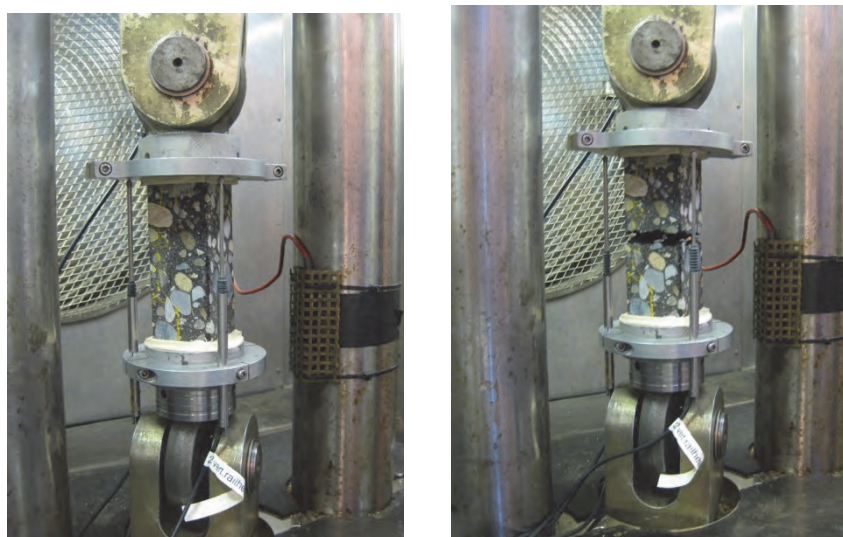
Figure 3.8. Set-up of the uniaxial tension test and the specimen. Before and after test

The tension test set up consists of a MTS 50 KN hydraulic actuator mounted in a rigid loading frame. The axial displacement was measured and controlled by three LVDT's fixed in an LVDT ring around the specimen. Dependent on the temperature different ranges of the LVDTs were used. For 5°C tests LVDTs with a range of ±1 mm were used whereas for 20°C and 30°C LVDTs with a range of ±5 mm and ±10 mm were used respectively. This set up is mounted in a temperature–controlled cabinet which has the ability to keep the cabin temperature constant in a range of -20°C to 80°C.

The specimens needed to be glued to the loading caps and were confined with 4 pieces of wood to avoid failure at the end of the specimen. The specimen was glued perpendicular to the cap and during the process of gluing the top and bottom cap were kept parallel to each other. Figure 3.9 shows the preparation of the specimen. It shows how the specimen is mounted in a rigid specimen holder to make sure that the top and bottom cap are in parallel position and that the specimen remains in the same position during gluing.

Figure 3.9. Glueing process

3.3.6. **Indirect Tensile Strength Test (ITS)**

The monotonic indirect tension strength test is a test to determine the tensile strength of the asphalt mixture by applying a strip loading on top of a thin disc. The same actuator and controller were used as in the MUCT. The test set-up is presented in Figure 3.10 whereas the stress distributions in vertical and horizontal direction are presented in Figure 3.11.

The ITS tests were performed at temperatures of 5°C, 20°C and 30°C and at displacement rates of 0.028 mm/s to 8.33 mm/s as shown in Table 3.8. The vertical and horizontal displacements are measured by means of attached LVDTs. From the results the indirect tensile strength, Poisson's ratio as well as the specimen's stiffness can be calculated.

The results can be compared to the results of the monotonic uniaxial tension test. On the one hand this could confirm the necessity of the relatively complex uniaxial tension test or on the other hand it could show that a simple ITS test suffices.

Figure 3.10. Indirect tension test set-up
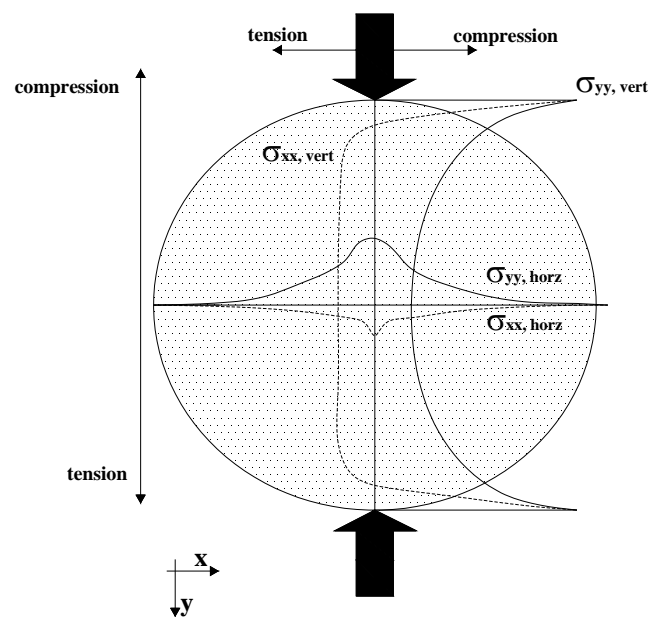
Figure 3.11. Stresses along the vertical; and horizontal cross section

The cylindrical specimens with a diameter of 100 mm and a thickness of 40 mm were drilled from the blocks as shown in Table 3.2. Only specimens with an air voids between 4 and 5% were used for the test. The testing program is described in Table 3.8.

Table 3.8. Test program of the Indirect tensile strength test

Indirect Tension Test (Monotonic)			
(°C)	(%/s)	[mm/s]	n
Temp	strain rate	Speed	nr of spec
5	0.01	0.0278	1
	0.1	0.2778	1
	0.5	1.3889	1
	1	2.7778	1
20	0.05	0.1389	1
	0.1	0.2778	1
	1	2.7778	1
	2	5.5556	1
30	0.1	0.2778	1
	1	2.7778	1
	2	5.5556	1
	3	8.3333	1

The tests were performed at strain rates similar to those in the MUTT. These 'expected' strain rates in the x direction are translated to the deformation rates in the y direction using Equation (3.2). The explanation of the shift factor mentioned in Equation (3.2) is given in Appendix 3B.

$$\dot{U}_y = \frac{\dot{\varepsilon}_x}{SF} ; \quad \dot{U}_y = \frac{\dot{\varepsilon}_x}{0.0036} \tag{3.2}$$

where

$\dot{U}_y$ = deformation rate at y direction (mm/s)

$\dot{\varepsilon}_x$ = horizontal strain rate (1/s)

SF = shift factor

3.3.7. Healing

During the Lintrack tests, rest periods of varying length did occur. When the test was running smoothly, a loading period of 0.125 s was followed by a rest period of 2.16 s before the next wheel passage occurred. Furthermore, rest periods of 2 days occurred during the weekends when Lintrack was not allowed to be operated. Finally, rest periods with duration of a few days or even as long as a few weeks or months did occur because of maintenance and repair work that needed to be done to the Lintrack apparatus. Therefore, it was important to find out the healing capability of the mastic of the copied mixture. Such information was not available for the original mastic and in the original analyses by Groenendijk [2] and Bhairo [1] a healing factor of 4 was assumed without knowing whether this value was correct or not.

Qiu [14] proposed a simple fracturing-healing-refracturing test, using a direct tension test on a bituminous mastic produced by mixing a 40/60 pen Q8 bitumen and Wigro filler at a weight ratio of 0.35 : 0.65.

Based on Qiu's work, samples were made by using a double edge curve shaped mold as shown in Figure 3.12. After cooling the specimens in a refrigerator, the samples were de-molded and placed in the 0°C chamber of a DTT machine for at least 2 hours.

The samples were fractured using a displacement speed of 100 mm/min at 0°C and were then healed by placing them back in the mold for certain rest periods and temperatures. Afterwards, the specimens were stored again at 0°C for 2 hours, de-molded and re-fractured using the same displacement speed and temperature. The rest periods and temperatures applied before re-fracturing are shown in Table 3.9.
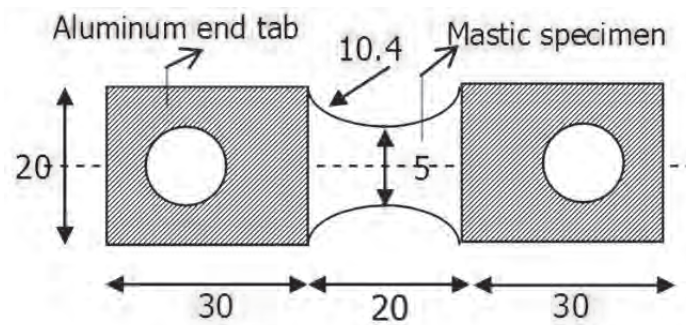
Figure 3.12. The double edge curve shaped of the DTT samples (all dimensions are in mm)

Table 3.9. Healing time and temperatures

Bituminous mastic pen 40/60		
T (°C)	Rest period (h)	n
10	3	1
	6	1
	24	1
20	3	1
	6	1
	24	1
40	3	1
	6	1
	24	1

3.3.8. Modification of the material
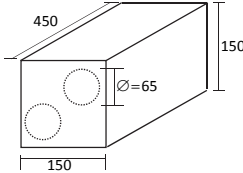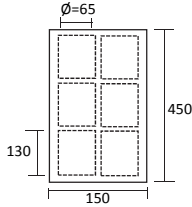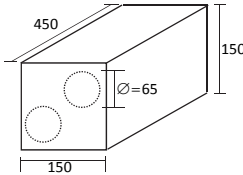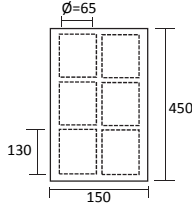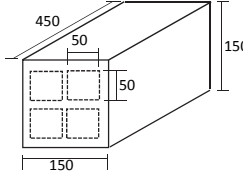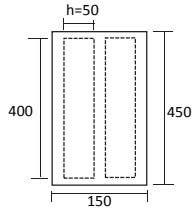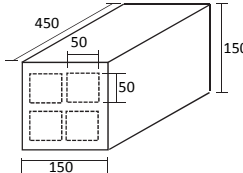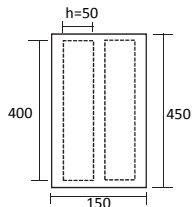
The modifier used in this research is a natural bitumen from Buton island Indonesia; the end product is called Retona®. The Retona® used in this study has a bitumen content of 35% and natural filler content of 65% by weight.

The production of the specimens is similar to that for making the GAC 40/60 mixture specimens which is explained in sub chapter 3.3.1. The Retona product is commonly used by replacing 20% of the bitumen content of the asphalt mixture. Therefore, the mixture design of the GAC 40/60 had to be slightly changed in order to get comparable mixtures from a gradation and volumetric point of view. The new mixture design which is called GAC 40/60+Retona is shown in Table 3.10. Table 3.11 gives an overview of the way the specimens were cut or drilled out of the GAC 40/60-Retona mixture blocks. More detail about the GAC 40/60+Retona tests and their results will be presented in chapter 5. The air voids of all specimens of GAC 40/60+Retona mixture varied from 2,9% to 6,0% (see Figure 3.13). Therefore, not all specimens could be used. Only specimens with air voids between 3.75% and 5.25% were used.

Table 3.10. Composition of the gravel asphalt concrete modified with Retona

Sieve size	% Weight (with Bitumen)					cumulative
(mm)	Gravel	River sand	'plaatzand'	Filler	Bitumen	
31.5 mm						
22.4 mm	5.22					5.22
16 mm	13.62					18.85
11.1 mm	12.44					31.28
8 mm	8.67					39.95
5.6 mm	8.56					48.52
4 mm	4.36					52.88
2 mm	0.75	1.01	0.15			54.79
500 μm		4.14	2.58			61.51
180 μm		4.82	16.57			82.89
90 μm				0.46		83.35
63 μm	0.16	0.31	6.44	0.17		90.44
passing 63 μm	0.05	0.02	0.03	4.19		94.73
bitumen 40/60					3.08	97.80
Bitumen Retona					0.77	98.57
Fines coming from Retona				1.43		100.00
Total	100.00					

Table 3.11. Overview of specimen's geometry and the test plan gravel asphalt concrete modified with Retona

Test	Dimension (mm) (shape) n	Coring/sawing (all in mm)	Top view (all in mm)
Monotonic Uniaxial Compression test	∅65*130 (Cylinder) 18		
Monotonic Uniaxial Tension test	∅65*130 (Cylinder) 18		
Four Point Bending test for Stiffness	50*50*400 (Beam) 4		
Four Point Bending test for Fatigue	50*50*400 (Beam) 9		
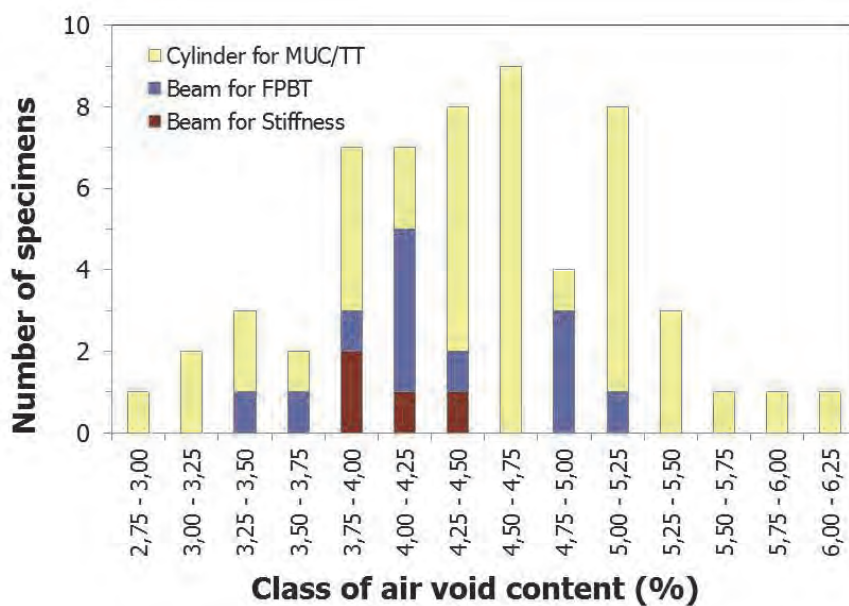
Figure 3.13. Air voids distribution of GAC 40/60+Retona specimens

3.4.   Analysis

The test results were used to develop a model that can predict the fatigue behavior of a GAC mixture. It was used to calculate the damage distribution of the Lintrack sections on the basis of Miner's law. The model for gravel asphalt concrete will be presented in chapter 4 and in chapter 5 the model for modified gravel asphalt concrete will be presented.

3.5.   Summary

This chapter started with the presentation and discussion of the approach that was followed to achieve the goals of this study being: to simulate more appropriately the fatigue behaviour of a real pavement in the laboratory, to determine the fatigue relationships of Gravel Asphalt Concrete specimens (GAC 2010) and, furthermore, to make comparisons between the predicted fatigue life obtained using the GAC 2010 fatigue relationship and fatigue life observed on accelerated pavement test sections (Lintrack 1990). Another goal of this research was to determine the effects of modifying the asphalt mixture with RETONA.

The preparation of specimens using the shear box compactor was presented and discussed. After that the tests which were performed on the GAC mixture and the Retona modified mixture were described.

3.6.   References

[1]   P. D. Bhairo, "Comparison of the predicted and Observed Pavement Life of LINTRACK Test Lane Va," Delft University of Technology, Delft, The Netherlands, 1997.
[2]   J. Groenendijk, "Accelerated Testing and surface cracking of asphaltic concrete pavements," PhD, Delft University of Technology, Delft The Netherlands, 1998.
[3]   J. Groenendijk and C.H. Vogelzang, "Pavement Performance Under LINTRACK Accelerated Loading, Extending measurement report and interpretation report section Vb," Delft University of Technology, Delft, The Netherlands, 1998.
[4]   F. H. v. Leeuwen, "Attachment: Construction Test Sections of GAC Type 57 at The Lintrack site of Delft University of Technology (In Dutch)," DWW (Dients Weg- en Waterbouwkunde), The Netherlands, 1990.
[5]   F. P. Pramesti, A. A. A. Molenaar, M.F.C. van de Ven, J. Qiu, and M.F. Woldekidan, "Comparison of Two Beam Fatigue Tests," *Journal of Testing and Evaluation,* 2014.

[6]   J. Qiu, N. Li, F. P. Pramesti, A.A.A. Molenaar, and M.F.C. van de Ven, "Evaluating Laboratory Compaction of Asphalt Mixtures using the Shear Box Compactor," *Journal of Testing and Evaluation,* vol. 40, p. 9, 2012.

[7]   NEN-EN-12697, "Bituminous Mixtures-Test methods for hot mix asphalt," in *Part 24; Resistance to fatigue*, ed: Comite Europeen de Normalisation, 2007.

[8]   J. Groenendijk, "Equivalence between a Practical-Loading Pulse and Loading Frequency for Four Point Bending Test in Retrospect to the Comparison of Measured and Calculated Asphalt Stiffness (in Dutch), Internal report," Delft University of Technology, Delft The Netherlands, 1992.

[9]   S.R. Bouman, A.A.A. Molenaar, C.A.P.M. van Gurp, and C.H. Vogelzang, "Lintrack Response Measurements; Comparison of Measured and Predicted Asphalt Strain (part I and II) (in Dutch), Report nr 7-91-209-17 and 7-91-209-18," Delft University of Technology, Delft The Netherlands, 1991.

[10]   M.R. Poot, M.F.C. van de Ven, and A. Cocurullo, "Asphalt Testing, Practical Manual CT 4830," ed: TU Delft, 2008.

[11]   J. Qiu, A.A.A. Molenaar, M.F.C. Van De Ven, and S. Wu, "Development of An autonomous Setup for Evaluating Self Healing capability of Asphalt Mixtures," in *2012 Annual Meeting of Transportation Research Board*, 2012.

[12]   S. Vismara, A.A.A. Molenaar, M. Crispino, and M.R. Poot, "Towards a Better Understanding of the Benefits of Geosynthetics Embedded in Asphalt Pavements," in *2012 Annual Meeting of Transportation Research Board*, Washington 2012.

[13]   Koninklijk Nederlands Meteorologisch Instituut (KNMI). (Accessed: 11 October 2010). *KNMI Data Centre - Observations & computational models*. Available: https://data.knmi.nl/portal/KNMI-DataCentre.html

[14]   J. Qiu, M.F.C. van de Ven, S. Wu, J. Yu, and A.A.A. Molenaar, "Investigating the Self Healing Capability of Bituminous Binders " *Int. Journal Road Materials and Pavement Design ICAM 2009,* vol. 10, 2009.

This page is intentionally left blank

Appendix 3A
Relationship between strain rates and stiffness of the Lintrack sections

The strain rates which were applied in the mechanical tests e.g. monotonic uniaxial tension and compression tests were determined based on the strain rates that were calculated at the bottom of the asphalt layer in the Lintrack sections.

Since Groenendijk [1] showed that the ten strain gauges installed in the Lintrack gave a large amount of scatter, it was highly impractical to determine the Lintrack strain rates from the available strain gauge information. Therefore it was decided to calculate the strain rates by means of the BISAR computer program. The calculations were performed for Lintrack sections I and VA.

3.A.1. BISAR input

The input data for the BISAR simulations are shown in Table 3A1.

Table 3A1. The inputs of the BISAR simulations

	Section I	Section VA
Wheel load	75 kN	75 kN
AC Thickness	0.15 m	0.08 m
The load area**	circle with a radius of 0.165 m.	circle with a radius of 0.165 m.
Subgrade stiffness***	160 MPa	160 MPa
Poisson's ratio all layer	0.35	
AC Stiffness	In the simulations six asphalt stiffness values were used being: 1000; 3000; 5000; 7000; 9000 and 11,000 MPa	
Position to be assessed	Layer 1, (xi; yi; 0.15)	Layer 1, (xi; yi; 0.08)

** Corresponding with the gross tyre pavement contact area
*** back calculated from FWD measurements Bouman [2].

3.A.2. BISAR output

The output of BISAR the simulations on Lintrack section I and VA is shown in table 3A2 and Table 3A3 respectively.

Table 3A2. The stress and the strain values at position of (0; 0; 0.15) of Lintrack section I

E1	E2	σ_{XX}	σ_{YY}	σ_{ZZ}	ε_{XX}	ε_{YY}	ε_{ZZ}	U_{XX}	U_{YY}	U_{ZZ}
(MPa)	(MPa)	(MPa)	(MPa)	(MPa)	µstrain	µstrain	µstrain	(µm)	(µm)	(µm)
1000	162	0.960	0.960	-0.404	765.7	765.7	-1076	0	0	812.6
3000	162	1.842	1.842	-0.242	427.2	427.2	-510.3	0	0	617.9
5000	162	2.266	2.266	-0.1837	307.4	307.4	-354	0	0	535.4
7000	162	2.544	2.544	-0.152	243.8	243.8	-276.1	0	0	485.3
9000	162	2.75	2.75	-0.131	203.7	203.7	-228.5	0	0	450.2
11000	162	2.914	2.914	-0.117	175.9	175.9	-196	0	0	423.6

Table 3A3. The stress and the strain values at position of (0; 0; 0.08) of Lintrack section VA

E1	E2	σ_{XX}	σ_{YY}	σ_{ZZ}	ε_{XX}	ε_{YY}	ε_{ZZ}	U_{XX}	U_{YY}	U_{ZZ}
(MPa)	(MPa)	(MPa)	(MPa)	(MPa)	µstrain	µstrain	µstrain	(µm)	(µm)	(µm)
1000	162	0.907	0.907	-0.656	819.4	819.4	-1291	0	0	1128
3000	162	2.567	2.567	-0.485	612.7	612.7	-760.5	0	0	948.2
5000	162	3.56	3.56	-0.401	490.8	490.8	-578.5	0	0	854.5
7000	162	4.271	4.271	-0.349	414	414	-476.9	0	0	792.1
9000	162	4.826	4.826	-0.312	360.7	360.7	-410	0	0	746.1
11000	162	5.282	5.282	-0.284	321.2	321.2	-362	0	0	709.9

3.A.3. Relationship between strain and stiffness

Using the results shown in Table 3A2 and 3A3, plots of the peak strains in the xx, yy and zz directions as a function of asphalt stiffness could be made. They are presented in Figure 3A1 and 3A2.
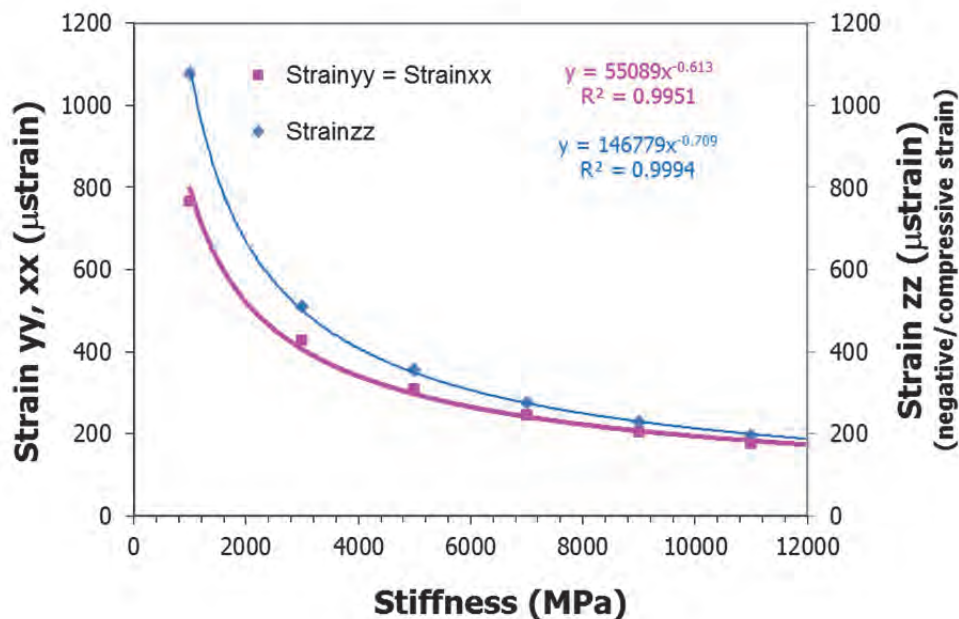
Figure 3A1. Relationship between strain and AC modulus stiffness of section I
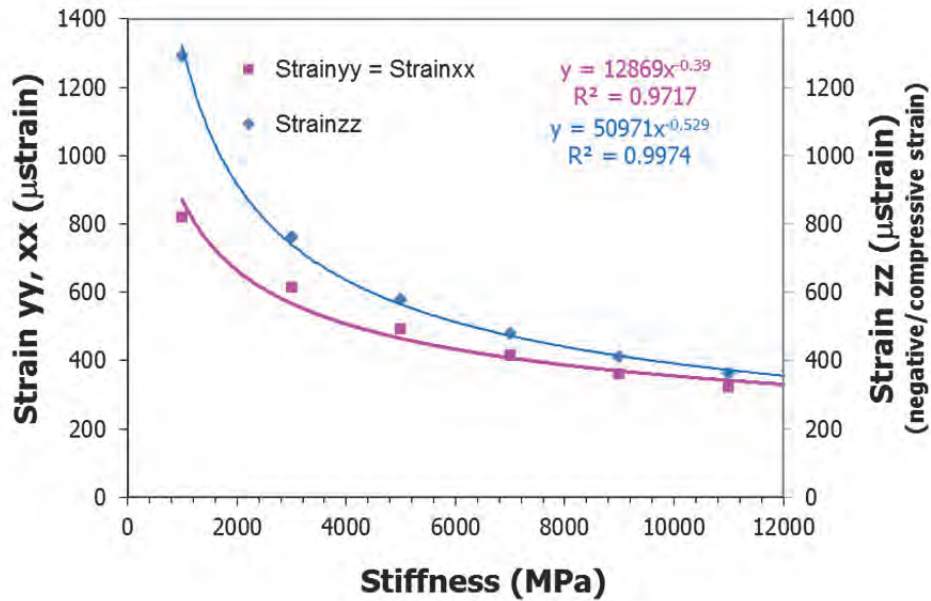
Figure 3A2. Relationship between strain and AC modulus stiffness of section VA

3.A.4. Determination of the strain rate

The strain rate can be determined as the change of strain with respect to time (see Equation 3A.1). Where t is the time required to reach d distance which can be determined using Equation 3A.2. The calculation results are recapitulated in Tables 3A4 and 3A5 for section I and VA consecutively.

$$\dot{\varepsilon} = \frac{\varepsilon}{t} \times 100\% \tag{3A.1}$$

where:

$\dot{\varepsilon}$ = strain rate (%/s)
ε = strain (m/m)
t   = time required to reach d distance (s)

$$t = \frac{d}{S} \tag{3A.2}$$

where:

d   = longitudinal distance from the location of the peak strain to the location where the strain equals 0 (m) (see Figure 3A3)
S   = speed (m/s)
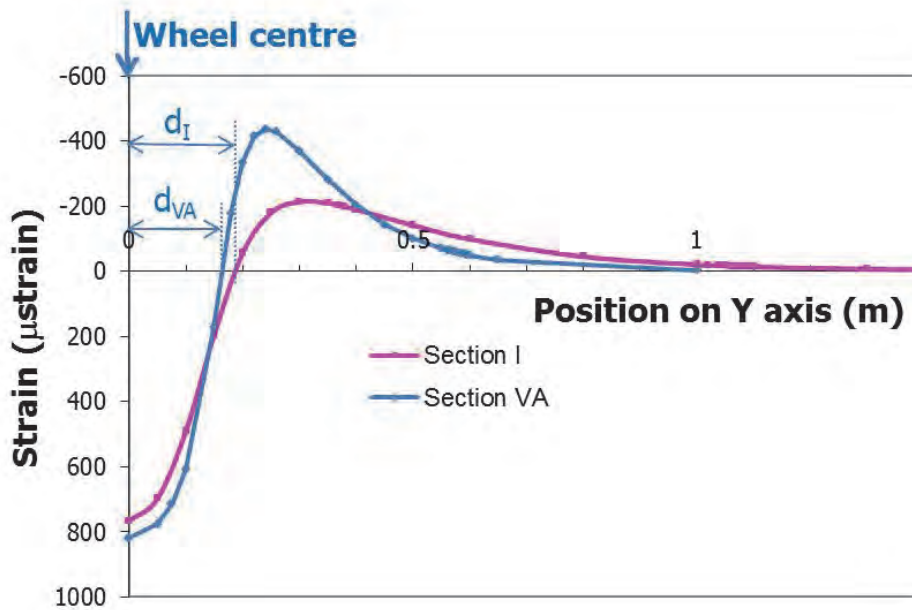
Figure 3A3. ε_{YY} of GAC Lintrack Section I and VA, at the bottom of asphalt layer, Smix=1000 MPa

Table 3A4. Simulation results for section I for position (0; 0; 0.15) being the bottom of the asphalt layer

Stiffness	Speed		Result from Bisar		Time	Strain rate	
			Max YY µstrain	y-coord when YY µstrain=0			
S_{mix}	S		ε		d	t	$\dot{\varepsilon}$
Mpa	km/h	m/s	µm/m	m/m	m	s	m/m/s	%/s
(0)	(1)	(2)	(3)	(4)	(5)	(6)=(5)/(2)	(7)=(4)/(6)	(8)=(7)x100
1000	20	5.556	765.7	7.7E-04	0.187	0.034	0.02	**2.27**
3000	20	5.556	427.2	4.3E-04	0.222	0.040	0.01	**1.07**
5000	20	5.556	307.4	3.1E-04	0.245	0.044	0.007	**0.70**
7000	20	5.556	243.8	2.4E-04	0.263	0.047	0.005	**0.51**
9000	20	5.556	203.7	2.0E-04	0.281	0.051	0.004	**0.40**
11000	20	5.556	175.9	1.8E-04	0.299	0.054	0.003	**0.33**

*(i) is the number of column

Table 3A5. Simulation results for section VA for position of (0; 0; 0.08) being the bottom of the asphalt layer

Stiffness	Speed		Result from Bisar		y-coord when YY μstrain=0	Time	Strain rate	
			Max YY μstrain					
S_{mix}	S		ε		d	t	$\dot{\varepsilon}$	
Mpa	km/h	m/s	μm/m	m/m	m	s	m/m/s	%/s
(0)	(1)	(2)	(3)	(4)	(5)	(6) =(5)/(2)	(7) =(4)/(6)	(8) =(7)x100
1000	20	5.556	819.4	8.2E-04	0.165	0.0297	0.03	**2.76**
3000	20	5.556	612.7	6.1E-04	0.178	0.03204	0.02	**1.91**
5000	20	5.556	490.8	4.9E-04	0.189	0.03402	0.014	**1.44**
7000	20	5.556	414	4.1E-04	0.197	0.03546	0.011	**1.17**
9000	20	5.556	360.7	3.6E-04	0.205	0.0369	0.009	**0.98**
11000	20	5.556	321.2	3.2E-04	0.212	0.03816	0.008	**0.84**

3.A.5. Relationship between strain rate and stiffness

The relationship between the stiffness and the strain rate for Lintrack sections I and VA can be formulated using power model as depicted in Equations 3A.3 and 3A.4 respectively. The relationships are shown in graphical form in Figure 3A5.

$$\dot{\varepsilon}=628.2\,S_{mix}^{-0.805} \qquad\qquad (3A.3)$$

$$\dot{\varepsilon}=90.11\,S_{mix}^{-0.493} \qquad\qquad (3A.4)$$
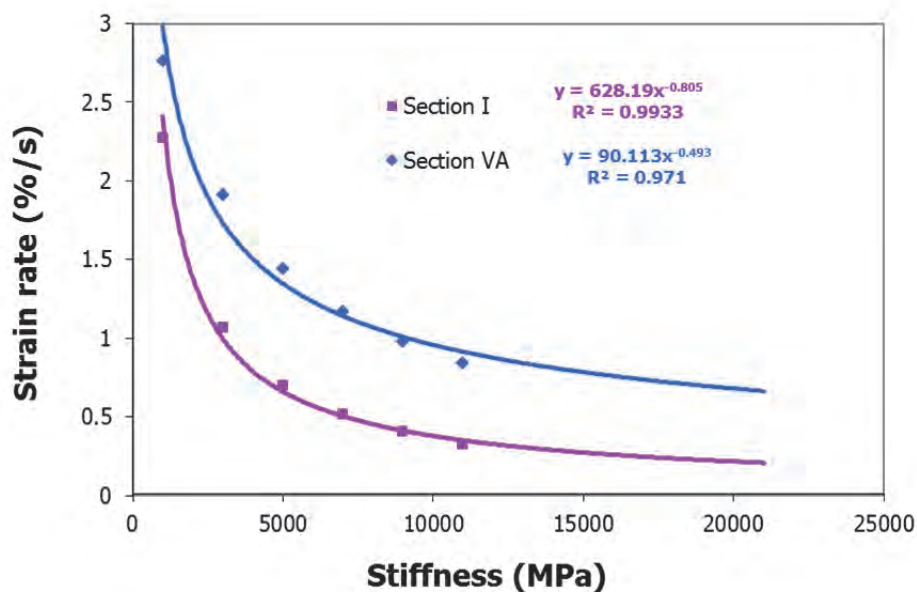
Figure 3A5. Stiffness versus strain rate of GAC Lintrack section I and VA

3.A.6. References

[1]   J. Groenendijk, "Accelerated Testing and surface cracking of asphaltic concrete pavements," PhD, Delft University of Technology, Delft The Netherlands, 1998.

[2]   S.R. Bouman, A.A.A. Molenaar, C.A.P.M. van Gurp, and C.H. Vogelzang, "Lintrack Response Measurements; Comparison of Measured and Predicted Asphalt Strain (part I and II) (in Dutch), Report nr 7-91-209-17 and 7-91-209-18," Delft University of Technology, Delft The Netherlands, 1991.

Appendix 3B
Relation between strain rate and deformation rate in Indirect Tensile Test

From Indirect Tensile Test (ITT) as discussed in sub chapter 3.3.6 one obtains data on the force vs the specimen's horizontal and vertical deformation. The deformation rate which is applied on the test can be determined from the relation between strain rate and deformation rate.

3.B.1. Relation of stress, strain and deformation for ITT specimen

As the vertical loading yields horizontal deformation, the strain rate of specimen can be reliably measured at the specimen's centre line. However this strain measurement is almost impossible due to the fact that this central region is where the crack initiates. Therefore the relation between displacement and strain rate can be explained from the plane stress conditions that occur and assuming linear-elastic material response.

Hondros [1] explains that the radial and tangential stresses at x and y direction as depicted in Figure 3B.1 can be obtained using Equation 3B.1 to 3B.4, assuming that the body forces are negligible. These equations relate the stresses to the pressure applied to the specimen. Having the stresses, the strain can be obtained and the deformation might be calculated using Equation 3B.5 to 3B.7 [2].

Figure 3B.1. Geometry and notation of polar stress component in ITT specimen [3]

$$\sigma_{\theta y} = \frac{2P}{\pi at}\left[\frac{\left(1 - \frac{r^2}{R^2}\right)\sin 2\alpha}{\left(1 - \frac{2r^2}{R^2}\cos 2\alpha + \frac{r^4}{R^4}\right)} - \tan^{-1}\left(\frac{\left(1 + \frac{r^2}{R^2}\right)}{\left(1 - \frac{r^2}{R^2}\right)}\tan\alpha\right)\right] \qquad (3B.1)$$

$$\sigma_{ry} = -\frac{2P}{\pi at}\left[\frac{\left(1 - \frac{r^2}{R^2}\right)\sin 2\alpha}{\left(1 - \frac{2r^2}{R^2}\cos 2\alpha + \frac{r^4}{R^4}\right)} + \tan^{-1}\left(\frac{\left(1 + \frac{r^2}{R^2}\right)}{\left(1 - \frac{r^2}{R^2}\right)}\tan\alpha\right)\right] \qquad (3B.2)$$

$$\sigma_{\theta x} = -\frac{2P}{\pi at}\left[\frac{\left(1 - \frac{r^2}{R^2}\right)\sin 2\alpha}{\left(1 + \frac{2r^2}{R^2}\cos 2\alpha + \frac{r^4}{R^4}\right)} + \tan^{-1}\left(\frac{\left(1 - \frac{r^2}{R^2}\right)}{\left(1 + \frac{r^2}{R^2}\right)}\tan\alpha\right)\right] \qquad (3B.3)$$

$$\sigma_{rx} = \frac{2P}{\pi at}\left[\frac{\left(1-\dfrac{r^2}{R^2}\right)\sin 2\alpha}{\left(1+\dfrac{2r^2}{R^2}\cos 2\alpha + \dfrac{r^4}{R^4}\right)} - \tan^{-1}\left(\frac{\left(1-\dfrac{r^2}{R^2}\right)}{\left(1+\dfrac{r^2}{R^2}\right)}\tan\alpha\right)\right] \qquad (3B.4)$$

where
P	= load applied (N)
a	= width of loading strip (mm)
t	= specimen thickness (mm)
r	= distance to the centre of the specimen (mm)
R	= Radius of the specimen (mm)
α	= Half of the top angle of the triangle between loading strip and the centre of the specimen

$$\varepsilon_x = \frac{1}{E}\left(\sigma_{rx} - \upsilon\sigma_{\theta x}\right) \qquad (3B.5)$$

$$\varepsilon_y = \frac{1}{E}\left(\sigma_{ry} - \upsilon\sigma_{\theta y}\right) \qquad (3B.6)$$

where
E	= Modulus of elasticity (MPa)
ε_x , ε_y	= strain in x and y directions
σ_{rx} , σ_{ry}	= radial stresses along x and y axes (MPa)
$\sigma_{\theta x}$, $\sigma_{\theta y}$	= tangential stresses along x and y axes (MPa)
ν	= Poisson's ratio

$$U_x = \int_{-R}^{R}\varepsilon_x dr$$

$$U_x = \frac{1}{E}\int_{-R}^{R}\left(\sigma_{rx} - \upsilon\sigma_{\theta x}\right)dr$$

$$\qquad (3B.7)$$

$$U_y = \int_{-R}^{R}\varepsilon_y dr$$

$$U_y = \frac{1}{E}\int_{-R}^{R}\left(\sigma_{ry} - \upsilon\sigma_{\theta y}\right)dr$$

where:
U_x , U_y	= Total specimen deformations along x and y axes (mm)

3.B.2. Relation between strain rate and deformation rate

By numerically integrating the above mentioned equations, the relation between vertical deformation rate and horizontal strain rate at the center of the specimen can be determined. This relation is given by means of Equation 3B.8.

$$\dot{\varepsilon}_{x,r=0} = SF \cdot \dot{U}_{y,tot} \qquad (3B.8)$$

where

$\dot{U}_{y,tot}$ = deformation rate in the y direction (mm/s)

$\dot{\varepsilon}_{x,r=0}$ = horizontal strain rate (1/s)

SF = shift factor

Figure 3B.2 shows the radial and tangential stress distribution along the x and y axes, with R = 50 mm, a = 12.7 mm and t = 40 mm. For a specimen with a radius (R) of 50 mm and width of the loading strip (a) of 12.7 mm, the shift factor (SF) is 0.00364. This value is similar with the shift factor value used by Erkens [2] for the ITT with similar loading strip's width and specimen's radius but with the thickness of 25 mm. It should be noted that a different SF values applies for specimens with a different radius and thickness and for a test set up with a different loading strip width.
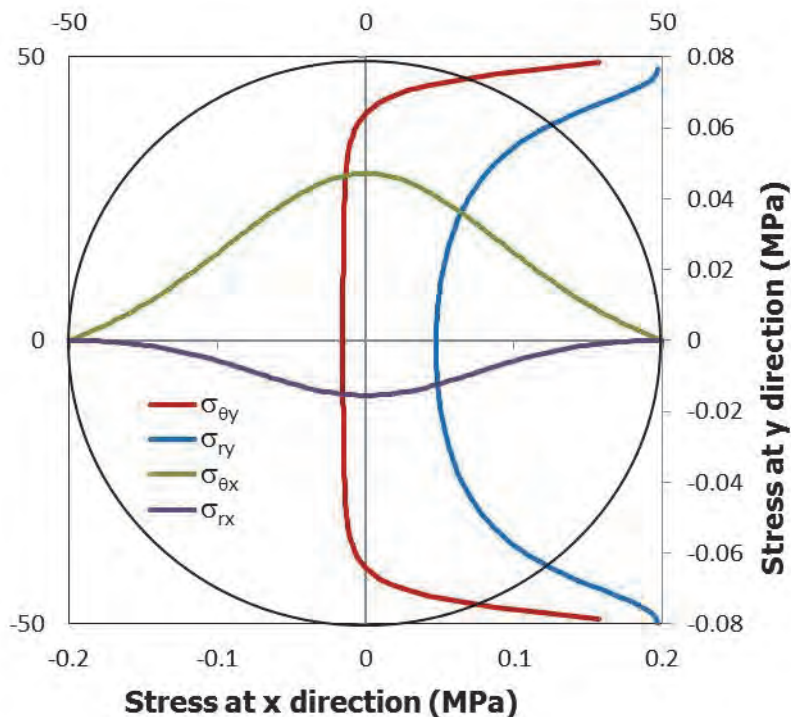
Figure 3B.2. Stress distribution along the principal axes with R = 50 mm, a = 12,7 mm

3.B.3. References

[1]   J.R. Hondros, "The Evaluation of Poisson's Ratio and the Modulus of Materials of a Low Tensile Resistance by the Brazilian (Indirect Tension) Test with Particular Reference to Concrete," *Austrian Journal of Applied Science,* vol. 10, pp. 243-268, 1959.

[2]   S. M. J. G. Erkens, "Asphalt Concrete Response - Determination, Modeling and Prediction," PhD, Delft University of Technology, Delft The Netherlands, 2002.

[3]   W.O. Hadley, W.R. Hudson, and T.W. Kennedy, "A Method of Estimating Tensile Properties of Materials Tested in Indirect Tension, Center for Highway Research," The University of Texas Austin, 1970.

This page is intentionally left blank

Chapter 4
Characterization of a gravel asphalt concrete base course mixture

As mentioned earlier, the main topic of this thesis is to re-analyze the Lintrack APT sections which were tested by the laboratory of Road and Railway Engineering at the Delft University of Technology The Netherlands. The reason for this is that it was not possible in earlier research to arrive to a good match between the predicted and observed performance of these sections and such a match is needed in order to be able to make reliable pavement life predictions. If one cannot predict the life of a carefully monitored test section how then the life of a real pavement can be predicted? Part of the mismatch might have been caused by the fact that the laboratory fatigue data used were determined at loading frequencies (30 Hz) which were completely different from the loading frequencies which occurred in the Lintrack experiments (3 – 8 Hz). Other factors (such as the unknown effect of healing) might have played a role as well.

As part of the re-analysis it was decided to characterize the asphalt mixture in such a way that an improved fatigue analysis (taking into account correct loading frequencies) would be possible. Since the original test sections did not exist anymore, the asphalt mixture as used in the Lintrack sections had to be reproduced based on the data from the original mixture composition. This was possible because the original mixture composition was well defined.

This chapter describes the results of the tests that were conducted on a gravel asphalt concrete (GAC) mixture identical to the mixture used in the Lintrack APT sections. Firstly, the characteristics of the components of the GAC are described. Secondly, the mixture's mechanical properties are determined by means of monotonic uniaxial compression and tension tests, indirect tension strength tests, four-point bending (4PB) tests and Beam on Elastic Foundation (BOEF) tests.

The four point bending (4PB) test was employed to study the fatigue properties of the mixture as this test is commonly used for pavement design purposes. The BOEF test was also performed since it is thought to provide a better representation of the real loading and boundary conditions occurring in pavements. The pavement can be seen as a long beam on top of a foundation (soil) and in the BOEF test asphalt beams resting on a rubber foundation were tested. The fatigue properties resulting from these two tests are described, compared and discussed. The mechanical properties resulting

from the other tests mentioned above are used to determine the yield surface line of the material. The yield surface will be used in analyzing the fatigue models obtained from the 4PB test and BOEF tests. This chapter ends with a summary of the main findings and conclusions.

4.1.   Characterization of the mixture components

The composition of the mixture used in this study and the specimen production has been explained in subchapter 3.3.1. In the following chapter, the characteristics of the GAC components will be discussed. Furthermore, the GAC mixture produced for this study and the GAC mixture of Lintrack sections will be compared.

4.1.1. Materials

No specific information is available about the characteristics of the gravel used in the Lintrack sections, only that the Lintrack test sections consisted of river gravel 0/32. The gravel used in this research is coming from typical river gravel 4/32 and 0/16 available in the market, resulting in a Gravel Asphalt Concrete (GAC) 57 type 0/32 hot mix which complies with the Dutch standards. The gravel has a density of around 2600 kg/m3 which was measured using a vacuum pycnometer. The results of these measurements are shown in Table 4.1.

Table 4.1. The density of the mixture component

Component	Density
	kg/m3
Aggregate 1 (Gravel 16-32)	2546*
Aggregate 2 (Gravel 4-16)	2622*
Aggregate 3 (Gravel 0-4)	2635*
Sand 1 (Rivierzand/River sand)	2671**
Sand 2 (Plaatzand/Foreshore sand)	2678**
Filler (Wigro)	2778**

*   Determined using vacuum-pycnometer
** Determined using ultra-pycnometer

The densities of the fine materials such as sand and filler were measured with an ultra-pycnometer. Two types of sand were used for making the mixture namely foreshore sand and river sand while Wigro filler was used as filler. The Wigro filler is produced by grinding limestone which is mined in a limestone quarry in Winterswijk, the Netherlands. Table 4.2 shows the grain size distribution of Wigro filler used. The density of the filler was 2778 kg/m3 (see Table 4.1). This value is in the range of NEVUL product specification for Wigro [1], which is in between 2680 kg/m^3 and 2880 kg/m^3.

The densities of the sands used for making the specimens are also shown in Table 4.1. The gradations of both sands are shown in Table 3.1 in chapter 3.

Table 4.2. Grain size distribution of Wigro filler [2]

Grain size distribution	Unit	value
63 μm	%(m/m)	17
90 μm	%(m/m)	10
2 mm	%(m/m)	0

4.1.2. Bitumen

To produce the gravel asphalt concrete mixture, a 40/60 pen bitumen was used which is commonly used in the Netherlands for base course layers. Table 4.3 shows the values of the penetration, softening point and the penetration index of the bitumen that was recovered from the GAC beam specimens. The penetration value of the virgin bitumen 40/60 is 30.8 (0.1mm) which is actually outside the 40/60 range. Reasons for this could not be found albeit that the bitumen (obtained as 40/60) was in stock for quite some time.

Table 4.3. Properties and source of the recovered 40/60 bitumen

	Pen [0.1 mm]	Softening Point [°C]	Penetration Index	Source
Recovered bitumen 40/60	19.2	59.5	-1.05	Q8: Kuwait Petroleum B.V.

The Dynamic Shear Rheometer was used to investigate the viscoelastic properties of the bitumen. These tests were performed using an AR 2000 Dynamic Shear Rheometer (DSR) (see Figure 4.1.). The machine has a torque capacity up to 0.2 Nm and is equipped with an environmental testing chamber; the temperature is accurately controlled by means of electrical heating in combination with nitrogen gas for cooling. The test results are commonly expressed in terms of the complex shear modulus (G*) and the phase angle (ϕ), both as function of temperature and frequency.

Figure 4.1. Dynamic shear rheometer machine and liquid nitrogen vessel

In this test, a thin layer of bitumen is placed in between two circular parallel plates (a type of test geometry available in the DSR). This layer normally has a diameter of 25 mm and a thickness of 1 mm for tests at temperatures above 20°C and a diameter of 8 mm and a thickness of 2 mm for temperatures below 20°C [3]. Prior to the test, a calibration was performed which takes into account effects of inertia and machine compliance factors. During the test, the lower plate is fixed while the upper plate rotates back and forth in a certain oscillating frequency creating shearing action, as depicted by Figure 4.2.

Readings of the applied torque and measuring the deformation provide the material response. By taking into account inertia and machine compliance factors, the torque and angular rotation signals deliver fundamental material properties such as complex shear modulus |G*|, complex shear compliance |J*|, and the phase angle ϕ.

The derivation of the equation to calculate the complex modulus based on the strain and the stress values as measured by the DSR is explained in detail by Woldekidan [14] and Hagos [15].
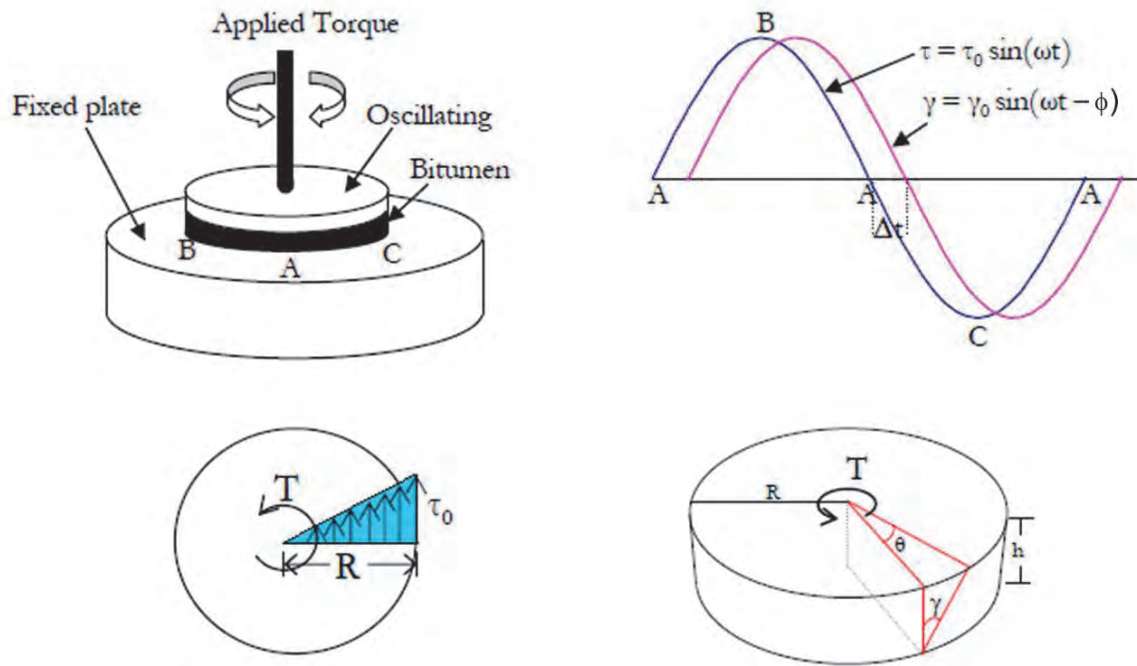
Figure 4.2. Dynamic shear rheometer (DSR) setup and working principle [4]

The DSR tests were carried out at various temperatures ranging from -10°C to 60°C and frequencies ranging from 0.05 Hz to 50 Hz. Using the Time-Temperature superposition principle, master curves of the complex modulus and phase angle at a reference temperature of 15°C were developed. This principle was used to shift the data obtained at various temperatures with respect to time or frequency to a selected reference temperature. The Williams-Landel-Ferry (WLF) Equation 4.1 was employed to accomplish this shifting process.

$$\text{Log } a_T = \frac{-C_1\left(T\text{-}T_0\right)}{C_2+\left(T\text{-}T_0\right)} \qquad\qquad (4.1)$$

where:

C_1, C_2 = constants
T = temperature [°C]
T_0 = reference temperature [°C]
a_T = shift factor

Woldekidan [4] introduced a new approach to develop a master curve based on the Huet Sayegh model (HS) called the Modified Huet Sayegh model (MHS). The creep compliance of the MHS model can be obtained by adding the compliance of a linear dashpot to the original HS model as shown in Equation 4.3. The complex modulus can now be determined as the inverse function of the creep compliance (see Equation 4.2)[5].

$$\left| G^{*}\left(\omega \right)_{MHS} \right| = \left| \frac{1}{J^{*}\left(\omega \right)_{MHS}} \right| \tag{4.2}$$

$$J^{*}\left(\omega \right)_{MHS} = \frac{G^{'}}{\left| G^{*}\left(\omega \right) \right|^{2}} - i.\left[\frac{G^{''}}{\left| G^{*}\left(\omega \right) \right|^{2}} + \frac{1}{\eta_{3}\omega} \right] = J^{'}\left(\omega \right) - i.J^{''}\left(\omega \right) \tag{4.3}$$

where:

$\left\| G^{*}\left(\omega \right)_{MHS} \right\|$	= magnitude of the complex shear modulus of the Modified HS model
$J^{*}(\omega)_{MHS}$	= the complex creep compliance of the MHS model
$J'(\omega)$	= storage creep compliance of the MHS model
$J''(\omega)$	= loss creep compliance of the MHS model
G'	= storage shear modulus of the original HS model
G''	= loss shear modulus of the original HS model
$\|G^{*}(\omega)\|$	= magnitude of the complex shear modulus of the original HS model
η_{3}	= the linear dashpot parameter
i	= complex number notation

The expression for the storage and loss modulus values of the original HS model is given by [6]:

$$G^{'} = G_{0} + A.\frac{G_{\infty} - G_{0}}{A^{2} + B^{2}} \quad \& \quad G^{''} = B.\frac{G_{\infty} - G_{0}}{A^{2} + B^{2}} \tag{4.4}$$

$$A = 1 + \delta_{1}\frac{\cos\left(m_{1}\frac{\pi}{2} \right)}{(\omega\tau)^{m_{1}}} + \delta_{2}\frac{\cos\left(m_{2}\frac{\pi}{2} \right)}{(\omega\tau)^{m_{2}}} \& B = \delta_{1}\frac{\sin\left(m_{1}\frac{\pi}{2} \right)}{(\omega\tau)^{m_{1}}} + \delta_{2}\frac{\sin\left(m_{2}\frac{\pi}{2} \right)}{(\omega\tau)^{m_{2}}} \tag{4.5}$$

Where:

G_{∞}	= instantaneous shear modulus value
G_{0}	= rubbery shear modulus value
τ	= time constants
m_{1}, m_{2}	= parabolic dashpot coefficients
δ_{1}, δ_{2}	= model parameters, where $\delta_{2} = 1$

Meanwhile:

$$\delta_1 = \frac{\tau_1 \left(G_\infty - G_0 \right)}{\eta_1} \tag{4.6}$$

Where:

η_1 = the linear dashpot parameter 1

The frequency sweep results of the recovered bitumen 40/60 are shown in Figure 4.3, whereas Figure 4.4 shows the G^* and phase angle master curves of the recovered bitumen.
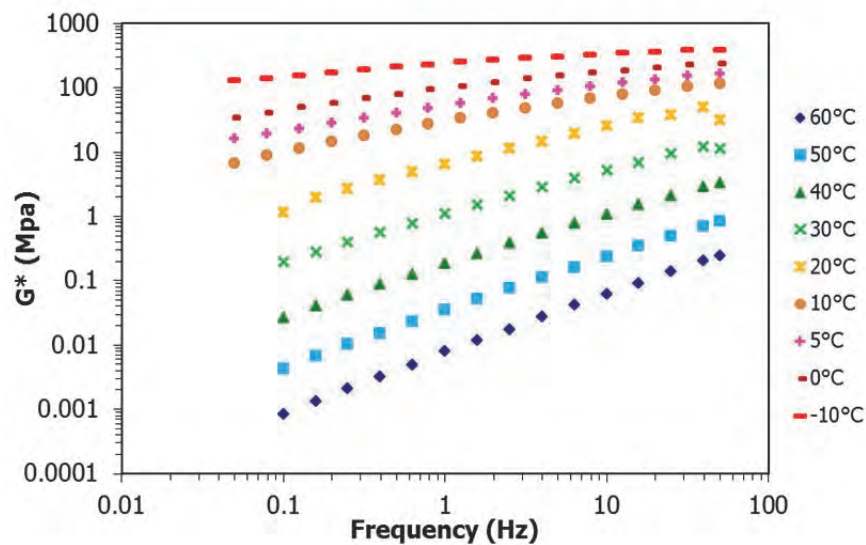
Figure 4.3. Measured Complex Modulus of recovered bitumen pen 40/60 at various temperatures as a function of frequency

Saal & Labout [7] proposed a relation between the bitumen penetration and the G^* resulting from DSR tests. In 1998, Molenaar [8, 9] also published a similar relation which is shown in Equation 4.7. By determining the G^* value of the recovered bitumen 40/60 at the temperature of 25°C and frequency of 0.15 Hz, the penetration value of the recovered bitumen can be calculated.

$$\text{Log}\left(\text{Pen}_{25°C \, [dmm]} \right) = \frac{7.845 - \text{Log}G^*_{25°C, \, 0.15Hz}}{1.642} \tag{4.7}$$

Using Equation 4.7 a bitumen penetration value of 16.5 dmm was derived. This value is lower than the value resulting from penetration test determined in the laboratory as shown in Table 4.4 but taking into account the accuracy of the penetration test, the agreement between the measured and predicted pen values can be rated as fairly good.
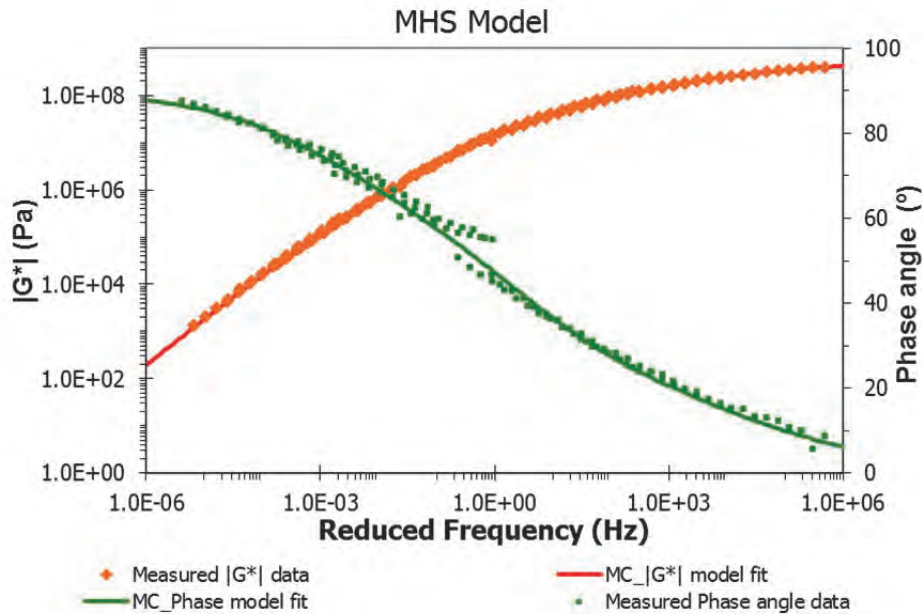
Figure 4.4. Master curve of 40/60 recovered bitumen at reference temperature of 15°C

It should be noted that Van den Bergh [10] in his research concluded that for a hard bitumen, pen values predicted using G* are to be preferred above those measured with the penetration test.

Table 4.4. The G* and penetration value of recovered bitumen 40/60

Bitumen	Penetration value (Laboratory test)		$G^*_{25°C;\ 0.15Hz}$	Penetration value (Equation 4.7)
	I	II		
	dmm	dmm	Pa	dmm
Recovered 40/60	19.2	18.7	7.05E+05	16.5

4.1.3. Mixture properties

As explained in chapter 3, the specimens tested in this study were produced using a Shear Box Compactor with a target air voids in the range of 4% to 5% representing a specimen density of 2324 kg/m^3 to 2365 kg/m^3. This was done because the produced mixture should be a copy of the mixture which was used in the Lintrack APT sections.

After the Lintrack GAC sections were constructed, some cores and slabs were drilled and sawn. The volumetric properties of these specimens were then determined and the results are shown in Table 4.5. In the beginning, the measurements were carried out by RHED in 1990, followed in 1991 by Watimena [11], van de Ven [12] and Sassen [13] in the same year. Besides determining the volumetric properties of the asphalt concrete, Watimena and Sassen also used the specimens to determine the AC fatigue behavior and the initial dynamic stiffness modulus.

In 1994, Groenendijk used non-destructive nuclear measurements to determine the density of the Lintrack sections. Sabha (in 1995) determined the densities of cores of the bottom layer of Lintrack section 1 while Bhairo (in 1997) did the same for section I and VA for loaded parts of the sections and parts which were not subjected to the Lintrack wheel loads.

Having the objective to produce specimens with similar volumetric characteristics, the production process of the specimens used in this thesis was carefully performed from the mixture design to the drilling/cutting process. In total as many as 140 beams and cylinders of the GAC mixture were sawn and drilled from 30 slabs. The comparison of the average density and air voids of those specimens to the values measured on samples taken from the GAC Lintrack sections and reported in previous studies [11-16] is presented in Table 4.5.

Table 4.5. Comparison of density, bitumen and air voids between the GAC produced for this study (GAC 2010-Pramesti) and the GAC of the Lintrack sections

		Density (kg/m^3)			Air voids (%)			Bitumen content (%)		
		average	st dev	n	average	st dev	n	average	st dev	n
Lintrack Top	1990	2380	13	20	4.3	0.3	12	4	0.3	12
Bottom		2362	12	20	4.8	0.6	12	4.1	0.3	12
All		2371	16	40	4.6	0.5	24	4	0.3	24
Van de Ven & Watimena	1991	2325	10	20	NA			NA		
Sassen	1991	2330	15	12	NA			NA		
Groenendijk	1994	2350			NA			NA		
Sabha	1995	2373	12	51	NA			NA		
Bhairo	1997	2384			NA			NA		
Pramesti	2010	2353	24	140	4.6	0.73	140	4.0	0.03	140

From Table 4.5 it is clear that the density and air voids of the GAC specimens produced in 2012 are in the same range as the density and air voids reported for the GAC Lintrack sections.

From several GAC beams that were produced by the author, some amount of bitumen was recovered. Penetration tests and a Ring & Ball tests were carried out on the recovered bitumen. The results were compared to the penetration and Ring & Ball test as determined on the bitumen recovered from Lintrack section in 1991. Table 4.6. shows this comparison.

Table 4.6. Comparison of penetration, softening point and penetration index of the recovered bitumen of GAC 2010 with recovered bitumen of GAC 1990 from Lintrack sections

		Penetration (0.1 mm)		Softening Point(°C)		Penetration index	
		average	n	average	n	average	n
GAC	Top	35		55.5		-0.7	
1990	Bottom	44		52		-1.0	
GAC 2010		19.2	3	59.5	2	-1.05	2

It must be concluded that copying the characteristics of the bitumen was not really successful. The fact that the bitumen used in this thesis had a penetration below 40 will have attributed to this. Later on some discussion will be given about how these differences might have affected mixture stiffness and fatigue characteristics.

4.1.4. Self-healing capacity of the mastic

The healing test performed in this work was similar to the test carried out by Qiu [17] as explained in the subchapter 3.3.7. It is considered as a fracturing-healing-re-fracturing mastic Direct Tension Test (DTT), where the mastic is composed of filler mixed with bitumen.
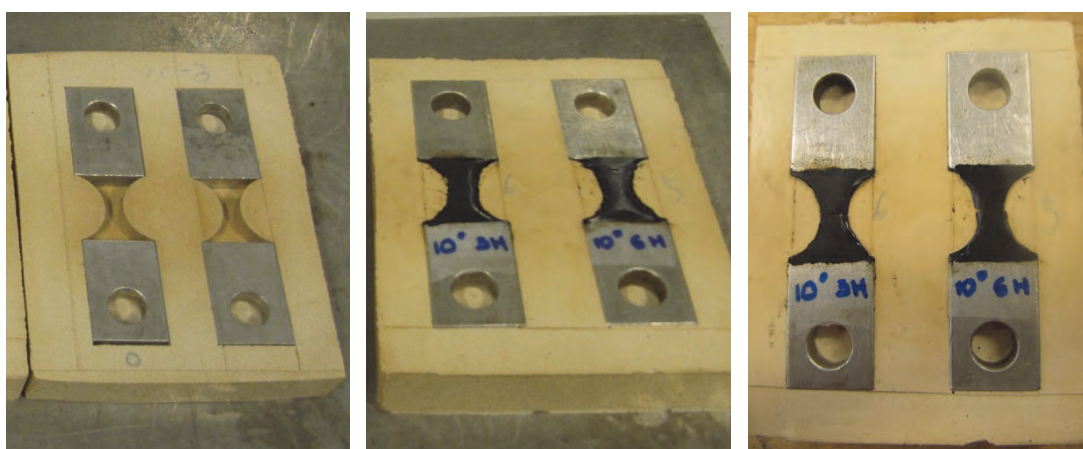
Figure 4.5. The double edge curve shaped mold of the DTT sample (left), bitumen mastic poured into the mold (middle) and starting the healing process by placing the fractured specimen back in the mold (right)

The samples for this study were made by using a double edge curve shaped mold as shown in Figure 4.5. The samples were fractured at a displacement rate of 100 mm/min at 0°C and were then healed by placing them back in the mold for a certain rest period and a certain temperature (see Table 3.9.). Then the specimens were de-molded and re-fractured in the same way, after conditioning them again in the DTT chamber at 0°C for 2 hours.

Table 4.7. Tensile strength before and after healing (kN)

Temperature	10°C		20°C		40°C	
Rest Period (hour)	Before	After	Before	After	Before	After
3	0.066	0.000	0.166	0.044	0.110	0.100
6	0.109	0.023	0.091	0.070	0.113	0.117
24	0.114	0.048	0.075	0.065	0.116	0.113

The tensile strength before and after rest period are shown in Table 4.7. Figure 4.6. shows a typical displacement versus load graph as obtained by means of the test. Figure 4.7. shows the healing percentage of mastic for different rest periods and different temperatures. The healing percentage shows the tensile strength before rest period divided by the tensile strength after rest period.
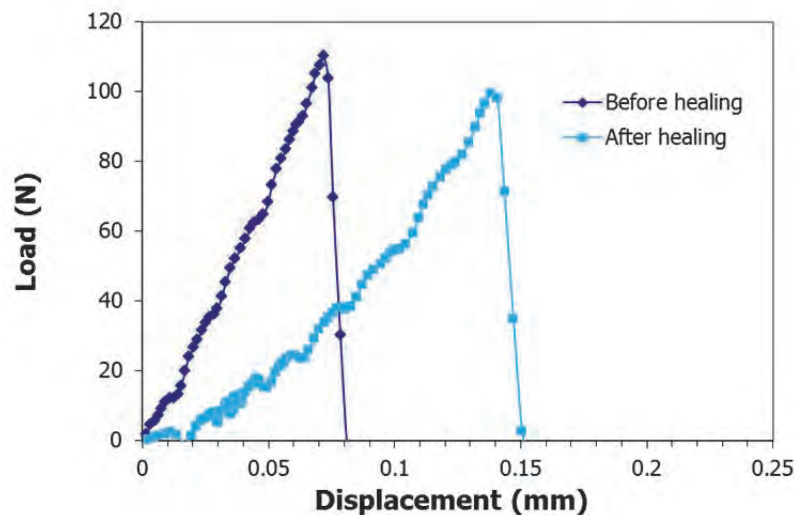
Figure 4.6. Typical result of the tension test on mastic sample before and after healing, at 0°C, 100 mm/min and with a rest period of 3 hours at a healing temperature of 40°C

From Figure 4.7 it can be seen that fractured specimens even show some healing at a temperature as low as 10°C. At higher temperatures significant healing occurred while at 40°C the specimen healed completely after a rest period of 6 hours. It is mentioned again that Figure 4.7 shows healing of fractured specimens. It is fair to expect that specimens which are not fractured but would show some internal micro damage would clearly show a better healing performance [18].
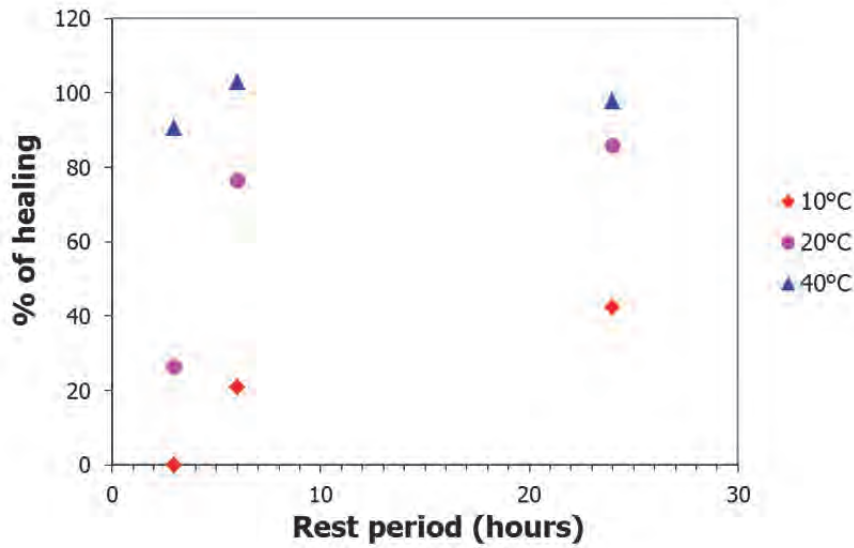
Figure 4.7. Healing of bituminous mastic pen 40/60

Qiu [18, 19] constructed a strength recovery master curve to model the time-temperature dependency of the self-healing process of bitumen pen 70/100 and SBS polymer modified bitumen. A typical Christensen-Anderson S shaped model for the complex modulus master curves was used as shown in Equation 4.8 [10, 11]. The Arrhenius equation (see Equation 4.9) was employed to determine the time-temperature superposition shift factor.

$$H(t,T) = 100 * \left\{ 1 + \left(\frac{m}{t^* \alpha_T} \right)^{\frac{\log 2}{n}} \right\}^{-\frac{n}{\log 2}} \quad (4.8)$$

$$\text{Log } \alpha_T(T) = \frac{\Delta E_a}{2.303 R} \left(\frac{1}{T} - \frac{1}{T_0} \right) \quad (4.9)$$

where,
H(t,T) = Healing percentage at a reference temperature of T°C (%)
t   = Healing time (hours)
m, n   = model parameters;
α_T = time-temperature superposition shift factor;
ΔE_a = apparent activation energy, J/mol;
R   = universal gas constant, 8.314 J /(mol ·K);
T   = temperature (K);
T_0 = reference temperature (K).

Using the same approach, the strength recovery master curve for bitumen mastic 40/60 used in the GAC mixture was developed for a reference temperature of 15°C. The related model is shown in Equation 4.10 and the master curve is presented in Figure 4.8.

$$H(t,T) = 100 * \left\{ 1 + \left(\frac{21.82}{t * \alpha_T} \right)^{\frac{\log 2}{0.192}} \right\}^{-\frac{0.192}{\log 2}} \qquad (4.10)$$

$$\text{Log } \alpha_T(T) = 5406.085 \left(\frac{1}{T} - \frac{1}{T_0} \right) \qquad (4.11)$$
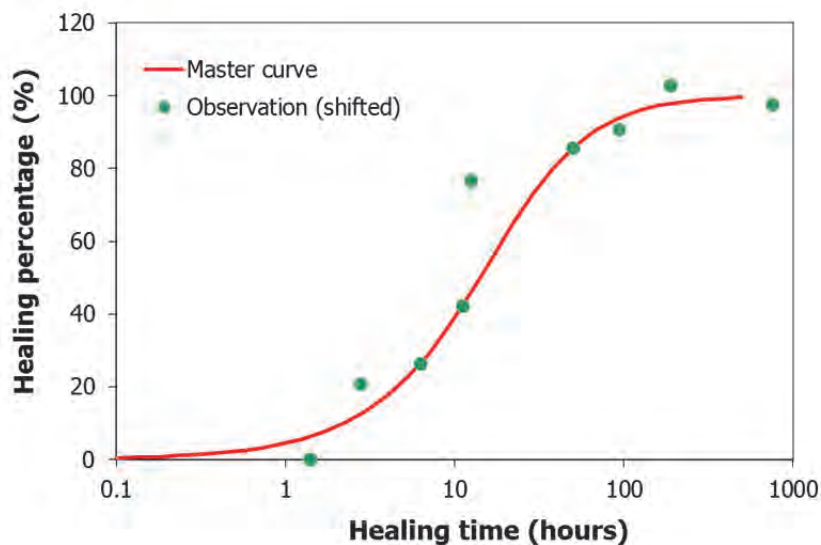
Figure 4.8. Self-healing master curve of the bituminous mastic 40/60 at Tref of 15°C

Given the results obtained from the healing tests it seems reasonable to assume that healing of fractured cracks will not occur between two successive load repetitions at temperatures of 10°C and lower. However, when there is only micro damage, healing can be expected to take place. This is supported by the finding of Qiu et al [21] on the self-healing characteristic of bituminous mastics. It is mentioned that one of the important factors that influence the healing behavior of bituminous mastics is the crack phase. A higher self-healing capability can be obtained when the crack phase is smaller.

Related to the healing due to the rest periods during the Lintrack tests because of maintenance and not operating Lintrack during the weekends, Groenendijk noticed some recovery (recovery in terms of stiffness) of the Lintrack AC stiffness. This 'recovery' only occurred in the beginning of the test when seemingly the pavement still has a self-healing capability. However, at the end of the test when the pavement showed significant structural damage, the mixture stiffness did not recover during the rest periods.

All in all this means that assuming a healing factor of 4 as was done in the previous analyses is a rather crude simplification of reality which most probably is wrong. Temperature, duration of the rest periods as well as damage progression all need to be taken into account.

4.2.   Mechanical behavior of Gravel Asphalt Concrete

The following tests were performed for characterizing the mechanical behavior of the gravel asphalt concrete.
- Monotonic uniaxial tension and compression tests to determine yield surfaces as a function of temperature and strain rate.
- Four point bending tests to determine the stiffness of the mixture as a function of frequency and temperature
- Four point bending fatigue tests at various loading frequencies and temperatures relevant for the Lintrack conditions
- Beam on elastic foundation fatigue tests to determine the effect of a continuous support of the beam on fatigue results

Cylindrical specimens as well as beams were needed for this test program and these specimens were obtained by coring and sawing them from the blocks that were prepared with the press box compactor. The test plan and the layout of how the cores and beams were taken from the asphalt blocks were explained in chapter 3, Table 3.2.

4.2.1. Monotonic Uniaxial Compression test (MUCT)

A number of Monotonic Uniaxial Compression tests were performed on several specimens at different strain rates and temperatures; Table 3.7 shows the test conditions. One of the failed specimens is shown in Figure 4.9. The picture shows that the specimen had collapsed completely from top to bottom. However, some specimens also showed shear failure.

Sub chapter 3.3.4. explained the test setup of the compression test and its test program. Compressive stress versus compressive axial and radial tensile strain curves are shown in Figure 4.10, 4.11 and 4.12. The specimens were tested at temperatures of 5°C, 20°C and 30°C respectively.
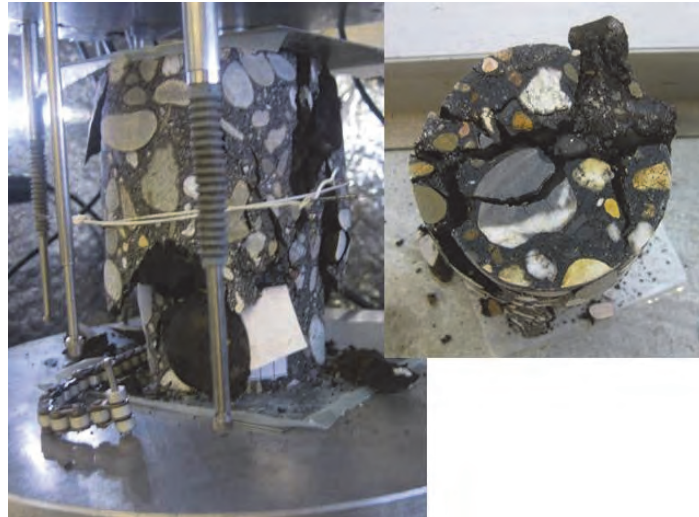
Figure 4.9. Failure of a specimen tested in compression at 5°C and at target strain rate of 1%/s. Side and top view.
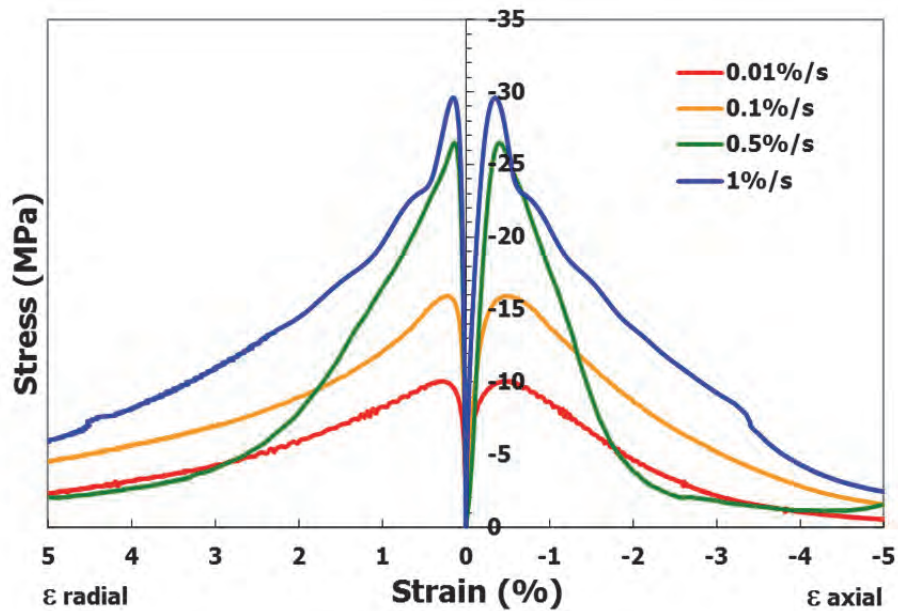
Figure 4.10. Compressive stress as a function of axial and radial strains at different strain rates at 5°C
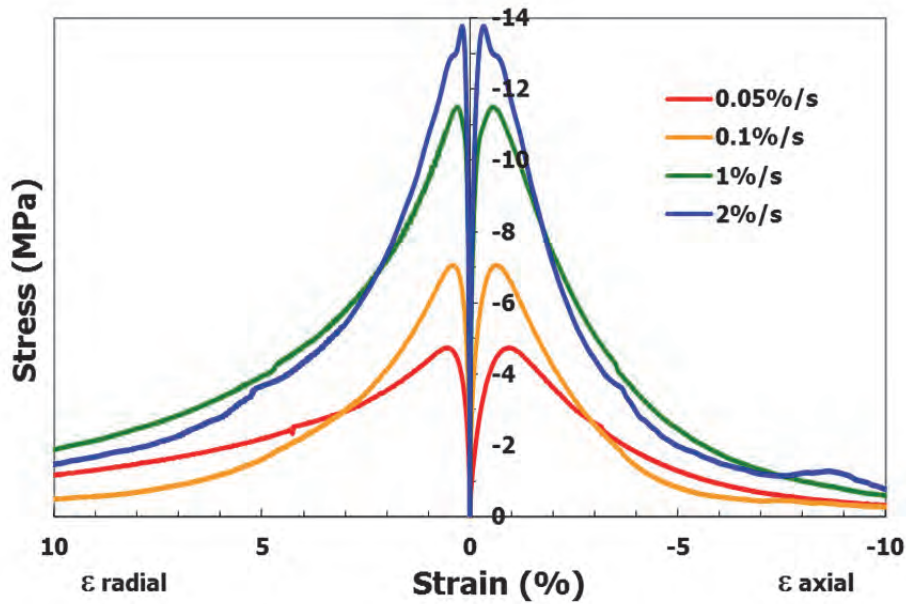
Figure 4.11. Compressive stress as a function of axial and radial strains at different strain rates at 20°C
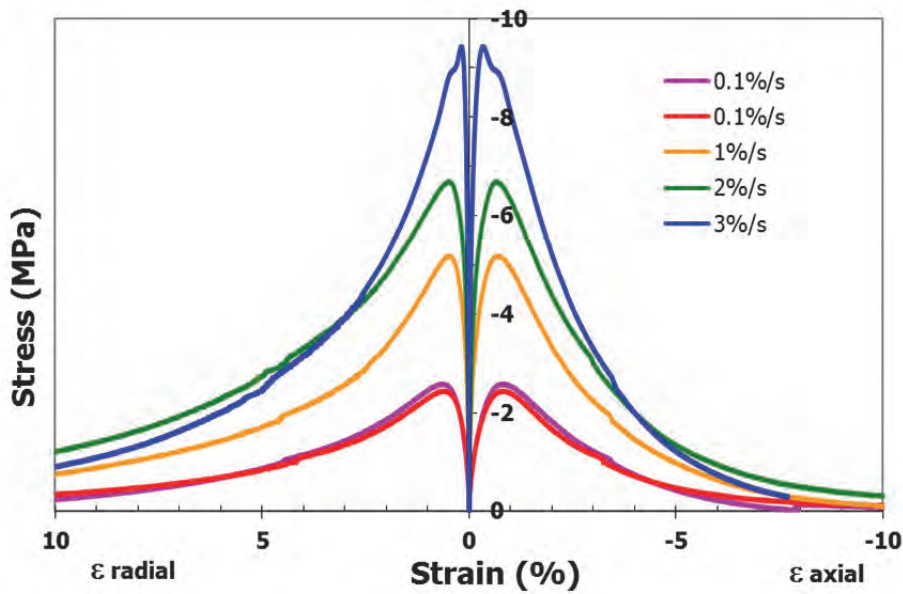
Figure 4.12. Compressive stress as a function of axial and radial strains at different strain rates at 30°C

The stress-strain curve was used to calculate the (tangent) E modulus in the MUCT as well as in the Monotonic Uniaxial Tension Test (MUTT) (to be discussed later). The modulus values were calculated by doing linear regression using data points collected when the stress was increasing from the 5% to 20 % of the maximum stress. The value of 5 % is chosen to avoid the influence of a possible touching/stretching effect in the beginning of the

test. The secant modulus is calculated simply by dividing the maximum stress by the strain at this maximum stress (Figure 4.13).

Poisson's ratio is calculated from the axial strain-radial strain curve over the same stress range as was used for calculation of the tangent E modulus. This is shown in Figure 4.14.
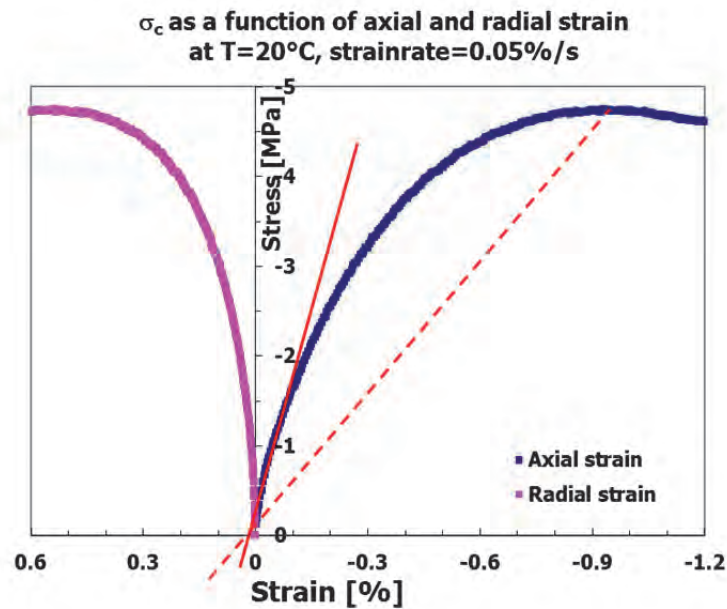
Figure 4.13. Sketch of the calculation of the tangent (solid line) and the secant Modulus (dashed line)
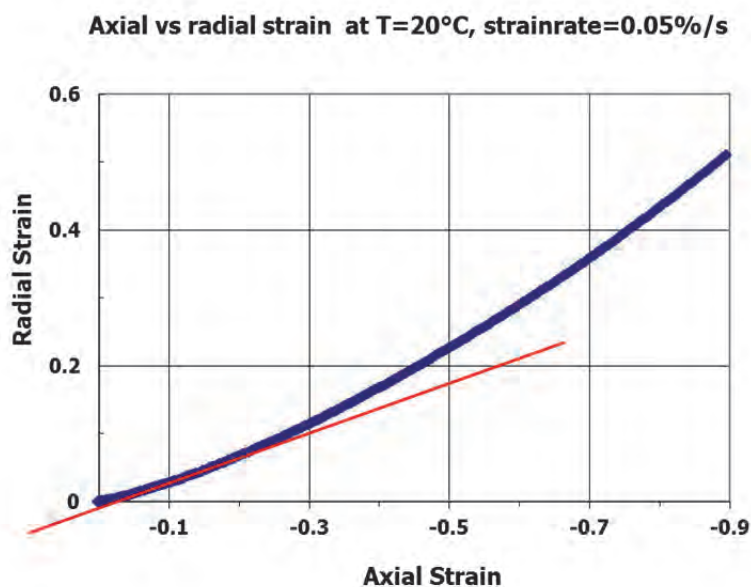
Figure 4.14. Sketch of the calculation of the Poisson's ratio (red line)

4.2.1.1. Correction of compression test results due to test set-up issues

It is recalled that the specimen was mounted in between a friction reduction system (on the top and at the bottom) and two loading platens. Since the displacement was measured between the two loading platens, this implied that not only the deformation over the total height of the specimen was measured but also deformations that might have occurred in the friction reduction system (FRS). It might even be possible that the measured deformations were affected by deformations of the loading frame. If this is the case then the measured modulus of the specimen would be lower than what it should be, especially when measuring small deformations (this is at lower temperatures and/or higher strain rates). In order to determine this effect, a similar test was performed using a steel specimen with the same dimensions and a known elastic modulus.

4.2.1.2. Monotonic Uniaxial Compression test using a steel specimen

A monotonic compression test on a steel specimen was done to investigate the effect of the two thin layers of the friction reduction system and the loading frame. The friction reduction system, which was placed on the top and bottom side of the specimen, consisted of a biological plastic, a thin steel plate and a thin layer of grease smeared in between them. Three LVDTs with a range of 2 mm were used to measure the deformation.

The test was done after 2 hour preconditioning in the force controlled mode at a loading speed of 0.02 kN/s. The test is summarized in Table 4.8. The results of this test are presented in Figure 4.15.

Table 4.8. Material and test conditions

Feature	material	Descriptor	Test condition
Specimen	Steel	$E = 2.1 \times 10^5$ MPa H = 130 mm $\varnothing$ = 65 mm	1. Steel specimen with friction reduction on the top and the bottom side 2. Force control with loading rate of 0.02 kN/s
Friction reduction	Biological plastic	E = unknown H = 0.05 mm	3. T = 20°C 4. Preload = 0.15 kN
	Grease	E = unknown H = unknown	5. Maximum Force = 60 kN 6. 2 hours precondition before start the test

During the initial phase of the test, the deformation increased rapidly with only a limited increase in force. This implies that a major portion of the

displacement at low load levels develops in the friction reduction system. This was followed by a linear phase at load levels higher than 30 kN, where a stiffness of 63,654 MPa is calculated. This stiffness is about 3 times lower than the stiffness of the steel specimen which is around 210,000 MPa.

This indicates that although the deformation of the FRS has come to an end, there is still an influence of -most probably- the loading frame to the development of the displacement. However, this influence can be ignored because the important properties were calculated in the initial phase of the test. Later on it will be shown that tests on a Delrin specimen showed that this 'correction' is sufficient to obtain a correct modulus value.

Figure 4.15 clearly shows that the FRS causes a significant displacement and, thus, has an effect on the overall displacement measured especially in the beginning of the test. This effect should be considered in the calculation of Young's modulus of the specimen (tangent modulus) which is based on the slope in the beginning of the load – displacement curve.
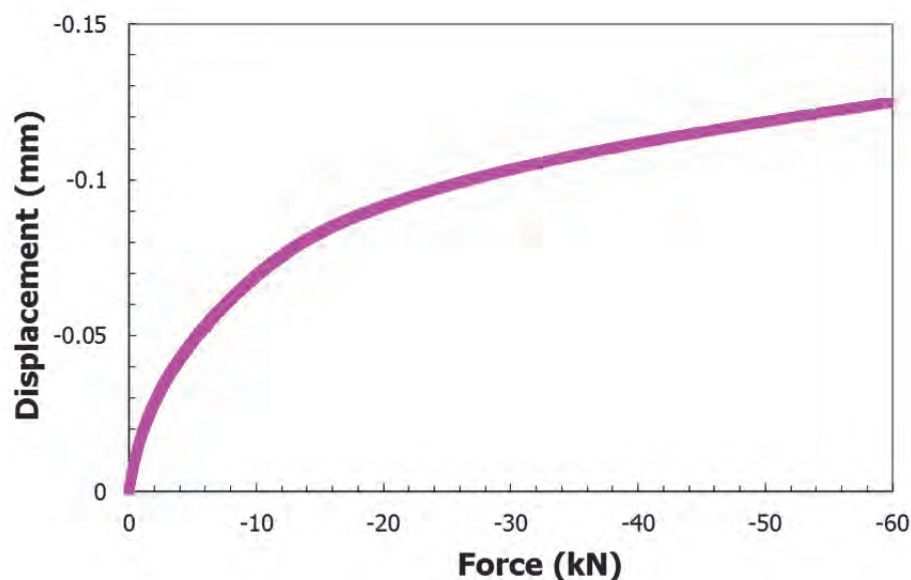
Figure 4.15. Applied force versus measured displacement during a compression test on a steel cylinder with plastic & grease as friction reduction system.

To exclude this effect, a relation between the stress and the displacement of the FRS/frame was developed. The stress-displacement curve shown in the fuchsia colored curve depicted in Figure 4.16 is best described by means of the following equation:

$$d_{correction} = a\sigma + b\sigma^c \qquad (4.12)$$

Where d is the displacement measured (in mm) and σ is the stress (in MPa). The constants that give the best fitting model are shown in equation 4.13. This fitted model is shown as a purple line in Figure 4.16.

For $0 \leq \sigma \langle 15$ MPa

$$d_{correction} = -0.5998\,\sigma + 0.6295\,\sigma^{0.9869}$$

For $\sigma \geq 15$ MPa

$$d_{correction} = 0.118\,mm$$

(4.13)
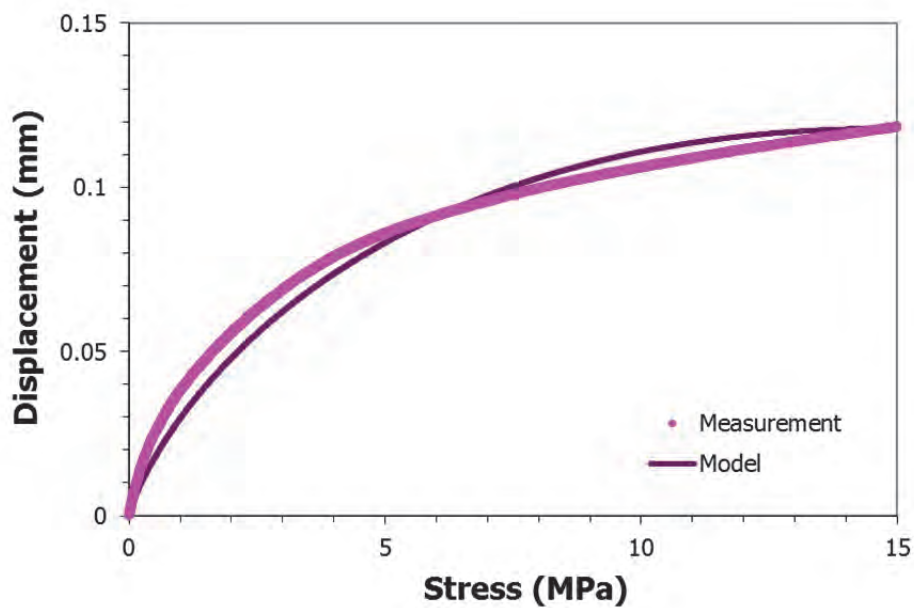
Figure 4.16. Stress versus displacement of a compression test on a steel cylinder using a friction reduction system

Equation 4.13 was used to calculate the correction value to be applied on the measured displacement, given the applied stress. Figure 4.17 shows how the correction affects the displacement in case of a GAC cylinder tested at a temperature of 20°C and a strain rate of 1%/s. This correction adjusted the specimen modulus elasticity from 5337 MPa to 10241 MPa (see Table 4.9). Moreover Figure 4.18 also shows that the axial strain at the labimum stress is shifted from -0.67% to -0.58%.
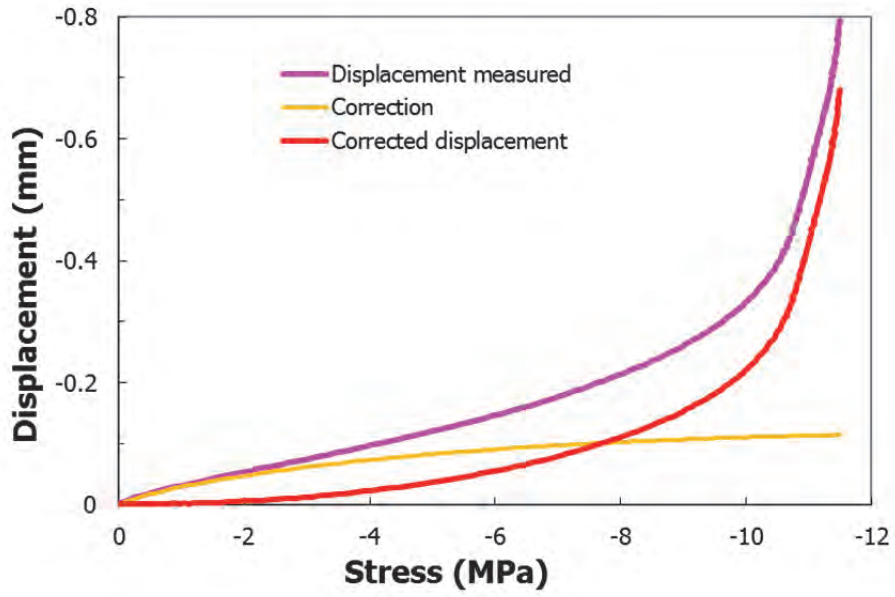
Figure 4.17. The original displacement measured for GAC 40/60 at T=20°C and $\dot{\varepsilon}$ =1%/s and the correction as a function of the stress
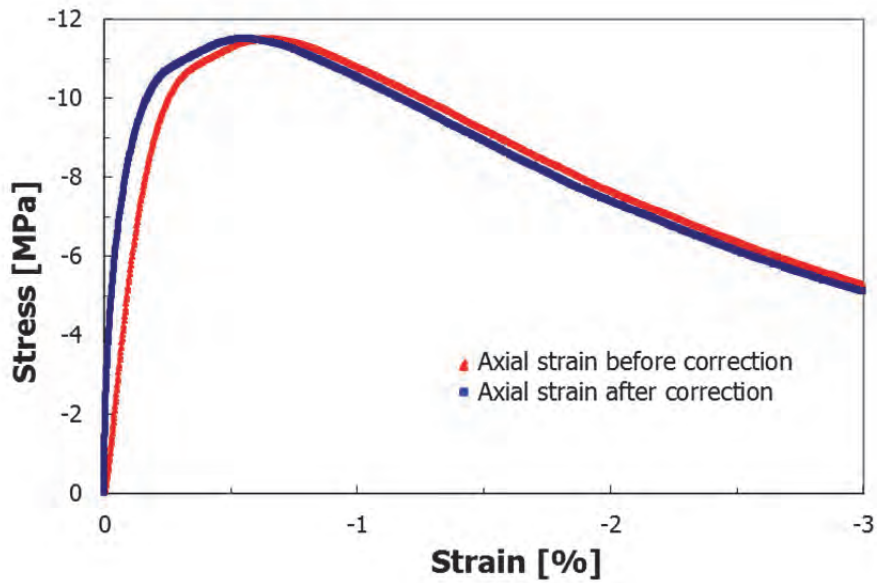
Figure 4.18. Axial strain-stress relation of GAC 40/60 tested at T=20°C and $\dot{\varepsilon}$ =1%/s. Before and after correction

4.2.1.3.   Validation using a Delrin (POM) cylinder

A compression test was performed on a Delrin[1] specimen to validate the correction model mentioned above. The dimension of the Delrin cylinder was identical to the GAC and steel specimen, so with a height of 130 mm and a diameter of 65 mm. The test condition and the friction reduction system employed were similar to the one mentioned in Table 4.8.
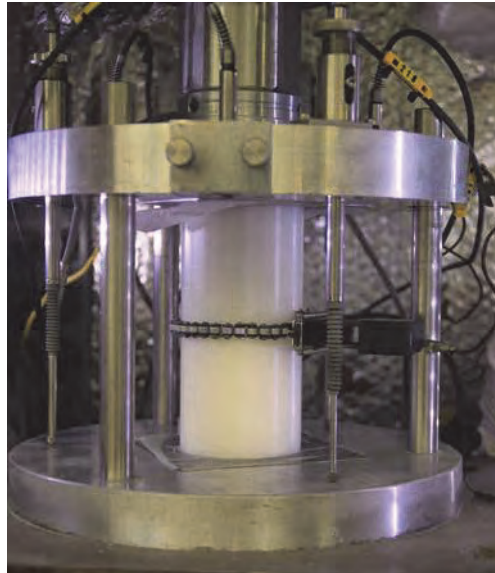
Figure 4.19. Delrin specimen in the set-up to validate the test method

Displacement measured as a function of stress is shown as fuchsia dots in Figure 4.20. Meanwhile the corrected value is presented as blue dots. The tangential modulus determined by means of linear regression on the measured and corrected data is 2210 MPa and 3278 MPa respectively. The latter value is relatively close to the well-known reference value of Delrin (POM) which has a compressive modulus of around 3100 MPa at 20°C [20]. These findings suggests that the correction equation (Equation 4.13) developed based on the test procedure using a steel specimen is also applicable for specimens which have a lower stiffness such as asphalt concrete specimens.

---

[1] Delrin is the trade name of a homopolymer acetal or polyoxymethylene (POM) produced by DuPont
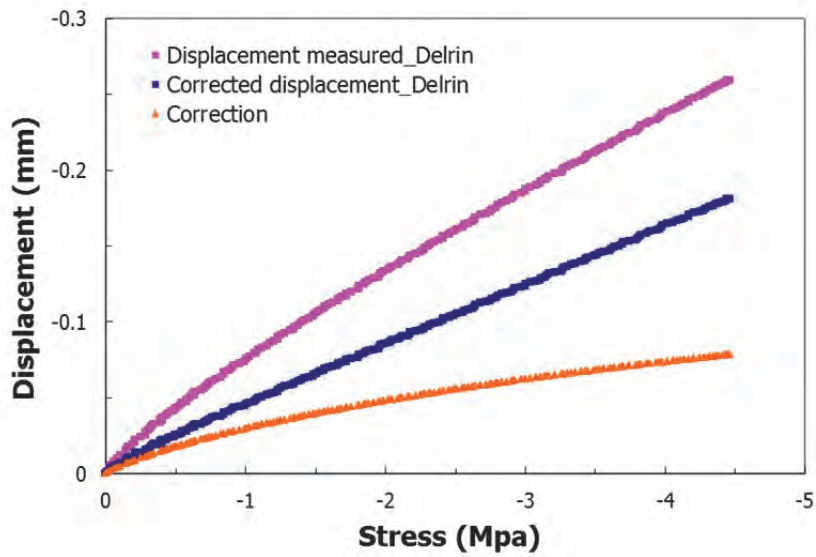
Figure 4.20. The original displacement measured for Delrin at T=20°C and $\dot{\varepsilon}$ = 0.1%/s and the correction as a function of the stress
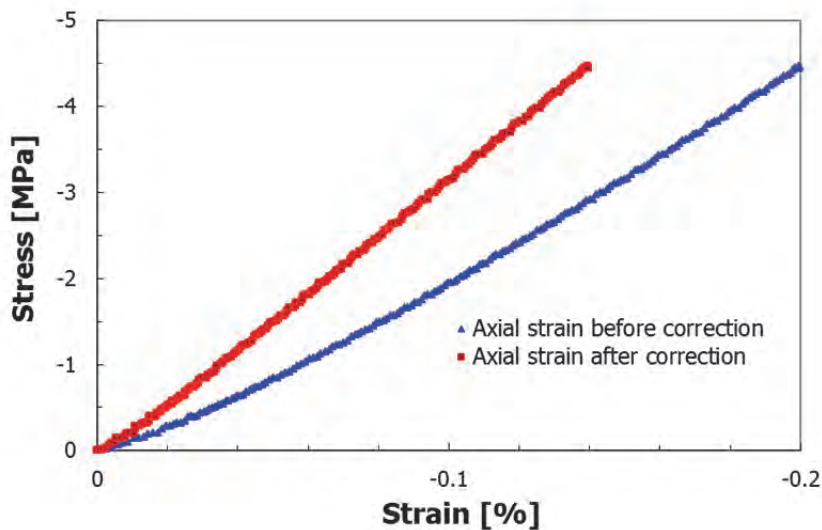
Figure 4.21. Axial strain-stress relation of Delrin tested at T=20°C and $\dot{\varepsilon}$ = 0.1%/s. Before and after correction

Applying the correction procedure on the E modulus values originally reported in Table 4.9 column 3 resulted in the values presented in Table 4.9 column 4. In the same way the Poisson's ratio values were adjusted. In Figure 4.22 the radial strain of the Delrin specimen as a function of the corrected axial strain is shown. From this figure a Poisson's ratio of 0.39 was calculated.

Figure 4.22. Corrected axial strain versus radial strain of the Delrin specimen in the MUCT at T=20°C and a strainrate of 0.1 %/s.

Table 4.9. Original and corrected E modulus values obtained from the compression tests.

T	Actual Strain rate	E mod before correction	E mod after correction	Ratio	Poisson's ratio before correction	Poisson's ratio after correction	Ratio
°C	%/s	Mpa	Mpa				
GAC							
5	0.0098	4863	7653	1.57	0.28	0.45	1.63
5	0.0993	5241	9340	1.78	0.12	0.21	1.81
5	0.5719	8170	11024	1.35	0.19	0.25	1.36
5	1.2645	8084	27515	3.40	0.11	0.37	3.42
20	0.0496	905	1028	1.14	0.31	0.36	1.14
20	0.0993	2059	2548	1.24	0.38	0.48	1.25
20	1.0063	5337	10241	1.92	0.27	0.52	1.93
20	2.6276	6538	13830	2.12	0.31	0.67	2.13
30	0.1001	556	613	1.10	0.61	0.67	1.10
30	0.1000	466	564	1.21	0.55	0.60	1.10
30	1.0179	1485	1782	1.20	0.52	0.63	1.22
30	2.0246	2293	2978	1.30	0.46	0.61	1.34
30	3.8790	4489	7700	1.72	0.33	0.57	1.72
Delrin							
20	0.1000	1926	2999	1.56	0.24	0.39	1.63

One should take into account that the correction procedure only applies for the test set-up and friction reduction system as used in the tests described here. It is obvious that each system has its own correction procedure.

The results obtained by means of the monotonic uniaxial compression test are displayed in Table 4.10. It is observed from the table that at high temperatures Poisson's ratio was higher than 0.5 showing that dilatation had occurred. This can be explained by the fact that this GAC contains big gravel stones up to the size of 32 mm in diameter, which can move in the radial direction when touching each other, especially at higher temperature when the bituminous mortar tends to be weaker.

Table 4.10. Summary of the monotonic uniaxial compression test results

	Target Strain rate	Actual Strain Rate	E mod	Secant Modulus	Poisson's ratio	f_c	Energy to peak	Total Energy
	%/s	%/s	MPa	MPa		MPa	J	J
5°C	0.01	0.010	7653	2144	0.45	-10.1	18.8	97.9
	0.1	0.099	9340	3428	0.21	-15.9	27.3	188.0
	0.5	0.572	11024	6656	0.25	-26.5	29.5	184.7
	1	1.265	27515	8439	0.37	-29.6	34.6	227.7
20°C	0.05	0.050	1028	508	0.36	-4.7	15.0	81.7
	0.1	0.099	2548	1064	0.48	-7.1	17.3	91.2
	1	1.006	10241	1989	0.52	-11.5	26.6	176.9
	2	2.628	13830	4247	0.67	-13.8	17.0	180.2
30°C	0.1	0.100	613	320	0.67	-2.6	7.0	34.0
	0.1	0.100	564	312	0.60	-2.4	6.4	35.7
	1	1.018	1782	741	0.63	-5.2	13.1	71.2
	2	2.025	3021	991	0.61	-6.7	16.7	100.8
	3	3.879	7700	2911	0.57	-9.4	11.7	112.4

4.2.2. Monotonic Uniaxial Tension test (MUTT)

For the uniaxial tension test, this study used the MUTT setup of the Road and Railway Engineering Laboratory of the Delft University of Technology. Sub chapter 3.5.5 explained the test set up and the procedure of the test. It is also extensively discussed and described by Erkens [21, 22]. The tension test was performed on 13 GAC specimens at different temperatures and strain rates.

Figure 4.23 shows a failed GAC specimen tested at the temperature of 30°C and strain rate of 0.1%/s. The figure shows what is called by some researchers [21, 23] 'localized failure' where the specimen breaks into two

parts and these two parts mostly remain undamaged. In case of figure 4.23, the specimen breaks in the middle and cracking is only taking place in the breaking area. All the specimens tested at 5°C, 20°C and 30°C show localized failure. Almost all of the specimen broke in the middle, only a specimen tested at 20°C and a specimen tested at 30°C broke at a fourth of its height. Figure 4.24, 4.25 and 4.26 show the result of the tests at temperatures of $5^{o}C$, $20^{o}C$ and $30^{o}C$ respectively. The figures present for each specimen the relation between the axial stress and strain.
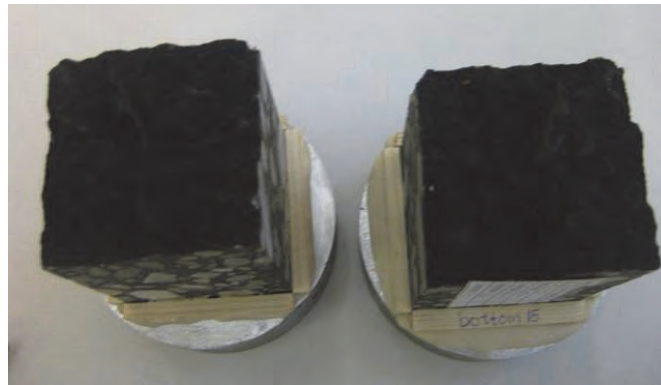
Figure 4.23. Failure of the specimen tested at 30°C and a strain rate of 0.1%/s
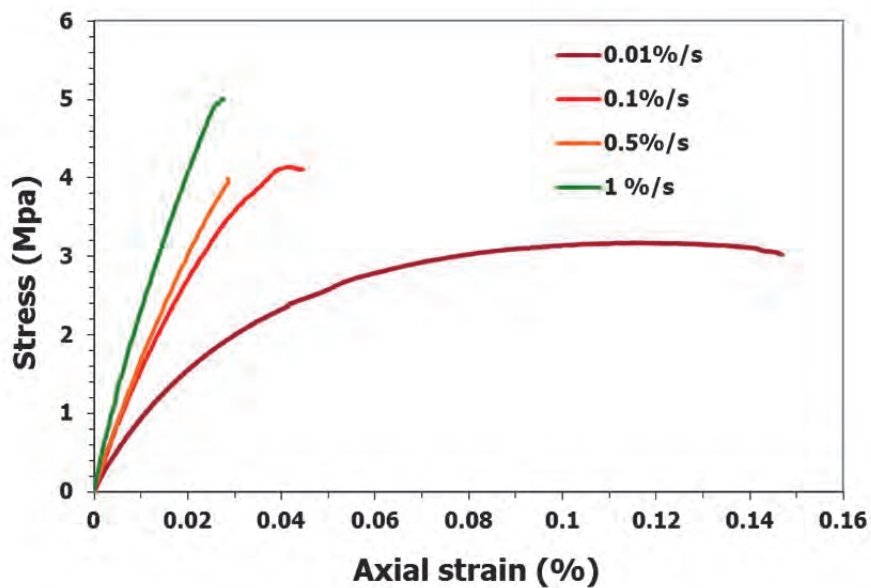
Figure 4.24. Tensile stress versus axial strain of GAC at 5°C
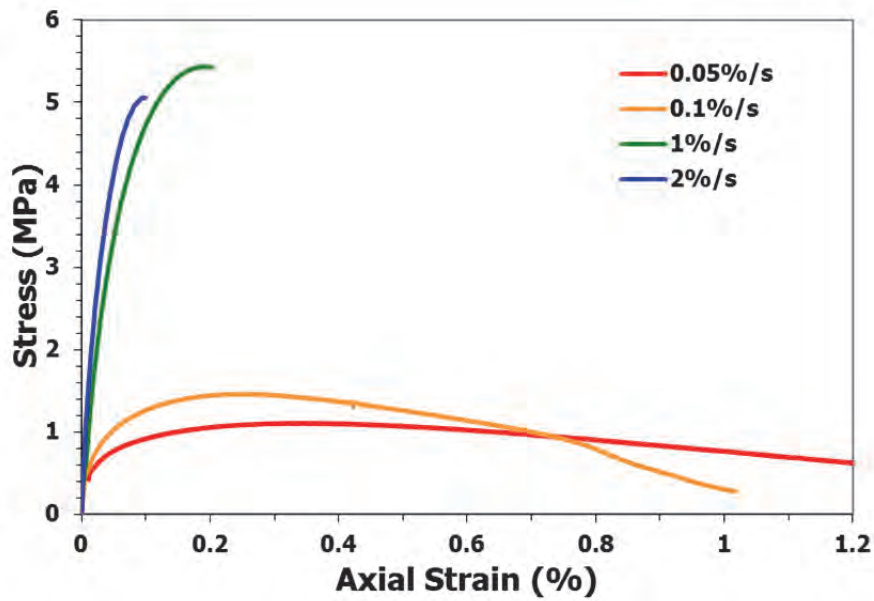
Figure 4.25. Tensile stress versus axial strain of GAC at 20°C
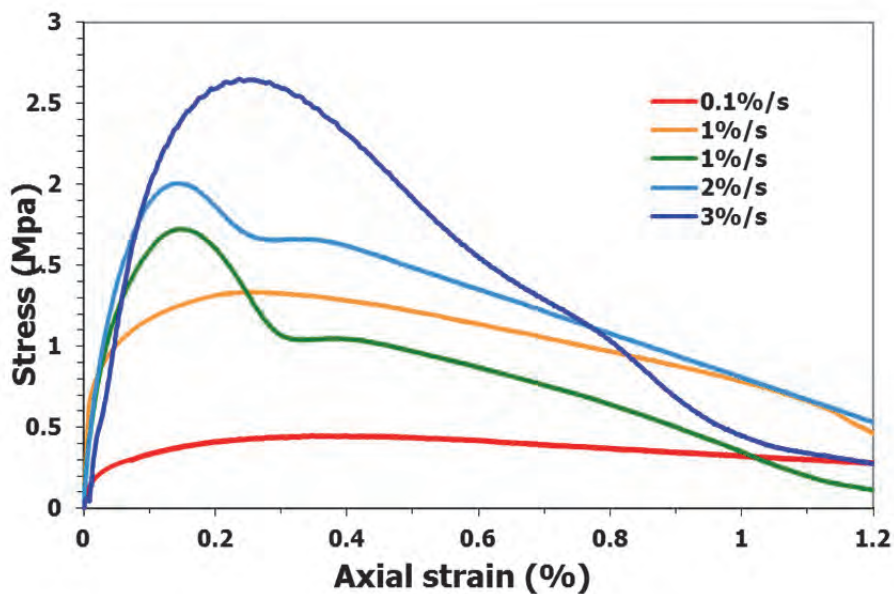
Figure 4.26. Tensile stress versus axial strain of GAC at 30°C

Table 4.11 shows the results of the monotonic uniaxial tension tests. The tangent and secant modulus were determined using the same approach as was used to determine the tangent and secant modulus from the compression tests (see sub chapter 4.2.2).

Table 4.11. Results of the monotonic uniaxial tension tests

T	Target Strain rate	Actual Strain Rate	E mod	Secant Modulus	f_t	Energy to peak	Total energy
°C	%/s	%/s	MPa	MPa	MPa	J	J
5°C	0.01	0.01	6162	2766	3.18	0.890	1.212
	0.1	0.10	16054	9948	4.14	0.351	0.391
	0.5	0.46	19199	14030	3.99	0.200	0.200
	1	0.77	23525	18147	5.01	0.269	0.269
20°C	0.05	0.05	493	318	1.11	1.044	4.294
	0.1	0.09	1153	587	1.46	0.994	3.622
	1	1.70	8817	2842	5.44	2.564	2.769
	2	2.91	16466	5109	5.06	1.172	1.172
30°C	0.1	0.09	273	130	0.45	0.412	1.997
	1	0.94	1916	536	1.34	1.026	4.377
	1	1.71	3923	1194	1.72	0.605	3.291
	2	2.64	5002	1427	2.01	0.673	5.449
	3	2.82	3158	1136	2.59	1.403	5.521
Delrin							
20	0.1	0.10	3542				

The total energy is defined as the amount of energy needed to break the specimen. It is the area under the force-displacement curve (see Figure 4.27). At high temperature, when the failure mechanism is ductile, the force will gradually decrease to zero. The total energy is then shown as E1. In the case of brittle failure, usually at low temperature, the force drops to zero after reaching the maximum value. Then the total energy is shown as E2.
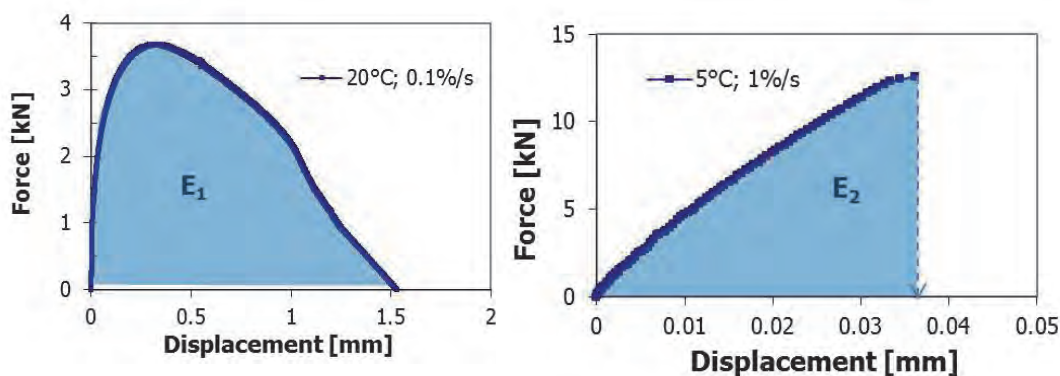
Figure 4.27. Typical force versus displacement at high and low temperatures

4.2.3. Validation MUTT using Delrin (POM) cylinder

A tension test was performed on a Delrin specimen to validate the set-up and measuring method (Figure 4.28). The dimension of the Delrin cylinder was

identical to the GAC specimen, so with a height of 130 mm and a diameter of 65 mm. The E-modulus as well as Poisson's ratio were measured for the Delrin specimen in the MUTT.

Figure 4.28. Delrin specimen in the set-up to validate the test method

The tangential modulus determined by linear regression on the measured data resulted in a E modulus of 3542 MPa and a Poisson's ratio of 0.4. Given the fact that the E modulus could be slightly higher because of the glued ends, both values are relatively close to the well-known reference values of Delrin (POM) which are around 3100 MPa and 0.4 at 20°C respectively [20].
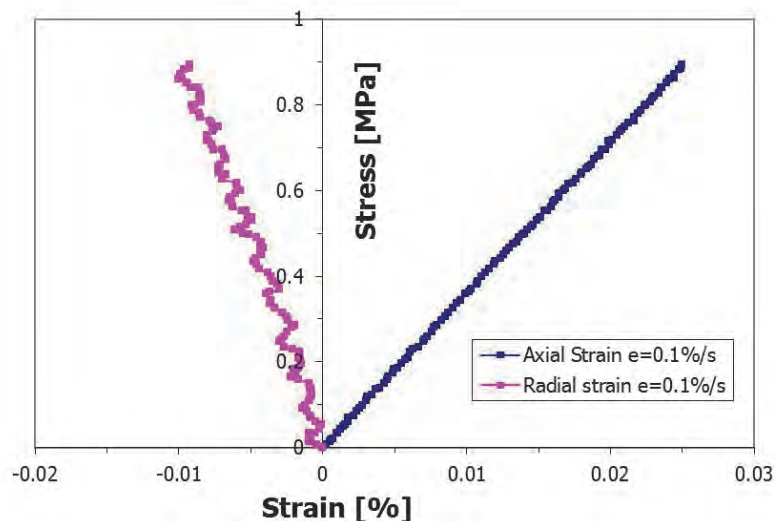
Figure 4.29. Axial and radial strain versus stress of the Delrin specimen in the MUTT at T=20°C and a strainrate of 0.1 %/s.

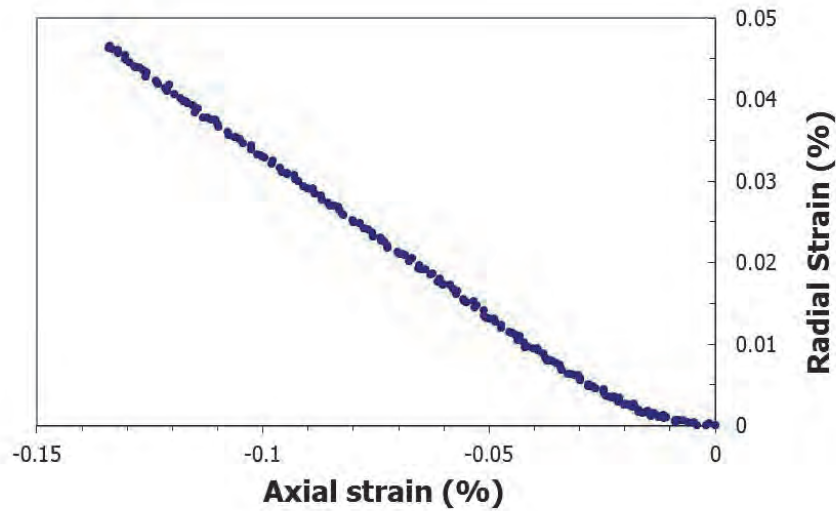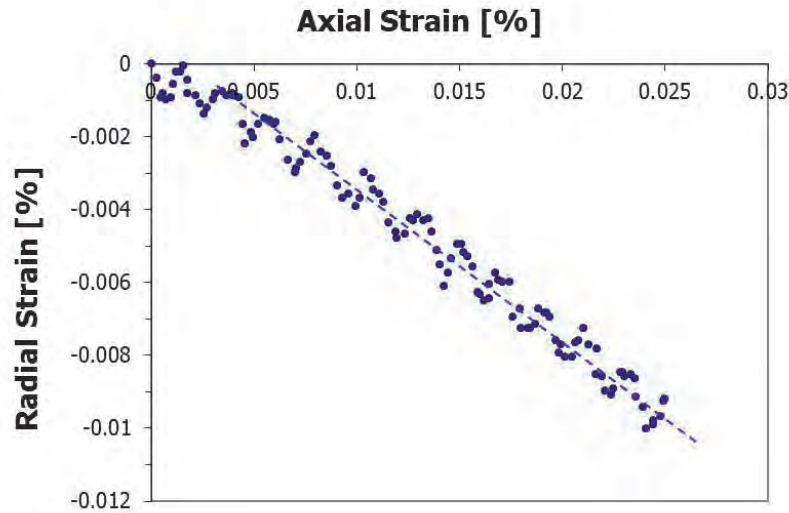**Figure 4.30.** Axial strain versus radial strain of the Delrin specimen in the MUTT at T=20°C and a strainrate of 0.1 %/s.

4.2.4. Modelling compressive and tensile strength

A general expression that gives the compressive and tensile strength as a function of temperature and loading rate was developed. Erkens proposed to use a non-linear relation since such a model showed to be the most realistic one [21]. The general expression is shown in Equation 4.14. Using an excel-solver function, all constants were derived; they are shown in Table 4.12 for both the compressive and tensile strength.

$$f_{c,t} = a \left[1 - \frac{1}{1 + \left[\dot{\varepsilon} \, e^{(b + \frac{c}{T})} \right]^d} \right] \tag{4.14}$$

Where:

f_c	= compressive strength (MPa)
f_t	= tensile strength (MPa)
$\dot{\varepsilon}$	= strain rate (%/s)
T	= temperature (K)
a, b, c & d	= regression constants

Table 4.12. Constants of Compressive and Tensile strength model of GAC

		a	b	c	d
GAC mix	f_c	-88.2	-79.32	21377	0.302
(Pramesti, 2014)	f_t	4.93	-75.43	22522	0.887

Figure 4.31 shows the actual data points together with the model predictions for the compressive strength and Figure 4.32 provides the actual data and the model for the tensile strength.
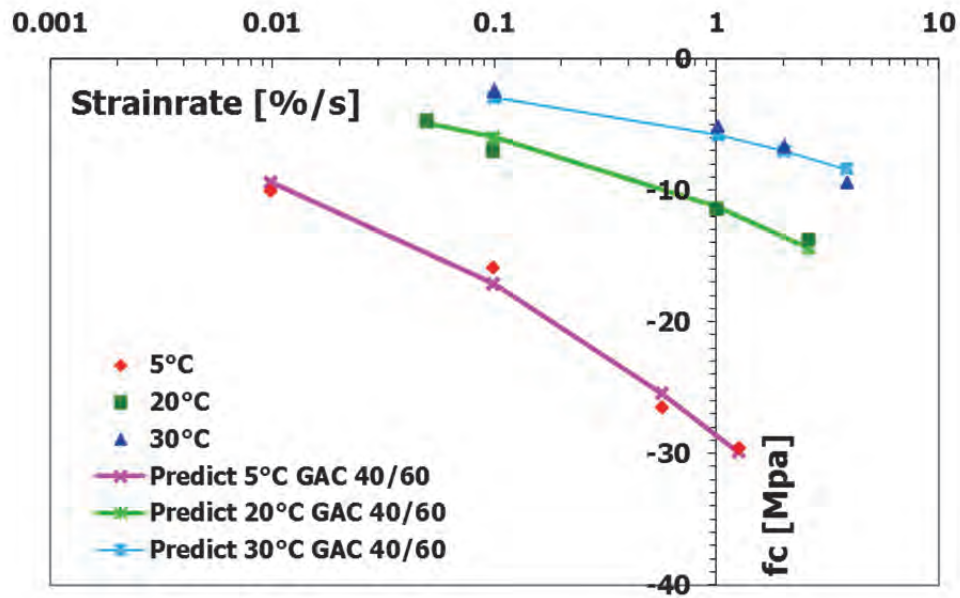
Figure 4.31. The compressive strength data and the model
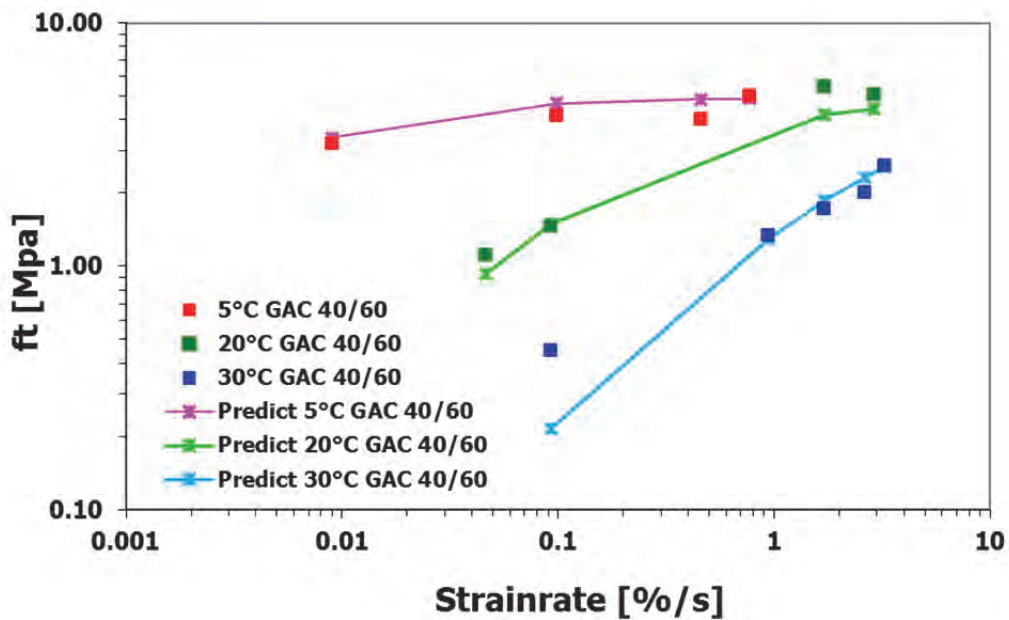
Figure 4.32. The tensile strength data and the model

4.2.5. Indirect Tensile Strength test

A monotonic indirect tensile test also provides information about the tensile strength. This test is widely used since the specimen can be easily produced and the test is relatively easy to perform. As a result, this splitting tensile test was also performed to obtain a tensile strength which can be calculated by [24]:

$$\sigma_{its} = \frac{2F}{\pi.l.D}$$

(4.15)

Where:

σ_{its}	= indirect tensile strength (MPa)
F	= maximum vertical load at failure (N)
l	= height of specimen (mm)
D	= diameter of specimen (mm)

The ITS test program and setup have been described in Subchapter 3.3.6; the tests were performed at displacement rates of 0.028 mm/s to 8.33 mm/s. The test results are presented in Figure 4.33 for 5°C, in Figure 4.34 for 20°C and in Figure 4.35 for 30°C.

An approach to determine the modulus of elasticity is presented in Equation 4.16. This equation is developed by Huurman [25] by means of a finite element simulation. It should be noted that in determining the constants mentioned in Equation 4.16, Huurman used an ITT specimen with diameter of 100 mm and thickness of 50 mm.

Since Poisson's ratio was not measured for the GAC specimens, the Poisson's ratio used in Equation 4.16 is taken from the monotonic tension tests (MUTT) performed on the Retona modified GAC specimens (see subchapter 5.2.2). For each temperature an average value was calculated from these tests. The ITS results are shown in Table 4.13.

$$E = \frac{(1.1892 * \upsilon + 0.2670) * F}{def_{hor} * l}$$

(4.16)

Where:

E	= Modulus elasticity (MPa)
υ	= Poisson's ratio
l	= height of the specimen (mm)
F/def$_{hor}$	= Initial slope of the force versus horizontal deformation (N/mm)

Table 4.13. Recapitulation of ITS results

T	Sample ID	Deformation rate	Actual strain rate	Air Voids	Indirect tensile strength ($\sigma_{its}=\sigma_{xx}$)	Poisson 's ratio	Stiffness (Huurman)
°C		(mm/s)	(%/s)	%	N/mm^2		MPa
5	25_9	0.028	0.010	4.36	2.54	0.21	7201
	25_7	0.278	0.104	4.19	3.98	0.21	15699
	25_6	1.389	0.489	4.21	5.46	0.21	16097
	25_3	2.778	0.955	4.2	5.14	0.21	19479
20	25_2	0.139	0.052	4.74	1.09	0.37	4979
	22_7	0.278	0.104	4.68	1.34	0.37	5057
	22_6	2.778	1.067	4.71	2.67	0.37	10339
	22_5	5.556	2.156	4.43	3.28	0.37	11941
30	22_3	0.278	0.103	5.09	0.70	0.38	1958
	22_4	2.778	1.057	4.87	1.54	0.38	5156
	22_2	5.556	2.156	3.95	2.09	0.38	7696
	22_1	8.333	3.238	4.89	1.78	0.38	4188
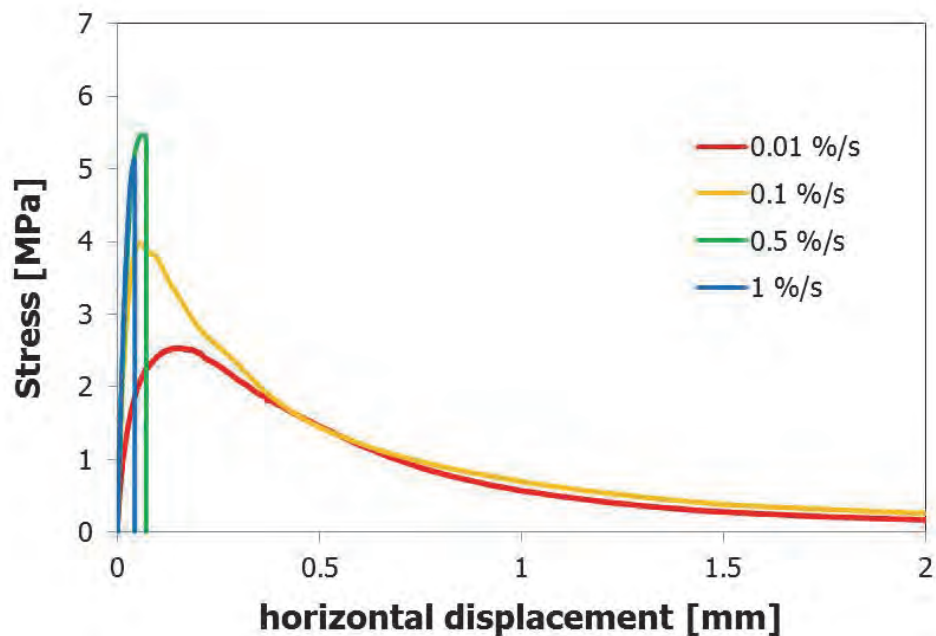
Figure 4.33. Horizontal stress versus horizontal displacement at 5°C
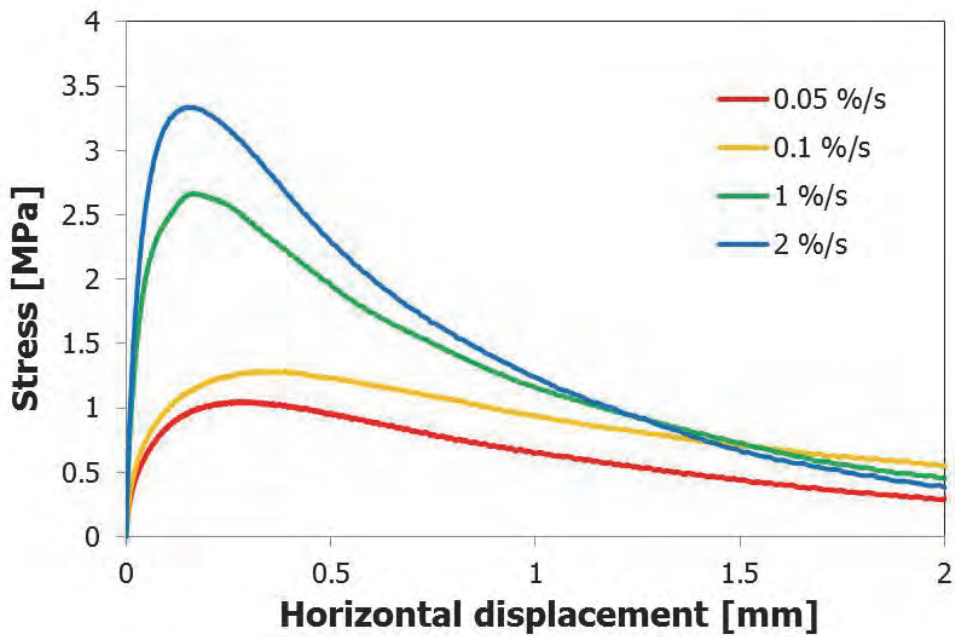
Figure 4.34. Horizontal stress versus horizontal displacement at 20°C
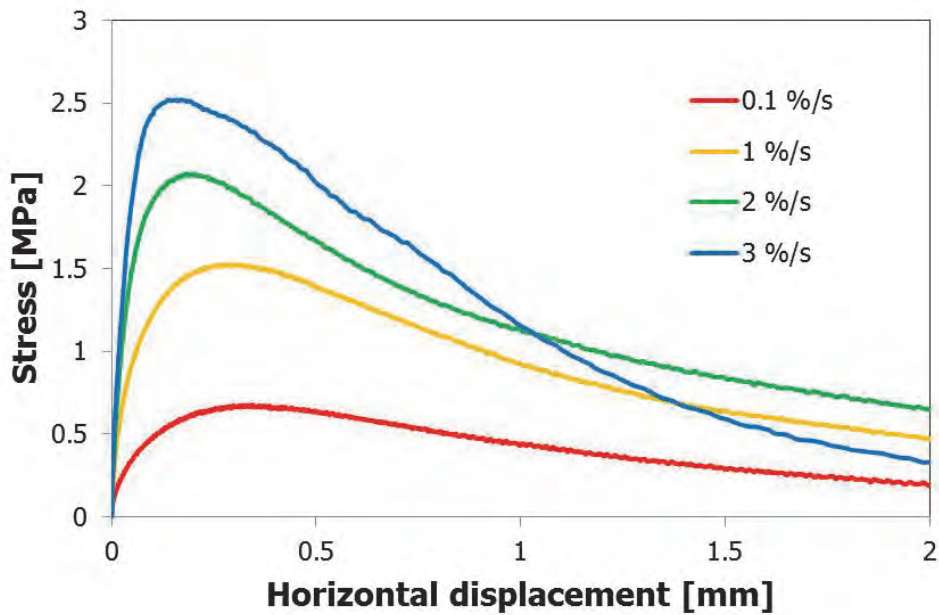
Figure 4.35. Horizontal stress versus horizontal displacement at 30°C

It is interesting to compare the tensile strength f_t and the tensile elastic modulus E_t derived from the uniaxial tension test with those obtained from the indirect tensile test.

The uniaxial tension test and the indirect tensile test were carried out at temperatures of 5°C, 20°C and 30°C and at strain rates ranging from 0.01 %/s to 3 %/s. Using the time-temperature superposition principle, master curves of the tensile strength f_t and the tensile elastic modulus E_t at reference

temperatures of 15°C and 20°C were developed. The Arrhenius equation (see Equation 4.9) was employed to determine the strain rate-temperature superposition shift factor. Furthermore, a typical Christensen-Anderson S shaped model as shown in Equation 4.17 was used to describe the tensile strength f_t and the tensile elastic modulus E_t as a function of strain rate.

$$f_t \text{ or } E_t = a_0 \left(1 - \exp^{\left(\frac{\dot{\varepsilon}}{a_1} \right)^{a_2}} \right)$$ (4.17)

where:

a₀, a₁, a₂   = constants
$\dot{\varepsilon}$ = strain rate [%/s]
f_t = tensile strength (N/mm²)
E_t = tensile elastic modulus (MPa)

To develop equation 4.17, the tensile strength from both tests (MUTT and ITT) and the strain rates measured were used as input. With the help of the solver option in the Excel spreadsheet, the constants a_0, a_1 and a_2 for these two different tests were determined.

Table 4.14 shows the constants of the tensile strength and the elastic modulus master curve at reference temperatures of 15°C and 20°C. Also the constants of the compressive elastic modulus master curve (from MUCT) are shown here. Figure 4.35 and Figure 4.36 shows the tensile strengths and the elastic modulus master curves at the temperature reference of 15°C respectively.

Table 4.14. Recapitulation of the constants a_0, a_1 and a_2 of the mastercurves

Master curve of		Ref temperature °C	Constant		
			a₀	a₁	a₂
Tensile strength	MUTT	15	4.75	0.12	0.58
		20	4.75	0.47	0.58
	ITS	15	5.53	0.60	0.40
		20	5.53	1.88	0.40
Elastic modulus	MUTT	15	20398.81	0.60	0.87
		20	20398.27	1.86	0.87
	ITS	15	21332.60	1.11	0.38
		20	18721.47	1.59	0.44
	MUCT	15	15952.07	0.39	0.70
		20	15953.08	1.32	0.70

Figure 4.36 shows that in the range of the measurements (0.01%/s to 1%/s) the tensile strength of the ITS is lower than the MUTT. The model also shows that the MUTT and ITS tensile strength values differ from each other at strain

rates lower than 0.05 %/s but are almost on top of each other at strain rates higher than 0.05 %/s. This implies that in cases where an uniaxial tensile test cannot be performed realistic tensile strength estimates can be obtained by means of the indirect tensile test which is easier to employ and the specimen is simpler to manufacture.

Figure 4.37 shows that only when the strain rate is higher than 1%/s, the tensile elastic modulus values of both tests are almost on top of each other.
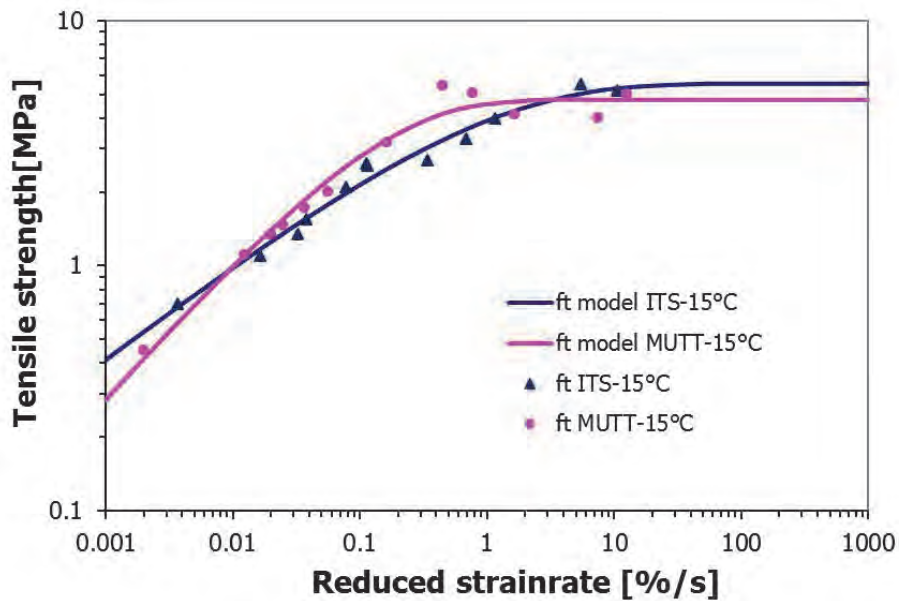
Figure 4.36. Mastercurve for GAC tensile strength as a function of strain rate
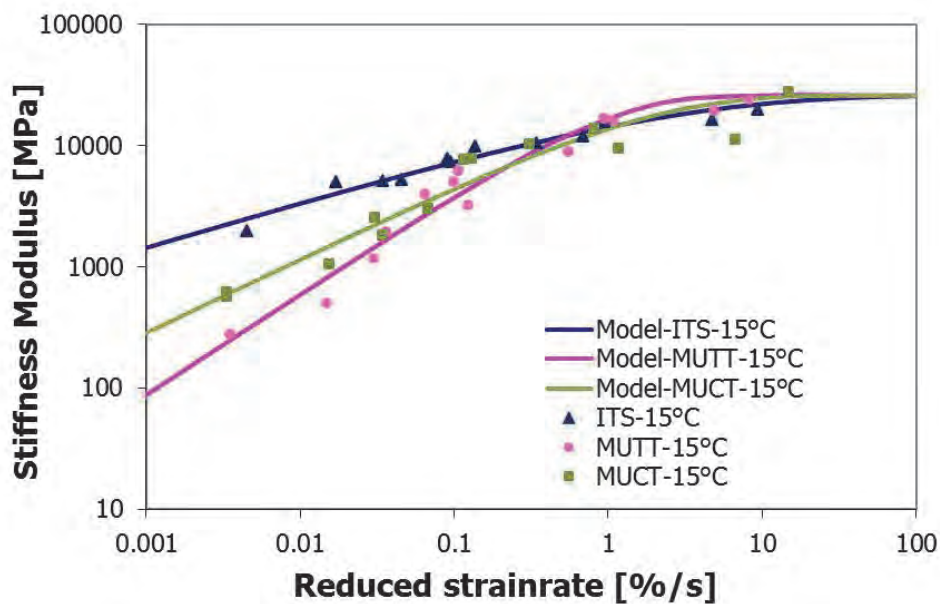
Figure 4.37. Mastercurve for GAC modulus as a function of strain rate

The elastic modulus master curve as a result of the monotonic uniaxial compression tests is also shown in Figure 4.37. It is interesting to note that the elastic modulus values resulting from the compression tests is in between those resulting from the ITS and uniaxial tension test. At low strain rates the compressive elastic modulus from the uniaxial test is higher than the tensile elastic modulus determined by means of the uniaxial test which is plausible because in the compression test at low strain rate -which represents high temperature due to the superposition of temperature-strainrate- the load will be carried up mainly by the aggregate skeleton rather than the bituminous mortar.

4.2.6. Stiffness testing by means of the 4PB test

The four point bending test was used to determine the flexural stiffness of the GAC asphalt mixture at different temperatures and frequencies. The temperature was ranging from 5°C to 30°C and the frequency was ranging from 0.5 Hz to 8 Hz. The sinusoidal strain controlled tests were performed at 50 μstrain (100 μstrain peak to peak) in which the stiffness was determined from the signals measured at the 100th cycle.
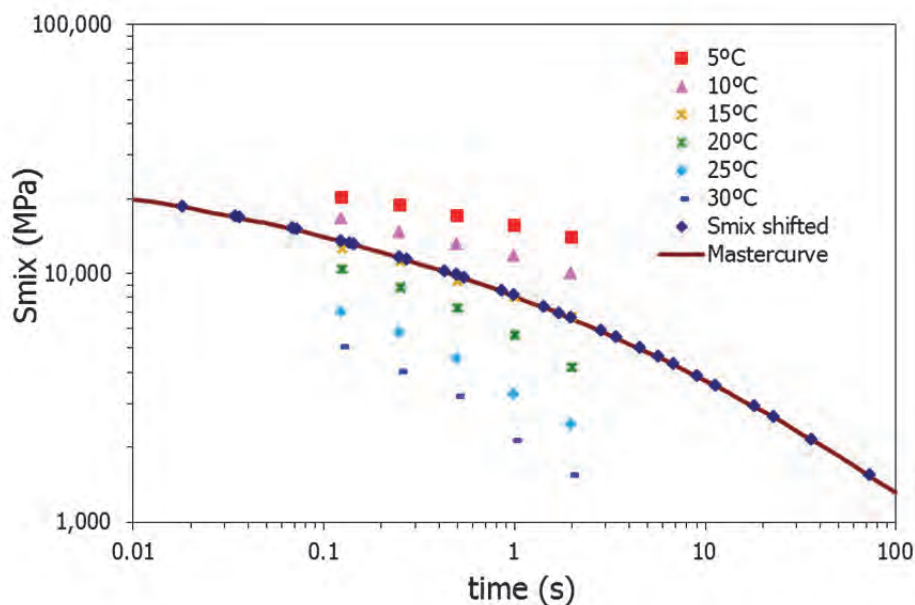
Figure 4.38. Flexural stiffness of gravel asphalt concrete mix (from four point bending test) as a function of loading time.

The results for each temperature are shown as data points in Figure 4.38. These results obtained at different temperatures and loading frequencies can be shifted such that a stiffness master curve at a selected reference temperature can be obtained. The Arrhenius relation shown in Equation 4.18 was employed to shift the data to a reference temperature of 15°C.

$$\text{Log } \alpha_T\left(T\right) = \frac{\Delta E_a}{2.303R}\left(\frac{1}{T} - \frac{1}{T_0}\right)$$

(4.18)

$$\alpha_T = \frac{f_{shifted}}{f}, \quad \alpha_T = \frac{t}{t_{shifted}}$$

(4.19)

$$t_{shifted} = \frac{t}{\alpha_T}$$

where,

α_T = time-temperature superposition shift factor;
ΔE_a = apparent activation energy, J/mol;
R = universal gas constant, 8.314 J /(mol · K);
T = temperature (K);
T_0 = temperature reference (K);
f = loading frequency (Hz);
$f_{shifted}$ = shifted frequency (Hz);
t = loading time (s);
$t_{shifted}$ = shifted loading time (s).

Many master curve models have been developed to describe the stiffness behavior of bituminous mixtures. A polynomial fit was used as done by Sabha [14] and Bhairo [16] to describe the stiffness of the Lintrack GAC mixture. This polynomial model is shown in Equation 4.20.

$$\text{Log}\left(S_{mix}\right) = a_0 - a_1\text{Logt} - a_2\left(\text{Logt}\right)^2 - a_3\left(\text{Logt}\right)^3$$

(4.20)

The relation between mix stiffness (S_{mix}) and loading time (t) at the reference of 15°C is shown in Equation 4.21.

$$\text{Log}\left(S_{mix}\right) = 3.9077 - 0.286\text{Logt} - 0.05\left(\text{Logt}\right)^2 - 0.002\left(\text{Logt}\right)^3$$

(4.21)

Table 4.15. Regression constants for master curves of GAC mixture

	Density (kg/m3)	T_{Ref} (°C)	a_0	a_1	a_2	a_3	R^2	Test
Bhairo	2375 – 2400	15	4.065	-0.292	-0.053	0.0028	0.999	DITT
Bhairo	2350 - 2375	15	3.916	-0.327	-0.050	-0.0001	0.997	DITT
Sabha	Not available	20	3.619	-0.382	-0.073	-0.0055	0.998	4PB Section 1
Sabha	Not available	20	3.599	-0.374	-0.069	-0.005	0.998	4PB All sections
Pramesti	2326-2340	15	3.908	-0.286	-0.05	-0.002	0.996	4PB
Pramesti	2326-2340	20	3.738	-0.342	-0.054	-0.002	0.996	4PB

*DITT: Dynamic indirect tensile tests

All regression constants of the master curves derived by Bhairo [16], Sabha [14] and this study (Pramesti) on GAC mixtures are shown in Table 4.15. Further, their graphs are presented in Figure 4.39.

The curves at 20°C show that at the same loading time GAC Pramesti has a higher stiffness than the Lintrack specimens tested by Sabha. This may be caused by the fact that GAC Pramesti's specimens contain a bitumen with a lower penetration and higher softening point than Sabha's specimens.

When comparing the Pramesti and Bhairo master curves at 15°C one will notice that they are approximately on top of each other, however, both master curves were derived from different types of test. Li [23], however, showed that the differences in stiffness as determined by means of a tension/compression test and a 4 PB tests are negligible.

Besides the different type of test, the age of the specimens will also have an influence on the master curve. The Sabha specimens were taken from what can be considered as a 'fresh' pavement (they were sawn in 1991 from a Lintrack section which was built in August 1990). The Pramesti specimens were approximately one to two months old when they were tested. Bhairo's specimens were drilled from the Lintrack section in 1995. Therefore, it is most likely that aging has influenced the stiffness of Bhairo's specimens.
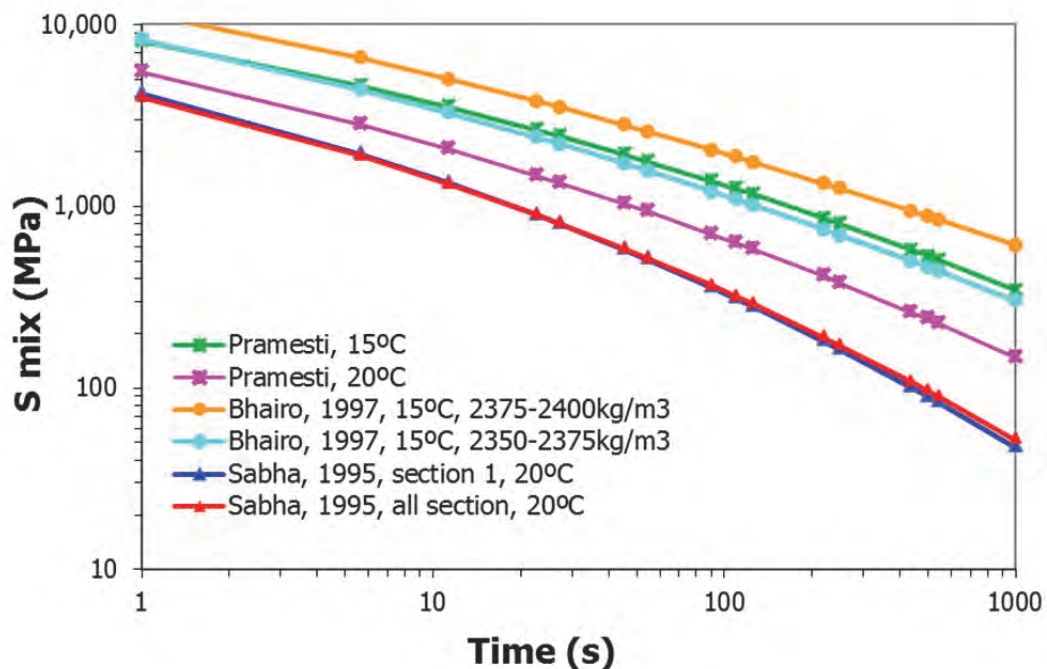
Figure 4.39. Comparison of GAC master curves from different researches

Nevertheless, it can be concluded that although Pramesti's mixtures contained a rather hard bitumen, the stiffness of these mixtures compared well with the stiffness values reported earlier.

Table 4.16. Modulus value at frequency of 3Hz and 8Hz

	Density (kg/m3)	Temperature (°C)	Smix at 3 Hz (MPa)	Smix at 8Hz (MPa)
Bhairo	2375 - 2400	15	15536	19168
Bhairo	2350 - 2375	15	11503	14810
Sabha	Not available	20	6098	8103
Sabha	Not available	20	5787	7659
Pramesti	2326 - 2340	15	10794	13402
Pramesti	2326 - 2340	20	7757	10124

4.2.7. Four Point Bending Fatigue tests

Fatigue tests were performed at 3 Hz and 8 Hz and temperatures of 5°C, 20°C and 30°C. The fatigue life was defined as the number of load repetitions at which the stiffness had reduced to 50% of its initial value. The results obtained on the individual beams are shown in Table 4.17.

Table 4.17. Recapitulation of the 4PB fatigue test result

			Specimen ID	Density	Air voids	Bitumen content	Strain level	Initial Stiffness	Nr of cycles to failure
	T	f		ρ	Va	Vb	ε	S_0	N_f
	°C	Hz		kg/m^3	%	%	μm/m	MPa	Cycle
1	5	3	OM01-01	2369	4.11	8.91	75	21,169	1,044,830
2		3	OM06-01	2361	4.28	8.90	87.5	17,998	656,270
3		3	OM02-01	2331	5.06	8.83	100	15,406	124,300
4		3	OM07-03	2320	4.53	8.87	112.5	17,751	143,220
5		3	OM01-02	2343	4.72	8.86	125	18,645	116,920
6		3	OM07-01	2348	4.62	8.87	137.5	17,350	44,870
7		3	OM05-04	2358	4.43	8.88	150	18,956	16,360
8		3	OM05-02	2348	4.99	8.83	162.5	17,904	29,840
9		3	OM01-04	2371	4.10	8.91	175	18,426	22,080
1	20	3	OM13-02	2355	4.18	8.91	75	7,628	631,360
2		3	OM11-03	2345	3.97	8.93	100	6,455	517,220
3		3	OM05-01	2295	5.04	8.83	125	5,758	234,940
4		3	OM13-01	2351	4.29	8.90	150	6,405	93,640
5		3	OM12-02	2324	5.02	8.83	175	5,618	59,200
6		3	OM13-03	2319	4.47	8.88	200	5,189	80,580
7		3	OM05-03	2340	5.10	8.82	225	5,502	20,320

Table 4.17. Recapitulation of the 4PB fatigue test result (Cont)

	T	f	Specimen ID	Density	Air void	Bitumen content	Strain level	Initial Stiffness	Nr of cycles to failure
				ρ	Va	Vb	ε	S_0	N_f
	°C	Hz		kg/m^3	%	%	µm/m	MPa	Cycle
1	5	8	OM12-03	2339	4.56	8.87	70	18,497	1,843,010
2		8	OM07-04	2348	4.07	8.92	75	20,005	887,070
3		8	OM08-03	2360	4.15	8.91	87.5	22,623	535,360
4		8	OM08-01	2341	4.78	8.85	100	21,480	132,650
5		8	OM08-04	2338	4.54	8.87	112.5	15,695	440,240
6		8	OM10-01	2341	4.82	8.85	125	18,571	188,230
7		8	OM11-01	2349	4.45	8.88	137.5	28,396	44,310
8		8	OM10-04	2353	4.08	8.92	150	19,858	39,270
9		8	OM10-03	2330	4.82	8.85	162.5	19,613	29,980
1	20	8	OM14-02	2337	4.74	8.85	75	9,003	1,200,780
2		8	OM14-03	2356	4.60	8.96	87.5	8,212	418,630
3		8	OM13-04	2344	4.63	8.87	100	8,799	215,590
4		8	OM16-02	2332	4.95	8.84	112.5	8,413	217,600
5		8	OM14-04	2416	4.74	8.85	125	9,372	108,150
6		8	OM14-01	2360	4.17	8.91	150	9,061	34,090
7		8	OM15-01	2348	4.49	8.88	175	8,623	29,460
1	30	8	OM18-03	2330	4.78	8.85	75	2,659	1,853,660
2		8	OM19-01	2333	4.97	8.83	100	2,912	827,830
3		8	OM19-02	2330	4.95	8.84	125	2,565	279,960
4		8	OM16-01	2346	5.09	8.82	137.5	2,642	208,590
5		8	OM18-04	2358	4.08	8.92	150	2,925	169,510
6		8	OM19-03	2385	4.37	8.89	162.5	3,017	122,910
7		8	OM19-04	2331	4.82	8.85	175	2,481	70,860

Based on the results shown in Table 4.17, fatigue relationships were developed using Equation 4.22 (see also Equation 3.1 in Chapter 3).

$$\mathrm{Log\,N} = \log a + n \log \varepsilon \qquad (4.22)$$

Where N_f is number of constant strain applications until the specimen reaches half of the initial stiffness, ε is applied strain (µm/m) and log a & n are regression constants. Table 4.18. shows the fatigue relationships for the different conditions.

Table 4.18. Fatigue formula and constants with ε in μm/m

Temp °C	Freq Hz	Formula	R^2	Log a	n
5	3	Log N = -4.835 Log ε + 15.046	0.916	15.046	-4.835
	8	Log N = -4.5845 Log ε + 14.64	0.876	14.64	-4.584
20	3	Log N = -3.0018 Log ε + 11.572	0.908	11.572	-3.001
	8	Log N = -4.3914 Log ε + 14.225	0.966	14.225	-4.391
30	8	Log N = -3.7672 Log ε + 13.379	0.987	13.379	-3.767
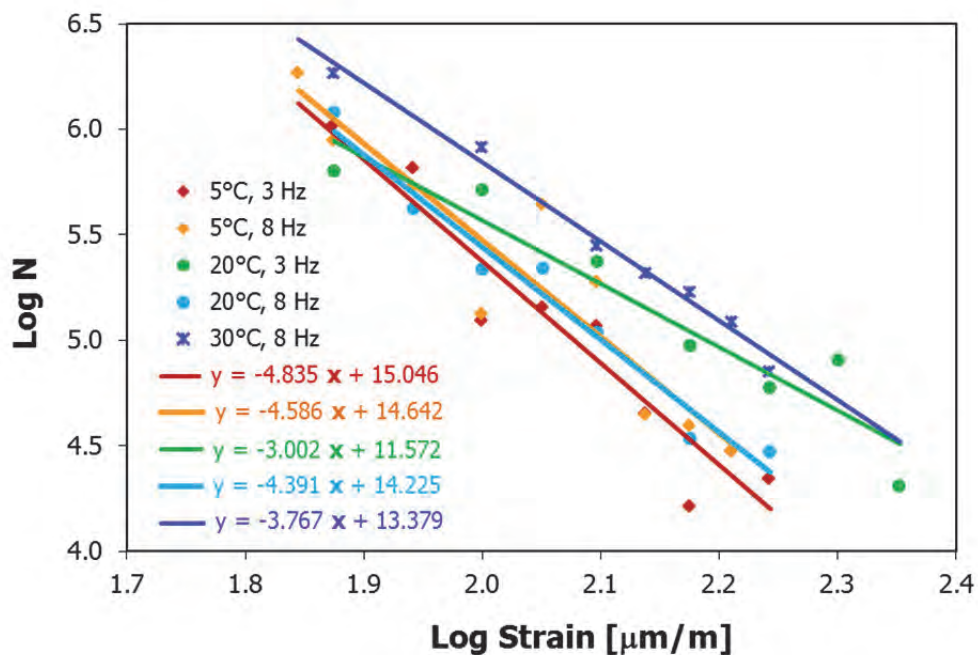
Figure 4.40. Gravel asphalt concrete fatigue lines

Table 4.18. shows that the slope of the fatigue lines decrease with increasing temperature and that the intercept value decreases with increasing temperature. A quite different slope is depicted on the 20°C-3Hz line (see Figure 4.40). It is because the data point at the lowest strain level (at Log strain =1.9) has a large effect on the fatigue relation and is not really in line with the other data points of the 20°C and 3Hz tests. Leaving out this lowest strain level increases the slope of the 20°C-3Hz line from -3.001 into -3.532 and the intercept from 11.572 into 12.759. It is obvious that taking out one single data point can influence the fatigue line significantly. This steeper 20°C-3Hz fatigue model is more 'parallel' with the other fatigue lines than the original one. However, in the next analysis the original 20°C-3Hz fatigue line will be used since no reason could be found for leaving out this single data point.

Table 4.19. Fatigue constants; comparison of Lintrack 1990 and GAC Pramesti results

	Temp °C	Freq Hz	R^2	Log a	n
Lintrack	0	30	0.94	16.57	-5.35
1990*	20	30	0.89	12.00	-3.43
GAC	5	3	0.916	15.046	-4.835
Pramesti		8	0.876	14.64	-4.584
	20	3	0.9079	11.572	-3.001
		8	0.966	14.225	-4.391
	30	8	0.987	13.379	-3.767

* Van de Ven [12] and Wattimena [11]
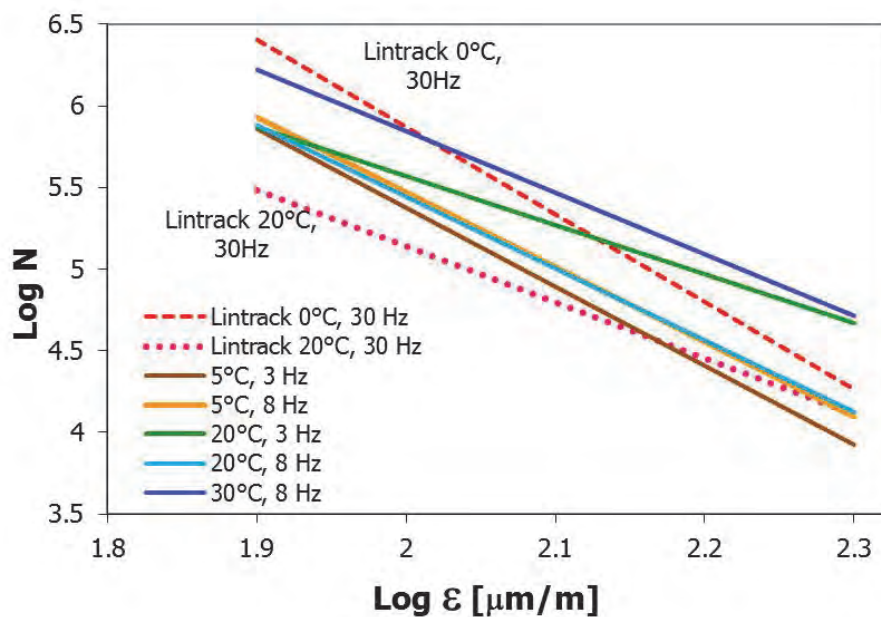
Figure 4.41. Four point bending test results from GAC 2010 (Pramesti) and GAC Lintrack 1990 (Van de Ven & Wattimena)

Table 4.19 and Figure 4.41 show the comparison between the GAC fatigue lines obtained from this experiment (Pramesti) and the GAC Lintrack fatigue lines. The GAC Lintrack 1990 fatigue lines were obtained from 4PB test performed at 30 Hz and 0°C and 20°C by Van de Ven and Wattimena [11, 12] on beams sawn from the Lintrack sections. Both fatigue lines from GAC Lintrack show that at an increasing temperature the intercept decrease and the absolute slope decrease. Also the effect of the loading frequency on the fatigue test results is clearly visible when the Wattimena/van de Ven results are compared with the results obtained by Pramesti.

In order to investigate the healing capacity of the GAC (Pramesti) mixture, a batch of beams which were previously tested at 5°C and 8 Hz were tested again nineteen months later. During these nineteen months the beams were stored at 15°C in a temperature controlled room. They were placed

horizontally on a flat support to assure that the beam remained in a straight position during storage. The results of these retests are shown in Table 4.20.

Table 4.20. Compilation of 4PB fatigue retests at a temperature of 5°C and a frequency of 8 Hz.

Speci-men ID	Strain level	1st test			2nd test			Redu-ced stiff-ness	Redu-ced fati-gue life
		Initial stiff-ness	50% stiff-ness	Fatigue life	Initial stiff-ness	50% stiff-ness	Fatigue life		
	ε	S_0	$S_{50\%}$	N	S_0	$S_{50\%}$	N		
	μm/m	MPa	MPa	Cycle	MPa	MPa	Cycle	%	%
OM12-03	70.0	18,497	9,249	1,843,010	17,920	8,960	640,340	3	65
OM07-04	75.0	20,005	10,003	887,070	19,839	9,920	557,430	1	37
OM08-04	112.5	15,695	7,848	440,240	17,709	8,855	344,560	-13	22
OM10-01	125.0	18,571	9,286	188,230	21,285	10,643	88,510	-15	53
OM11-01	137.5	28,396	14,198	44,310	20,881	10,441	76,760	27	-73
OM10-03	162.5	19,613	9,807	29,980	21,133	10,567	26,080	-8	13
OM02-02	150.0	9,552	4,776	24,400	9,418	4,709	21,500	1	12

* The 1st test was held in August 2010 and the 2nd test in March 2013
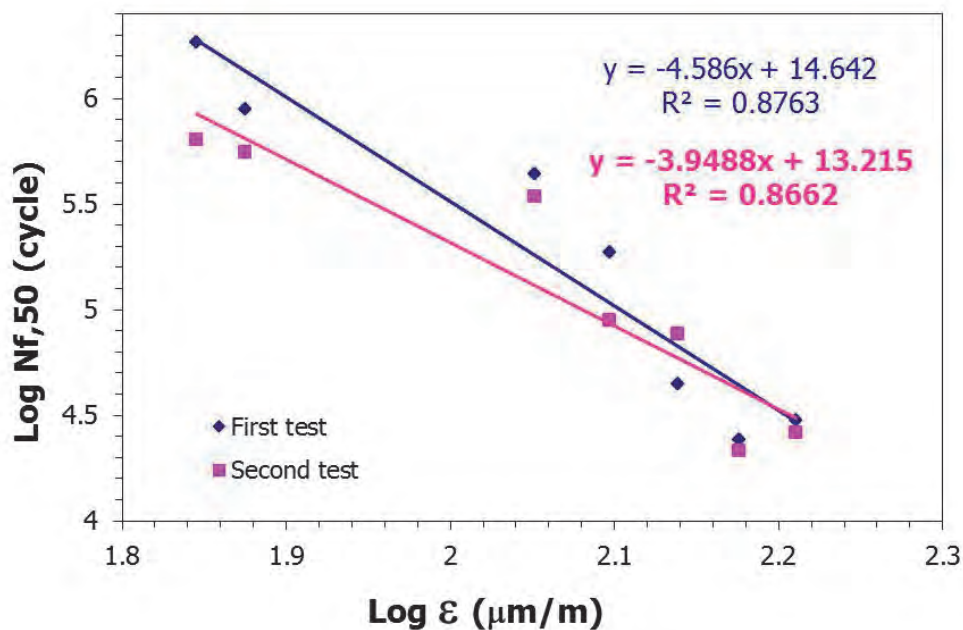
Figure 4.42. 4PB fatigue result and the retest result at temperature of 5°C and frequency of 8 Hz

From Figure 4.42 and Table 4.20 it can be seen that after 19 months the stiffness of the beams 'healed' to almost its initial value. Three out of seven specimens even reached a higher stiffness than the initial value. However, the fatigue life of those beams is less than the fatigue life from the 1st test. This indicates that some healing of the fatigue resistance did occur; especially the beams that were initially tested at high strain levels seemed to be healed

completely. The beams that were initially tested at lower strain levels did not heal completely. The results also indicate that healing in terms of recovery of strength should not be confused by healing in terms of recovery of stiffness! This is in line with findings reported by Qiu [19]. All in all the conclusion must be that the healing factor of 4 that was assumed in the previous analyses of the Lintrack sections as performed by Groenendijk [15] and which is used quite often in design analyses, is an overestimation of reality.

4.2.8. Beam on Elastic Foundation fatigue tests

The other test that was used for predicting the fatigue behaviour of the asphalt mixtures is the Beam on Elastic Foundation (BOEF) test. This test was selected because beam bending tests are never a good representation of reality. In reality, the asphalt layer is supported by the base layer and this support influences the damage propagation and re-distribution of stresses after initiation of damage. The need to perform a test like this became very clear after initial analyses of the performance of the Lintrack test sections were made using the 4PB test results described in the previous section. Those results showed that the predicted lifetime still did not match with the observed behaviour even though the new fatigue relations did take into account the loading frequency levels applied by the Lintrack device. The setup of the BOEF test and the applied loading is explained in chapter 3 and the results are shown in Table 4.21.

Table 4.21. Recapitulation of the BOEF fatigue test result at T=5°C and f=8 Hz

	Speci-men ID	Density	Air voids	Bitumen content	Applied load	Initial Stiffness	Nr of cycle to failure	Strain level*
		ρ	Va	Vb	P	S_0	N_{f50}	ε
		kg/m^3	%	%	kN	MPa	Cycle	μm/m
1	OM24-03	2322	5.10	8.81	1.50	27,697	2,359,690	102
2	OM27-03	2345	4.60	8.87	1.75	19,739	1,925,210	135
3	OM27-01	2363	3.93	8.93	2.00	21,146	309,770	200
4	OM27-02	2346	4.66	8.86	2.25	16,731	116,490	211
5	OM26-01	2369	4.34	8.89	2.50	14,133	10,430	289

*average cyclic strain (at the bottom of the beam) over 80% of the total load repetitions.

During the BOEF test, the recoverable (cyclic) and accumulated strains were measured. An example of the measured strains is given in Figure 4.43. At the beginning of the test the recoverable strain first decreases and then stays nearly constant for an appreciable period of time. As the test progresses and hairline cracks are formed at the bottom of the beam, the strains increase markedly until they reach a maximum value. From Figure 4.43 it is clear that the cyclic strain is mostly constant for almost 80% of the total load

repetitions. This average strain was used to compare the test to the 4PB test which is strain controlled.

The BOEF tests were continued until the beam broke. From the camera installed in front of the test set up a bottom up crack initiation and propagation was observed.

In order to be able to determine the modulus of the beam a finite element simulation was performed from which a relation could be developed between the applied load P, the strain at 8 mm above the bottom of the beam, ε, and the beam's stiffness, Smix. Figure 4.44 shows the mesh of the finite element simulation for the BOEF test. The relationship (P/ε) versus Smix as a result of this simulation is shown in Figure 4.45.
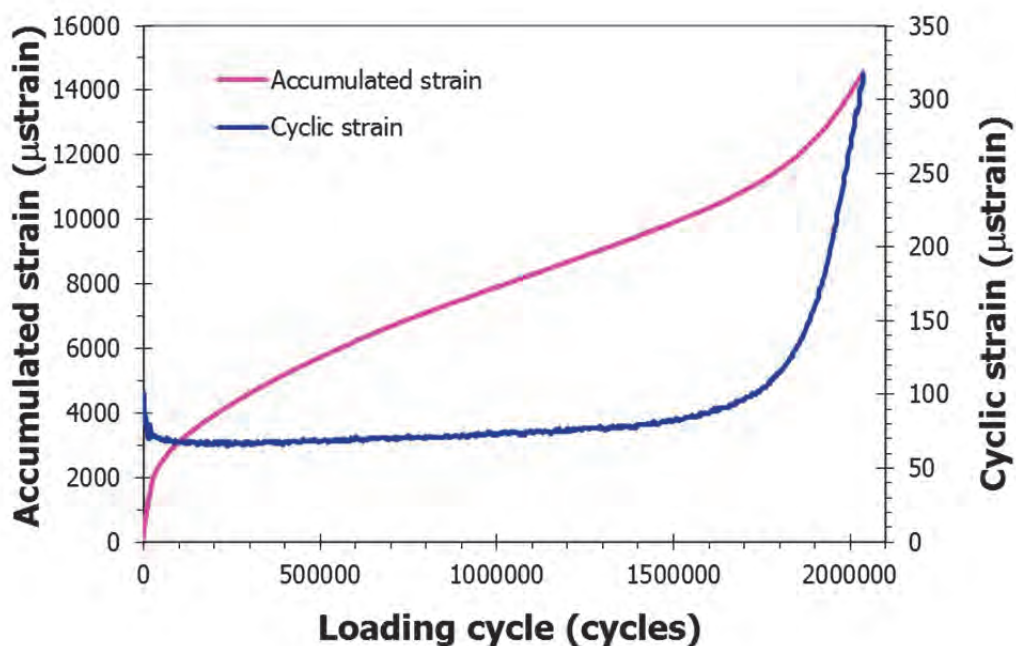
Figure 4.43. Typical development of the cyclic and accumulated strain during the BOEF fatigue test (P=1.75 kN) measured at 8 mm from the bottom of the beam using horizontal LVDT on position D
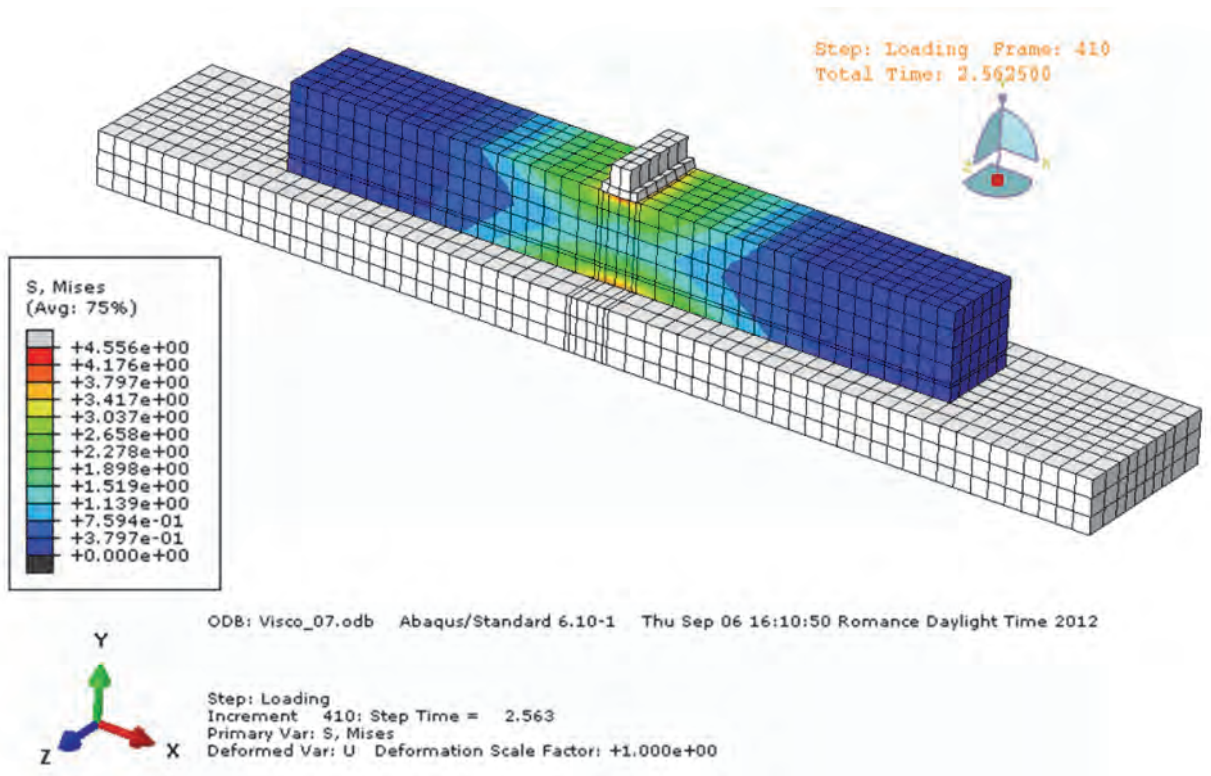
Figure 4.44. ABAQUS simulation of BOEF
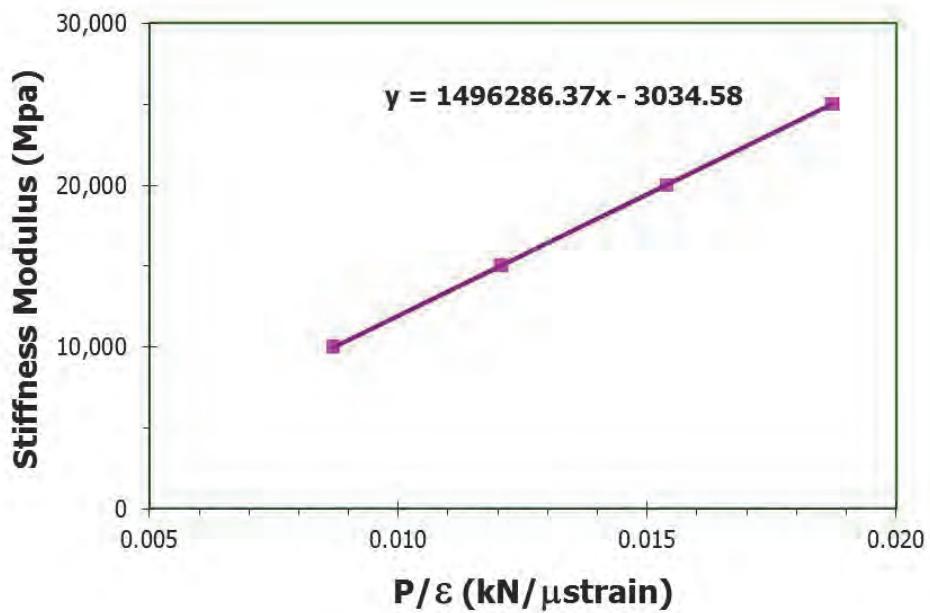
Figure 4.45. Relation between P/ε and the stiffness modulus of a beam on elastic foundation based on finite element simulations

From the BOEF tests, a BOEF fatigue relationship for GAC was determined; it is shown in Figure 4.46 together with the 4PB test fatigue line. It is recalled that both fatigue relationships are determined at 5°C and 8Hz.
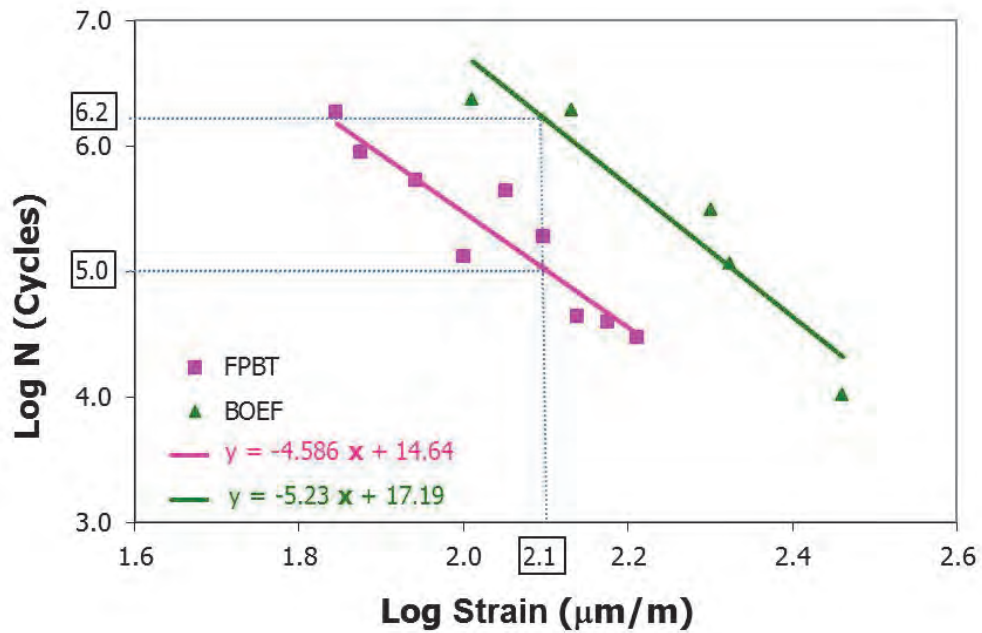
Figure 4.46. Fatigue line obtained from 4 PBT and BOEF test at 5°C and 8Hz

The two relationships shown in Figure 4.46 have approximately the same slope. However, the BOEF fatigue line has a much higher intercept with the vertical axis than the 4PB test fatigue line. At a strain level of 126 μm/m the BOEF fatigue line gives a fatigue life which is around 16 times higher than the fatigue life obtained in the 4PB test.

Figure 4.47 shows the change in cyclic and accumulated strain during the first 30 cycles of the BOEF fatigue test. This figure clearly shows, as was already observed in Figure 4.43, that in the beginning of the test the cyclic strain decreases while the accumulated strain increases.

In order to explain the unexpected development of the cyclic strain at the beginning of the test (it was expected that the cyclic strain at the beginning of the test would stay constant or would increase) a finite element simulation of the BOEF test was made using ABAQUS.
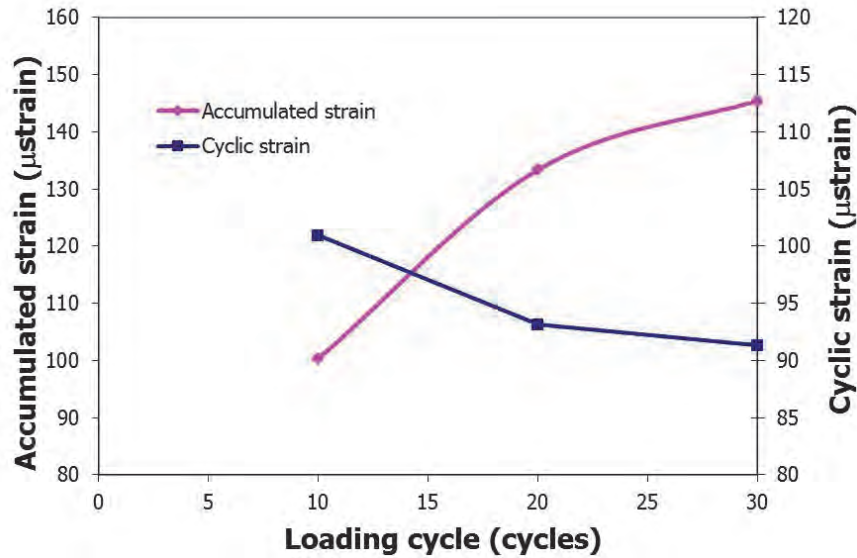
Figure 4.47. Cyclic and accumulated strain in the BOEF test during the first 30 loading cycles (P=1.75 kN)

In this simulation the steel plate and the rubber foundation were modelled as linear elastic materials. For the steel plate a Young's modulus of $2x10^5$ MPa and a Poisson's ratio of 0.3 were assumed. An elastic modulus of 6.5 MPa and a Poisson's ratio of 0.48 were assumed for the rubber subgrade. The asphalt beam was modelled as a visco-elastic material using a Prony series, of which the details are shown in Figure 4.48. The boundary condition which was applied at the bottom of steel plate implied that the displacement and rotation in all directions were fixed during the analysis. Since the beam was assumed to be laid freely on top of the rubber foundation, the interaction contact between the asphalt beam and the rubber foundation was specified as surface-to-surface-contact (standard) with a friction coefficient of 0.05. Vertically a hard-contact boundary condition was used, which implies that the bottom surface of the beam deforms in compliance with the top surface of the rubber.

The model parameters were calculated from information on the mixture stiffness and phase angle as a function of loading frequency as determined by means of 4PB tests. The stiffness & phase angle data were derived at temperatures ranging from 5°C to 30°C and frequencies ranging from 0.5 Hz to 8 Hz. All data were shifted to 5°C to obtain stiffness and phase angle values that were relevant for the BOEF test. The shifted data points are shown in Figure 4.49 together with the master curves. They were described using a sigmoidal-shape function [26] [27].
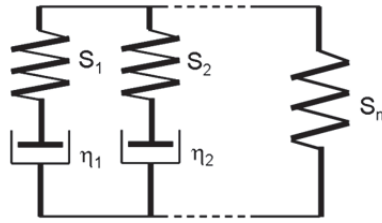
Figure 4.48. Prony series (Generalized Maxwell model) used in the ABAQUS simulations
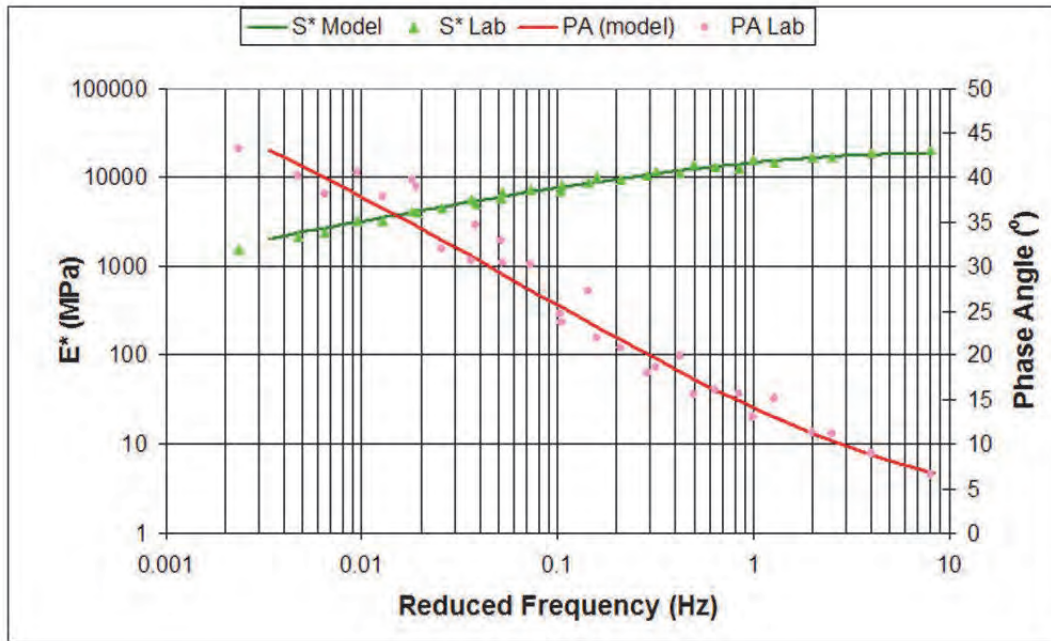
Figure 4.49. Master curve of Gravel asphalt concrete at T_{ref} = 5°C (PA = phase angle)

Table 4.22. Visco elastic material parameters (Prony coefficient)

S_0	18897	MPa		
ν	0.35			
i	1	2	3	4
τ_i (s)	2.65E-02	1.23E-01	2.05E-01	5.72E-01
α_i	1.77E-01	6.06E-02	1.82E-01	7.09E-02
i	5	6	7	8	9
τ_i (s)	9.54E-01	2.66E+00	7.40E+00	1.23E+01	3.44E+01
α_i	1.50E-01	1.20E-01	9.77E-02	1.04E-02	8.56E-02

The values for the 9 Prony elements that were needed to get a good fit of the master curves are shown in Table 4.22. The governing equations associated with the model are given in Equation 4.23 to 4.26.

$$S^* = S' + iS''$$
(4.23)

$$S'(\omega) = S_0 \left[1 - \sum_{i=1}^{N} \alpha_i \right] + S_0 \left[\sum_{i=1}^{N} \frac{\alpha_i \tau_i^2 \omega^2}{1 + \tau_i^2 \omega^2} \right]$$
(4.24)

$$S''(\omega) = S_0 \left[\sum_{i=1}^{N} \frac{\alpha_i \tau_i \omega}{1 + \tau_i^2 \omega^2} \right]$$
(4.25)

$$S(t) = S_0 \sum_{i=1}^{N} \left[1 - \alpha_i \left[1 - \exp\left(\frac{t}{t_i} \right) \right] \right]$$
(4.26)

Where:
$S'(\omega)$ = storage modulus as a function of frequency, ω [MPa];
$S''(\omega)$ = loss modulus as a function of frequency, ω [MPa];
S^* = complex modulus as a function of frequency, ω[MPa];
$S(t)$ = relaxation modulus as a function of time, t [MPa];
S_0 = stiffness of instantaneous response [MPa];
ω = applied angular frequency [rad/s];
α_i = model parameter, that is ith Prony S reduction ratio [-];
τ_i = model parameter, that is relaxation speed of the ith Prony [s];
n = number of components in the model [-].

The five haversine load levels of 1.5; 1.75; 2; 2.25 and 2.5 kN (P) as used in the BOEF test were also used in the BOEF ABAQUS simulation along with the constant preload of 0.05 x P. Due to the limited available computational capacity the FEM simulations have only been performed for the first 12 cycles.

As an example, Figure 4.50 shows the simulation results of the cyclic and accumulated strain at a 1.75 kN load. It is obvious that the simulations show a similar development of the cyclic and accumulated strain as was observed during the experiments (see Figure 4.47).
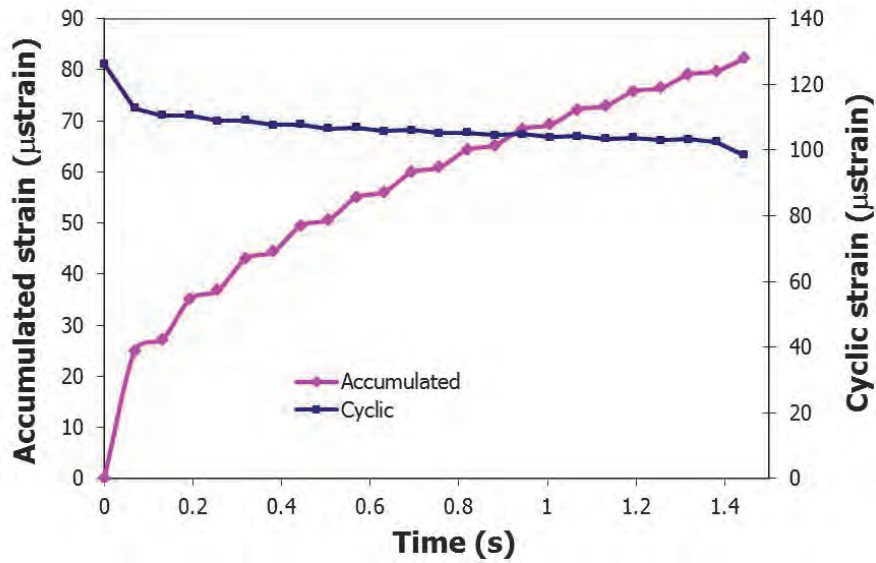
Figure 4.50. Cyclic and accumulated strain as calculated by means of ABAQUS. P=1.75 kN.
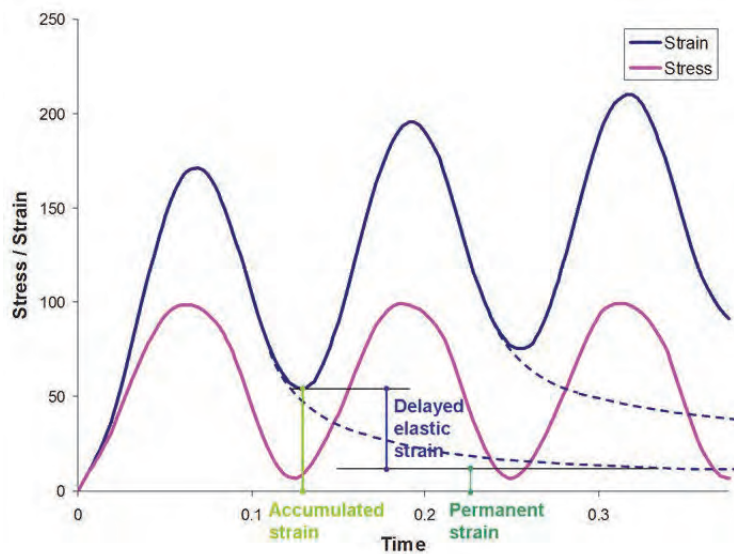
Figure 4.51. Sketch of the development of permanent, delayed and accumulated strain due to the haversine cyclic loading used in the BOEF test as a function of time.

The generalized Maxwell model does not allow to predict the development of any permanent deformation. The simulations, therefore, indicate that the accumulated strain consists of delayed elastic strain which could not recover because of the fact that the load pulses followed each other quickly without any rest period. Evidence for this is given in Figure 4.51 which gives a schematic representation of the load and associated strain cycles. Nevertheless, in the real BOEF test some permanent deformation will be generated during each loading cycle. The conclusion, therefore, is that the

accumulated strain as recorded during the BOEF tests mainly consists of accumulated not recovered delayed elastic strain and some accumulated permanent strain.

4.2.8.1. Crack propagation

A complete set of crack propagation pictures was obtained from one BOEF test. It was the BOEF test performed on beam OM 29_03 on which a 2.125 kN load was applied. The characteristics and a summary of the results are shown in Table 4.23. During the test a set of pictures was taken every 2 minutes (920 cycles). Some of the pictures are shown in Figure 4.52. Each picture was taken at a different stage; the first cycle captured by the camera was at 1,020 cycles (a) the last one was taken at the end of the test when the beam was completely fractured (e). This test is not included in the BOEF fatigue model due to a different cross section (dimensions) of the beam.

Table 4.23. Summary of the BOEF test on beam OM29_03, at 5°C and 8 Hz

Beam ID		OM29_03	
Density	ρ	2369	Kg/m3
Air voids	Va	4.22	%
Bitumen content	Vb	8.90	%
Applied load	P	2.125	kN
Initial Stiffness	S_0	22071	MPa
Nr of cycle to failure	N_{f50}	1,403,890	Cycles
Strain level	ε	135.8	μm/m
Nr of cycle to break	N_{break}	1,600,610	Cycles
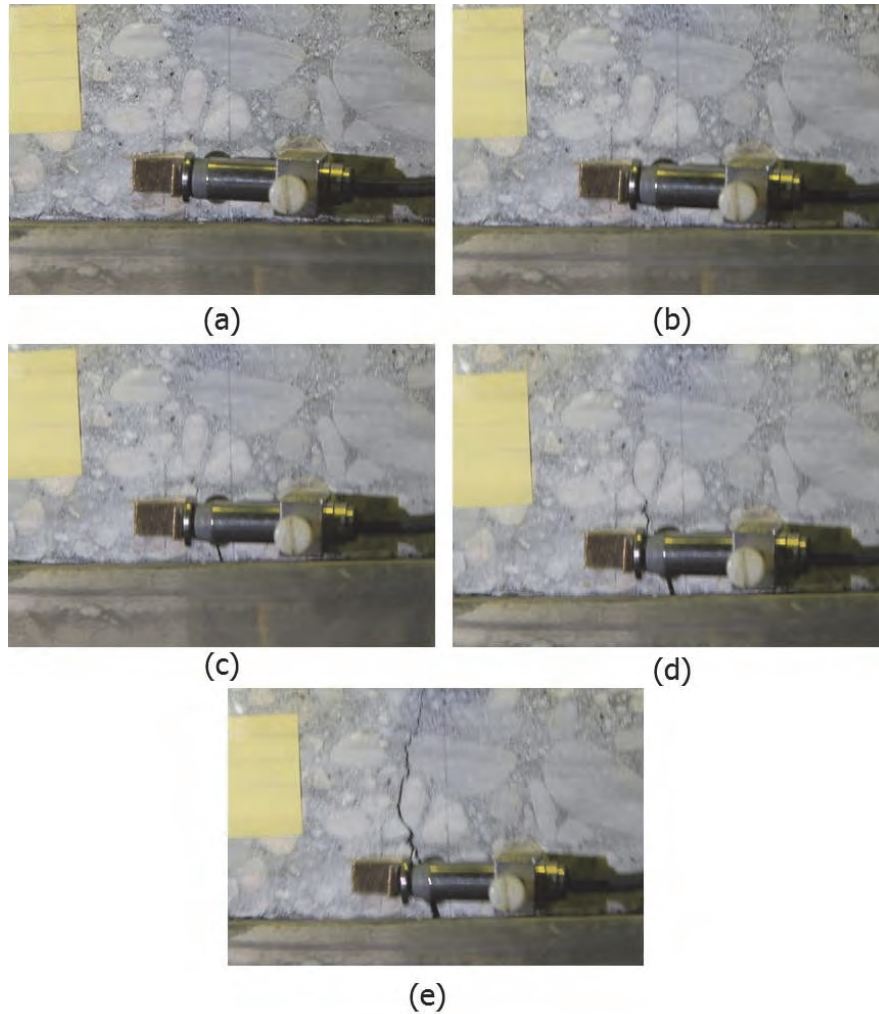
Figure 4.52. Bottom up crack propagation in a BOEF test
(a) at 1,020 loading cycles. (b) at 597,450 loading cycles. (c) at
1,403,750 loading cycles. (d) at 1,595,810 loading cycles and (e) at
1,600,610 loading cycles

Table 4.24 shows the number of load cycles and percentage of load cycles in relation to the percentage of crack length of this beam. The information given in Table 4.24 is visualized in Figure 4.53 which clearly shows the propagation of the crack. It is interesting to mention that at 100% of cycles/number of cycles to failure, where the stiffness reached 50% of its initial value, the crack length percentage is 28. The figure also shows that after the fatigue life is reached, the performance of the beam is quickly deteriorating until failure/break occurs.

Table 4.24. Number of load cycles and percentage of load cycles in relation to the percentage of crack length on beam OM 29_03.

n	$\dfrac{n}{N_{f50}}$ (%)	$\dfrac{\text{crack length}}{h}$ (%)	n	$\dfrac{n}{N_{f50}}$ (%)	$\dfrac{\text{crack length}}{h}$ (%)
1020	0	0	1329830	95	24
130620	9	2	1522850	108	40
140220	10	4	1593890	114	50
149820	11	6	1595810	114	56
161340	11	8	1596770	114	70
308220	22	9	1597730	114	80
356220	25	10	1598690	114	96
597450	43	11	1599650	114	100
638730	45	12	1600610	114	100
685770	49	14			

where:

n is number of load cycles applied; N_{f50} is number of cycles to failure, it is defined as the number of cycles at which the stiffness is 50% of the initial stiffness; h is the height of the beam (50.5 mm)
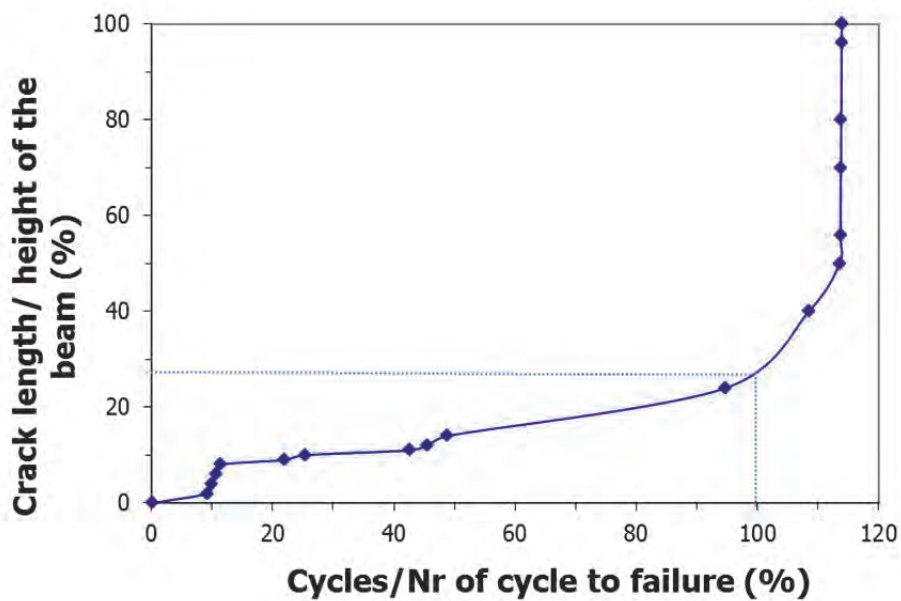
Figure 4.53. Crack propagation in the BOEF test

4.3. Relationship between stress state at the critical location in both fatigue tests and the yield surface

For a further analysis of the fatigue models the yield surface as determined from the compression and tension test results was employed. In this subchapter the relation between the stress state at the critical location in the 4PB and BOEF test and the yield surface will be analysed. Such an approach was suggested by Erkens [21] and Li [23].

4.3.1. Flow surface

The constitutive model used to describe the response of the asphalt mixture is based on the flow surface proposed by Desai and developed further by Scarpas, Erkens and Liu. The flow surface model given in Chapter 2, Equation 2.15 is represented in Equation 4.27, where the I_1 and J_2 mentioned in the equation are described in Equation 4.28 and 4.29 respectively.

$$F = \frac{J_2}{P_a^2} - \left[-\alpha \left(\frac{I_1-R}{P_a} \right)^n + \gamma \left(\frac{I_1-R}{P_a} \right)^2 \right] = 0 \tag{4.27}$$

$$I_1 = \sigma_1 + \sigma_2 + \sigma_3 \tag{4.28}$$

$$J_2 = \frac{1}{2} \left(\sigma_1^2 + \sigma_2^2 + \sigma_3^2 \right) = \frac{1}{6} \left[(\sigma_1 - \sigma_2)^2 + (\sigma_1 - \sigma_3)^2 + (\sigma_2 - \sigma_3)^2 \right] \tag{4.29}$$

The σ_i in those equations refers to the i-th principal stress.

Equation 4.27 can be pictured as a closed surface in the 3D space as shown in Chapter 2 Figure 2.39. In this equation, the parameters α and γ are controlled by the hardening and softening response, respectively. The parameter R is the tensile strength of the material when the deviatoric stress is zero while the parameter n determines the shape of the yield surface.

4.3.2. Determination of the yield surface from MUCT and MUTT results

Using the results of the monotonic uniaxial compression and tension tests, the parameters of the flow surface model can be expressed as function of strain rate and temperature. This method was elaborated by Scarpas [28], Erkens [2, 21, 22], Liu [29], Li [23], Medani [30].

In case of a uniaxial stress state where a stress with magnitude σ is applied, the yield surface can be expressed as follows:

$$\sigma_1 = \sigma$$
$$\sigma_2 = \sigma_3 = 0 \tag{4.30}$$
$$I_1 = \sigma_1 + \sigma_2 + \sigma_3 = \sigma$$

$$J_2 = \frac{1}{6} \left[(\sigma_1 - \sigma_2)^2 + (\sigma_1 - \sigma_3)^2 + (\sigma_2 - \sigma_3)^2 \right] = \frac{1}{3} \sigma^2 \tag{4.31}$$

Substituting Equation 4.30 and 4.31 into Equation 4.27 results in:

$$\frac{\sigma^2}{3P_a^2} = \left[-\alpha\left(\frac{\sigma\text{-}R}{P_a}\right)^n + \gamma\left(\frac{\sigma\text{-}R}{P_a}\right)^2 \right] \qquad (4.32)$$

Because the hardening parameter α is equal to zero at peak stress, Equation 4.32 simplifies to Equation 4.33.

$$\frac{1}{3}f_c^2 = \gamma\left(-f_c\text{-}R\right)^2$$
$$\frac{1}{3}f_t^2 = \gamma\left(f_t\text{-}R\right)^2 \qquad (4.33)$$

Where f_c is the compressive strength (MPa) and f_t is the tensile strength (MPa). R can be found from the uniaxial tension and compression data as the intercept with the I_1 axis of a line through the tensile and compressive strength results plotted in the I1-$\sqrt{}$J2 space. Therefore, using the results from the tension and compression tests, R can be determined as:

$$R = \frac{2\left|f_c\right| \cdot f_t}{\left|f_c\right|\text{-}f_t} \qquad (4.34)$$

Hence γ can be solved following:

$$\gamma = \frac{\left(\left|f_c\right| \cdot f_t\right)^2}{3\left(\left|f_c\right|\text{-}f_t\right)^2} \qquad (4.35)$$

4.3.3. Determination of the yield surfaces of the fatigue tests

To establish the yield surface line for each fatigue test, Equation 4.34 and 4.35 are employed, while the f_c and f_t were calculated using Equation 4.14 and the constants given in Table 4.12. The challenge was to determine the strain rate from the sinusoidal or haversine cyclic loading used in respectively the 4PB and the BOEF fatigue test.

A simplified procedure, originally proposed by Erkens and further discussed by Li [21, 23], was used to determine the strain rate. In this approach, the sinusoidal cyclic loading is considered as a triangle shaped signal with the same maximum strain level and time duration. Thus, the strain level can be simplified as a function of strain level divided by time duration when the strain changes from 0 to peak value, as depicted in Equation 4.36

$$\dot{\varepsilon} = \frac{\varepsilon_0}{t} \tag{4.36}$$

Where, ε_0 is the amplitude of the applied strain (m/m) and t is time duration when the strain changes from 0 to peak value (s).

4.3.3.1. 4PB fatigue test

The states of stress occurring in the 4PB fatigue test were calculated using Equation 4.37 and are plotted together with their related yield surfaces in Figure 4.54. The test conditions and the model parameters used to obtain this plot are presented in Table 4.25.

$$\sigma_{crit} = \frac{\frac{1}{2}P\,a}{\frac{1}{6}bh^2} \tag{4.37}$$

Where:

σ_{crit}	= critical stress (MPa)
P	= applied load (N)
a	= distance between load and nearest support (118.5 mm)
b	= specimen width (50 mm)
h	= specimen height (50 mm)

Table 4.25. Yield surface parameters of 4PB fatigue test

T	f	ε	$\dot{\varepsilon}$	fc	ft	R	γ
(°C)	(Hz)	(m/m %)	(%/s)				
5	**3**	0.0075	0.09	-16.721	4.648	12.875	0.106
		0.00875	0.105	-17.357	4.682	12.822	0.110
		0.01	0.12	-17.923	4.708	12.770	0.114
		0.01125	0.135	-18.433	4.729	12.720	0.117
		0.0125	0.15	-18.897	4.746	12.674	0.119
		0.01375	0.165	-19.325	4.760	12.630	0.122
		0.015	0.18	-19.721	4.772	12.589	0.124
		0.01625	0.195	-20.090	4.782	12.551	0.126
		0.0175	0.21	-20.436	4.791	12.516	0.128
5	**8**	0.007	0.224	-20.740	4.798	12.484	0.130
		0.0075	0.24	-21.069	4.805	12.451	0.132
		0.00875	0.28	-21.816	4.820	12.376	0.136
		0.01	0.32	-22.476	4.832	12.311	0.139
		0.01125	0.36	-23.069	4.841	12.254	0.142
		0.0125	0.4	-23.608	4.849	12.204	0.145
		0.01375	0.44	-24.101	4.855	12.159	0.147
		0.015	0.48	-24.557	4.860	12.118	0.149
		0.01625	0.52	-24.980	4.864	12.081	0.151

Table 4.25. Yield surface parameters of 4PB fatigue test (Cont)

T (°C)	f (Hz)	ε (m/m %)	ε̇ (%/s)	fc	ft	R	γ
20	**3**	0.0075	0.09	-5.807	1.462	3.907	0.119
		0.01	0.12	-6.299	1.737	4.796	0.107
		0.0125	0.15	-6.708	1.965	5.560	0.100
		0.015	0.18	-7.059	2.159	6.222	0.094
		0.0175	0.21	-7.369	2.326	6.799	0.090
		0.02	0.24	-7.647	2.472	7.306	0.087
		0.0225	0.27	-7.900	2.601	7.754	0.085
20	**8**	0.0075	0.24	-7.647	2.472	7.306	0.087
		0.00875	0.28	-7.980	2.640	7.892	0.084
		0.01	0.32	-8.279	2.785	8.392	0.082
		0.01125	0.36	-8.551	2.910	8.823	0.081
		0.0125	0.4	-8.801	3.021	9.198	0.080
		0.015	0.48	-9.248	3.206	9.813	0.078
		0.0175	0.56	-9.642	3.356	10.294	0.078
30	**8**	0.0075	0.24	-3.831	0.472	1.077	0.203
		0.01	0.32	-4.165	0.593	1.383	0.188
		0.0125	0.4	-4.443	0.704	1.674	0.176
		0.01375	0.44	-4.567	0.757	1.815	0.171
		0.015	0.48	-4.683	0.808	1.952	0.166
		0.01625	0.52	-4.792	0.857	2.087	0.162
		0.0175	0.56	-4.896	0.905	2.219	0.158
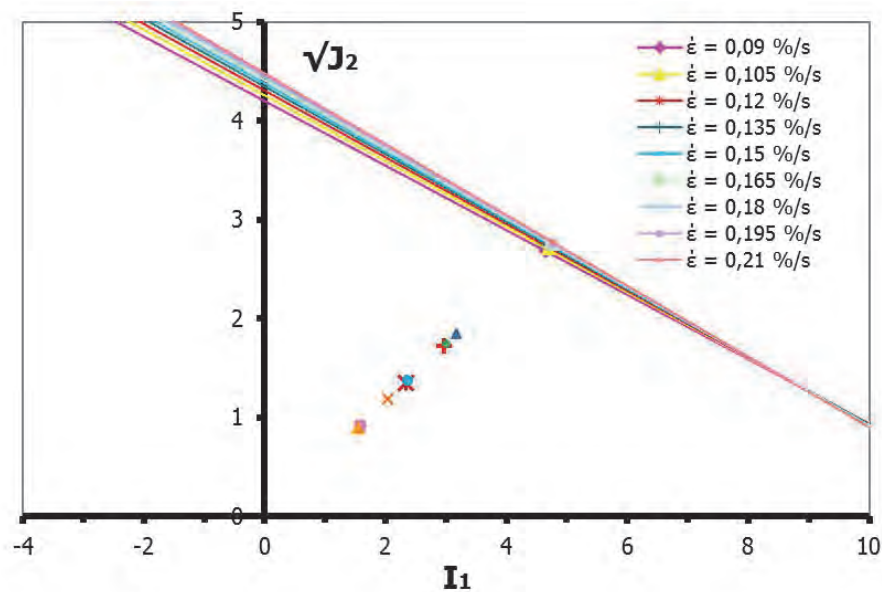
Figure 4.54.a. Yield surface and states of stress in the 4PB tests at 5°C and 3Hz
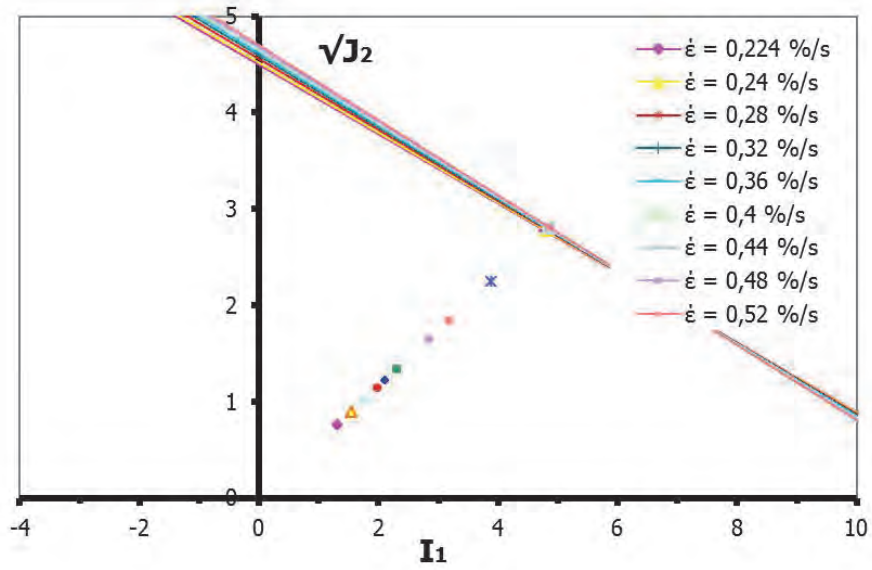
Figure 4.54.b. Yield surface and states of stress in the 4PB tests at 5°C and 8Hz
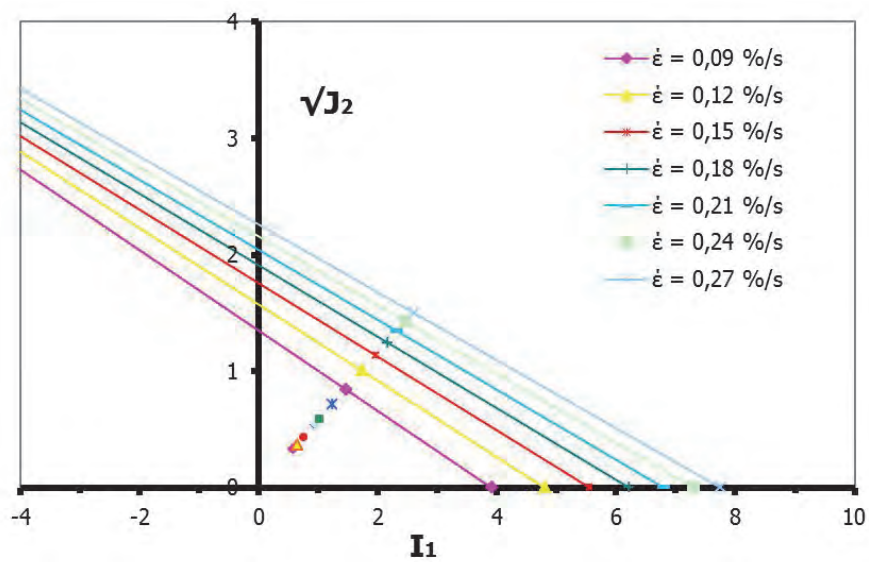
Figure 4.54.c. Yield surface and states of stress in the 4PB tests at 20°C and 3Hz
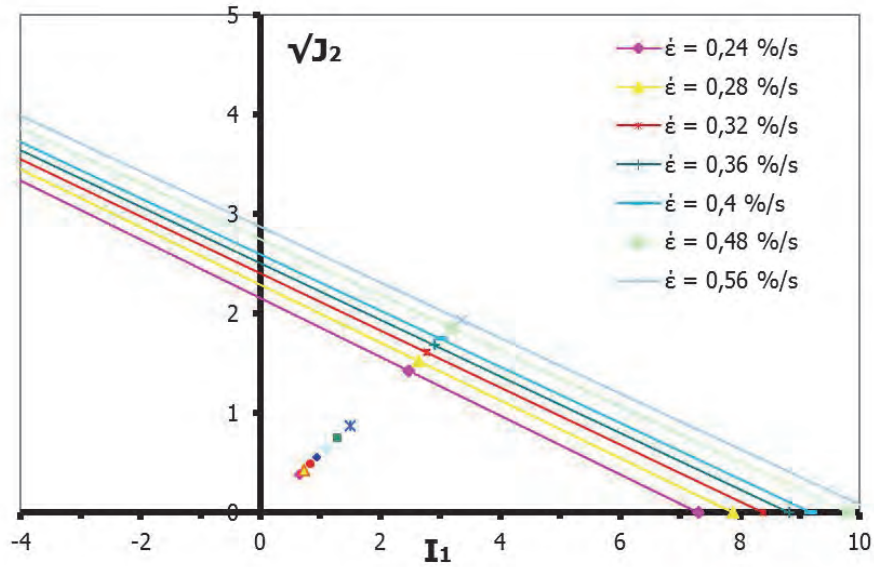
Figure 4.54.d. Yield surface and states of stress in the 4PB tests at 20°C and 8Hz
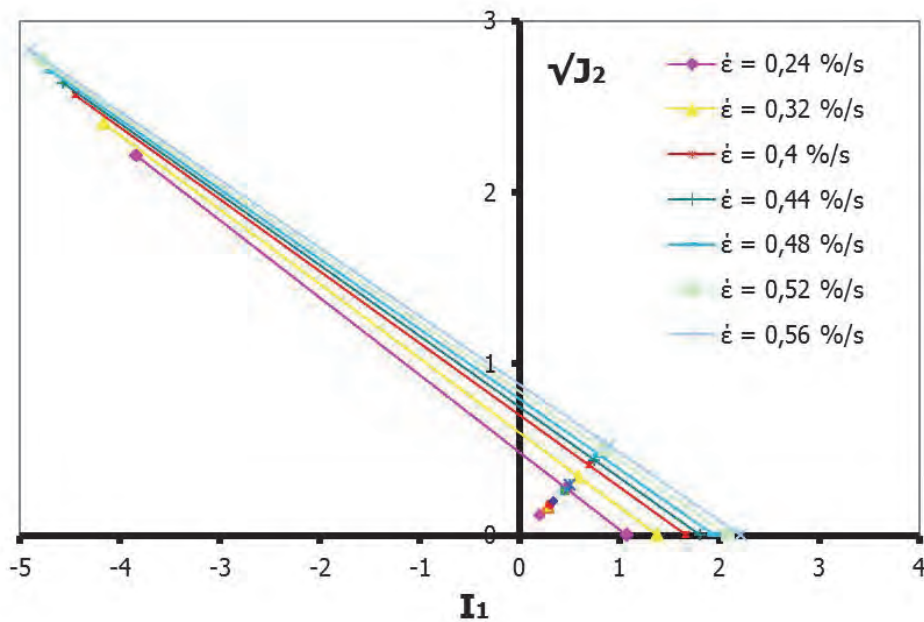
(e)

Figure 4.54.e. Yield surface and states of stress in the 4PB tests at 30°C and 8 Hz

From Figure 4.54 one can observe that at low temperatures the yield surfaces are hardly affected by the strain rate. Meanwhile at high temperatures (20°C and 30°C), the strain rate clearly affected the intercept of the failure lines.

The failure lines at low temperature intercept the ordinate and the abscissa at a higher point than the lines determined for the higher temperatures (20°C and 30°C). At higher temperatures the mixture is getting prone to damage

indicated by the smaller distance between the state stress of the fatigue tests and the failure lines.

The stress state points of the beams which were tested at low temperature indicate higher resistance to failure compared to the stress state points of the beams tested at a higher temperature. This is because of the smaller distance of the stress points to the related failure lines.

4.3.3.2. BOEF test

The yield surface parameters I_1 and $\sqrt{J_2}$ for the BOEF test were determined using Equation 4.34 and 4.35. The yield surface parameters for the BOEF fatigue tests are given in Table 4.26 and were determined in the following way. The BOEF tests were performed using a haversine load with a frequency of 8 Hz, similar to a loading time of 0.125 s so the strain rates were determined using Equation 4.36 using a "t" value of 0.0625 s. The tensile strain values were those measured during the test.

The stress conditions for each of the BOEF fatigue tests were determined by means of the earlier mentioned 3D FE simulations using ABAQUS. The input parameters and loading conditions of this simulation have been explained in subchapter 4.3.

From the result of this simulation the I_1 and $\sqrt{J_2}$ coordinate of each stress state point were determined using Equation 4.38. I_1 and $\sqrt{J_2}$ occurring in each of the BOEF tests as determined by means of ABAQUS simulations are presented in Table 4.27.

$$I_1 = \sigma_1 + \sigma_2 + \sigma_3$$

$$\sqrt{J_2} = \sqrt{\frac{1}{6}\left[\left(\sigma_1 - \sigma_2\right)^2 + \left(\sigma_1 - \sigma_3\right)^2 + \left(\sigma_2 - \sigma_3\right)^2\right]} \tag{4.38}$$

Table 4.26. Recapitulation of the yield surface parameters valid for the BOEF tests

T	f	P	$\dot{\varepsilon}$	fc	ft	R	γ
°C	Hz	kN	%/s	N/mm2	N/mm2		
5	8	1.5	0.164	-19.29	4.76	12.63	0.122
		1.75	0.217	-20.58	4.79	12.50	0.129
		2	0.320	-22.48	4.83	12.31	0.139
		2.25	0.338	-22.74	4.84	12.28	0.141
		2.5	0.462	-24.36	4.86	12.14	0.149

Table 4.27. Stresses at the bottom of the BOEF beams as calculated by means of ABAQUS and the associated I_1 and $\sqrt{J_2}$ values

P	σ_1	σ_2	σ_3	I_1	$\sqrt{J_2}$
kN	MPa	MPa	MPa	MPa	MPa
1.50	2.4366	-0.1183	0.1210	2.44	1.41
1.75	2.8429	-0.1379	0.1418	2.85	1.65
2.00	3.2556	-0.1578	0.1628	3.26	1.89
2.25	3.6559	-0.1771	0.1833	3.66	2.12
2.50	4.0623	-0.1966	0.2042	4.07	2.35
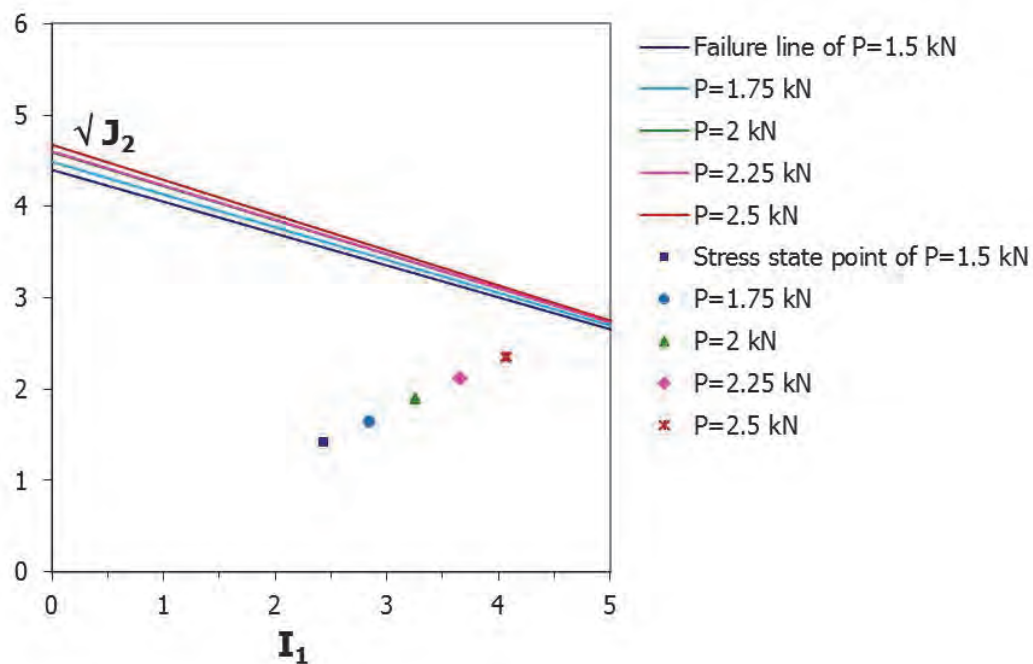
Figure 4.55. Yield surface and stress state points of GAC at 5°C and 8 Hz of the BOEF test

Figure 4.54 shows the stress conditions and the yield surfaces for the strain rates that occurred at the different BOEF tests. From the I_1-$\sqrt{J_2}$ plane (see Figure 4.55) it is observed that the different strain rates hardly influenced the location of the yield surfaces.

One will notice that the stress state positions of the BOEF tests are closer to the yield surface than the stress state positions of the 4PB tests. This can easily be explained by the fact in the BOEF test, 3D stress conditions occur. Further discussion on this matter will be presented in the following section.

4.3.4. The stress ratio

Figure 4.54 and 4.55 show that the states of stress of the different tests lay along a path starting at the origin (0,0) and continuing to the corresponding yield surface.

If the stress conditions in a material result in a point above the yield surface, then immediate failure will occur. The closer the stress state point is to the yield surface the closer it is to failure.

Li [31] introduced a variable R_Δ to indicate the safety margin to failure of the material at a certain stress state. The principle is illustrated in Figure 4.56 and is determined by means of Equation 4.39.

$$R_\Delta = \frac{\Delta_i}{\Delta_{tot}}$$

(4.39)
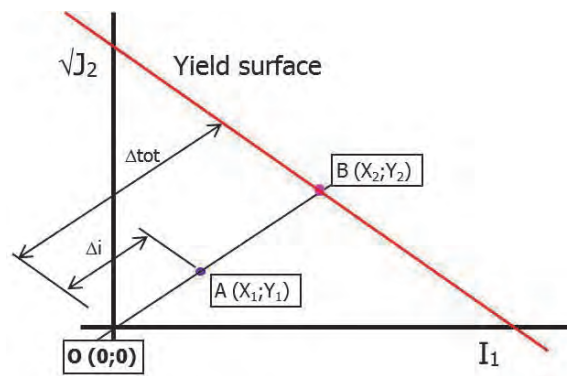
Figure 4.56. Sketch of Δ_i and Δ_{tot} on I_1-$\sqrt{J_2}$ space

The R_Δ value is in the range between 0 and 1. If this ratio approaches 1, it implies that the material approaches failure.

For each data point in Figure 4.54 and 4.55, the relation between the number of load repetitions until failure, N, and R_Δ, is determined. Tables 4.28 and 4.29 show the results from the 4PB and BOEF tests respectively. The relation between R_Δ and the fatigue life is shown in Figure 4.57.

Table 4.28. Stress ratios $R\Delta = \Delta_i/\Delta_{tot}$ and number of load repetitions to failure for the 4PB fatigue tests

T	f	R_Δ	log R_Δ	N	log N
°C	Hz	Δ_i/Δ_{tot}		cycles	
5	3	0.343	-0.465	1044830	6.019
		0.339	-0.470	656270	5.817
		0.329	-0.482	124300	5.094
		0.434	-0.363	143220	5.156
		0.491	-0.309	116920	5.068
		0.500	-0.301	44870	4.652
		0.625	-0.204	16360	4.214
		0.630	-0.201	29840	4.475
		0.664	-0.178	22080	4.344
5	8	0.272	-0.565	1843010	6.266
		0.323	-0.491	887070	5.948
		0.411	-0.386	533360	5.727
		0.437	-0.359	132650	5.123
		0.364	-0.439	440240	5.644
		0.476	-0.323	188230	5.275
		0.802	-0.096	44310	4.647
		0.588	-0.231	39270	4.594
		0.654	-0.184	29980	4.477
20	3	0.389	-0.410	631360	5.800
		0.367	-0.436	517220	5.714
		0.385	-0.415	234940	5.371
		0.435	-0.362	93640	4.971
		0.413	-0.384	59200	4.772
		0.412	-0.385	80580	4.906
		0.476	-0.323	20320	4.308
20	8	0.268	-0.572	1200780	6.079
		0.275	-0.561	418630	5.622
		0.301	-0.521	215590	5.334
		0.326	-0.486	217600	5.338
		0.368	-0.434	108150	5.034
		0.404	-0.394	34090	4.533
		0.447	-0.350	29460	4.469
30	8	0.422	-0.375	1853660	6.268
		0.484	-0.315	827830	5.918
		0.436	-0.360	279960	5.447
		0.455	-0.342	208590	5.319
		0.542	-0.266	169510	5.229
		0.531	-0.275	122910	5.090
		0.567	-0.247	70860	4.850

Table 4.29. Stress ratios $R\Delta = \Delta_i/\Delta_{tot}$ and number of load repetitions to failure for the BOEF fatigue tests

T	f	Δ_i/Δ_{tot}	log Δ_i/Δ_{tot}	N	log N
°C	Hz	R_Δ	Log R_Δ	cycles	
5	8	0.51	-0.290	2,359,690	6.373
		0.59	-0.226	1,925,210	6.284
		0.68	-0.170	309,770	5.491
		0.76	-0.120	116,490	5.066
		0.84	-0.077	10,430	4.018

(a) 4PB test

(b) BOEF test
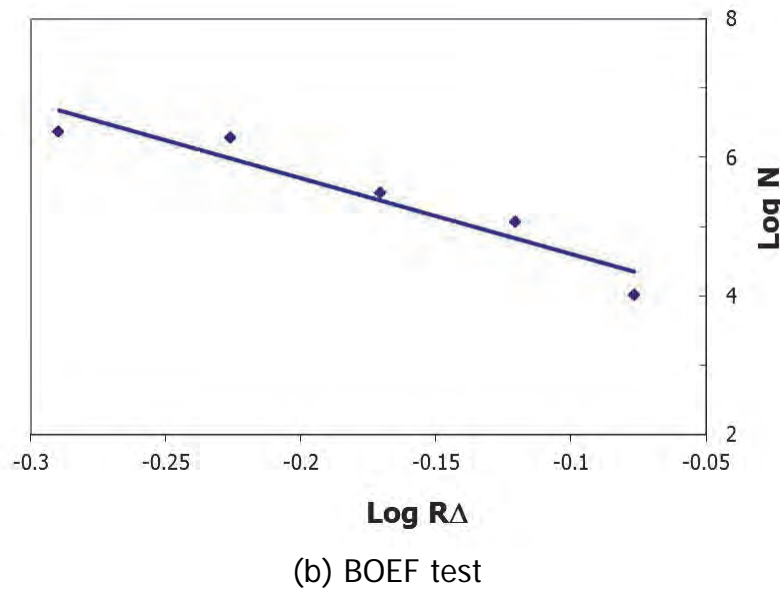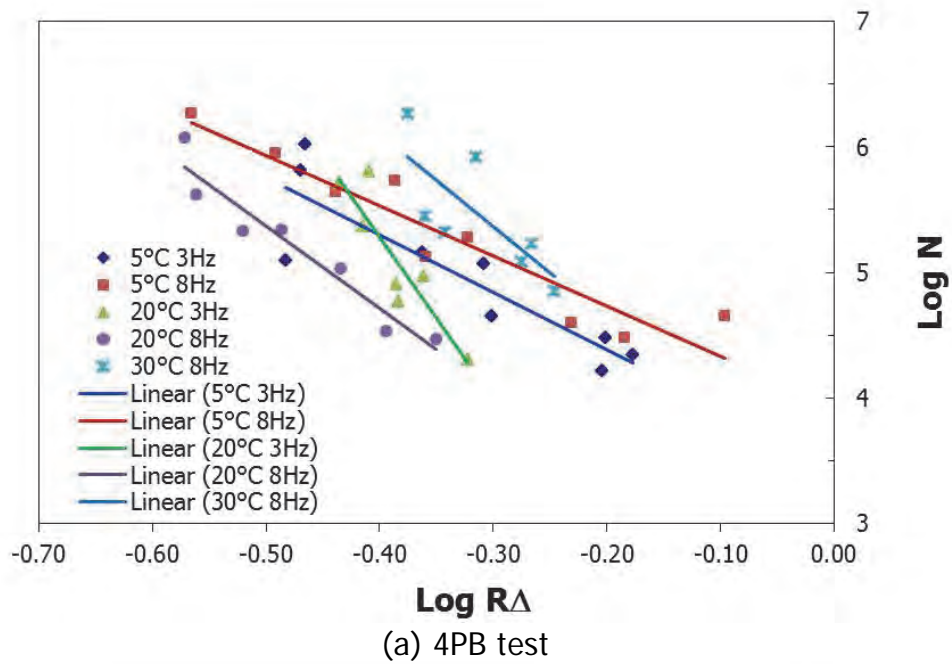
Figure 4.57. Relation between $R\Delta$ and the number of cycles to fatigue

The relation between the stress ratio and the number of load repetitions until failure for both the 4PB and BOEF fatigue test performed at the temperature of 5°C and frequency of 8 Hz are shown in Figure 4.58 in a log (a) and linear scale (b). Figure 4.58 (b) shows that at a certain stress ratio level, the fatigue life seems to go to infinity. This level can be called the endurance limit.

Log N
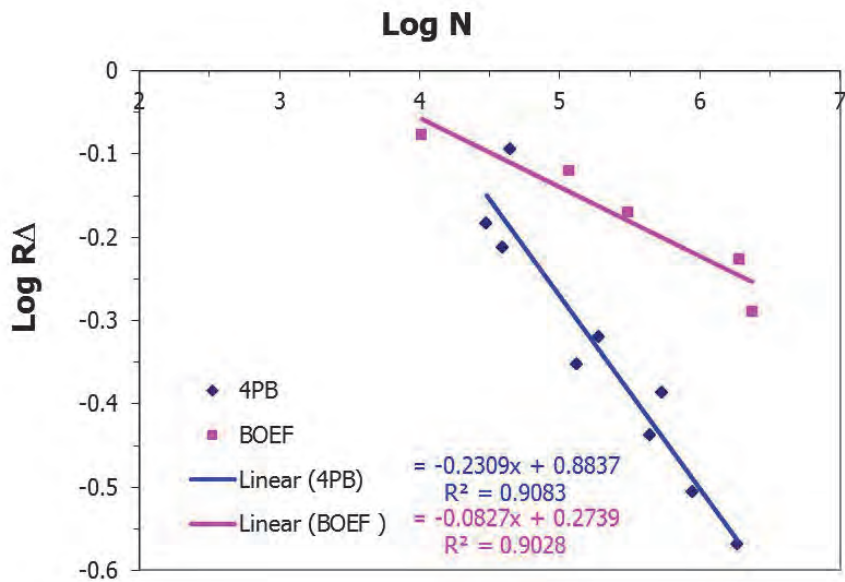
(a) in log scale
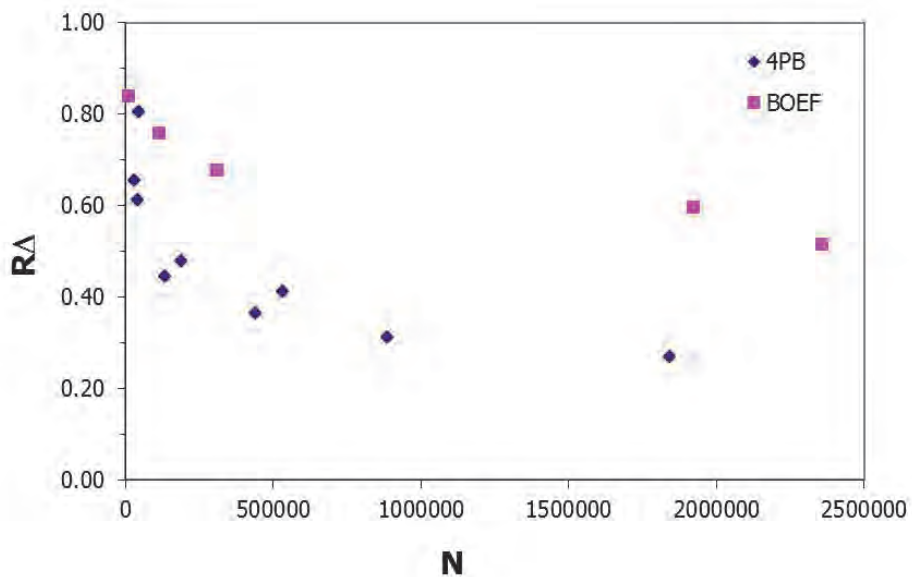
(b) in linear scale

Figure 4.58. N_f versus RΔ for the 4PB and BOEF test (Temp 5°C, frequency 8 Hz)

Similar tendencies were observed by Li who tested a DAC mixture by means of different fatigue test types and loading modes [23, 32]. Li proposed Equation 4.40 for capturing this behavior.

$$R_\Delta = R_0 - R_1 \left(1 - e^{-aN_f}\right)^b \tag{4.40}$$

Where R_0, R_1, a and b are regression coefficients.
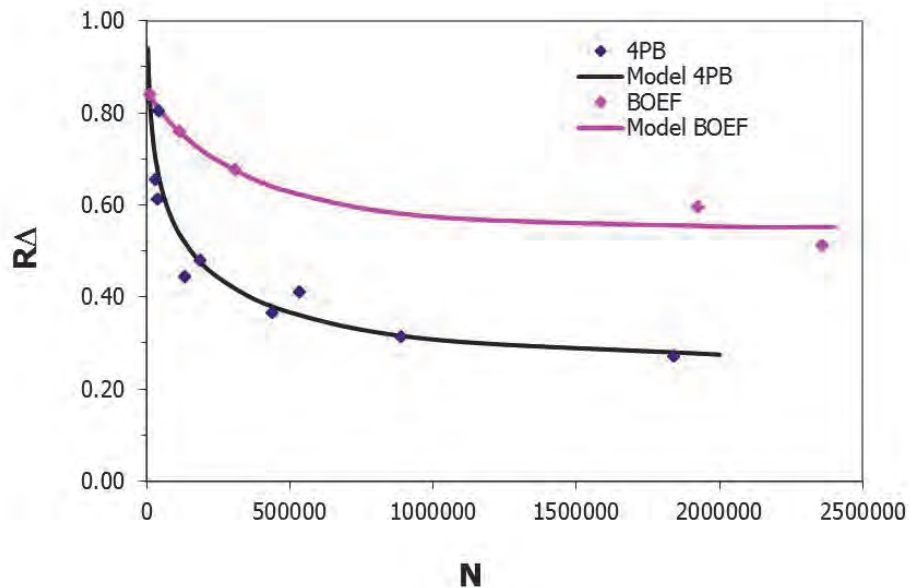
Figure 4.59. The relation between Nf and RΔ for 4PB and BOEF (Temp 5°C, frequency 8 Hz)

When using this equation to model the 4PB and BOEF test results obtained in this study, Figure 4.59 is obtained. The model parameters are presented in Table 4.30.

Table 4.30. General expression of RΔ as a function of N_f and the value of the R_{limit}

Test	Model : $R\Delta$	R^2	$R_{limit} = R_0\text{-}R_1$
4PB	$R\Delta_{4PB} = 0.785 - 0.518\left(1 - e^{-2.38 \times 10^{-6} Nf}\right)^{0.5176}$	0.84	**0.266**
BOEF	$R\Delta_{BOEF} = 0.853 - 0.302\left(1 - e^{-2.37 \times 10^{-6} Nf}\right)^{0.81}$	0.95	**0.551**

The model implies that at R values below a certain level no fatigue will occur. This R value, R_{limit}, is called the endurance limit and is equal to $R_0 - R_1$.

4.4.   Fatigue strain endurance limit

In Figure 4.60, all fatigue data in terms of tensile strain versus number of load repetitions to 50% stiffness reduction are shown. Like Figure 4.59, Figure 4.60 clearly shows that below a certain strain level the number of load repetitions to failure tends to go to infinity. This strain level is commonly called the strain fatigue endurance limit (ε_{limit}). Figure 4.60 indicates that a strain level of around 70 µm/m could be such a limit for all 4PB test results, independent of the testing conditions.
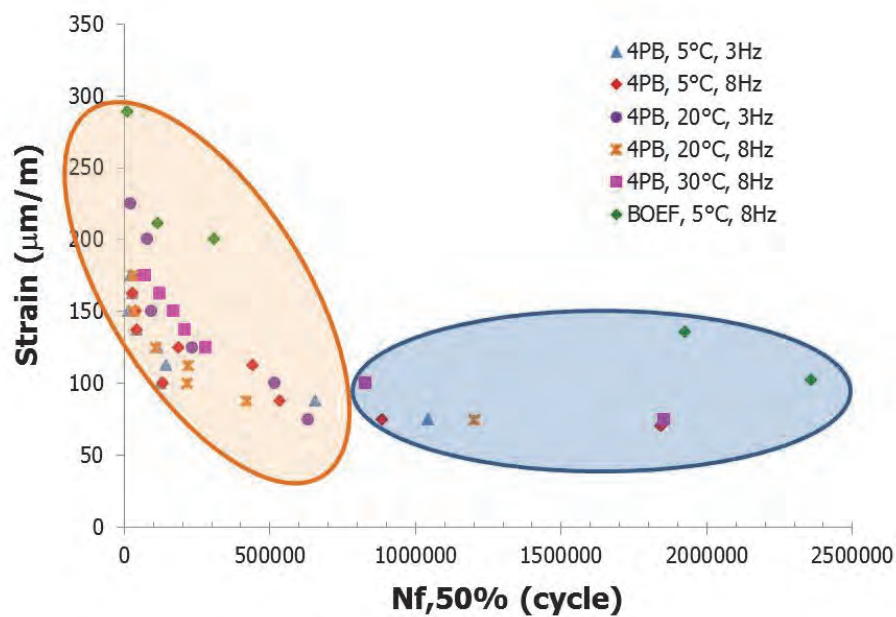
Figure 4.60. Plot of all 4PB and BOEF fatigue data

Taking into account the shape and the trend of the data points, the regression equation as proposed by Li [32] was used (Equation 4.41).

$$\varepsilon = \varepsilon_0 - \varepsilon_1 \left(1 - e^{-a N_f}\right)^b \tag{4.41}$$

Where ε is the strain level (in µm/m) and the other symbols are as previously defined.

When applied on 4PB and BOEF data, obtained at 5°C and 8 Hz, the results shown in Table 4.31 and Figure 4.61 were obtained.

For the sake of completeness also the 4PB strain endurance limit for the other test conditions were determined. They are shown in Table 4.32.

Table 4.31. General expression of ε as a function of N_f and the value of ε_{limit}

Test	Model : ε ($\mu m/m$)	R^2	$\varepsilon_{limit} = \varepsilon_0 - \varepsilon_1$ ($\mu m/m$)
4PB	$\varepsilon_{4PB} = 168.412 - 98.956\left(1 - e^{-2.65 \times 10^{-6} Nf}\right)^{0.7267}$	0.85	**69.5**
BOEF	$\varepsilon_{BOEF} = 322.62 - 207.75\left(1 - e^{-1 \times 10^{-6}\,Nf}\right)^{0.3992}$	0.96	**114.9**
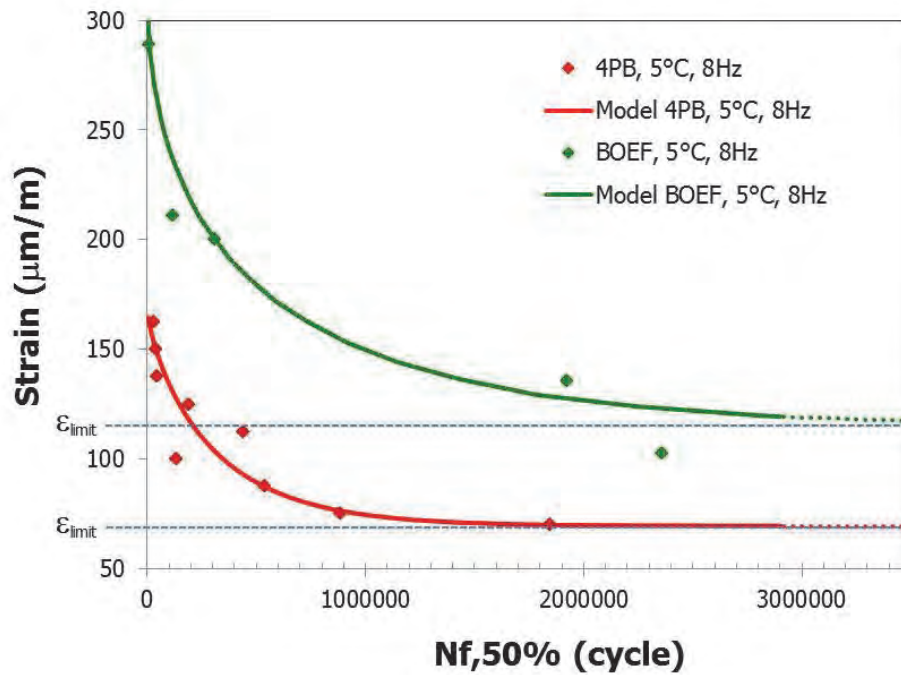
Figure 4.61. Strain endurance limits derived for the 4PB and BOEF tests at $5^\circ C$ and 8 Hz

Table 4.32. General expression of ε as a function of N_f for 4PB

4PB Test	Model : ε ($\mu m/m$)	R^2	ε_{limit} ($\mu m/m$)
$5^\circ C$, 3Hz	$\varepsilon = 173.628 - 93.137\left(1 - e^{-1.02 \times 10^{-5} Nf}\right)^{1.5838}$	0.90	79.4
$5^\circ C$, 8Hz	$\varepsilon = 168.412 - 98.956\left(1 - e^{-2.65 \times 10^{-6} Nf}\right)^{0.7267}$	0.85	69.5
$20^\circ C$, 3Hz	$\varepsilon = 270.157 - 176.697\left(1 - e^{-5.46 \times 10^{-6} Nf}\right)^{0.6052}$	0.92	93.5
$20^\circ C$, 8Hz	$\varepsilon = 167.163 - 92.337\left(1 - e^{-5.16 \times 10^{-6} Nf}\right)^{0.9223}$	0.95	74.8
$30^\circ C$, 8Hz	$\varepsilon = 185.197 - 110.241\left(1 - e^{-4.54 \times 10^{-6} Nf}\right)^{1.8203}$	0.97	75.0

4.5.   Findings

In this chapter the volumetric and mechanical characteristic of a gravel asphalt concrete mixture, that was a copy of the mixture used in the Lintrack tests, have been evaluated.

The investigation on the GAC volumetric characteristic has shown that the density and air voids values of GAC produced for this study are in the same range as the density and air voids of the GAC Lintrack sections. This means that the GAC Lintrack section material, which is no longer available, could adequately be reproduced. Unfortunately the recovered bitumen penetration was slightly different in which the penetration of the recovered bitumen from the reproduced GAC is lower than that of the recovered bitumen of Lintrack sections. Nevertheless, the mixture stiffness of the mixture produced in this study was in the same range as the stiffness of the original Lintrack sections. Therefore, it is believed that the mixture composition of this work adequately represents the original Lintrack mixture characteristics.

Healing tests performed on the pen 40/60 mastic showed that healing occurred at temperatures higher than 10°C, and rest periods higher than 5 hours. On the Lintrack test sections, this kind of 'recovery' only occurred in the beginning of the test when seemingly the pavement still has a self-healing capability. Furthermore, re-testing a batch of fatigue beams (5°C-8Hz) showed that after 19 months the stiffness of the beams had almost returned to its initial value. Complete healing in terms of the strength expressed by the fatigue life was not achieved. Therefore, using a healing factor of 4, as was done in previous research, seems to be an overestimation of reality.

Models to predict the compressive and tensile strength as a function of temperature and strain rate were developed. These models were used to define the yield surface as a function of temperature and strain rate.

One of the more significant findings that emerged from this study is the successful implementation of the beam on elastic foundation (BOEF) test as an alternative of the 4PB test. The fatigue lines from these two tests have approximately the same slope but the BOEF fatigue line has a much higher intercept. The fatigue life as determined with the BOEF test at a strain level of 126 μm/m was approximately 16 times longer than the fatigue life determined with the 4PB test.

The stress ratio RΔ may be used to indicate the "safety against failure". It is shown that at a certain RΔ, an endurance limit is reached. It was also shown that a similar limit in terms of tensile strain exists.

4.6.   References

[1]   NEVUL, "Activity 2010-2011, Certification 2011-2012, List of Recognized Brand Fillers (in Dutch)," ed. Venray, The Netherlands: Nevul, 2011-2012.

[2]   S.M.J.G. Erkens and M.R. Poot, "The Uniaxial Compression Test (Asphalt Concrete Response-ACRe)," Delft University of Technology, Delft The Netherlands, 2000.

[3]   G. Liu, "Characterization and Identification of Bituminious Materials Modified with Montmorillonite Nanoclay," Delft University of Technology, Delft The Netherlands, 2011.

[4]   M. F. Woldekidan, "Response Modelling of Bitumen, Bituminous Mastic and Mortar," PhD, Delft University of Technology, Delft The Netherlands, 2011.

[5]   M. F. Woldekidan, M. Huurman, and A. C. Pronk, "A modified HS model: Numerical applications in modeling the response of bituminous materials," *Finite Elements in Analysis and Design,* vol. 53, pp. 37-47, 6// 2012.

[6]   A. C. Pronk, "The Huet-Sayegh Model: A Simple and Excellent Rheological Model for Master Curves of Asphaltic Mixes. ," presented at the ASCE., Baton Rouge, Louisiana, USA, 2005.

[7]   R. N. J. Saal and J. W. A. Labout, "CHAPTER 9 - RHEOLOGICAL PROPERTIES OF ASPHALTS," in *Rheology*, F. R. Eirich, Ed., ed: Academic Press, 1958, pp. 363-400.

[8]   J.M.M. Molenaar and A.A.A. Molenaar, "Aspects of Constitutive Modelling of Asphalt.," presented at the The Eurasphalt & Eurobitume Congress 2000, Rheology of Bitumen, Barcelona, 2000.

[9]   J.M.M. Molenaar, "Rheology of Bitumen," presented at the Eurobitume workshop on "Performance Related Properties for Bituminous binders", May 3-6, Luxembourg, 1999.

[10]   W. V. d. Bergh, "The Effect of Ageing on the Fatigue and Healing Properties of Bituminous Mortars," PhD, Delft University of Technology, Delft, The Netherlands, 2011.

[11]   J. S. Wattimena, "Fatigue Testing GAC may 1991 (Lintrack) (in Dutch); Report 91482; NPC," Hoevelaken, 1991.

[12]   M.F.C. van de Ven, "Fatigue Testing GAC test section II (Lintrack DUT) (in Dutch); Report 91489; NPC," Hoevelaken, 1991.

[13]   J. A. Sassen, "Determination of the Initial Dynamic Stiffness Modulus of the Lintrack Test Sections," RHED, Delft, 1991.

[14]   H. Sabha, "Estimation of Crack Growth Parameters and Fatigue Characteristics of Asphalt Mixes Using Simple Test," Delft University of Technology, Delft, The Netherlands, 1995.

[15]   J. Groenendijk, "Accelerated Testing and surface cracking of asphaltic concrete pavements," PhD, Delft University of Technology, Delft The Netherlands, 1998.

[16]   P. D. Bhairo, "Comparison of the predicted and Observed Pavement Life of LINTRACK Test Lane Va," Delft University of Technology, Delft, The Netherlands, 1997.

[17]   M. Miradi, "Knowledge Discovery and Pavement Performance: Intelligent Data Mining," PhD, Delft University of Technology, Delft The Netherlands, 2009.

[18]   J. Qiu, M. van de Ven, S. Wu, J. Yu, and A. A. A. Molenaar, "Evaluating Self Healing Capability of Bituminous Mastics," *Experimental Mechanics,* vol. 52, pp. 1163-1171, 2012.

[19]   J. Qiu, "Self Healing of Asphalt Mixture," PhD, Delft University of Technology, Delft The Netherlands, 2012.

[20]   M.R. Poot, J.W. Bientjes, and A.C. Pronk, "Stab reference dataset for fatigue and dynamic stiffness properties. ," TU Delft Road and Railway Engineering, Delft, 2008.

[21]   S. M. J. G. Erkens, "Asphalt Concrete Response - Determination, Modeling and Prediction," PhD, Delft University of Technology, Delft The Netherlands, 2002.

[22]   S.M.J.G. Erkens and M. R. Poot, "The Uniaxial Tension Test (Asphalt Concrete Response-ACRe)," Delft University of technology, Delft The Netherlands, 2001.

[23]   N. Li, "Asphalt Mixture Fatigue Testing; Influence of Test Type and Specimen Size," PhD, Delft University of Technology, Delft The Netherlands, 2013.

[24]   M.R. Poot, M.F.C. van de Ven, and A. Cocurullo, "Asphalt Testing, Practical Manual CT 4830," ed: TU Delft, 2008.

[25]   M. Huurman and M.R. Poot, "Determination of the Burgers' parameters by application of the dynamic ITT," in *Advanced characterisation of pavement and soil engineering materials,* , Leiden, The Netherlands, 2007, pp. 111-121.

[26]   M. Woldekidan, M. Huurman, and A. Pronk, "Linear and Nonlinear Viscoelastic Analysis of Bituminous Mortar," *Transportation Research Record: Journal of the Transportation Research Board,* vol. 2370, pp. 53-62, 12/01/ 2013.

[27]   J. Qiu, M.F.C. van de Ven, E. Schlangen, A.A.A. Molenaar, and S. Wu, "Cracking and Healing Modelling of Asphalt Mixtures," in *7th RILEM International Conference on Cracking in Pavements*, 2012.

[28]   A. Scarpas, R. Al-Khoury, C. Van Gurp, and S. Erkens, "Finite element simulation of damage development in asphalt concrete pavements," in *Eighth International Conference on Asphalt Pavements*, Washington, 1997.

[29]   X. Liu, "Numerical modelling of porous media response under static and dynamic load conditions," PhD, Delft University of Technology, Delft The Netherlands, 2003.

[30]   T. O. Medani, "Design Principles of Surfacings on Orthotropic Steel Bridge Decks," PhD, Delft University of Technology, Delft The Netherlands, 2006.

[31]   N. Li, A. A. A. Molenaar, M. F. C. van de Ven, and S. Wu, "Characterization of fatigue performance of asphalt mixture using a new fatigue analysis approach," *Construction and Building Materials,* vol. 45, pp. 45-52, 8// 2013.

[32]   N. Li, A. C. Pronk, M. F. C. van de Ven, and A. A. A. Molenaar, "Estimation of Fatigue Endurance Limit by Using Monotonic Uniaxial Tension Test," Delft University of Technology, Juli 2009.

This page is intentionally left blank

Appendix 4A
Initiation of tertiary flow in the BOEF tests

In the BOEF test where a number of load cycles was applied to a beam specimen, the development of the accumulated strain vs the number of load repetitions was recorded. As mentioned in section 4.2.8 this accumulated strain consists partly of non-recovered delayed elastic strain and partly of permanent strain.

It has been stated by a number of researchers like Molenaar [1] and Kunst [2] that failure in repeated load controlled fatigue tests is because of creep and not so much because of fatigue. If repeated load controlled fatigue specimens fail in creep/accumulated deformation then it might be possible to define a creep/accumulated strain level at which the BOEF specimens were failing. Such a value would of course be dependent on the temperature and loading rate applied in the test but these were the same for all BOEF tests.

In this appendix an attempt has been made to define such a creep/accumulated strain level at which failure of the BOEF specimens occurred.

Vismara [3] mentioned that there are three stages of flow that occurred during the BOEF tests performed by her. Similar trends were observed in this research (see e.g. Figure 4A.1)
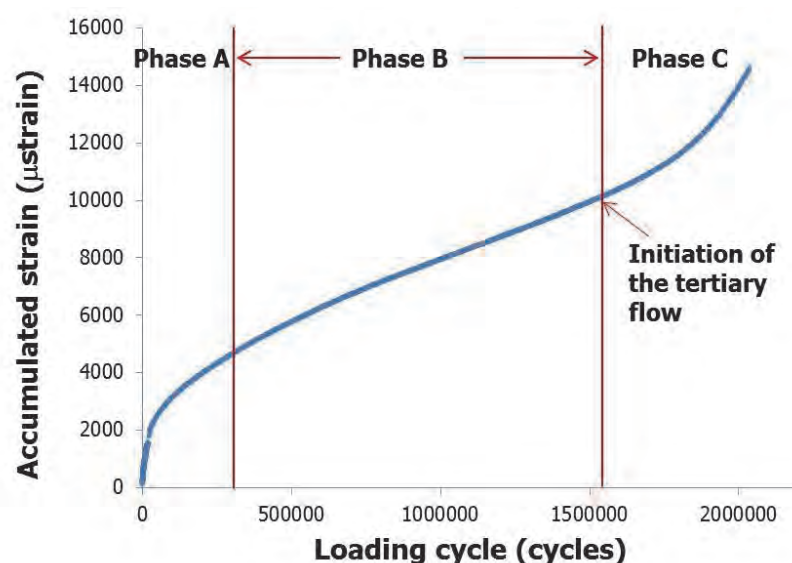
Figure 4A.1. The development of the accumulated strain during the BOEF test. P = 1.75 kN

These three stages (A, B and C) not only show the development of the accumulated strain as a function of the number of load repetitions but also show the development of the strain rate during the test. In phase A the strain rate is decreasing. In phase B the strain rate is relatively constant, while in phase C the strain rate is rapidly increasing and ultimately the specimen will fail . The third (C) phase is often called the 'Tertiary flow' phase.

In permanent deformation tests the initiation of this third phase is defined as the Flow Number (FN). This parameter is useful to indicate the beginning of the permanent deformation in asphalt mixture and to provide the required parameter for predicting rut depth based on laboratory tests [4].

The accumulated strain as a function of the number of load repetitions applied on the five BOEF tests is shown in Figure 4A.2. It looks like the initiation of the tertiary flow in the five BOEF tests occur at the same accumulated strain level but at different numbers of load cycles. So it looks like the earlier made hypothesis (the BOEF specimens fail at the same accumulated strain level) might be true.
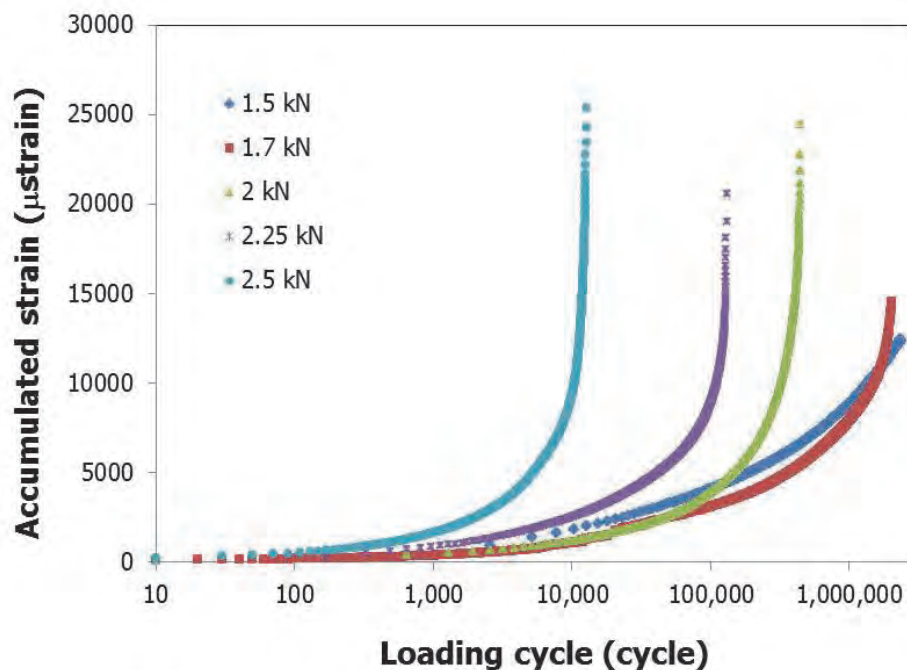
Figure 4A.2. The accumulated strain of the five BOEF tests as a function of the loading cycles at 5°C and 8 Hz.

4.A.1. Francken model

There are several methods to determine the initiation of the tertiary flow [4, 5]. Some of them are the Three stage, FNest, Francken and Stepwise method [5-8]

Ameri [4] in his paper evaluated and compared nine methods for calculating the tertiary flow initiation. He concluded that for a single specimen each different method does not yields the same results and there is high variability between them. He also concluded that for all asphalt mixtures he investigated, the Francken method has the lowest variability and therefore is highly recommended.

The Francken model is a composite mathematical model proposed by Biligiri et al [8] to express the relation between accumulated strain and number of loading cycles. This function is shown in Equation 4A.1.

$$\varepsilon_a(N) = AN^B + C\left(e^{DN} - 1\right) \qquad (4A.1)$$

where

ε_a = accumulated strain (microstrain)

N   = number of load cycles (-)

A, B, C and D   = regression constants

For determining the slope of the curve (the strain rate), equation 4A.1 is differentiated with respect to N as shown in Equation 4A.2.

$$\frac{d\varepsilon_a}{dN} = \left(A \times B \times N^{(B-1)}\right) + \left(C \times D \times e^{DN}\right) \qquad (4A.2)$$

The second derivative of the Equation 4A.1 is expressed in Equation 4A.3. From this equation the tertiary flow initiation is determined being the cycle number where the second derivative of the composite model changed from a negative to a positive value.

$$\frac{d^2\varepsilon_a}{dN^2} = \left(A \times B \times (B-1) \times N^{(B-2)}\right) + \left(C \times D^2 \times e^{DN}\right) \qquad (4A.3)$$

4.A.2. Determination of the Francken parameters for the BOEF tests

The procedure described above was applied to the BOEF test results. Figure 4A.5 shows the Francken model for BOEF test at P = 1.75 kN. It can be seen that the predicted accumulated strain fits to the measured accumulated strain with an R^2 of 0.999. The slope which was determined using Equation 4A.2, is

also shown in this Figure. The regression constants for all of the BOEF tests are depicted in Table 4A.1.

The result of the Equation 4A.3 for the BOEF test at P = 1.75kN is plotted in Figure 4A.6. The point when the 2nd derivative of the accumulated strain equals to zero is N = 1,134,170 cycles.
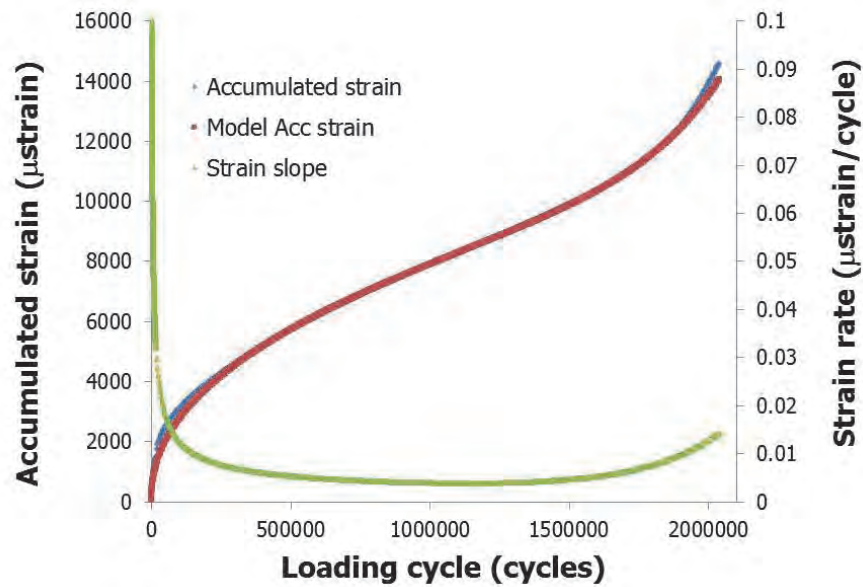
Figure 4A.5. The accumulated strain and strain rate for P = 1.75 kN
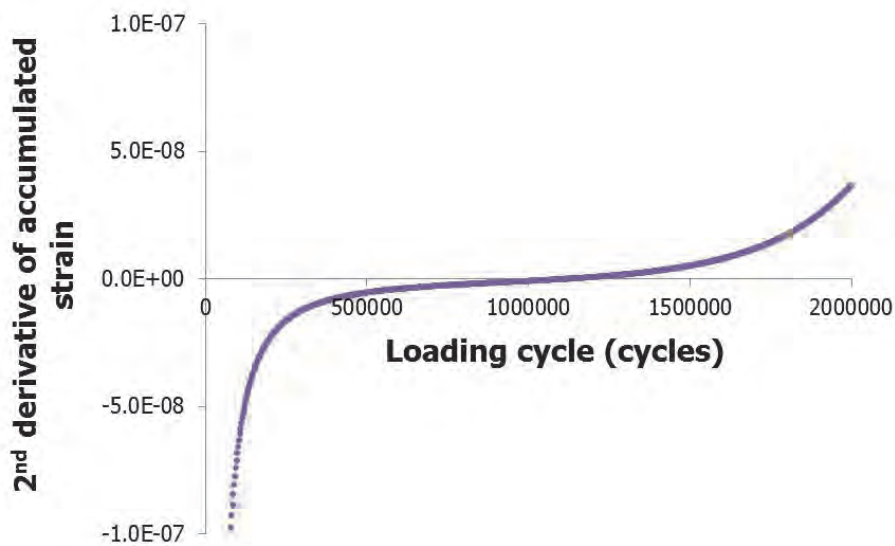
Figure 4A.6. The 2nd derivative of the accumulated strain as a function of the number of load cycles. P = 1.75 kN

Table 4A.1. Francken regression constants for five BOEF tests.

P kN	A	B	C	D	R^2
1.50	63.492	0.35770	8.61653	1.628E-06	0.999
1.75	14.942	0.45324	1.93783	3.640E-06	0.999
2.00	1.427	0.68780	0.70000	2.160E-05	0.916
2.25	37.001	0.45862	31.58001	3.946E-05	0.889
2.50	11.392	0.71343	0.11842	9.045E-04	0.998

Table 4A.2. The accumulated strain value at the initiation of the tertiary flow for BOEF tests

P	Number of cycle to fatigue	N when $\frac{d^2\varepsilon_a}{dN^2} = 0$	Strain rate when $\frac{d^2\varepsilon_a}{dN^2} = 0$ (min strain rate)	ε_a at the initiation of tertiary flow phase
kN	cycle	cycle	µstrain/cycle	µstrain
1.50	2,359,690	2,040,970	0.002	11705
1.75	1,925,210	1,134,170	0.004	8410
2.00	309,770	211,850	0.023	6636
2.25	116,490	55,690	0.057	5808
2.50	10,430	6,330	0.694	5906

The results given in Table 4A.2 show that the tertiary flow of the BOEF tests did not initiate at a similar accumulated strain level implying that the hypothesis "the BOEF tests failed at the same accumulated strain level" has to be rejected.

4.A.3. References

[1] J. M. M. Molenaar, "Performance Related Characterisation of the Mechanical Behaviour of Asphalt Mixtures," PhD, Delft University of Technology, Delft The Netherlands, 2003.

[2] P.A.J.C. Kunst and A.A.A. Molenaar, "Characterisation of the Deformation and Cracking Behavior of an Open Asphalt Concrete Mixture at low Temperatures and long Loading Times (in Dutch)," Technische Hogeschool Delft, Afdeling der Civiele Techniek, Laboratorium voor Weg- en Spoorwegbouwkunde, Delft, 1983.

[3] Stefania Vismara, A.A.A. Molenaar, Maurizio Crispino, and M.R. Poot, "Towards A Better Understanding Of The Benefits Of Geosynthetics Embedded 1 In Asphalt Pavements," in *2012 Annual Meeting of Transportation Research Board*, 2012.

[4] M. Ameri, A. H. Sheikhmotevali, and A. Fasihpour, "Evaluation and comparison of flow number calculation methods," *Road Materials and Pavement Design,* vol. 15, pp. 182-206, 2014.

[5] S. W. Goh and Z. You, "A simple stepwise method to determine and evaluate the initiation of tertiary flow for asphalt mixtures under

dynamic creep test," *Construction and Building Materials,* vol. 23, pp. 3398-3405, 2009.

[6]   F. Zhou, T. Scullion, and L. Sun, "Verification and Modeling of Three-Stage Permanent Deformation Behavior of Asphalt Mixes," *Journal of Transportation Engineering,* vol. 130, pp. 486-494, 2004.

[7]   A. R. Archilla, L. G. Diaz, and S. H. Carpenter, "Proposed method to determine the flow number from laboratory axial repeated loading tests in bituminous mixtures," in *Transportation Research Board 86th Annual Meeting*, 2007.

[8]   K. P. Biligiri, K. E. Kaloush, M. S. Mamlouk, and M. W. Witczak, "Rational modeling of tertiary flow for asphalt mixtures," *Transportation Research Record: Journal of the Transportation Research Board,* vol. 2001, pp. 63-72, 2007.

Chapter 5
Asphalt Buton modified GAC base course mixture
-comparison to the unmodified GAC mixture-

In chapter 4 the characterization of the Gravel Asphalt Concrete (GAC) base course mixture was described. In this chapter the results of the same test program as carried out on the GAC mixture modified by incorporating Asphalt Buton (Asbuton) are presented. Asbuton – a natural "rock-like" bitumen available in Indonesia – has shown potential as a modifier of or additive to conventional bitumen as well as bitumen replacement. Therefore, it is very interesting to study its effects on mixture characteristics such as stiffness, fatigue and permanent deformation resistance. As the literatures [1-6] show that this modifier is very promising in enhancing these characteristics, the investigations will enable us to compare the characteristics of both mixture compositions (reference and modified) as well as to explore the long term performance of Asbuton modified GAC mixtures. Such an analysis could be of benefit for the road agencies in Indonesia.

In this research, Refined Buton Asphalt (Retona) produced from Asbuton was introduced as modifier. First, Asbuton and its refining process resulting in Retona are presented in this chapter. Next, the results of monotonic uniaxial compression and tension tests, four point bending tests and healing tests are presented and used to characterize the stiffness and fatigue properties of the Retona modified mixture. Comparisons with the mechanical properties of the original GAC mixture will be presented and discussed in each section.

5.1.   Asphalt Buton (Asbuton)

Among the more than 17.000 islands of the Indonesia archipelago (see Figure 5.1), Buton is an island south east of Sulawesi (Celebes) located at 5° 22′ S and 122° 51′ E. This island has abundantly available natural rock asphalt usually called Asbuton which stands for Asphalt Buton. Astuti [7] reported that the deposits found are about 300 million tons spread over an area of 70.000 ha. A report taken from the website of the Research and Development Agency of the Ministry of Public Works, Government of Indonesia, shows that the proven deposits are twice the size as reported by Astuti. Although precise data on the Asbuton deposits are not available, one can safely say that large

quantities are available for future use and that the potential of the resources are huge.

On Buton this natural asphalt is found as brownish black asphaltic porous rock which is lightweight and consists of mineral, bitumen, and water. The local government site reported that the bitumen content varies between 10% to 40% [8], while another source reported that its content varies between 15% to 35% [9]. Asbuton itself has been recognized since the 1920's when the Dutch Geologist Hetzel studied the deposits. He published a complete geologic map of Buton Island in 1936. Afterwards, Buton became famous for its late Triassic oil shales and tertiary tar sands. Asbuton has been mined at many places on Buton Island, such as Kabungka, Lawele, Winto, Wariti, Waisiu, Rongi and Ereke with Kabungka and Lawele as the biggest mining sites. Since 1980 the resources in Kabungka (the hard asphalt) and since 2003 in Lawele (the softer asphalt) have been mined. However, full exploitation is limited and used as cheap conventional road material substituting petroleum asphalt. This is mainly because the characteristics of Asbuton are not well studied.
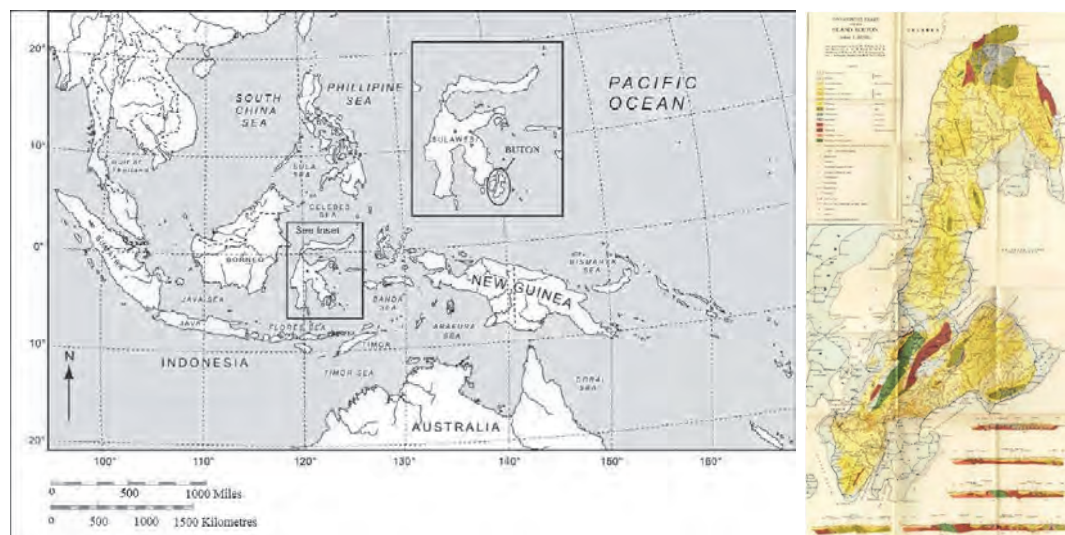
Figure 5.1. Buton Island and the geologic map created by Hetzel 1936

Conventional Asbuton bitumen is normally extracted from the crushed rock by diluting it using some solvent. After 3-4 days, this laborious time consuming process might result in a granular material with varying bitumen content. This is the reason why a new refinement process has been developed leading to what is branded as Refined Buton Asphalt (Retona).

The process is started by blasting rock by means of dynamite. The results are lumps or chunks of about 200 mm in size. This material is then loaded into trucks and stored at the plant for further crushing using a hammer mill. The result is an aggregate with a size of about 25 mm which then is delivered to a

chemical plant for bitumen extraction. In this plant an acid-alkaline chemical reaction takes place in which Asbuton is diluted with an inorganic solvent. In principle, the higher the amount of inorganic solvent used, the higher the bitumen content obtained. For instance, Retona 60 means 60% of the material is bitumen and the rest is natural filler. The refinement is not a cheap process, the higher the bitumen content targeted, the higher the cost will be, since more amount of inorganic solvent is required.

The Retona used in this study is Retona 35 which consists of 35% bitumen and 65% filler. This type of Retona is used because it is available in the market and relatively cheap compared to the standard bitumen. Usually 20% of this type of Retona is added as a modifier to the other 80% bitumen which normally has a penetration of 60/70. In this work the term Retona refers to Retona 35.

In determining the mixture composition of modified GAC with Retona, care has to be given to the fact that because of the amount of Retona filler that is added, the amount of original filler of the GAC mixture should be reduced. This is shown in chapter 3 Table 3.10.

The chemical and mineral composition of the extracted Asbuton mined in Kabungka and Lawele region is described by Siswosoebrotho [1] and is shown in Table 5.1 and 5.2. These tables are assumed to describe the chemical and mineral composition of the Retona since its raw material is mined in the Kabungka and Lawele region.

Table 5.1. Chemical component of extracted bitumen of Asbuton mined in Kabungka and Lawele[1]

Component	Content	
	Asbuton Kabungka	Asbuton Lawele
Precipitate:		
Asphaltene content,%	46.92	39.45
Solution of maltenes:		
Nitrogen bases (N), %	29.04	27.01
1st Acidaffins (A1),%	6.6	9.33
2nd Acidaffins (A2),%	8.43	12.98
Paraffins (P),%	8.86	11.23
Parameter Maltene		
= (N+A1)/(P+A2)	2.06	1.5
Nitrogen bases/Parafin		
= N/P	3.28	2.41

Using Rostler's chemical precipitation procedure [10, 11], the chemical components of the bitumen extracted from Asbuton were determined. Table 5.1 shows that the material is rich in asphaltenes, followed by Nitrogen bases.

Table 5.2 shows that the extracted filler of Asbuton mainly consists (more than 70%) of calcium carbonate ($CaCO_3$) or lime.

Table 5.2. Chemical properties of mineral (extracted filler) of Asbuton mined in Kabungka and Lawele[1]

Component	Source of deposit	
	Kabungka	Lawele
$CaCO_3$	86.66	72.9
$MgCO_3$	1.43	1.28
$CaSO_4$	1.11	1.94
CaS	0.36	0.52
H_2O	0.99	2.94
SiO_2	5.64	17.06
Al_2O_3 +Fe_2O_3	1.52	2.31
Residue	2.29	1.05

5.1.1. Infrared spectroscopy of Retona bitumen and filler

The gradation of Retona natural rock asphalt is shown in Table 5.3. as provided by PT Olah Bumi Mandiri, the company which produces Retona.

Table 5.3. Gradation analysis of Retona

Sieve Number	Size	
ASTM	mm	% passing
3/8"	9.50	100
4	4.75	32
8	2.36	0.3
10	2.00	0.2

In order to determine the bitumen content and to further characterize Retona, an extraction of the natural rock asphalt has been carried out. The bitumen recovery process, based on NEN-EN 12697-3, was performed using a Centaur 2 MSE® centrifuge, a vacuum pump, microfiber filter paper (with 1.6 μm particle retention in liquid), and dichloromethane as a solvent. Use of the filter paper of 1.6 μm might allow smaller particles to pass during the extraction. The possible presence of this fine material in the recovered binder will be explained when discussing the FTIR results.

The extraction was started by placing 25 g of Retona in four sample-tube-centrifuges to which 30 ml dichloromethane was added. The next step was stirring the contents of the tubes until the Retona granular was dissolved. The insoluble material was segregated from the bitumen solution by centrifuging the tubes at a speed of 3000 revolutions per minute for 20 minutes. The

centrifuging resulted in a dark bitumen-dichlorometane solution while the solid part of Retona remained at the bottom of the tube. The bitumen-dichlorometane solution then needed to be filtered through a pressure filter using a partial vacuum in the Erlenmeyer (See Figure 5.2 right). This bitumen-dichlorometane solution was then collected in an aluminum container

In the next step more solvent was added to the remaining solid part in the tubes and the process was repeated by stirring the content of the tubes and centrifuging again. The process needed to be repeated until the dissolved bitumen was clean which was indicated by the light color of both the dissolved liquid and the solid part. When the bitumen solution was totally clean, the process was continued by evaporating the solvent by leaving it for 24 hours in the fume chamber. The extracted bitumen and extracted filler were then ready for further testing.

Figure 5.2. The Centaur 2 centrifuge (left) and the Erlenmeyer (right), connected to the vacuum pump, with the microfiber filter paper

(a)   (b)

Figure 5.3. (a) From left to the right are the dichloromethane+dissolved bitumen after 1st, 4th and 7th process (b) From left to the right are the granular Retona in original form, the extracted filler, and the extracted bitumen.

Figure 5.2 shows the centrifuge and the Erlenmeyer connected to the vacuum pump. Figure 5.3 shows the dissolved bitumen (a) and the original Retona together with the extracted filler and bitumen (b). Table 5.4 shows the result of the extraction. The results indicate that the bitumen content of the granular Retona is on average 35% by weight.

Table 5.4. Result of the Retona extraction [%]

Material	Value
Bitumen	35.0
Filler	64.7
Water	0.3

Table 5.5 shows that about 50% of the extracted filler of Retona particles are smaller than 75 μm. When modifying GAC with Retona, this gradation should be taken into account. How this is done is described in Chapter 3, Table 3.10.

Table 5.5. Gradation analysis of the extracted filler of Retona fraction

Sieve Number		
ASTM	Size	% passing
8	2.36 mm	100
16	1.18 mm	99
30	600 μm	96
50	300 μm	88
100	150 μm	77
200	75 μm	56

Table 5.6. Properties of the extracted bitumen of Retona

Property	Value	Units
Penetration (25°C, 100 g, 5 s)	8	0.1 mm
Softening Point	77.9	°C
Ductility (25°C, 5 cm/min)	23.0	cm
Solubility in C_2HCl_3	93.9	% weight
Flash Point, COC	256	°C
Specific Gravity	1.104	(g/cm^3)
Loss of weight after TFOT (163 °C, 5hrs)	0.751	% weight
Penetration after TFOT (25°C, 100 g, 5 s)	30.3	% of origin
Softening Point after TFOT	87.8	°C
Ductility after TFOT (25°C, 5 cm/min)	0	cm

*TFOT: Thin film oven test (aging test)

The properties of the extracted bitumen from Retona are given in Table 5.6. The table shows that the penetration at 25°C is 8 dmm which implies that the extracted bitumen can be classified as a very hard bitumen. Penetration

values between 3 and 4 are also reported for bitumen extracted from the Kabungka Asbuton region by several researchers [1, 12].

The composition of the extracted bitumen was characterized by Fourier transform infrared spectroscopy (FTIR). FTIR spectra were collected using a Perkin–Elmer Spectrum 100 Series spectrometer equipped with a universal Attenuated Total Reflectance (ATR) unit, allowing a non-destructive analysis of the bitumen. The ATR analysis only requires a very small sample, so only a few drops of bitumen were placed on top of the ATR crystal. The internal reflectance of the infrared beam into the ATR crystal creates an evanescence wave which extends into the sample. The sample absorbs energy in a particular region of the infrared spectrum and the attenuated infrared beam is then collected by the detector. The spectra were recorded in the wavenumber range of 4000–600 cm^{-1} with 4 cm^{-1} resolution, and 5 scans were collected each time [13, 14]. The principle of the FTIR-ATR is shown in Figure 5.4.
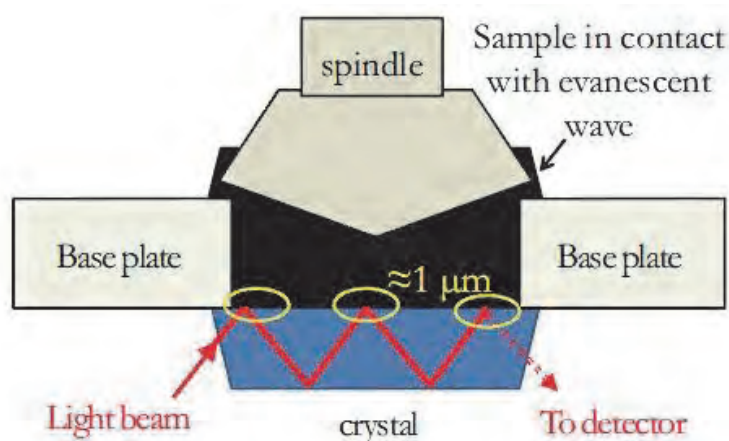
Figure 5.4. Scheme of FTIR principle [14]

The infrared spectra of the virgin bitumen 40/60 used for the GAC mixture and the extracted bitumen from Retona are shown in Figure 5.5. The red line shows the virgin 40/60 pen bitumen while the blue line shows the extracted Retona bitumen. The strong peaks within the 2850–2960 cm^{-1} regions are typical C-H stretching vibrations of aliphatic chains. The C-H asymmetric deforming into CH_2 and CH_3, and the C-H symmetric deforming into CH_3 vibrations were observed at 1458.2 cm^{-1} and 1375.2 cm^{-1} respectively. The peak at 1030 cm^{-1} was ascribed to S=O stretching vibrations. The small peaks within the 740–910 cm^{-1} region were typical C-H vibrations of benzene rings [15, 16]. Most of the peaks and valleys in the spectra of both specimens match each other. As can be seen from Figure 5.5 the two lines have similar functional groups. One difference is depicted by the presence of a peak at 1702 cm^{-1} in the Retona bitumen line which most probably is an effect of ageing resulting in a C=O group (van den Bergh [14]), or a result of the extraction procedure.

The two lines only differ in shape at the 1702 cm^{-1} wavenumber, which indicates an organic functional group. This cannot be caused by mineral particles of Retona (smaller than 1.6 μm) which are inorganic.
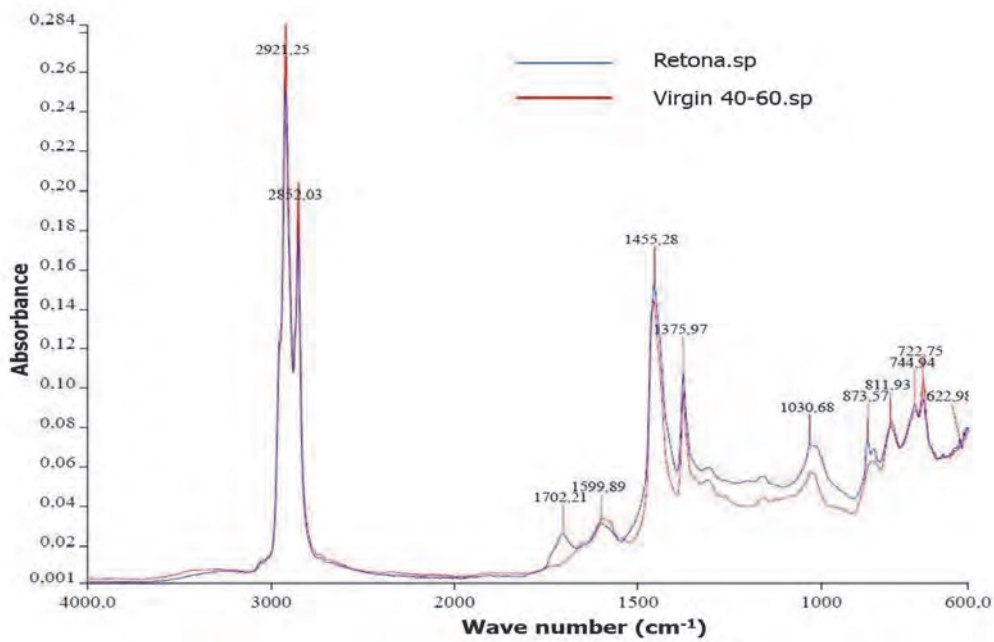
Figure 5.5. The FTIR spectra of the bitumen extracted from Retona and bitumen 40/60
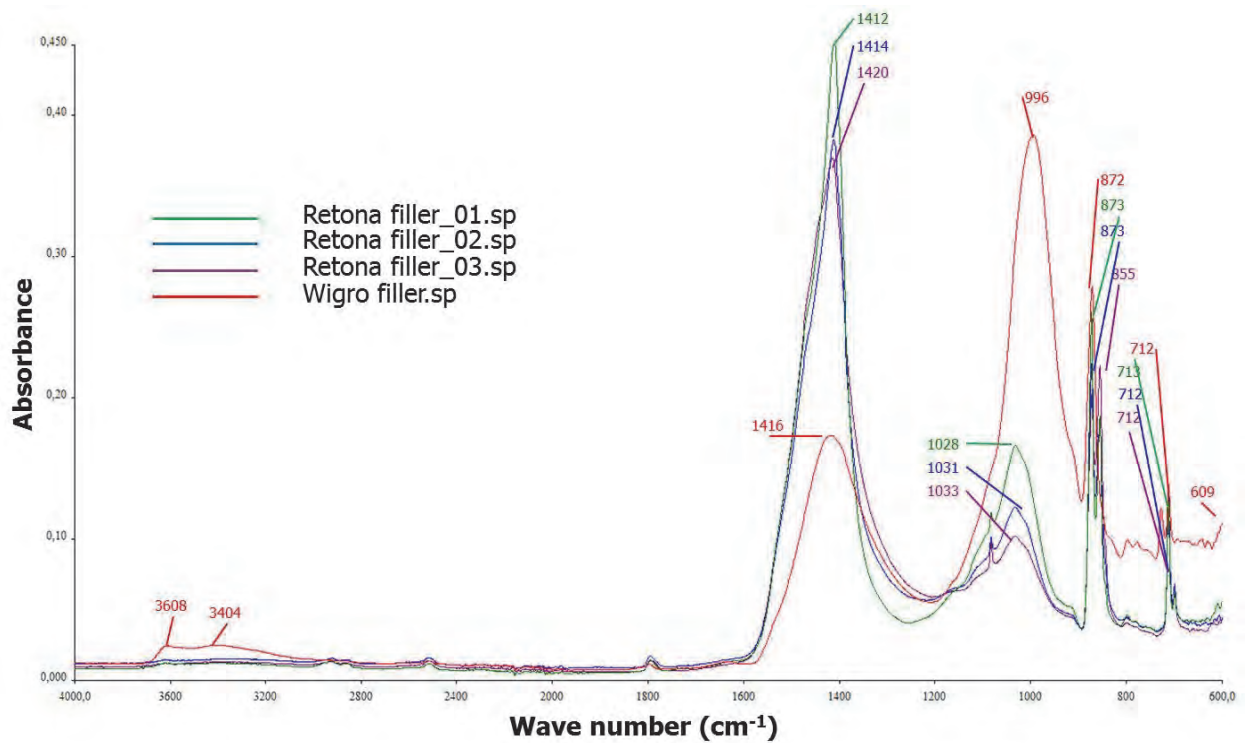
Figure 5.6. The FTIR spectra of the filler extracted from Retona and Wigro filler

Chapter 5._F. P. Pramesti

FTIR tests were also carried out to determine the composition of the extracted Retona aggregate particles. Figure 5.6 shows the spectra of three extracted Retona specimens and one Wigro specimen. Obviously most of the functional groups found on the Wigro filler are also found on the extracted Retona fillers. According to Lanzon et al [17], the transmittance bands at 711 cm^{-1}, 877 cm^{-1} and especially the strong band at 1415 cm^{-1} shown in the Figure 5.6 can be assigned to calcite. The main differences between the extracted Retona filler and Wigro filler are at the 3608 cm^{-1} and 3404 cm^{-1} peak which apparently belong to OH only found in the Wigro filler.

5.1.2. Rheology of the Retona bitumen

The viscoelastic properties of the extracted Retona bitumen were determined using an AR 2000 Dynamic Shear Rheometer (DSR), see Figure 4.1. The principles of the test have been explained in subchapter 4.1.2.

For the Retona bitumen, the tests were carried out from -10°C to 60°C at a range of frequencies. Using the time-temperature superposition principle, master curves of the complex modulus and phase angle at a reference temperature of 15°C were developed by employing the Williams-Landel-Ferry (WLF) Equation 4.1.

As was done for the 40/60 bitumen recovered from the GAC mixture (see chapter 4), the Modified Huet Sayegh model (MHS); introduced by Woldekidan [18], was used to develop the master curve for the bitumen recovered from the Retona.
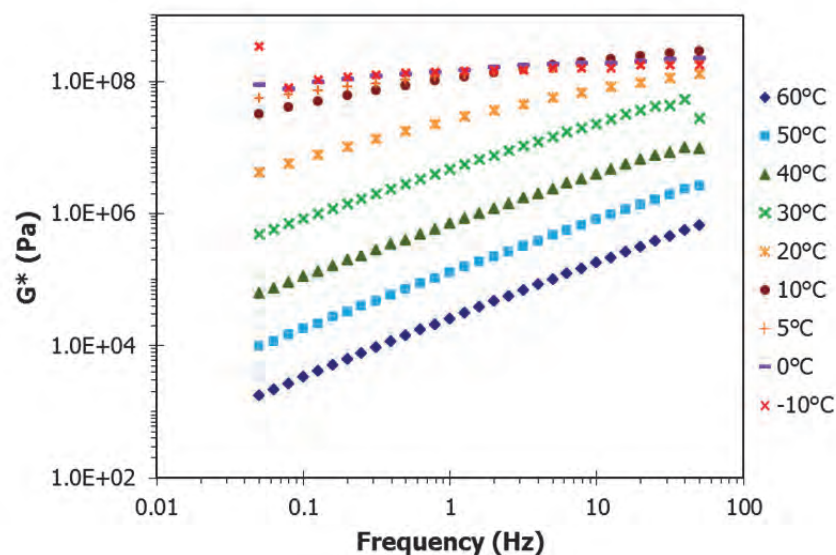
Figure 5.7 Complex Modulus of the extracted Retona bitumen at various temperatures and frequencies
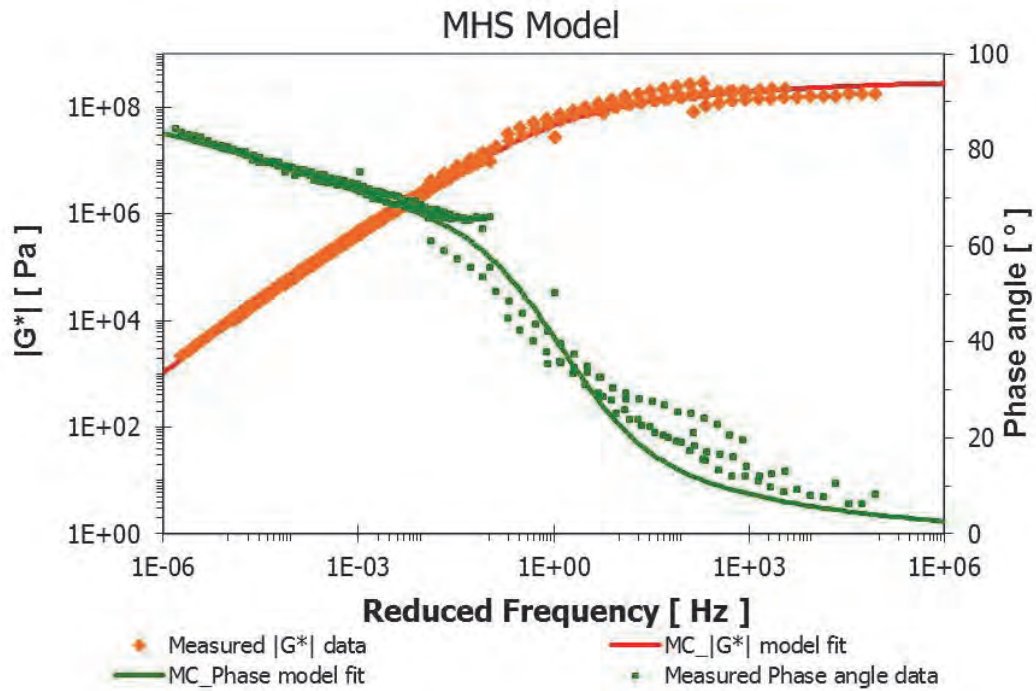
Figure 5.8 Master curve of extracted bitumen Retona at a reference temperature of 15°C
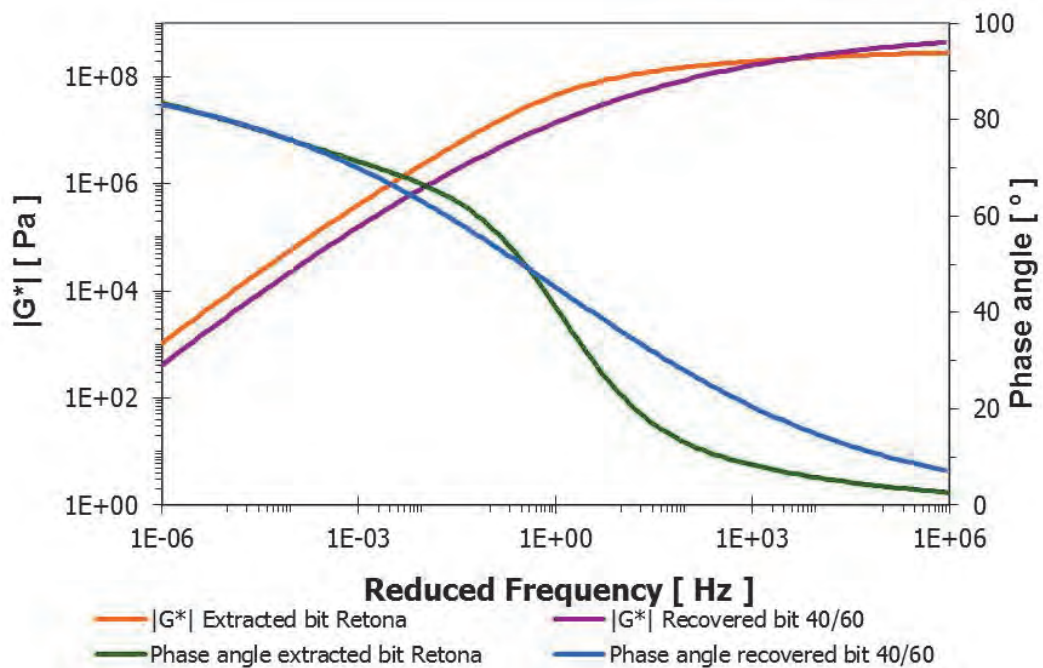
Figure 5.9 Master curve of recovered bitumen 40/60 and extracted bitumen Retona at a reference temperature of 15°C

Figure 5.7 shows the results of the frequency sweeps of the extracted Retona bitumen. The master curves for G^* and the phase angle are shown in Figure 5.8. Figure 5.9 shows that in the frequency range, which is relevant for pavements (10^{-2} Hz $<$ f $<$ 10^2 Hz), the Retona bitumen is stiffer and has a lower phase angle than the recovered 40/60 bitumen.

5.1.3. Self-healing capacity of the mastic

As mentioned before the Retona mastic used in this research consisted of 35% bitumen and 65% fine aggregate particles by weight. To determine the healing capacity of Retona mastic, a similar test procedure as explained in sub chapter 4.1.4., was carried out. The test program can be found in Table 5.7.

Table 5.7. Healing temperatures and rest periods

Retona mastic		
T (°C)	Rest period (h)	n
10	3	1
	6	1
	24	1
20	3	1
	6	1
	24	1
40	3	1
	6	1
	24	1

The healing percentage was calculated by the following equation

$$H = \frac{S_{\text{re-fracture}}}{S_{\text{fracture}}} \times 100\%$$
(5.1)

whereas S_{fracture} is the strength of the original fractured specimens and $S_{\text{re-fracture}}$ is the strength of the re-fractured specimens. The Retona mastic healing capacity is shown in the Figure 5.10. A comparison with the mastic of the reference mixture, made of pen 40/60 bitumen + Wigro filler, is presented in Figure 5.11.
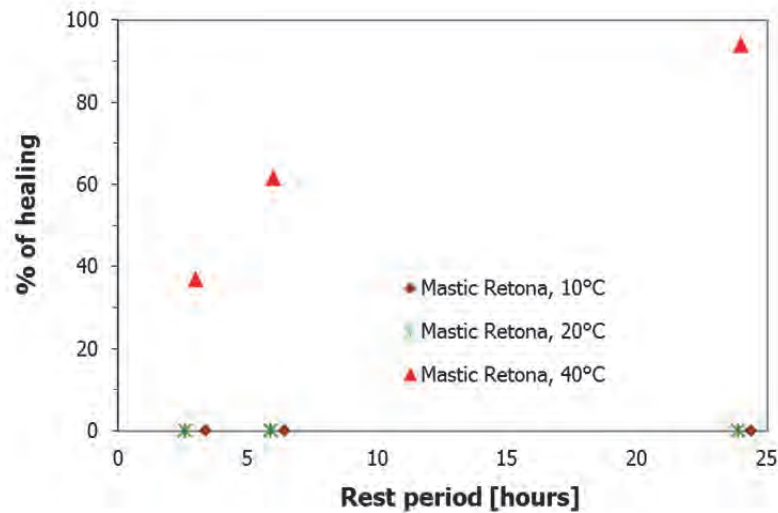
Figure 5.10. Healing of the strength of bituminous mastic Retona
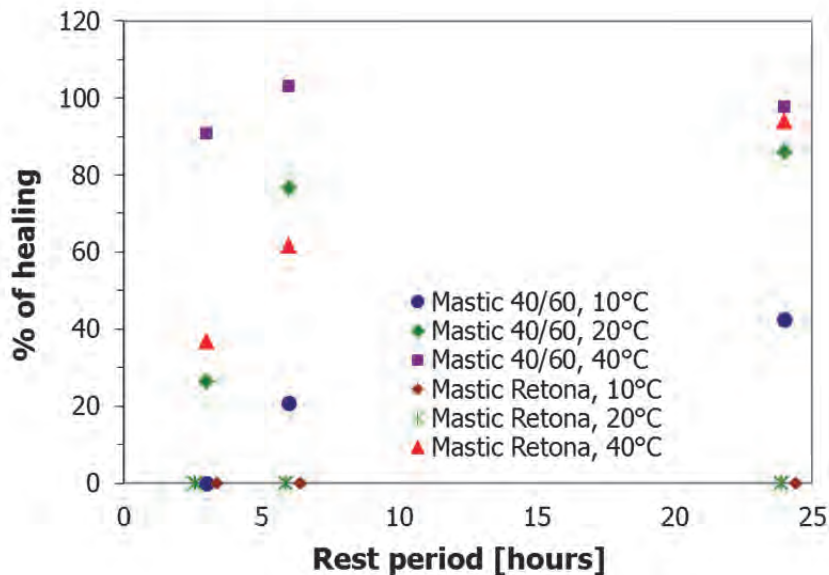
Figure 5.11. Healing of the strength of bituminous mastic 40/60 and Retona

Figure 5.11 clearly shows that the Retona mastic shows a poor healing capacity compared to the reference mastic. Only at a temperature of 40°C healing could be observed of about 36% to 94% depending on the length of the rest period.

With the available penetration data of the recovered 40/60 bitumen and the extracted Retona bitumen of 19 and 8 respectively, a relation between the penetration of the extracted bitumen and the healing percentage of the mastic of both Retona and bit 40/60 can be plotted (see Figure 5.14). The figure only shows the healing at 40°C, since at 10°C and 20°C the Retona did not show any healing.
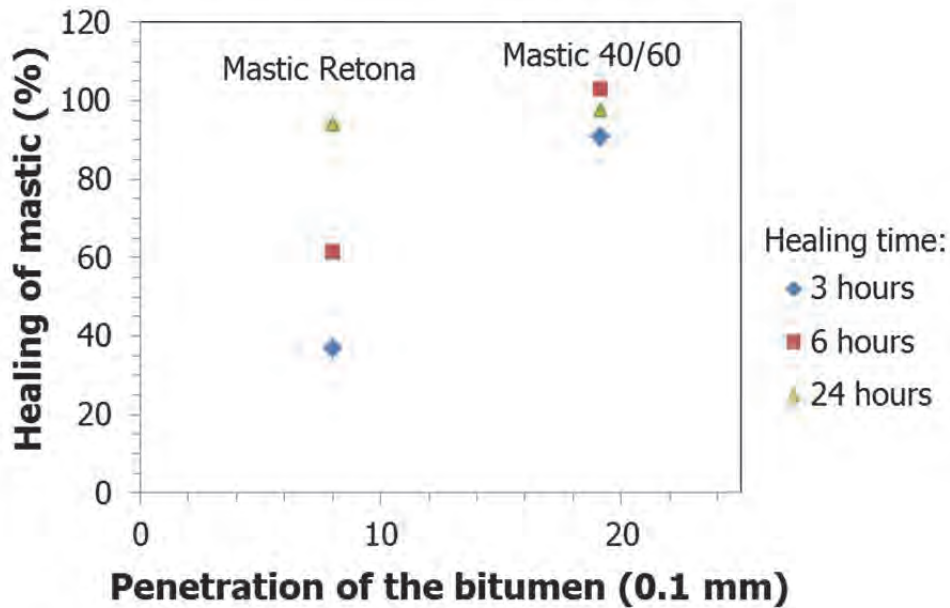
Figure 5.12. Healing percentage of the strength of Retona and bitumen 40/60+filler at 40°C versus the penetration value of the recovered bitumen

5.2. Mechanical Properties of Gravel Asphalt Concrete-Retona

Modification of conventional bitumen 40/60 GAC by adding Retona (Asbuton natural asphalt) might lead into an interesting insight. The question is to what extent this new mixture shows a better strength and fatigue performance. In order to answer this question, some specimens were prepared by modifying the mix design of the GAC. The modification was carried out by replacing 20% of the bitumen 40/60 with Retona 'bitumen'. The new mix design was shown in Table 3.10. The mixture ingredients were then used to make slabs with a similar procedure as explained in sub chapter 3.3.1. After that test specimens were cut or drilled as shown in Table 3.11.

5.2.1. Monotonic Uniaxial Compression test (MUCT)

The specimens of the gravel asphalt concrete modified with Retona had a diameter of 65 mm and a height of 130 mm. Similar to the MUCT for GAC 40/60, the MUCT for GAC 40/60+Retona was performed at 3 temperatures and different strain rates which are shown in Table 5.8. The details of the test setup were explained in sub chapter 3.3.4.

Table 5.8. Test program of MUCT for GAC 40/60+Retona

Temp (°C)	Target Strain $\acute{\varepsilon}$ (%/s)	Nr of specimen	Temp (°C)	Target Strain $\acute{\varepsilon}$ (%/s)	Nr of specimen	Temp (°C)	Target Strain $\acute{\varepsilon}$ (%/s)	Nr of specimen
5	0.01	1	20	0.05	1	40	0.1	1
	0.1	1		0.1	1		1	1
	0.5	1		1	1		2	1
	1	1		2	1		3	1

(a)

(b)

(c)
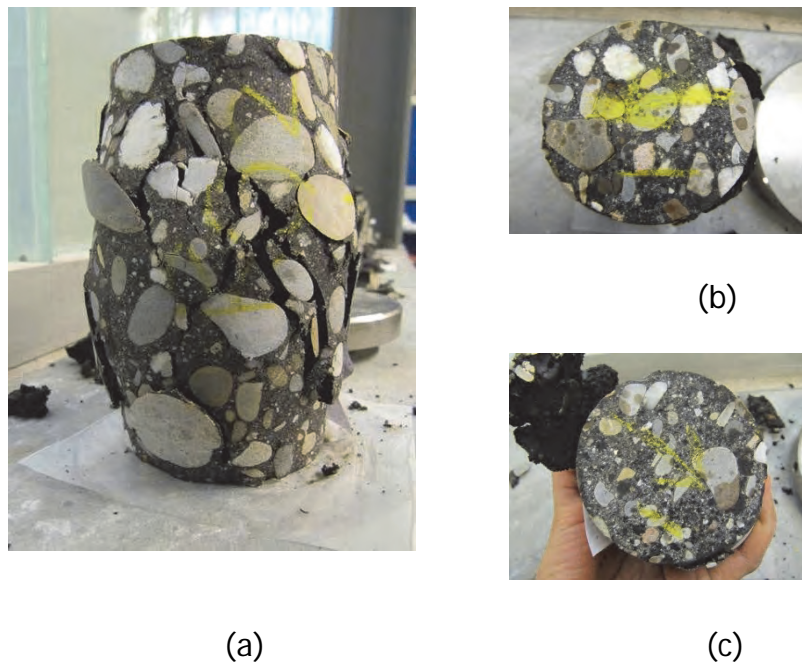
Figure 5.13. (a) Failed specimen of GAC modified Retona after a compression test at a temperature of 40°C and a strain rate of 3%/s. (b) Top side of failed specimen. (c) Bottom side of failed specimen.

An example of a failed specimen is shown in Figure 5.13 (a). Three out of thirteen specimens had a top and bottom side which did not show damage (see Figure 5.13 (b) and (c)). The barrel–shape shows that there was still some friction at the contact surface between specimen and loading plate. The outcomes of the compression test are load and axial and radial deformations at specific temperatures and deformation rates. From the calculation of the force and deformation into stress and strain, the axial and radial strain at the peak stress can be determined.

As was done in the analysis of the compression tests on the GAC 40/60 mixture, a correction to the axial strain measured from the compression test GAC 40/60+Retona was carried out. The procedure was explained in Chapter

4.2.1. The correction for the axial strain did affect the value of the modulus of elasticity and Poisson's ratio; Table 5.9 shows the influence of this correction.

Table 5.9. Original and corrected E modulus values obtained from the compression tests on GAC 40/60+Retona

T	Actual Strain rate	E mod before correction	E mod after correction	ratio
°C	%/s	Mpa	Mpa	
GAC+Asbuton				
5	0.0100	4141	7188	1.74
5	0.1037	4736	6628	1.40
5	0.3322	4466	8445	1.89
5	1.0727	4649	13602	2.93
20	0.0495	856	1655	1.93
20	0.0983	1133	2043	1.80
20	1.0279	5510	8529	1.55
20	2.7365	4051	9653	2.38
40	0.0988	135	158	1.18
40	1.0189	413	771	1.87
40	2.1328	541	757	1.40
40	3.1510	832	1572	1.89
40	11.4884	1382	2540	1.84
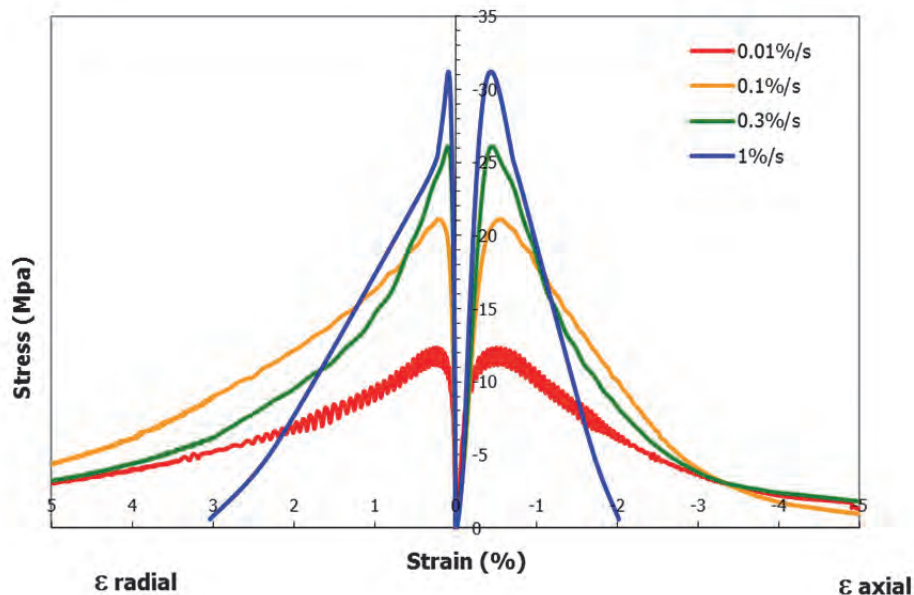
Figure 5.14. Compressive stress as a function of axial and radial strain at different strain rates at 5°C of GAC 40/60+Retona
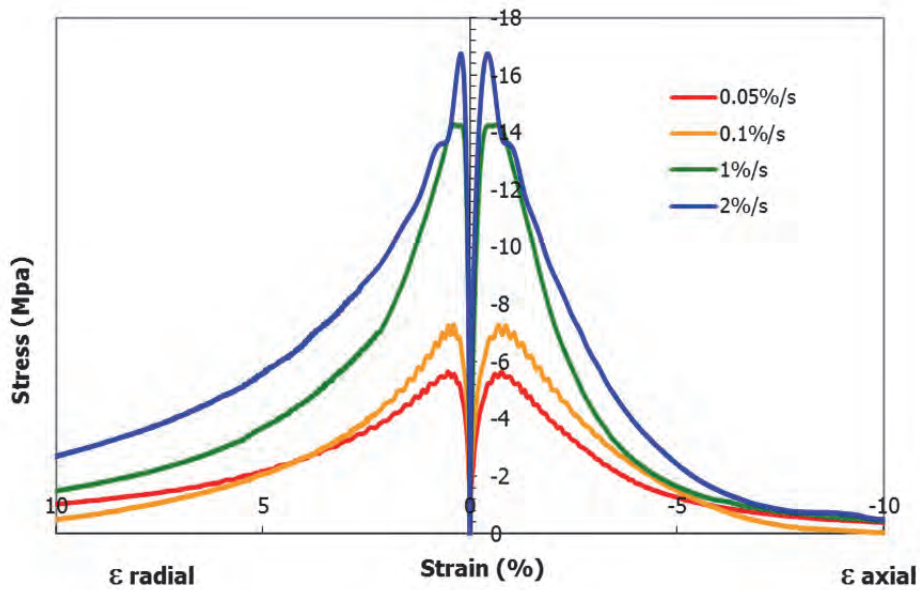
Figure 5.15. Compressive stress as a function of axial and radial strain at different strain rates at 20°C of GAC 40/60+Retona
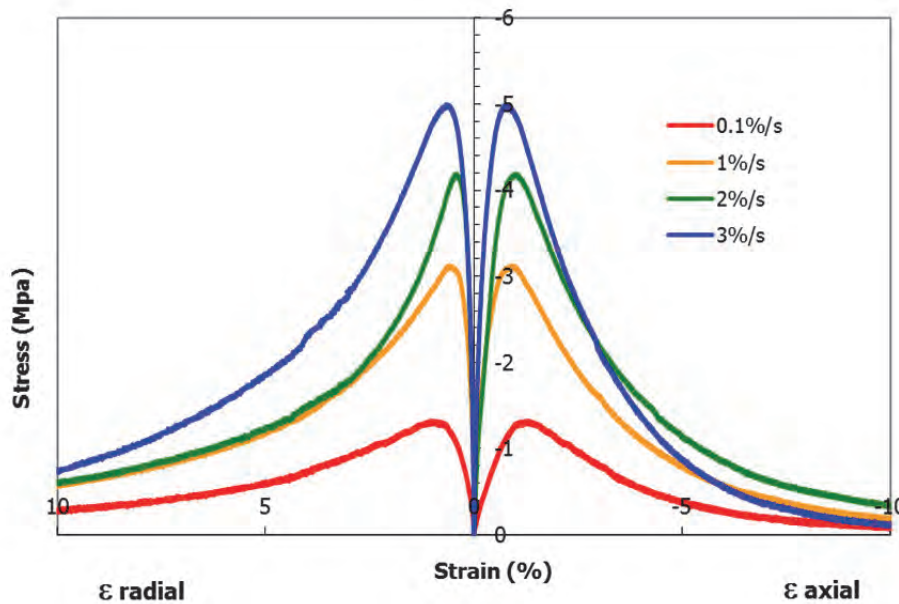
Figure 5.16. Compressive stress as a function of axial and radial strain at different strain rates at 40°C of GAC 40/60+Retona

The radial strain and corrected axial strain versus stress for each temperature and strain rate are shown in Figure 5.14, Figure 5.15 and Figure 5.16. A summary of the test results is given in Table 5.10. Poisson's ratio was determined by means of linear regression on the axial and radial strain at the beginning of the test, which is from 5% to 20% of the maximum stress. The same procedure was carried out to determine the E modulus from the axial strain and stress.

Table 5.10. Summary of the monotonic uniaxial compression test results for GAC 40/60+Retona

T	Target Strain rate	Actual Strain Rate	E Mod	Secant Modulus	Poisson's ratio	The axial strain at peak stress	The radial strain at peak stress	f_c	Energy to peak	Total Energy
°C	%/s	%/s	MPa	MPa		%	%	MPa	J	J
5	0.01	0.010	7188	2434	0.15	-0.51	0.23	-12.3	21.8	121.5
	0.1	0.10	6628	3863	0.17	-0.54	0.20	-21.1	32.6	179.4
	0.5	0.33	8445	5760	0.11	-0.45	0.09	-26.1	29.9	205.0
	1	1.07	13602	7214	0.17	-0.43	0.087	-31.2	34.1	63.5
20	0.05	0.05	1655	736	0.51	-0.77	0.530	-5.7	15.5	90.2
	0.1	0.10	2043	1050	0.46	-0.70	0.391	-7.3	17.9	104.2
	1	1.03	8529	2190	0.31	-0.65	0.359	-14.3	35.7	175.7
	2	2.74	9653	3825	0.46	-0.43	0.226	-16.7	25.4	202.8
40	0.1	0.10	158	100	0.49	-1.32	1.03	-1.32	5.2	22.6
	1	1.02	771	338	0.45	-0.93	0.58	-3.13	9.6	50.1
	2	2.13	757	426	0.24	-0.99	0.41	-4.19	12.2	68.7
	3	3.15	1572	620	0.62	-0.81	0.67	-4.99	13.9	68.1

Note: Total energy is the total area under the axial stress vs axial strain plot

During the tests sometimes a slight difference between the targeted strain rate and the actual strain rate occurred because the valve, which regulates the hydraulic oil into the actuator, could not perfectly follow the target displacement at high speeds. In the analysis and modelling the actual strain rate is used.

In order to develop a generalized failure model for the Retona modified GAC mixture, the compressive strength needed to be expressed as a function of loading rate and temperature. Based on the general S-shaped relation Equation 5.2 proposed by Erkens [19] a relation between compressive strength and the loading rate and temperature was developed which is shown in Equation 5.3.

$$f_c = a \left[1 - \frac{1}{1 + \left[\dot{\varepsilon}\, e^{(b + \frac{c}{T})} \right]^d} \right] \tag{5.2}$$

Where:

f_c	= compressive strength (MPa)
$\dot{\varepsilon}$	= strain rate (%/s)
T	= temperature (K)
a, b, c & d	= regression constants

$$f_c = -48.97 \left[1 - \cfrac{1}{1 + \left[\dot{\varepsilon} e^{\left(-78.36 + \frac{22198.8}{T}\right)} \right]^{0.355}} \right]$$ (5.3)

Figure 5.17.a shows the data and the predicted compressive strength as a function of strain rate for the GAC 40/60+Retona at three temperatures.
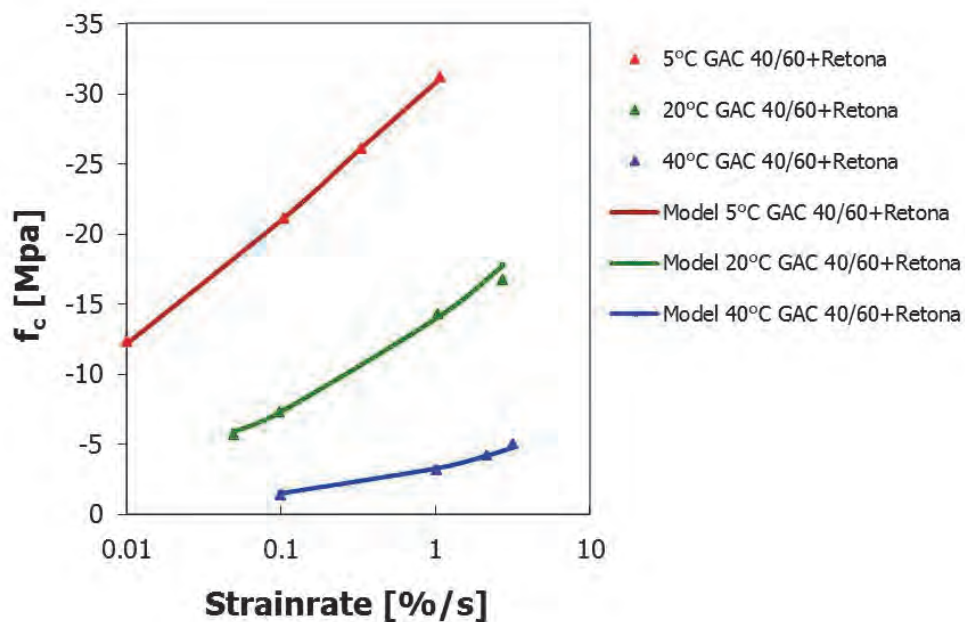
Figure 5.17.a. The compressive strength of GAC 40/60+Retona

Figure 5.17.b shows the predicted compressive strength as a function of strain rate for both the reference GAC 40/60 and the GAC40/60+Retona mixture at 5°C, 20°C and 40°C.

It can be seen that the addition of Retona increases the compressive strength of the mixture especially at lower temperatures. However, at a temperature of 40°C the addition of Retona does not increase the compressive strength of the mixture significantly.
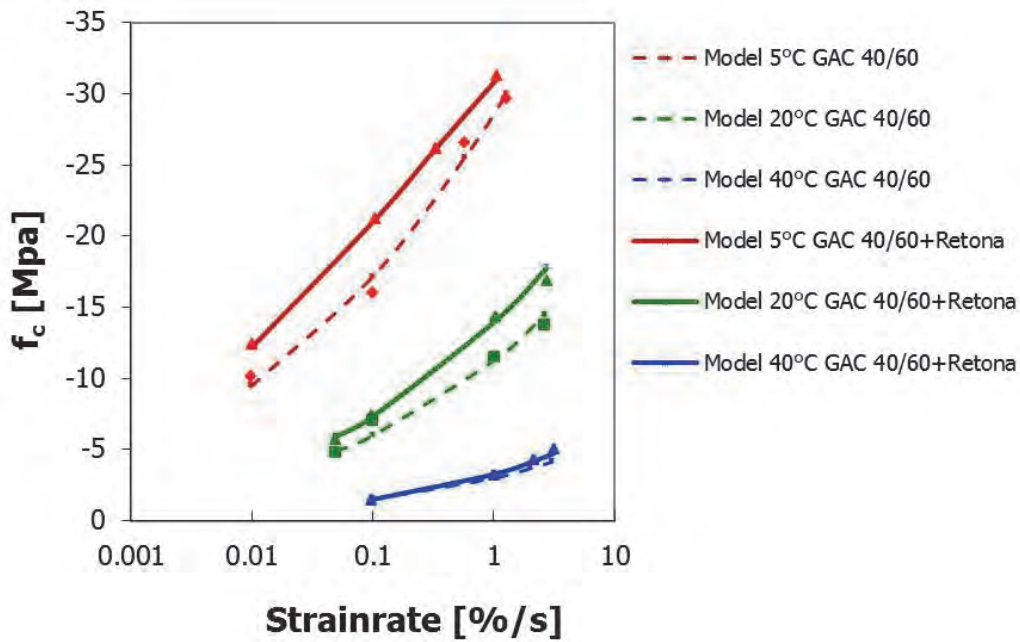
Figure 5.17.b. The compressive strength of GAC 40/60+Retona and the GAC 40/60

5.2.2. Monotonic Uniaxial Tension test (MUTT)

The MUTT for GAC 40/60+Retona was carried out using the test setup that is described in sub chapter 3.3.5. The specimens used for this test were cylinders with a diameter of 65 mm and a height of 130 mm. The test program is shown in Table 5.11.

Table 5.11. The test program of MUTT for GAC 40/60+Retona (1 specimen per condition)

Temp °C	Target Strain $\acute{\epsilon}$ (%/s)	Temp °C	Target Strain $\acute{\epsilon}$ (%/s)	Temp °C	Target Strain $\acute{\epsilon}$ (%/s)
5	0.01	20	0.05	40	0.1
	0.1		0.1		1
	0.5		1		2
	1		2		3

Figure 5.18 gives an example of the failure of a GAC 40/60+Retona test sample tested at 20°C and the strain rate of 0.01%/s. The test result shows that the specimen was breaking into two parts with minimum damage on the rest of the specimen. The specimen did break at the weakest part and in the case of the specimen shown in Figure 5.20, the weakest part seems to be the part where a white quartz aggregate particle was. It is important to note that sometimes the river gravel consisted of white quartz. Seven out of fifteen specimens broke in the middle while the other failed in an area between 1/4 and 1/10 of the height of the specimen.

Figure 5.18. Typical failure at 5°C around the aggregate -adhesive- (right: test at 5°C and 1%/s) and at 20°C through an aggregate particle (left: test at 20°C and 0.01%/s;

For each test the axial and radial deformation as well as the force was measured using a load-cell, axial LVDTs and a radial chain. The result was then calculated into stress and strain both in axial and radial direction. Figure 5.19, Figure 5.20 and Figure 5.21 present the results in the form of stress as a function of axial and radial strain. At low temperatures and high strain rates the specimen suddenly broke when the stress reached the maximum value.
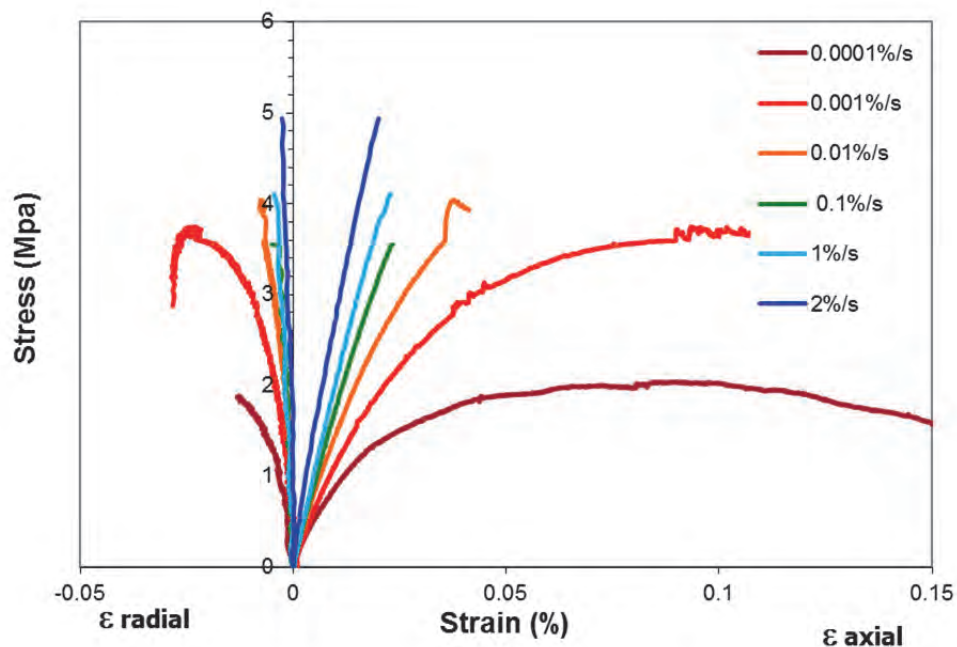
Figure 5.19. Tensile stress versus radial and axial strain of GAC Retona at 5°C

Tests performed at high temperature and high strain rate show more than one 'peak' indicating that the feedback gain (P) was probably too high, resulting in an 'overshoot'. However, this was necessary to obtain an accurate initial strain rate as targeted.
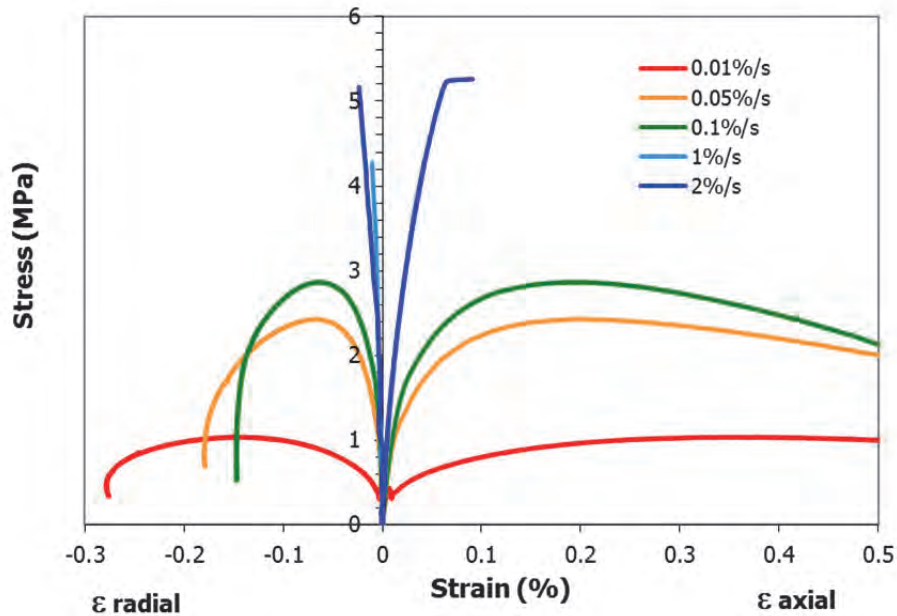
Figure 5.20. Tensile stress versus radial and axial strain of GAC Retona at 20°C
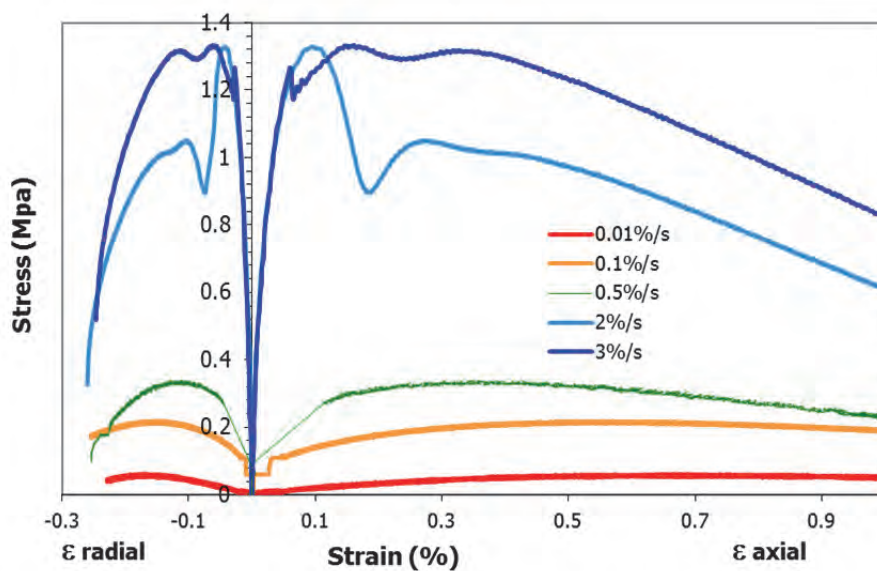
Figure 5.21. Tensile stress versus radial and axial strain of GAC Retona at 40°C

The actual strain rate, tensile strength, E modulus as well as the Poisson's ratio are summarized in Table 5.12.

Table 5.12. Summary of the GAC 40/60 +Retona monotonic uniaxial tension test results

T	Target Strain rate	Actual Strain Rate	E mod	Sec Modu-lus	Poisson's ratio	The axial strain at peak stress	The radial strain at peak stress	f_t	Energy to peak	Total Energy
°C	%/s	%/s	MPa	MPa		%	%	MPa	J	J
5	0.0001	0.0001	6135	2270	0.27	0.090	-0.024	2.05	0.639	1.783
	0.001	0.001	8787	4015	0.23	0.093	-0.023	3.75	1.078	1.568
	0.01	0.009	14626	10689	0.23	0.038	-0.008	4.04	0.379	0.440
	0.1	0.100	18684	15186	0.17	0.023	-0.004	3.55	0.199	0.199
	1	0.355	19883	16412	0.18	0.025	-0.004	4.16	0.268	0.268
	2	0.867	39460	24629	0.18	0.021	-0.003	5.14	0.258	0.258
20	0.01	0.009	497	304	0.41	0.342	-0.138	1.04	1.274	4.040
	0.05	0.046	2414	1229	0.37	0.198	-0.066	2.43	1.731	7.926
	0.1	0.092	3588	1491	0.35	0.192	-0.063	2.86	1.998	8.075
	1	1.212	14784	4316	0.34	0.056	-0.012	4.75	0.722	0.722
	2	2.447	19564	8480	0.37	0.062	-0.024	5.26	0.916	0.916
40	0.01	0.009	18	9	0.39	0.666	-0.169	0.06	0.118	0.371
	0.1	0.092	51	39	0.32	0.569	-0.155	0.22	0.443	1.547
	0.5	0.361	161	80	0.37	0.425	-0.130	0.34	0.616	2.059
	2	1.730	1778	389	0.44	0.270	-0.103	1.05	1.239	5.052
	3	3.342	4888	1637	0.45	0.160	-0.062	1.33	0.787	6.770

The total energy was calculated by determining the area under the force-displacement curve (as explained in chapter 4.2.2). In case of brittle failure where the force suddenly drops to zero this could be done quite accurately whereas for ductile failure sometimes at the end of the test the curves need to be extrapolated to zero. In those cases the curve couldn't reach zero completely because of the limitation of the LVDT's range.

Again, using the general S-shaped relation depicted in Equation 5.2, a tensile strength model was developed and the result is shown in Equation 5.4. Figure 5.22.a shows the model together with the data points.

$$f_t = 4.62 \left[1 - \frac{1}{1 + \left[\dot{\varepsilon} e^{\left(-90.57 + \frac{27572.68}{T} \right)} \right]^{0.685}} \right] \qquad (5.4)$$

Where:

f_t	= tensile strength (MPa)
$\dot{\varepsilon}$	= strain rate (%/s)
T	= temperature (K)
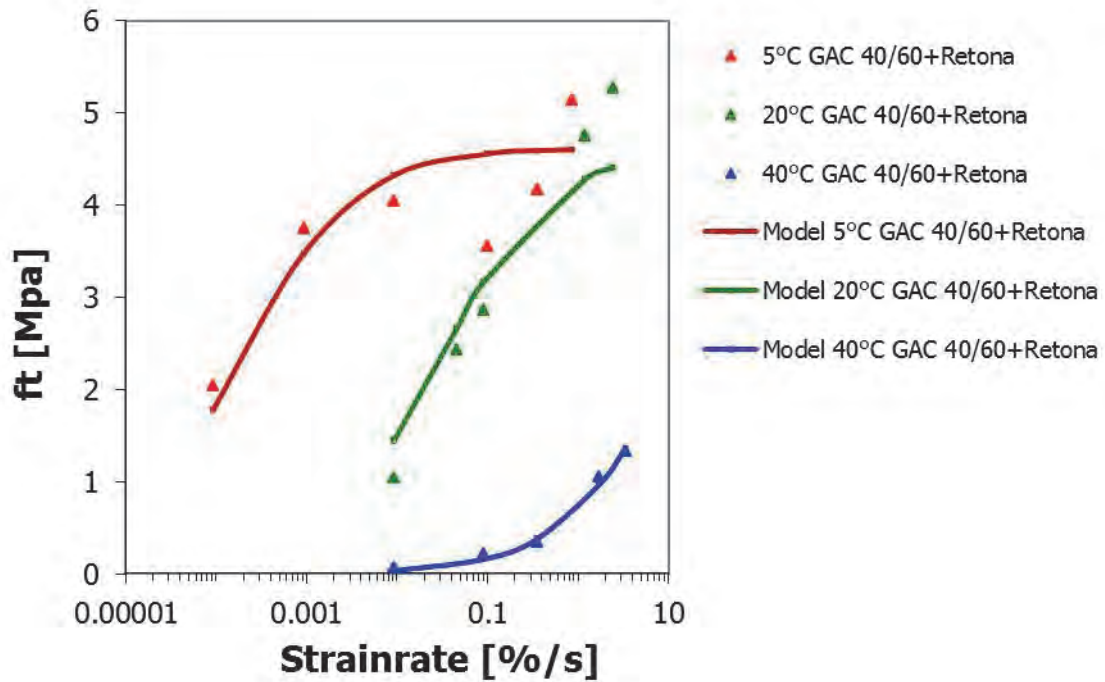
Figure 5.22.a. The Tensile strength of GAC 40/60+Retona
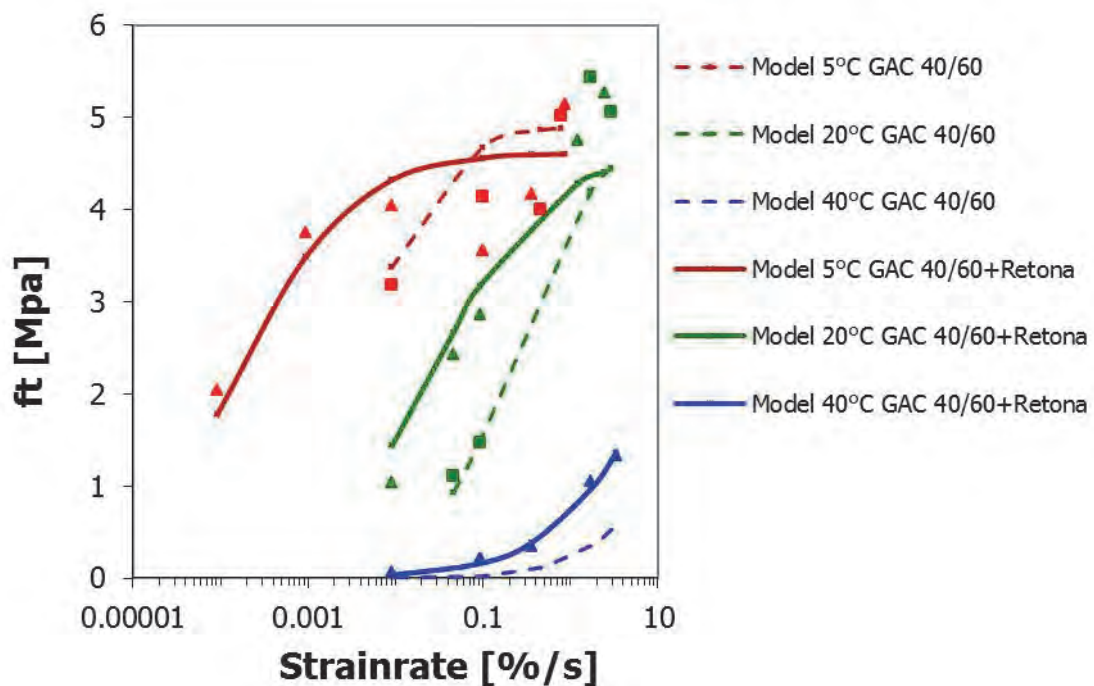
(b)

Figure 5.22.b. Comparison of the tensile strength of GAC 40/60+Retona to the tensile strength of GAC 40/60 mixture

The comparison between the tensile strength predictions of GAC 40/60+Retona and GAC 40/60 is shown in Figure 5.22.b. Since the GAC 40/60 was tested at 5°C, 20°C and 30°C, while the GAC 40/60+Retona was tested at 5°C, 20°C and 40°C, a GAC 40/60 tensile model at 40°C was developed to

make an overall comparison of both mixtures possible. This model is presented in Figure 5.22.b with the dashed blue line. At 40°C the GAC 40/60+Retona shows a higher tensile strength compared to GAC 40/60, whereas at 5°C and 20°C the GAC 40/60+Retona shows a higher tensile strength only at a strain rate less than about 0.1%/s and 2%/s respectively.

The 5°C and 20°C data given in Table 4.11 and Table 5.12 are combined in Table 5.13, to make it possible to compare the secant and tangent stiffness, the strain at peak stress and the energy values at these temperatures.

Since the GAC 40/60 was tested at 30°C and the GAC 40/60+Retona at 40°C, a straight forward comparison of these properties could not be made and models has to be used.

At 5°C and 20°C the strain level at peak stress is lower for the GAC 40/60+Retona, indicating a more brittle behavior. The same can be concluded when comparing the moduli and energy values. Higher stiffness and lower energy values are found for the GAC 40/60+Retona. Only at 20°C and low strain rates the energy values for the GAC 40/60+Retona are higher.

Table 5.13. Properties comparison of the GAC 40/60 and the GAC 40/60+Retona

T	$\dot{\varepsilon}$	ε_x	ε_{x-R}	E	E_R	E_{Sec}	E_{Sec-R}	E_P	E_{P-R}	E_{Tot}	E_{Tot-R}
°C	%/s	%	%	MPa	MPa	MPa	MPa	J	J	J	J
5	0.01	0.115	0.038	6162	14626	2766	10689	0.890	0.379	1.212	0.440
5	0.1	0.042	0.023	16054	18684	9948	15186	0.351	0.199	0.391	0.199
5	0.5	0.028	0.025	19199	19883	14030	16412	0.200	0.268	0.200	0.268
5	1	0.028	0.021	23525	39460	18147	24629	0.269	0.258	0.269	0.258
20	0.05	0.348	0.198	493	2414	318	1229	1.044	1.731	4.294	7.926
20	0.1	0.249	0.192	1153	3588	587	1491	0.994	1.998	3.622	8.075
20	1	0.191	0.056	8817	14784	2842	4316	2.564	0.722	2.769	0.722
20	2	0.099	0.062	16466	19564	5109	8480	1.172	0.916	1.172	0.916

$\dot{\varepsilon}$: Target Strain rate
ε_x : The axial strain at peak stress
ε_{x-R} : The axial strain at peak stress (Retona)
E : E modulus
E_R : E modulus (Retona)
E_{Sec} : Secant Modulus
E_{Sec-R} : Secant Modulus (Retona)
E_P : Energy to peak
E_{P-R} : Energy to peak (Retona)
E_{Tot} : Total energy
E_{Tot-R} : Total energy (Retona)

5.2.3. Flexural stiffness testing (4PB)

The flexural stiffness tests were conducted using the 4PB test set up at temperatures ranging from 5°C to 40°C and at frequencies ranging from 0.5 Hz to 8 Hz. These tests were carried out in the strain controlled mode at 50 μstrain (100 μstrain peak to peak). The stiffness was determined from the signals measured at the 100th cycle.

The test results at various temperatures were shifted to a chosen reference temperature of 30°C, which is the average temperature in Indonesia's urban area. A master curve for the mixture stiffness was developed based on these shifted data. A polynomial equation was used to form the master curve and is shown in Figure 5.23. The relation between mix stiffness (S_{mix}) and loading time (t) at a reference temperature of 30°C is shown in Equation 5.5.

$$Log\left(S_{mix}\right) = 4.363 - 0.120\log t - 0.098\left(\log t\right)^2 + 0.012\left(\log t\right)^3 \qquad (5.5)$$
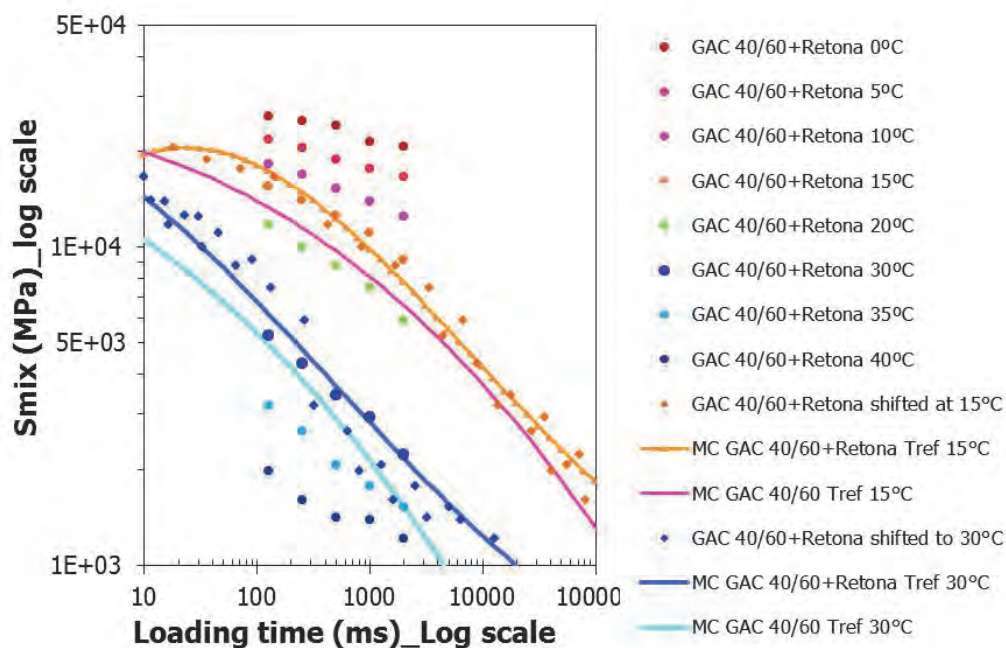
Figure 5.23. Master curve (MC) of gravel asphalt concrete with and without Retona at reference temperatures of 15°C and 30°C

As can be seen from the mastercurve of GAC 40/60+Retona at T reference of 30°C, the stiffness is higher than 10,000 MPa, at loading times lower than 30 ms, while at a T reference of 15°C the stiffness is higher than 20.000 MPa at loading times lower than 30 ms.

Furthermore, when comparing the mastercurve of the GAC 40/60 with Retona with the mastercurve of the GAC 40/60 without Retona, it seems that the addition of 20% of Retona bitumen in the mixture, increases the stiffness of

the GAC 40/60 at 30°C with 30% (on average) and with 20% (on average) at 15 °C.

5.3. Fatigue Properties of Gravel Asphalt Concrete – Retona

5.3.1. Four point bending fatigue tests

The objective of this test was to obtain a fatigue life model for GAC 40/60+Retona mixtures. The procedure and the specimen used in this test are the same as the ones explained in sub chapter 4.2.5. The tests were carried out at a temperature of 30°C and a frequency of 8 Hz and are compared with the tests that have been done for the GAC 40/60 mixture at these conditions.

Nine beams of the GAC 40/60+Retona mixture have been tested. The results are presented in Table 5.14. The fatigue life as a function of strain is shown in Equation 5.6. In this equation, N is the number of load repetitions until failure (cycles) and ε is the strain level (μm/m). The fatigue life is defined as the number of cycles at which the stiffness has reached half of its initial value.

$$LogN = -4.0185 \log \varepsilon + 14.007 \tag{5.6}$$

Figure 5.24 shows the fatigue line of the GAC 40/60 mixture and the GAC 40/60+Retona mixture. From the figure it can be seen that the slopes of the two lines are almost the same but the GAC 40/60 modified with 20% Retona shows a marginal higher intercept than the GAC 40/60's line. The figure shows that at 30°C the fatigue life of the mixture modified with Retona is on average of 1.28 times higher than the fatigue life of the unmodified mixture.

Table 5.14. Summary of the fatigue test results on GAC 40/60+Retona obtained at 30°C and 8Hz

Specimen ID	Density	Air voids	Bitumen content	Strain level	Initial Stiffness	Nr of cycle to failure	Applied load
ID		Va	Vb		S_0	N_{f50}	
	(kg/m^3)	%	%	μm/m	MPa	Cycle	kN
RM10-02	2399	4.83	8.71	75	4967	3,207,110	0.132
RM10-03	2375	4.45	8.75	87.5	4327	1,952,500	0.132
RM11-03	2377	4.05	8.79	100	4731	694,730	0.163
RM11-01	237	4.88	8.71	112.5	4485	656,420	0.176
RM10-01	2400	3.98	8.79	125	4680	255,620	0.207
RM11-04	2352	5.01	8.7	137.5	4681	195,370	0.22
RM09-04	2381	4.03	8.79	150	4244	337,030	0.226
RM09-01	2371	4.88	8.71	162.5	4597	156,760	0.27
RM10-04	2379	4.13	8.78	175	4149	80,190	0.262
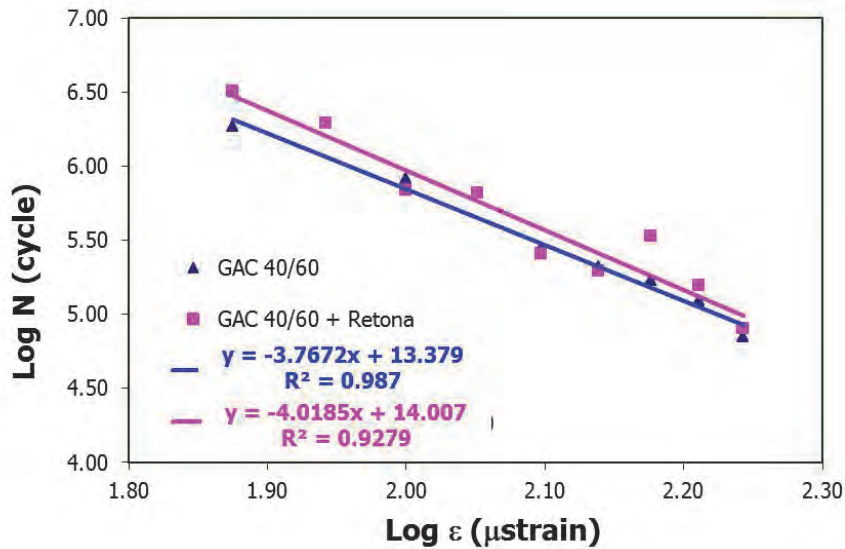
Figure 5.24. Fatigue line of GAC 40/60 and GAC 40/60+Retona at a temperature of 30°C and a frequency of 8 Hz

In terms of tensile strain vs number of load repetitions, the GAC+Retona mixture also showed an endurance limit. By means of Equation 4.41 (see Chapter 4) the endurance limit of both mixtures is calculated. The comparison between the endurance limit of the GAC mixture and the GAC+Retona mixture is shown in Figure 5.25 and Table 5.15. The ε_{limit} of GAC+Retona is higher than the ε_{limit} of GAC unmodified.
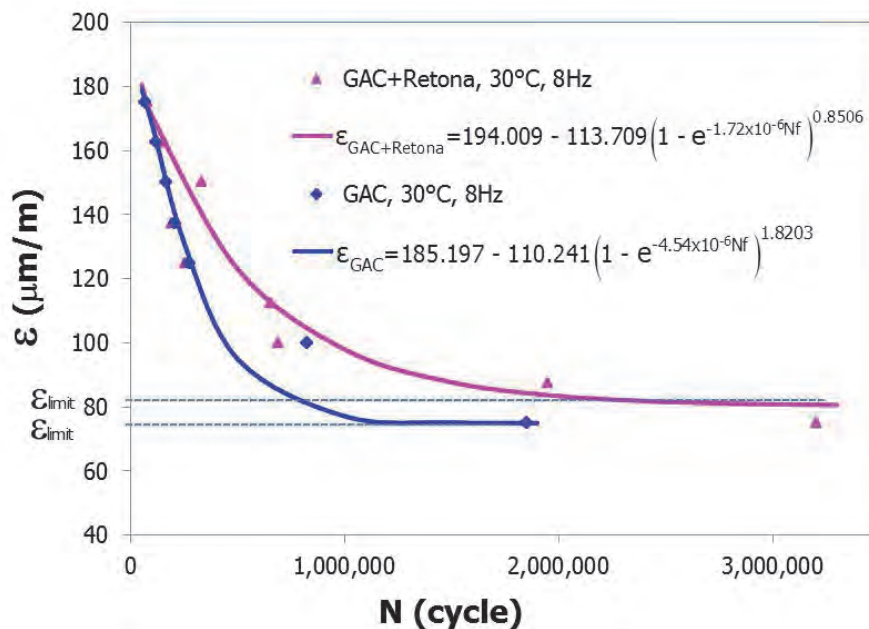
Figure 5.25. Strain endurance limits of GAC and GAC+Retona mixture, tested at 30°C and 8 Hz

Table 5.15. General expression of ε and the value of ε_{limit} for GAC mixture and GAC+Retona mixture determined using the 4PB test at 30°C and 8Hz

Mixture	Model : ε (μm/m)	R^2	$\varepsilon_{limit} = \varepsilon_0 - \varepsilon_1$ (μm/m)
GAC + Retona	$= 194.009 - 113.709\left(1 - e^{-1.72\times10^{-6}Nf}\right)^{0.8506}$	0.90	**80**
GAC	$= 185.197 - 110.241\left(1 - e^{-4.54\times10^{-6}Nf}\right)^{1.8203}$	0.97	**75**

5.3.2. Fatigue analysis of GAC 40/60 and GAC 40/60+Retona, a case study

In order to investigate the effect of Retona on the pavement fatigue life, a simple pavement design analysis has been performed.

A two layer pavement system was considered consisting of a 120 mm thick asphalt layer on top of a subgrade with an elastic modulus of 100 MPa. The asphalt layer is a gravel asphalt concrete 40/60 layer. The pavement is designed to sustain a wheel load of 50kN at a loading frequency loading of 8 Hz. At the average temperature of the pavement of 30°C, the stiffness modulus of the GAC asphalt layer is 5050 MPa. The tyre-pavement contact area is considered to be a circle with a radius of 149 mm.

The BISAR computer program was used to determine the tensile strain at the bottom of the asphalt layer. The results are shown in Table 5.16.

A similar simulation was performed for an asphalt layer of gravel asphalt concrete modified with Retona. At 30°C, the stiffness modulus of the GAC40/60+Retona layer is 5300 MPa (see Figure 5.25). The results are shown in Table 5.17.

Table 5.16. BISAR results obtained on the gravel asphalt concrete pavement
GAC 40/60

Layer	Thick-ness	Young's Modulus	Poisson's Ratio	Load	Normal Stress	Shear Stress	R	Load Position	
	(m)	(MPa)		Nr	(MPa)	(Pa)	(m)	X (m)	Y (m)
1	0.12	5050	0.35	1	0.7169	0	0.149	0	0
2		100	0.35						

Position Number	Layer Number	X-Coordinate (m)	Y-Coordinate (m)	Depth (m)
1	1	0	0	0
2	1	0.149	0	0
3	1	0	0.149	0
4	1	0	0	0.12

Position Number	Stress			Strain		
	XX	YY	ZZ	XX	YY	ZZ
	(MPa)	(MPa)	(MPa)	µstrain	µstrain	µstrain
1	-2.652	-2.652	-0.7169	-291.7	-291.7	225.7
2	-1.451	-1.868	-0.3584	-133	-244.6	159.1
3	-1.868	-1.451	-0.3584	-244.6	-133	159.1
4	2.319	2.319	-0.1305	307.6	307.6	-347.3

Table 5.17. BISAR results obtained on the gravel asphalt concrete modified
with Retona pavement
GAC 40/60+Retona

Layer	Thick-ness	Young's Modulus	Poisson's Ratio	Load	Normal Stress	Shear Stress	R	Load Position	
	(m)	(MPa)		Nr	(MPa)	(Pa)	(m)	X (m)	Y (m)
1	0.12	5300	0.35	1	0.7169	0	0.149	0	0
2		100	0.35						

Position Number	Layer Number	X-Coordinate (m)	Y-Coordinate (m)	Depth (m)
1	1	0	0	0
2	1	0.149	0	0
3	1	0	0.149	0
4	1	0	0	0.12

Position	Stress			Strain		
Number	XX	YY	ZZ	XX	YY	ZZ
	(MPa)	(MPa)	(MPa)	µstrain	µstrain	µstrain
1	-2.687	-2.687	-0.7169	-282.2	-282.2	219.7
2	-1.479	-1.899	-0.3584	-129.9	-236.9	155.4
3	-1.899	-1.479	-0.3584	-236.9	-129.9	155.4
4	2.358	2.358	-0.1271	297.6	297.6	-335.4

The fatigue life equation of the GAC 40/60+Retona mixture is shown in Equation 5.6. In chapter 4 the fatigue life of GAC 40/60 at 30°C and 8Hz has been reported in Table 4.18 and is given again in Equation 5.7, where N is in cycles and ε is in µm/m.

$$Log\ N = -3.7672 \log \varepsilon + 13.379 \tag{5.7}$$

Based on the strain at the bottom of the asphalt layer calculated with BISAR, the number of load repetitions until failure for both asphalt mixture can be obtained using the equations above mentioned. The recapitulation is shown in Table 5.18.

Table 5.18. Fatigue life of the GAC 40/60 and GAC 40/60+Retona pavements "Ratio" should be below "N"

	GAC 40/60	GAC 40/60+ Retona	
ε_{xx}	307.6	297.6	µstrain
n	-3.7672	-4.0185	
Log a	13.379	14.007	
N	10,145	11,660	cycle
Ratio N	1.15		

The ratio N which is defined as the ratio between GAC 40/60+Retona fatigue life and the GAC 40/60 fatigue life is 1.15, indicating the potential of obtaining a longer service life by modifying asphalt mixtures with Retona.

5.3.3. Yield surface

Based on the results of the tension and compression tests, yield surfaces were developed showing at which combinations of normal and shear stresses the asphalt mixture will fail. Since the tensile and compressive strength of asphalt mixtures are dependent on loading time and temperature, also the yield surfaces are dependent on loading time and temperature. Figure 5.26 shows the yield surfaces for the GAC 40/60 mixture and the GAC 40/60+RETONA mixture. The parameters σ and τ are defined in the Mohr-Coulomb criterion.
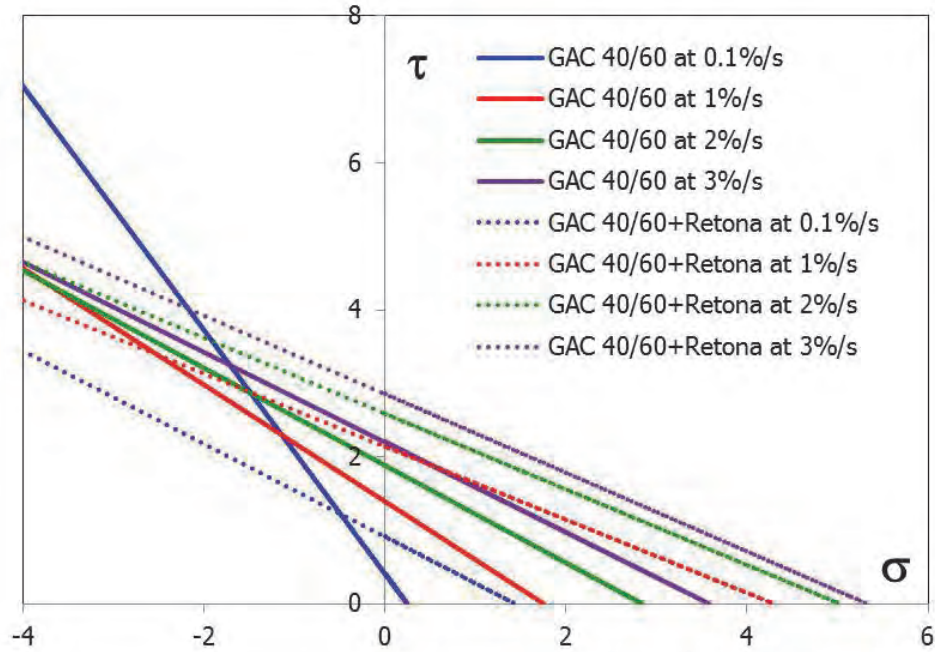
Figure 5.26. Yield surfaces of GAC 40/60 and GAC 40/60+Retona, at 30°C and different strain rates

The Mohr-Coulomb type criterion is mathematically expressed as:

$$\tau = c - \sigma \cdot \tan \varphi \qquad (5.8)$$

where:
τ = shear stress, (MPa);
σ = normal stress, (MPa);
c = cohesion, (MPa);
φ = angle of internal friction, (°).

Variables c and φ can be derived from the uniaxial tensile (f_t) and uniaxial compressive (f_c) test data using Equations 5.9 and 5.10.

$$\varphi = \arcsin \left(\frac{f_c + f_t}{f_c - f_t} \right) \qquad (5.9)$$

$$c = \frac{f_t \cdot (1 + \sin \varphi)}{2 \cos \varphi} = -\frac{f_c \cdot (1 - \sin \varphi)}{2 \cos \varphi} \qquad (5.10)$$

Uniaxial compression and tension tests on GAC 40/60 and GAC 40/60+Retona specimens have been performed. The results for GAC 40/60 are presented in Chapter 4 in which the compressive and tensile strength model parameters are presented in Table 4.12. Whereas the compressive and tensile strength

model for GAC 40/60+Retona are presented in Equation 5.3 and 5.4 respectively.

Figure 5.26 clearly shows that the yield surfaces of the Retona modified mixture are well above the yield surfaces of the reference mixture indicating that the Retona modified mixture has a higher resistance to 3D stress conditions.

5.3.4. Resistance to permanent deformation

Although no specific tests were performed to determine the resistance to permanent deformation, some remarks with respect to it can be made. This can be done based on the information about the mixture stiffness and the yield surfaces for the reference mixture and the Retona mixture.

For the hypothetical pavement described in subchapter 5.3.2, yield lines of both the unmodified and Retona modified GAC were determined. At the temperature of 30°C and the frequency of 8 Hz, the strain rate for unmodified GAC and Retona modified GAC are 1.55%/s and 1.5%/s respectively. The yield lines of both pavements are depicted in Figure 5.27.

The Mohr-Coulomb circles shown in Figure 5.27.a and 5.27.b are the MC circles at positions 1, 2, 3 and 4 as shown in the Table 5.16 and 5.17 respectively. It shows that for both mixtures, the MC circle at position 2 and 3 are on top of each other.

The fact that the stiffness of both mixtures is approximately the same, is the reason that almost the same stresses will occur in asphalt pavements made with the reference GAC mixture and the Retona modified asphalt provided that the loads are the same and the pavement structures are similar. This means that at a similar point in the pavement, the τ and σ value will almost be the same. The distance of this stress state point to the respected yield line is, however, much larger for the pavement with RETONA modified mixture than for the pavement with the reference mixture. This implies that failure and permanent deformation is less likely to occur in the Retona modified mixture than in the reference mixture.
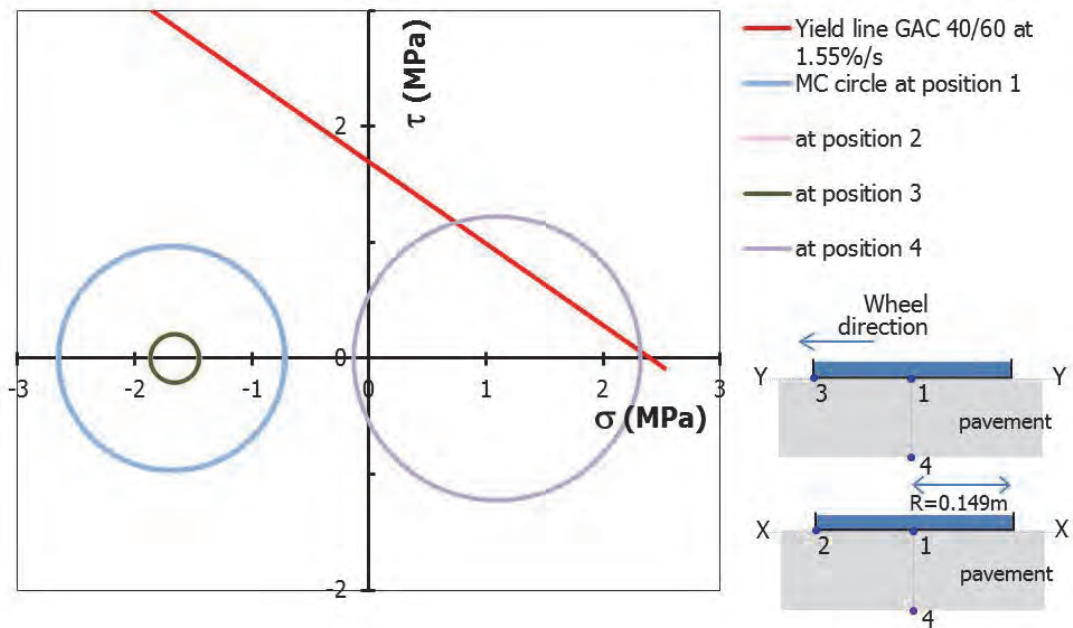
Figure 5.27. a. MC circles at the surface and at the bottom of asphalt layer, GAC mixture, at 30°C-8Hz.
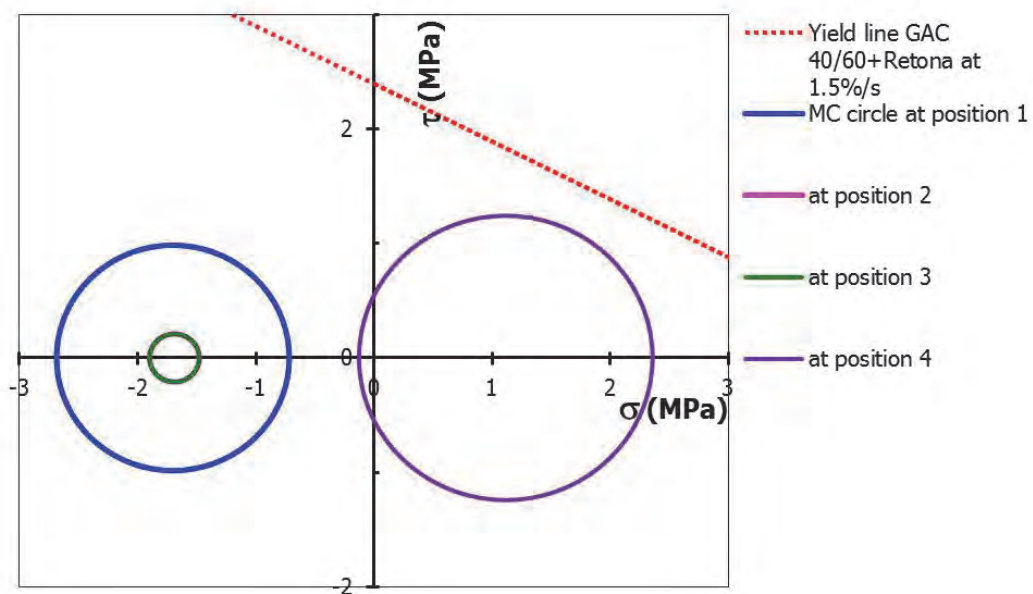
Figure 5.27. b. MC circles at the surface and at the bottom of asphalt layer, GAC+Retona mixture, at 30°C-8Hz.

5.4.   Findings and Conclusions

The characteristics and behavior of the GAC mixture modified with Retona, a kind of natural asphalt from Buton island Indonesia, were investigated by means of tests like DSR, penetration and softening point for the binder, and MUCT and MUTT, and also FPBT for stiffness and fatigue of the micture. Also healing strength tests on the mastic were performed.

The healing capacity for strength of the mastic with Retona is less compared to the healing capacity of the reference mastic made with 40/60 bitumen + Wigro filler. At temperatures of 10°C and 20°C the Retona modified mixture shows no healing. This was to be expected as the Retona bitumen is much stiffer than the 40/60 bitumen.

Comparison of the mechanical properties of the GAC mixture with and without Retona modification demonstrates some interesting facts. The compressive and tensile strength of the GAC mixture modified with Retona are higher than the unmodified GAC, especially at low strain rates. The 4PB test showed that the stiffness of GAC 40/60 modified with Retona is higher than the GAC 40/60 unmodified.

A simple pavement design analysis showed that at 30°C and 8Hz the GAC mixture modified by Retona has on average a 1.28 times longer fatigue life than the unmodified mixture. This may be beneficial for the implementation of Retona modified mixtures in tropical countries such as Indonesia. It was also shown that the Retona modification resulted in a mixture which has a higher resistance to permanent deformation.

Although application of Retona 35 shows some benefits, the improvements in mixture characteristics are not really spectacular. Higher application rates of Retona 35 and or using Retona types that contain higher amounts of bitumen (for example Retona 60) will most probably give more significant improvements of the characteristics of asphalt mixtures.

Finally, it is remarked that application of higher amounts of Retona in areas where large temperature differences can occur between day and night or between seasons might not be feasible because of the hardness of the Retona bitumen.

5.5.   References

[1]   Siswosoebrotho. B.I., N. Kusnianti, and W. Tumewu, "Laboratory Evaluation Of Lawele Buton Natural Asphalt In Asphalt Concrete Mixture," *Proceeding Of the Eastern Asia Society for Transportation Studies,* vol. 5, pp. 857-867, 2005.

[2]   S. P. Hadiwardoyo, E. S. Sinaga, and H. Fikri, "The influence of Buton asphalt additive on skid resistance based on penetration index and temperature," *Construction and Building Materials,* vol. 42, pp. 5-10, 2013.

[3]   F. Affandi, "The performance of bituminous mixtures using Indonesia natural asphalt," in *25th ARRB Conference – Shaping the future: Linking policy, research and outcomes* Perth, Australia, , 2012.

[4]   B. S. Subagio, B. I. Siswosoebrotho, and R. H. Karsaman, "Development Of Laboratory Performance Of Indonesian Rock Asphalt (Asbuton) In Hot Rolled Asphalt Mix," *Journal Of the Eastern Asia Society for Transportation Studies,* vol. 4, pp. 436-448, 2003.

[5]   B. S. Subagio, R. H. Karsaman, J. Adwang, and I. Fahmi, "Fatigue Performance of HRA (Hot Rolled Asphalt) and Superpave® Mixes Using Indonesian Rock Asphalt (ASBUTON) as Fine Aggregates and Filler," *Journal Of the Eastern Asia Society for Transportation Studies,* vol. 6, pp. 1207-1216, 2005.

[6]   B. S. Subagio, H. Rahman, S. Hendarto, and F. J. Philips, . "Stiffness Modulus Of Asphaltic Concrete Wearing Course (Ac-Wc) Mix Containing Retona Blend 55®: Theoretical and Experimental Analysis.," *Proceeding Of the Eastern Asia Society for Transportation Studies,* 2009.

[7]   T. Astuti, "Study of Resistance to Fatigue Cracking of Asphalt Mixes with Refined Buton Natural Asphalt (Retona)," Master Thesis, International Institute for Infrastructutal Hidraulic & Environmental Engineering, IHE, Delft, The Netherlands, 2002.

[8]   Southeast Sulawesi Provincial Site. (1999, Accessed at 14 July 2014). *Southeast Sulawesi Provincial Site; Buton Asphalt (In Bahasa).* Available: http://sultra.tripod.com/ASPAL_BUTON.htm

[9]   D. Widhiyatna, R. Hutamadi, and Sutrisno. (2007) Review On Buton Asphalt Resources Conservation (in Bahasa). *Geological Resources Bulletin.*

[10]   F. S. Rostler and R. M. White, "Influence of chemical composition of asphalts on performance, particularly durability," *ASTM Special Technical Publication,* 1960.

[11]   F. S. Rostler and H. W. Sternberg, "Compounding Rubber with Petroleum Products - Correlation of Chemical Characteristics with Compounding Properties and Analysis of Petroleum Products Used as Compounding Ingredients in Rubber," *Industrial & Engineering Chemistry,* vol. 41, pp. 598-608, 1949.

[12]   Anwar Yamin, Kazuyuki Kubo, Iwao Sasaki, and S. Ueno, "Japan Indonesia Cooperation on the Research in Asbuton," in *14th REAAA Conference* Kuala Lumpur Malaysia, 2013.

[13]   E. T. Hagos, "The Effect of Aging on Binder Properties of Porous Asphalt Concrete," PhD, Delft University of Technology, Delft The Netherlands, 2008.

[14]   W. V. d. Bergh, "The Effect of Ageing on the Fatigue and Healing Properties of Bituminous Mortars," PhD, Delft University of Technology, Delft, The Netherlands, 2011.

[15] D. Q. Sun, "A Study on Xinjiang Asphaltite as an Asphalt Modifier. Part I: Composition, Structure, and Thermal Behavior," *Petroleum Science and Technology,* vol. 30, pp. 307-315, 2012.

[16] J. Qiu, "Self Healing of Asphalt Mixture," PhD, Delft University of Technology, Delft The Netherlands, 2012.

[17] M. Lanzón, A. Garrido, and P. García-Ruiz, "Stabilization of sodium oleate as calcium oleate in cement-based mortars made with limestone fillers," *Construction and Building Materials,* vol. 25, pp. 1001-1008, 2011.

[18] M. F. Woldekidan, "Response Modelling of Bitumen, Bituminous Mastic and Mortar," PhD, Delft University of Technology, Delft The Netherlands, 2011.

[19] S. M. J. G. Erkens, "Asphalt Concrete Response - Determination, Modeling and Prediction," PhD, Delft University of Technology, Delft The Netherlands, 2002.

Appendix 5A
Ratio of compressive modulus and tensile modulus

It is interesting to look at the Elastic modulus in tension and compression in the gravel asphalt concrete mixture. They are usually considered to be equal. However, dividing the compressive modulus by the tensile modulus at the similar strain rate shows a typical trend of this ratio. The real data of the GAC specimens (also with Retona) comply with this trend which indicates that this modulus ratio is dependant of temperature and strain rate (See Figure 5A.1).
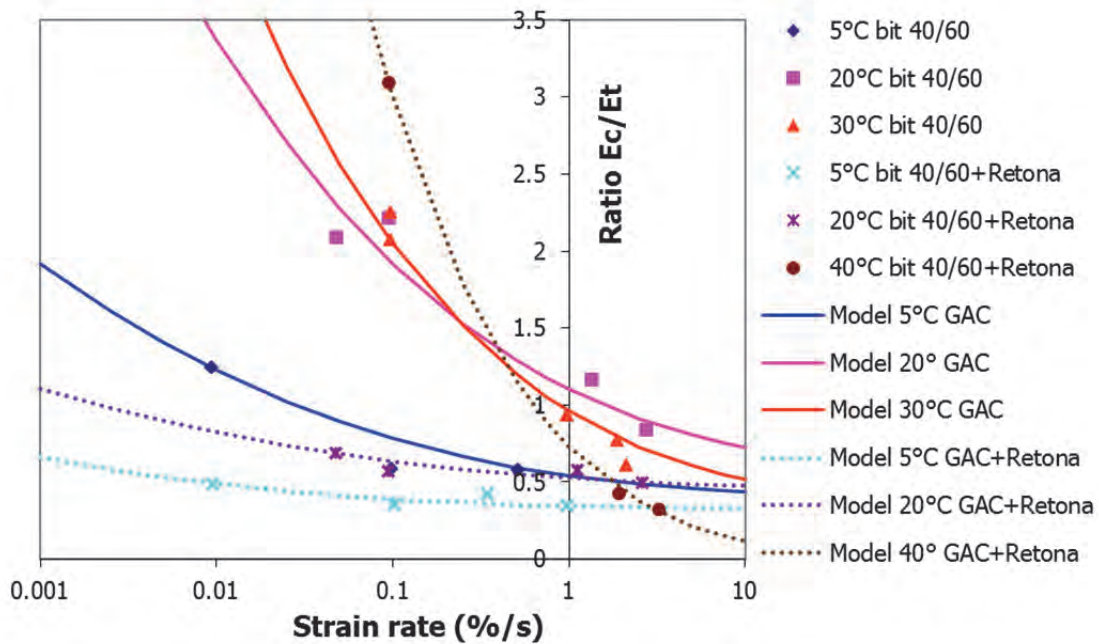
Figure 5A.1. Compressive modulus divided by tensile modulus as a function of strain rate for GAC (solid line) and GAC with Retona (dashed line)

Based on the trend of the data points, a typical S-shaped model as shown in Equation 5A.1 was used to describe the relation between the ratio of modulus and the strain rate. Table 5A.1 shows the parameters of the model at different temperature both for GAC and GAC+Retona mixtures.

$$\frac{E_c}{E_t} = a_0 + a_1 \left\{ e^{-\left(\frac{\dot{\varepsilon}}{a_2}\right)^{a_3}} \right\} \tag{5A.1}$$

Where:
E_c = compressive Modulus (MPa)
E_t = tensile Modulus (MPa)
$\dot{\varepsilon}$ = strain rate (%/s)
a_n = model parameters

Table 5A.1. Parameters of Ec/Et ratio model at several temperatures

Model Parameter	5°C GAC	20°C GAC	30°C GAC	5°C GAC +Retona	20°C GAC +Retona	40° GAC +Retona
a_0	0.39	0.54	0.35	0.32	0.45	0.00
a_1	15.62	54.56	90.06	4.45	6.95	395.24
a_2	2.18E-07	1.10E-07	1.00E-07	1.18E-07	1.00E-07	6.23E-08
a_3	0.10	0.10	0.10	0.10	0.09	0.11

From the graph it can be seen that for GAC 0/32 (with or without Retona) there is a clear trend that the ratio Ec/Et is decreasing with increasing strain rate. It also can be seen that the slope of the graphs at high temperatures (20°C to 40°C) is steeper than the slope of the graphs at low temperatures (5°C). Furthermore at high temperatures, and especially at low strain rates, the compressive modulus is more dominant over the tensile modulus than at low temperatures.

Chapter 6
Comparison of predicted fatigue life with cracking performance observed on Lintrack test sections

6.1. Introduction

This chapter discusses the comparison that has been made between the lifetime observed on Lintrack gravel asphalt concrete (GAC) test sections and the lifetime predicted using fatigue relationships that were obtained from 4PB and BOEF fatigue laboratory tests.

For the comparison of pavement performance predictions with actual performance indicators like cracking, permanent deformation, raveling, etc., or to calibrate pavement life predictions with actual pavement life, one has to define the meaning of "end of pavement life". Therefore, also in this dissertation the question what is "end of pavement life" should be solved first before a comparison of predicted and actual pavement life can be made.
In this paragraph, the issue of "end of pavement life" will be first discussed along general lines. After that, the "end of pavement life" issue for the Lintrack test sections will be discussed.

In the AASHTO pavement design manual [1], the end of pavement life is defined as the moment at which the present serviceability index has decreased to a certain value which is dependent on the importance of the pavement structure. Further, reliability concepts are applied in the manual which allow to define the pavement life as the number of load repetitions at which a certain percentage of the paved area has reached a predefined serviceability value.

The present serviceability index is controlled by three types of defects being cracking, permanent deformation and pavement roughness or unevenness. The unevenness parameter (roughness) is by far the most important parameter and studies on the AASHO Road Test data showed that the amount of cracking strongly correlates with pavement roughness [2].

Also in the Highway Design Model, the riding quality is taken as the prime parameter in defining "end of pavement life" [3]. Usually end of pavement life is defined in this case as the moment at which the vehicle operating costs start to increase fast. This moment coincides with the moment at which also

the pavement roughness starts to increase rapidly [3]. According to the Highway Design Model, pavement roughness is affected by raveling, potholing, permanent deformation and cracking, and the model shows how these damage types are affecting each other.

In many countries, the moment at which maintenance is applied is determined by the amount and severity of the different damage types that appear. In some cases, like on the main highways in the Netherlands, one damage type is dominant over other damage types. To a very large extent, raveling of the porous asphalt surface layers of the Dutch highways controls when maintenance is applied on pavements having such a wearing course. This moment, however, is much earlier than the moment at which the pavement would have reached its end of pavement life in terms of structural bearing capacity. This implies that a distinction needs to be made between the structural life of a pavement, which is related to the pavement's capacity to carry the traffic loads, and the functional life of a pavement (surface) which is related to the ability of the pavement to provide enough service to the road user in terms of skid resistance, noise reduction, evenness and safety. Of course structural defects will affect the functional performance but situations are known where the pavement is completely cracked but still offers sufficient service to the road user because it is still rather smooth and safe to drive on.

Although generalizing things is a dangerous thing to do, one could state that in case of thin pavements an insufficient pavement strength will have an immediate negative effect on the functional pavement life because the lack of structural capacity will not only result in cracking but also in, for example, pothole formation and permanent deformation which have a strong negative impact on the functional performance. On thick pavements, however, structural performance of the entire structure will hardly influence the functional performance of the surface layer and maintenance because of functional defects will always be needed well before structural maintenance is needed.

Moreover, the minimum condition levels and the area over which these minimum condition levels are allowed to occur depend on the importance of the road and are not the same in each country. In the Netherlands, for instance, the maintenance standards are much higher than those in other countries.

All this makes it almost impossible to come up with one single definition for "end of pavement life".

When calibrating fatigue models one usually tries to match fatigue life, determined by calculating the tensile strain at the bottom of the asphalt layer, using appropriate fatigue relationships and Miner's law, with the amount of cracking that is observed at the pavement surface. It has already been mentioned in chapter 2 that this approach can be severely flawed by the fact that the cracking visible at the pavement surface is quite often top-down

cracking and, then, has nothing to do with the damage which is calculated at the bottom of the asphalt layer. This problem also occurred when analyzing the Lintrack sections. As was stipulated by Groenendijk [4], much of the initial surface cracks were initiated during compaction and later on progressed due to the applied wheel loads. However, the strain measurements showed a clear increase in strain and the asphalt modulus, which was back calculated from falling weight deflection measurements, showed a clear decrease with increasing number of load repetitions. Both parameters do indicate that fatigue damage did initiate and propagate. Figure 6.1 shows how the average value of the back calculated modulus decreased for each of the Lintrack sections and Figure 6.7 shows an example of the increasing tensile strains in relation to the applied number of load repetitions.

$$S_{mix} = 17159 - 15419\left(1 - e^{-(4.5E-07)N}\right)^{0.86}$$

(a) Section I

$$S_{mix} = 10682 - 7018\left(1 - e^{-(1.4E-05)N}\right)^{6.37}$$

$$S_{mix} = 12098 - 6018\left(1 - e^{-(2.9E-06)N}\right)^{1.73}$$

(c) Section VB
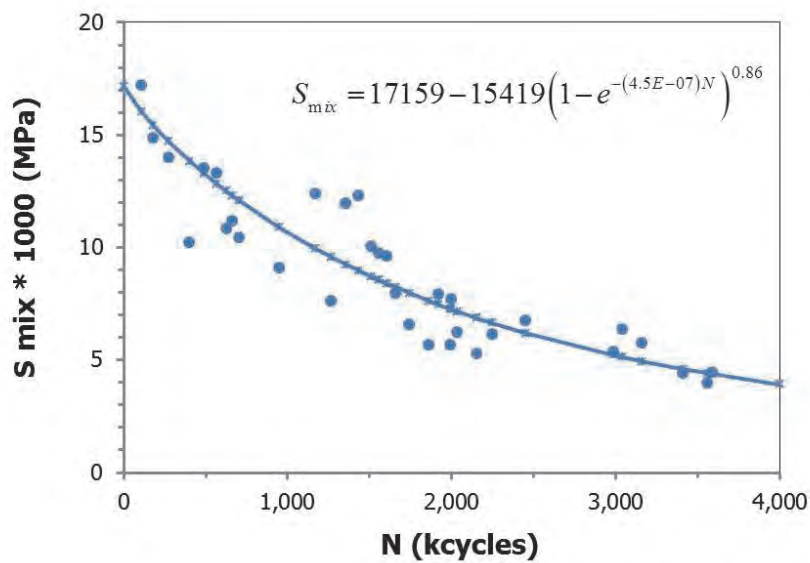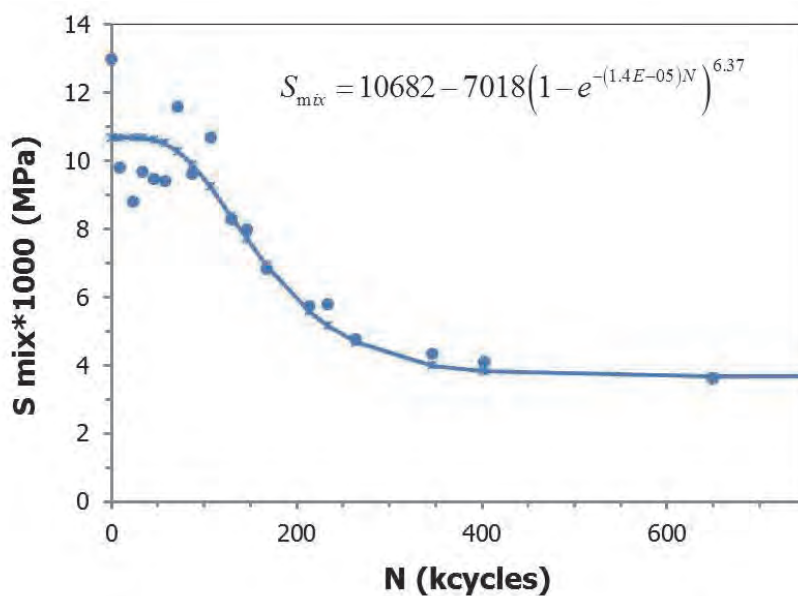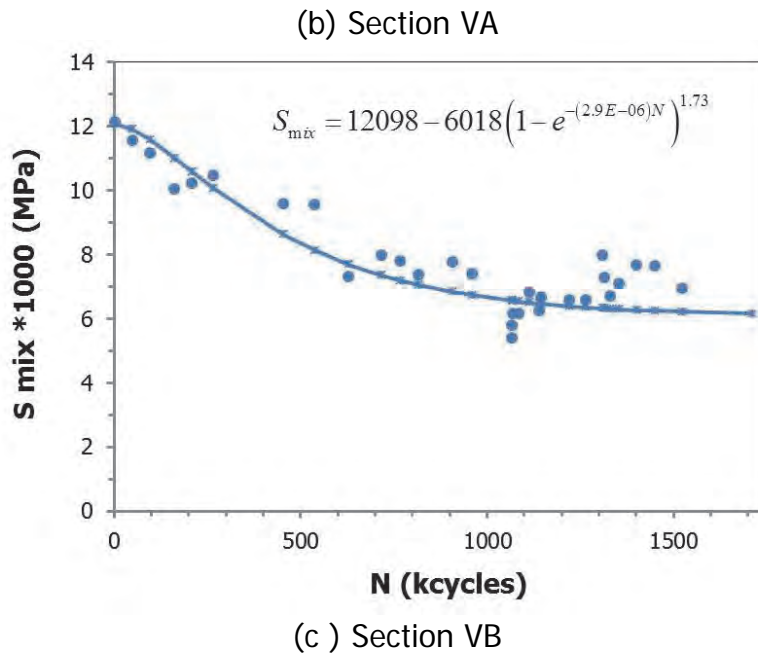
Figure 6.1. Deterioration of Smix for Lintrack sections I, VA and VB (no temperature correction is applied)

Based on this information the following approach was adopted to compare the predicted number of load repetitions to failure with the observed number of load repetitions. It consisted of the following steps:

a. determine the pavement life, defined as the moment at which the back calculated modulus equals 50% of its original value, for different probability of survival levels;
b. determine the amount of cracking at the pavement life as calculated under item a;
c. determine the amount of permanent deformation at each calculated pavement life.

The observation aspect is carried out in several steps and is discussed in detail in section 6.2.

The prediction aspect based on the laboratory test is discussed in section 6.3 and it consists of the following steps:

a. calculate the tensile strain at the bottom of the asphalt layer at different temperatures;
b. determine the pavement life at different probability of survival levels using the 4PB and BOEF fatigue relations;
c. determine to what extent the observed longitudinal cracks were a result of permanent deformation.

In predicting the Lintrack sections lifetime the cumulative damage ratio according to Miner, $\Sigma n_i/N_{fi}$, is employed. The n_i is the actual number of load repetitions at temperature 'i' and N_{fi} is the allowable number of load repetitions at temperature 'i' calculated using the fatigue prediction model. In this research two types of models have been used. The first is based on four

point bending fatigue tests, which is the common way to determine the fatigue resistance of asphalt mixtures in the Netherlands. The second model has been derived from beam on elastic foundation (BOEF) tests which are believed to give a better representation of what happens in reality. In chapter 4 it has already been shown that significant differences in outcome exist between the two tests.

Comparison of the observed and predicted values end of pavement life is discussed in section 6.7. In cases when observation and prediction showed a disparity, a shift factor needed to be introduced. In addition, cracking and permanent deformation are evaluated because both features are visible, easy to measure and they provide additional information for the pavement life analyses and feedback for determining the shift factor.

6.2. Lintrack sections, the observations

6.2.1. Observed cracking

This section is devoted to describe the distress in the form of cracking that was observed during the full scale accelerated testing performed on three GAC Lintrack sections.

During the Lintrack tests the progression of the crack pattern at the surface was recorded using two techniques. The first one was by taking photographs of the test lane (regularly) and the second by drawing the cracks on transparent plastic sheets (regularly). To enable a simple and accurate description of the position of any crack, rectangular grids of 0.40×0.60 m^2 were drawn on the test lane. The total crack pattern of Lintrack section I, VA and VB at the end of the loading/testing is shown in Figure 6.2, 6.3 and 6.4 [4-6].

As mentioned in chapter 2, the surface area of the Lintrack sections was 16 m long and 4 m wide. However, the surface area that was loaded was 12.8 m long and 2.4 m wide and on this area the crack observations were made, as shown in Figure 6.2., 6.3, and 6.4. The green and blue dots in the figures describe the position of the five longitudinal and five transversal strain gauges respectively. The strain gauges were placed close to the bottom of the asphalt layer.

The development of the cracked area during the repeated loadings was calculated from the visual observations mentioned above and is shown in Figure 6.5. In this figure the development of the cracked area is shown as a function of the number of load cycles applied which is shown as percentage of the total number of loads.

The amount of cracking was determined in the following way; an imaginary grid with cell sizes of 100 × 100 mm was laid over the travelled pavement surface. The percentage of the cells in which one or more cracks are visible is reported as the percentage cracked area. It should be kept in mind that the thinner VA and VB sections showed a denser crack pattern than the thicker section I and, therefore, showed a higher percentage cracked area at the end of the test than section I.
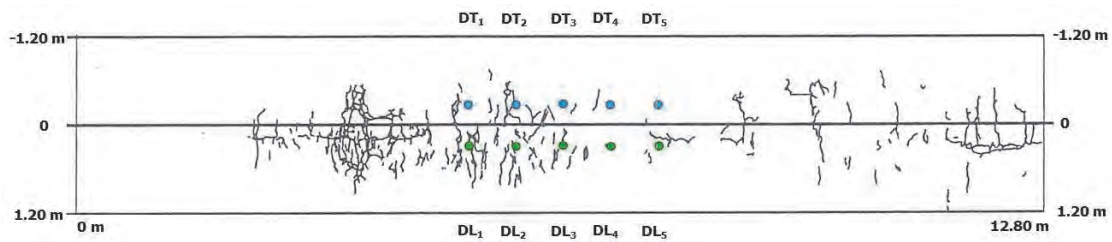
Figure 6.2. Crack pattern of Lintrack section I after 4 Million cycles, wheel load 75 kN, 150 mm thickness
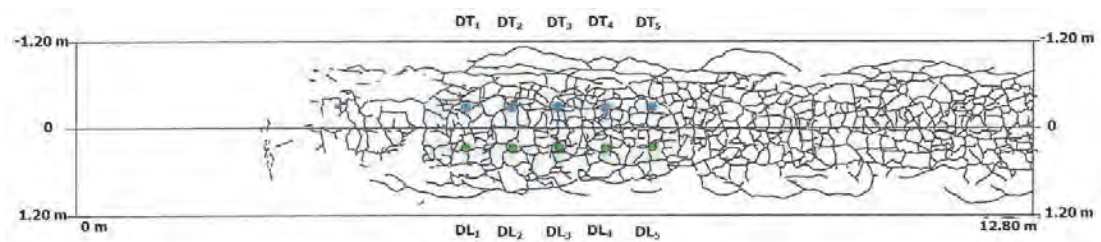
Figure 6.3. Crack pattern of Lintrack section VA after 650 kilocycles, wheel load 75 kN, 80 mm thickness
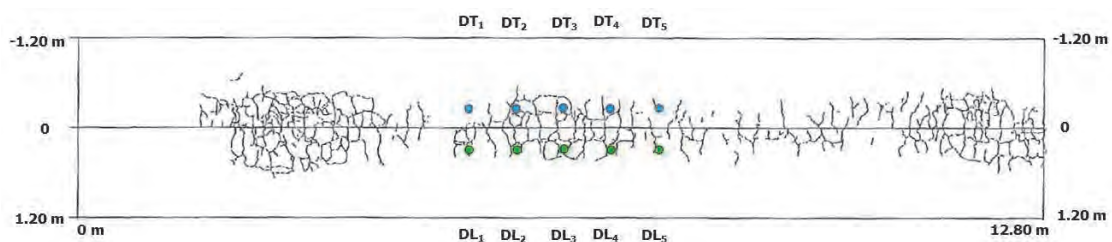
Figure 6.4. Crack pattern of Lintrack section VB after 1722 kilocycles, wheel load 50 kN, 80 mm thickness

Figure 6.5 shows that the development of the cracked area of section I is not fast at the beginning, and at the end it is not even fully cracked. Only about 20% of the area suffered from cracking. For section VA, which is only 80 mm thick, the loading was the same as for section I (75 kN) resulting in a fast development of cracks in the beginning of the test. This section 'crumbled' under the heavy load. Cracking developed less fast on Section VB, which also was 80 mm thick, mainly because the applied load on that section was 50 kN instead of 75 kN used on section VA. As will be discussed later on in more

detail, there is clear evidence that section VA was overloaded resulting in a fast cracking development.

(a)

(b)
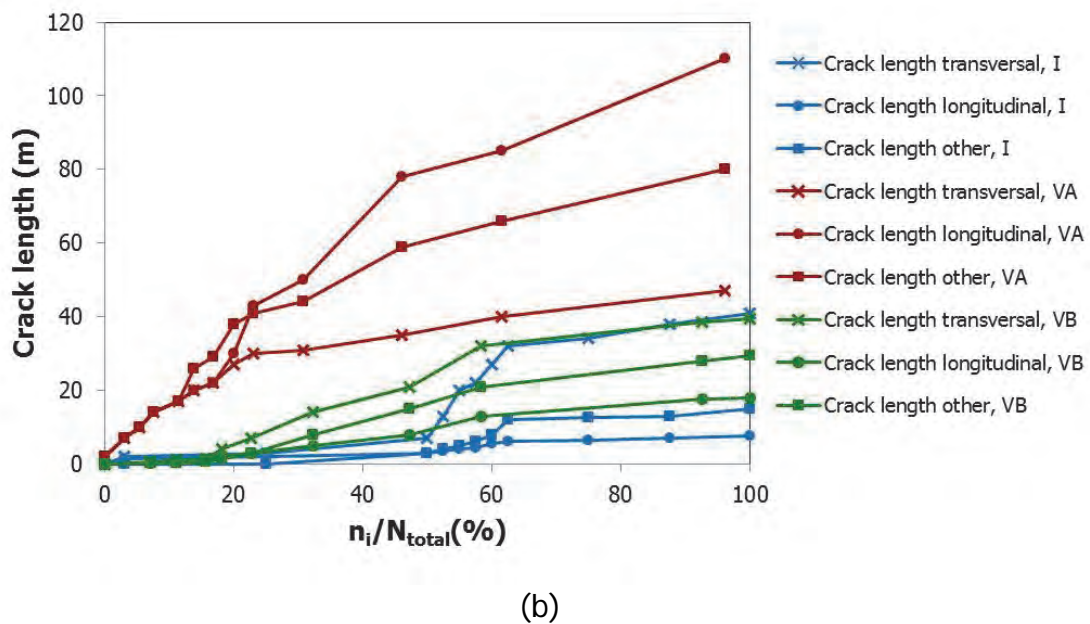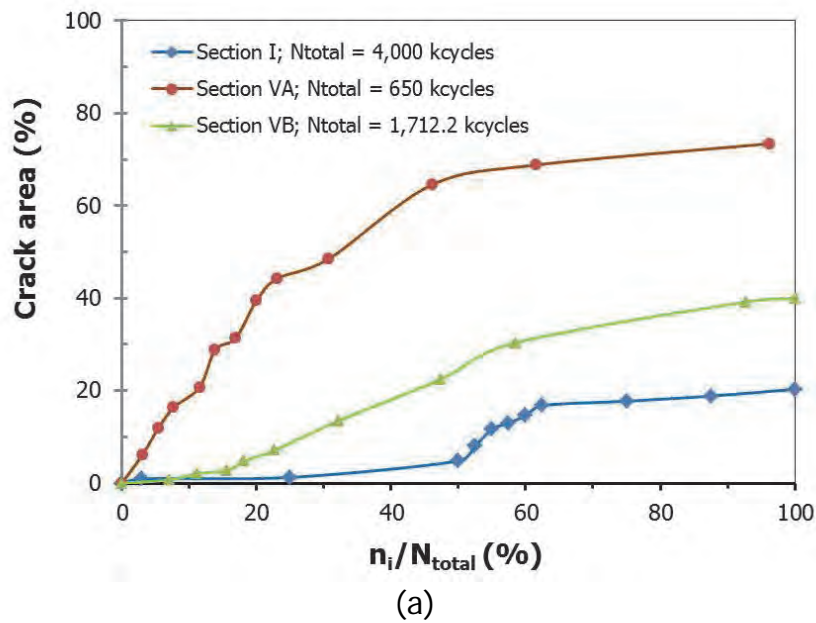
Figure 6.5. (a) Development of the percentage cracked area on Lintrack sections I, VA, VB based on 100x100 grid size area (b) Development of crack length observed on Lintrack sections I, VA and VB

During the tests strain measurements were carried out as well. As already mentioned in subchapter 2.8.2., also the increase in the measured tensile strain is giving information about damage development. Information on this is given in Figures 6.7.
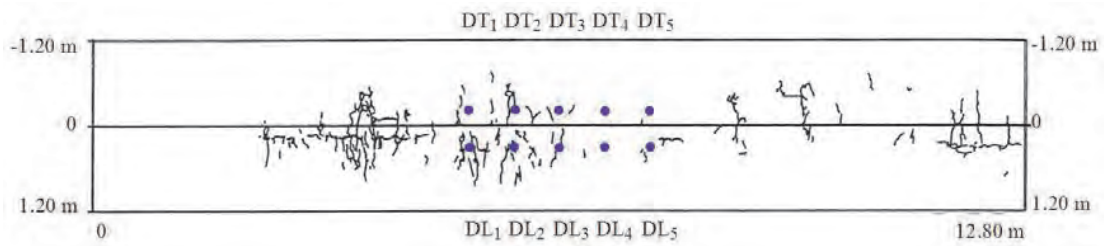
Figure 6.6. Overview of cracks observed on Lintrack section I after 2,5 M cycles (adapted from Groenendijk [4])
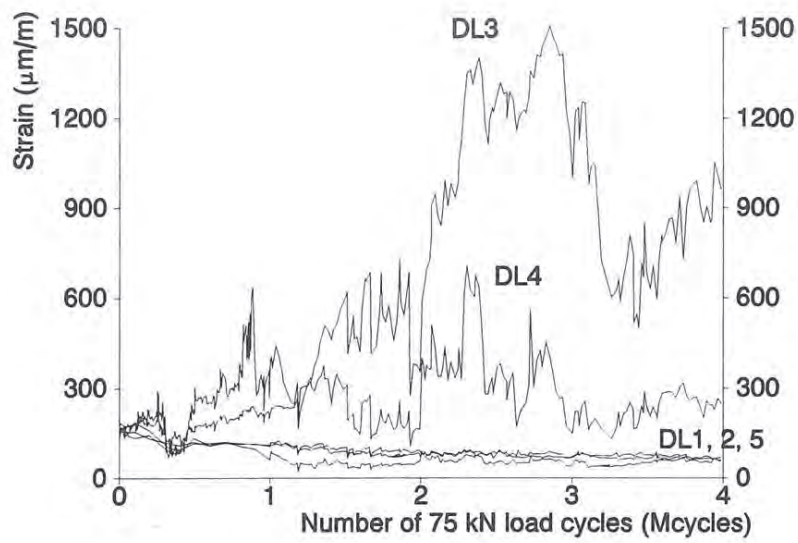
(a) Longitudinal gauges
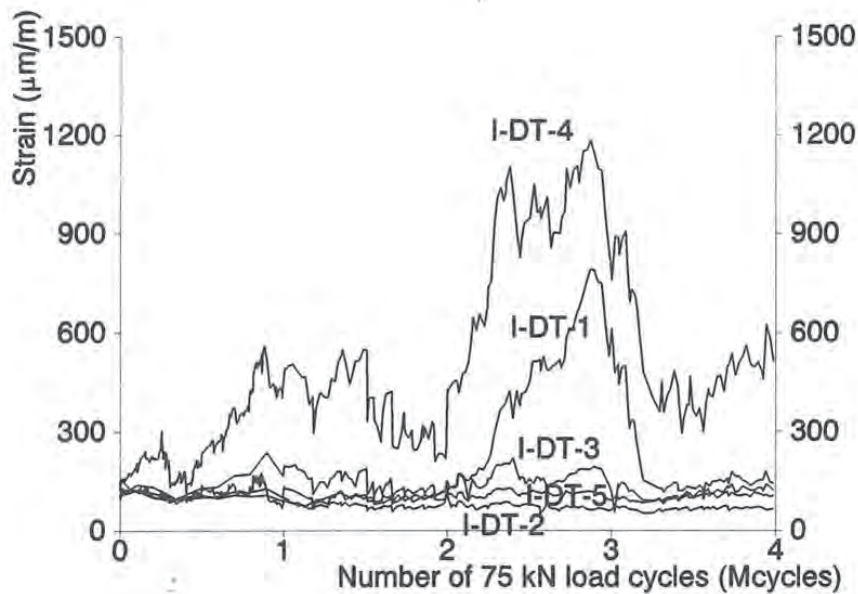
(b) Transversal gauges

Figure 6.7. Strain peak development in longitudinal and transversal direction (Lintrack section I, corrected to 15°C)

Based on Figure 6.7, it is clear that in section I only transversal strain gauge IDT 4 was measuring an increase in tensile strain from the very beginning of the test. IDT 1 only showed an increase after about $2 * 10^6$ repetitions while IDT 2, 3 and 5 showed an increase after approximately $3.2 * 10^6$ repetitions. If it is assumed that the moment at which the tensile strain increases is the moment of initiation of cracking, then it is clear that not all the cracks visible at the pavement surface can be classified as classical fatigue cracks growing from the bottom of the asphalt layer to the top. This has been further substantiated by plotting the occurrence of cracks after 2.5 million load repetitions in relation to the location of the transversal strain gauges (see Figure 6.6).

When combining Figure 6.7 with Figure 6.6 it becomes obvious that at position IDT4 and IDT5 no cracking is visible after 2.5 million load repetitions while at the other locations cracks are visible. All in all this implies that damage that is 'measured' at the bottom of the asphalt layer did not show up as visible cracks at the top of the pavement.

The difference between 'measuring damage' and 'seeing damage' explained above complicates attempts in matching observed with predicted damage. Although 'measuring damage' during accelerated pavement tests, in terms of measuring the increase in tensile strains at the bottom of the asphalt layer in the horizontal as well as lateral direction, is quite laborious, it is needed in order to be able to correlate predictions to observations.

6.2.2. Permanent deformation

Permanent deformation occurring in the Lintrack sections was measured by a transverse profilograph comprising of an aluminium frame bridging the test lane and guiding the measuring wheel which travels across the pavement. Permanent deformation was defined as 'rut depth' and the results of the measurements are shown in Figure 6.8.

The graph shows the development of permanent deformation as function of the number of load repetitions expressed as percentage of the total applied number of load repetitions. Section VA shows excessive permanent deformation development in the early stages of loading. It is recalled that this section carried a similar tyre load (75 kN) as section I but was much thinner than section I.
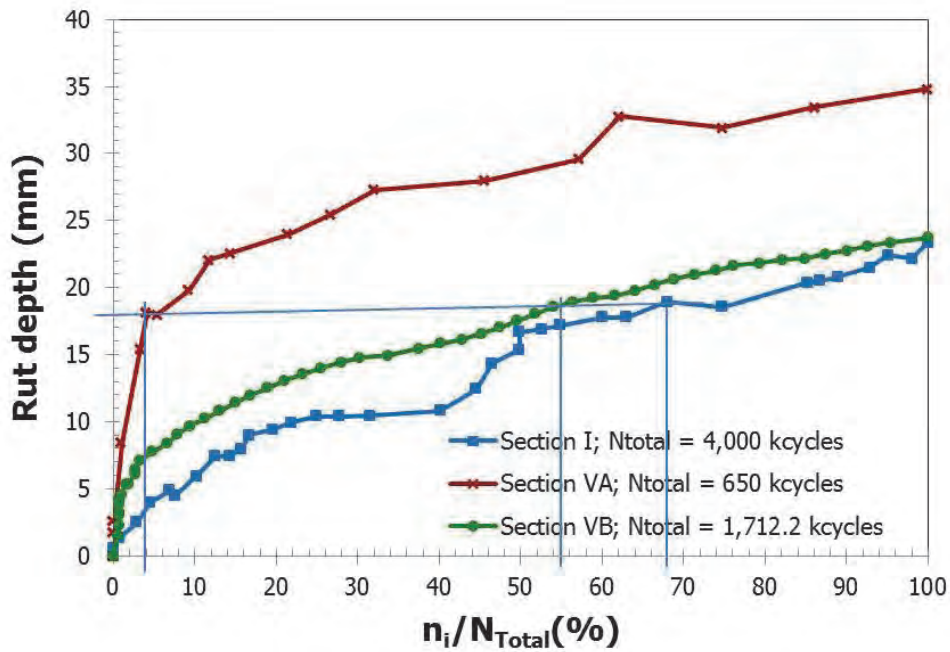
Figure 6.8. Rutting of Lintrack sections I, VA and VB

According to the Dutch maintenance standard for motorways, maintenance action should be taken if the rutting depth reaches 18 mm. Based on this criterion, maintenance is supposed to be carried out at 4%, 55% and 68% of total loading for section VA, VB and I respectively. Later in this chapter a discussion will be presented to determine the relation between the end of the structural pavement life in terms of cracking and the amount of permanent deformation. This is necessary because at some of the sections, shear deformation occurred resulting in a sharp curvature of the asphalt layer which certainly has contributed to the development of cracking. Figures 6.9 (a) to (c) show the development of rut depth profiles on sections I, VA and VB.
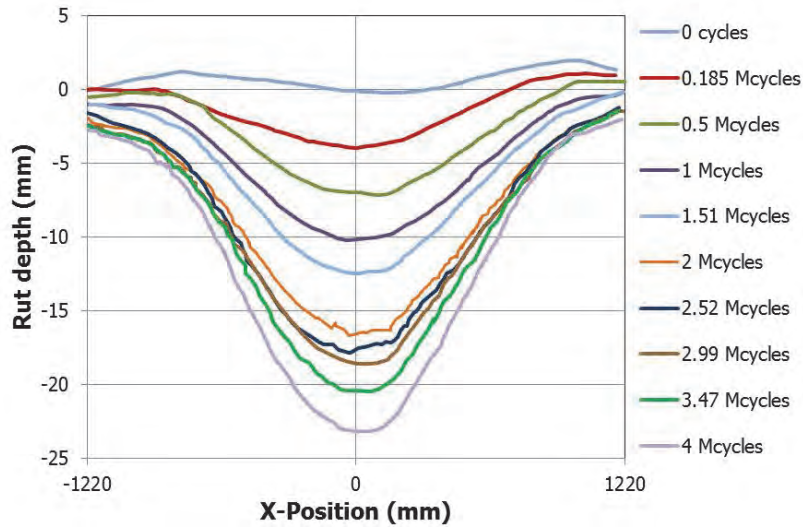
(a) Section I
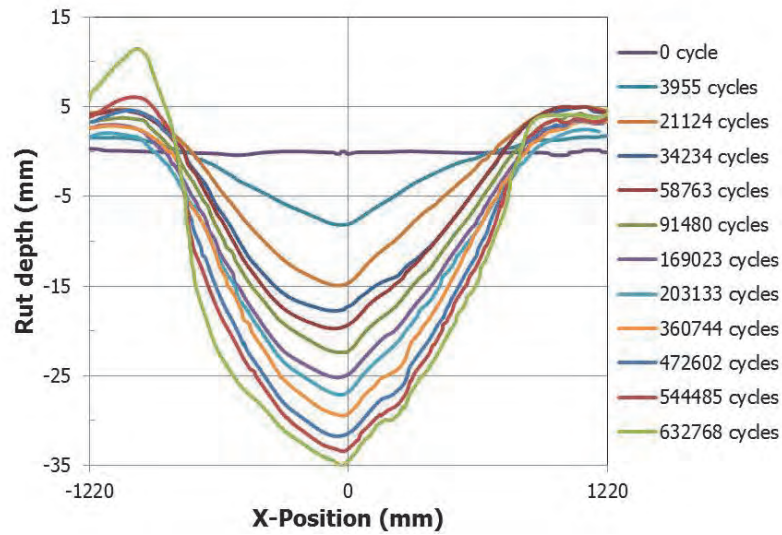
(b) Section VA
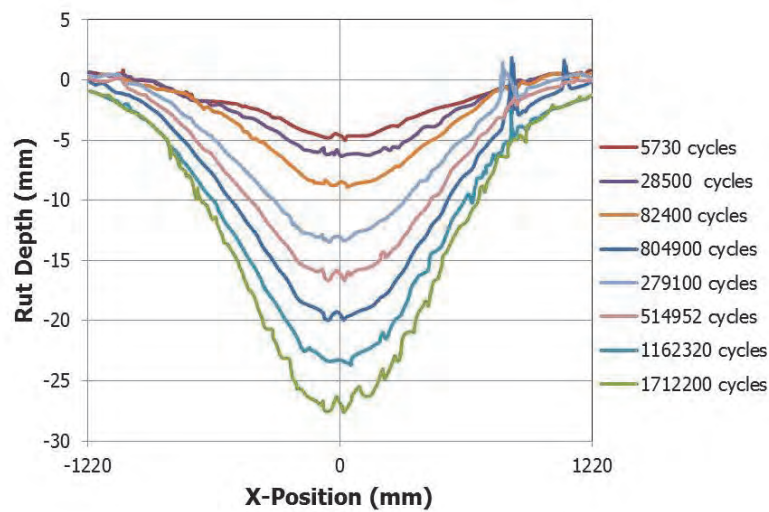
(c) Section VB

Figure 6.9. Rut depth profile of each Lintrack section at several loading cycles

6.2.3. Determination of the pavement life from the back-calculated modulus

The layer stiffnesses were calculated from falling weight deflectometer (FWD) test results using the MISS computer program. The pavement was assumed to act like a two layer system. A detailed explanation of the computer program and calculation procedure can be found in Van Gurp [7], Groenendijk [4], and Bhairo [6].

The FWD measurements were carried out on all sections on the pavement surface above the ten strain gauges location point (DT1 to DT5 and DL1 to DL5). The stiffness evolution in relation to the number of load repetitions is shown in the Figure 6.10 a, b and c. By examining the initial stiffness of each measurement, the fatigue life can be determined straightforwardly from these pictures by determining the number of load repetitions at which the modulus had reduced to 50% of its initial value. A stiffness reduction of 50% was assumed to represent end of pavement life because this is also done when evaluating 4PB fatigue test results. The stiffness values shown are the raw data which means that they are not corrected for temperature influences. Temperature corrections were not applied because van Gurp [7] showed that at a certain amount of cracking such corrections are not applicable anymore.

Table 6.1 summarizes the results of the fatigue life estimations based on back-calculated asphalt stiffness values for each of the ten measurement locations of each section. The fatigue lives presented in the table show large variations. This implies that the determination of the end of the pavement life cannot be defined by means of a single number since even in one section different fatigue life values were obtained at different locations.

(a) Section I
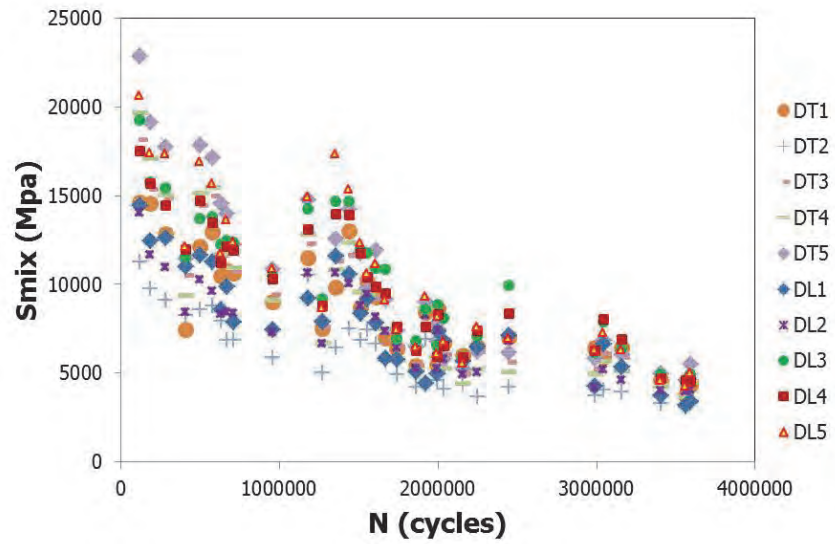
(b) Section VA
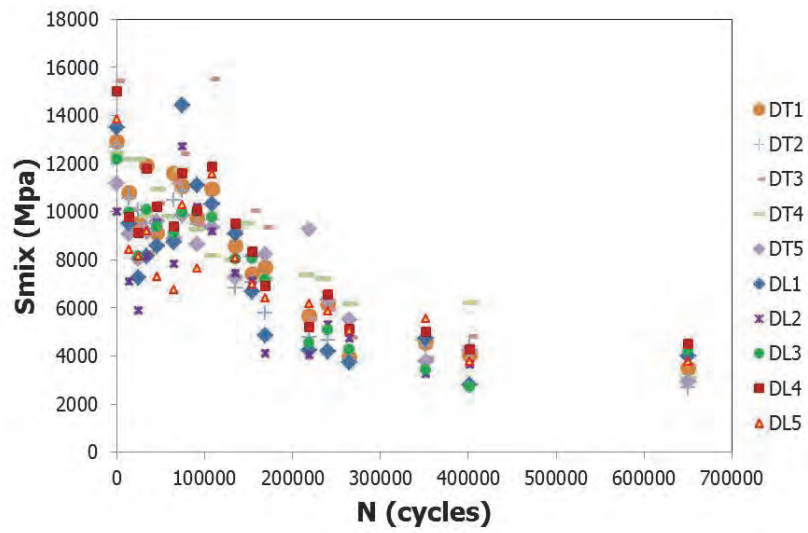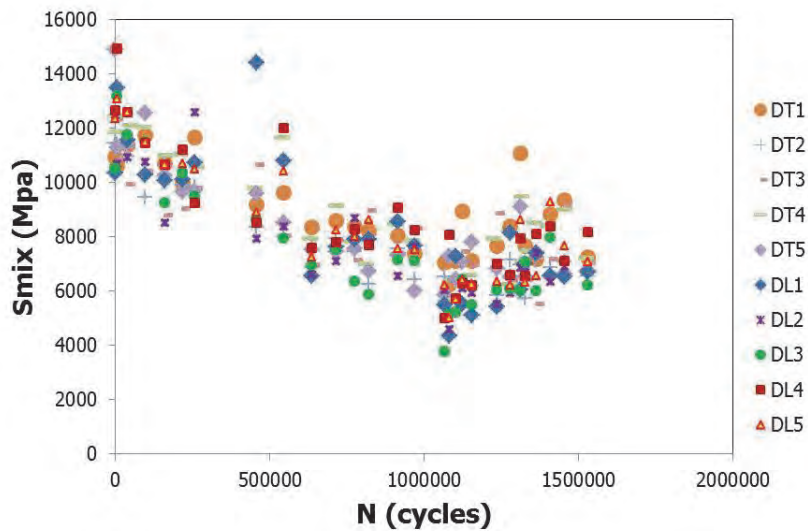
(c) Section VB

Figure 6.10. Back calculated AC stiffness of Lintrack sections

Table 6.1. Back-calculated AC stiffness based on individual strain gauges

Strain gauges	Lintrack section I			Lintrack section VA			Lintrack section VB		
	$S_{initial}$	N at $0.5S_{init}$	Rank	$S_{initial}$	N at $0.5S_{init}$	Rank	$S_{initial}$	N at $0.5S_{init}$	Rank
	MPa	cycles		MPa	cycles		MPa	cycles	
DL1	14,439	1,620,000	8	13,512	154,000	1	10,327	630,000	1
DL2	14,062	1,250,000	4	9,991	165,000	5	12,475	1,050,000	8
DL3	19,207	1,270,000	7	12,168	190,000	7	10,521	760,000	3
DL4	17,513	1,700,000	10	15,000	162,000	3	12,648	990,000	4
DL5	20,651	1,255,000	5	13,852	155,000	2	12,331	1,040,000	6
DT1	14,597	1,650,000	9	12,925	200,000	8	10,935	1,700,000	10
DT2	11,256	1,260,000	6	12,703	163,000	4	11,455	1,070,000	9
DT3	18,173	1,245,000	3	15,418	190,000	6	12,357	1,030,000	5
DT4	19,680	400,000	1	12,435	266,000	10	12,450	1,045,000	7
DT5	22,825	855,000	2	11,167	265,000	9	14,885	710,000	2

The fatigue life values obtained in Table 6.1 can also be presented by means of a probability curve. For this purpose it was assumed that the calculated fatigue lives could be represented by means of a normal distribution. This is shown in Figure 6.11 for section I, VA, and VB. The bell type curves describe the probability function of the fatigue life of each section in terms of number of load repetitions at which the stiffness of the asphalt layer had reduced to 50% of its initial value.

The distribution of the fatigue lives determined in this way was between 200 to 2,900; 25 to 349 and from 350 to 1,390 kcycle for section I, VA and VB respectively.

Chapter 6. _F. P. Pramesti
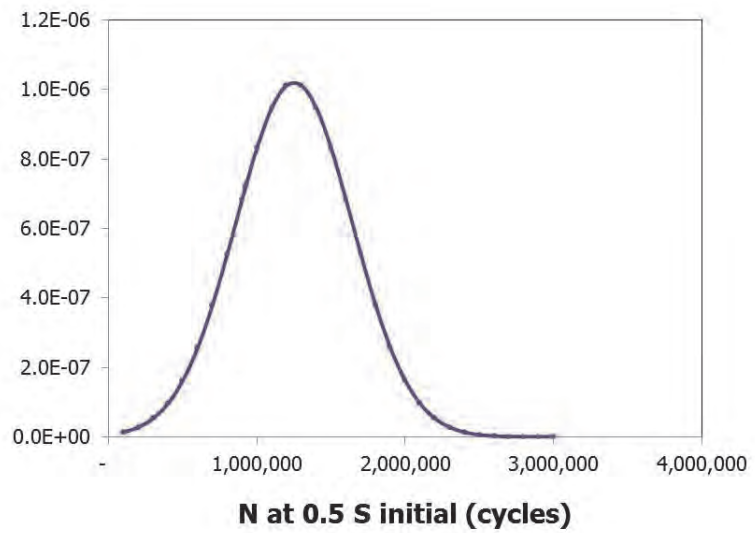
(a) Section I
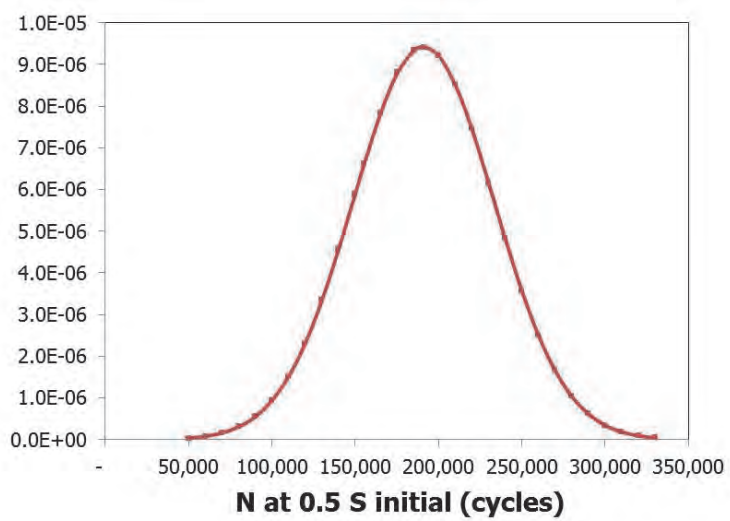
(b) Section VA

(c) Section VB
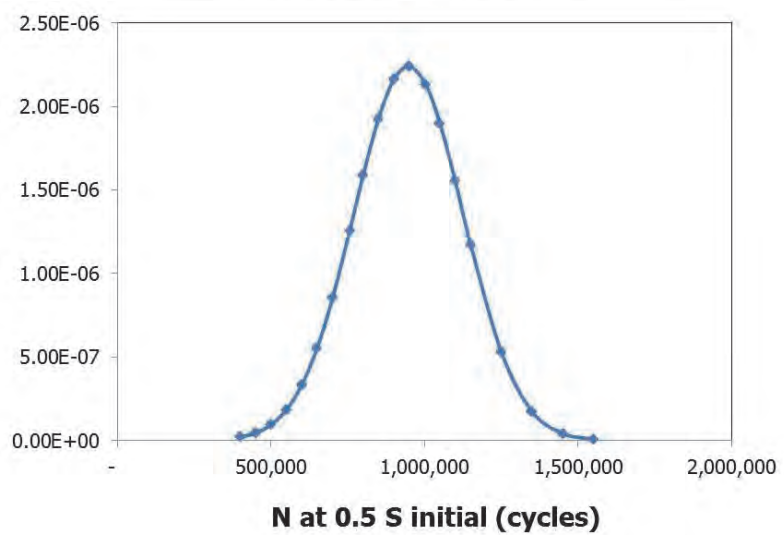
Figure 6.11. Normal distribution of fatigue life based on the back-calculated AC stiffness

6.3. Prediction of 4PB and BOEF fatigue relations for conditions different from the test conditions

In chapter 4 the fatigue relations developed by means of the 4 PB and BOEF test were described. Although these tests were done at frequencies similar to those occurring in the Lintrack tests, they were only done at a few temperatures. The Lintrack sections, however, were subjected to a wide temperature range. This section describes how fatigue relations for each of the temperature conditions occurring in the Lintrack tests were derived from the tests that were performed in the laboratory.

6.3.1. 4PB fatigue parameters for a wide range of temperatures

The 4PB fatigue test provided information about the fatigue behavior of the gravel asphalt concrete at temperatures of 5°C, 20°C and 30°C and loading frequencies of 3 Hz and 8 Hz. The failure point Nf was defined as the number of cycles where the stiffness is half the initial value. The obtained fatigue lines are shown in Figure 4.40 (and Table 4.18) and are expressed by Equation 6.1.

$$N_f = a\varepsilon^n$$
$$LogN_f = Log\,a + n\,Log\varepsilon$$

(6.1)

Where N_f is the number of constant displacement applications until the specimen reached half of its initial stiffness, ε is the applied tensile strain (μm/m), while Log a and n are regression constants.

According to Groenendijk [4], the pavement temperature during the Lintrack performance test varied from 0°C to 30°C. As mentioned before, the loading frequencies of 3 and 8 Hz were close to the loading rates caused by the Lintrack wheel while the temperatures were selected such that the fairly wide range of temperatures which occurred during the Lintrack tests were covered In order to be able to estimate the fatigue relation for conditions which differed from the test conditions, fatigue line constants n and Log a in Equation 6.1 needed to be determined for other conditions.

6.3.1.1. Relationship between n (slope of the fatigue line) and Smix

Schapery [8] showed that the slope of the fatigue relation 'n' is related to the inverse of the slope of the stiffness master curve 'm' and that n = f (2/m). Molenaar [9] and Medani and Molenaar [10] proved this to be the case but also showed that the void content of the mixture should be taken into account. The relationship between the log (loading time) and the log (mixture

stiffness) is non-linear; at short loading times (implying a high mixture stiffness) the 'm' value is low, implying a high value for 'n'. At long loading times, however, the 'm' value is higher, implying that 'n' is lower in the lower stiffness range. Because of these interactions, a relationship between the fatigue constant 'n' and the stiffness of the mixture was developed.

In order to get a more reliable relationship, the data set which was presented in Table 4.18 was extended by adding GAC 4PB test data which were collected at the time of the construction of the Lintrack sections. For these later data the reader is referred to van de Ven [11], Wattimena [12] and Groenendijk [4]. These fatigue relations were developed from 4PB test on beam specimens sawn from the Lintrack sections.

The best fit between the slope of the fatigue relation, n, and the mixture stiffness S_{mix} is shown in Figure 6.12 and Equation 6.2.

$$n = -0.099 \frac{S_{mix}}{1000} - 2.942 \qquad (6.2)$$

where n is the slope of the fatigue relationship and Smix is the stiffness of the mixture (MPa)
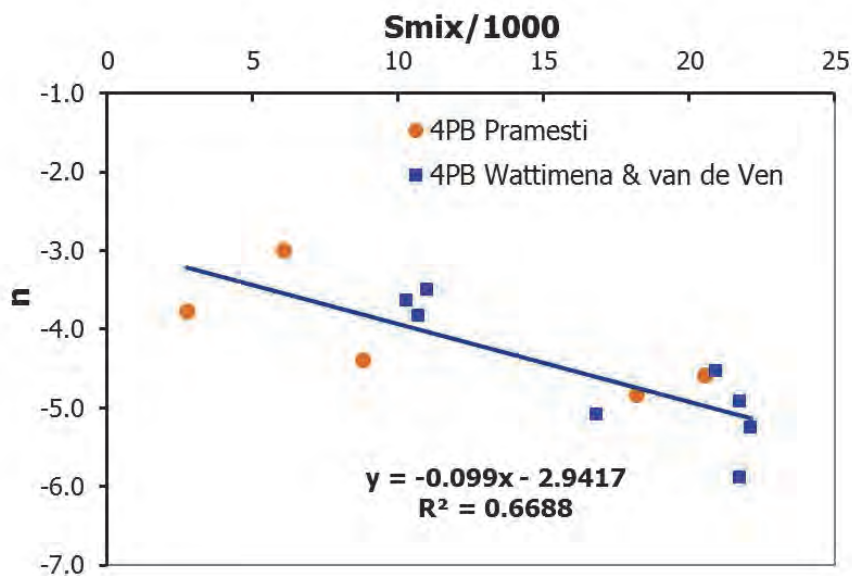
Figure 6.12. Relation between n and Smix

This relationship allows appropriate n values to be selected at all S_{mix} conditions which occurred during testing of the Lintrack sections.

6.3.1.2. Relationship between Log a and n

Molenaar [9], when analyzing several fatigue researches showed that the parameters Log a and n are correlated. Later on Molenaar and Medani [10] showed that the constant Log a is dependent on a number of factors including the mixture stiffness while Groenendijk [4] and Li [13] explained that the constant Log a is also affected by the specimen size. For reasons of simplicity it was decided to follow the approach adopted by Molenaar in 1983 in developing a relationship between Log a and n. Again the GAC fatigue lines from the 4PB tests by Pramesti and those by Wattimena & van De Ven were used (see Figure 6.13). The relation is shown in Equation 6.3. The figure shows that a very good relationship between Log a and n was obtained and, therefore, it was decided to use this relationship for estimating Log a at mixture stiffness conditions occurring during the Lintrack tests.

Log a = -2.136 n + 4.925   (6.3)

where n and Log a are fatigue constants
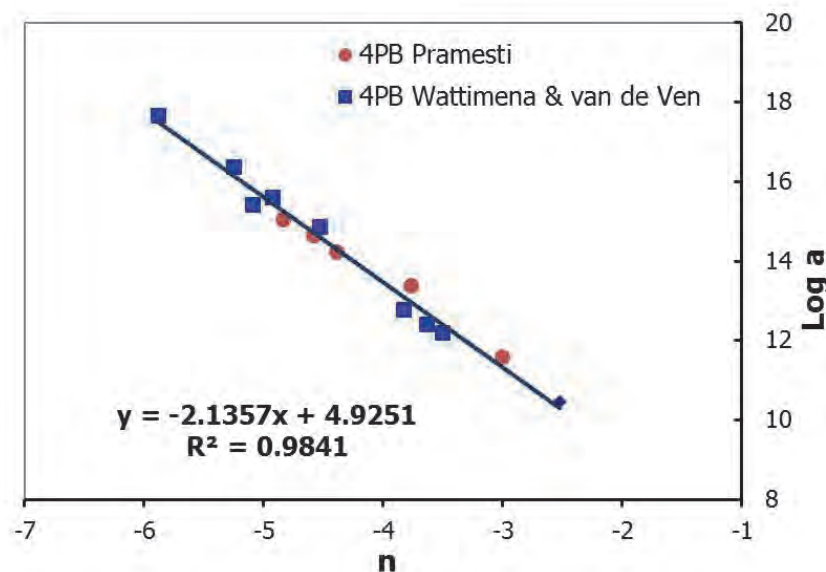
Figure 6.13. Relation between n and Log a

6.3.2. BOEF fatigue parameters for a wide range of temperatures

As has been described in chapter 5, the BOEF tests were only performed at 5°C and 8 Hz. In order to be able to estimate the BOEF fatigue constants for other conditions, an approach different from the one used to estimate the 4PB test constants needed to be adopted. The approach followed in this study closely follows the approach as used by Sabha [14] and Groenendijk [4, 5] in their research.

6.3.2.1. Application of Paris' law to estimate Log a and n

Groenendijk [4] applied the principles of fracture mechanics to analyze 4PB fatigue test results in a fundamental way. Crack, or damage, growth was analyzed using Paris' law which is $dc/dN = A K^n$ where dc/dN is the crack growth per load cycle, A and n are material parameters and K is the stress intensity at the tip of the crack. Groenendijk concluded that 4PB test results could be modelled by means of Equation 6.4.

$$N = \frac{h^{\left(1-\frac{n}{2}\right)}}{AS_{mix}^n} \int_{c_0/h}^{c_f/h} \frac{d\left(c/h\right)}{\left[1.99\left(\frac{c}{h}\right)^{0.5} - 2.47\left(\frac{c}{h}\right)^{1.5} + 12.97\left(\frac{c}{h}\right)^{2.5} - 23.17\left(\frac{c}{h}\right)^{3.5} + 24.8\left(\frac{c}{h}\right)^{4.5}\right]^n} \varepsilon^{-n} \qquad (6.4)$$

where

$$h^{\left(1-\frac{n}{2}\right)}$$

and

$$\int_{c_0/h}^{c_f/h} \frac{d\left(c/h\right)}{\left[1.99\left(\frac{c}{h}\right)^{0.5} - 2.47\left(\frac{c}{h}\right)^{1.5} + 12.97\left(\frac{c}{h}\right)^{2.5} - 23.17\left(\frac{c}{h}\right)^{3.5} + 24.8\left(\frac{c}{h}\right)^{4.5}\right]^n}$$

are entities that represent the geometry and damage development parameters of the specimens.

For the BOEF test a similar equation can be developed but with different geometry and damage development parameters. When all specimens, like in this research, have the same geometry, these two entities, however, are not important when the ratio of the number of load repetitions to failure at two different conditions is determined. When the ratio N_{Smix1} over N_{Smix2} is determined (this is the ratio of lifetimes at a particular strain level but determined at, for instance, different temperatures), the geometry parameter and the damage propagation parameter can be eliminated from the equation. Therefore, to determine the number of load repetitions when the BOEF test is performed at other test conditions (temperature and loading frequency) only

the parameters $\dfrac{1}{AS^n_{mix}}$ and ε^{-n} have to be taken into account. Hence for the BOEF test Equation 6.4 can be rewritten into Equation 6.5 which in turn can be rewritten as Equation 6.6.

$$N = \frac{1}{AS^n_{mix}} \varepsilon^{-n} \ast \text{constant} \tag{6.5}$$

$$N = a \, \varepsilon^{-n} \ast \text{constant} \tag{6.6}$$

Where
N   : Number of load repetitions to failure
A, n : material properties controlling damage growth; they are dependent of the type of material and the experimental conditions (waveform, temperature and frequency)
S_{mix} : stiffness of the asphaltic material (MPa)
ε : applied strain (m/m)

The log equation of the fatigue line model is shown in Equation 6.7. This equation complies with equation 6.1.

$$\log N = \log a - n \log \varepsilon \tag{6.7}$$

The value of "Log a" for 5°C is known from the BOEF fatigue test, hence, the "Log a" for a different temperature can be determined using Equation 6.8.

$$\log a_{i^oC} = \frac{\left(\dfrac{1}{AS^n_{mix}} \right)_{i^oC}}{\left(\dfrac{1}{AS^n_{mix}} \right)_{5^oC}} \ast \log a_{5^oC} \tag{6.8}$$

6.3.2.2. Determination of Log a and n using the Jacobs-Groenendijk approach

Groenendijk/Jacobs and Molenaar/Medani proposed methods to estimate the constants of fatigue relationships. Both methods will be described hereafter and the results will be compared. Finally, a decision will be made on the method to be used for this research.

Equation 6.8 shows that the material properties 'A' , 'n' and 'S_{mix}' need to be known. Jacobs [15] proposed equation 6.9 to predict A and Groenendijk [4] has suggested a procedure to implement it. This procedure was applied on the GAC Pramesti dataset and the results are given in Table 6.2.

$$LogA = d - 2a\log(\sigma_m) - b\frac{n}{2}\log 2\Gamma_m - c\frac{n}{2}\log(S_{mix})$$ (6.9)

Where:

a,b,c,d = regression coefficients depending on mix type (Jacobs reported a = 0.39, b = -0.04, c = 0.62, d = -1.29 for dense asphalt concrete and stone matrix asphalt). It is realized that these values might not be really applicable to the GAC used in this study.

σ_m = tensile strength (MPa)

Γ_m = fracture energy (Nmm/mm^2)

n = fatigue constant

Smix = stiffness modulus of the mix determined from the master curves

Table 6.2a. The compilation / calculation of a and n for different temperatures

T	t (time period)	S_{mix}	n	σm	Γ	Log A
°C	ms	Mpa		MPa		
	(1)	(2)	(3)	(4)	(5)	(6)
0	125	22880	5.428	4.810	0.049	-9.267
5	125	20088	5.190	4.654	0.069	-8.823
10	125	16844	4.880	4.436	0.105	-8.254
15	125	13401	4.497	4.145	0.172	-7.567
20	125	10124	4.057	3.781	0.285	-6.798
25	125	7267	3.577	3.348	0.456	-5.984
30	125	4962	3.077	2.860	0.671	-5.163

*(i) is number of column

Table 6.2b. The compilation / calculation of a and n for different temperatures

T	A	$A*S_{mix}{}^{\wedge}n$	$1/A*S_{mix}{}^{\wedge}n$	a	log a	n_{obs}
°C						
	(7)	(8)	(9)	(10)	(11)	(12)
0	5.41E-10	2.48E+14	4.03E-15	8.40E-16	-15.076	
5	1.50E-09	3.22E+13	3.10E-14	6.46E-15	-14.190	5.230
10	5.57E-09	2.34E+12	4.27E-13	8.88E-14	-13.052	
15	2.71E-08	9.85E+10	1.02E-11	2.11E-12	-11.675	
20	1.59E-07	2.84E+09	3.53E-10	7.34E-11	-10.134	
25	1.04E-06	6.75E+07	1.48E-08	3.08E-09	-8.511	
30	6.87E-06	1.61E+06	6.21E-07	1.29E-07	-6.889	

The procedure to determine the values which are shown in Table 6.2 is as follows:

Step 1

Determine the master curve at the temperatures of interest. The master curve is expressed by means of a polynomial equation (Equation 6.10). Over the stiffness range of interest, this polynomial model gives the best fit to the stiffness modulus data measured by means of the 4PB test for stiffness (see Table 6.3). Column (2) of Table 6.2 shows the calculated stiffness values.

$$LogS_{mix} = a_0 + a_1 \log t + a_2 (\log t)^2 + a_3 (\log t)^3 \tag{6.10}$$

$$t = \frac{1000}{f} \tag{6.11}$$

Where:

S_{mix} : the stiffness modulus of the mixture at certain temperature and loading time (MPa)

a_i : Coefficients of the master curve

t : loading time (ms)

f : frequency (Hz)

Table 6.3. The coefficients of the master curve, the Smix model, and Smix observed at different temperatures

Reference temperature (°C)	a_0	a_1	a_2	a_3	S_{mix} at f = 8 Hz	S_{mix} observed at f = 8 Hz
0	4.404	0.0203	-0.0146	-0.00250	22880	-
5	4.398	0.0099	-0.0215	-0.00230	20088	20032
10	4.397	-0.0178	-0.0254	-0.00231	16844	16478
15	4.378	-0.0482	-0.0293	-0.00231	13401	12426
20	4.343	-0.0818	-0.0330	-0.00231	10124	10313
25	4.291	-0.1181	-0.0367	-0.00230	7267	6930
30	4.222	-0.1569	-0.0401	-0.00230	4962	5053

Step 2

Determine the relation between n and Smix. Based on Pramesti's GAC fatigue data set (from the 4PB and BOEF's fatigue lines) as displayed in Table 6.4, the relation between Log S_{mix} and n is determined using an S curve model which is shown in Equation 6.12 and Figure 6.14.a.

$$n = 507.088 \left\{ 1 - e^{ -\left[\left(\frac{LogS_{mix}}{16.209} \right)^{3.45} \right] } \right\} \tag{6.12}$$

Since the Smix for each temperature is known, the n for other temperatures can be determined. They are shown in column (3) of Table 6.2. It should be

noted that at the Smix of the Lintrack sections, Equation 6.2 and Equation 6.12 give approximately the same value for n. However, for the 4PB case the n values observed are closer to the n model depicted in Equation 6.2 whereas in the case of the BOEF the n value is closer to the n model of Equation 6.12.; this is also shown in Figure 6.14b.

Table 6.4. Overview of the fatigue tests on GAC, n and related stiffness

Fatigue test	T	t (time period)	n	S_{mix}
	°C	ms		Mpa
GAC 4PB	5	333.33	4.835	17745
GAC 4PB	5	125	4.584	20088
GAC 4PB	20	333.33	3.001	7757
GAC 4PB	20	125	4.391	10124
GAC 4PB	30	125	3.767	4962
GAC BOEF	5	125	5.230	20088
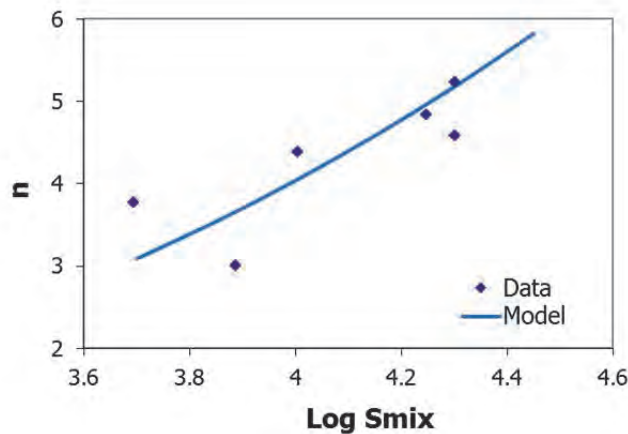
Figure 6.14.a. The relation of n estimation and the stiffness of the mixture
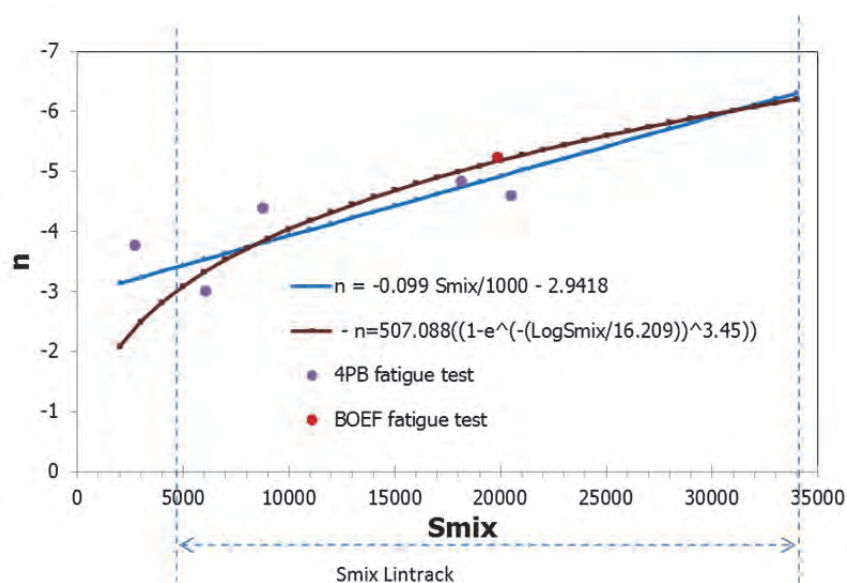
Figure 6.14.b. n estimation and the stiffness of the mixture using Equation 6.2 and 6.12.

Step 3
Perform uniaxial tensile tests to failure. These tests were done and the details
have been explained in sub chapters 3.3.5 and 4.2.2. The test results are
shown in Table 6.5.

Table 6.5. Summary of the MUTT results

T	E mod	Tensile strength (σ_m)	Fracture energy (Γ)
°C	MPa	MPa	Nmm/mm2
5	6,162	3.18	0.245
5	16,054	4.14	0.078
5	19,199	3.99	0.042
5	23,525	5.01	0.054
20	493	1.11	0.898
20	1,153	1.46	0.718
20	8,817	5.44	0.577
20	16,466	5.06	0.240
30	273	0.45	0.401
30	1,916	1.34	0.888
30	3,923	1.72	0.663
30	5,002	2.01	1.085
30	3,158	2.59	1.103

Step 4
Determine the relation between the mixture stiffness and tensile strength and
between the mixture stiffness and the fracture energy. The relation of the
tensile strength and fracture energy to the stiffness of the mixture are
described by means of S curves. The equations are shown in Equation 6.13
and 6.14. The values of σ_m and Γ are shown in column (4) and (5) of Table
6.2.

$$\sigma_m = 6.68 \left\{ 1 - e^{-\left(\frac{LogS_{mix}}{4.153}\right)^{4.983}} \right\} \tag{6.13}$$

$$Log\Gamma = 3.257 - 5.413 \log S_{mix} \, 2.396 \left(\log S_{mix}\right)^2 - 0.312 \left(\log S_{mix}\right)^3 \tag{6.14}$$
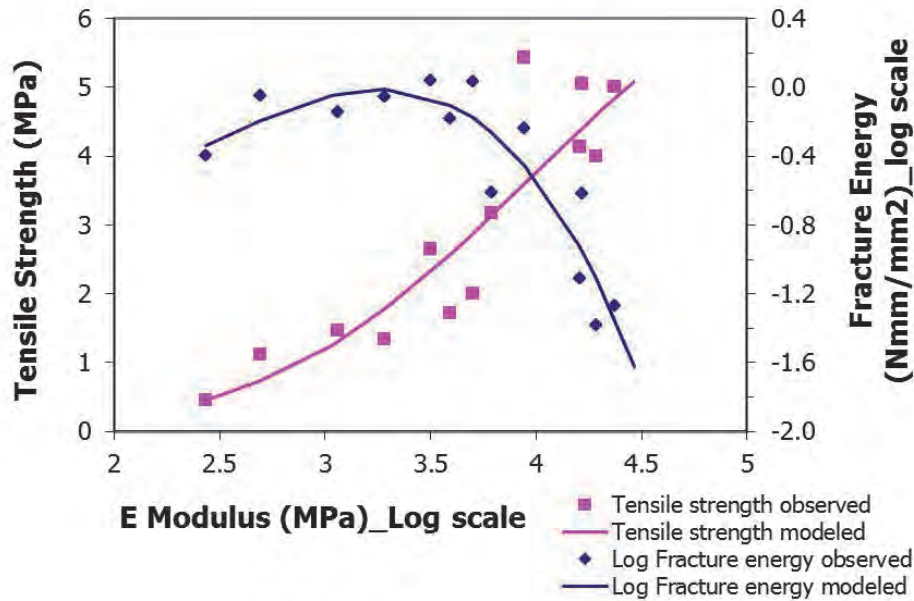
Figure 6.15. The tensile strength and the fracture energy versus stiffness of the mixture

Step 5
Since all the parameters needed are known, Log A and A can be calculated using Equation 6.9. The results are shown in Table 6.2 column (6) and (7).

Step 6
Determine 'a' and 'log a' using Equation 6.8. The 'n' and 'log a' parameters of the fatigue line are shown in Table 6.2 column (3) and (11). These columns show the value of **n** and **Log a** for other temperatures applicable to the BOEF fatigue lines.

By using the fatigue constants in step 6, the BOEF fatigue lines for other temperatures were determined and are shown in Figure 6.16. It can be seen from Figure 6.16 that the fatigue slopes decrease with increasing temperature. The fatigue line of 5°C modeled has a bit lower slope than the fatigue line of 5°C observed, as the n of the model is a little bit lower than the n from the observation although both fatigue lines have similar Log a. The figure also shows that the intercept of the fatigue lines decreases with the increasing temperature.
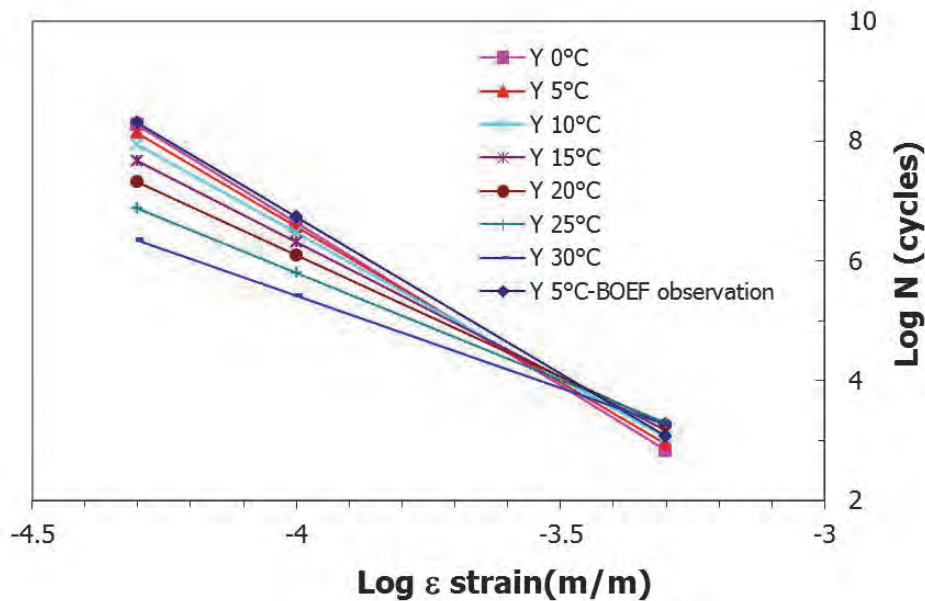
Figure 6.16. Fatigue line prediction for other temperatures based on BOEF fatigue line (Where Log A is calculated using Jacobs' equations)

6.3.2.3. Determining Log A and n using the Medani-Molenaar approach

Medani-Molenaar [16] used the test results of Molenaar [9] and Jacobs [15] to derive a relationship between Log A, n and Smix as shown in Equation 6.15. The coefficient of determination R^2 of the model is 0.888.

$$LogA = -2.890 - 0.308n - 0.739n^{0.273\log S_{mix}}$$ (6.15)

The procedure to calculate A and n is as follows:

Step 1
Similar to the procedure explained in the previous sub chapter, this approach also starts with the determination of the stiffness master curve at the reference temperatures. By using the same equation and input, the result is similar to the result presented in Table 6.2. It is presented in Table 6.6 column (2).

Step 2
Determine the n value using Equation 6.12.

Step 3
Since all the parameters needed by Equation 6.15 are known, A can be calculated and the results can be found in Table 6.6 column (5).

Step 4
Again, similar as step 6 of Groenendijk's procedure, 'log a' for other temperatures can be calculated using Equation 6.8. The 'n' and 'log a' parameters of the fatigue lines are shown in Table 6.6 column (3) and (8). Figure 6.17 presents the fatigue lines of the BOEF test for several temperatures.

Like the fatigue lines resulting from the Jacobs-Groenendijk approach, the slopes of the fatigue lines from Medani Molenaar decrease with increasing temperature whereas the intercept which is represented as 'Log a' increases with increasing temperature.

Both approaches show a 'rotation' of the fatigue lines at around 3.2×10^{-4} strain (316 μstrain) where the slope decreasing with increasing temperature. It is also shown that both the modeled and observed fatigue line at 5°C have almost the same slope and intercept.

Table 6.6. The compilation / calculation of a and n for different temperature

T	t	S_{mix}	n	Log A	A	$\frac{1}{A*S_{mix}\wedge n}$	a	log a	n_{obs}
°C	ms	Mpa							
(1)	(2)	(3)	(4)	(5)		(6)	(7)	(8)	(9)
0	125	22880	5.428	-10.094	8.05E-11	2.71E-14	9.38E-16	-15.028	
5	125	20088	5.190	-9.602	2.50E-10	1.87E-13	6.46E-15	-14.190	5.230
10	125	16844	4.880	-8.995	1.01E-09	2.35E-12	8.13E-14	-13.090	
15	125	13401	4.497	-8.296	5.06E-09	5.44E-11	1.88E-12	-11.725	
20	125	10124	4.057	-7.557	2.77E-08	2.03E-09	7.01E-11	-10.154	
25	125	7267	3.577	-6.824	1.50E-07	1.03E-07	3.55E-09	-8.450	
30	125	4962	3.077	-6.134	7.34E-07	5.81E-06	2.01E-07	-6.697	
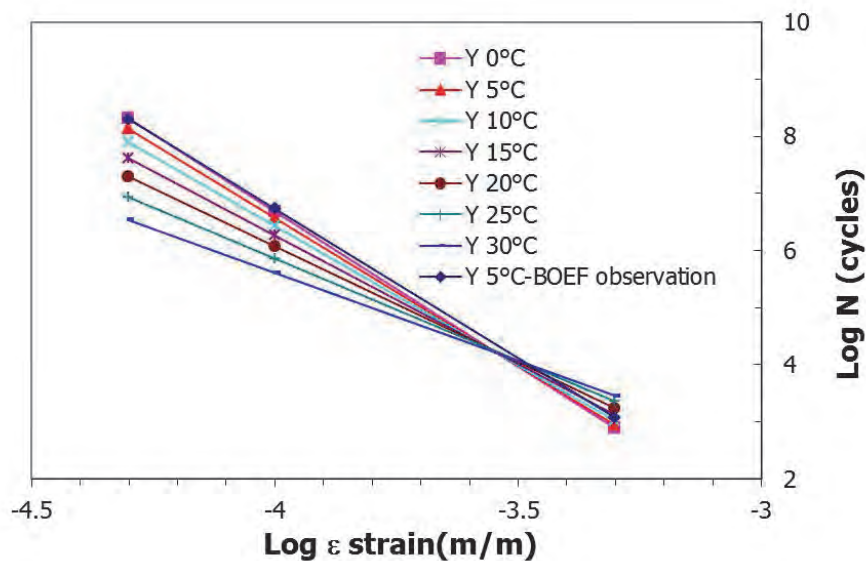
Figure 6.17. BOEF fatigue line predictions for other temperatures (Log A is calculated using the Medani-Molenaar equations)

6.3.2.4. Recapitulation of n and Log a

Table 6.7 shows the recapitulation of fatigue line's constants as a result of the Jacobs- Groenendijk and the Medani-Molenaar approach. It should be noted that for the constants showed in Table 6.7, the strain level is in microstrain (μm/m).

Table 6.7. Summary of fatigue line's constants*

Temperature °C	Jacobs-Groenendijk		Medani-Molenaar	
	Log a	n	Log a	n
0	17.490	5.43	17.538	5.43
5	17.192	5.23	17.192	5.23
10	16.227	4.88	16.189	4.88
15	15.308	4.50	15.258	4.50
20	14.209	4.06	14.190	4.06
25	12.954	3.58	13.015	3.58
30	11.571	3.08	11.763	3.08

* ε in μm/m

It seems that the differences between the two procedures are not large; they are in the range of 0% to 1.63% (and average of 0.44%). For the next analysis it was decided to use the Log a and n values from Jacobs-Groenendijk approach. The reason for this choice is the fact that the Jacobs-Groenendijk approach makes use of material properties such as tensile strength and fracture energy. These properties were also determined for the GAC mixture investigated in this research (see chapter 4) whereas the Medani-Molenaar approach is just a regression equation in which measured material properties cannot be used.

6.4. Prediction of pavement fatigue life at different probability of failure levels

It is a well-known fact that when fatigue cracking occurs, the pavement will not show cracks from one day to the other. Cracking develops gradually in time because the tensile strains are varying over the length of the pavement due to the variation in the thickness and in the stiffness of the layer. Also the fatigue characteristics are not a "constant", simply because of the fact that the material composition varies along the road. The way in which these variations are influencing crack development is schematically shown in Figure 6.18.
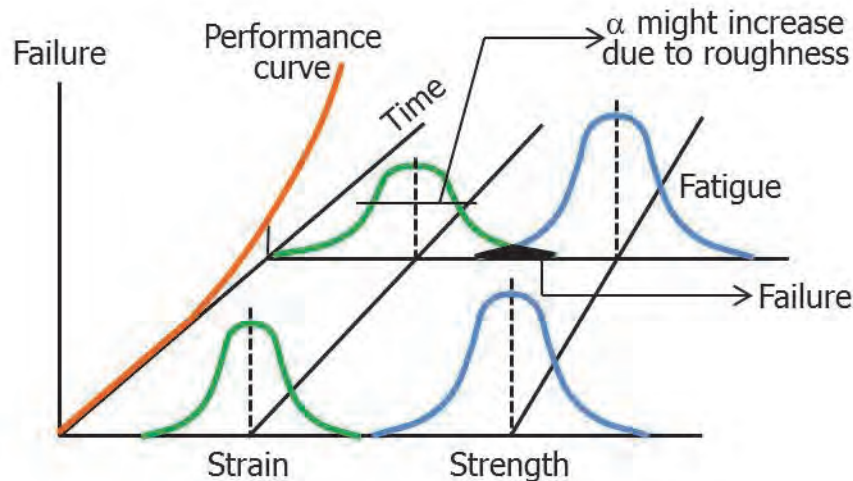
Figure 6.18. Scheme of the development of the strain and the strength of asphalt pavement over time [17]

The figure given above nicely shows what the influence factors are in the development of crack. They are:
- Variation in the tensile strain
- Variation in the fatigue characteristics

This concept also applies to the Lintrack test sections. Earlier studies [9], have shown that the major cause for variation in pavement life is the variation in the fatigue characteristics. Because of this and because sufficient information on the variation in the asphalt layer thickness was not available, it was decided not to take into account the variation in strain level. Accordingly, the reliability analyses only took into account the variation in fatigue characteristics.

The variation in fatigue characteristics was taken into account in the following way. The fatigue relation that is derived from the 4PB or the BOEF test is actually the "average" fatigue line. However, confidence limits around this average relationship can be derived using the available data.

Conceptually the confidence level can be summarized and presented using Figure 6.19. NP0.5 describes the average fatigue model. Assuming that the data is normally distributed, one can determine the desired confidence level $(1-\alpha)$. Based on this confidence limit the lower bound is taken as $N_{P\alpha/2}$ and the upper bound as $N_{P(1-\alpha/2)}$. The $N_{P\alpha/2}$ represents the probability of fatigue life at $\alpha/2$.
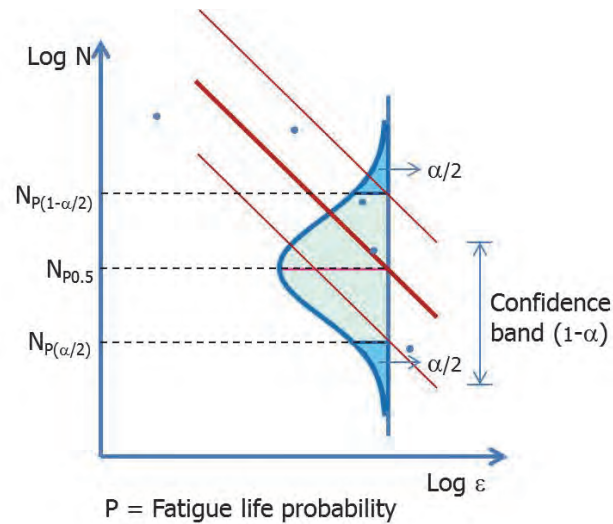
Figure 6.19. The scheme of fatigue life probability

Figure 6.19 shows a two-sided tolerance limit which is based on Equation 6.16, for N_P less than 0.5 ($N_{P\alpha/2}$), and Equation 6.17 for NP more than 0.5 ($N_{P(1-\alpha/2)}$).

$$LogN_P = Log\,a + nLog\,\varepsilon - t\,s\sqrt{\frac{1}{d}}$$ (6.16)

$$LogN_P = Log\,a + nLog\,\varepsilon + t\,s\sqrt{\frac{1}{d}}$$ (6.17)

In Equation 6.16 and 6.17, "t" is a multiplier (factor) tabulated as a function of the confidence level (1-α), probability γ and the number of data points d. "s" is the standard deviation which is given by Equation 6.18. In this equation d is the number of data. Y in this equation is the observed Log N and $\hat{Y}$ is the predicted Log N.

$$s = \left\{ \frac{\sum_{i=1}^{d}\left(Y_i - \hat{Y}_i\right)^2}{d-2} \right\}^{\frac{1}{2}}$$ (6.18)

As an example, the fatigue line resulted from the BOEF test will be analyzed in this section. The BOEF fatigue line parameters are shown in Figure 6.20, whereas 'n' is -5.2303 and 'Log a' is 17.192 (ε in μm/m). The 'n' parameter of the fatigue lines at different probabilities is the same as the original value, which is -5.2303. Meanwhile the 'Log a' parameter of the fatigue lines at different probabilities, named as Log a', are determined using Equation 6.19 and Equation 6.20.

For N_P less than 0.5 ($N_{P(\alpha/2)}$):

$$Log\,a' = Log\,a - t\,s \sqrt{\left(\dfrac{\sum X_i}{d\sum\left(X_i-\overline{X}\right)^2}\right)} \qquad (6.19)$$

For N_P more than 0.5 ($N_{P(1-\alpha/2)}$):

$$Log\,a' = Log\,a + t\,s \sqrt{\left(\dfrac{\sum X_i}{d\sum\left(X_i-\overline{X}\right)^2}\right)} \qquad (6.20)$$

By increasing the probability of failure from 0.1 to 0.9 with steps of 0.1, the Log a′ of the fatigue lines at those probability values are determined. The recapitulation of the fatigue parameters Log a′ and n is shown in Table 6.8. Thus, it can be said that the Log a′ values in this table are the values of Log a which belong to a certain reliability level (for example, $P_{0.1}$). The fatigue lines that are valid for a certain reliability level are presented in Figure 6.20.

Table 6.8. Fatigue parameter, n and Log a′ of BOEF

	n	Log a′
$Y_{NP0.1}$	-5.2303	16.940
$Y_{NP0.2}$	-5.2303	17.041
$Y_{NP0.3}$	-5.2303	17.102
$Y_{NP0.4}$	-5.2303	17.149
$Y_{NP0.5}$	**-5.2303**	**17.192**
$Y_{NP0.6}$	-5.2303	17.235
$Y_{NP0.7}$	-5.2303	17.282
$Y_{NP0.8}$	-5.2303	17.343
$Y_{NP0.9}$	-5.2303	17.444
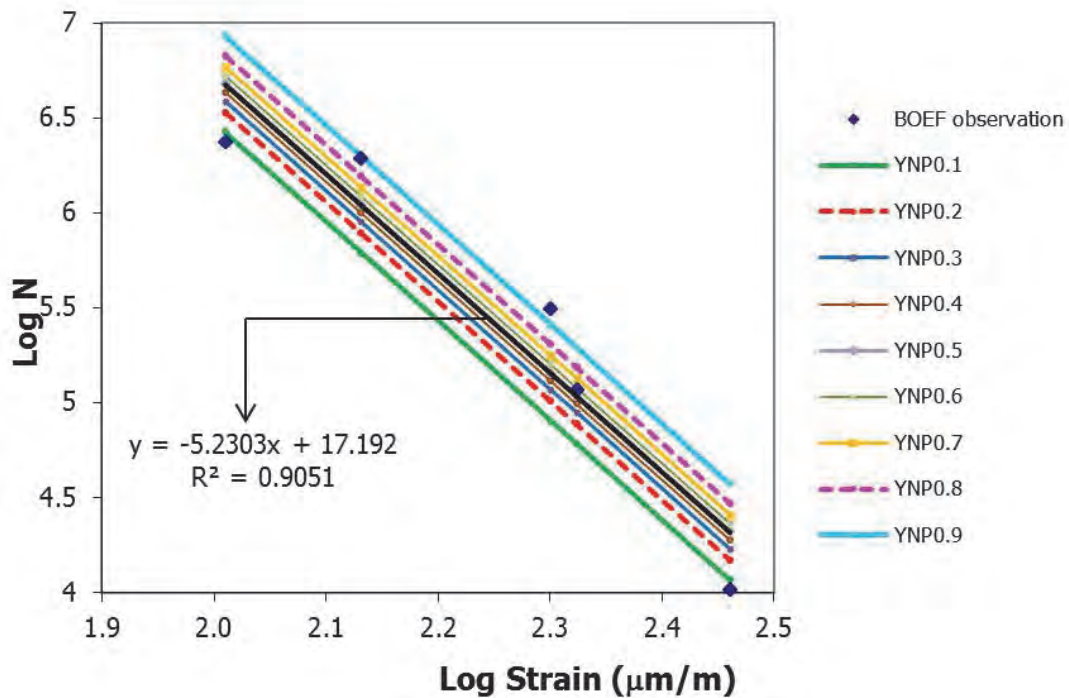
Figure 6.20. Probability of fatigue failure of GAC 40/60 as determined with the BOEF test at 5°C and 8Hz

In Figure 6.20, YNPi represents the fatigue relation which can be used to determine the number of load repetitions to failure with a probability of failure of i.

6.5. Determining fatigue life at a probability of failure level of 20%

In this sub-chapter the calculations made to determine the number of load repetitions to failure at a probability level of 20% are presented as an example. This is done to make the reader familiar with the various steps that needed to be undertaken to allow such analyses to be made. There is no specific reason for taking the 20% probability of failure results as an example. Also the results obtained at other probability levels could have been used for this purpose.

6.5.1. Stiffness during Lintrack loading

During the Lintrack tests, the pavement temperature was not constant due to the fact that on the test site there was no temperature controller. To compensate that shortcoming, the pavement was covered with a mobile hall that protected the pavement from direct exposure to sun and rain. Thus, he ambient air temperature is the only factor that influenced the pavement temperature.

The daily air temperature data during the Lintrack tests were obtained from the KNMI (Koninklijk Netherlands Meteorologisch Instituut or The Royal Dutch Meteorological Institute) database. These temperature data were used to determine the stiffness of the asphalt layer. The stiffness values were calculated using equation 6.21 which gives the stiffness at a frequency of 8 Hz.

$$S_{mix} = 0.0289T^3 + 6.3815T^2 - 857.27T + 24189 \qquad (6.21)$$

where S_{mix} is the stiffness (MPa) and T is the temperature (°C).

6.5.2. Strain at the bottom layer of Lintrack sections

The strain at the bottom of the asphalt layer was determined using a relationship between the stiffness and the strain at the bottom of the layer. These relations were derived from BISAR simulations made for Lintrack section I, VA and VB. The input data for the BISAR simulations are shown in Table 6.9.

Table 6.9. The inputs of the BISAR simulation

	Section I	Section VA	Section VB
Wheel load	75 kN	75 kN	50 kN
AC Thickness	0.15 m	0.08 m	0.08 m
The load area**	circle with a radius of 0.165 m.	circle with a radius of 0.165 m.	circle with a radius of 0.165 m.
Subgrade stiffness***	160 MPa	160 MPa	160 MPa
Poisson's ratio all layer	0.35	0.35	0.35
AC Stiffness	In the simulation six asphalt mixture stiffness values were used ranging from 1000 to 11,000 MPa with the increment of 2000 MPa.		

** Corresponding with the gross tyre pavement contact area
*** back calculated from FWD measurements Bouman [18].

The relation between the mix stiffness and the calculated strain at the bottom of the asphalt layer was best represented by a power model which is shown in Equation 6.26, 6.27 and 6.28 for section I, VA and V respectively.

Section I

$$\varepsilon = 55089 S_{mix}^{-0.6133} \qquad (6.22)$$

Section VA

$$\varepsilon = 12869 S_{mix}^{-0.3899} \qquad (6.23)$$

Section VB

$$\varepsilon = 8580 S_{mix}^{-0.3899}$$ (6.24)

Where:

ε   :   strain μm/m
S_{mix} :   stiffness (MPa)

6.5.3. Cumulative damage analysis of the Lintrack sections using the 4PB fatigue results

As mentioned before, the cumulative amount of damage was calculated using Equation 6.25.

$$\sum D = \sum_{i=1}^{m} \frac{n_i}{N_i}$$ (6.25)

Where ni is the number of load repetitions applied during period i and Ni is the allowable number of load repetitions for that period. m indicates the number of loading periods.

During the Lintrack tests there were rest periods in between the successive loadings. It is well known that due to the visco-elastic behaviour of AC, this condition -especially when the temperatures are high- could allow micro cracks to heal. Therefore, the number of allowable load repetitions that is calculated from laboratory test results is usually multiplied with a "healing factor" (H). H is the correction factor for healing and the values reported in the literature are ranging from 1 to 20. The value depends on the amount and type of bitumen used in the mixture [19] as well as the loading time to rest period ratio. In the Netherlands this factor is commonly taken as H = 4 for GAC mixtures [4].

In Chapters 3.3.7 and 4.1.4, the experimental program and results of healing tests performed on the GAC *mastic* have been presented. These results came from fracture-healing-refracture tests and did not consider the healing of micro damage. The tests also did not include healing that might occur at the aggregate-mastic interface. This, however, is an important issue since examination of the crack interfaces showed that cracking in GAC is predominantly adhesive cracking. Because of all these unknowns, it was decided to set the healing factor initially at H = 1.

Besides this correction, another correction factor called "lateral wander" (LW) has to be taken into account. This correction considers the fact that the real traffic loads are not always applied on the same transverse location. LW was calculated using the actual lateral wander during the Lintrack tests and the lateral wander reduction chart of RHED [7]. This chart shows that the

magnitude of LW depends on the thickness and stiffness of the top layer as well as the stiffness of the subgrade (See Figure 6.21).
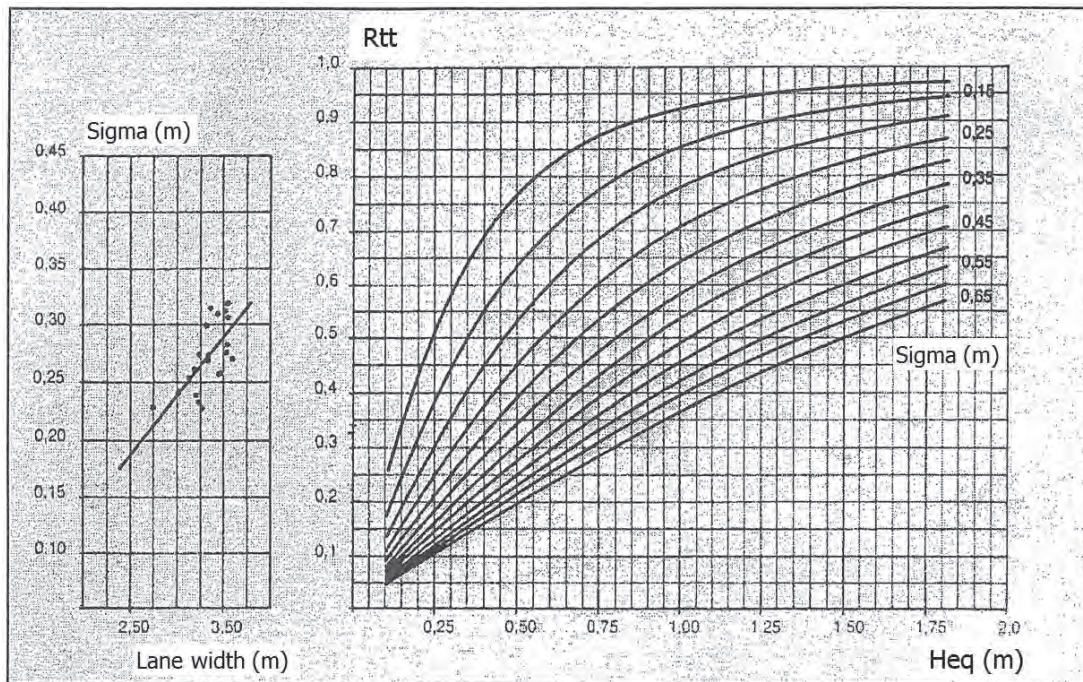
Figure 6.21. Reduction factor for lateral wander (RHED)

During the Lintrack tests the loads were applied using a certain lateral wander pattern. This lateral wander pattern followed a Gaussian distribution with a standard deviation of σ = 0.30 m [4, 6] (see Figure 6.22). With the thickness and the value of the lateral wander correction (Table 6.10), a relation between the lateral wander and the stiffness for each section could be determined (see Figure 6.23.a and b). These functions are shown in Equation 6.26 for section I and 6.27 for section VA and VB.
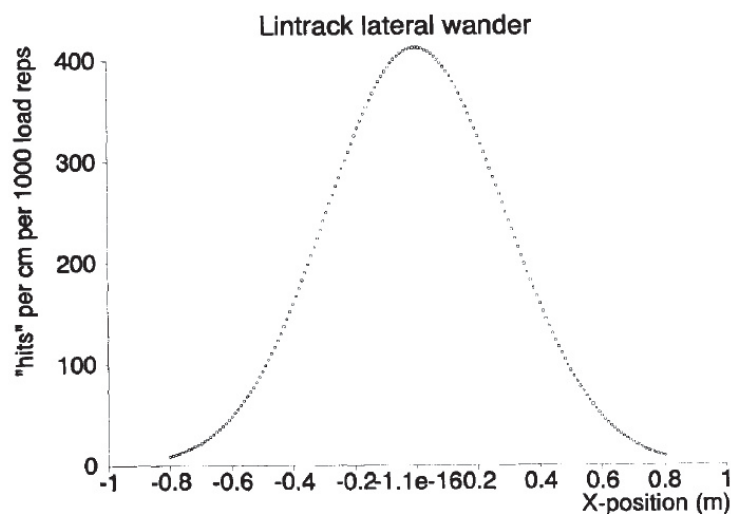
Figure 6.22. Truncated Gausian distribution of Lintrack lateral wander (after Groenendijk)

Table 6.10. Lateral wander for Lintrack section I, VA and VB at several stifness value

Lin-track section	lane width m	σ	T C	f Hz	S_{mix} MPa	h_i m	$S_{subgrade}$ MPa	h_e m	R_{tt}	LW $=1/R_{tt}$
I	4	0.3	0	8	23586	0.15	160	0.71	0.52	1.92
			5		20032			0.67	0.5	2.00
			10		16478			0.63	0.475	2.11
			15		12426			0.57	0.44	2.27
			20		10313			0.54	0.42	2.38
			25		6930			0.47	0.375	2.67
			30		5053			0.42	0.35	2.86
VA	4	0.3	0	8	23586	0.08	160	0.38	0.32	3.13
&			5		20032			0.36	0.29	3.45
VB			10		16478			0.34	0.275	3.64
			15		12426			0.31	0.255	3.92
			20		10313			0.29	0.24	4.17
			25		6930			0.25	0.21	4.76
			30		5053			0.23	0.19	5.26

$y = 26.724x^{-0.262}$
$R^2 = 0.9992$

(a) Section I

Figure 6.23. Lintrack lateral wander as a function of Smix.
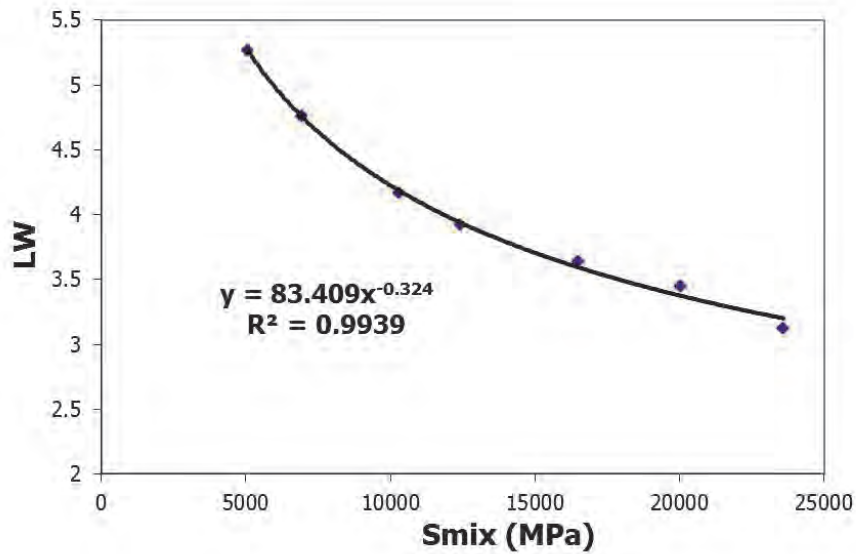
(b) Section VA and VB

Figure 6.23. Lintrack lateral wander as a function of Smix.

LW for section I:

$$LW = 26.724 \, S_{mix}^{-0.262} \qquad (6.26)$$

LW for section VA and VB:

$$LW = 83.409 \, S_{mix}^{-0.324} \qquad (6.27)$$

When the healing and the lateral wander correction factors mentioned are known, the Ni-field could be calculated by means of Equation 6.28 [6].

$$Nfi_{field} = Nfi_{lab} * H * LW \qquad (6.28)$$

Where:
H   :   healing correction = 1
LW   :   lateral wander correction

Table 6.11, 6.12 and 6.13 show the ni/Ni calculation of model $N_{P0.2}$ for section I, VA and VB respectively. In order to precisely calculate the cumulative damage ratio, daily loading data applied during testing of each Lintrack section and daily temperature were used. The daily loading data are listed in the third column of those tables. The tables do not give the results for each and every day. These data can, however, be made available on request.

Table 6.11. Cumulative damage analysis of Lintrack **section I** using 4PB model $N_{P0.2}$

(1)	(2)	(3)	(4)	(5)	(6)	(7)	(8)	(9)	(10)	(11)	(12)	(13)	(14)
D	T	ni	*10³	Smix	ε	n	Log a	Nfi,lab	H	LW	Nfi-field	n_i/Nf_i	$\Sigma n_i/Nf_i$
	°C	cycles	cycles	Mpa	μm/m			cycles			cycles		
1	7.2	8000	8	18,358	134	-4.70	14.98	96,031	1	2.04	195,970	0.04	0.04
2	6.6	8000	16	18,817	132	-4.74	15.07	103,880	1	2.03	210,620	0.04	0.08
3	6.4	8000	24	18,971	131	-4.76	15.10	106,646	1	2.02	215,766	0.04	0.12
4	5.5	8000	32	19,672	128	-4.82	15.25	120,100	1	2.00	240,689	0.03	0.15
5	4.8	8000	40	20,224	126	-4.58	14.57	87,167	1	1.99	173,426	0.05	0.20
6	2.1	0	40	22,417	118	-5.08	15.81	189,869	1	1.94	367,708	0.00	0.20
7	2.2	0	40	22,334	119	-5.07	15.79	187,287	1	1.94	363,060	0.00	0.20
8	7	6000	46	18,511	133	-4.72	15.01	98,575	1	2.04	200,726	0.03	0.23
9	5.3	6000	52	19,829	128	-4.58	14.57	82,462	1	2.00	164,916	0.04	0.26
10	2.7	6000	58	21,921	120	-5.03	15.71	174,930	1	1.95	340,767	0.02	0.28
⋮	⋮	⋮	⋮	⋮	⋮	⋮	⋮	⋮	⋮	⋮	⋮	⋮	⋮
1021	17.1	0	3976	11,540	178	-4.06	13.58	27,327	1	2.30	62,979	0.00	36.27
1022	16.1	0	3976	12,162	172	-4.12	13.71	30,970	1	2.27	70,400	0.00	36.27
1023	15.9	24000	4000	12,288	171	-4.13	13.73	31,756	1	2.27	71,992	0.33	36.60

(1) Day number; (2) Temperature; (3) Daily loading; (4) Cumulative loading; (5) Stiffnesss; (6) Strain at the bottom of layer 1; (7) Fatigue model parameter, n; (8) Fatigue model parameter, Log a; (9) Nfi,lab : Nfi using 4PB model $N_{P0.2}$; (10) Healing correction; (11) Lateral wander correction; (12) Nfi, field; (13) Damage; (14) Cumulative Damage.

Table 6.12. Cumulative damage analysis of Lintrack **section VA** using 4PB model $N_{P0.2.}$

(1)	(2)	(3)	(4)	(5)	(6)	(7)	(8)	(9)	(10)	(11)	(12)	(13)	(14)
D	T	ni	*10³	Smix	ε	n	Log a	Nfi,lab	H	LW	Nfi-field	n_i/Nf_i	$\Sigma n_i/Nf_i$
	°C	cycles	cycles	Mpa	μm/m			cycles			cycles		
1	17.6	5400	5.4	11,235	339.02	-4.04	13.52	2,024	1	4.06	8,223	0.66	0.66
2	17.8	4600	10	11,114	340.45	-4.02	13.49	2,007	1	4.08	8,183	0.56	1.22
3	18.6	3900	13.9	10,637	346.32	-3.98	13.40	1,941	1	4.14	8,027	0.49	1.70
4	20.8	7300	21.2	9,379	363.75	-3.86	13.14	1,763	1	4.31	7,594	0.96	2.67
5	22.2	3900	25.1	8,619	375.94	-3.79	12.98	1,652	1	4.43	7,314	0.53	3.20
6	22.2	0	25.1	8,619	375.94	-3.79	12.98	1,652	1	4.43	7,314	0.00	3.20
7	18.9	0	25.1	10,461	348.59	-3.96	13.36	1,917	1	4.16	7,971	0.00	3.20
8	16.9	0	25.1	11,663	334.11	-4.08	13.61	2,082	1	4.01	8,357	0.00	3.20
9	17.8	0	25.1	11,114	340.45	-4.02	13.49	2,007	1	4.08	8,183	0.00	3.20
10	18.6	0	25.1	10,637	346.32	-3.98	13.40	1,941	1	4.14	8,027	0.00	3.20
⋮	⋮	⋮	⋮	⋮	⋮	⋮	⋮	⋮	⋮	⋮	⋮	⋮	⋮
206	2.5	5100	636.7	22,086	260.48	-5.05	15.74	3,493	1	3.26	11,400	0.45	59.24
207	3	7800	644.5	21,675	262.39	-5.01	15.66	3,434	1	3.28	11,276	0.69	59.93
208	2.9	5500	650	21,757	262.01	-5.02	15.67	3,446	1	3.28	11,302	0.49	60.42

Table 6.13. Cumulative damage analysis of Lintrack **section VB** using 4PB model $N_{P0.2}$

(1)	(2)	(3)	(4)	(5)	(6)	(7)	(8)	(9)	(10)	(11)	(12)	(13)	(14)
D	T	ni	*10³	Smix	ε	n	Log a	Nfi,lab	H	LW	Nfi-field	n_i/Nf_i	$\Sigma n_i/Nf_i$
	°C	cycles	cycles	Mpa	μm/m			cycles			cycles		
1	18.6	4656	4.656	10,637	230.90	-3.98	13.40	9,743	1	4.14	40,291	0.12	0.12
2	16.2	0	4.656	12,099	219.60	-4.12	13.69	11,358	1	3.97	45,051	0.00	0.12
3	15.8	0	4.656	12,351	217.84	-4.14	13.75	11,649	1	3.94	45,897	0.00	0.12
4	15.9	13644	18.3	12,288	218.28	-4.13	13.73	11,576	1	3.95	45,686	0.30	0.41
5	15.7	22070	40.37	12,415	217.40	-4.15	13.76	11,723	1	3.93	46,112	0.48	0.89
6	15.6	17840	58.21	12,478	216.97	-4.15	13.77	11,797	1	3.93	46,327	0.39	1.28
7	15.4	15160	73.37	12,606	216.11	-4.16	13.80	11,947	1	3.91	46,761	0.32	1.60
8	15.7	14874	88.24	12,415	217.40	-4.15	13.76	11,723	1	3.93	46,112	0.32	1.92
9	13.7	0	88.24	13,716	209.11	-4.27	14.03	13,294	1	3.81	50,629	0.00	1.92
10	13.7	0	88.24	13,716	209.11	-4.27	14.03	13,294	1	3.81	50,629	0.00	1.92
⋮	⋮	⋮	⋮	⋮	⋮	⋮	⋮	⋮	⋮	⋮	⋮	⋮	⋮
524	3.7	22950	1.680	21,106	176.77	-4.96	15.54	25,017	1	3.31	82,859	0.28	27.22
525	4.1	22200	1.703	20,783	177.83	-4.93	15.47	24,378	1	3.33	81,147	0.27	27.49
526	4.6	9500	1.712	20,383	179.19	-4.58	14.57	17,332	1	3.35	58,057	0.16	27.65

(1) Day number; (2) Temperature; (3) Daily loading; (4) Cumulative loading; (5) Stiffnesss; (6) Strain at the bottom of layer 1; (7) Fatigue model parameter, n; (8) Fatigue model parameter, Log a; (9) Nfi,lab : Nfi using 4PB model $N_{P0.2}$; (10) Healing correction; (11) Lateral wander correction; (12) Nfi field; (13) Damage; (14) Cumulative Damage.

6.5.4. Cumulative damage analysis of the Lintrack sections using the BOEF fatigue results

Similar calculations were also carried out using the BOEF fatigue lines. The determination of n and Log a is explained in subchapter 6.3.2. Equations 6.26 and 6.27 are used to determine the lateral wander correction, LW.

The results of the cumulative damage calculations are presented in Tables 6.14, 6.15 and 6.16 for Section I, Section VA and Section VB respectively. Figures 6.28, 6.29 and 6.30 present the result in a graphical form. Furthermore, a recapitulation of the important values is given in Table 6.17.

Table 6.14. Cumulative damage analysis of Lintrack **section I** using BOEF model $N_{P0.2}$

(1)	(2)	(3)	(4)	(5)	(6)	(7)	(8)	(9)	(10)	(11)	(12)	(13)	(14)
D	T	ni	*10³	Smix	ε	n	Log a	Nfi,lab	H	LW	Nfi-field	n_i/Nf_i	$\Sigma n_i/Nf_i$
	°C	cycles	cycles	Mpa	µm/m			cycles			cycles		
1	7.2	8000	8	18,358	133.68	5.03	-13.72	581,940	1	2.05	1,193,404	0.0067	0.01
2	6.6	8000	16	18,817	131.67	5.07	-13.87	654,822	1	2.04	1,334,222	0.0060	0.01
3	6.4	8000	24	18,971	131.01	5.09	-13.92	681,083	1	2.03	1,384,772	0.0058	0.02
4	5.5	8000	32	19,672	128.13	5.15	-14.14	812,840	1	2.01	1,637,066	0.0049	0.02
5	4.8	8000	40	20,224	125.97	5.23	-14.34	1,136,517	1	2.00	2,272,434	0.0035	0.03
6	2.1	0	40	22,417	118.26	5.39	-14.97	1,582,400	1	1.95	3,079,931	0	0.03
7	2.2	0	40	22,334	118.53	5.38	-14.94	1,551,783	1	1.95	3,023,269	0	0.03
8	7	6000	46	18,511	133.00	5.04	-13.77	605,288	1	2.05	1,238,604	0.0048	0.03
9	5.3	6000	52	19,829	127.51	5.23	-14.34	1,066,789	1	2.01	2,144,054	0.0028	0.03
10	2.7	6000	58	21,921	119.90	5.35	-14.82	1,407,280	1	1.96	2,755,146	0.0022	0.04
⋮	⋮	⋮	⋮	⋮	⋮	⋮	⋮	⋮	⋮	⋮	⋮	⋮	⋮
1021	17.1	0	3,976	11,540	177.71	4.26	-11.05	83,573	1	2.32	193,509	0	10.15
1022	16.1	0	3,976	12,162	172.08	4.34	-11.34	101,484	1	2.28	231,778	0	10.15
1023	15.9	24000	4,000	12,288	171.00	4.36	-11.39	105,512	1	2.28	240,327	0.0999	10.25

(1) Day number; (2) Temperature; (3) Daily loading; (4) Cumulative loading; (5) Stiffnesss; (6) Strain at the bottom of layer 1; (7) Fatigue model parameter, n; (8) Fatigue model parameter, Log a; (9) Nfi,lab : Nfi using BOEF model $N_{P0.2}$; (10) Healing correction; (11) Lateral wander correction; (12) Nfi field; (13) Damage; (14) Cumulative Damage.

Table 6.15. Cumulative damage analysis of Lintrack **section VA** using BOEF model $N_{P0.2.}$

(1)	(2)	(3)	(4)	(5)	(6)	(7)	(8)	(9)	(10)	(11)	(12)	(13)	(14)
D	T	ni	*10³	Smix	ε	n	Log a	Nfi,lab	H	LW	Nfi-field	n_i/Nf_i	$\Sigma n_i/Nf_i$
	°C	cycles	cycles	Mpa	µm/m			cycles			cycles		
1	17.6	5400	5.4	11,235	339.02	4.22	-10.90	5,336	1	4.06	21,679	0.25	0.25
2	17.8	4600	10	11,114	340.45	4.20	-10.85	5,241	1	4.08	21,368	0.22	0.46
3	18.6	3900	13.9	10,637	346.32	4.13	-10.61	4,880	1	4.14	20,182	0.19	0.66
4	20.8	7300	21.2	9,379	363.75	3.94	-9.96	4,027	1	4.31	17,347	0.42	1.08
5	22.2	3900	25.1	8,619	375.94	3.82	-9.53	3,576	1	4.43	15,831	0.25	1.32
6	22.2	0	25.1	8,619	375.94	3.82	-9.53	3,576	1	4.43	15,831	0.00	1.32
7	18.9	0	25.1	10,461	348.59	4.11	-10.52	4,752	1	4.16	19,760	0.00	1.32
8	16.9	0	25.1	11,663	334.11	4.28	-11.11	5,684	1	4.01	22,813	0.00	1.32
9	17.8	0	25.1	11,114	340.45	4.20	-10.85	5,241	1	4.08	21,368	0.00	1.32
10	18.6	0	25.1	10,637	346.32	4.13	-10.61	4,880	1	4.14	20,182	0.00	1.32
⋮	⋮	⋮	⋮	⋮	⋮	⋮	⋮	⋮	⋮	⋮	⋮	⋮	⋮
206	2.5	5100	636.7	22,086	260.48	5.36	-14.87	22,273	1	3.26	72,693	0.07	12.16
207	3	7800	644.5	21,675	262.39	5.33	-14.75	21,217	1	3.28	69,670	0.11	12.27
208	2.9	5500	650	21,757	262.01	5.33	-14.78	21,424	1	3.28	70,264	0.08	12.35

Table 6.16. Cumulative damage analysis of Lintrack **section VB** using BOEF model $N_{P0.2}$

| (1)	(2)	(3)	(4)	(5)	(6)	(7)	(8)	(9)	(10)	(11)	(12)	(13)	(14)
D	T	ni	$*10^3$	Smix	ε	n	Log a	Nfi,lab	H	LW	Nfi-field	n_i/Nf_i	$\Sigma n_i/Nf_i$
	°C	cycles	cycles	Mpa	μm/m			cycles			cycles		
1	18.6	4656	4.656	10,637	231	4.13	-10.61	26,061	1	4.14	107,773	0.043	0.04
2	16.2	0	4.656	12,099	220	4.33	-11.31	35,082	1	3.97	139,152	0	0.04
3	15.8	0	4.656	12,351	218	4.37	-11.42	36,874	1	3.94	145,286	0	0.04
4	15.9	13644	18.3	12,288	218	4.36	-11.39	36,418	1	3.95	143,726	0.095	0.14
5	15.7	22070	40.37	12,415	217	4.37	-11.45	37,337	1	3.93	146,865	0.150	0.29
6	15.6	17840	58.21	12,478	217	4.38	-11.48	37,806	1	3.93	148,462	0.120	0.41
7	15.4	15160	73.37	12,606	216	4.40	-11.53	38,761	1	3.91	151,711	0.100	0.51
8	15.7	14874	88.24	12,415	217	4.37	-11.45	37,337	1	3.93	146,865	0.101	0.61
9	13.7	0	88.24	13,716	209	4.54	-12.01	47,946	1	3.81	182,597	0	0.61
10	13.7	0	88.24	13,716	209	4.54	-12.01	47,946	1	3.81	182,597	0	0.61
⋮	⋮	⋮	⋮	⋮	⋮	⋮	⋮	⋮	⋮	⋮	⋮	⋮	⋮
524	3.7	22950	1.680	21,106	177	5.28	-14.58	168,503	1	3.31	558,102	0.041	5.97
525	4.1	22200	1.703	20,783	178	5.25	-14.49	160,265	1	3.33	533,472	0.042	6.01
526	4.6	9500	1.712	20,383	179	5.23	-14.34	179,975	1	3.35	602,865	0.016	6.02

(1) Day number; (2) Temperature; (3) Daily loading; (4) Cumulative loading; (5) Stiffnesss; (6) Strain at the bottom of layer 1; (7) Fatigue model parameter, n; (8) Fatigue model parameter, Log a; (9) Nfi,lab : Nfi using BOEF model $N_{P0.2}$; (10) Healing correction; (11) Lateral wander correction; (12) Nfi field; (13) Damage; (14) Cumulative Damage.

6.5.5. 4PB and BOEF based predictions of the number of load repetitions to failure at a probability of failure of 20% versus surface cracking.

The cumulative damage $\Sigma ni/NFi$ as a function of the cumulative load repetitions for sections I, VA and VB are shown in Figures 6.24 a, b and c. The cumulative damage is compared with the development of the percentage cracked area. From the graphs, it can be seen that the cumulative damage calculated using the BOEF fatigue lines test are always lower than the cumulative damages calculated with the 4PB test fatigue lines.

One could hypothesize that the % area which shows cracking at a certain number of load repetitions equals the probability of failure at that number. The figures hereafter show that this is not the case. It should be mentioned, however, that such comparisons are difficult to make because the estimation of the "% cracked area" depends on the definitions used. Nevertheless, one can conclude that the number of load repetitions at which ni/Ni = 1 (at a probability of failure level of 20%) does not correspond with the number of load repetitions at which 20% of the area is cracked.
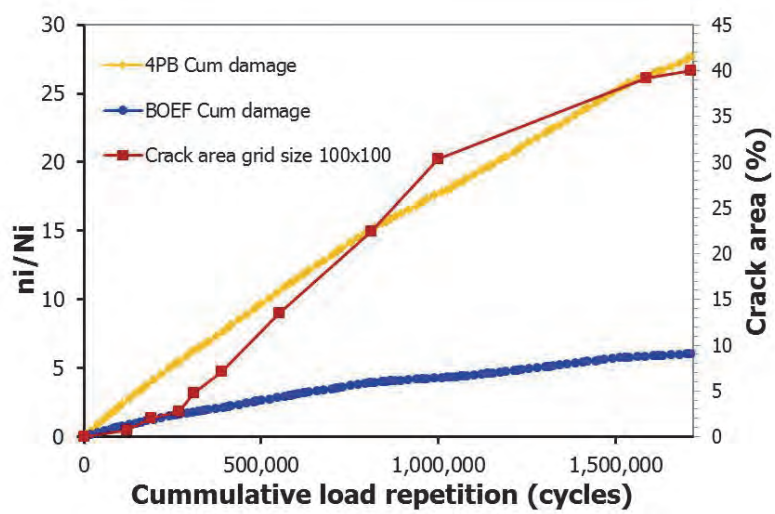
(a) Section I
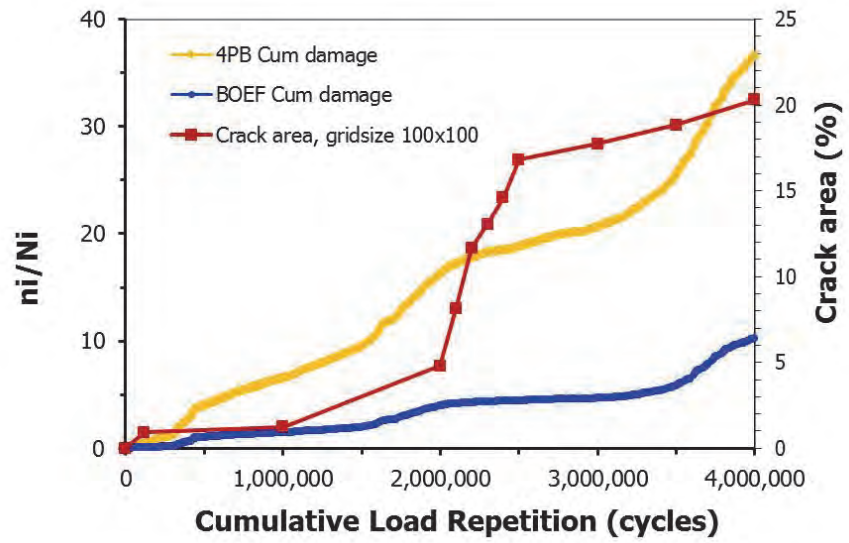
(b) Section VA
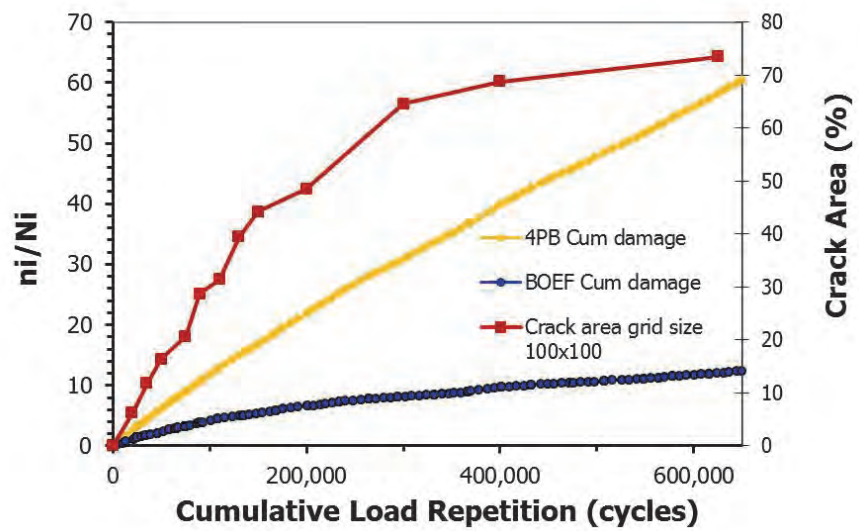
(c) Section VB

Figure 6.24. Development of cumulative damage and cracked area in Lintrack

6.5.6. Conclusions

From the analyses given in the previous sub chapter it can be concluded that using the BOEF fatigue relationship results in a much slower development of the n/N ratio than when the 4PB fatigue relationships are used. As mentioned earlier, the BOEF test is believed to be a better representation of reality, because the tested beam is fully supported just like a real pavement layer is and because the load signal is much more realistic than was used in the 4PB constant displacement tests. Therefore, it was decided to perform additional analyses only by using the BOEF fatigue relationship.

6.6. Cumulative damage analyses at different probability of failure levels

The analysis described in section 6.5 was performed to determine the number of load repetitions to a probability of failure of 20%. The same calculations were repeated to obtain the number of load repetitions to failure at several probability of failure levels. As mentioned in section 6.5.6 these calculations were only done using the BOEF fatigue relationships. The results are shown in Table 6.17.

Since the number of load repetitions to obtain a Miner's ratio of 1 is known for each probability of failure level, a curve showing the lifetime distribution could be constructed for each section. Assuming that the distribution is normal, this curve is developed using the normal distribution function in Excel. Figure 6.25 a, b and c show these distributions for section I, VA and VB respectively.

Table 6.17. Number of load cycles at $\Sigma ni/Nfi=1$

Probability	N at $\Sigma ni/Nfi$ BOEF = 1		
	Section I	Section VA	Section VB
NP0.1	418,000	16,250	108,370
NP0.2	466,500	19,850	147,930
NP0.3	618,500	22,350	176,070
NP0.4	749,500	24,430	198,370
NP0.5	929,000	25,100	218,920
NP0.6	1,096,000	29,700	257,040
NP0.7	1,288,000	34,100	292,690
NP0.8	1,496,000	39,000	351,020
NP0.9	1,624,000	52,100	479,108

Figure 6.25 shows the distribution of the probability where the cumulative area under the bell curve is equal to 1.

(a) Section I
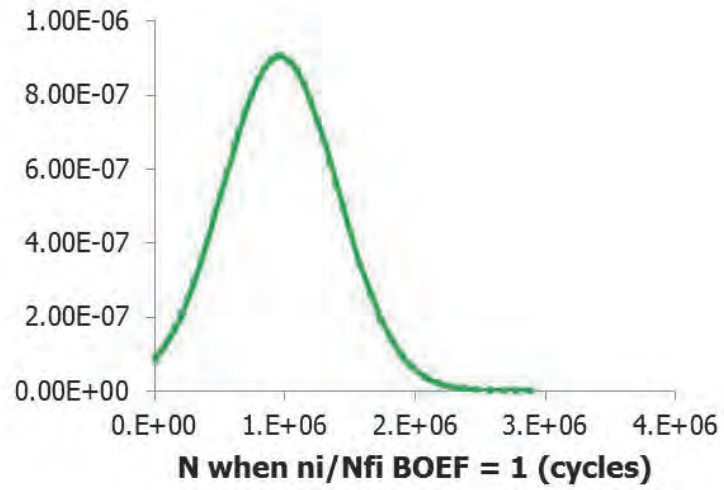
(b) Section VA
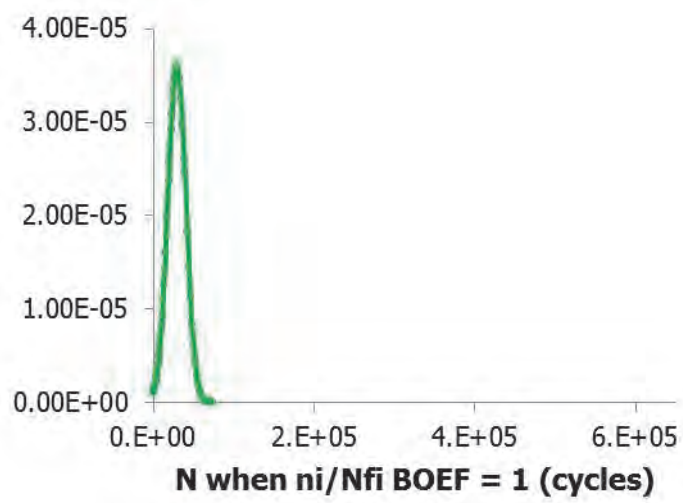
(c) Section VB

Figure 6.25. Normal distribution of the predicted number of load cycles to failure based on the BOEF fatigue model for the three Lintrack sections

6.7. Comparison of observed and predicted end of pavement life and comparison with observed amount of cracking and permanent deformation at the end of pavement life

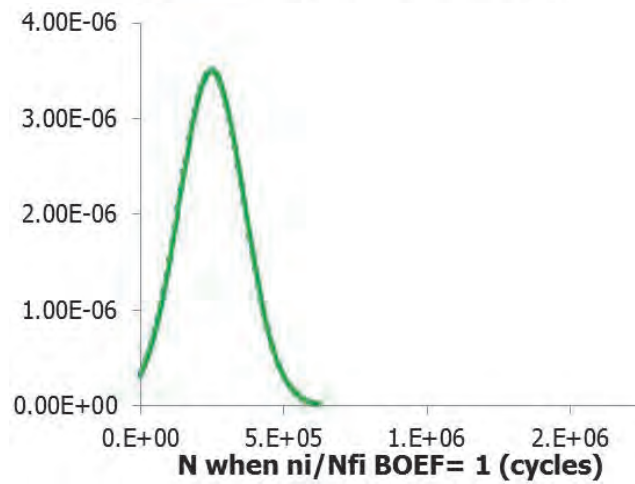The comparison of the fatigue life determined from the back calculated asphalt layer stiffness and the fatigue life using the BOEF fatigue relationships as well as the ratio between those two lifetimes are presented in Table 6.18. It is interesting to note that the difference between both lifetimes is the smallest for the thicker section I. In analysing the differences one has to keep in mind that N_{BOEF} is actually the number of load repetitions to initiation of cracking at the bottom of the layer while $N_{stiffness}$ takes into account damage propagation. This implies that $N_{stiffness}$ should always be higher than N_{BOEF}. The observed differences in the $N_{stiffness}$ / N_{BOEF} ratios of section I and sections VA/VB might, therefore, indicate that crack propagation develops relatively slower in the thinner sections than in the thicker section.

**Table 6.18.** Fatigue life at the probability of failure of 20% and 50%

Section	$N_{P0.2}$			$N_{P0.5}$		
	BOEF	Back-calc stiffness	Ratio $N_{stiffness}/N_{BOEF}$	BOEF	Back-calc stiffness	Ratio $N_{stiffness}/N_{BOEF}$
I	618,000	922,000	1.5	982,000	1,252,000	1.3
VA	17,890	155,400	8.7	28,210	191,100	6.8
VB	157,800	795,800	5.0	252,100	946,800	3.8

Figures 6.26, 6.27 and 6.28 give detailed information about the cumulative distribution curves of N_{BOEF} and N_{stiff} together with the progression in cracked area, crack length and permanent deformation.

In these three figures the red lines show the distribution of the lifetime based on the back-calculated stiffness (observation). Whereas the green lines show the distribution of the predicted number of load cycles to failure based on the BOEF fatigue model (prediction-BOEF). In Figure 6.26.(a), 6.27.(a), and 6.28.(a), the distribution of observed and predicted fatigue life are presented with the development of the crack length over the load cycles for section I, VA and VB respectively. Figure 6.26.(b), 6.27.(b), and 6.28.(b) show the distribution of the observed and predicted fatigue life together with the development of the cracked area (determined using a grid size of 100 x 100 mm) in relation to the number of load cycles. Figure 6.26.(c), 6.27.(c), and 6.28.(c) show the distribution of observed and predicted fatigue life together with the development of the rut depth.
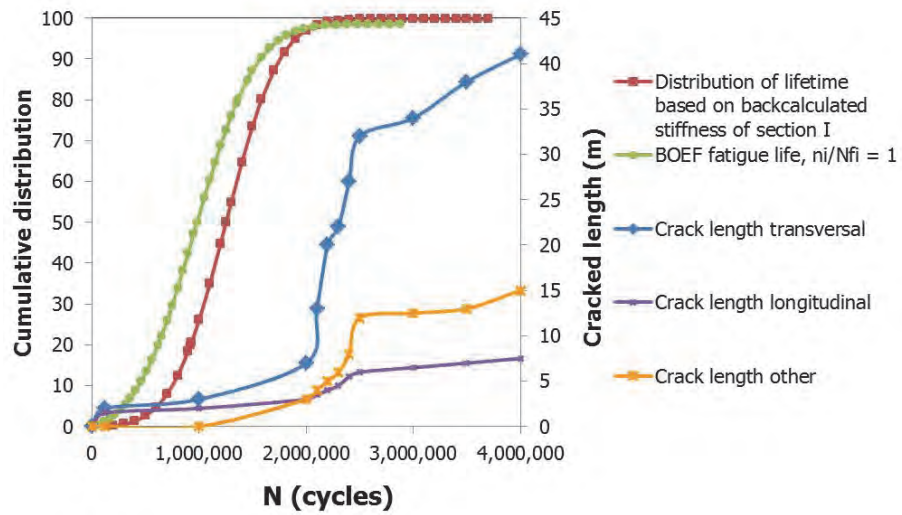
(a)
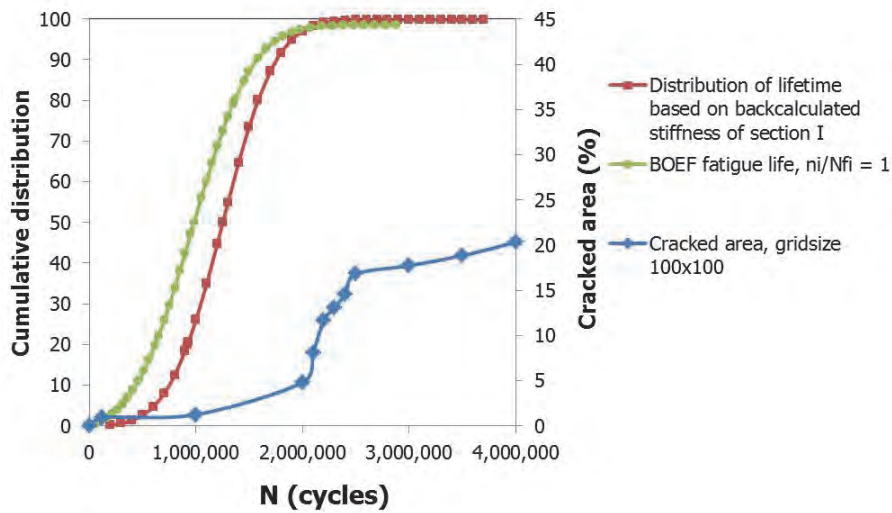
(b)
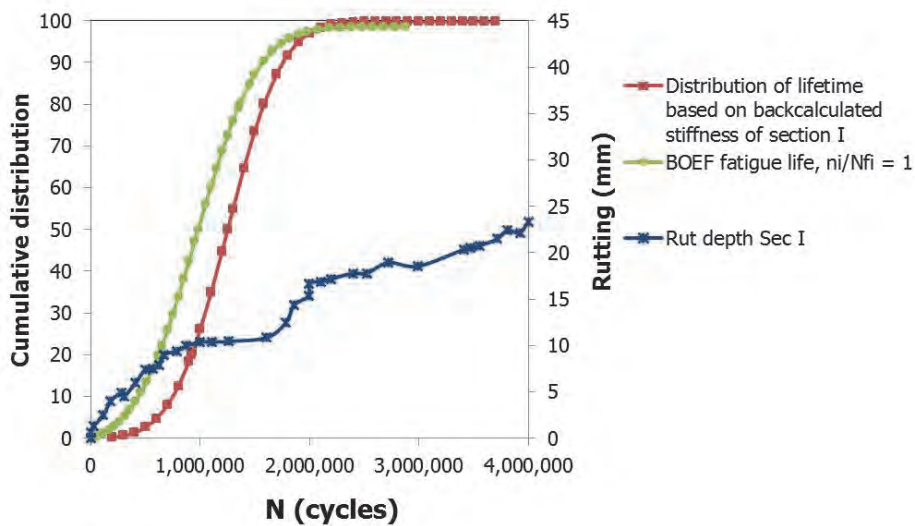
(c)

Figure 6.26. Predicted fatigue lives of Lintrack section I, compared with (a). crack length. (b) cracked area and (c) permanent deformation.

(a)

(b)

(c)

Figure 6.27. Predicted fatigue lives of Lintrack section VA, compared with (a). crack length. (b) cracked area and (c) permanent deformation.

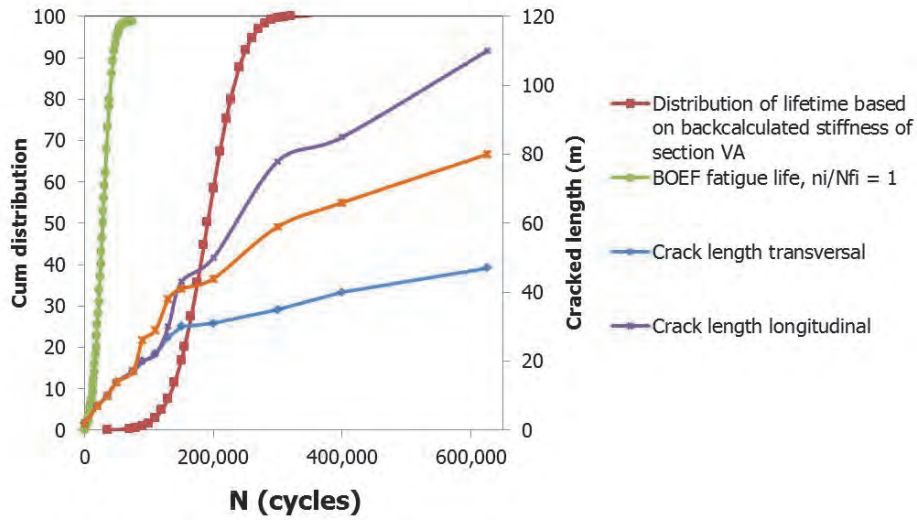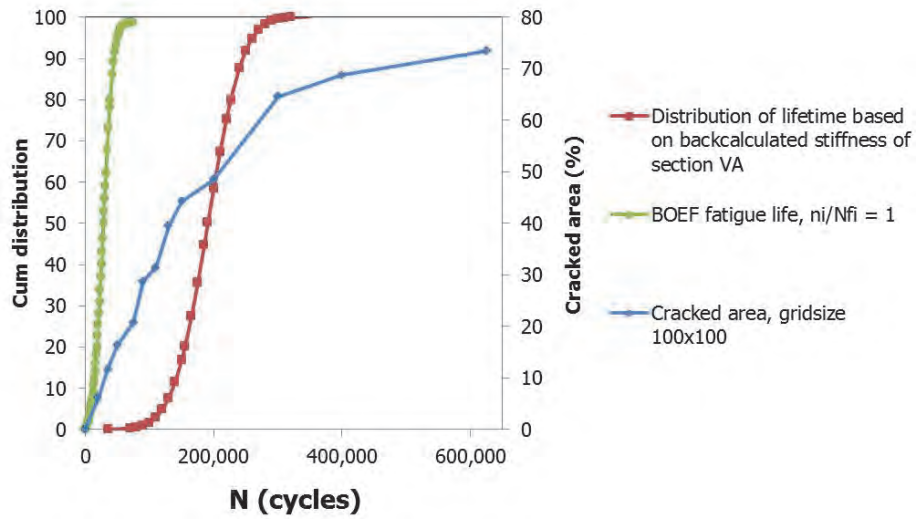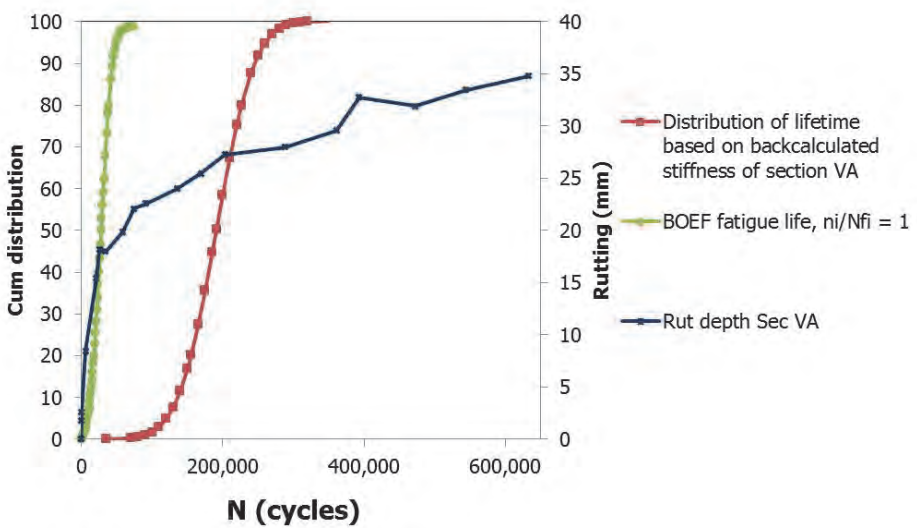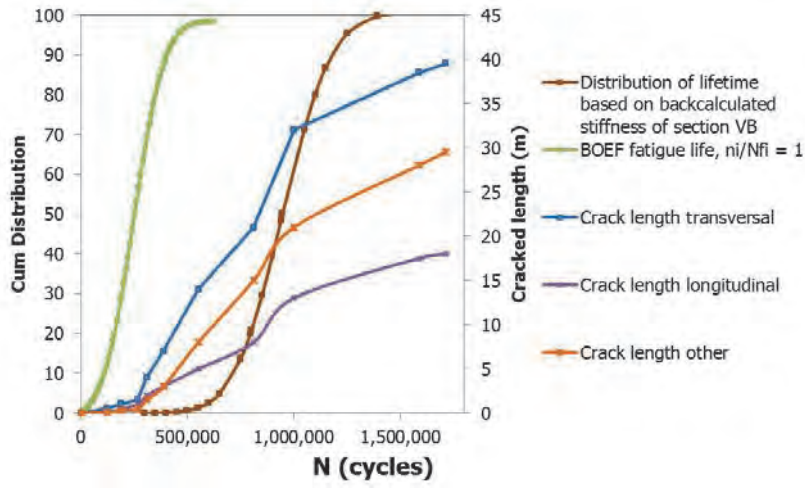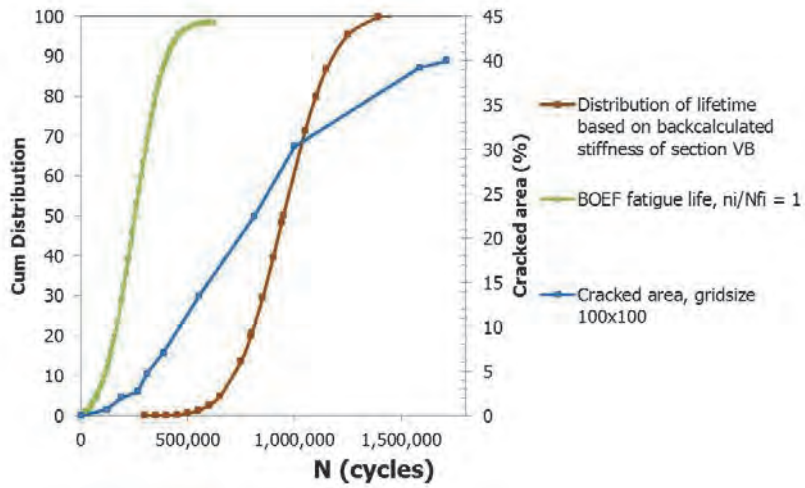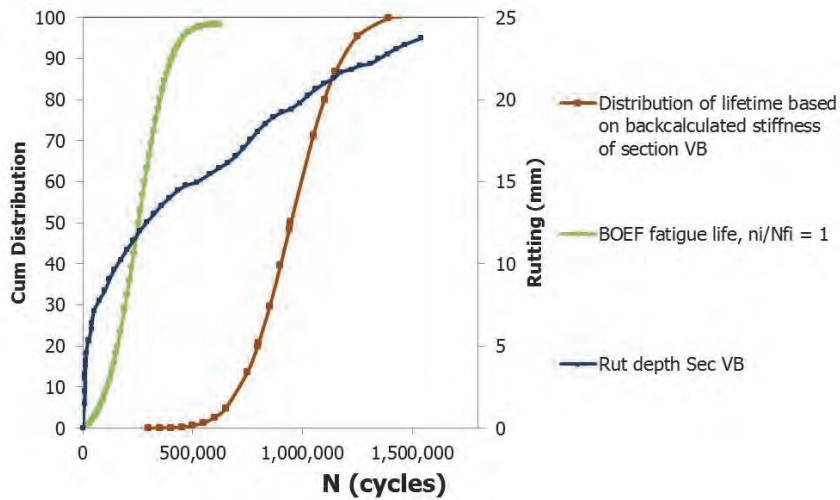**Figure 6.28.** Predicted fatigue lives of Lintrack section VB, compared with (a). crack length. (b) cracked area and (c) permanent deformation.

The amount of crack length, cracked area and permanent deformation at NP0.2 and NP0.5 are recapitulated in Table 6.19. In this table the values of the predicted and observed NP0.2 and NP0.5 are also shown. It is recalled that NP0.2 and NP0.5 were obtained when the pavement reached its fatigue life in terms of the number of load repetitions when the asphalt stiffness has reached half of its initial value at the probability of 20% and 50% respectively. For sections I and VB it appears that the cracked area started to develop at the predicted BOEF NP0.2 values. Also the crack length in sections I and VB are about the same at that number of load repetitions. Different 'cracked area' and 'crack length' values are found for section VA compared to sections I and VB. This is most probably caused by the fact that section VA was severely overloaded.

It is noticed that the observed values of crack length, cracked area and permanent deformation for Section VA are large and are almost the same at the observed NP0.2 and NP0.5. This is indicating that section VA was rapidly deteriorating in terms of back-calculated stiffness which again is pointing to section VA being overloaded.

Table 6.19. Crack length, cracked area and permanent deformation at the predicted and observed pavement life

Section	Predicted/Obser-ved of pavement life at NPx	Crack length transv.	Crack length longit.	Crack length other	Crack ed area	Permanent deformation
	(cycle)	(m)	(m)	(m)	(%)	(mm)
Predicted BOEF (NP0.2)						
I	618,000	2.6	1.8	0.0	1.1	7.9
VA	17,890	6.5	6.5	6.5	5.6	14.0
VB	157,800	0.8	0.3	0.2	1.4	10.0
Observed (NP0.2)						
I	922,000	2.9	2.0	0.0	1.2	10.1
VA	155,400	30.1	43.8	41.3	44.7	24.9
VB	795,800	20.6	7.8	14.6	22.0	18.0
Predicted BOEF (NP0.5)						
I	982,000	3.0	2.0	0.0	1.2	10.3
VA	28,210	8.6	8.6	8.6	9.3	18.1
VB	252,100	1.4	0.9	0.5	2.6	11.9
Observed (NP0.5)						
I	1,252,000	4.0	2.3	0.8	2.2	10.4
VA	191,100	30.8	48.8	43.5	47.8	26.7
VB	946,800	28.9	11.6	19.3	28.1	19.4

In the following subsections more comments will be made about a possible relationship between cracking and permanent deformation.

6.7.1. Crack length

The crack length was classified as the length of the crack in the transversal, longitudinal and other directions.
- Longitudinal cracks have an angle deviating less than ±20 degrees from the Y-axis (Y-axis is in the direction of travel).
- Transversal cracks deviate less than ±20 degrees from the X direction.
- Other cracks refer to the remaining cracks.

Cracks in section VA developed already in the very beginning of the loading and its development is faster compared to section I and VB (see Figure 26.a. 27.a . and 28.a.).

For section I and VB, the dominant mode is transversal cracking with more than 45% of total crack length. For section VA, longitudinal cracking is dominant (46%), followed by 'other' (34%) and transversal (20%) cracks.

6.7.2. Definition of "cracked area" and its consequences on matching observed with predicted fatigue performance

As mentioned before, a grid size of 100 x 100 mm was used in this study to determine the area that showed cracking. It will be clear, however, that the choice of the grid size influences the number that reflects the size of the cracked area. The larger the grid size, the higher the total cracked area will be. The definition of "cracked area" and more particular the selection of the grid size has consequences for the definition of a failed pavement from a cracked area point of view. This is further elaborated in this section.

By using a grid size of 50 x 2400 for section I, Groenendijk found that at the moment when the pavement reaches the 'pavement life' (50% stiffness) criteria, the cracked area was equal to approximately 20% (See Figure 6.29).
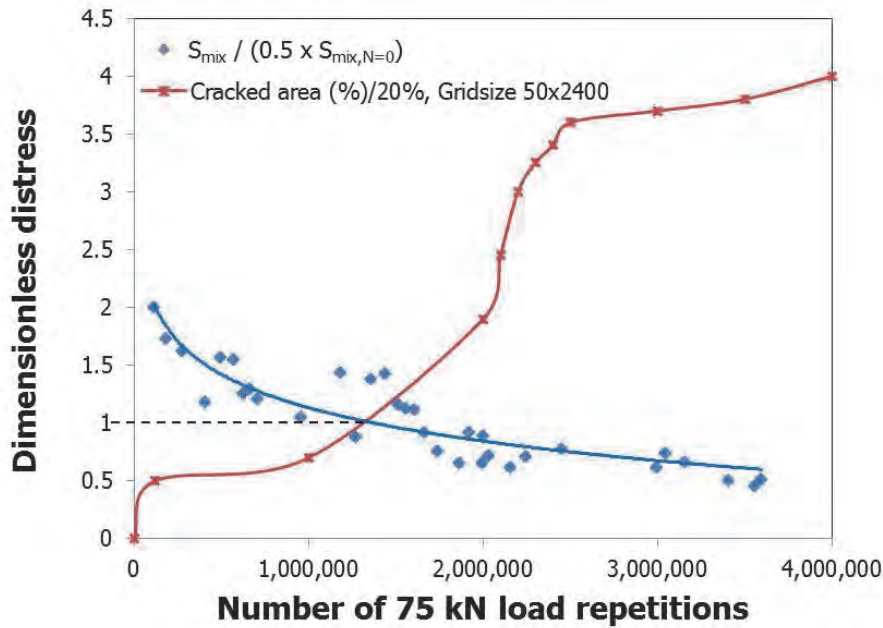
Figure 6.29. The observed fatigue life of Lintrack section I and the cracked area (grid size 50 x 2400), after Groenendijk [4]

Other researchers [20-22] also tried to relate cracking visible at the pavement surface to pavement damage (Miner's ratio). Ali and Tayabji [20] for example, correlated the percentage of fatigue cracking to the damage ratio where the allowable number of passages to failure was determined using the Asphalt Institute and Shell fatigue models. Their model showed that the cracking percentage is less than 10% when the damage index reaches 1. The MEPDG [21] assumes that when fatigue cracking has extended over 50% of the total lane area, a damage percentage of 100% is reached. Prowell [22] reported that three sections of the NCAT 2003 test track were defined as failed when fatigue cracking was exceeding 20% of the total lane area. These examples show that different researchers use different ways to define a pavement to be failed.

Table 6.20. Different criteria determined for end of pavement life based on cracked area

	End of pavement life	Crack area criteria
Groenendijk [4]	50% back-calculated stiffness	cracked area = 20%
Ali & Tayabji [20]	Damage index = 1	fatigue cracking < 10%
MEPDG [21]	Damage index = 1	fatigue cracking > 50%
The NCAT 2003 [22]	Damage index = 1	fatigue cracking > 20%

*Damage index = Miner's cumulative damage

The analyses presented in this thesis have shown that it is very difficult to relate damage which is visible at the pavement surface to a damage ratio which is calculated numerically. The reasons for this are that not all cracking observed at the pavement surface is bottom-up fatigue cracking. It should be

remembered that the fatigue life calculations are actually estimating the initiation of bottom up cracking instead of top down cracking. Therefore, unless it is proven that most of the cracking is bottom up cracking, relating surface cracking with fatigue life will be inaccurate. Analyses of the three Lintrack sections showed that pavement thickness as well as the way how the percentage cracked area is determined, are also affecting the result. Unfortunately in none of the references cited above, these factors were considered.

6.7.3. Permanent deformation and structural pavement life

Before the existence of any relationship between permanent deformation and the structural pavement life (cracking) will be discussed, attention is called for the fact that all permanent deformation in each of the Lintrack pavement sections was caused by permanent deformations in the sand subgrade. Deformations in the asphalt layer itself made, if present, only a very small contribution to the total deformation.

As mentioned in chapter 2, the World Bank's HDM3 model shows that there is a relationship between the rut depth and the amount of cracking. In that model the average rut depth depends on the amount of cracking in the following way

Average rut depth = f (% cracked area * mean monthly precipitation)

Since the Lintrack sections were covered, they were protected against the influence of precipitation making MMP (mean monthly precipitation) = 0. This implies that the HDM3 model could not be used for the Lintrack sections to determine whether cracking would influence permanent deformation or vice versa. It is, however, very well possible that permanent deformation affects the occurrence of cracking because if a significant rut depth develops, significant curvature of the pavement occurs, which possibly cannot be followed by the asphalt layer without cracking. So cracking could develop as a result of creep.
In an attempt to determine whether there is some correlationship between permanent deformation (rutting) and cracking, the Tables 6.21 and 6.22 were developed.

Table 6.21. Amount of cracking at an average rut depth of 18 mm

Section	I	VA	VB
Area cracked (%)	16.9	8.3	21.9
N	2,559,448	25,545	793,136
Amount of transverse cracking [m]	32.2	8.1	21
Amount of longitudinal cracking [m]	6.1	8.1	7.8

Chapter 6. _F. P. Pramesti

Table 6.22. Rut depth at which % cracked area started to increase rapidly

Section	I	VA	VB
Rut depth (mm)	16.6	Could not be determined	12.1
N	2,000,000		267,200

Especially Table 6.21 is of importance since it shows that the amount of longitudinal cracking at 18 mm rut depth was approximately the same for all three sections. Furthermore, Table 6.22 shows that progressive development of cracking seems to occur when the rut depth is around 15 mm or larger. Hence from these limited results it indeed seems to appear that rut depth and cracking are to some extent related to each other.

This finding was the reason why a deeper look into the relationship between rut depth and the amount of cracking was undertaken. Especially the relationship between the rut depth and longitudinal cracking was investigated since this seemed to be the most logical relationship if a relation between rut depth and cracking would exist.

6.8. Permanent deformation and longitudinal cracking

6.8.1. Permanent/creep strain and radius of curvature of the rut depth profile

From the theory of slabs it is known that a simple relation exists between the radius of curvature of a deflection profile and the tensile strain at the bottom of the slab. The relation is shown in Equation 6.29 where (ε_x) is the horizontal strain at the bottom, h is the thickness of the slab and (Rx) is the radius of curvature.

$$\varepsilon_x = \frac{h}{2R_x} \qquad\qquad (6.29)$$

In this study this relationship was used to calculated the creep/permanent strain as a result of permanent deformation. When a rut depth profile is modelled as an arc, with the length of the chord defining the base of the arc being W and the height measured at the midpoint of the arc's base is H, then the radius of this arc can be estimated using Equation 6.30.
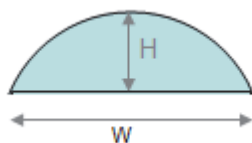
$$Radius = \frac{H}{2} + \frac{W^2}{8H} \qquad\qquad (6.30)$$
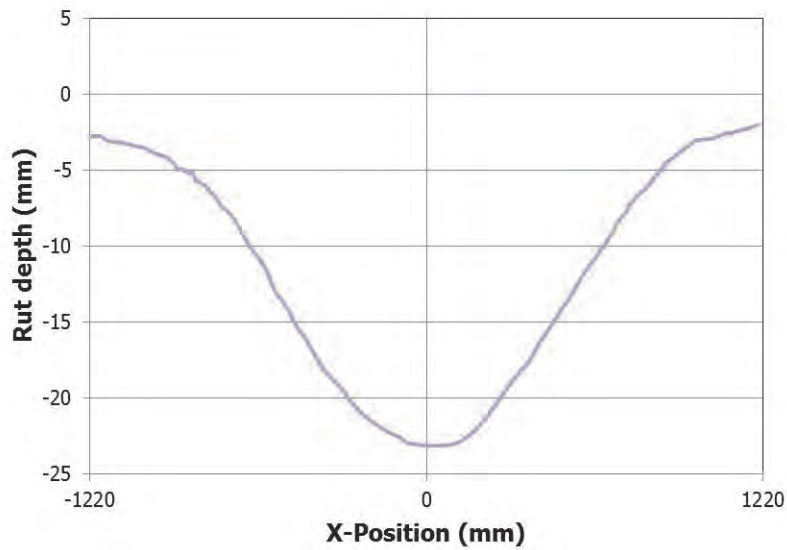
Figure 6.30. Rut depth profile of Section I at 4x10^6 number of load repetitions

When applying this principle on the curvature as a result of rut depth formation, then the challenge is to define H. This is because there is uncertainty of how big the arc should be. This uncertainty results in several possibilities for the radius (R) value. A trial on the rut depth profile that was measured after 4x10^6 load repetitions on section I (see Figure 6.30) was performed.

The relation between H and R and between H and ε is shown in Figure 6.31. The figure shows that there is an optimum value of H that gives the maximum strain. The minimum radius is reached at H=2.49 mm which is 10.75% of the total rut depth of 23.2 mm at 4*10^6 load repetitions. Another three trials also resulted in a similar value. For that reason this percentage of 10.75% is used to determine the height of the other rut depth profiles. It should be noted, however, that not all of the rut depth profiles had an optimum value of H. However, this 10.75% is used to make a consistent calculation in determining R.
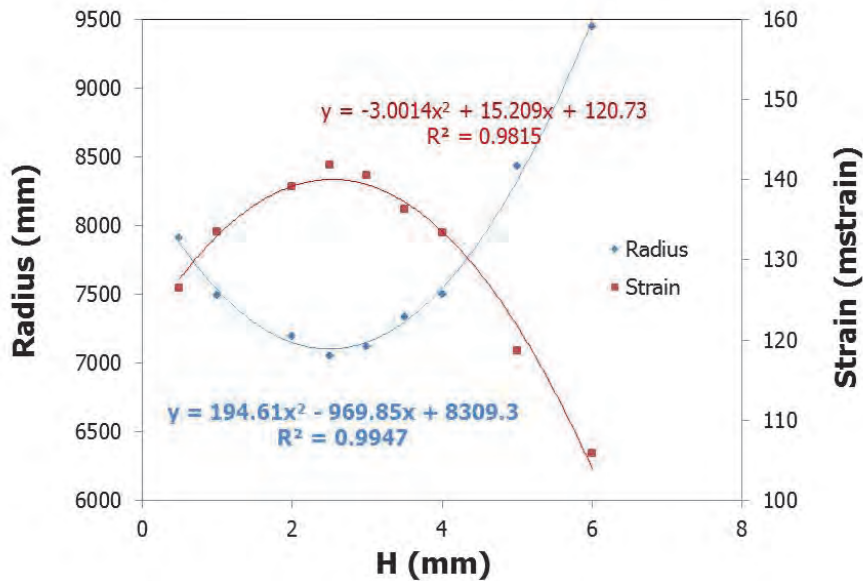
Figure 6.31. The possible radii and permanent strains of the rut depth profile at N=4x10^6 cycles as a function of H

Because of the irregular shape of the rut depth profiles, the W at a certain H could not be easily determined. Then, each rut depth profile was described using a polynomial function. They are shown in Figure 6.32 as dashed lines. These 'new' lines improved significantly the determination of the width of the arc (W) at a certain H value.

Based on the crack pattern shown in Figure 6.3, section VA is the only section that shows a significant amount of longitudinal cracking. The longitudinal cracking appears in the outer side of the wheel path. Figure 6.9.b shows that at the outer sides of the wheel path also deformation in the shape of ridges developed (in the area from the -1220 to -800 and from 800 to 1220). Then, for this section, two deformations will be analysed which are the rut depth between -800 to 800 and the high ridge between -1220 to -800.
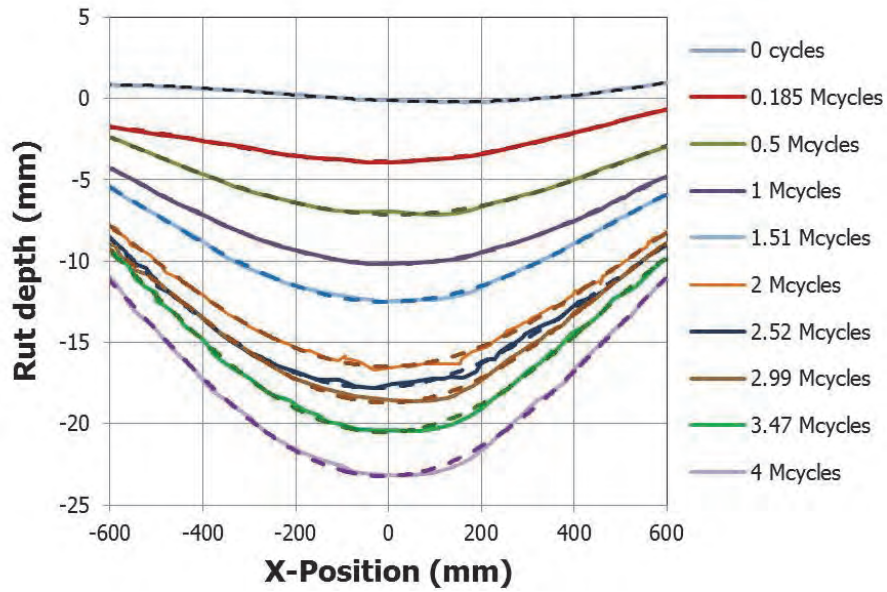
(a) section I at the X-position from -600 mm to 600 mm
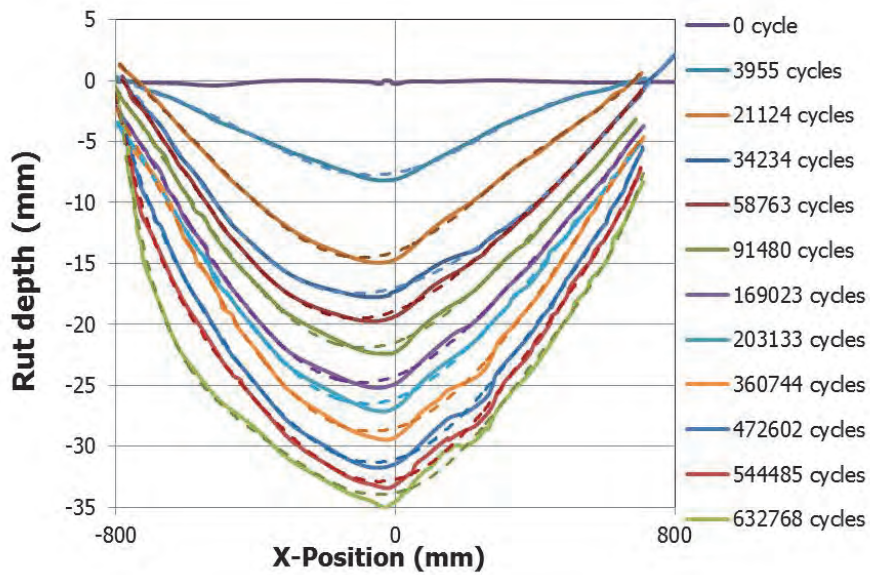
(b) section VA at the X-position from -800 mm to 800 mm
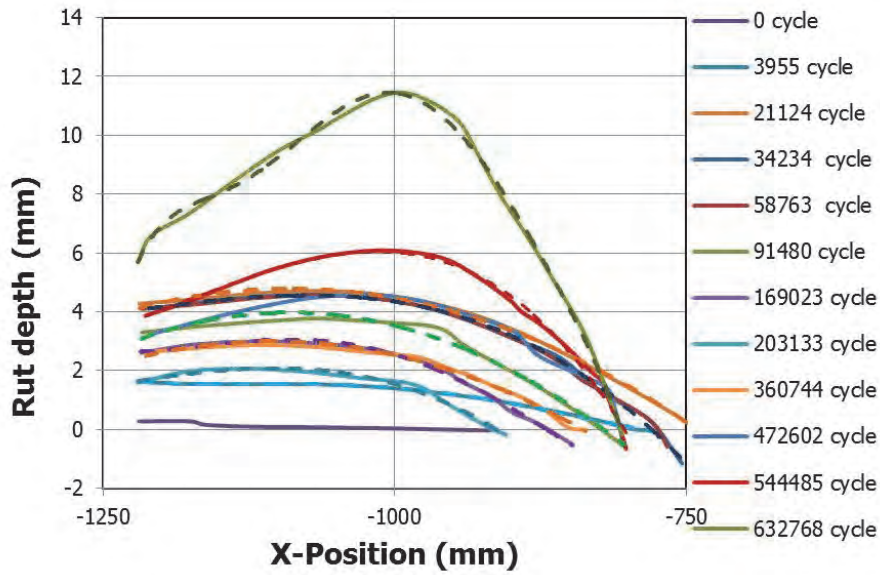
(c) Section VA at the X-position from -1220 mm to -800 mm
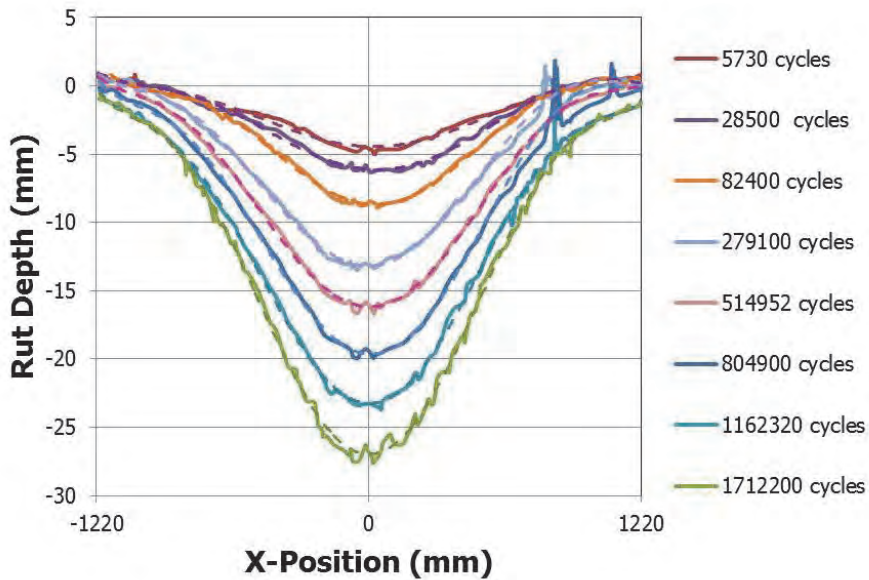
(d) Section VB at the X-position from -1220 mm to 1220 mm

Figure 6.32. Polynomial function of the rut profile (dashed line) at several loading cycles

By using these new rut depth profiles, W was estimated. Hence the radii and the permanent strain could then be determined using Equation 6.30 and 6.29 consecutively. As an example, the results of the calculation for the rut depth profiles of section I are shown in Table 6.23. The relation between the permanent strain and the number of load cycles can be seen in Figure 6.35. An S curve relation between the permanent strain and the number of load repetitions was developed and presented in this figure.

Table 6.23. Recapitulation of the Radii and permanent strain at certain number of load repetitions (Section I)

N	Maximum rut depth (Y)	H (10.75% * Y)	W	Radius	ε (permanent strain)	
cycles	mm	mm	mm	mm	%	µstrain
0	-0.20	0.02	120	84853.43	0.05	471
185000	-3.88	0.42	400	47931.59	0.08	835
500000	-7.14	0.77	380	23529.29	0.17	1700
1000000	-10.18	1.09	460	24165.4	0.17	1655
1510000	-12.51	1.34	420	16403.41	0.24	2439
2000000	-16.49	1.77	480	16252.45	0.25	2461
2520000	-17.79	1.91	500	16338.85	0.24	2448
2990000	-18.72	2.01	440	12029.66	0.33	3325
3470000	-20.52	2.21	480	13055.09	0.31	3064
4000000	-23.23	2.50	500	12514.06	0.32	3196

6.8.2. Relationship between the rut depth and the radius of curvature and between the rut depth and the permanent strain.

Before the relation between the permanent/creep strain and cracking will be discussed, first some attention will be paid to the relation between the rut depth and the radius of curvature and the relation between rut depth and permanent strain obtained from the data using the procedure described in the previous paragraph.

The relation between the rut depth and radius and between rut depth and permanent strain as determined from the data obtained on the three sections are shown in Figure 6.33 and 6.34. Figure 6.33 shows a nonlinear relation between the rut depth and the radius. However, the three sections show a similar pattern which can be represented by means of a logarithmic trend line. Meanwhile the relation between rut depth and permanent strain presented in Figure 6.34 shows a linear relation between the rut depth and the permanent strain.
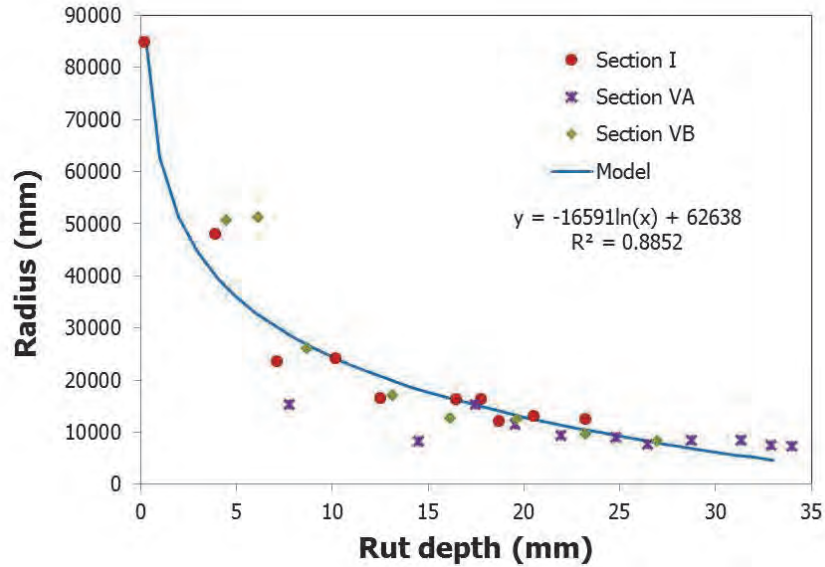
Figure 6.33. Relation between rut depth and radius
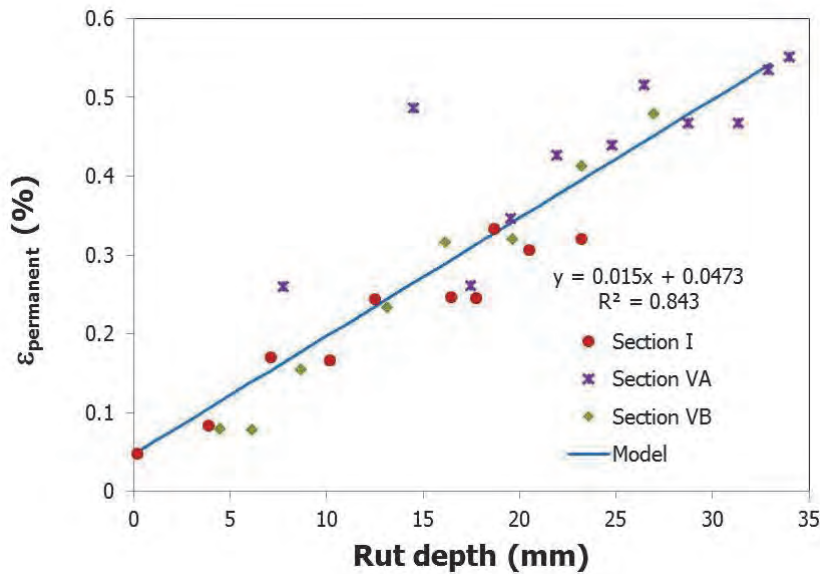
Figure 6.34. Relation between rut depth and permanent/creep strain

Figure 6.34. is an interesting one because it shows that there is a rather good correlation between rut depth and permanent strain which is independent of the layer thickness. This relationship, however, might be dependent on the amount of lateral wander.

6.8.3. Rut depth, permanent strain and cracking in section I

Figure 6.35 shows the relationship that was developed between the number of load repetitions and the permanent strain. For the sake of completeness it is recalled that the permanent strain is acting at the bottom of the asphalt layer in the transversal direction and could, therefore, give rise to longitudinal cracking in the centre of the wheel path.
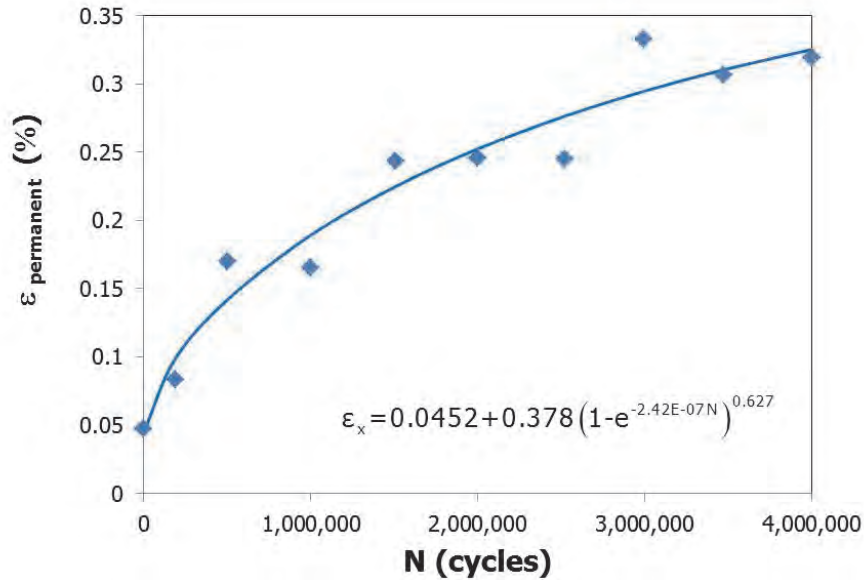
Figure 6.35. Development of the permanent strain in Section I

Figure 6.36 and Figure 6.37 show the development of the crack length and cracked area subsequently with respect to the number of load repetitions.

Both figures show that the crack development was rather slow until $2x10^6$ load repetitions but also that the crack lengths increased significantly after $2*10^6$ cycles. At that number of load repetitions, the permanent strain value is around 0.25% and the rut depth around 17 mm (see also Figure 6.32.a.).

Figure 6.36. Development of the permanent strain and crack length in Section I

Chapter 6. _F. P. Pramesti
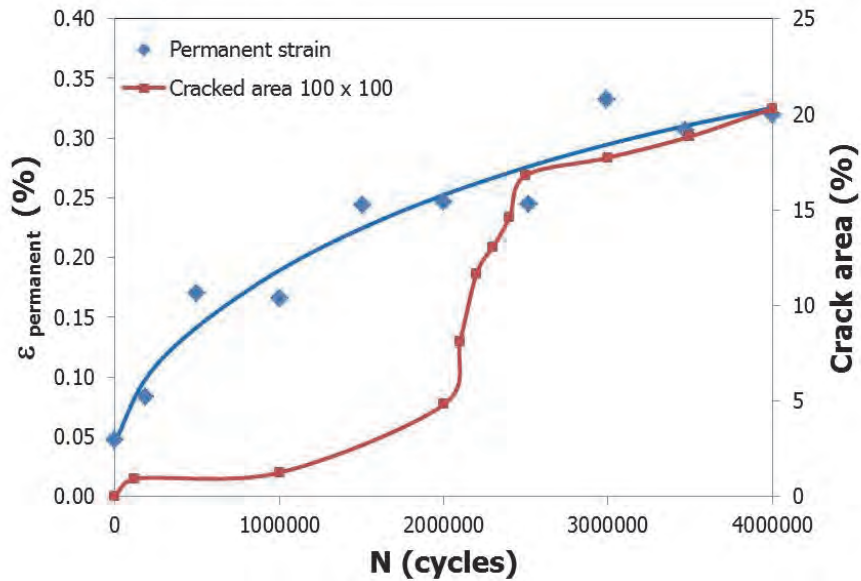
Figure 6.37. Development of the permanent strain and cracked area in Section I

6.8.4. Rut depth, permanent strain and cracking in section VA

For Section VA, the recapitulation of the radii and permanent strain is presented in two parts. The first part in Table 6.24 shows the radii and permanent strains at the x position between -800 to 800 (the rut depth area), whereas Table 6.25 shows the radii and permanent deformation at the x position from -1220 to -800 (the ridge area).

Table 6.24. Recapitulation of the Radii and permanent strain at certain number of load repetitions (Section VA) between -800 to 800

N	Maximum rut depth (Y)	H (10.75% * Y)	W	Radius	ε (permanent strain)	
cycles	mm	mm	mm	mm	%	µstrain
3955	-7.76	0.83	320	15344	0.26	2607
21124	-14.50	1.56	320	8211	0.49	4872
34234	-17.48	1.88	480	15329	0.26	2609
58763	-19.52	2.10	440	11535	0.35	3468
91480	-21.91	2.35	420	9364	0.43	4272
169023	-24.76	2.66	440	9092	0.44	4399
203133	-26.46	2.84	420	7754	0.52	5159
360744	-28.75	3.09	460	8560	0.47	4673
472602	-31.33	3.37	480	8552	0.47	4677
544485	-32.88	3.53	460	7486	0.53	5343
632768	-33.96	3.65	460	7247	0.55	5520

Table 6.25. Recapitulation of the Radii and permanent strain at certain number of load repetitions (Section VA) from -1220 to -800

N	Maximum rut depth (Y)	H (10.75% * Y)	W	Radius	ε (permanent strain)	
cycles	mm	mm	mm	mm	%	μstrain
3955	1.62	0.18	240	40452	0.10	989
21124	4.71	0.52	230	12765	0.31	3134
34234	4.56	0.50	230	13190	0.30	3033
58763	4.57	0.50	270	18137	0.22	2205
91480	3.83	0.42	230	15714	0.25	2545
169023	3.06	0.34	170	10724	0.37	3730
203133	2.07	0.23	150	12346	0.32	3240
360744	3.00	0.33	180	12258	0.33	3263
472602	4.50	0.49	190	9121	0.44	4385
544485	6.00	0.66	160	4851	0.82	8246
632768	11.44	1.26	120	1431	2.80	27961

$$\varepsilon_x = 0.0664 + 0.7063\left(1 - e^{-9.52E\text{-}08\,N}\right)^{0.149}$$
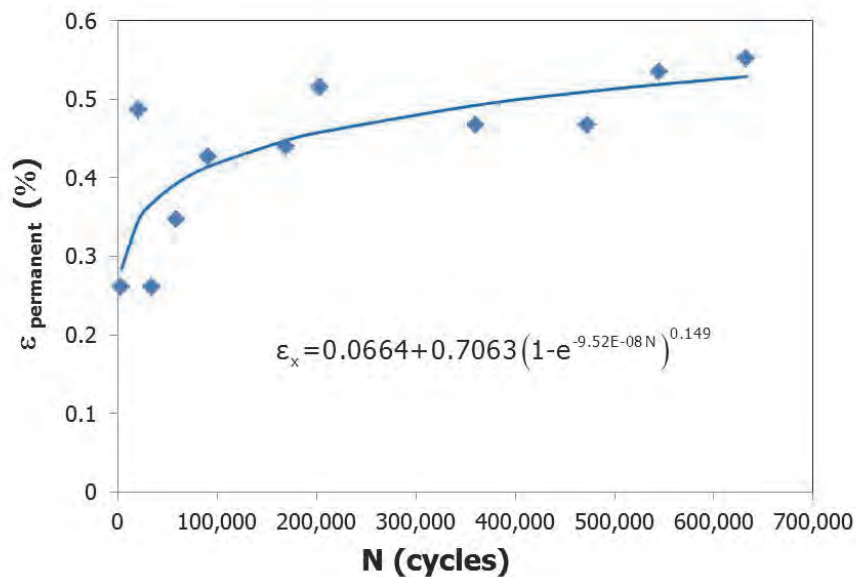
Figure 6.38.a. Development of the permanent strain at Section VA, from -800 to 800; the rut valley
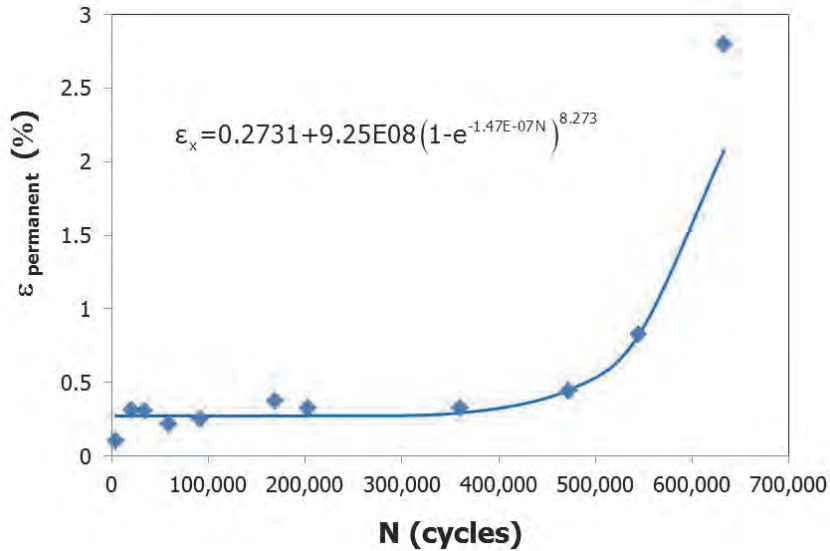
Figure 6.38.b. Development of the permanent strain at Section VA, from -1220 to -800; the rut ridge

Figure 6.38 shows the relation between permanent strain and the number of load cycles. Figure 6.38.a shows immediate and rapid increase of the permanent strain during the first 100,000 load repetitions while it developed at a much slower pace after 100,000 load repetitions. On the other hand Figure 6.38.b, which represents the development of the permanent strain at the top of the ridge, shows that the permanent strain was rather constant at around 0.25% for a rather long period but increased dramatically after 500 kcycles.

In Figure 6.39 and 6.40, the development of the permanent strain at the related number of load repetitions is compared with the development of the crack length and cracked area. Both figures show that cracking started immediately.
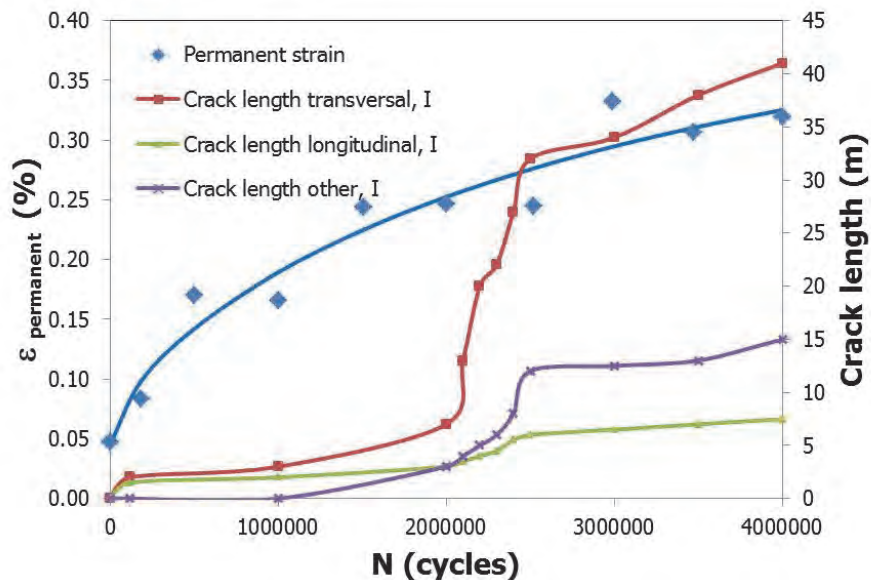

Figure 6.39. Development of the permanent strain and crack length in Section VA
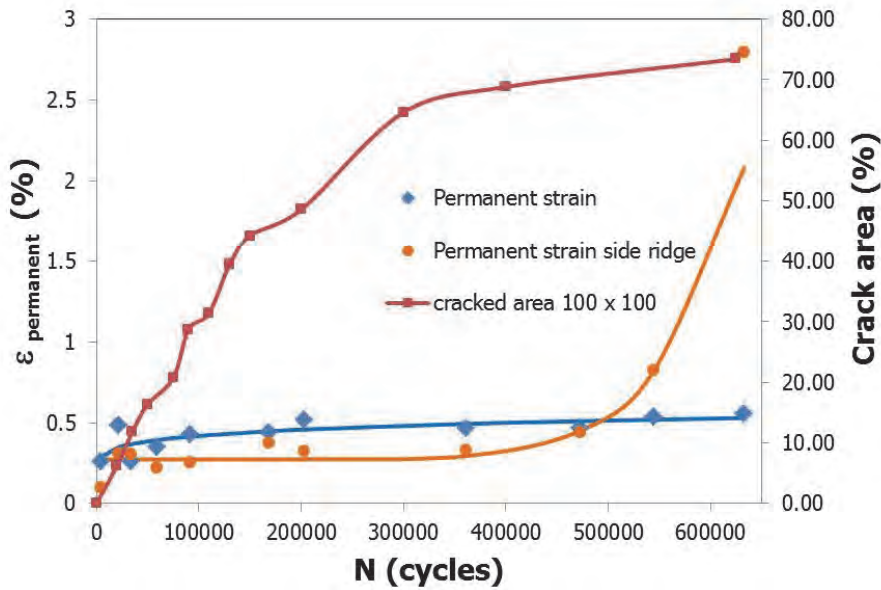
Figure 6.40. Development of the permanent strain and cracked area in Section VA

Section VA is the section that shows quite a number of longitudinal cracks (see also Figure 6.3). This type of cracking was not only present in, or near, the centre of the wheel path, as was also the case in section I and VB, but many of these longitudinal cracks were also present at the edges of the rut profiles in section VA. These cracks were less present in Section VB and quite rare in Section I. From Figure 6.38a it can be concluded that after 75000 load repetitions, when the permanent strain had reached a value of 0.4%, the permanent strain is not increasing rapidly anymore. It seems as if the 0.4% strain is about the maximum the pavement can take. At that moment the rut depth is 22 mm and the cracked area is 20%.

Figure 6.38b seems to indicate that a permanent strain of 0.4% is about the maximum the pavement can take because a very rapid increase in strain is observed after this strain level has been reached (at 450,000 load repetitions). Taking into consideration the size of the cracked area at that moment (see Figure 6.40) the pavement can be considered to be completely failed.

6.8.5.   Rut depth, permanent strain and cracking in section VB

For Section VB, the curvature radii and permanent strains are presented in Table 6.26 and the resulting relation between the number of load repetitions and permanent strain is shown in Figure 6.41.

Table 6.26. Recapitulation of the radii and permanent strain at certain number of load repetitions (Section VB) From -1220 to 1220 (rut depth)

N	Maximum rut depth (Y)	H (10.75% * Y)	W	Radius	ε (permanent strain)	
cycles	mm	Mm	mm	mm	%	μstrain
5730	-4.45	0.48	440	50563	0.08	791
28500	-6.15	0.66	520	51152	0.08	782
82400	-8.68	0.93	440	25946	0.15	1542
279100	-13.16	1.41	440	17107	0.23	2338
514952	-16.18	1.74	420	12680	0.32	3154
804900	-19.64	2.11	460	12529	0.32	3193
1162320	-23.25	2.50	440	9685	0.41	4130
1712200	-26.98	2.90	440	8346	0.48	4793

The equation shown on the figure:

$$\varepsilon_x = 0.03503 + 1.2364\left(1 - e^{-6.68E-08\,N}\right)^{0.463}$$
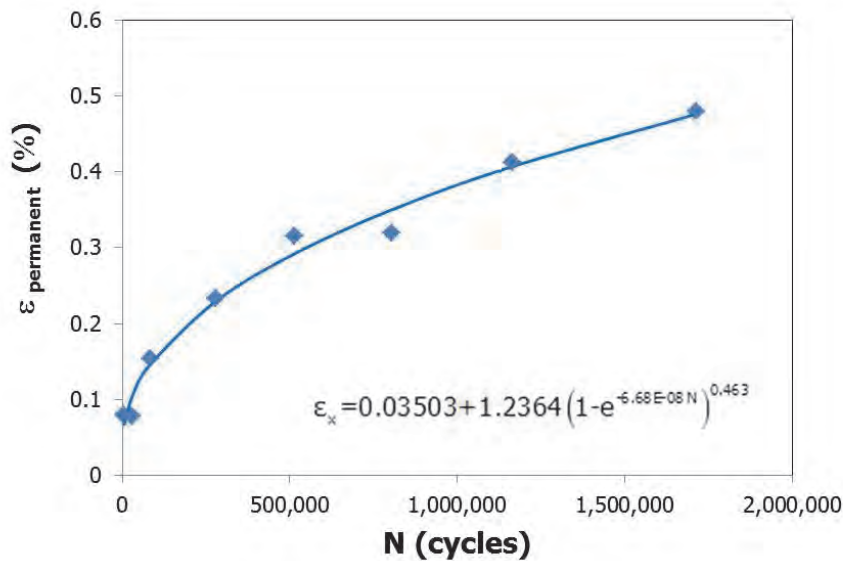
Figure 6.41. Development of the permanent strain in Section VB

Figure 6.42 and 6.43 show that the cracks started to develop at around 278,000 cycles. At that point, the permanent strain is around 0.23% and the rut depth 13 mm. The 0.4% strain level is reached after approximately 1.1 million load repetitions and at that moment the cracked area amounts 32%. The rut depth at that moment was 22 mm.
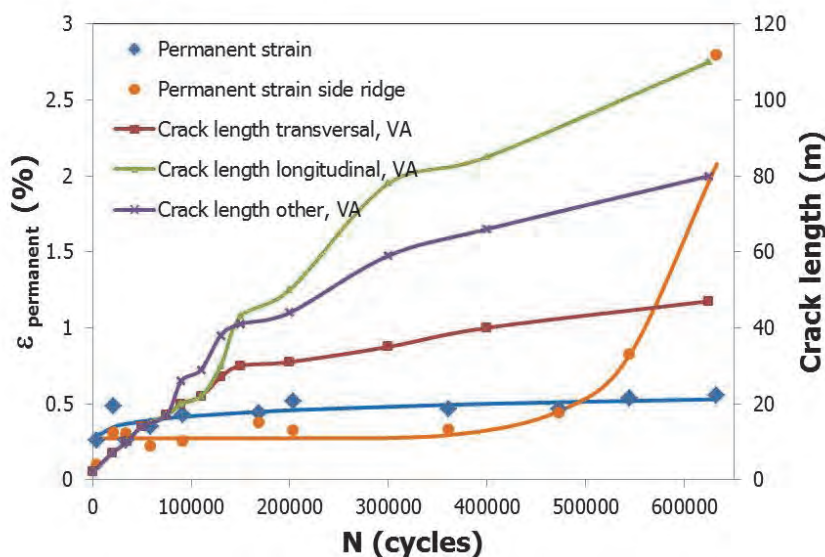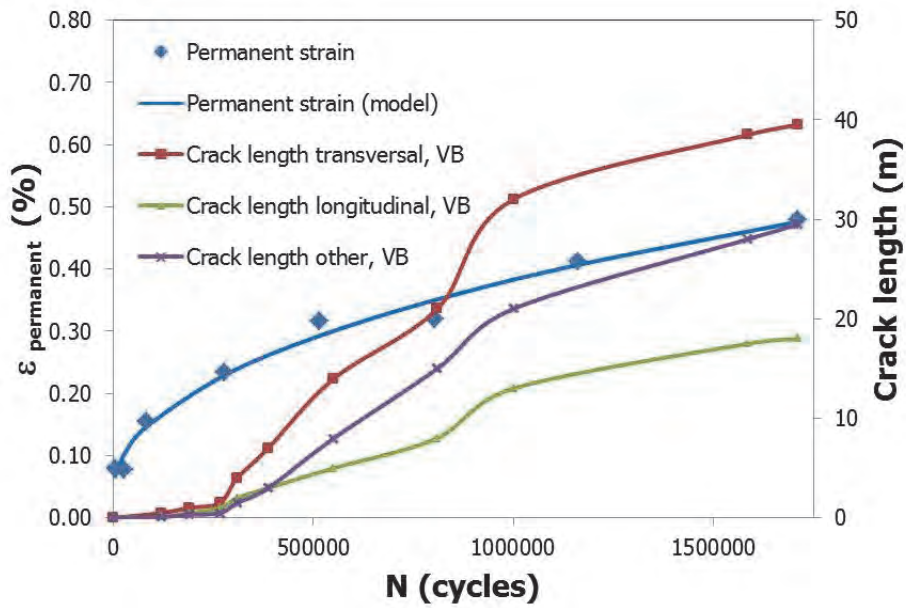
Figure 6.42. Development of the permanent strain and crack length in Section VB
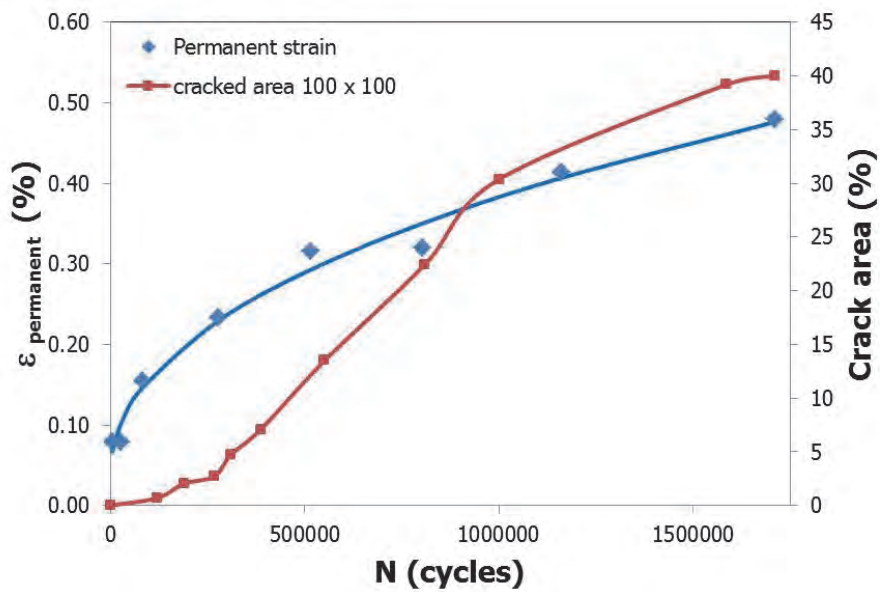
Figure 6.43. Development of the permanent strain and crack area in Section VB

6.8.6. Summary of findings with respect to the relationship between rut depth and cracking

The most important findings with respect to the relation between permanent deformation and cracking are summarized in Table 6.27.

Table 6.27. Summary of findings with respect to the relationship between rut depth and cracking.

Section	I	VA	VB
Nr of load repetitions at which cracking starts to increase	2,000,000		267,200
Permanent strain when cracking starts to increase	0.25%		0.23%
Rut depth when cracking starts to increase	16.6 mm		12.1 mm
Nr of load repetitions at which permanent strain equals 0.4%		75,000	1,000,000
Rut depth at a permanent strain of 0.4%		22 mm	22 mm
Cracked area when permanent strain equals 0.4%		20%	32%

From the results shown in Table 6.27 it appears that at a rut depth of around 15 mm, crack development starts to accelerate and that at a rut depth of 20 mm the sections can considered to be failed. It should be noticed that these findings are based on the performance of the Lintrack sections where permanent deformation was a result of deformation of the subgrade and NOT because of the asphalt layer. It is, however, noteworthy that these findings closely agree with the definitions of failure as used in the pavement evaluation and overlay design system as developed by the Transport and Road Research Laboratory in the UK which are shown in Table 6.28 [23].

Table 6.28. Classification of pavement condition according to Croney [23]

Classification	Visible evidence
Sound	No cracking. Rutting beneath 2-m straightedge less than 10 mm.
Critical	(a) No cracking. Rutting between 10 and 20 mm. (b) Cracking confined to a single crack in the wheel-track, with rutting less than 20 mm.
Failed	Cracking extending over the area of the wheel-track and/or rutting greater than 20 mm.

In any case the results show that permanent deformation and structural performance were closely related in case of the Lintrack pavements. These findings also explain the complexity of finding a relationship between Miner's fatigue damage ratio and the amount of cracking; cracking of the Lintrack sections is not only because of fatigue but also because of permanent deformation.

6.9.   Conclusions

Many researchers have tried to match observed with predicted fatigue life. In this study such an effort has also been made by studying the initiation and progression of damage as observed on accelerated pavement test sections and by predicting their fatigue life using linear elastic multilayer analyses and fatigue relationships developed from laboratory tests.

In this chapter, the fatigue performance of three accelerated pavement test sections (Lintrack 1990) was discussed. Parameters that were thought to be of importance for determining the pavement life were studied, being cracking (including crack length and cracked area) as well as permanent deformation and back-calculated stiffness of the asphalt layer.

The results of two beam fatigue laboratory tests, 4PB test and BOEF test, have been used to develop fatigue models. Using probability concepts, the so called N_{Px} (N_{Px} = number of load repetitions to failure at probability level x) fatigue life was determined based on the 4PB and BOEF fatigue results.

When comparing the lifetime based on the reduction of the back-calculated stiffness, with the fatigue life as predicted with the 4PB and BOEF fatigue lines, the BOEF based predictions exhibited a better agreement indicated by a smaller shift factor between "stiffness reduction" and "fatigue" based predictions for all Lintrack sections. Therefore, BOEF test based fatigue models are highly recommended to predict pavement life in practice.

From the analyses it appeared that healing did not play a major role and its potential effect could be neglected. nevert, it is not recommended to take a healing factor into account in countries with a moderate climate like the Netherlands.

Furthermore, an attempt was made to relate the BOEF based fatigue life predictions to the amount of cracking that was visible at the surface of the Lintrack sections. As mentioned before, a probabilistic approach was used to determine the fatigue life. Nevertheless, it was not possible to get a good match between the predicted fatigue life and the cracking observed at the pavement surface.

In this study, it was found that the observed cracking was not merely caused by fatigue but also by permanent deformation.

This study showed that part of the observed longitudinal cracking in the Lintrack sections is quite strongly related to rutting. This statement is based on the following findings:
  - Progressive development of cracking seemed to occur when the rut depth was around 15 mm or larger.

- The rut depth profile analyses showed that there is a rather good correlation between rut depth and permanent/creep strain which is independent of the layer thickness.
- It is clear that correlating the calculated pavement life to the cracked area is not recommended since quite some visible cracking, especially in VA and VB, must have been caused by rutting and some cracking must have been top down cracking initiated by compaction during construction. That permanent deformation did have an influence on the cracking performance was nicely shown when analysing the behaviour of Section VA. There it appeared that the ridge that developed next to the rut depth clearly corresponded with the longitudinal cracking observed in that area.

6.10.   References

[1]   AASHTO, "AASHTO Guide for Design of Pavement Structures 1993," ed. Washington D.C., 1993.

[2]   S.P. Jain, B.F. McCullough, and W.R. Hudson, "Flexible Pavement Design System - Second Generation, Incorporating Fatigue and Stochastic Concepts," Research Report 123-10, Center for Highway Research, the University of Texas at Austin, Austin, 1971.

[3]   W.D.O. Paterson, *Road Deterioration and Maintenance Effects*. Baltimore, U.S.A.: John Hopkins University Press, 1987.

[4]   J. Groenendijk, "Accelerated Testing and surface cracking of asphaltic concrete pavements," PhD, Delft University of Technology, Delft The Netherlands, 1998.

[5]   J. Groenendijk and C.H. Vogelzang, "Pavement Performance Under LINTRACK Accelerated Loading, Extending measurement report and interpretation report section Vb," Delft University of Technology, Delft, The Netherlands, 1998.

[6]   P. D. Bhairo, "Comparison of the predicted and Observed Pavement Life of LINTRACK Test Lane Va," Delft University of Technology, Delft, The Netherlands, 1997.

[7]   C. A. P. M. van Gurp, "Characterization of seasonal influences on asphalt pavements with the use of falling weight deflectometers," PhD, Delft Unversity of Technology, The Netherlands, 1995.

[8]   R. A. Schapery, "A Theory of Crack Growth in Visco-Elastic Media," Report MM 2764-73-1, Mechanics and Materials Research Centre, Texas A & M University, 1973.

[9]   A.A.A. Molenaar, "Structural Performance and Design of Flexible Road Construction and Asphalt Concrete Overlays," PhD, Delft University of Technology, Delft The Netherlands, 1983.

[10]   T.O. Medani and A. A. A. Molenaar, "A Simplified Practical Procedure for Estimation of Fatigue and Crack Growth Characteristics of Asphaltic Mixes," *International Journal of Road Materials and Pavement Design,* vol. 1, 2000.

[11]   M.F.C. van de Ven, "Fatigue Testing GAC test section II (Lintrack DUT) (in Dutch); Report 91489; NPC," Hoevelaken, 1991.

[12]   J. S. Wattimena, "Fatigue Testing GAC may 1991 (Lintrack) (in Dutch); Report 91482; NPC," Hoevelaken, 1991.

[13]   N. Li, "Asphalt Mixture Fatigue Testing; Influence of Test Type and Specimen Size," PhD, Delft University of Technology, Delft The Netherlands, 2013.

[14]   H. Sabha, "Estimation of Crack Growth Parameters and Fatigue Characteristics of Asphalt Mixes Using Simple Test," Delft University of Technology, Delft, The Netherlands, 1995.

[15]   M. M. J. Jacobs, "Crack Growth in Asphaltic Mixes," PhD Thesis Delft University of Technology, Delft, The Netherlands, 1995.

[16]   T. O. Medani, "Design Principles of Surfacings on Orthotropic Steel Bridge Decks," PhD, Delft University of Technology, Delft The Netherlands, 2006.

[17]   A.A.A. Molenaar, "Design of Flexible Pavement, Lecture Note E54 Structural Pavement Design, Part III," Delft University of Technology, Delft the Netherlands, September 1994.

[18]   S.R. Bouman, A.A.A. Molenaar, C.A.P.M. van Gurp, and C.H. Vogelzang, "Lintrack Response Measurements; Comparison of Measured and Predicted Asphalt Strain (part I and II) (in Dutch), Report nr 7-91-209-17 and 7-91-209-18," Delft University of Technology, Delft The Netherlands, 1991.

[19]   A.A.A. Molenaar, "Design of Flexible Pavement, Lecture Note CT 4860 Structural Pavement Design," Delft University of Technology, Delft the Netherlands, 2007.

[20]   H. A. Ali and S. D. Tayabji, "Evaluation of mechanistic-empirical performance prediction models for flexible pavements," *Transportation research record: journal of the Transportation Research Board,* vol. 1629, pp. 169-180, 1998.

[21]   M. M. El-Basyouny and M. Witczak, "Calibration of the Alligator Fatigue Cracking Model for the 2002 Design Guide," *Transportation Research Record: Journal of the Transportation Research Board. Transportation Research Board of the National Academies, Washington, D.C.,* vol. 1919, pp. 77–86, 2005.

[22]   B. D. Prowell, "Estimate of Fatigue Shift Factors Between Laboratory Tests and Field Performance," *Transportation Research Record: Journal of the Transportation Research Board,* vol. 2181, pp. 117-124, 2010.

[23]   D. Croney, *The Design and Performance of Road Pavements. Transport and Road Research Laboratory.* London: Her Majesty's Stationery Office, 1977.

Chapter 7
Modelling of surface cracking

7.1.   Introduction

As has been discussed in the literature survey, surface cracking (top down cracking) is a major problem in flexible pavements and it appears that most of the longitudinal cracking in the wheel paths of thicker asphalt pavements is top down cracking rather than bottom up cracking. As was indicated by Groenendijk [1], also the Lintrack sections showed a lot of top down cracking although most of it was initiated by compaction rather than a result of repeated wheel loads.

The prevailing appearance of top-down cracking observed in a pavement remains problematic and is in contrast with conventional theory. In theory, cracks should propagate bottom-up as the highest flexural stress develops at the bottom-side of the asphalt layers. To elucidate the phenomenon, various explanations have been proposed. Baladi et al [2] identify four aspects that may activate this type of cracking; material, construction, thermal and load-induced aspects. Low fracture energy and aging in the material can cause the pavement to crack. Longitudinal joints and segregation of the mixture during construction may induce the crack initiation while thermal stresses certainly influence crack propagation.

Baladi, further, assert that among the factors identified, tension and shear load induced factors are admittedly noticed as the most influential factors in the surface cracking phenomenon. Vehicle tires unquestionably exert complex tensile and shear stresses on the pavement surface. The repetition of these high tensile and shear stresses at the surface and near-surface region will, according to Baladi et al, result in damage initiation, leading to fatigue life reduction. This process accelerates because of stresses due to thermal cycles and asphalt aging which is reducing the fracture resistance of the asphalt mixture.

The Lintrack tests performed in the 1990's provide valuable data to study the top-down cracking behavior of a pavement subjected to long term cyclic loading. Proper analysis will supply insight how this top surface cracking relates to fatigue life. This chapter focusses on surface cracking and finite element simulations are used to study this phenomenon.

Groenendijk [1] performed Finite Element simulations on a Lintrack section using CAPA (Computer Aided Pavement Analysis) which was developed by Scarpas et al [3]. The simulations were performed to examine the influence of a non-uniform 3D tyre contact stress distribution, aging of the top of the asphalt layer and intentional pre-cracks on the critical stress at the asphalt concrete surface. The asphalt was considered as elastic material but the failure criterion used was valid for DAC (Dense Asphalt Concrete) instead of GAC. DAC data were used since there were not enough GAC material data available at that time.

The result of Groenendijk's study provided valuable insight for the simulation carried out in this thesis. Groenendijk explained that modelling the contact pressure distribution in more detail could not explain the occurrence of critical stress conditions at the tire-pavement interface, although a realistic modelling of the contact stresses resulted in higher stresses in the near surface area than those predicted by means of the commonly used homogeneously distributed vertical contact stress distribution. It was also shown that aging of the top of the asphalt layer had an influence on the stress distribution in the near surface area, but it could also not explain the surface cracking phenomenon, although it had a higher influence than detailing the load. The factor that might cause surface damage is an overloaded/underinflated tire. The simulations in which some surface cracking was assumed to be already present showed that the stress along the crack edge can be high enough to cause crack propagation. However, the crack will only propagate horizontally (longitudinally or transversally) when the crack tip is loaded by a moving wheel.

In spite of these results a renewed attempt was made to explain surface/top-down cracking. The "improvements" compared to Groenendijk involve a more detailed non-uniform tire-pavement contact stresses distribution calculated using CSIR's Tyrestress database, modeling the asphalt layer as a viscoelastic material and applying the GAC yield criterion.

Analysis based on linear viscoelastic material properties makes it possible to study the evaluation of a buildup of residual, unrecovered, stresses and strains that might develop in the Lintrack sections due to the low loading speed. As mentioned in Chapter 6, unrecovered strain as a result of permanent deformation (rutting) was one of the causes of the longitudinal surface cracking occurring at the edge of the wheel path in sections VA and VB.

Although the finite element simulations will be performed for only four loading cycles (with three rest period), some development of unrecovered strains will most probably be observed.

7.2.   Model parameters and description

When a tire load is applied on a pavement surface, complex 3D contact stresses are developing underneath the tire ribs. The study in this sub chapter intends to analyze the influence of the non-uniform contact stress distribution in the tire-pavement interface on the development of damage at the pavement surface and at the near surface area of the GAC layer.

To compute and simulate the behavior of a pavement and its interaction with the complex tire loading, a 3D finite element model was built using ABAQUS v6.13 [4]. The pavement modelling involved; (i) determination of the tire contact stress; (ii) modelling of surface stresses in the GAC mixture based on viscoelastic material behavior.

A description of the pavement and the tire load is given in the following subchapters.

7.2.1.   Lintrack section I

Lintrack section I had a 150 mm thick GAC layer; its length was $16x10^3$ mm and it had a width of $4x10^3$ mm. Although the temperature during the test varied considerably, a constant temperature of 5°C was assumed for the analysis. The speed was 20 km/h resulting in a loading frequency of 8 Hz. Based on the GAC master curve, the stiffness of the asphalt concrete is 18,850 MPa at 5°C. The 150 mm asphalt layer was laid on top of $5x10^3$ mm well compacted and consolidated sand [1]. This subgrade was simulated as an elastic material with an elastic modulus of 160 MPa.

7.2.2.   The tire load

In the Lintrack tests, a super single radial truck tire was used with a more or less rectangular contact area (see Figure 7.1). Its width was constant (independent on the wheel load) and equal to the tread width, meanwhile the length of the contact area varied depending on the wheel load and inflation pressure. In the case of Lintrack section 1, the wheel load was 75kN and the tire was inflated to 950 kPa, resulting in a contact area as shown in Figure 7.1 The super single radial tire has a steel carcass with a high structural stiffness. This can carry a substantial part of the tire load, giving a 'localised' high contact stress. Table 7.1 summarizes the characteristics of the tire and the loading exerted in the contact area.

Figure 7.1 frame (1) exhibits the imprint of the tire capturing the contact area. Subsequently frame 2 depicts the dimension of contact area on which the meshing of load (frame 3) in ABAQUS is based.

Table 7.1. Contact area of Lintrack super single tyre (Bridgestone V steel rib R160A, 425/65 R 22,5)

Measured at loading cycles:	cycles	300.000	4.000.000
Load	kN	75	75
Inf press	MPa	0.95	0.95
Gross width	mm	300	294
Length	mm	270	298
Shape		rectangle	rectangle
gross area	mm2	81000	87612
rad eq.circle	mm	161	167
av contact pressure	MPa	0.93	0.86
net area	mm2	62370	67944
Rad eq circle	mm	141	147
av contact pressure	MPa	1.2	1.1
Groove width	mm	15, 13, 13, 13, 15	15, 12, 12, 12, 15
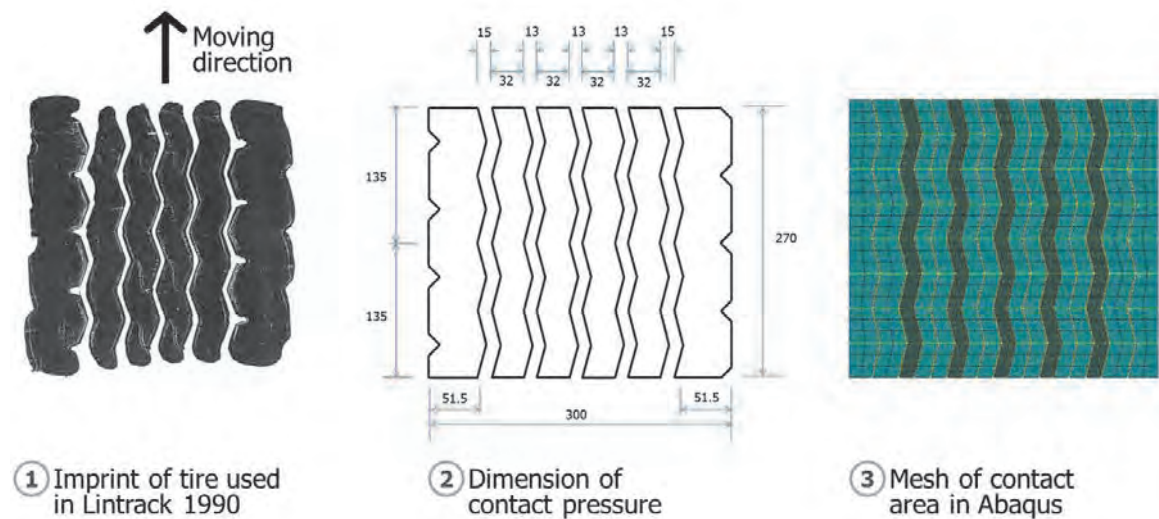
Figure 7.1. Super single tyre used for Lintrack section I (Bridgestone V steel rib R160A, 425/65 R 22,5; wheel load 75kN; inflated to 950 kPa), Sketch of wheel load surface and the tire load surface in ABAQUS

7.2.3. Meshing

A 3D finite element mesh was implemented using ABAQUS v6.13. A half 3D FE mesh in the longitudinal direction was used, as shown in Figure 7.2.

The coarser mesh was employed in the far field while the finer mesh was implemented near the loading area along the wheel path. The finite element mesh dimension was based on the contact width of the tire ribs and the width of the grooves.

(a)   (b)
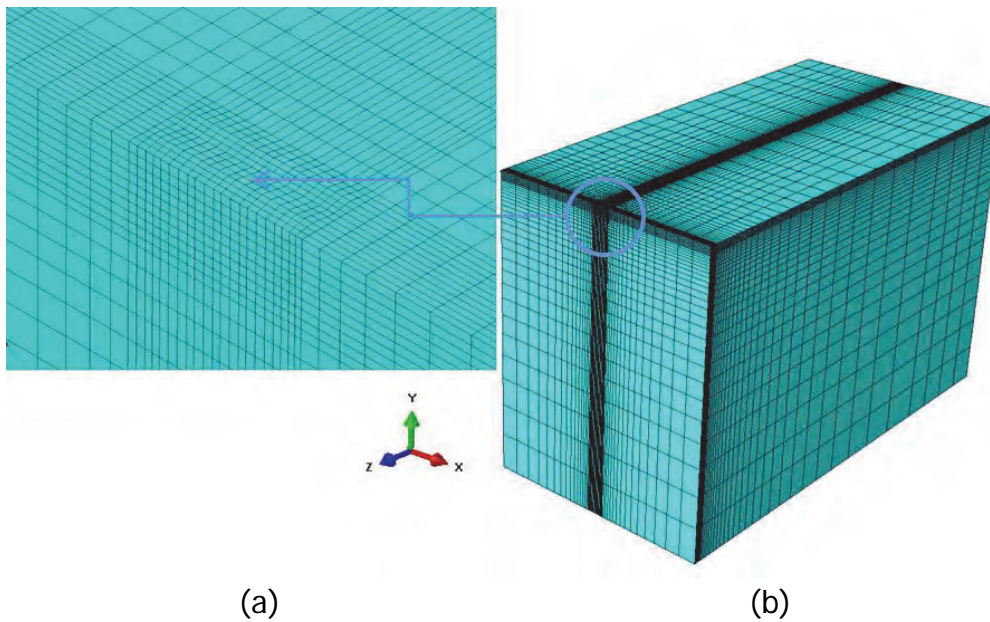
Figure 7.2. Finite element mesh (a) loading area (b) half length of the Lintrack Section I

7.2.4. Loading

The load for the finite element simulations was dictated by the contact pressure pattern. The vertical, transversal and longitudinal 'reaction' on the pavement due to the tire load area were derived using the Tyrestress software [5, 6] for a typical super single tyre 425/65 R 22,5; wheel load 75kN; inflated to 950 kPa.
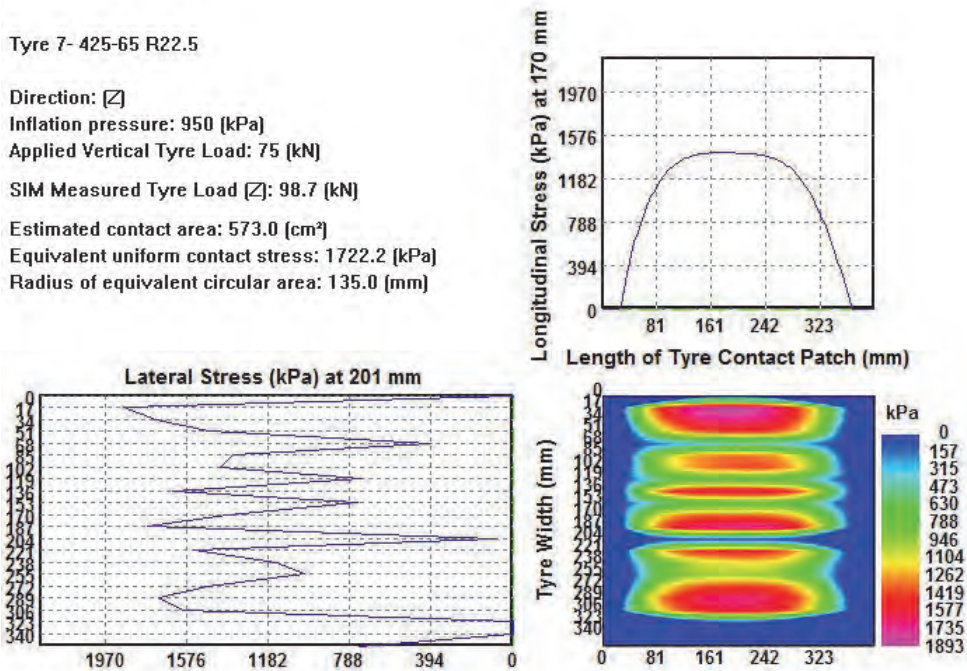
Figure. 7.3. Contact stress area of Super single tyre R160A, 425/65 R 22.5 from Tyrestress[®]

The contact pressure in the vertical direction is shown in Figure 7.3. The tangential stress direction is shown in Figure 7.4. The magnitude of the load pressure applied on the 17 surfaces is shown in Table 7.2.
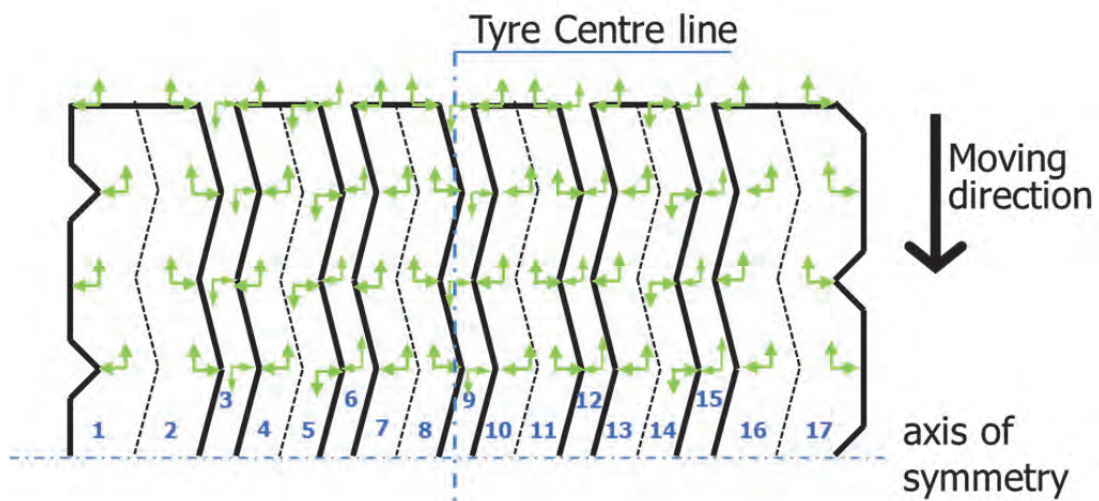
Figure. 7.4. Schematic illustration of the tangential stresses in the pavement contact area

Table 7.2. Magnitude of the contact pressure in the vertical, longitudinal and transversal direction

Surface	Vertical Y	Transversal X	Longitudinal Z
		(MPa)	
1	-1.738	-0.184	-0.060
2	-1.284	0.197	-0.002
3	-0.307	0.082	0.032
4	-1.199	-0.131	-0.030
5	-1.222	0.176	0.057
6	-0.663	-0.130	-0.033
7	-1.528	-0.017	-0.070
8	-1.528	-0.017	-0.070
9	-0.645	0.106	0.070
10	-1.300	-0.228	-0.098
11	-1.617	0.144	-0.004
12	-0.054	-0.014	0.000
13	-1.406	-0.133	-0.066
14	-0.980	0.145	0.053
15	-0.899	-0.233	-0.097
16	-1.309	-0.154	-0.066
17	-1.412	0.226	-0.090
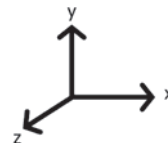
Comparison of Table 7.2 with Figure 7.4 immediately shows a problem that arose during modelling of the contact pressures. Table 7.2 shows that at surfaces 3, 6, 9, 12 and 15 vertical and horizontal stresses are acting while these areas are actually grooves and one would therefore expect the stresses

at these surfaces to be zero. The Tyrestress program, however, gave non zero stress values for these surfaces and because of that stresses were modelled to occur at groove surfaces 3, 6, 9, and 12. In order to simplify the analyses, no variation in the longitudinal direction was assumed.

For the viscoelastic simulation, the tire loading was moving at a speed of 20 km/h which was typical for the speed at which the Lintrack tests were performed. The length of the pavement is 16×10^3 mm, however, the pavement length over which the speed was 20 km/h is only 12×10^3 mm. The deceleration and acceleration at the end and the beginning of the path was neglected. The time needed for the wheel to arrive back to the same point is 2.16 second. The loading pattern in the middle of the pavement is shown in Figure 7.5.

Figure 7.5. The haversine loading

7.2.5. Prony series

The asphalt concrete was modeled as a visco-elastic material using Prony series. The model consists of several parallel Prony elements, each having a serial spring (S_n) and dashpot (η_n) element (Maxwell model), and is shown in Figure 7.6.

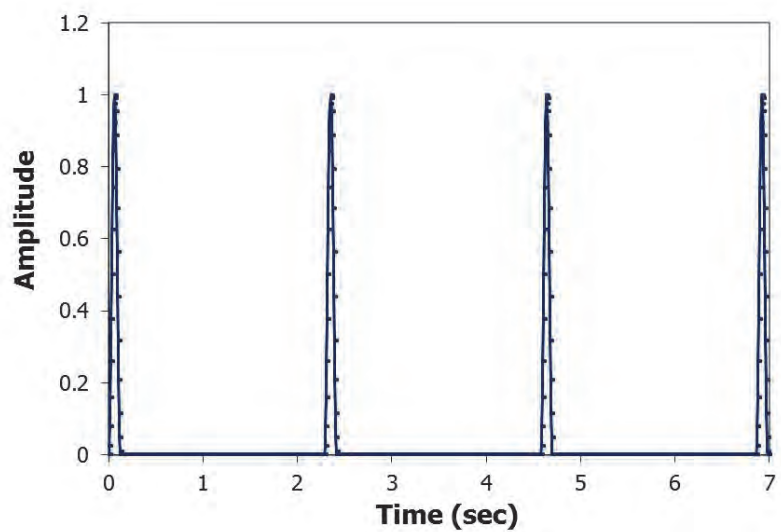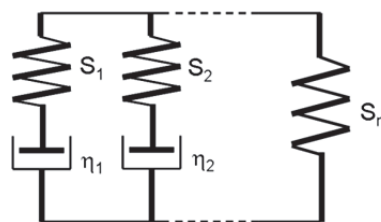**Figure 7.6.** Prony series used in the Lintrack section I simulations

The model parameters were calculated from the mixture stiffness and phase angle data which were determined as a function of the loading frequency by means of 4PB tests. The stiffness & phase angle data were derived at temperatures ranging from 5°C to 30°C and frequencies ranging from 0.5 Hz to 8 Hz. The shifted data points are shown in Figure 4.3 and the master curve according to the Modified Huet Sayegh model [7], [8] is shown in Figure 4.4.

The values for the 9 Prony elements needed to get a good fit of the master curves are shown in Table 7.3. The governing equations associated with the model are given in equation (7.1) to (7.4).

$$S^* = S' + iS'' \tag{7.1}$$

$$S'(\omega) = S_0 \left[1 - \sum_{i=1}^{n} \alpha_i \right] + S_0 \left[\sum_{i-1}^{n} \frac{\alpha_i \tau_i^2 \omega^2}{1 + \tau_i^2 \omega^2} \right] \tag{7.2}$$

$$S''(\omega) = S_0 \left[\sum_{i-1}^{n} \frac{\alpha_i \tau_i \omega}{1 + \tau_i^2 \omega^2} \right] \tag{7.3}$$

$$S(t) = S_0 \sum_{i=1}^{n} \left[1 - \alpha_i \left[1 - \exp\left(\frac{\tau}{\tau_i} \right) \right] \right] \tag{7.4}$$

Where:
S'(ω)	= storage modulus as a function of frequency, ω (MPa);
S''(ω)	= loss modulus as a function of frequency, ω (MPa);
S^*	= complex modulus as a function of frequency, ω (MPa);
S (t)	= relaxation modulus as a function of time, t (MPa);
S_0	= stiffness of instantaneous response (MPa);
ω	= applied angular frequency (rad/s);
α_i	= model parameter, i.e ith Prony S reduction ratio (-);
τ_i	= model parameter, i.e. relaxation speed of the ith Prony (s);
n	= number of components in the model (-).

Table 7.3. Visco elastic material parameters (Prony coefficient)

S_0:	18897	MPa
ν:	0.35	

i	τ_i (s)	α_i
1	0.026	0.177
2	0.123	0.061
3	0.205	0.182
4	0.572	0.071
5	0.954	0.150
6	2.656	0.120
7	7.396	0.098
8	12.343	0.010
9	34.372	0.086

7.3.   Gravel asphalt concrete failure criterion

The GAC's failure behaviour was described using the Mohr-Coulomb (MC) criterion which basically states that the strength of materials is controlled by the cohesion (c) and the angle of internal friction (φ). The Mohr-Coulomb criterion is mathematically expressed as:

$$\tau = c - \sigma \cdot \tan\varphi \qquad (7.5)$$

where:
τ = shear stress, (MPa);
σ = normal stress, (MPa);
c = cohesion, (MPa);
φ = angle of internal friction, (°).

Variables c and φ can be derived from the uniaxial tensile and compressive test data. The parameters φ and c can be calculated using Equation 7.6 and 7.7 subsequently.

$$\varphi = \arcsin\left(\frac{f_c + f_t}{f_c - f_t}\right) \qquad (7.6)$$

$$c = \frac{f_t \cdot (1 + \sin\varphi)}{2\cos\varphi} = -\frac{f_c \cdot (1 - \sin\varphi)}{2\cos\varphi} \qquad (7.7)$$

Uniaxial tension and compression tests on GAC specimens have been performed and the results are presented in Chapter 4. The tensile (f_t in MPa) and compressive strength (f_c in MPa) as a function of temperature (T in Kelvin) and strain rate ($\dot{\varepsilon}$ in %/s) are presented in sub chapter 4.2.3 and represented in Equation 7.8 and 7.9.

$$f_c = -82.38\left[1 - \frac{1}{1 + \left[\dot{\varepsilon}\, e^{(-79.53 + \frac{21534}{T})}\right]^{0.305}}\right] \qquad (7.8)$$

$$f_t = 4.93\left[1 - \frac{1}{1 + \left[\dot{\varepsilon}\, e^{(-75.43 + \frac{22522}{T})}\right]^{0.887}}\right] \qquad (7.9)$$

In Appendix 3.A, the relationship between the mix stiffness (S_{mix}) and the calculated strain rate ($\dot{\varepsilon}$) are presented as determined by means of BISAR calculations on the Lintrack sections. The relationship for section I is shown in Equation 7.10 and Figure 7.7.

$$\dot{\varepsilon} = 628.19\, S_{mix}^{-0.805} \tag{7.10}$$
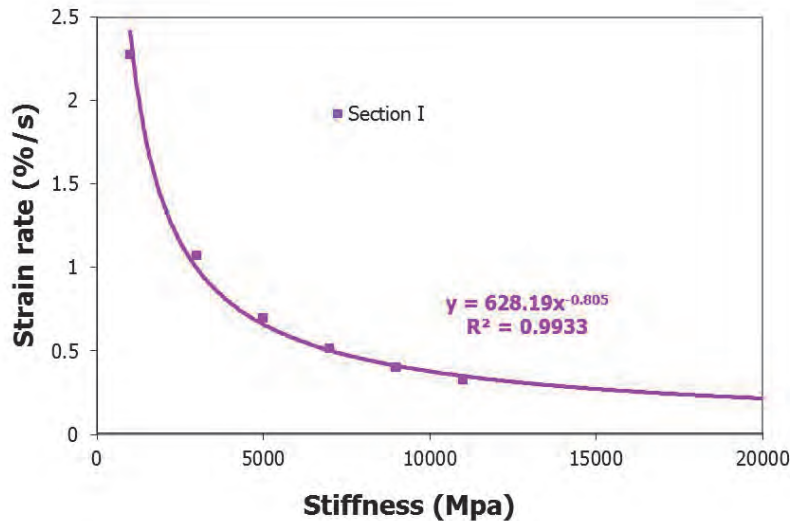
Figure 7.7. Relationship between Smix and strain rate of Lintrack section I

At a mixture stiffness of 18,850 MPa (at 8Hz and 5°C), a strain rate of 0.227%/s is obtained. Furthermore, by using Equation 7.8 and 7.9, a uniaxial tensile strength of 4.8 MPa and uniaxial compressive strength of -20.8 MPa were attained.

The failure criterion is expressed as a line touching the two Mohr-Coulomb (MC) circles resulting from the compression and tension test. The large MC circle in Figure 7.8 represents the uniaxial compressive test; the compressive strength is plotted at the negative x-axis. From the uniaxial tensile test, the smaller circle was derived and the tensile strength is plotted at the positive x-axis (see Figure 7.8).
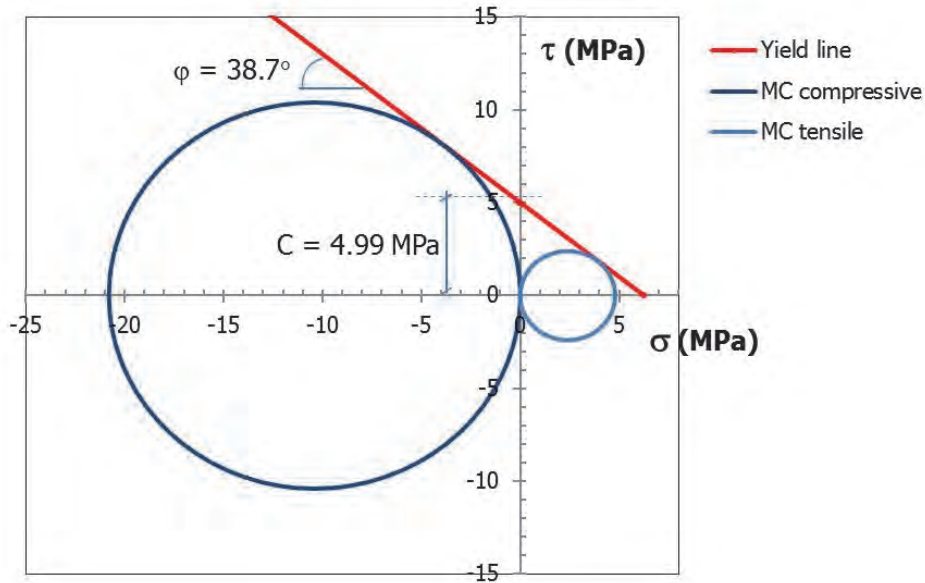
Figure 7.8. Stress based failure line of GAC at the temperature of 5°C and the strain rate of 0.227%/s

With the mixture stiffness of 18,800 MPa the tensile and compressive strain at failure under those conditions are 254 μm/m and -1,101 μm/m respectively.

A strain based failure criterion was then expressed as a line touching the two Mohr-Coulomb (MC) strain circles resulting from the compression and tension test. The large MC circle in Figure 7.9 represents the compressive strain at failure (the compressive strain is plotted at the negative x-axis) and from the uniaxial tensile test, the smaller circle was derived (the tensile strain is plotted at the positive x-axis, see Figure 7.9).
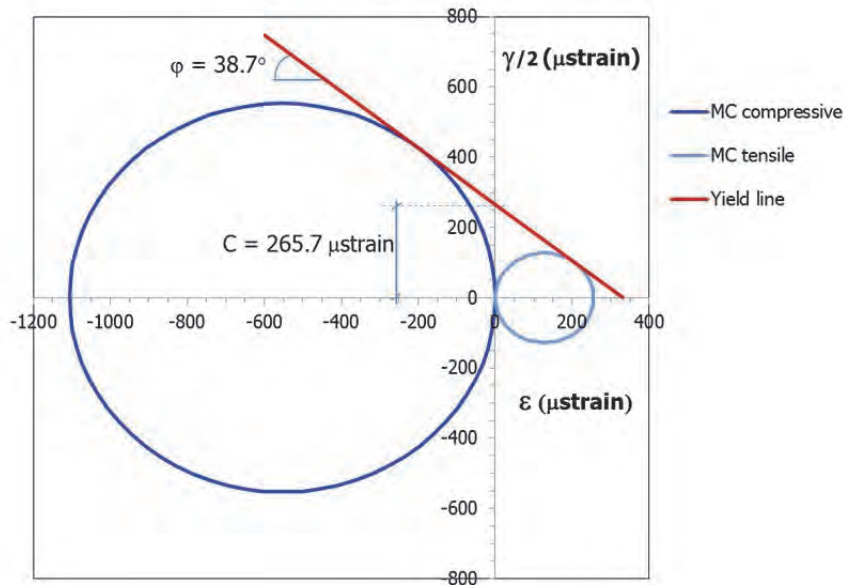
Figure 7.9. Strain based failure line of GAC at the temperature of 5°C and the strain rate of 0.227%/s

7.4. Top down versus bottom up cracking

7.4.1. Stress based MC circle

By using the results of the ABAQUS analyses, stress based MC circles were determined for several locations in the pavement; they are shown in Figure 7.10 to 7.13. Figure 7.10 depicts the MC circle of the nodes at four positions at the surface of the asphalt layer. The four positions are at the left and right outer edge, at the middle under the rib of the tyre and at the edge of the middle groove.

Not only the stresses at the pavement surface were calculated but also those at near surface positions at a depth of 15 and 30 mm from the surface. The MC circles at the surface and near surface nodes are shown in Figure 7.11.

Figure 7.12 exhibits the MC circles of the nodes at the bottom of the asphalt layer. The four positions are similar to those of Figure 7.10 but instead of under the tire, these positions are at 150 mm under the asphalt surface.

Figure 7.10 shows that the response of the pavement surface to the tire loading is dominated by a combination of compressive and shear stresses. In addition, the figure shows that these stress states vary as a function of the point under the tire. The largest value of the combined shear and compressive stress is found in the point representing the edge of the middle groove (purple circle).

The MC circles at the surface and near surface shows that the farther the distance from the surface the smaller the MC circle is (see Figure 7.11). The smallest combination of shear and compressive stress in this figure is shown by the MC circle at 4** (outer edge right, 30 mm from surface), however, this small circle is as close to the yield line as the MC circle at location 4 to the yield line is. This indicates that point 4** has a similar probability to failure as point 4 (outer edge right, at the surface).

At the bottom of the pavement (See Figure 7.12), however, horizontal tensile stresses dictate the pavement response to the applied load. The stress states at the bottom of the asphalt layer, both under the middle rib (green circle) and under the edge of middle groove (purple circle) are on top of each other. Also the stress states at the left and right outer edge (blue and orange circle) are almost the same.
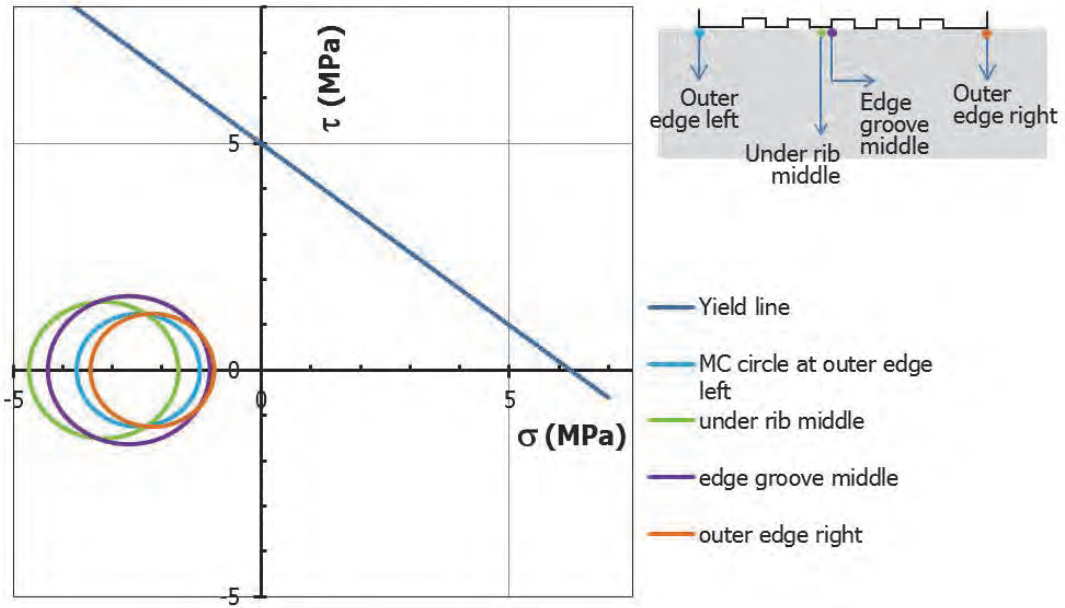
Figure. 7.10. Stress based MC circle at the pavement surface
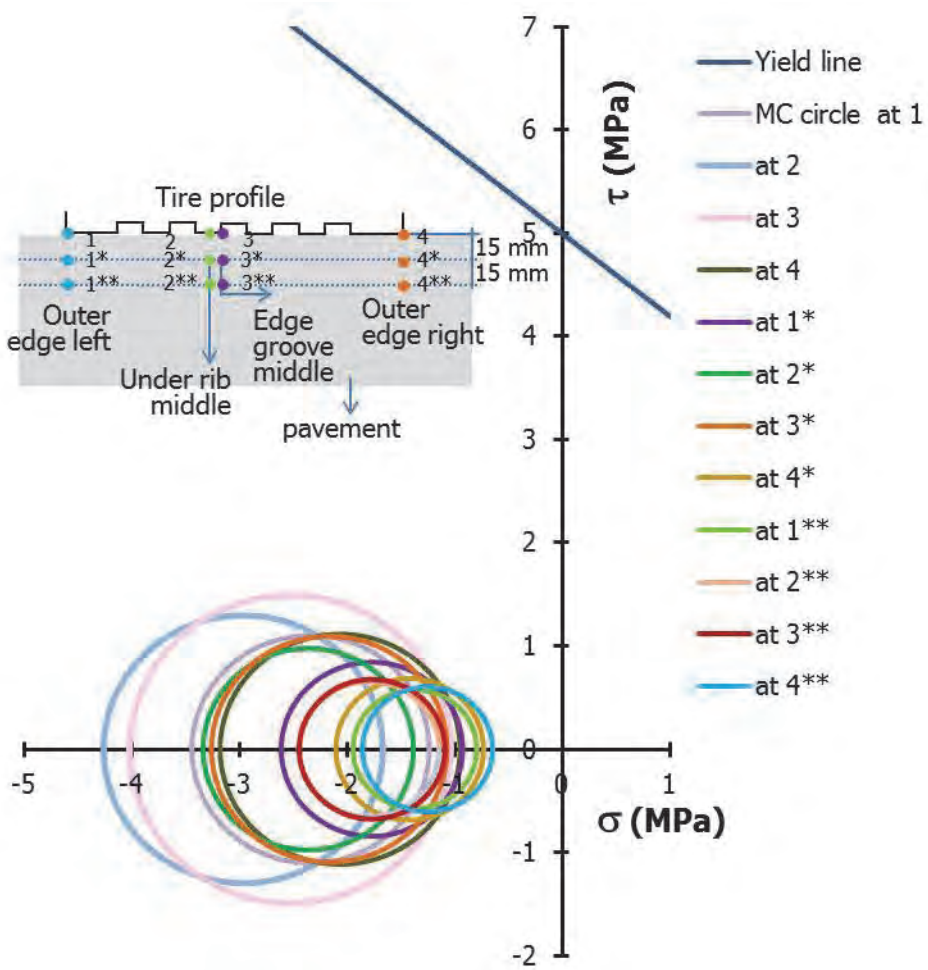
Figure. 7.11. Stress based MC circle at the near surface
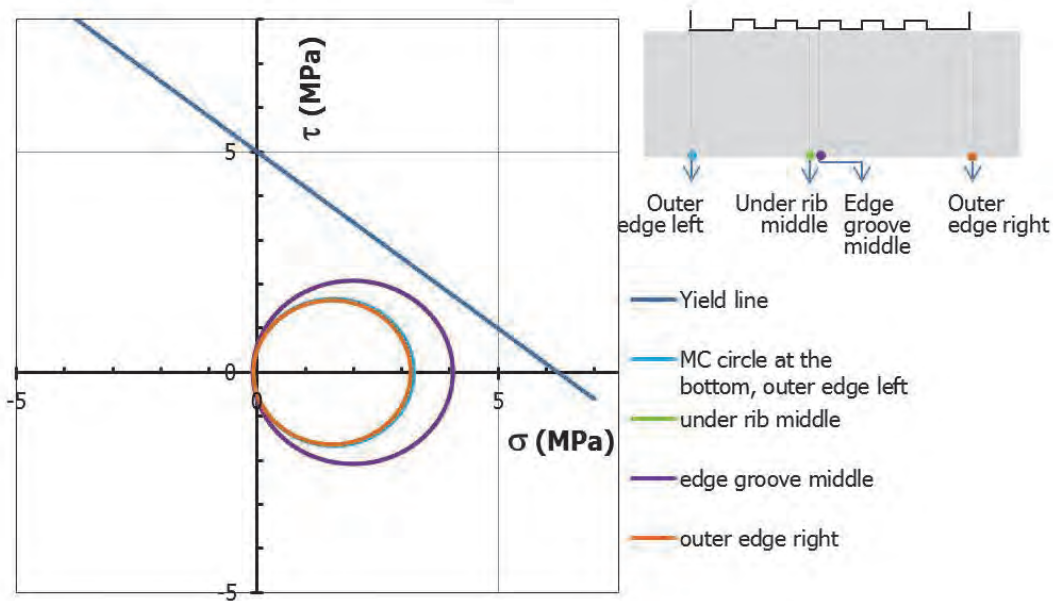
Figure. 7.12. Stress based MC circle at the bottom of asphalt layer
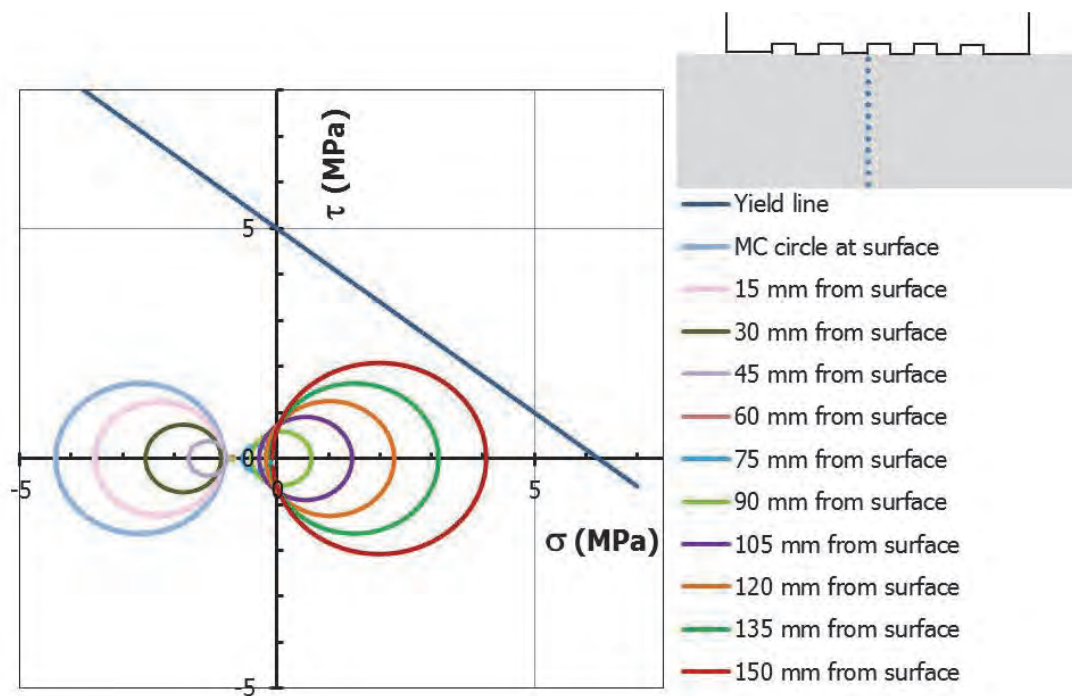
Figure. 7.13. Stress based MC circle over the height of asphalt layer.

Figure 7.13 presents the values of MC circles of the nodes over the height of the asphalt layer together with the failure line. The graph indicates that failure at the pavement surface is unlikely to occur. It implies that the more detailed analysis presented in this chapter did not shed any new light on the top down cracking problem. These results are in agreement with the results published by Groenendijk [1] and Wang et al [9]. Further, both studies showed that an intentional pre-crack in the pavement 3D model is needed to create tensile induced crack failure in the near-surface area.

7.4.2. Strain based MC circle

The strain values resulting from the ABAQUS analyses at the surface and near surface as determined for the analyzed pavement are shown in Table 7.4. Positions 1, 2, 3 and 4 show the strain values at the surface. The i* positions show the strain values at 15 mm under the surface. Whereas the i** positions show the strain values at 30 mm under the surface.

Table 7.4. Recapitulation of the strain at the surface and near surface (μstrain)

Position	ε principal (ε max)	ε mid	ε principal (ε min)	ε_{xx}	ε_{yy}	ε_{zz}	ε_{xy}	ε_{xz}	ε_{yz}	Center	Radius
1	84	-118	-121	-112	77	-121	-72	0	1	-19	103
2	89	-133	-154	-154	89	-133	-4	0	-1	-32	122
3	116	-141	-149	-140	115	-149	37	0	-4	-16	133
4	90	-114	-116	-107	83	-116	72	0	-1	-13	103
1*	77	-90	-96	-61	48	-96	-124	0	0	-9	86
2*	58	-99	-109	-98	58	-109	-1	0	0	-26	83
3*	80	-107	-120	-119	80	-107	19	0	1	-20	100
4*	76	-83	-94	-62	55	-94	105	0	1	-9	85
1**	64	-68	-79	-46	30	-68	-121	0	0	-8	71
2**	36	-74	-76	-74	36	-76	-6	0	0	-20	56
3**	40	-76	-77	-77	40	-76	6	0	0	-19	58
4**	65	-67	-76	-48	36	-67	112	0	0	-6	70

The Strain MC circles of the 12 positions are shown in Figure 7.14. It can be seen from this figure that the further the distance from the surface the smaller the MC circle is. Moreover, the figure shows that a significant principal tensile strain of about 120 μm/m is present at location 3 at the edge of the middle rib. The lowest principal tensile strain of approximately 40 μm/m is indicated by the smallest MC circles which occur at 2** and 3** (under the middle rib and the edge of the middle rib, 30 mm from surface).
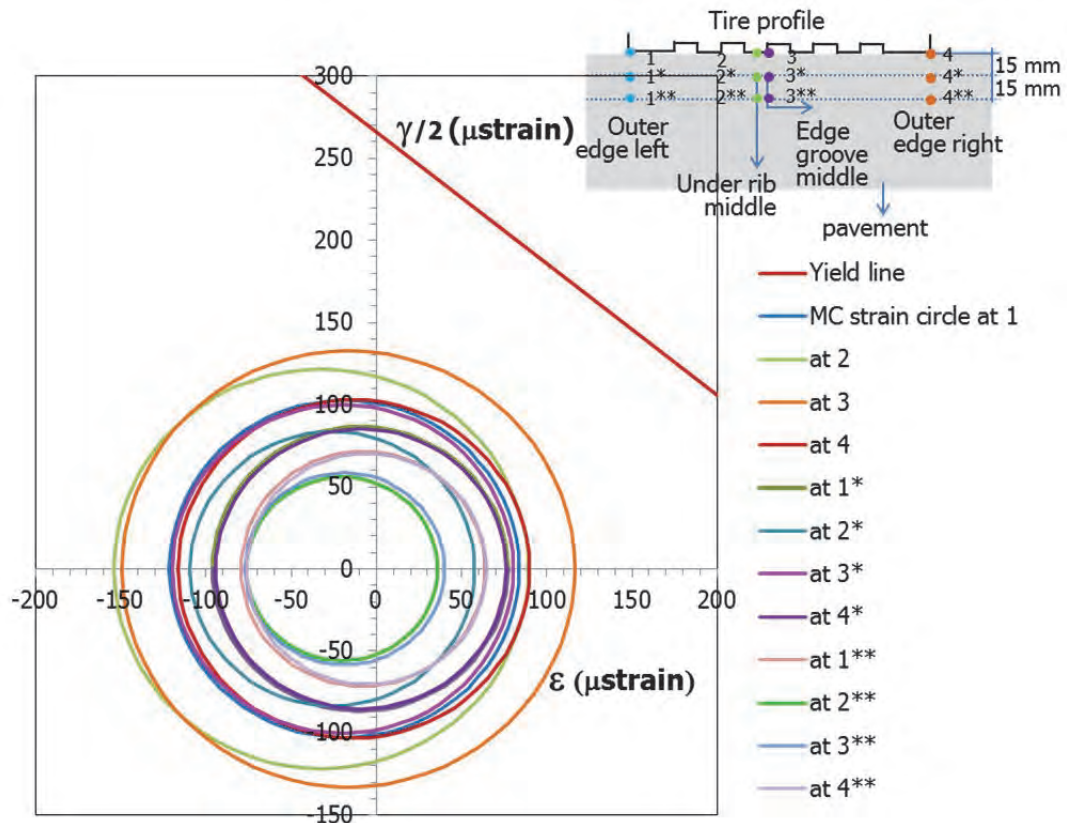
Figure. 7.14. Strain based MC circles at the surface and near surface of the pavement

The strain based MC circles over the height of the asphalt layer under the center of the tire are shown in Figure 7.15. Meanwhile the strain based MC circles over the height of the asphalt layer at the edge of the tire are depicted in Figure 7.16. Figure 7.15 was developed based on the data presented in Table 7.5, whereas Figure 7.16 was based on Table 7.6.

Table 7.5. Recapitulation of the strain over the height of asphalt pavement at the center of the tire (µstrain)

From surface (mm)	εprincipal (ε max)	ε mid	εprincipal (ε min)	ε_{xx}	ε_{yy}	ε_{zz}	ε_{xy}	ε_{xz}	ε_{yz}	Center	Radius
0	116	-141	-149	-140	115	-149	37	0	-4	-16	133
15	80	-107	-120	-119	80	-107	19	0	1	-20	100
30	40	-76	-77	-77	40	-76	6	0	0	-19	58
45	11	-46	-47	-47	11	-46	4	0	0	-18	29
60	-13	-17	-19	-19	-14	-17	3	0	0	-16	3
75	11	8	-36	8	-36	11	2	0	0	-13	24
90	38	34	-59	34	-59	38	2	0	0	-11	48
105	66	61	-83	61	-83	66	1	0	0	-8	74
120	95	90	-109	90	-109	95	1	0	0	-7	102
135	127	121	-139	121	-139	127	1	0	0	-6	133
150	164	155	-176	155	-176	164	0	0	0	-6	170
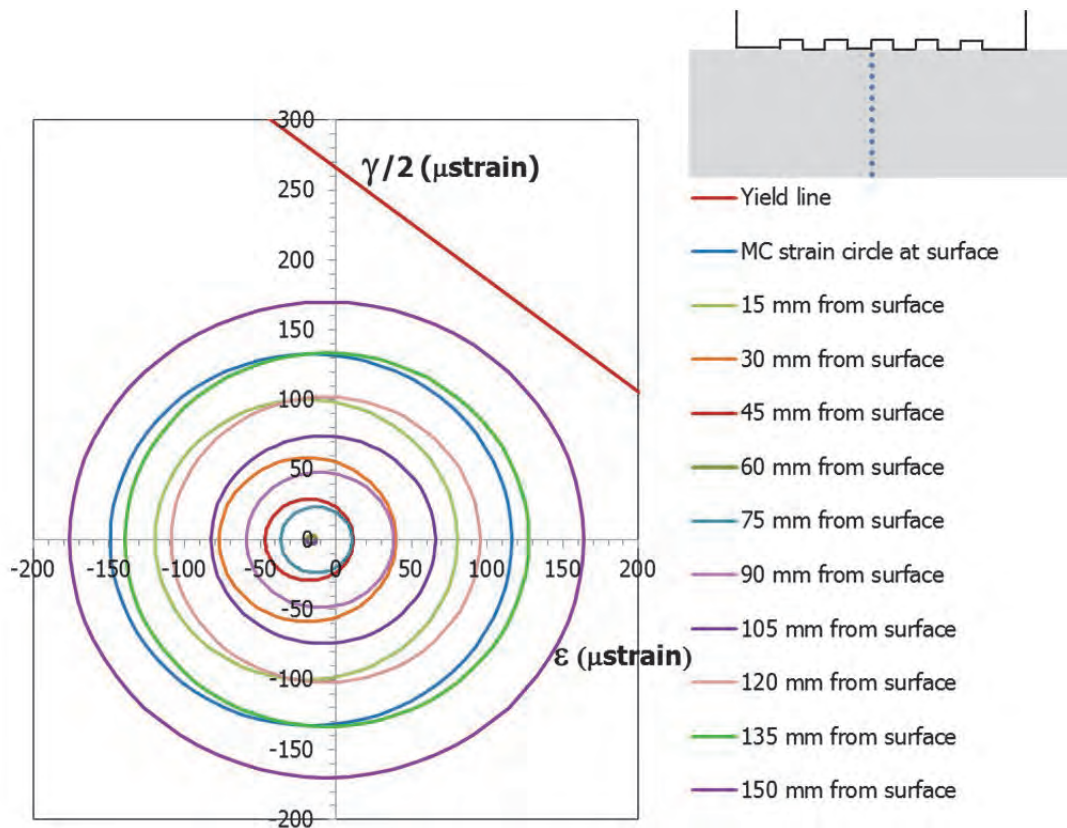
Figure. 7.15. Strain based MC circles over the height of the pavement (center)

Table 7.6. Recapitulation of the strain over the height of asphalt pavement under the edge of the tire (µstrain)

From surface (mm)	εprincipal (ε max)	ε mid	εprincipal (ε min)	ε_{xx}	ε_{yy}	ε_{zz}	ε_{xy}	ε_{xz}	ε_{yz}	Center	Radius
0	84	-118	-121	-112	77	-121	-72	0	1	-19	103
15	77	-90	-96	-61	48	-96	-124	0	0	-9	86
30	64	-68	-79	-46	30	-68	-121	0	0	-8	71
45	57	-42	-73	-29	13	-42	-123	0	0	-8	65
60	54	-17	-71	-13	-4	-17	-124	0	0	-9	62
75	53	7	-71	4	-22	7	-121	0	0	-9	62
90	55	31	-74	21	-41	31	-113	0	0	-10	65
105	59	56	-80	39	-60	56	-98	0	0	-10	70
120	81	68	-91	58	-81	81	-76	0	0	-5	86
135	109	80	-107	77	-105	109	-46	0	0	1	108
150	139	98	-131	98	-131	139	-4	0	0	4	135
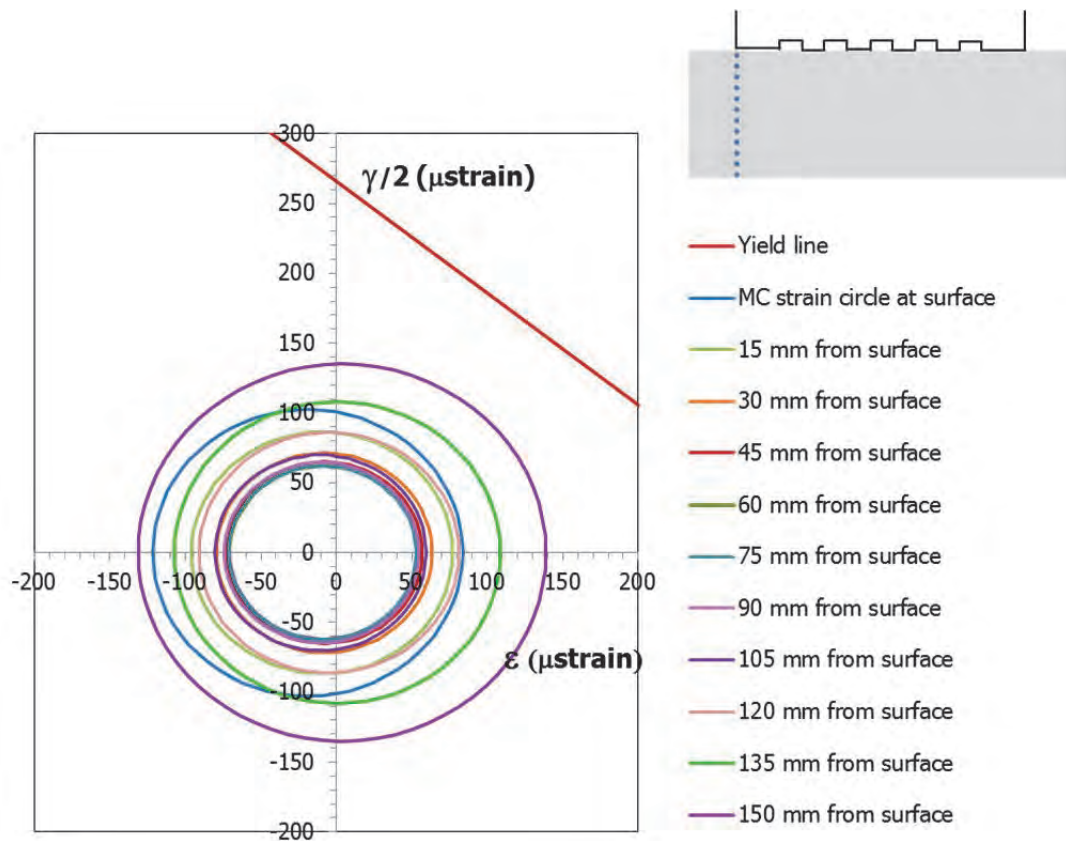
Figure. 7.16. Strain based MC circle over the height of the pavement (under the edge of tire)

The principal tensile strain changes over the height of the asphalt pavement. For the 150 mm thick asphalt layer used in this simulation, the tensile strain value is high at the surface, decreases over the height and then increases again and reaches its maximum value at the bottom of the asphalt pavement. These values will be dependent on the stiffness modulus, a lower stiffness will result in higher strain values. Although not taken into account in this analysis the stiffness will most probably also vary over the height of the asphalt pavement thickness due to temperature and other climatic influences as well as differences in compaction.

The stress based analysis could not explain the top-down cracking phenomenon. However, the initiation of the surface cracking might be explained using the strain based approach.

The analysis of the principal strain presented above shows that significant tensile strain values do occur at the surface and moderate values at the near surface. Although the principal strain values at the surface are somewhat lower than at the bottom, these values are considered significant enough to induce surface fatigue cracking.

7.4.3. Stress and strain based MC circles obtained from the simulation of pavement response at a high temperature

The need to perform simulations at high temperature is twofold. Firstly it was considered necessary to study the effect of a lower stiffness on the principal tensile strains and secondly, to gain insight how surface cracking might develop in an asphalt pavement in a tropical country. The daily temperature in a tropical country like Indonesia, is between 22°C to 33°C whereas the pavement surface temperature is between 29°C to 43°C [10]. Therefore it was decided to do the simulation at 40°C.

The Prony elements needed for a good fit of the master curve at the reference temperature of 40°C are shown in Table 7.7.

Table 7.7. Visco elastic material parameters (Prony coefficient) at 40°C

S_0:	18897	MPa
ν:	0.35	
i	τ_i (s)	α_i
1	1.884E-05	0.177
2	8.755E-05	0.061
3	1.461E-04	0.182
4	4.069E-04	0.071
5	6.7898E-04	0.150
6	1.891E-03	0.120
7	5.266E-03	0.098
8	8.787E-03	0.010
9	2.447E-02	0.086

The results of the simulation at 40°C are presented adjacent to the results from the previous simulation at 5°C, both at the surface and at the bottom of the asphalt layer. Figure 7.17 shows principal stress results and Figure 7.18 shows the principal strain results. The figures also show the position of the rib and the groove of the tyre.

Figures 7.17.a and b show the maximum and the minimum principal stress at the surface and at the bottom respectively. The plots show that only compressive stresses occur at the pavement surface. Meanwhile the plot of the stress conditions occurring at the bottom of the asphalt layer show the occurrence of a tensile principal stress. High absolute values of compressive stress at the surface and tensile stress at the bottom are indicated at the temperature of 5°C. According to these stress conditions, cracks will not initiate at the surface but at the bottom of the asphalt layer. If the effects of lateral wander and overloaded/underinflated wheel loads are neglected, the bottom up cracking will initiate under the centre of the tyre at the bottom of the asphalt layer.

The principal strains at the surface and at the bottom of the asphalt layer are shown in Figure 7.18.a and b. The plots show high tensile strains both at the surface and at the bottom. The principal strain value increases with increasing temperature. Although the tensile strain at the surface is lower than the value at the bottom, it is high enough to induce surface fatigue cracking.
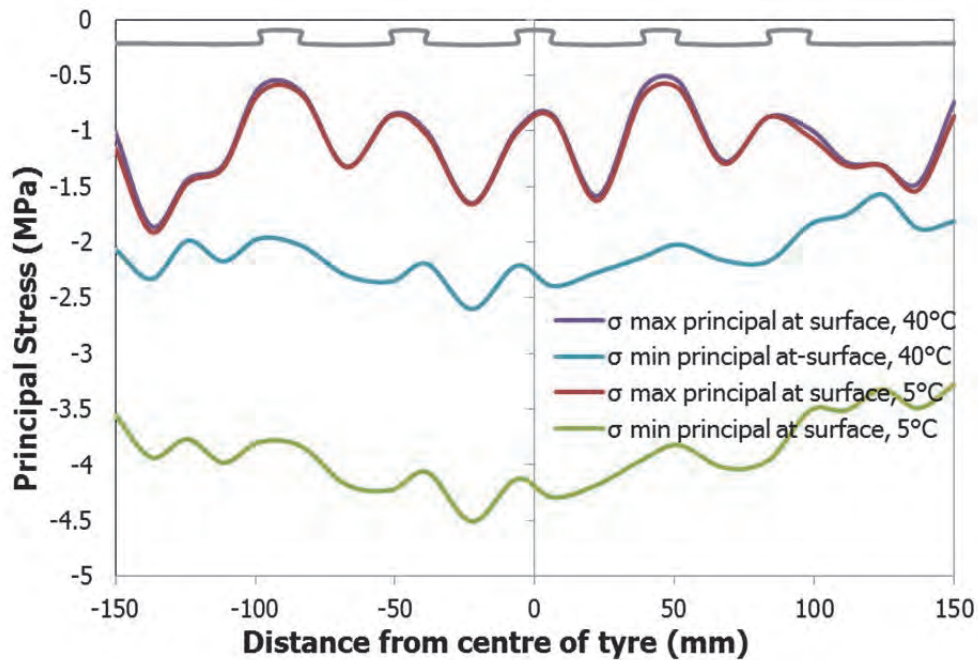
Figure 7.17.a. The principal stress at the surface of Lintrack Section I from the FEM simulation at 5°C and 40°C
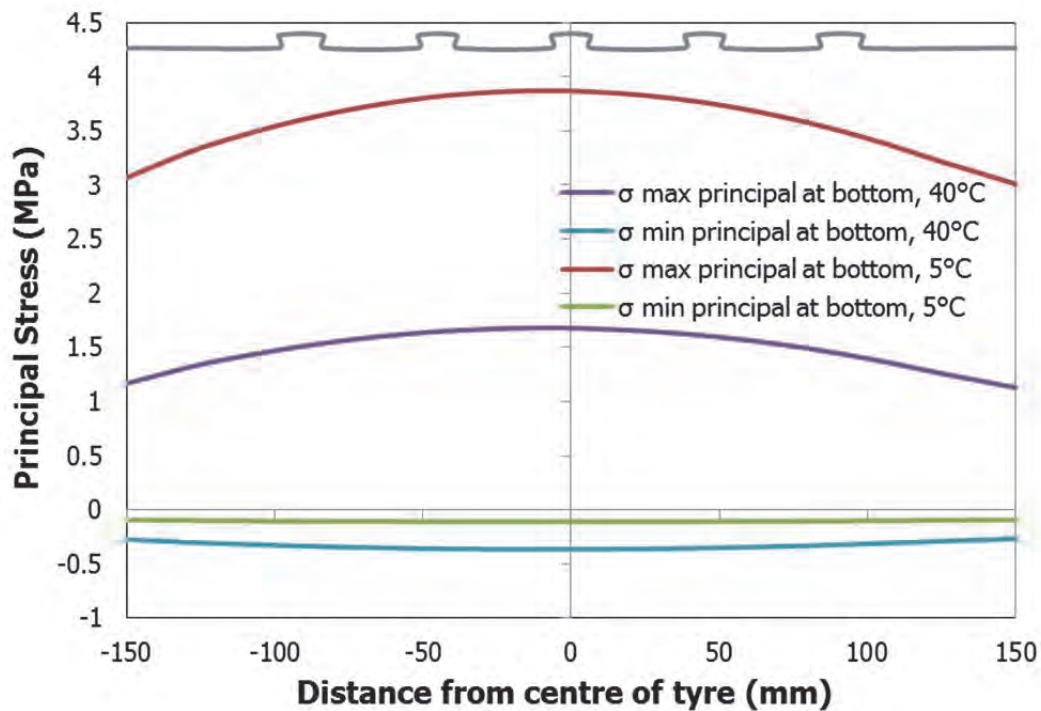
Figure 7.17.b. The principal stress at the bottom of Lintrack Section I from the FEM simulation at 5°C and 40°C

As can be seen in Figure 7.18.a, the highest principal tensile strain at the temperature of 40°C occurs under the edge of the middle rib of the tyre. This figure also shows for some points the direction of the critical principal strains (see the insertion).
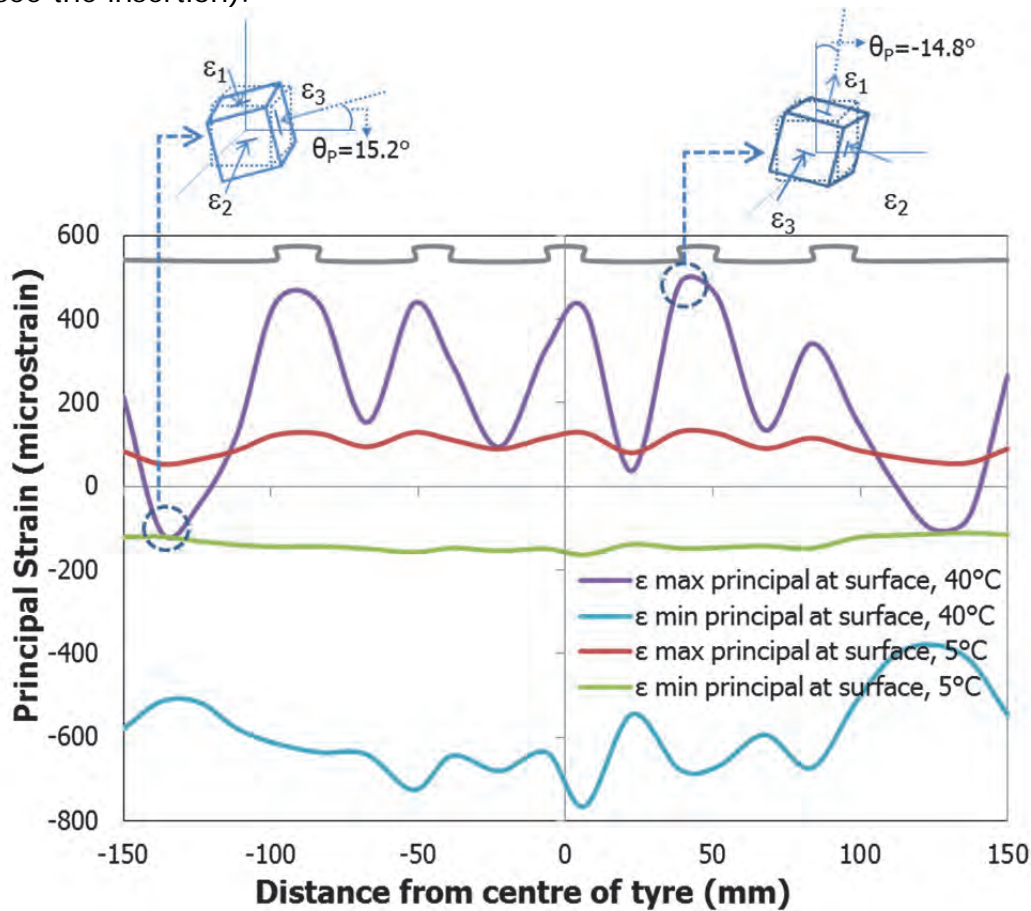
Figure 7.18.a. Principal strain at the surface of Lintrack Section I obtained from the FEM simulations at 5°C and 40°C

Table 7.9 and 7.10 shows the recapitulation of the strain at the surface at temperatures of 5°C and 40°C respectively. The values presented in these tables are the strain values at the nodes along the axis of symmetry of the contact pressure (The axis of symmetry is illustrated in Figure 7.4). Column 1 of both Table 7.9 and 7.10 represents the distance from the centre line of the tyre. Figure 7.18.a has been developed based on column 2 and 4 of these two tables.

Table 7.9. Recapitulation of the strain at the surface at 5°C (μstrain)

Distance from centre of tyre	ε principal (ε max)	$\boldsymbol{\varepsilon}$ max abs	ε principal (ε min)	ε_{xx}	ε_{yy}	ε_{zz}	ε_{xy}	ε_{xz}	ε_{yz}
-150	84	-121	-121	-112	77	-121	-72	0	1
-137.125	53	-120	-120	-118	52	-119	-23	0	-1
-124.25	65	-131	-131	-96	65	-131	15	-1	-2
-111.375	87	-140	-140	-118	86	-140	25	0	2

Table 7.9. Recapitulation of the strain at the surface at 5°C (μstrain) (cont)

Distance	ε principal (ε max)	ε max abs	ε principal (ε min)	ε_{xx}	ε_{yy}	ε_{zz}	ε_{xy}	ε_{xz}	ε_{yz}
-98.5	123	-144	-144	-129	120	-144	56	1	-5
-83.5	126	-144	-144	-142	125	-140	-37	0	4
-67.5	95	-149	-149	-124	95	-149	4	0	1
-51.5	129	-158	-158	-157	128	-145	31	1	-4
-38.5	111	-147	-147	-146	109	-135	-40	0	4
-22.5	89	-154	-154	-154	89	-133	-4	0	-1
-6.5	116	-149	-149	-140	115	-149	37	0	-4
6.5	128	-163	-163	-162	127	-139	-36	0	3
22.5	80	-138	-138	-128	79	-138	-23	-1	2
38.5	130	-148	-148	-143	126	-145	69	0	-8
51.5	127	-147	-147	-143	123	-134	-65	0	7
67.5	91	-143	-143	-119	90	-143	18	0	-2
83.5	115	-148	-148	-148	115	-130	1	1	-1
98.5	87	-122	-122	-120	85	-117	-47	0	1
111.375	71	-117	-117	-109	70	-117	-22	-1	-1
124.25	58	-114	-114	-89	58	-114	1	-1	-1
137.125	57	-111	-111	-105	55	-111	26	-1	-1
150	90	-116	-116	-107	83	-116	72	0	-1

Table 7.10. Recapitulation of the strain at the surface at 40°C (μstrain)

| Distance from centre of tyre	ε principal (ε max)	ε max abs	ε principal (ε min)	ε_{xx}	ε_{yy}	ε_{zz}	ε_{xy}	ε_{xz}	ε_{yz}
-150	213	-579	-579	-441	75	-448	-601	-1	10
-137.125	-111	-514	-514	-474	-151	-417	-189	1	-8
-124.25	-42	-516	-516	-272	-59	-516	123	-12	-19
-111.375	127	-580	-580	-434	108	-580	207	-3	15
-98.5	438	-614	-614	-520	380	-612	470	6	-40
-83.5	436	-636	-636	-612	412	-570	-305	1	36
-67.5	153	-641	-641	-443	149	-641	32	-4	6
-51.5	437	-726	-726	-711	422	-606	259	4	-30
-38.5	292	-644	-644	-612	260	-516	-335	1	31
-22.5	94	-680	-680	-673	86	-500	-36	-3	-8
-6.5	330	-636	-636	-557	303	-635	305	0	-37
6.5	424	-765	-765	-745	404	-547	-298	2	27
22.5	37	-545	-545	-464	6	-544	-196	-5	13
38.5	482	-676	-676	-598	405	-606	572	3	-69
51.5	453	-671	-671	-600	382	-515	-541	-1	58
67.5	135	-594	-594	-417	118	-593	152	-2	-16
83.5	342	-673	-673	-673	342	-494	8	5	-11
98.5	162	-516	-516	-453	99	-391	-393	2	5
111.375	9	-406	-406	-381	-13	-398	-183	-4	-12
124.25	-102	-379	-379	-228	-102	-378	3	-10	-5
137.125	-70	-416	-416	-374	-112	-358	217	-4	-9
150	264	-546	-546	-414	132	-408	598	4	-10
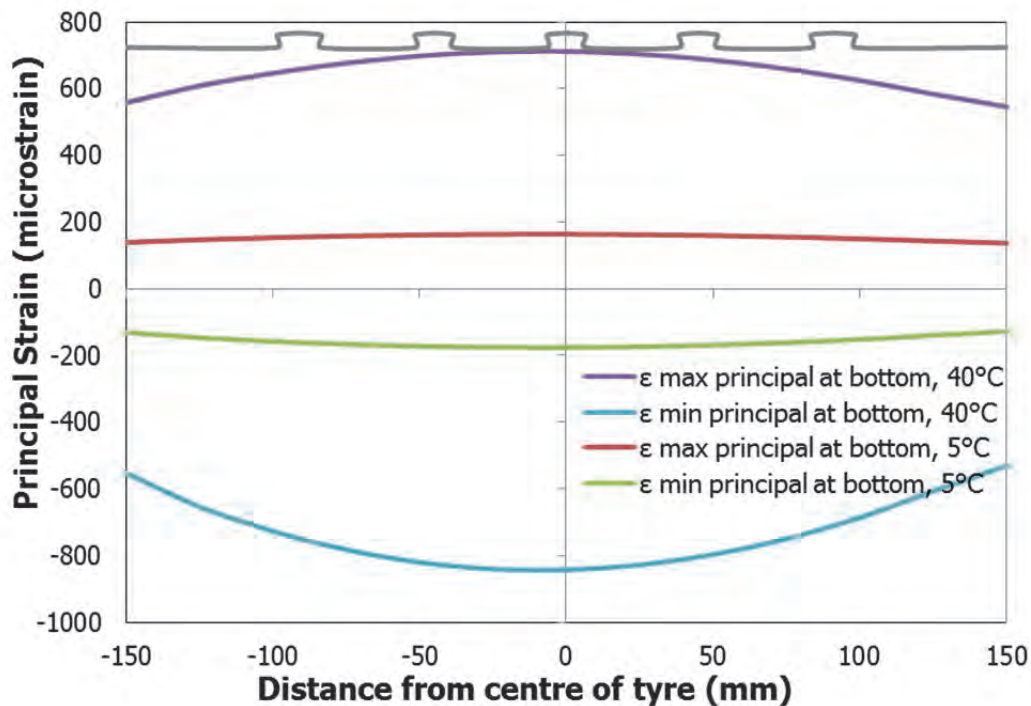
Figure 7.18.b. Principal strains at the bottom of Lintrack Section I obtained from the FEM simulations at 5°C and 40°C

The simulation results indicate that the principal strain at high temperature can be used to explain surface cracking occurring at high pavement temperatures.

7.5. Development of stress and strain over time

Because some researchers (e.g Gerritsen e.a. [11]) stated that residual stresses also might contribute to the development of surface cracking, the development of these residual stresses was analysed by applying four load repetitions to the pavement structure. The simulation results for these four loading cycles are shown in Figure 7.19 to 7.20. These figures show the maximum principal stress and strain response to the wheel load under the centre of the wheel load at the top and bottom of the asphalt pavement.

Due to the time-dependent viscoelastic nature of the GAC materials, it can be expected that as a result of the cyclic loading, residual stresses will develop. Figure 7.19b shows that at the higher temperature the residual stress is higher than the residual stress at the lower temperature. These residual stresses develop but then reduce to 0 because of relaxation.
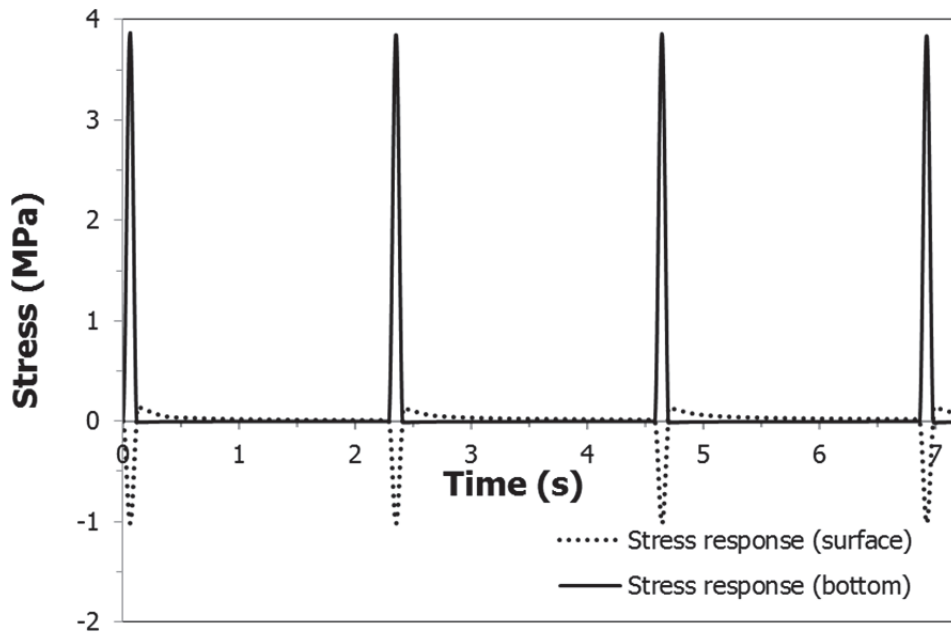
Figure 7.19.a. Development of the max principal stress over time for 4 loading cycles (at the surface and at the bottom of asphalt pavement) at 5°C
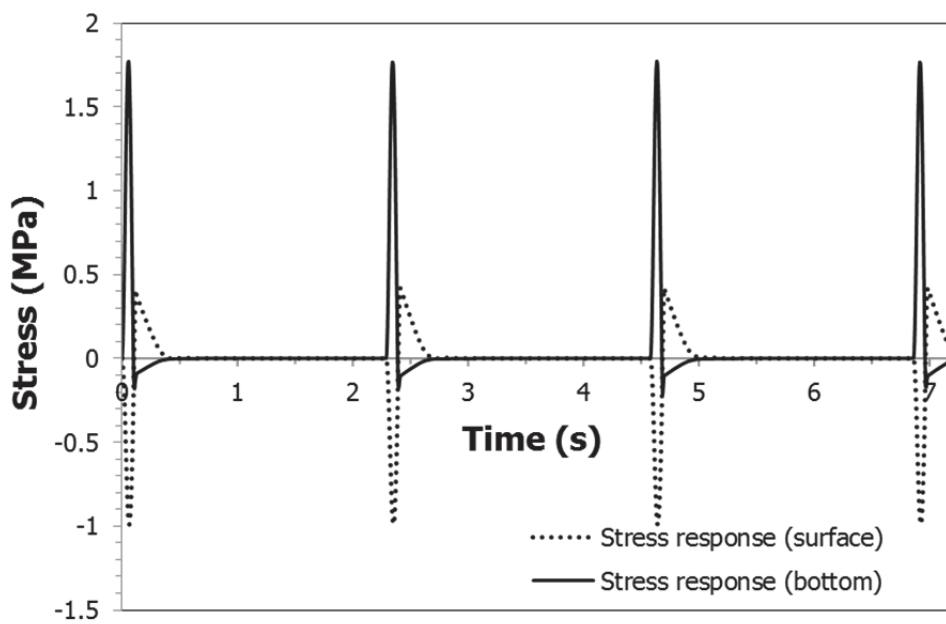
Figure 7.19.b. Development of the max principal stress over time for 4 loading cycles at the surface and at the bottom of asphalt pavement at 40°C
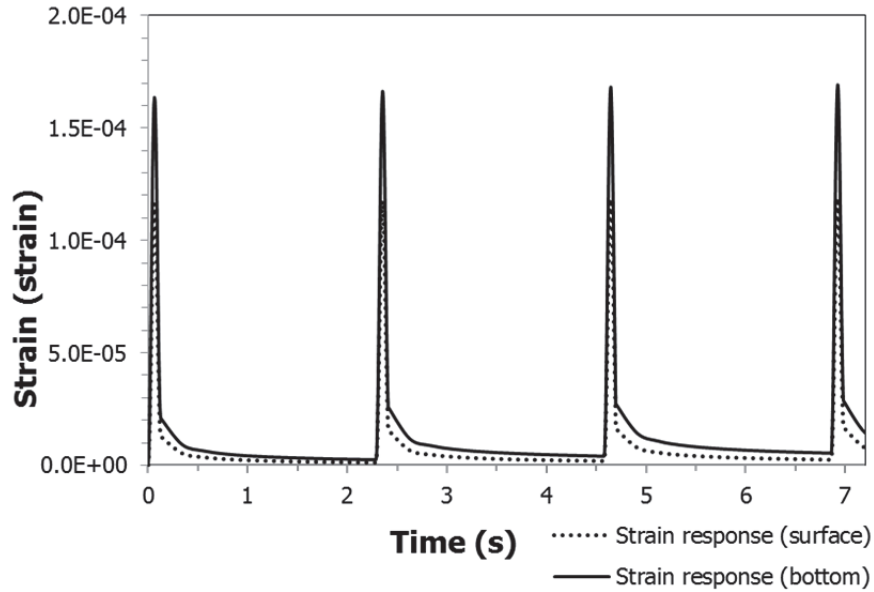
Figure 7.20.a. Development of the max principal strain over time for 4 loading cycles at 5°C
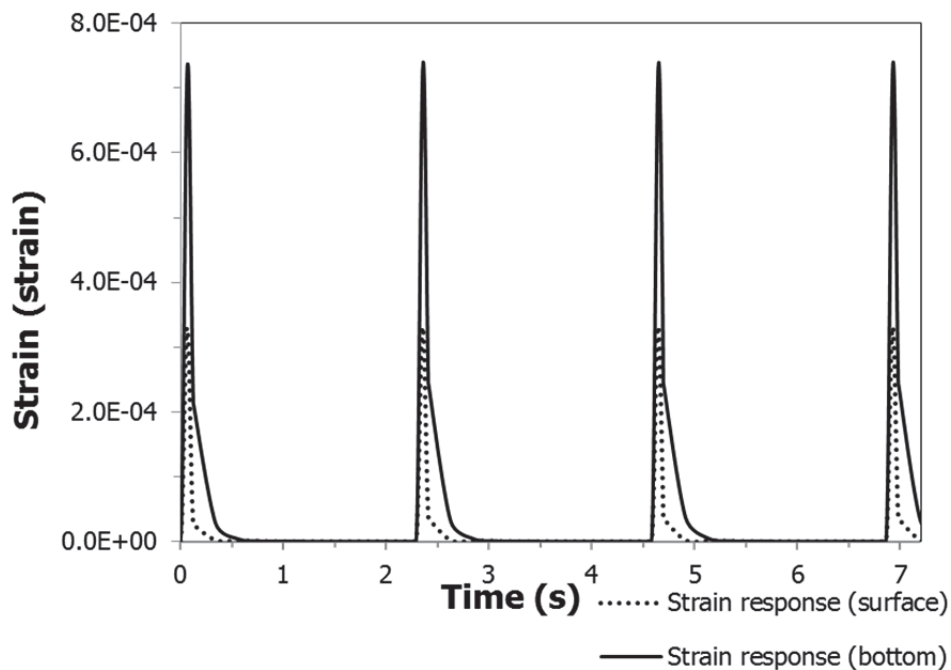
Figure 7.20.**b.** Development of the max principal strain over time for 4 loading cycles at 40°C

Figure 7.20.a shows that at 5°C temperature some delayed strain occurs at the end of each loading cycle. However, this delayed strain can hardly be observed in the 40°C simulation.

These results indicate that crack development at the pavement surface due to residual stresses will not occur for the conditions (temperature and loading time) assumed in the simulations.

7.6.   Number of load repetitions to failure, relating BOEF and FEM results

In chapter 6, lifetime analyses have been made based on the tensile strain which occurs at the bottom of the asphalt layer. The fatigue relationship needed for these analyses were based on BOEF fatigue tests. In this section the stress and strain conditions at the pavement surface and at the bottom of the asphalt layer were analysed using MC circles. In order to complete the picture it was decided to show in this section how MC circles can be used for pavement fatigue analyses.

Each of the MC circles shown in Figure 7.13 can be used to predict the number of load repetitions to failure by using the results obtained from the BOEF test. Figure 7.21 shows the MC circles of the GAC BOEF fatigue tests at 5°C and 8 Hz in the σ-τ space as well as the failure line. Through each MC circle, a line which is parallel to the failure line was drawn. These lines, which are shown in Figure 7.21 as dashed lined, can be seen as a representation of the number of load repetitions to failure at a certain combination of normal and shear stresses.
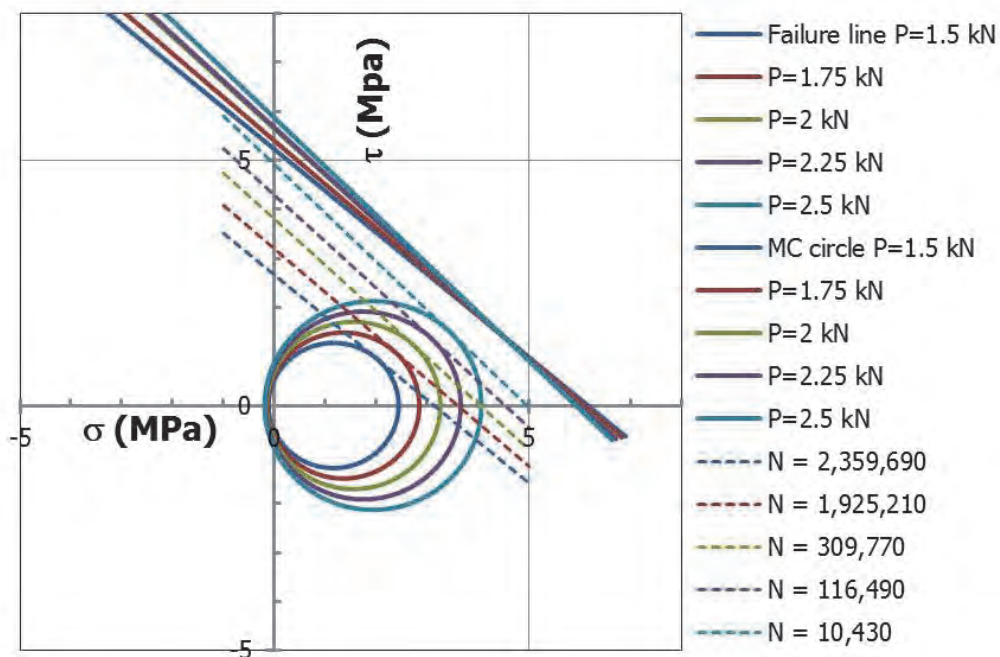
Figure 7.21.Failure line, MC circle and related number of load repetition to failure of GAC BOEF test at 5°C and 8 Hz

The general expression of the failure line relationship is expressed in Equation 7.5. Meanwhile the general expression of the lines touching the circles and parallel to the failure line of the BOEF tests at different load levels is presented in Equation 7.11. Each stress circle is representing a number of load repetitions. The bigger the circle the less load repetitions can be taken and vice versa.

$$\tau = c' - \sigma \tan\varphi \qquad (7.11)$$

Figure 7.22 illustrates the relation between the tangent line and the failure line. Delta is the ratio of the distance of the tangent line to the origin (a) to the distance of the failure line to the origin (b). The relation is presented in Equation 7.12.
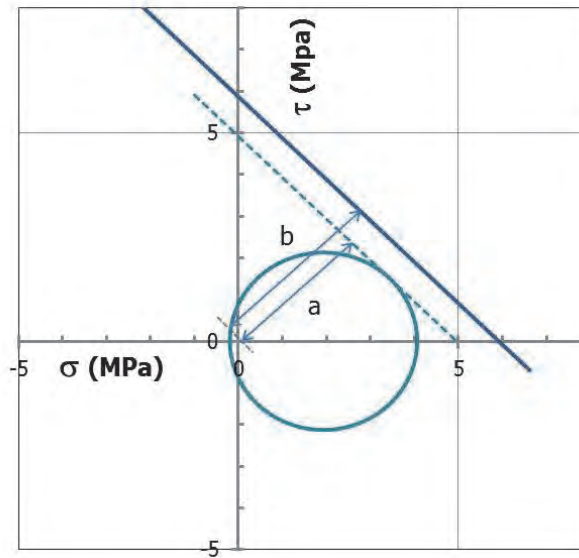
Figure 7.22.Failure line and tangent lines to the MC circles of the GAC BOEF test at 5°C and 8 Hz

$$\Delta = \frac{a}{b} \qquad (7.12)$$

In Table 7.11 the c, $\tan\varphi$ and c' parameters, are presented, as well as Δ. Furthermore, a relation between Δ and N was developed which is shown in Figure 7.23.

Table 7.11. Parameters of the failure line and tangent lines and number of load repetitions to failure of the BOEF tests performed at 5°C - 8Hz

P	N	f_c	f_t	Failure line c	$\tan\varphi$	Tangent line c'	Distance from (0;0) b	a	Δ
kN	cycles	MPa	MPa	MPa		MPa			a/b
1.5	2,359,690	-22.59	4.83	5.23	-0.850	2.66	3.98	2.03	0.51
1.75	1,925,210	-24.02	4.85	5.40	-0.888	3.19	4.04	2.39	0.59
2	309,770	-26.10	4.87	5.64	-0.941	3.80	4.11	2.77	0.67
2.25	116,490	-26.39	4.88	5.67	-0.948	4.29	4.12	3.11	0.76
2.5	10,430	-28.14	4.89	5.86	-0.991	4.91	4.17	3.49	0.84
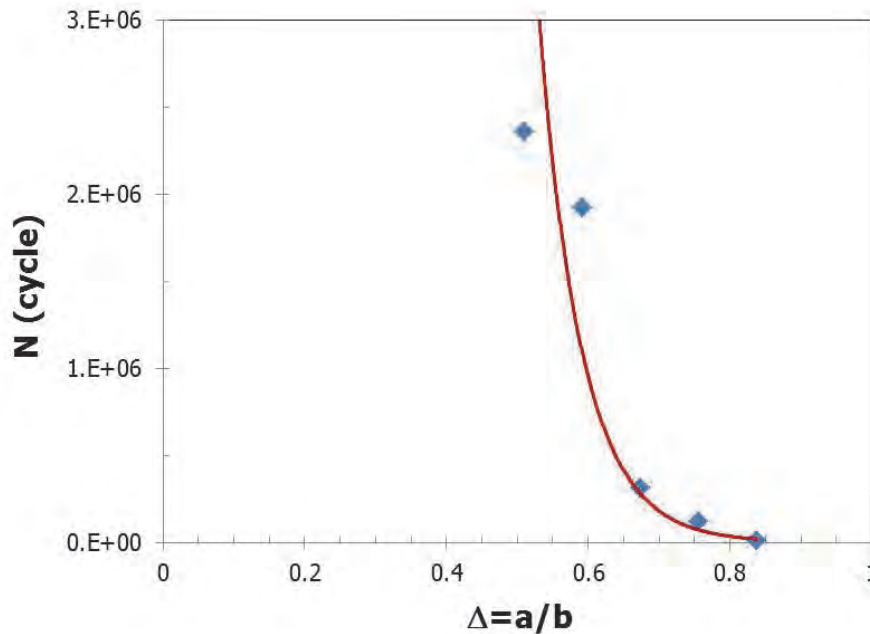
Figure 7.23. Relation between Δ and number of load repetition to failure (N)

Equation 7.13 was derived based on Figure 7.23 and was subsequently used to determine the number of load repetitions to failure at the bottom of Lintrack section I; the results are represented in Table 7.12.

$$N = 2.0087E + 10 \cdot e^{-16.596\Delta}$$
$$R^2 = 0.94$$

(7.13)

Table 7.12. Number of cycles to failure

Node number	Distance from surface	c	tanφ	c'	b	A	Δ	N
	(mm)						a/b	cycle
295	150	4.99	-0.801	4.25	3.90	3.32	0.85	14,810

Table 7.12 shows that failure at the bottom of the asphalt layer occurs when the number of load repetitions is approximately 1.4×10^4 cycles. This number should still be corrected for the effect of lateral wander.

It will be clear that, given the size and position of the MC circles in the MC space, similar analyses were not performed for the locations at and near the surface of the pavement.

It will also be clear that a similar analysis could have been made using the strain based MC circles.

7.7. Conclusions

A finite element simulation has been performed on the Lintrack section I pavement. The tire load was represented by a non-uniform tyre contact stresses distribution. The influence of tire contact stresses on crack development at the surface was analyzed at two different temperature conditions being 5°C and 40°C.

The simulations, in which the actual contact pressure distribution applied during the Lintrack tests was used, showed that significant tensile strains develop at the pavement surface. Although they were somewhat lower than the tensile strains occurring at the bottom of the asphalt layer, they are considered to be high enough to be responsible for surface fatigue cracking both at low and high temperatures.
It should be noted that the occurrence of surface cracking could not be explained by means of a stress based analysis.

A general expression of the number of load repetitions to failure for the Gravel Asphalt Concrete mixture at 5°C has been developed as a function of the ratio between the distance of the MC circle to the origin and the distance of the failure line to the origin. This model enables the determination of the fatigue life of the GAC material at a certain state of stress.

7.8. References

[1]   J. Groenendijk, "Accelerated Testing and surface cracking of asphaltic concrete pavements," PhD, Delft University of Technology, Delft The Netherlands, 1998.

[2]   J.R. Hondros, "The Evaluation of Poisson's Ratio and the Modulus of Materials of a Low Tensile Resistance by the Brazilian (Indirect Tension) Test with Particular Reference to Concrete," *Austrian Journal of Applied Science,* vol. 10, pp. 243-268, 1959.

[3]   A. Scarpas, "CAPA-3D Finite Elements System User's Manual, Parts I, II and III, ," Department of Structural Mechanics, Faculty of Civil Engineering, Delft University of Technology, Delft, The Netherlands, 1992.

[4]   ABAQUS inc, "ABAQUS User's Manual Version 6.6. ," ed: Pawtucket, RI, 2006.

[5]   M. De Beer, J. W. Maina, Y. van Rensburg, and J. M. Greben, "Toward Using Tire-Road Contact Stresses in Pavement Design and Analysis," *Tire Science And Technology,* vol. 40, pp. 246-271, 2012.

[6]   M. De Beer, C. Fisher, Y. Van Rensburg, J. Greben, and J. Maina, "Framework for Tyre Contact Stress Information System (T-CSIS): Project A-1," *Report: SANRAL/SAPDM/A-1/2010-003, Revision of the South African Pavement Design Method. Project Focus Area: Traffic Demand Analysis, Version: 3rd Draft Report (unpublished),* 2011.

[7]   M. Woldekidan, M. Huurman, and A. Pronk, "Linear and Nonlinear Viscoelastic Analysis of Bituminous Mortar," *Transportation Research Record: Journal of the Transportation Research Board,* vol. 2370, pp. 53-62, 12/01/ 2013.

[8]   J. Qiu, M.F.C. van de Ven, E. Schlangen, A.A.A. Molenaar, and S. Wu, "Cracking and Healing Modelling of Asphalt Mixtures," in *7th RILEM International Conference on Cracking in Pavements*, 2012.

[9]   H. Wang, H. Ozer, I. Al-Qadi, and C. Duarte, "Analysis of Near-Surface Cracking under Critical Loading Conditions Using Uncracked and Cracked Pavement Models," *Journal of Transportation Engineering,* vol. 139, pp. 992-1000, 2013.

[10]   Suwardo, "Investigation of Skid Resistance of Road Pavement Using the Wessex Skid Tester (In Bahasa Indonesia)," *Media Teknik UGM,* vol. 27, 2005.

[11]   A.H. Gerritsen, C.A.P.M. van Gurp, J.P.J. M. van der Heide, A.A.A. Molenaar, and A.C. Pronk, "Prediction and Prevention of Surface Cracking in Asphaltic Pavement," in *International Conference on the Structural Design of Asphalt Pavement*, Ann Arbor, MI, USA, 1988, pp. 378-391.

Chapter 8
Conclusions and recommendations

8.1   Introduction

The main goal of the study was to determine a relationships between the fatigue life predicted for 3 Lintrack sections that were tested in the 1990's and the fatigue life observed on these sections; this is elaborated in Chapter 6. In an attempt to explain surface cracking a finite element simulation on Lintrack section I was performed; this is presented in Chapter 7. All necessary material data were obtained on a copy of the Lintrack mixture (GAC 1990), called mixture GAC 2010. The tests performed and results obtained are presented in Chapter 4. Furthermore, the strength, stiffness and fatigue resistance of the GAC mixture modified with RETONA is described in Chapter 5.

This chapter presents the general conclusions and recommendations resulting from the entire research program. The detailed conclusions at the various stages of the research were presented at the end of each chapter.

8.2   General conclusions

- It has been shown that it is very difficult to relate cracking visible at the surface of the pavement to fatigue damage that has been calculated to initiate at the bottom of the asphalt layer. To a large extent this is due to the fact that cracking which is visible at the pavement surface is top-down cracking, which cannot be explained by means of the afore mentioned analysis.
- In relation to the previous conclusion it is, furthermore, concluded that it was impossible to solve the problem of matching theory to practice by using results that have been obtained elsewhere because of different and sometimes weak definitions of "end of pavement life".
- It has been shown that the pavement life based on reduction of the asphalt stiffness is longer than the pavement life calculated on the basis of damage initiation at the bottom of the asphalt layer. It is clear that crack/damage principles need to be applied to explain the difference between both lifetimes.
- It has been shown that it is not useful to base thickness design predictions on fatigue relationships developed by means of the 4PB test. The BOEF test is to be preferred for those purposes.

- In pavement design analyses quite often a factor that takes into account the healing of asphalt mixtures during rest periods is considered. This research, however, has shown that healing in terms of stiffness does occur until a certain amount of damage has been reached, but that healing in terms of fatigue strength is not likely to occur. It is, therefore, concluded that it is not wise to take into account healing of fatigue characteristics of asphalt mixtures in design analyses.
- The existence of an endurance fatigue limit has been shown. This limit should be used when designing "long life" or "perpetual" pavements.
- It has been shown that permanent deformation (in this study this was permanent deformation of the subgrade) can have a large effect on the formation of longitudinal cracks at the edges of the wheel paths.
- Finite element simulations using detailed tyre–pavement contact pressure modelling have shown that significant tensile strains do develop at the pavement surface as a result of the applied wheel load. This tensile strain at the pavement surface is of such a magnitude that it will most probably initiate fatigue cracking at the pavement surface. It should be noted however that a stress based analysis doesn't result in the same conclusion.
- This research has shown that modifying GAC type mixtures with Retona results in mixtures with an increased fatigue and permanent deformation resistance for climatic conditions prevailing in Indonesia.

8.3 Recommendations

The fatigue lifetime predictions were based on assuming linear elastic behavior of the pavement materials and assuming that Miner's law is the correct way to calculate the damage accumulation due to traffic loads of different magnitude. Furthermore, only the number of load repetitions to crack initiation could be calculated. Based on these shortcomings the following recommendations are made.

- Making pavement life predictions using advanced models is the way to go and their development is, therefore, highly recommended. Such models should take into account crack initiation, crack propagation, stress redistribution because of damage development, etc.
- Surface cracking should be analyzed using these advanced models and by taking into account, where applicable, effects of aging, moisture, frost, etc.
- It is, furthermore, recommended to re-analyze the applicability of Miner's law for making predictions on fatigue performance as result of a wide wheel load spectrum.
- It is strongly recommended to further develop the BOEF test and laboratory wheel tracking tests since they allow realistic fatigue performance studies to be made including investigations on healing, effects of moisture, etc.

- With respect to Retona it is strongly recommended to study the effect of modifying mixtures with higher amounts of Retona 35 and or Retona types that contain a higher percentage of bitumen.

This page is intentionally left blank

About the author

Florentina Pungky Pramesti was born in Madiun, Indonesia. Pungky graduated from Universitas Brawijaya, Malang, in 1997 with a BSc in Civil Engineering after presenting her final project on '*Improvement of peat soils bearing capacity with geotextile*'. She won a scholarship to continue her study and received her master degree in 2001 from Institut Teknologi Bandung (ITB) where she defended her research in '*Management of highway*'.

Then, she joined the Civil Engineering Department, UNS, Indonesia. As a lecturer she taught and conducted research in transport and traffic engineering. She conducted consultancy to several engineering projects and served the community by offering her professional expertise.

In 2010, she joined the Road and Railway Engineering Section in the Faculty of Civil Engineering and Geosciences of Delft University of Technology after she won a scholarship from the Directorate General of Higher Education, Ministry of National Education, the Government of Republic of Indonesia and joined Section of Materials and Environment. Under supervision of Prof. Molenaar and Ass. Prof. van de Ven, she investigated the fatigue of asphalt pavements. She studied the results of accelerated tests which were performed in the 1990's on three pavement sections by means of the full scale testing facility called Lintrack. She reconstructed the asphalt mixture that was used in those tests for fatigue and other tests. From these lab tests she attempted to match fatigue lifetime predictions and observations. She also conducted research on the modification of the Gravel Asphalt Concrete used in the Lintrack (GAC 1990) with Asbuton – a natural rock-like bitumen available in Indonesia- to find out the benefits of using Retona.

She is married to Senot Sangadji and they have a boy, Quanta A. Sangadji. She enjoys singing in the choir, cooking, and spending quality time with her family and friends.

Publications:

1. **F.P. Pramesti**, A.A.A. Molenaar and M.F.C. van de Ven, *The Prediction Of Fatigue Life Based On Four Point Bending Test*, 2nd International Conference on rehabilitation and Maintenance in Civil Engineering, 8 - 10 March 2012, Solo, Indonesia.
2. **F.P. Pramesti**, A.A.A. Molenaar and M.F.C. van de Ven, *Fatigue Cracking of Gravel Asphalt Concrete; Cumulative Damage Determination*, 7th RILEM 2012 International Conference on Cracking in Pavements, 20 - 22 June 2012, Delft, The Netherlands.
3. **F.P. Pramesti**, A.A.A. Molenaar and M.R. Poot, *Effects of modifying Bitumen with Asbuton on the Mechanical Characteristics of Asphalt Mixtures*, 15th Australian Asphalt Pavement Association 2013, International Flexible Pavements Conference, Brisbane Australia, 22-25 September 2013.
4. **F.P. Pramesti**, A.A.A. Molenaar, M.F.C. van de Ven, J. Qiu, and M.F. Woldekidan, *Comparison of Two Beam Fatigue tests*, 4th International Conference on Asphalt Materials, Guangzhou, China, 6-8 November 2013,
5. A.A.A. Molenaar, N. Li, and **F.P. Pramesti**, *Fatigue Characterization of Asphalt Mixtures for Designing Long Life Pavements*, 15th Australian Asphalt Pavement Association 2013, Internationale Flexible Pavements Conference, Brisbane Australia, 22-25 September 2013.
6. A.A.A. Molenaar, **F.P. Pramesti**, and N. Li, *Bridging the Gap between Laboratory Fatigue and Field Performance*, 14th Road Engineering Association of Asia & Australia (REAAA) Conference, Kuala Lumpur-Malaysia, 26-28 March 2013.
7. Qiu. J, Li. Ning, **F.P. Pramesti**, A.A.A. Molenaar and M.F.C. van de Ven, *Evaluating laboratory Compaction of Asphalt Mixtures using the shear Box Compactor*, Vol 40. Issue 12, Journal of Testing and Evaluation, ASTM, 2012.
8. **F.P. Pramesti**, A.A.A. Molenaar, M.F.C. van de Ven, J. Qiu, and M.F. Woldekidan, *Comparison of Two Beam Fatigue tests*, Vol 42. Issue 5, Journal of Testing and Evaluation, ASTM, 2014.

Duc in altum

ABBREVIATIONS

4PB	:	Four Point Bending
AASTHO	:	American Association of State Highway and Transportation Officials
ABAQUS	:	A general purpose finite element program distributed by ABAQUS Ltd
ACRe	:	Asphalt Concerete Response
ANN	:	Artificial Neural Network
APT	:	Accelerated Pavement Testing
ASBUTON	:	Asphalt Buton
ATR	:	Attenuated Total Reflectance
BISAR	:	Bitumen Stress Analysis in Roads computer program
BOEF	:	Beam on Elastic Foundation
CAPA	:	Computer Aided Pavement Analysis
CIRCLY	:	CIRCular loads and LaYered system. A computer software for mechanistic pavement design and analysis defined by the AUSTROADS Guide to Pavement Technology.
CROW	:	*Centrum voor Regelgeving en Onderzoek in de Grond-, Water- en Wegenbouw en de Verkeerstechnie*k (Center for Regulatory and Research in Soil, Water and Road and Traffic Engineering)
CSIR	:	Council of Scientific & Industrial Research
DAC	:	Dense Asphalt Concrete
DL	:	Dynamic asphalt strain gauge in Longitudinal direction
DSR	:	Dynamic Shear Rheometer
DT	:	Dynamic asphalt strain gauge in Transversal direction
DTT	:	Direct Tension Test
DUT	:	Delft University of Technology
EME	:	*Enrobe a Module Eleve*
EMPA	:	*Eidgenössische Materialprüfungs- und Forschungsanstalt.* (Swiss Federal Laboratories for Materials Science and Technology)
FEM	:	Finite Element Modelling
FORCE	:	First OECD Road Common Experiment
FRS	:	Friction Reduction System
FTIR	:	Fourier Transform Infrared Spectroscopy
FWD	:	Falling Weight Deflection
GAC	:	Gravel Asphalt Concrete
HDM	:	Highway Design Manual
HISS	:	Hierarchical Single Surface
HS	:	Huet Sayegh
HVS	:	Heavy Vehicle Simulator
I	:	Name of Pavement test section of Lintrack
ITS	:	Indirect Tension Strength Test
ITT	:	Indirect Tension Test

KENLAYER	:	A computer software for pavement analysis and design
KNMI	:	*Koninklijk Netherlands Meteorologisch Instituut* (The Royal Dutch Meteorological Institute)
LDVT	:	Linear Variable Differential Transformer
Lintrack	:	Linear Tracking apparatus
MC	:	Mohr-Coulomb
MEPDG	:	Mechanistic-Empirical Pavement Design Guide
MHS	:	Modified Huet Sayegh
MISS	:	Moduli Information System Software. A computer software used for the backcalculation of the layer moduli.
MLS	:	Mobile Load Simulator
MMP	:	Mean Monthly Precipitation
MTS	:	Material Testing Systems
MUCT	:	Monotonic Uniaxial Compression Test
MUTT	:	Monotonic Uniaxial Tension Test
NCAT	:	National Center for Asphalt Technology
NEVUL	:	*NEderlandse vereniging van fabrikanten en importeurs van VULstof voor bitumineuze werken* (Branche organisation for filler)
OECD	:	Economic Co-operation and Development
PA	:	Phase Angle
PAC	:	Porous Asphalt Concrete
POM	:	Polyoxymethylene
RETONA	:	Refined Buton Asphalt
RHED	:	Road and Hydraulic Engineering Division
RRRL	:	Railroad Research Laboratory
SCB	:	Semi Circular Bending
SCW	:	*Studie Centrum Wegenbouw* (Study centre for road construction)
SF	:	Shift Factor
SHRP-NL	:	Strategic Highway Research Program for The Netherlands
SMA	:	Stone Mastic Asphalt
SPDM	:	The Shell Pavement Design Manual
SPDM	:	The Shell Pavement Design Manual
TxMLS	:	The Texas Mobil Load Simulator
UTC	:	Uniaxial Tension Compression Test
VA	:	Name of Pavement test section of Lintrack
VB	:	Name of Pavement test section of Lintrack
VEROAD	:	Viscoelastic Road Analysis Delft
VISCOROUTE	:	A software to evaluate the effects of moving loads on transport infrastructure made of materials with viscoelastic behavior
VRSPTA	:	Vehicle-Road Surface Pressure Transducer Array
WLF	:	William-Landel-Ferry
WTT	:	Wheel Tracking Test

TUDelft